

Advances in Optical Technologies

# Recent Advances in Semiconductor Surface-Emitting Lasers

Guest Editors: Krassimir Panajotov, Rainer Michalzik,  
and Kent D. Choquette





---

# **Recent Advances in Semiconductor Surface-Emitting Lasers**

Advances in Optical Technologies

---

## **Recent Advances in Semiconductor Surface-Emitting Lasers**

Guest Editors: Krassimir Panajotov, Rainer Michalzik,  
and Kent D. Choquette



---

Copyright © 2012 Hindawi Publishing Corporation. All rights reserved.

This is a special issue published in "Advances in Optical Technologies." All articles are open access articles distributed under the Creative Commons Attribution License, which permits unrestricted use, distribution, and reproduction in any medium, provided the original work is properly cited.

## Editorial Board

Mustafa A. G. Abushagur, USA  
Partha P. Banerjee, USA  
Ralph Barry Johnson, USA  
Augusto Belendez, Spain  
Steve Blair, USA  
Maria Luisa Calvo, Spain  
Pierre Chavel, France  
Zhongping Chen, USA  
Fu-Pen Chiang, USA  
Petr Eliseev, USA  
Michael A. Fiddy, USA  
Patti Gillespie, USA

Richard B. Hoover, USA  
Zoran Ikonc, UK  
Saulius Juodkasis, Australia  
Mark A. Kahan, USA  
Alexander A. Kaminskii, Russia  
Qiang Lin, China  
Liren Liu, China  
Qingming Luo, China  
Daniel Malacara, Mexico  
Mikhail Noginov, USA  
Ci-Ling Pan, Taiwan  
Markus Pessa, Finland

Giancarlo C. Righini, Italy  
Joseph Rosen, Israel  
Jos Lui's Santos, Portugal  
Colin J. R. Sheppard, Singapore  
Kiyoshi Shimamura, Japan  
Jagdish P. Singh, USA  
Yinglin Song, China  
Theo Tschudi, Germany  
Leonid P. Yaroslavsky, Israel  
Jianping Yin, China  
Yong Zhao, China

# Contents

**Recent Advances in Semiconductor Surface-Emitting Lasers**, Krassimir Panajotov, Rainer Michalzik, and Kent D. Choquette

Volume 2012, Article ID 234163, 2 pages

**Numerical Self-Consistent Analysis of VCSELs**, Robert Sarzała, Tomasz Czystanowski, Michał Wasiak, Maciej Dems, Łukasz Piskorski, Włodzimierz Nakwaski, and Krassimir Panajotov

Volume 2012, Article ID 689519, 17 pages

**Semiconductor Disk Lasers: Recent Advances in Generation of Yellow-Orange and Mid-IR Radiation**, Mircea Guina, Antti Härkönen, Ville-Markus Korpijärvi, Tomi Leinonen, and Soile Suomalainen

Volume 2012, Article ID 265010, 19 pages

**Spin-Controlled Vertical-Cavity Surface-Emitting Lasers**, Nils C. Gerhardt and Martin R. Hofmann

Volume 2012, Article ID 268949, 15 pages

**Single-Fiber Bidirectional Optical Data Links with Monolithic Transceiver Chips**, Alexander Kern, Sujoy Paul, Dietmar Wahl, Ahmed Al-Samaneh, and Rainer Michalzik

Volume 2012, Article ID 729731, 8 pages

**Advances in Red VCSEL Technology**, Klein Johnson, Mary Hibbs-Brenner, William Hogan, and Matthew Dummer

Volume 2012, Article ID 569379, 13 pages

**Single Mode Photonic Crystal Vertical Cavity Surface Emitting Lasers**, Kent D. Choquette, Dominic F. Siriani, Ansas M. Kasten, Meng Peun Tan, Joshua D. Sulkin, Paul O. Leisher, James J. Raftery Jr., and Aaron J. Danner

Volume 2012, Article ID 280920, 8 pages

**Collective Micro-Optics Technologies for VCSEL Photonic Integration**, V. Bardinal, T. Camps, B. Reig, D. Barat, E. Daran, and J. B. Doucet

Volume 2011, Article ID 609643, 11 pages

**Wafer-Fused Optically Pumped VECSELs Emitting in the 1310-nm and 1550-nm Wavebands**, A. Sirbu, N. Volet, A. Mereuta, J. Lyytikäinen, J. Rautiainen, O. Okhotnikov, J. Walczak, M. Wasiak, T. Czystanowski, A. Caliman, Q. Zhu, V. Iakovlev, and E. Kapon

Volume 2011, Article ID 209093, 8 pages

**Cavity Solitons in VCSEL Devices**, S. Barbay, R. Kuszelewicz, and J. R. Tredicce

Volume 2011, Article ID 628761, 23 pages

**Surface-Emitting Metal Nanocavity Lasers**, Martin T. Hill and Milan J. H. Marell

Volume 2011, Article ID 314952, 8 pages

**Nonlinear Dynamics of Vertical-Cavity Surface-Emitting Lasers**, Krassimir Panajotov, Marc Sciamanna, Ignace Gatare, Mikel Arteaga, and Hugo Thienpont

Volume 2011, Article ID 469627, 16 pages

**Progress on High-Speed 980 nm VCSELs for Short-Reach Optical Interconnects**, Alex Mutig and Dieter Bimberg

Volume 2011, Article ID 290508, 15 pages

## Editorial

# Recent Advances in Semiconductor Surface-Emitting Lasers

**Krassimir Panajotov,<sup>1,2</sup> Rainer Michalzik,<sup>3</sup> and Kent D. Choquette<sup>4</sup>**

<sup>1</sup> Department of Applied Physics and Photonics, Vrije Universiteit Brussel, Pleinlaan 2, 1050 Brussels, Belgium

<sup>2</sup> Georgi Nadjakov Institute of Solid State Physics, Bulgarian Academy of Sciences, 72 Tzarigradsko Chaussee Boulevard, 1784 Sofia, Bulgaria

<sup>3</sup> Institute of Optoelectronics, Ulm University, Albert-Einstein-Allee 45, 89081 Ulm, Germany

<sup>4</sup> Department of Electrical and Computer Engineering, University of Illinois, 208 North Wright Street, Urbana, IL 61801, USA

Correspondence should be addressed to Krassimir Panajotov, kpanajot@b-phot.org

Received 23 August 2012; Accepted 23 August 2012

Copyright © 2012 Krassimir Panajotov et al. This is an open access article distributed under the Creative Commons Attribution License, which permits unrestricted use, distribution, and reproduction in any medium, provided the original work is properly cited.

This special issue 1 of *Advances in Optical Technologies* contains 12 review papers highlighting the most recent and impressive achievements and exciting new concepts in the field of semiconductor surface-emitting lasers. Hereafter we briefly summarize its content.

Two review articles present advances in the development of semiconductor disk lasers (SDLs). M. Guina et al. from Tampere University of Technology review SDLs producing yellow-orange and mid-IR radiation for high-impact applications in medicine, spectroscopy, or astronomy. They demonstrate dilute nitride (GaInNAs) gain mirror SDLs with more than 11 W output power in the wavelength range 1180–1200 nm and subsequent intracavity frequency doubling to generate yellow-orange radiation with power exceeding 7 W. For the 2–3  $\mu\text{m}$  wavelength range, they use GaSb gain mirrors and achieve the shortest pulses of 384 fs obtained from SDLs at 2  $\mu\text{m}$ . A paper from the group of E. Kapon at the Swiss Federal Institute of Technology in collaboration with the Technical University of Lodz, Poland reviews the progress in SDLs based on wafer-fused InAlGaAs/InP-AlGaAs/GaAs gain mirrors for telecommunication wavelengths. Continuous-wave (CW) output powers of 2.7 W at 1550 nm, 4.8 W at 1480 nm, and 6.6 W at 1300 nm have been demonstrated, as well as second-harmonic emission at 650 nm wavelength with a record output of 3 W and Raman fiber lasers with 0.5 W emission at 1600 nm.

A. Mutig and D. Bimberg from the Technische Universität Berlin, Germany, review the progress on high-speed 980 nm vertical-cavity surface-emitting lasers (VCSELs) for short-reach optical interconnects, reporting direct modulation rates exceeding 40 Gbit/s and excellent temperature stability.

The major device concepts leading to these impressive achievements are presented.

A review paper from the group of R. Michalzik at Ulm University, Germany, presents the monolithic integration, fabrication, and electro-optical properties of AlGaAs/GaAs-based transceiver (TRx) chips for 850 nm wavelength optical links. Two design concepts are presented, based on a VCSEL and a monolithically integrated PIN-type photodiode for 62.5 and 50  $\mu\text{m}$  core diameter multimode fiber (MMF) or metal-semiconductor-metal photodetector for 100 or 200  $\mu\text{m}$  large-area fibers. The feasibility of upgrading standard MMF networks to handle true bi-directional data rates of up to 10 Gbit/s is demonstrated.

K. Johnson et al. from Vixar company in Plymouth, USA, review the advances in red VCSEL technology for medical and industrial sensing, printing, scanning, and lower cost interconnects based upon plastic optical fiber. Some of the state-of-the-art red VCSEL performance demonstrations include output power of 14 mW CW at room temperature, a record maximum temperature of 105°C for CW operation at an emission wavelength of 680 nm, time to 1% failure at room temperature of approximately 200,000 hours, lifetime in a 50°C, 85% humidity environment in excess of 3500 hours, digital data rates of 3 Gbit/s, and peak pulsed array powers greater than 100 mW.

K. D. Choquette et al. from the University of Illinois, in collaboration with the Rose-Hulman Institute of Technology, Terre Haute, and the United States Military Academy West Point, all from the USA, and with the National University of Singapore, review the design, fabrication, and performance of photonic crystal VCSELs for enhanced single-transverse

mode operation. They demonstrated that by control of the refractive index and loss created by the photonic crystal, operation in the Gaussian mode can be ensured, independent of the lasing wavelength.

N. Gerhardt and M. Hofmann from the Ruhr-University Bochum, Germany, review the progress in spin-controlled VCSELs. By means of optical excitation and numerical simulations, they present superior properties compared to conventional devices such as threshold reduction, spin control of the emission, or even much faster dynamics. Possible concepts for room-temperature electrical spin injection without large external magnetic fields are summarized, and the progress on the field of purely electrically pumped spin-VCSELs is reviewed.

M. I. Hill and M. I. H. Marell from the Technische Universiteit Eindhoven, The Netherlands, review the advances in surface-emitting metal nanocavity lasers. Two different realized versions of these nanopillar devices, one with a trapped cutoff mode in the pillar, another with a mode that propagates along the pillar, have been demonstrated.

K. Panajotov et al. from the Vrije Universiteit Brussel, Belgium, in collaboration with Supélec in Metz, France, and the Universidad Pública de Navarra in Pamplona, Spain, review the VCSEL nonlinear dynamics induced by optical injection, optical feedback, current modulation, and mutual coupling. For the case of orthogonal optical injection, they demonstrate a new Hopf bifurcation that delimits the injection locking region and a new resonance tongue that is due to first-order transverse mode injection locking. Similarly, the underlying polarization mode competition leads to chaotic-like behavior in case of gain switching and to anticorrelated polarization dynamics in the regimes of low-frequency fluctuations and self-pulsations induced by optical feedback. Polarization dynamics, however, improves chaos synchronization between unidirectionally coupled VCSELs.

R. Sarzała et al. from the Technical University of Lodz, Poland in collaboration with the Vrije Universiteit Brussel, Belgium, review the progress in self-consistent modeling of optical, electrical, thermal, and carrier transport phenomena taking part in VCSELs. Versatile numerical methods for nitride, arsenide, and phosphide VCSELs emitting light from violet to near-infrared with either gain guiding by a tunnel junction or index guiding by oxide or photonic crystal aperture are presented, focusing on enhancing the single-transverse-mode operation.

V. Bardinal et al. from LAAS-CNRS and Université de Toulouse, France, review the main recent technological approaches to combine micro-optical elements with VCSELs in order to control their output beam and to improve their photonic integration. They detail their integration techniques of self-aligned polymer microlens fabrication for beam collimation and short-distance beam focusing.

Finally, S. Barbay and R. Kuszelewicz from Laboratoire de Photonique et de Nanostructures at CNRS, Marcoussis, in collaboration with J. Tredicce from the Institut Non Linéaire de Nice, both in France, review the advances on the experimental study of cavity solitons (CS) in VCSELs during the past decade. They emphasize on the design and fabrication of electrically or optically pumped broad-area VCSELs used for

CS formation, review different experimental configurations and discuss CS applications for all-optical processing of information and for VCSEL characterization.

## Acknowledgments

It was our great pleasure and honor to work for the success of this special issue. We thank the contributors for their careful writing and report on significantly new results. Many thanks go to all referees for their hard and prompt work. As a result, this special issue provides a relevant snapshot of the most recent advances to the field, and we hope that it will motivate further work on the basis of these findings, concepts, and applications. We thank the editorial staff of *Advances in Optical Technologies* for their kind attention and their efforts in making this special issue possible.

*Krassimir Panajotov  
Rainer Michalzik  
Kent D. Choquette*

## Review Article

# Numerical Self-Consistent Analysis of VCSELs

Robert Sarzała,<sup>1</sup> Tomasz Czyszanowski,<sup>1</sup> Michał Wasiak,<sup>1</sup> Maciej Dems,<sup>1</sup> Łukasz Piskorski,<sup>1</sup> Włodzimierz Nakwaski,<sup>1</sup> and Krassimir Panajotov<sup>2,3</sup>

<sup>1</sup>Institute of Physics, Technical University of Lodz, Wolczanska 219, 93-005 Lodz, Poland

<sup>2</sup>Department of Applied Physics and Photonics, Vrije Universiteit Brussel, Pleinlaan 2, 1050 Brussels, Belgium

<sup>3</sup>Institute of Solid State Physics, 72 Tzarigradsko Chaussee Boulevard, 1784 Sofia, Bulgaria

Correspondence should be addressed to Tomasz Czyszanowski, tomasz.czyszanowski@p.lodz.pl

Received 1 July 2011; Accepted 20 February 2012

Academic Editor: Kent D. Choquette

Copyright © 2012 Robert Sarzała et al. This is an open access article distributed under the Creative Commons Attribution License, which permits unrestricted use, distribution, and reproduction in any medium, provided the original work is properly cited.

Vertical-cavity surface-emitting lasers (VCSELs) yield single-longitudinal-mode operation, low-divergence circular output beam, and low threshold current. This paper gives an overview on theoretical, self-consistent modelling of physical phenomena occurring in a VCSEL. The model has been experimentally confirmed. We present versatile numerical methods for nitride, arsenide, and phosphide VCSELs emitting light at wavelengths varying from violet to near infrared. We also discuss different designs with respect to optical confinement: gain guidance using tunnel junctions and index guidance using oxide confinement or photonic crystal and we focus on the problem of single-transverse-mode operation.

## 1. Introduction

Currently there are two distinctly different classes of Fabry-Perot semiconductor diode lasers: edge-emitting lasers (EELs) and vertical-cavity surface-emitting lasers (VCSELs). Because of the details of their structure, VCSELs have a number of unique features that distinguish them from conventional EELs [1]: inherent single-longitudinal-mode operation, low-divergence nonastigmatic circular output beams, low threshold current at room-temperature (RT) continuous-wave (CW) operation, device geometry suitable for integration into two-dimensional laser arrays, compatibility with vertical-stacking architecture, the ability to be modulated at very high frequencies, and the possibility of *in situ* testing.

While EELs usually emit many longitudinal modes around the maximal optical gain wavelength, VCSELs emit a single longitudinal mode at the wavelength determined by the cavity design. Therefore, EEL cavities are always tuned to their maximal optical gain but those of VCSELs may be intentionally detuned, which gives an additional degree of freedom to the VCSEL design. As a result, designers of EELs can propose devices emitting radiation of wavelength solely determined by their activeregions. In the case of VCSELs, however, it is possible to design a device emitting radiation

at wavelength somewhat different (practically always longer) from that associated with their active-region structure.

Computer simulations of laser operation enable anticipating the laser performance in more efficient and inexpensive way than the trial-and-error method. However, VCSEL modelling is a very involved task because of its multilayered structure (sometimes containing as many as several hundred layers) often of nonplanar or buried-type architecture, with many heterojunctions, graded layers, strained layers, quantum wells (QWs), quantum dots (QDs) or quantum wires, superlattices, oxide and oxidized layers, or mesa structures, and so forth. Therefore, in advanced VCSEL models, all material and structure parameters should be functions of the local material composition. Additionally, physical phenomena taking place during the VCSEL operation, that is, optical, electrical, thermal, and mechanical phenomena, are interrelated. These interactions create a network of mutual interrelations. Therefore comprehensive VCSEL modelling should have self-consistency, where as many as possible interactions between individual physical phenomena taking place within the VCSEL should be accounted for.

Following the general principles given in [2], the comprehensive self-consistent VCSEL model should contain the following mutually interrelated parts.

- (1) A three-dimensional (3D) optical model describing, for successive cavity modes, their modal gain and loss, lasing thresholds, emission wavelengths, and optical field distributions within the laser cavity.
- (2) A 3D electrical model characterizing the current spreading between the top and the bottom contacts through the centrally located active region, the injection of carriers of both polarity into the QW or QD active region, and their subsequent radiative or non-radiative recombination after radial out-diffusion within the active region and the possible overbarrier carrier leakage.
- (3) A thermal model characterizing generation of a heat flux (nonradiative recombination, reabsorption of spontaneous radiation as well as volume and barrier Joule heating), its 3D flow from heat sources towards a heat sink, and its 3D spreading within a heat sink.
- (4) A recombination model describing phenomena within the QW or QD active region, that is, furnishing information about the optical gain process being the result of radiative bimolecular recombination (to enable determination of the active-region optical gain spectrum) as well as nonradiative monomolecular and Auger recombinations.
- (5) a piezoelectric model (important in nitride materials) first describing mechanical stresses within the VCSEL structure necessary to determine the piezoelectric polarization and then introducing piezoelectric and spontaneous polarization effects leading to some modifications of potential distributions especially important in quantum wells (QWs).

Additionally in a comprehensive VCSEL model, as many as possible linear and nonlinear interactions between the above individual optical, electrical, thermal, recombination, mechanical, and piezoelectric phenomena should be taken into account with the aid of the self-consistent approach including the effects of

- (i) thermal focusing, that is, the temperature dependence of refractive indices,
- (ii) self-focusing, that is, dependence of refractive indices on carrier concentration,
- (iii) gain-induced wave guiding, that is, the temperature, carrier concentration, and wavelength dependences of the extinction coefficient,
- (iv) temperature (and sometimes also carrier concentration) dependence of thermal conductivities,
- (v) temperature and carrier concentration dependences of electrical conductivities,
- (vi) the temperature, carrier concentration, and wavelength dependences of optical gain,
- (vii) temperature and carrier concentration dependences of the energy gaps,
- (viii) quantum-confined Stark effect (QCSE), that is, an impact of spontaneous and piezoelectric polarization

on the QW potential distribution leading to reduced overlapping of the wave functions of electrons and holes trapped within the QW, raising both their QW levels and carriers enhanced escape possibilities.

Truly comprehensive VCSEL models constitute an advanced and integrated tool for studying all aspects of VCSEL performance in the whole complexity of all interrelated physical phenomena taking part in their operation. 3D profiles of all model parameters within the whole device volume should be determined in each calculation loop not only by the various chemical composition of the layers, but by the self-consistent calculation algorithm which takes into account current 3D profiles of temperature, current density, carrier concentration, mode radiation intensity, and mechanical stresses. Reaching such self-consistency is especially important for modelling high-power and/or high-temperature VCSEL operation. Such a comprehensive VCSEL model has been reported by Sarzała and Nakwaski [3] and Sarzała [4], and its validity has been confirmed experimentally for QD VCSELs in [5]. Above the lasing threshold, the spatial-hole-burning (SHB) effect should also be taken into account [6–8]. A local increase in a lasing intensity of the already excited lowest-threshold mode enhances (as a result of a stimulated emission) recombination of active-region carriers leading to a decrease in their concentration and a decrease in the local optical gain at places of high mode radiation intensity. The modal optical gain of this lowest-threshold mode saturates (or may even be reduced) which may favour excitation of the next transverse mode of an intensity spatial profile better suited to this new optical gain profile. Therefore, the above-threshold analysis of a VCSEL operation requires considering the SHB effect.

Similar to a chain being as strong as its weakest link, a model is as exact as its least precise part. Therefore, it is useless to improve the more accurate parts of the model and not to care about less exact portions. All parts of the model should exhibit similar accuracy. In any individual case, a reasonable compromise should be reached between high modelling fidelity and its practical convenience depending on a main modelling goal, importance and urgency of expected results, available equipment, and also financial possibilities. Rigorous modelling from the first principles is usually very time-consuming and often requires powerful supercomputers equipped with enormous memory. Sometimes such modelling is justified but very often more approximate (but quicker and cheaper) models are acceptable and provide important technological suggestions. The computational cost of applying a scalar or a vectorial optical model, a simplified or a more involved drift-diffusion electrical model, Fermi's Golden Rule or a many-body optical gain determination, and so forth, has to be compared before the modelling approach is chosen. Additionally, it should be taken into consideration that rigorous models are very time-consuming, which practically excludes their application in self-consistent modelling. Often, modelling errors due to the lack of self-consistency are worse than those created by using a simpler approximate method.

The main goal of the current paper is to present versatile numerical methods for nitride, arsenide, and phosphide VCSELs emitting light at wavelengths varying from violet to near infrared. We also discuss different device designs with respect to optical confinements: gain guidance using a tunnel junction and index guidance using an oxide or Photonic Crystal. We also restrict our discussion to the problem of enhanced single transverse-mode operation. Such operation is required in several VCSEL applications as, for example, telecommunications and gas detection. Single mode operation can only be achieved for small aperture in standard index-guided VCSELs, which limits the available single-mode output [5]. Higher-output large-size index guided VCSELs usually exhibit multimode operation, especially at higher temperatures. This results from the considerable current-crowding effect near the active-region edges, which—despite the smooth radial carrier diffusion profile in the active region—still favours higher-order transverse modes [5, 8]. In gain-guided VCSELs, on the other hand, single-mode operation is possible for broader active regions, at the expense of higher threshold currents. So as one can see, the requirements of higher-power single-mode operation and low lasing threshold usually contradict each other. Nevertheless, various approaches of enhancing the single-mode VCSEL output power have been reported [8–14].

Even if the VCSEL is single mode, there still can be observed polarization switching between two orthogonal polarisations of the fundamental mode. In a number of applications such polarization switching cannot be tolerated. For this reason, the polarization stabilization is an important issue in the design of modern VCSELs. Traditional, commonly used VCSELs have geometries with cylindrical symmetry and are usually grown on (100)-oriented substrates. Thus, they have no a priori defined polarization, that is, the LP-polarized modes can be oriented in any direction perpendicular to the VCSEL symmetry axis. In practice, there is always some small anisotropy induced by residual strain introduced during fabrication and the electrooptic effect. Therefore, the electric field of the fundamental mode (LP mode) is almost always linearly polarized along [011] or [011] crystallographic axis, while the one of the first-order modes is perpendicular [15]. During the operation of the laser, a change of temperature, current, or stress can induce polarization switching, that is, the VCSEL starts emitting light in the polarization orthogonal to the previous one. This effect can be a subject to bistability, hysteresis or random dynamic behavior [16, 17]. Furthermore, optical feedback [18] or optical injection [19] can introduce even more polarization instabilities in the system. There exist several methods for providing polarization control in VCSELs. They can be attributed to one of the following groups: introduction of anisotropic gain, use of noncircular resonators or polarization-dependent mirrors, an external feedback, and finally application of photonic crystals. Here, we are focused on the numerical design of the optimal photonic crystal aimed for stabilization of polarization in VCSELs.

The paper is organized as follows. Section 2 describes the theoretical self-consistent model of physical phenomena taking part in VCSEL, and Section 3 concerns the

experimental validation of the model based on a 1300 nm QD VCSEL. Comparison of scalar and vectorial optical models for 400 nm nitride VCSEL is presented in Section 4. Optimization of oxide-confined VCSELs is presented in Section 5. Design rules of photonic crystal VCSELs for enhanced single-mode and single-polarization operation are given in Sections 6 and 7, respectively. Finally, in Section 8 we conclude.

## 2. Numerical Model

The simulated performance characteristics of VCSELs are determined with the aid of numerical models presented in this section. Typically, personal computers are used in simulation process, and the resulting calculation time to achieve a single result of any characteristic varies from several minutes to one day. The shorter calculation times arise from using 1D or 2D electrical and thermal models combined with 2D scalar optical approach, while the longer duration occurs when using all 3D models and vectorial optics.

### 2.1. Optical Models

**2.1.1. Scalar Optics.** The scalar optical approach for VCSEL simulation was introduced by Hadley [20] and latter modified by Wenzel and Wünsche [21]. In this effective-frequency method (EFM) the optical field  $E(r, z, \varphi)$  is assumed to be linearly polarized and spatially separated:

$$E(r, z, \varphi) = E_{r,z}(r, z)E_r(r) \exp(iL\varphi), \quad (1)$$

where  $z$  is the direction of the light propagation in the VCSEL,  $r$  is the radial coordinate in the plane of epitaxial layers,  $\varphi$  is the azimuthal coordinate, and  $L = 0, 1, 2, \dots$  is the azimuthal mode number. The above enables reducing the wave equation within the VCSEL resonator to the following two mutually interrelated nearly-one-dimensional wave equations along the axial and the radial VCSEL directions:

$$\begin{aligned} \left[ \frac{d^2}{dz^2} + k_0^2 \varepsilon \right] E_{r,z} &= \nu_{\text{eff}}(r) k_0^2 \sqrt{\varepsilon n_g} E_{r,z}, \\ \left[ \frac{d^2}{dr^2} + \frac{1}{r} \frac{d}{dr} - \frac{L^2}{r^2} + \nu_{\text{eff}}(r) k_0^2 \langle \sqrt{\varepsilon n_g} \rangle_r \right] E_r^L(r) &= \nu k_0^2 \langle \sqrt{\varepsilon n_g} \rangle_r E_r^L(r). \end{aligned} \quad (2)$$

For simplicity, we assigned  $\varepsilon \equiv \varepsilon(r, z)$  and  $E_{r,z} \equiv E_{r,z}(r, z)$ ,  $\nu_{\text{eff}}$  to represent the effective frequency,  $k_0$  is the vacuum wave number,  $\varepsilon$  is the dielectric constant of the layer, and  $n_g$  is the group index. The boundary conditions (BCs) are realized by the introduction of the region in which the solutions of the (2) are assumed as decaying functions [22]. The last layer that is responsible for decaying of the field in the radial direction is placed 20  $\mu\text{m}$  from the edge of the active region. The dimensionless complex parameter  $\nu$  plays the role of an eigenvalue.

**2.1.2. Vectorial Optics.** The computational efficient vectorial approach to VCSELs described in this section is based on

the plane wave admittance method (PWAM) [19]. The main objective of the method is the transformation of Maxwell's equations to a form of the characteristic equation, which will be utilized in the further vectorial analysis of the VCSEL. To this aim, the Cartesian coordinate system is oriented in such a way that the  $x$ - $y$  plane is parallel to the epitaxial layers, whereas the  $z$  direction is the direction of the light propagation. Then, Maxwell's equations can be expressed in the form

$$\begin{aligned}\nabla \times \mathbf{E}(x, y, z, t) &= -\mu\mu_0 \frac{\partial \mathbf{H}(x, y, z, t)}{\partial t} \\ \nabla \times \mathbf{H}(x, y, z, t) &= \varepsilon\varepsilon_0 \frac{\partial \mathbf{E}(x, y, z, t)}{\partial t}\end{aligned}\quad (3)$$

with  $\mu$ ,  $\mu_0$  being the magnetic permittivity diagonal tensors for the material and vacuum, respectively, and  $\varepsilon$ ,  $\varepsilon_0$  being the respective diagonal tensors of dielectric constant.  $\mathbf{E}$  and  $\mathbf{H}$  are the vectors of the electric and magnetic fields. We further assume that

- (1) harmonic time dependence of the fields is of the form  $\sim \exp(i\omega t)$ , with  $\omega$  being the angular frequency of the propagating wave in the vacuum,
- (2) the structure consists of uniform (in the propagation  $z$ -direction) parallel layers, which yields Maxwell's set of the equations in the static form

$$\begin{aligned}\nabla \times \mathbf{E}(x, y, z) &= -i\omega\mu\mu_0\mathbf{H}(x, y, z), \\ \nabla \times \mathbf{H}(x, y, z) &= i\omega\varepsilon\varepsilon_0\mathbf{E}(x, y, z).\end{aligned}\quad (4)$$

Eliminating the  $z$ -components of the electric and magnetic fields from the above equations results in

$$\begin{aligned}\partial_z^2 \begin{bmatrix} E_x \\ E_y \end{bmatrix} &= \frac{1}{\omega^2\varepsilon_0\mu_0} \begin{bmatrix} -\partial_x \frac{1}{\varepsilon_z} \partial_x - \omega^2\varepsilon_0\mu_y\mu_0 & \partial_x \frac{1}{\varepsilon_z} \partial_y \\ -\partial_y \frac{1}{\varepsilon_z} \partial_x & \partial_y \frac{1}{\varepsilon_z} \partial_y + \omega^2\varepsilon_0\mu_x\mu_0 \end{bmatrix} \\ &\times \begin{bmatrix} -\partial_y \frac{1}{\mu_z} \partial_y - \omega^2\mu_0\varepsilon_x\varepsilon_0 & \partial_y \frac{1}{\mu_z} \partial_x \\ -\partial_x \frac{1}{\mu_z} \partial_y & \partial_x \frac{1}{\mu_z} \partial_x + \omega^2\mu_0\varepsilon_y\varepsilon_0 \end{bmatrix} \begin{bmatrix} E_x \\ E_y \end{bmatrix}.\end{aligned}\quad (5)$$

The electromagnetic fields as well as the magnetic and electrical permittivities are decomposed in orthonormal complete basis of exponential functions:

$$\begin{aligned}\Phi_u &= \sum_{n,m}^N \tilde{\Phi}_u^{n,m} \varphi_{n,m}, \\ \eta_u &= \sum_{n,m}^\infty \tilde{\eta}_u^{n,m} \varphi_{n,m},\end{aligned}\quad (6)$$

where  $\Phi_u$  are the arbitrary field components of the electric or magnetic field,  $\eta_u$  are the components of magnetic or electric

permittivity, and  $u = x, y, z$ . The basis functions have been defined in the form of product of two functions, which satisfy the orthonormality and completeness of the basis:

$$\varphi_{n,m} = \exp\left(i\left(\frac{2\pi n}{L_x} + k_x\right)x + i\left(\frac{2\pi m}{L_y} + k_y\right)y\right), \quad (7)$$

where  $L_x$  and  $L_y$  correspond to the dimensions of the calculation window along the  $x$  and  $y$  axis and  $k_x$  and  $k_y$  are corresponding components of wavevector in the  $x$ - $y$  plane. Using these assumptions modifies the set of (5) to the form in which fields and permittivities are replaced with coefficients of exponential expansions:

$$\begin{aligned}\partial_z^2 \begin{bmatrix} \tilde{E}_y^n \\ \tilde{E}_x^n \end{bmatrix} &= -\frac{1}{k_0^2} \begin{bmatrix} (\mathbf{G} + \mathbf{k})(\mathbf{G}'' + \mathbf{k})\tilde{\kappa}_z^{\mathbf{G}'' - \mathbf{G}} - k_0^2\tilde{\mu}_x^{\mathbf{G}'' - \mathbf{G}} \\ (\mathbf{G} + \mathbf{k})(\mathbf{G}'' + \mathbf{k})\tilde{\kappa}_z^{\mathbf{G}'' - \mathbf{G}} \\ -(\mathbf{G} + \mathbf{k})(\mathbf{G}'' + \mathbf{k})\tilde{\kappa}_z^{\mathbf{G}'' - \mathbf{G}} \\ k_0^2\tilde{\mu}_y^{\mathbf{G}'' - \mathbf{G}} - (\mathbf{G} + \mathbf{k})(\mathbf{G}'' + \mathbf{k})\tilde{\kappa}_z^{\mathbf{G}'' - \mathbf{G}} \end{bmatrix} \\ &\times \begin{bmatrix} (\mathbf{G} + \mathbf{k})(\mathbf{G}'' + \mathbf{k})\tilde{\gamma}_z^{\mathbf{G}'' - \mathbf{G}} - k_0^2\tilde{\varepsilon}_y^{\mathbf{G}'' - \mathbf{G}} \\ (\mathbf{G} + \mathbf{k})(\mathbf{G}'' + \mathbf{k})\tilde{\gamma}_z^{\mathbf{G}'' - \mathbf{G}} \\ -(\mathbf{G} + \mathbf{k})(\mathbf{G}'' + \mathbf{k})\tilde{\gamma}_z^{\mathbf{G}'' - \mathbf{G}} \\ k_0^2\tilde{\varepsilon}_x^{\mathbf{G}'' - \mathbf{G}} - (\mathbf{G} + \mathbf{k})(\mathbf{G}'' + \mathbf{k})\tilde{\gamma}_z^{\mathbf{G}'' - \mathbf{G}} \end{bmatrix} \begin{bmatrix} \tilde{E}_y^{\mathbf{G}} \\ \tilde{E}_x^{\mathbf{G}} \end{bmatrix}.\end{aligned}\quad (8)$$

The boundary conditions assumed for the set of equations are fulfilled by absorbing perfectly matched layers [23]. The final set (8) can be written as

$$\partial_z^2 \bar{\mathbf{E}} = \mathbf{R}_H \mathbf{R}_E \bar{\mathbf{E}} \equiv \mathbf{Q}_E \bar{\mathbf{E}}. \quad (9)$$

In the same manner one arrives at the equation for magnetic field:

$$\partial_z^2 \bar{\mathbf{H}} = \mathbf{R}_E \mathbf{R}_H \bar{\mathbf{H}} \equiv \mathbf{Q}_H \bar{\mathbf{H}}. \quad (10)$$

Equations (9) and (10) can be solved in a base, which reduces the matrices  $\mathbf{Q}_E$  and  $\mathbf{Q}_H$  to diagonal forms:

$$\begin{aligned}\partial_z^2 \hat{\mathbf{E}} + \Gamma_E^2 \hat{\mathbf{E}} &= 0, \\ \partial_z^2 \hat{\mathbf{H}} + \Gamma_H^2 \hat{\mathbf{H}} &= 0,\end{aligned}\quad (11)$$

where  $\hat{\mathbf{E}}$  and  $\hat{\mathbf{H}}$  stand for electric and magnetic fields in the new base and can be defined as

$$\begin{aligned}\hat{\mathbf{E}} &= \mathbf{T}_E^{-1} \bar{\mathbf{E}}, \\ \hat{\mathbf{H}} &= \mathbf{T}_H^{-1} \bar{\mathbf{H}},\end{aligned}\quad (12)$$

where the matrices  $\mathbf{T}_E$  and  $\mathbf{T}_H$  diagonalize  $\mathbf{Q}_E$  and  $\mathbf{Q}_H$ , respectively:

$$\begin{aligned}\mathbf{T}_E^{-1} \mathbf{Q}_E \mathbf{T}_E &= \Gamma_E^2, \\ \mathbf{T}_H^{-1} \mathbf{Q}_H \mathbf{T}_H &= \Gamma_H^2.\end{aligned}\quad (13)$$

The solution of (11) has the well-known form of a standing wave:

$$\begin{aligned}\hat{\mathbf{E}}(z) &= \cosh(i\Gamma_E z) \mathbf{A}_E + \sinh(i\Gamma_E z) \mathbf{B}_E, \\ \hat{\mathbf{H}}(z) &= \cosh(i\Gamma_H z) \mathbf{A}_H + \sinh(i\Gamma_H z) \mathbf{B}_H.\end{aligned}\quad (14)$$

Additionally, the fields  $\hat{\mathbf{E}}(z)$  and  $\hat{\mathbf{H}}(z)$  and their  $z$ -derivatives satisfy the continuity condition on the interface between the layers, that is,

$$\begin{bmatrix} \hat{\mathbf{H}}_0^{(i)} \\ -\hat{\mathbf{H}}_d^{(i)} \end{bmatrix} = \begin{bmatrix} \mathbf{Y}_1^{(i)} & \mathbf{Y}_2^{(i)} \\ \mathbf{Y}_2^{(i)} & \mathbf{Y}_1^{(i)} \end{bmatrix} \begin{bmatrix} \hat{\mathbf{E}}_0^{(i)} \\ \hat{\mathbf{E}}_d^{(i)} \end{bmatrix}, \quad (15)$$

where subscripts 0 and  $d$  correspond to the bottom and the top of the layer, respectively,

$$\begin{aligned} \mathbf{y}_1 &= \alpha_{\mathbf{H}} \tanh^{-1}(i\Gamma_{\mathbf{E}}d), \\ \mathbf{y}_2 &= -\alpha_{\mathbf{H}} \sinh^{-1}(i\Gamma_{\mathbf{E}}d), \\ \alpha_{\mathbf{H}} &= (\mathbf{T}_{\mathbf{E}}^{-1}\mathbf{R}_{\mathbf{H}}\mathbf{T}_{\mathbf{H}})^{-1}\Gamma_{\mathbf{E}}. \end{aligned} \quad (16)$$

Transformation of the fields from layer  $i$  to layer  $i+1$  is given by

$$\begin{aligned} \hat{\mathbf{E}}_0^{(i+1)} &= (\mathbf{T}_{\mathbf{E}}^{(i+1)})^{-1}\mathbf{T}_{\mathbf{E}}^{(i)}\hat{\mathbf{E}}_d^{(i)} \equiv \mathbf{t}_{\mathbf{E}}^{(i)}\hat{\mathbf{E}}_d^{(i)}, \\ \hat{\mathbf{H}}_0^{(i+1)} &= (\mathbf{T}_{\mathbf{H}}^{(i+1)})^{-1}\mathbf{T}_{\mathbf{H}}^{(i)}\hat{\mathbf{H}}_d^{(i)} \equiv \mathbf{t}_{\mathbf{H}}^{(i)}\hat{\mathbf{H}}_d^{(i)}. \end{aligned} \quad (17)$$

The above relations of the field transformation between and within the layers can be employed to determine the characteristic equation by forcing boundary conditions, that is, zeroing of the field on the upper-most and lower-most layer boundaries. This allows finding the characteristic values of the problem, that is, the effective emission wavelength of the VCSEL, as well as the characteristic vectors, which determine the distribution of the electromagnetic field within the structure. Furthermore, one can choose a matching interface, which should be placed at a maximum of standing wave to reduce numerical error. That leads to the following relation between electric fields in neighboring layers:

$$\mathbf{T}_{\mathbf{H}}^{(m)}\mathbf{Y}_{\text{up}}^{(m)}\hat{\mathbf{E}}_d^{(m)} = \mathbf{T}_{\mathbf{H}}^{(m)}\mathbf{Y}_{\text{down}}^{(l)}\hat{\mathbf{E}}_d^{(l)}, \quad (18)$$

where

$$\mathbf{Y}^{(i)} = -\left(\mathbf{y}_2^{(i)}\left(\mathbf{t}_{\mathbf{H}}^{(i)}\mathbf{Y}^{(i-1)}\left(\mathbf{t}_{\mathbf{E}}^{(i)}\right)^{-1} - \mathbf{y}_1^{(i)}\right)^{-1}\mathbf{y}_2^{(i)} + \mathbf{y}_1^{(i)}\right), \quad (19)$$

that is, the matrices  $\mathbf{Y}$  are determined from a recurrence relation starting from the bottom  $\mathbf{Y}_{\text{up}}^{(m)}$  and the top  $\mathbf{Y}_{\text{down}}^{(m)}$  of the VCSEL. Thus, (18) results in

$$\left(\mathbf{T}_{\mathbf{H}}^{(m)}\mathbf{Y}_{\text{up}}^{(m)}\left(\mathbf{T}_{\mathbf{E}}^{(m)}\right)^{-1} - \mathbf{T}_{\mathbf{H}}^{(m)}\mathbf{Y}_{\text{down}}^{(l)}\left(\mathbf{T}_{\mathbf{E}}^{(l)}\right)^{-1}\right)\bar{\mathbf{E}} = \mathbf{Y}\bar{\mathbf{E}} = 0, \quad (20)$$

which is the characteristic value equation. The solution of (20) determines the complex emitted wavelength. The imaginary part of wavelength determines the modal gain of the propagating wave.

**2.2. Electrical Model.** We utilize a finite-element (FE) electrical model of the VCSEL, which takes into account in a natural way the interplay of drift and diffusion currents for both electrons and holes. Current spreading can be determined from

a three-dimensional (3D) potential distribution  $V(r, z, \varphi)$  by solving the Laplace equation:

$$\text{div}[\sigma(r, z, \varphi)\text{grad}(V(r, z, \varphi))] = 0, \quad (21)$$

where  $\sigma$  denotes the 3D profile of electrical conductivity and  $r$ ,  $z$ , and  $\varphi$  represent a cylindrical coordinate system with the  $z$ -axis directed along the device axis. From now on, the following notation  $\vec{r} = (r, z, \varphi)$  will be used. For all the layers of the laser structure (except the active region), the conductivity  $\sigma$  depends on the material composition and doping, as well as on local temperature and local carrier concentration:

$$\sigma(\vec{r}) = en(\vec{r})\mu(\vec{r}). \quad (22)$$

In (22),  $e$  is the electron charge,  $n$  the carrier concentration, and  $\mu$  the carrier mobility.

Generation and recombination phenomena within the active region provide the nonzero right-hand side of (21) (known as the Poisson equation in this case). Their relative influence is difficult to analyze theoretically. Therefore, they will be taken symbolically into account with the aid of an effective conductivity  $\sigma_{\text{pn}}$  of the active-region material. Its value can be found using the differential Ohm law and the classical diode equation:

$$\sigma_{\text{pn}}(r) = \frac{\beta_{\text{pn}}j_{\text{pn}}(r)d_{A,E}}{\ln\left[\left(j_{\text{pn}}(r)/j_s\right) + 1\right]}, \quad (23)$$

where  $j_{\text{pn}}$  is the p-n junction current density,  $j_s$  the reverse p-n saturation current density, and  $d_{A,E}$  the cumulative active-region thickness including not only the active layers but also the barrier layers between them.

To obtain the 3D potential profile for the whole laser structure, it should be matched (using a self-consistent approach) with the aid of boundary conditions at all boundaries between the layers. The 3D current density  $j(\vec{r})$  can then be found within the whole device volume from the differential Ohm law:

$$j(\vec{r}) = -\sigma(\vec{r})\text{grad}[V(\vec{r})]. \quad (24)$$

Thereafter, the carrier density profile  $n_A(r)$  within the active layer may be determined from the diffusion equation below threshold:

$$\begin{aligned} D_A \left[ \frac{\partial^2 n_A(r)}{\partial r^2} + \frac{1}{r} \frac{\partial n_A(r)}{\partial r} \right] - An_A(r) - Bn_A^2(r) \\ - Cn_A^3(r) + \frac{j_{\text{pn}}(r)}{ed_A} = 0, \end{aligned} \quad (25)$$

where  $D_A$  is the ambipolar diffusion coefficient,  $(A)$  is the monomolecular (on point defects) nonradiative recombination constant,  $(B)$  the bimolecular recombination constant, and  $(C)$  the Auger recombination coefficient.

**2.3. Thermal Model.** We utilize a FE thermal VCSEL model, for which the same mesh as the one generated for the

FE electrical calculations is applied. The heat conduction equation

$$\text{div}[\lambda_T(\vec{r})\text{grad}(T(\vec{r}))] = -g_T(\vec{r}) \quad (26)$$

may be solved in this way for the whole VCSEL structure. In the above equation,  $\lambda_T$  stands for the 3D thermal conductivity coefficient and  $g_T$  for the 3D volume density of heat sources.

Nonradiative recombination and reabsorption of spontaneous radiation within the active region together with the volume Joule heating in all layers and the barrier Joule heating in the contacts are usually the main heat sources in the laser. The 3D heat flux spreading in the heat sink is determined by assuming that its external walls are kept at ambient temperature. With the exception of some specific cases, the mesa sidewalls and top laser facet are assumed to be thermally isolated because of the negligible heat abstraction mechanisms.

**2.4. Overthreshold Model.** The active-region carrier concentration distribution  $n_A$  is described by a time-independent (steady state) diffusion equation with adiabatic boundary conditions in one or two dimensions, that is, the active region is assumed to be so thin that  $n_A$  does not depend on  $z$ :

$$\kappa\Delta n_A(\vec{r}) - L(T, n_A) + S(\vec{r}) = 0, \quad (27)$$

where  $\kappa$  is the diffusion constant,  $L$  are the carrier losses, which depend on the carrier concentration and local temperature (see (28)), and  $S$  describes the carrier source (see (29)). The losses in the threshold case consist of three recombination processes: monomolecular, bimolecular, and Auger:

$$L(T, n_A) = An_A + Bn_A^2 + Cn_A^3, \quad (28)$$

where the recombination coefficients  $A$ ,  $B$ , and  $C$  may depend on the temperature. The sources are just the carriers injected into the active region of thickness  $d$ :

$$S(\vec{r}) = \frac{j_\perp}{ed}, \quad (29)$$

where  $j_\perp$  denotes the current density in the direction perpendicular to the active region.

Now we want to add to our threshold model the ability to describe phenomena connected with the presence of a strong electromagnetic field, which causes the stimulated recombination of the carriers in the active region (where the optical gain is positive). This phenomenon is called spatial hole burning. We will simulate it by adding another (negative if the gain is positive) carrier source in the carrier diffusion equation. Since our equation assumes a steady state, we must assume that the stimulated recombination rate does not depend on time. This requires that the modes are stable—they do not change in time. This assumption may not be valid in many edge emitting lasers, but in VCSELs it is very natural. In case of single-mode operation, the stimulated emission losses are described by the following formula:

$$L_{\text{st}}(n_A, T, x, y) = P \frac{2g(n_A, T, \vec{r})M(\vec{r})}{(1-R)\hbar\omega \int_S M}, \quad (30)$$

where  $P$  is the output power,  $g$  is the optical gain,  $M$  the mode profile,  $R$  is the reflectivity of the output mirror (the other one is assumed to reflect 100%), and  $\hbar\omega$  is the photon energy. Adding the above term to (27) results in the above-threshold carrier diffusion equation. For a given voltage  $U$ , which determines the temperature and carrier distribution, we find such a value of  $P$ , which gives such a carrier (and hence optical gain) distribution that the total modal gain is equal to 0.

In case of the multimode operation, stimulated emission losses for each mode are added. Each mode has its own power, gain, mode distribution, and photon energy. In this case we formally need to solve a system of  $n$  equations for the power  $U$  of each mode (where  $n$  is the number of modes).

### 3. Experimental Validation of the Model

The experimental validation of the model is based on the measured characteristics of a  $1.3\ \mu\text{m}$  quantum dot (QD) oxide-confined (OC) VCSEL structure (Figure 1) as described in [24].

The current flow is defined by selective oxidation of an AlAs layer placed at antinode position of the mode. The active region is composed of five groups of three 8 nm thick  $\text{In}_{0.15}\text{Ga}_{0.85}\text{As}$  QWs, each of which containing one InAs QD layer. In each group, located close to the successive antinode positions of the optical standing wave within the cavity, the QWs are separated by 32 nm thick GaAs barriers. Additional single InGaAs QWs containing single QD layers are placed at the beginning and the end of the active region. The cavity is bounded by two  $\text{Al}_{0.9}\text{Ga}_{0.1}\text{As}/\text{GaAs}$  distributed Bragg reflectors (DBRs).

Figure 2 presents the comparison of the results obtained with the aid of the self-consistent model with measurement. Good agreement between theoretical and experimental results is evident. In the model we do not consider spontaneous emission, therefore the theoretical total emitted power increases sharply from the lasing threshold, which is slightly less than 6 mA. While the emitted power increases in a single-fundamental-mode regime, the carrier concentration decreases in the center of the active region, where stimulated recombination is the most intense because of spatial hole burning. Hence, the first-order mode  $\text{LP}_{11}$  can be excited since more carriers are located closer to the radial borders of the active region.

It is clearly seen that the  $\text{LP}_{11}$  mode appears at around 8 mA. For larger currents, although the total efficiency remains almost unchanged, the fundamental mode power decreases, while the higher-order mode quickly increases. Very exact agreement between experimental and theoretical plots shown in Figure 2 confirms validity of computer simulation.

Figure 3 presents a dependence of the RT CW lasing threshold currents of the  $1.3\ \mu\text{m}$  top-emitting In(Ga)As/GaAs QD GaAs-based VCSELs on diameters  $d_A$  of their active regions. If we take into consideration that the final shape of an oxide aperture is not a perfect circle, but it resembles rather an ellipse, which is followed by an exactness of the  $d_A$  determination not better than about  $2\ \mu\text{m}$ , experimental

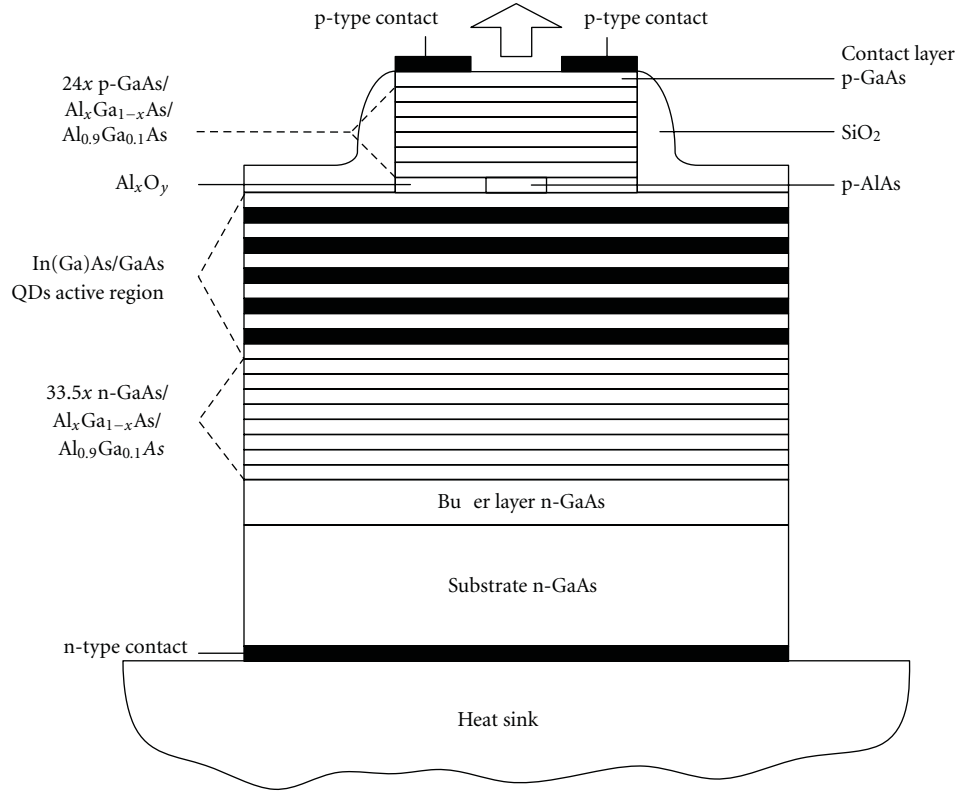


FIGURE 1: A mesa structure of the  $1.3 \mu\text{m}$  top-emitting oxide-confined (OC) In(Ga)As/GaAs quantum-dot GaAs-based VCSEL.

results agree quite well with theoretical ones. The lowest lasing threshold of  $4.95 \text{ mA}$  has been anticipated for  $d_A = 6 \mu\text{m}$ . In the case of smaller VCSELs, the radial size of the active region is too small to effectively confine the optical field. This causes a radical increase in its penetration into the passive areas around the central active region leading to a considerable increase in the lasing threshold observed in Figure 3. In VCSELs with larger active regions, current injection into the active region becomes increasingly nonuniform (current-crowding effect close to the active-region edge), which is followed by an excitation of higher-order transverse modes with higher thresholds than the fundamental mode.

#### 4. Comparison of Self-Consistent Models Assuming Scalar and Vectorial Optical Approaches

Simple scalar optical approaches based on the general assumption of the optical field within the laser cavity in the form of a plane wave [22] reveal very good accuracy in comparison with experiment as shown in the preceding section. However, modern designs of VCSELs are often equipped with relatively small active regions to reduce their lasing thresholds. The cavity size becomes comparable to the laser wavelength so that the above plane wave assumption is no longer valid. Then, the much more complicated vectorial optical approaches have to be used, which require solving six

coupled equations for all components of both electric and magnetic fields. These algorithms are very involved, which increases the time taken to complete calculations by a factor of up to one hundred as compared to the scalar calculations. However, simplified scalar optical models sometimes give approximately correct results even beyond their confirmed range of validity. In such cases it may be unnecessary to use the full vectorial model.

We examine the limits of the scalar optical approach by comparing the threshold of a nitride VCSEL with more rigorous vectorial optical calculation. The reliability of the optical models used in the self-consistent analysis, that is, the plane wave admittance method and the effective frequency method, has been proved by comparison of their results obtained for the benchmark VCSEL structure from the COST-268 with those reported in [24]. The main conclusion drawn is that larger discrepancy occurs for the modal gain than for the emission wavelength and that the difference between them becomes larger for higher-order modes and smaller apertures where diffraction processes are essential [25].

Let us consider a possible structure of the GaN-based VCSELs (Figure 4) emitting at  $400 \text{ nm}$ . The structure and parameters used in the simulations are described in [26]. Our self-consistent simulation model is used to determine possible room-temperature CW performance characteristics of GaN-based VCSELs. We consider the fundamental  $\text{LP}_{01}$  scalar mode and the fundamental vectorial  $\text{HE}_{11}$  mode as well as the first-order  $\text{LP}_{11}$  scalar mode and corresponding

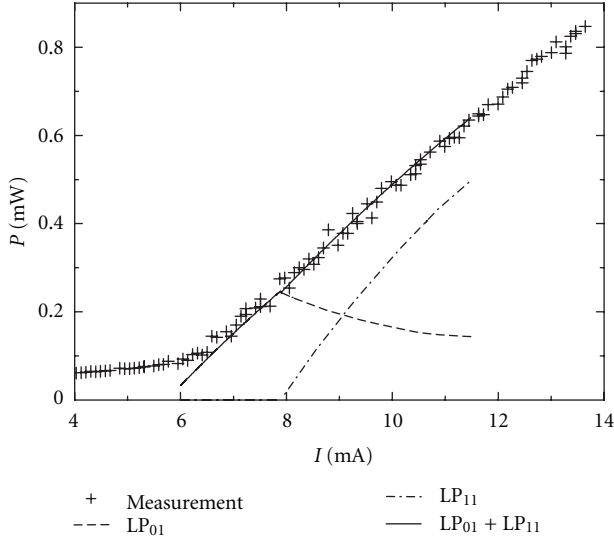


FIGURE 2: RT (18°C) CW light-current characteristic of the 10  $\mu\text{m}$  diameter 1.3  $\mu\text{m}$  InAs/GaAs quantum-dot GaAs-based oxide-confined (OC) VCSEL: crosses: experimental points, lines: theoretical curves; dash line: the LP<sub>01</sub> mode, dot-dash line: the LP<sub>11</sub> mode, and solid line: both the LP<sub>01</sub> and the LP<sub>11</sub> modes. Exactness of an output power measurement is not worse than 0.01 mW and that of an operation current is  $-0.1$  mA.

three vectorial HE<sub>21</sub>, TE<sub>01</sub>, and TM<sub>01</sub> first-order modes [27]. These three vectorial modes degenerate to the LP<sub>11</sub> mode in the scalar limit, but, as the difference between these three modes is rather small, we restricted our simulation to the HE<sub>21</sub> mode only.

RT CW threshold current of a particular mode  $I_{\text{th}}$  (Figure 5(a)) increases superlinearly with increasing  $r_A$ , mostly as a result of a steadily increasing active-region size. A possible impact of the active-region temperature (at threshold, its maximal value is increased from about 320 K for  $r_A = 2 \mu\text{m}$  to as high as 375 K for  $r_A = 8 \mu\text{m}$ , see Figure 5(b)) is ambiguous. It is followed by slightly lower and somewhat shifted material optical gain and some deterioration of other material properties but, at the same time, the radial thermal focusing leads to better optical confinement. Nevertheless, for too large active regions (i.e., for  $r_A > 8 \mu\text{m}$ ), the VCSEL does not reach the lasing threshold at all, probably because of its excessively high active-region temperature.

For relatively large active regions (Figure 5(a)), the first-order vectorial HE<sub>21</sub> mode becomes the lowest-threshold one. This is a consequence of the changes in the carrier-density radial profile for larger active regions (see Figure 5(c)) with its maximum close to the active-region edge. In addition, the first-order vectorial mode exhibits lower lasing threshold than that of the scalar one. The impact of diffraction losses in these large-size devices is reduced.

For a VCSEL design equipped with a tunnel junction and an n-type radial-current-spreading layer (instead of the p-type one), both the above optical methods have been found to give accurate results for the fundamental transverse mode, which confirms the general opinion that the scalar effective

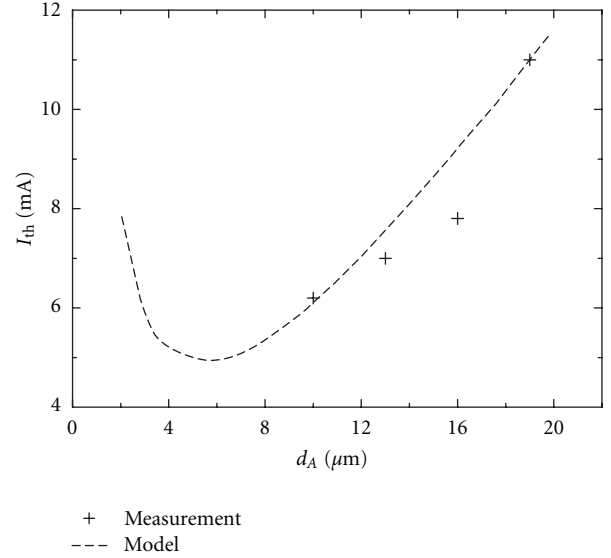


FIGURE 3: Dependence of the RT (18°C) CW threshold currents  $I_{\text{th}}$  of the 1.3  $\mu\text{m}$  top-emitting In(Ga)As/GaAs quantum-dot GaAs-based OC VCSELs on diameters  $d_A$  of their active regions: crosses: experimental points and dash line: simulation curve. Exactness of the diameter  $d_A$  seems to be not better than about  $2 \mu\text{m}$  because a final shape of an oxide aperture is not a perfect circle, but it resembles rather an ellipse.

frequency method yields reasonable results even beyond the range of its confirmed validity. Larger discrepancies are found for first-order transverse modes and for larger (or very small) active regions. For the same carrier concentration, the modal gain of the fundamental mode is usually somewhat higher (and the lasing threshold slightly lower), when it is determined using the vectorial approach, than that in the case of scalar one. The above is partly compensated by diffraction losses, not included in scalar approaches, which are more important for higher-order modes and smaller active regions. Therefore, contrary to the fundamental mode, modal gain determined for the same carrier concentration is higher (and the lasing threshold lower) for the first-order mode using the scalar optical approach than in the case of the vectorial one, especially in smaller devices. To summarize this comparison, simplified scalar optical approaches have been found to give approximately good results for fundamental transverse modes, but their accuracy is somewhat worse for first-order and higher-order modes as well as for large or very small VCSEL diameter.

## 5. Simulation of Oxide-Confined VCSELs

In this paragraph we consider various designs of oxide-confined (OC) VCSELs using our self-consistent model. We explore structures that produce single-mode operation for relatively large optical apertures, which enables high-power lasing.

A typical double-intracavity-contacted structure (with two ring contacts) of a 1.3  $\mu\text{m}$  OC GaAs-based (GaIn)(NAs)/GaAs quantum-well VCSEL with a single oxide aperture

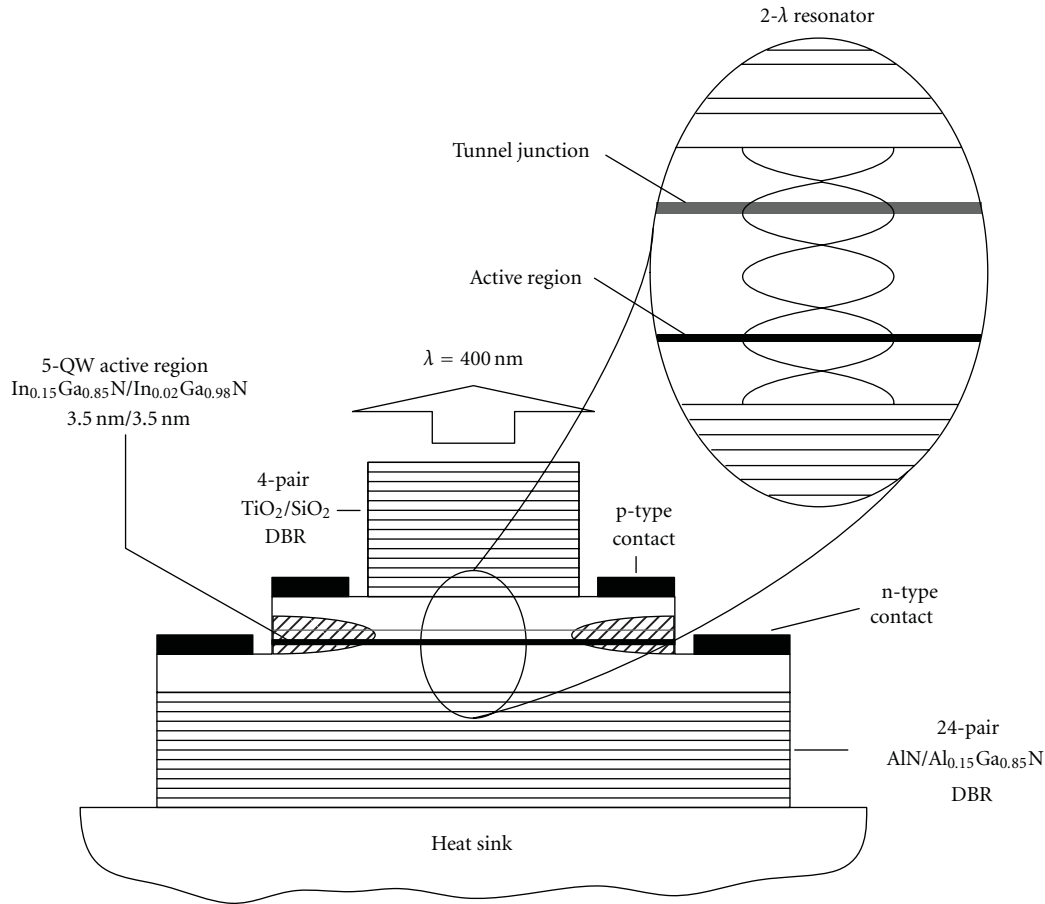


FIGURE 4: Structure of the modeled GaN-based VCSEL with the active region composing 5 quantum wells (MQW) and the tunnel junctions (TJ).

is shown in Figure 6 [28]. A radial selective oxidation is proposed to create an oxide aperture of radius  $r_A$  which serves as both an electrical (to funnel current spreading from annular contact towards the central active region) and an optical aperture (to confine an optical field in a radial direction). In the standard VCSEL structure, both the active region and the oxide aperture are located at the antinode positions of the optical standing wave (Figure 6). So the VCSEL is working as an index-guided (IG) device with a strong radial built-in index confinement.

Lasing thresholds of cavity modes depend on the overlap of their intensity profiles with the optical-gain distribution. The latter is directly associated with a radial profile of the threshold current density injected into the VCSEL active region (Figure 7), becoming in these double intracavity contacted VCSELs more and more nonuniform with increasing active-region radius  $r_A$  [25, 26]. Therefore, for larger  $r_A$  it is found that higher-order transverse modes become the lowest-threshold modes, which limits the desired Gaussian mode operation to relatively small active region diameter. These conclusions are confirmed in Figure 8 which shows the wavelength and maximum threshold gain of the lowest-threshold transverse LP modes versus the radius of the active region. As expected, fundamental mode operation is

possible in small VCSELs with an active-region radius not exceeding  $3 \mu\text{m}$ . An increase in the active-region size creates an increasing order of the lowest-threshold transverse mode.

The radial built-in index guiding (IG) is the strongest for an oxide aperture localized at an antinode position of the standing optical wave within the VCSEL cavity. Let us analyze the impact of the reduced waveguiding, which happens with a gradual shift of the aperture towards a node position in a VCSEL with a large active region diameter of  $20 \mu\text{m}$  (Figure 9). As one can see for relatively small shifts of the aperture, the radial built-in IG is still sufficient to confine the optical field with a very low threshold gain. However, when the aperture is shifted too far from the antinode position, the IG becomes ineffective and is replaced by the gain guiding (GG) mechanism, which requires much higher gain to reach the lasing action. As shown in Figure 9, a dramatic increase in the threshold gain from about  $1750 \text{ cm}^{-1}$  to as high as  $4900 \text{ cm}^{-1}$  occurs with a shift of the aperture. At the same time, instead of the high-order LP transverse modes, the fundamental LP<sub>01</sub> mode becomes the lowest-threshold mode. A similar behaviour may also be seen in Figure 10 for a VCSEL with a much smaller active-region diameter of only  $4 \mu\text{m}$ . In this case for all aperture positions, the fundamental mode remains the lowest-threshold mode, although its threshold

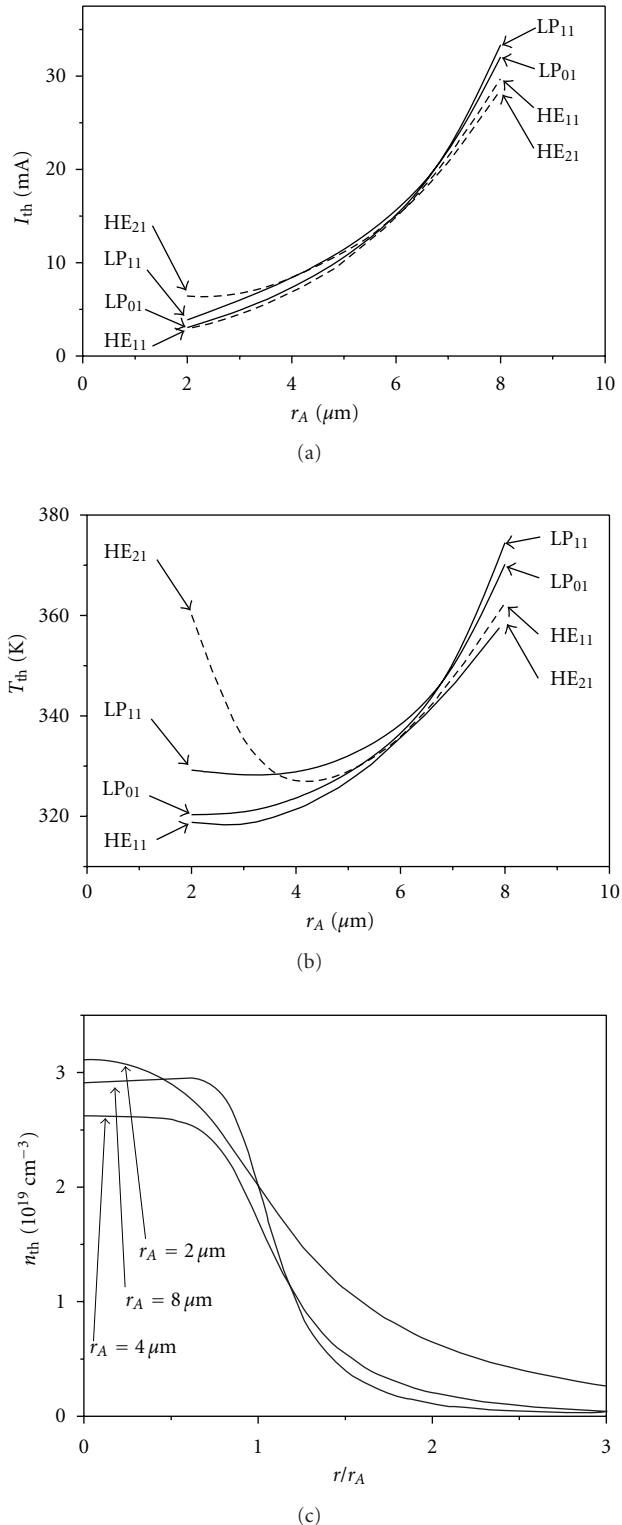


FIGURE 5: (a) RT CW threshold current of the particular modes  $I_{th}$  determined with the aid of the fully self-consistent approach for two, the lowest-order scalar and vectorial transverse, modes versus the active-region radius  $r_A$ . (b) The highest active-region temperature  $T_{th}$  in the threshold of the particular modes determined versus the radius of the active region  $r_A$ . (c) Radial profiles of the RT CW threshold carrier concentration  $n_{th}(r)$  determined for VCSELs equipped with active regions of various radii  $r_A$ .

for the GG regime is nearly six times higher than that for the IG one.

As expected, the single-fundamental-mode operation is achieved in IG VCSELs only for relatively small active regions but their lasing threshold remains very low even for VCSELs with the largest active regions considered. By contrast in GG VCSELs, the single-fundamental-mode operation is ensured for all devices, but their lasing thresholds are considerably higher.

The standard OC VCSEL with two identical oxide apertures [27] is equipped with a 3-wavelength-long cavity with apertures positioned exactly at the standing-wave antinode positions on both sides of its active region. The layered structure is very similar to that of the  $1.5\lambda$  cavity VCSEL with a single aperture: both DBR mirrors and the active region are identical, and only the n-type and p-type spacers are readjusted to create the  $3\lambda$  cavity and to locate both apertures at antinode positions. The operation of such a VCSEL with two identical oxide apertures has been theoretically analyzed in [28]. As expected, the threshold gain turns out to be somewhat lower than that of the  $1.5\lambda$  cavity IG VCSEL, but the desired single-fundamental-mode operation is again confined to small active regions of diameters not exceeding  $7 \mu\text{m}$ , which is consistent with experimental results reported by Degen et al. [29]. A further increase in the active-region size is followed by a gradual increase in the mode order of the lowest-threshold transverse mode.

Let us consider a new approach [30, 31] proposed to enhance the single mode operation in larger OC VCSELs with two oxide apertures: one of them is shifted to the node position, where it behaves as an electrical aperture only, whereas the second aperture remains at antinode position (the spacer thicknesses are properly adjusted). In this design the diameters of the two apertures may be changed independently giving an additional degree of freedom. In particular, the radial current spreading between the annular n-side and p-side contacts and the central active region and the radial optical waveguiding may be optimized independently.

Since the kinetics of the oxidation is strongly dependent on temperature but also on compositions and thicknesses of oxidized (AlGa)As layers [32], it is possible that apertures of different diameters may be produced in one oxidation process.

The proposed VCSEL structure is a radial equivalent of the separate-confinement-heterostructure (SCH) [33, 34], which is created in the direction perpendicular to layer boundaries (Figure 11). In the SCH active region, both the carrier confinement in the thin active region and the field confinement within the wider cavity are produced independently by two (inner and outer) heterojunction pairs. By analogy, the proposed VCSEL structure shown in Figure 12 is able to independently create an active-region current-density profile and a radial optical index guiding with the aid of two different oxide apertures is called the separate-confinement-oxidation (SCO) structure [32] (Figure 11).

The impact of a steadily reduced radius  $r_E$  of the electrical aperture on the RT CW lasing threshold of a  $20 \mu\text{m}$  diameter SCO VCSEL is shown in Figure 13. As expected, when the

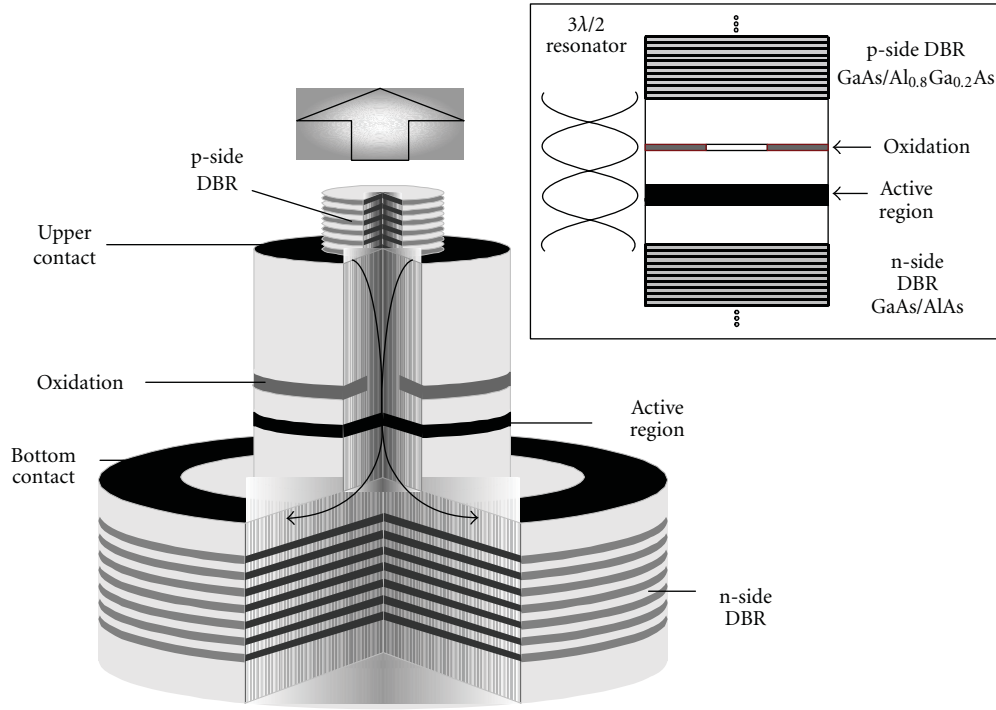


FIGURE 6: A typical double-intracavity-contacted structure of standard GaAs-based oxide-confined (OC) VCSEL with a single oxide aperture located at an antinode position of the optical standing wave within the VCSEL  $1.5 \lambda$  cavity.

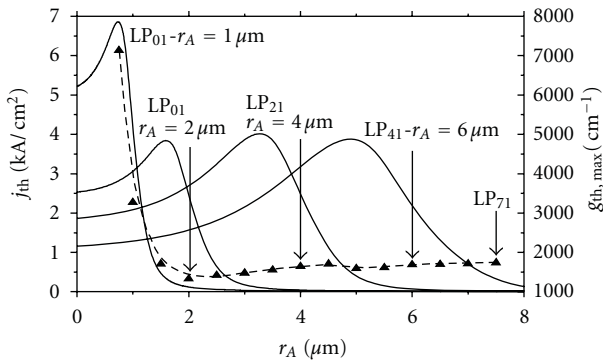


FIGURE 7: Radial profiles of the threshold current densities  $j_{th}$  of the indicated lowest-threshold LP modes determined for different radii  $r_A$  of the active region of the index-guided double-intracavity-contacted  $1.5 \lambda$  cavity GaInNAs/GaAs DQW VCSEL.

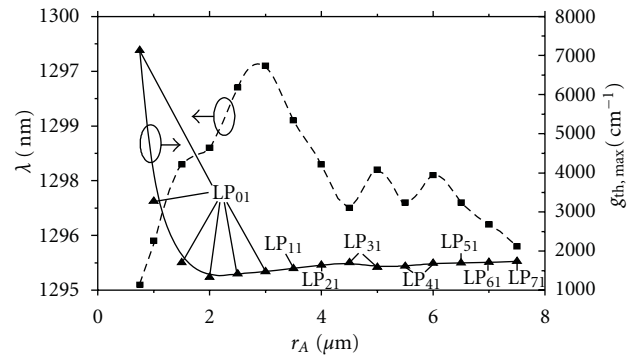


FIGURE 8: Wavelengths  $\lambda$  of the indicated lowest-threshold cavity modes (dashed curve) and their maximal threshold optical gain  $g_{th,max}$  (solid curve) in the index-guided  $1.5 \lambda$  cavity double-intracavity-contacted GaInNAs/GaAs DQW VCSEL.

oxide apertures are of the same size ( $r_A = r_E$ ), the high-order transverse  $LP_{12}$  mode exhibits the lowest RT CW lasing threshold. A decrease of  $r_E$  creates a gradual decrease in the mode order, accompanied by a considerable increase of the lasing threshold (Figure 13) and an active-region temperature increase  $\Delta T_{A,max}$  (Figure 14). For diameters of the electrical aperture smaller than  $15 \mu m$ , the desired stable single-fundamental-mode operation is achieved. The threshold optical gain is initially reduced because of a better overlap between both the distributions of the mode intensity and the optical gain; for smaller electrical apertures, the threshold optical gain increases again due to increased

losses in the passive areas. For decreasing  $r_E$  in Figure 13, the threshold current,  $I_{th}$ , reaches its maximum value at  $r_E \approx 7.5 \mu m$  and then continuously reduces because of the reduction of the active-region area. The wavelength of the lowest-threshold transverse mode depends on its penetration into the low-refractive-index oxide layer, which is larger for the higher-order transverse modes than for the lowest-order  $LP_{01}$  one. That is why the  $LP_{01}$  fundamental mode exhibits the longest wavelength.

Our theoretical model of the proposed SCO VCSEL configuration is consistent with the experimental work by Samal et al. [35]. As in the SCO VCSEL, two apertures

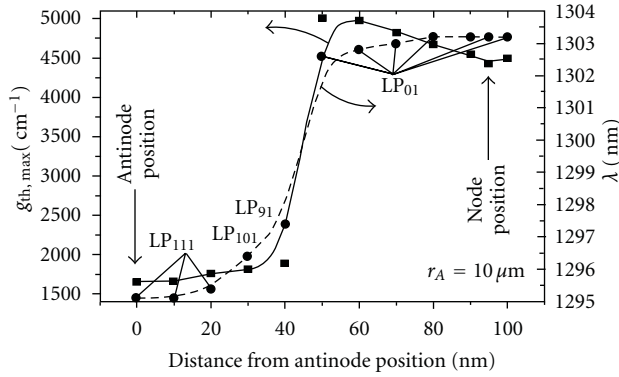


FIGURE 9: Maximal RT CW threshold optical gain  $g_{th,max}$  (solid line) and wavelength  $\lambda$  (dashed line) of the indicated lowest-threshold LP modes for 20  $\mu\text{m}$  diameter 1.5  $\lambda$  cavity double-intracavity-contacted GaInNAs/GaAs DQW VCSEL as a function of the distance of the oxide aperture from its antinode position within a laser cavity.

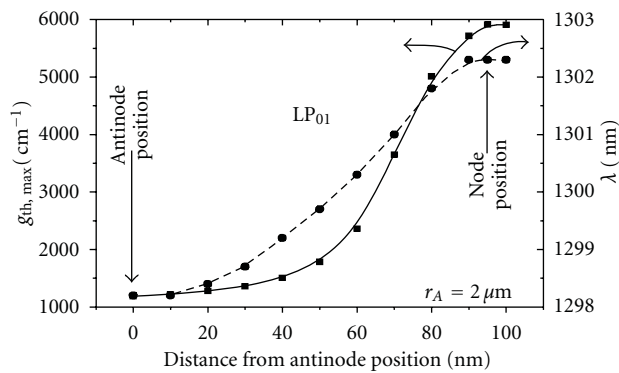


FIGURE 10: Maximal RT CW threshold optical gain  $g_{th,max}$  (solid line) and wavelength  $\lambda$  (dashed line) of the indicated lowest-threshold LP<sub>01</sub> mode determined for the 4  $\mu\text{m}$  diameter 1.5  $\lambda$ -cavity double intracavity contacted GaInNAs/GaAs DQW VCSEL as a function of the distance of the oxide aperture from its antinode position within a laser cavity.

of different diameters on both sides of the VCSEL active region are utilized leading to dramatically improved mode selectivity. However, there are insufficient details (such as cavity length) given in this paper to compare this structure with ours. Assuming that the active region is located at the antinode position, the larger aperture is placed close to the next antinode position, so it behaves as both an electrical and optical aperture. However, the second aperture is located relatively far from the active region. Nevertheless, Samal et al. [35] have observed single-fundamental-mode operation of their VCSELs with two oxide apertures, whereas their VCSEL with only one oxide aperture located close to the antinode position emits the high-order LP<sub>31</sub> transverse mode, which is consistent with our model.

## 6. Simulation of Photonic Crystal VCSELs

In this section we present numerical analysis of PhC VCSELs, which is aimed primarily at designing a PhC pattern that

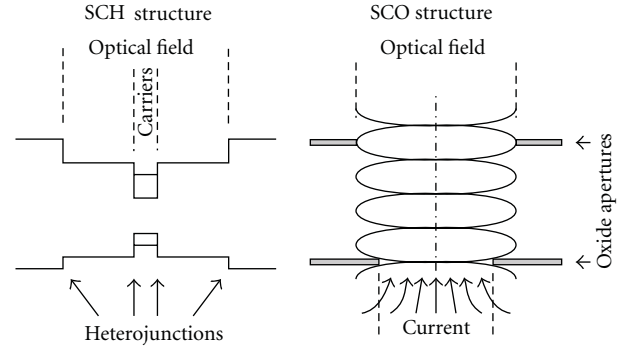


FIGURE 11: A comparison of the separate-confinement-heterostructure (SCH) and the separate-confinement-oxidation (SCO) structures.

assures single-mode operation and simultaneously reduction of the threshold current with respect to the VCSEL without the PhC. To fully reflect the complexity of the phenomena taking place in PhC VCSEL operation, a self-consistent model comprising three-dimensional, vectorial optical, thermal, electrical, and recombination submodels is used in the analysis.

For simulation purposes we have chosen an InP-based, 1300-nm AlInGaAs VCSEL with tunnel junction carrier injection described in [36]. The lattice constant of PhC and hole diameter equal 3.2 and 1.6  $\mu\text{m}$ , respectively. Although the results presented here are obtained for this particular device, we believe that such phenomena as the dependences of threshold current on electrical aperture and etching depth are quite general and would show qualitatively the same trends for other PhC VCSELs. However, the optimized parameters cannot be used straightforwardly for PhC VCSELs based on different material systems mostly because of the different wavelength of emission.

In the analysis we consider the fundamental (HE<sub>11</sub> mode which relates to scalar mode LP<sub>01</sub>) and the first-order mode (HE<sub>21</sub> mode being the vectorial analog to the LP<sub>11</sub> mode) and we determine their threshold characteristics. Specifically we calculate their threshold currents as a function of etching depth, which is presented in Figure 15. An increase of the etching depth in the range from 0 to 5  $\mu\text{m}$  leads to an increase in both threshold currents, which reveals that shallow holes cause leakage of the light and therefore higher modal losses. As soon as the holes become deep enough to interact with the mode, the threshold currents  $I_{th}$  of both modes start to decrease with etching depth. Holes etched through the top DBR and into the cavity assure threshold current close to a minimum value. Further increase in the etch depth does not change significantly the threshold current. The existence of such a plateau is due to the maximum mode confinement for the etching through the cavity, where the intensity of the mode is the largest.

The threshold current dependences on etching depth are qualitatively similar for the two modes: they display maxima at a certain etching depth. The HE<sub>21</sub> mode interacts weaker with the PhC than the HE<sub>11</sub> mode; because the HE<sub>21</sub> mode is less confined, more light of HE<sub>21</sub> is escaping to the air

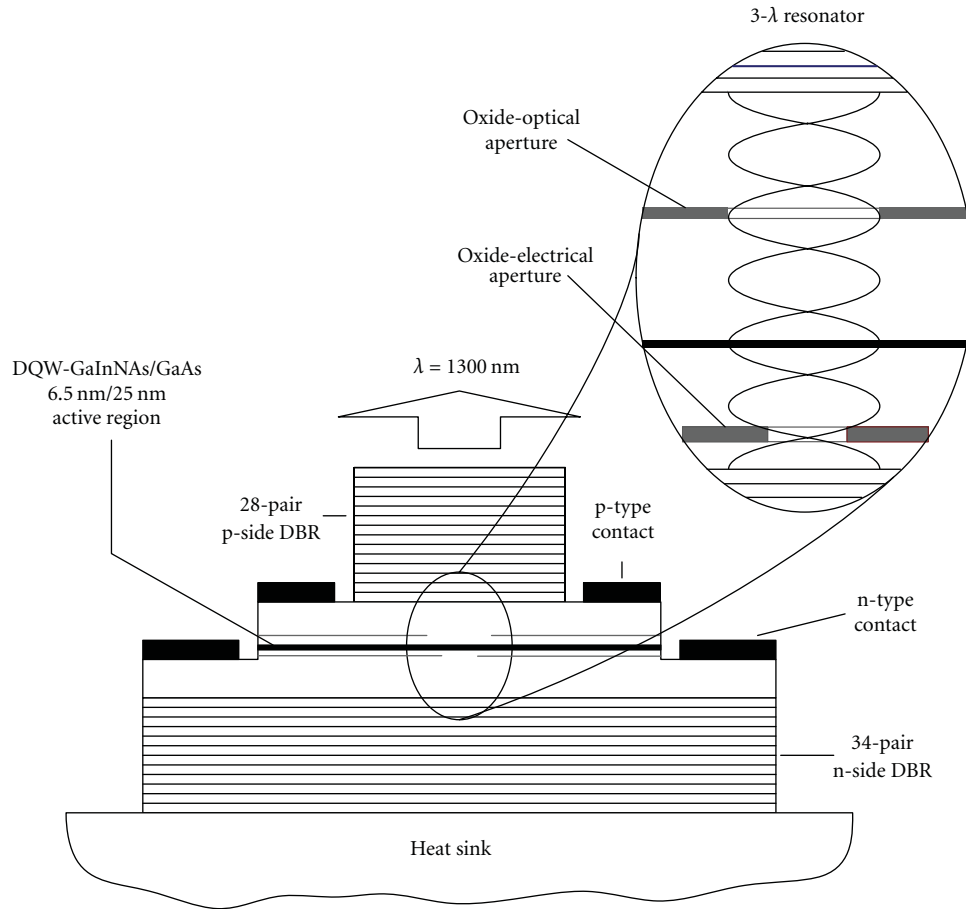


FIGURE 12: The considered structure of the  $1.3 \mu\text{m}$   $3 \lambda$  cavity SCO GaInNAs/GaAs DQW VCSEL.

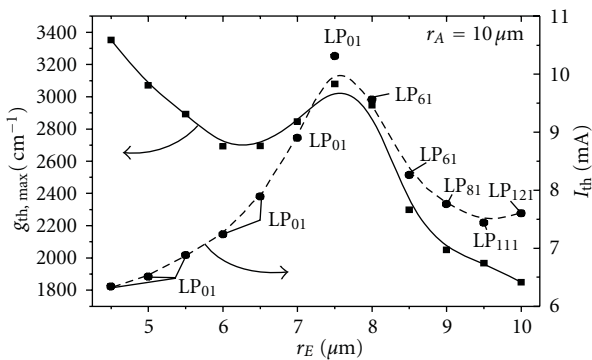


FIGURE 13: Impact of the radius  $r_E$  of the electrical aperture on the RT CW maximal threshold gain  $g_{th,max}$  and threshold current  $I_{th}$  of the indicated lowest-threshold transverse LP modes determined for the large-size  $20 \mu\text{m}$  diameter SCO VCSEL.

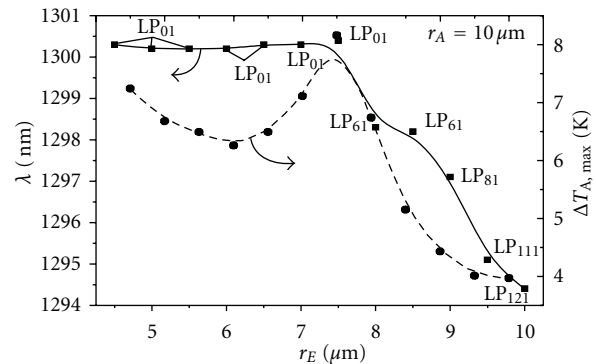


FIGURE 14: Impact of the radius  $r_E$  of the electrical aperture on the RT CW maximal active-region temperature increase  $\Delta T_{A,max}$  and wavelength  $\lambda$  of the indicated lowest-threshold transverse modes of the large-size  $20 \mu\text{m}$  diameter SCO VCSEL.

holes hence deeper holes are necessary to achieve similar confinement to that observed for the fundamental mode. This behavior causes the first-order mode to suffer large losses for an etching depth, which is sufficient to confine the fundamental mode and to lower its threshold current. By proper optimization of the PhC, such as etching depth

and optical aperture diameter, it is possible to simultaneously achieve low threshold current and strong higher-order mode discrimination in PhC VCSELs [37, 38]. In the hatched region in Figure 15, the threshold current for the  $HE_{11}$  mode is lower and simultaneously the differences of the threshold currents of the  $HE_{21}$  and  $HE_{11}$  modes are larger than in the

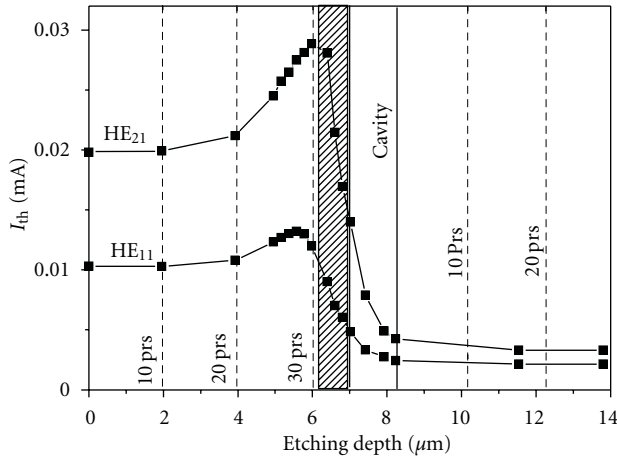


FIGURE 15: Threshold currents of the  $HE_{11}$  and  $HE_{21}$  modes as a function of the etching depth. The borders of the cavity and successive ten pairs of top and bottom DBRs are assigned by vertical lines. The region of strong discrimination and low threshold is assigned by hatched rectangle.

case of VCSEL without PhC; this indicates the optimal range of etching depths assuring high modal discrimination.

One can determine the region of optimal lattice constant and etching depth of a PhC pattern as shown Figure 16. For the sake of comparison, these regions are calculated for a tunnel junction VCSEL and for a proton-implanted VCSEL. These VCSEL structures differ by the relatively uniform gain spatial distribution in the first case and the strong current crowding in the second one [38].

## 7. Simulation of Photonic Crystal VCSELs for Enhanced Polarization Control

For several years, PhCs have been successfully used for providing birefringence and dichroism in Photonic Crystal fibers, although there are not many works for such PhC application in VCSELs. So far, only one such successful experimental attempt is reported in [39], where photonic crystal with elliptical holes is applied to provide stable polarization lasing. In that work, the stabilization of polarization with over 20 dB polarization mode suppression ratio (PMSR) is achieved with hexagonal lattice PhC with air holes elongated along the  $K$  and  $M$  crystallographic directions. Quite importantly, the PhC effect is accompanied by an anisotropic current injection that according to our investigations is the main reason of the observed dichroism. If we neglect this effect, we can observe that for the structure presented in Figure 17 modal dichroism is negligible; however, a slight frequency separation appears, as shown in Figure 18. This separation can be used to promote one of the polarizations due to the better overlap with the gain profile.

As can be seen from Figure 18, the hole structure with elliptical holes provides approximately 180 GHz frequency separation and no dichroism. From a practical point of view, this is not enough to ensure stable single polarization of the emitted light. Hence, we propose another design, based

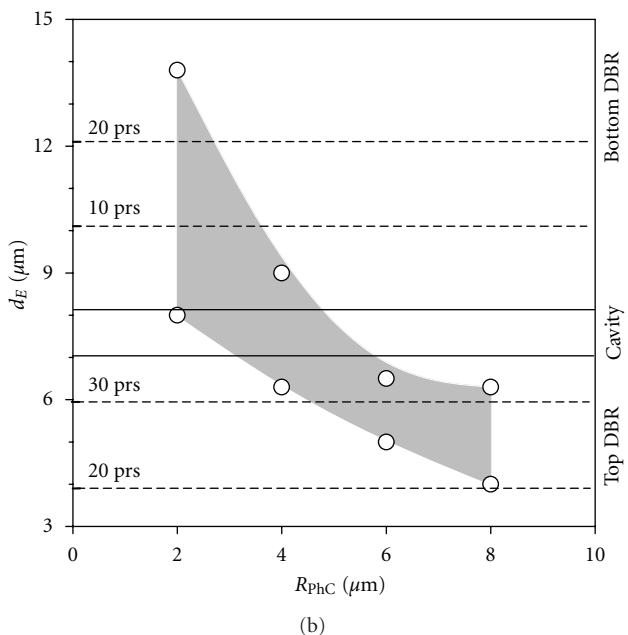
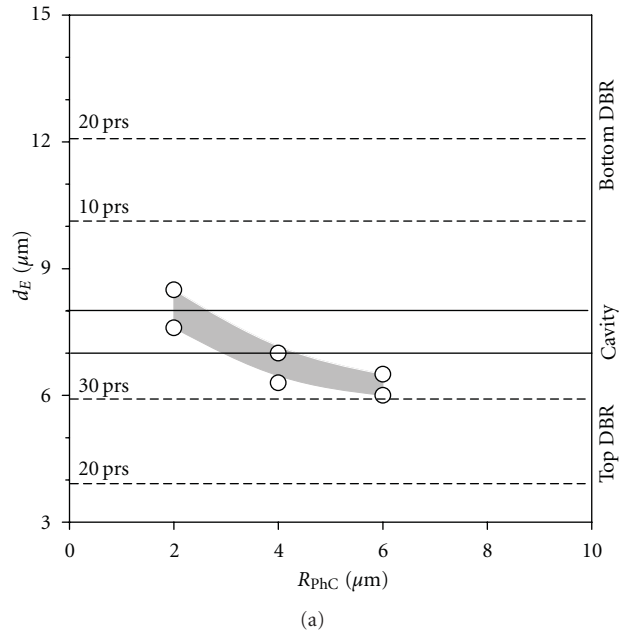


FIGURE 16: Regions of low threshold and strong mode discrimination (gray field) mapped in the plane of etching depth and optical aperture  $R_A$  for  $a/L = 0.5$  in the case of VCSEL with tunnel junction (a) and proton implanted (b).

on dichroic optical fiber [40]. The hole structure presented in Figure 19 provides over 7% dichroism and more than 400 GHz of frequency splitting between the two orthogonally polarized fundamental modes.

The optical mode is confined by the photonic crystal pattern of Figure 19 with  $C_6$  symmetry broken by four holes with diameter two times larger than the other holes. The factor of two-hole diameter enhancement is important, as its decrease quickly reduces the birefringence and dichroism, while further increase is hard to achieve due to the resulting

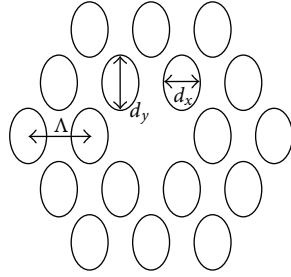


FIGURE 17: Schematic diagram of elliptical photonic crystal.

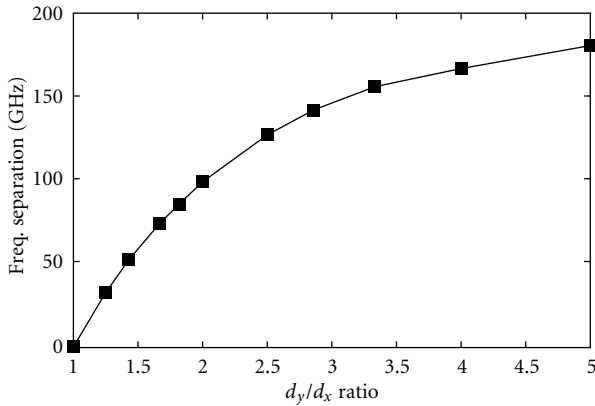


FIGURE 18: Resonant frequency separation of the  $x$ - and  $y$ -polarized modes for the structure with elliptical holes as a function of the  $d_x/d_y$  ratio.

thin walls between holes. The computed birefringence and dichroism of this structure are presented in Figures 20 and 21. It turns out that a small hole in the middle plays crucial role for the polarization stabilization as it increases the overlap of the mode with the region where the large holes are located and thus the crystal symmetry is broken. Figure 22 shows electric field profiles for the two orthogonal polarizations with different sizes of this hole.

### 8. Conclusions

We have presented a detailed self-consistent way of modeling the various physical phenomena that occur within a VCSEL. The simulation comprises thermal, electrical, optical, and gain submodels. All of the submodels are combined in a self-consistent manner. Such an approach allows consideration of nonlinear effects occurring during the laser emission, such as spatial hole burning. We first showed the conformity of the numerical model with experimental results. In particular, we have shown that the model reproduces very precisely the experimental characteristics of both emitted power as a function of current and threshold current versus the diameter of oxide aperture.

Modern designs of VCSELs are often equipped with relatively small active regions to reduce their lasing thresholds, and, as result, diffraction effects become significant. In order to precisely analyze such devices, more accurate

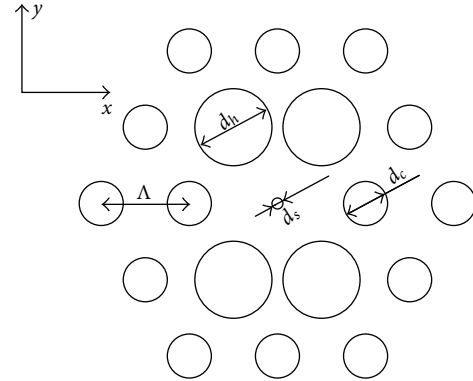


FIGURE 19: Schematic diagram of birefringent photonic crystal for light confinement in polarization-stable VCSEL.

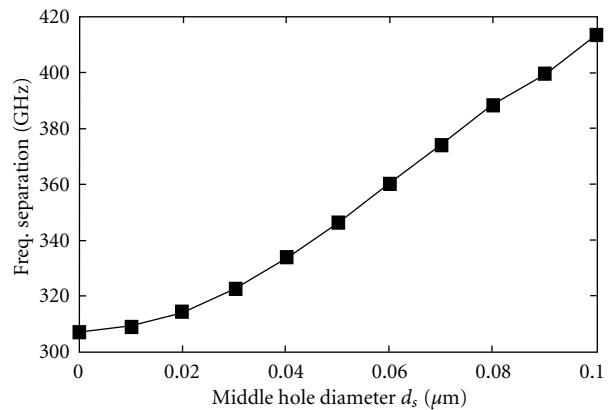


FIGURE 20: Frequency separation between the two orthogonal linearly polarized fundamental VCSEL modes as a function of the middle hole diameter.

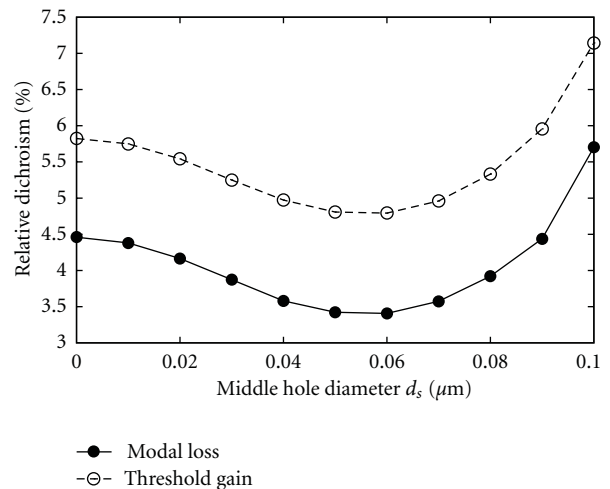


FIGURE 21: Relative loss/threshold gain difference between the two orthogonal polarized VCSEL fundamental modes as a function of the middle hole diameter.

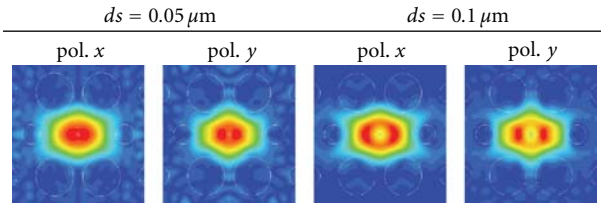


FIGURE 22: Electrical field profiles of both polarizations for the birefringent PhC structure for two different sizes of the middle hole.

vectorial models are necessary since simple scalar models are applicable only for optical apertures several times larger than the wavelength of the cavity mode. Our comparative analysis showed that the scalar model is accurate for the fundamental mode and standard devices. Higher-order mode analysis, devices with narrow or very wide apertures—for which subtle thermal issues affecting waveguiding become prominent—should be analyzed with vectorial optical models. Our self-consistent model has been used to design oxide-confined VCSELs that exhibit stable, single-mode operation. The typical VCSEL structure with an oxide layer positioned at an antinode position provides strong optical confinement, which favors high-order modes for broader than  $6 \mu\text{m}$  optical apertures.

The way to support single-mode operation for broader apertures is through weakening of the optical confinement. That can be realized by shifting the oxide layer away from the antinode position. Such approach assures single-mode operation, at the expense of a rapidly growing threshold current. The design comprises two oxidations: one layer in a field node position and another one in an antinode position. The first narrower oxide aperture funnels the current, while the second thicker oxide aperture confines the mode. Such a design provides stable single-mode operation up to electrical diameters as large as  $15 \mu\text{m}$ .

Another analyzed method to achieve stable single-mode operation that additionally reduces the threshold current is the introduction of a photonic crystal pattern of holes into the VCSEL. We showed that precise numerical simulation can predict the photonic crystal parameters that lead to improving the VCSEL performance with respect to mode discrimination and high power simultaneously. To assure not only the single-mode but also single-polarization operation, additional patterning of the photonic crystal is necessary. We presented the modeling of a photonic crystal VCSEL with an irregular geometry of holes, which enables large polarization mode suppression ratio.

Numerical modeling is a very powerful tool for designing VCSELs and exploring new phenomena. It is much cheaper than the trial and error method and allows for predicting behaviors of devices that do not yet exist. However, the assumptions used in deriving the models, the VCSEL parameters, and boundary conditions should be very closely related to the experiment. The step that should be always done first for a VCSEL model is its calibration with the measurements. This might be a time-consuming process but it is necessary to keep the theoretical analysis attached to reality.

## Acknowledgments

The authors wish to thank Professor K. D. Choquette for his kind assistance in editing the manuscript. This work is supported by Grant no. N N515 533338 from the Polish Ministry of Science and Higher Education (MNiSzW) and by the Swiss National Science Foundation (SNF) through Grant SCOPES IZ73ZO.128019, COST MP0702.

## References

- [1] H. Li and K. Iga, Eds., *Vertical-Cavity Surface-Emitting Laser Devices*, vol. 6 of *Springer Series in Photonics*, Springer, Berlin, Germany, 2002.
- [2] W. Nakwaski, “Principles of VCSEL designing,” *Opto-electronics Review*, vol. 16, no. 1, pp. 18–26, 2008.
- [3] R. P. Sarzała and W. Nakwaski, “Optimization of  $1.3 \mu\text{m}$  GaAs-based oxide-confined (GaIn)(NAs) vertical-cavity surface-emitting lasers for low-threshold room-temperature operation,” *Journal of Physics*, vol. 16, pp. S3121–S3140, 2004.
- [4] R. P. Sarzała, “Designing strategy to enhance mode selectivity of higher-output oxide-confined vertical-cavity surface-emitting lasers,” *Applied Physics A*, vol. 81, no. 2, pp. 275–283, 2005.
- [5] D. Xu, C. Tong, S. F. Yoon et al., “Room-temperature continuous-wave operation of the In(Ga)As/GaAs quantum dot VCSELs for the  $1.3 \mu\text{m}$  optical-fibre communication,” *Semiconductor Science and Technology*, vol. 24, no. 5, Article ID 055003, 2009.
- [6] J. Dellunde, A. Valle, and K. A. Shore, “Transverse-mode selection in external-cavity vertical-cavity surface-emitting laser diodes,” *Journal of the Optical Society of America B*, vol. 13, no. 11, pp. 2477–2483, 1996.
- [7] A. Valle, “Selection and modulation of high-order transverse modes in vertical-cavity surface-emitting lasers,” *IEEE Journal of Quantum Electronics*, vol. 34, no. 10, pp. 1924–1932, 1998.
- [8] M. Wasiak, “Quantum-enhanced uniformity of carrier injection into successive quantum wells of multi-quantum-well structures,” *Physica E*, vol. 41, pp. 1253–1257, 2009.
- [9] H. J. Unold, S. W. Z. Mahmoud, R. Jäger, M. Grabherr, R. Michalzick, and K. J. Ebeling, “Large-area single-mode VCSELs and the self-aligned surface relief,” *IEEE Journal on Selected Topics in Quantum Electronics*, vol. 7, no. 2, pp. 386–392, 2001.
- [10] D.-S. Song, S.-H. Kim, H.-G. Park et al., “Single-fundamental-mode photonic-crystal vertical-cavity surface-emitting lasers,” *Applied Physics Letters*, vol. 80, pp. 3901–3903, 2002.
- [11] D. Zhou and L. J. Mawst, “High-power single-mode antiresonant reflecting optical waveguide-type vertical-cavity surface-emitting lasers,” *IEEE Journal of Quantum Electronics*, vol. 38, no. 12, pp. 1599–1606, 2002.
- [12] A. Haglund, J. S. Gustavsson, J. Vukušić, P. Modh, and A. Larsson, “Single fundamental-mode output power exceeding 6 mW from VCSELs with a shallow surface relief,” *IEEE Photonics Technology Letters*, vol. 16, no. 2, pp. 368–370, 2004.
- [13] B. Kögel, M. Maute, H. Halbritter et al., “High singlemode output power from long-wavelength VCSELs using curved micro-mirrors for mode control,” *Electronics Letters*, vol. 41, no. 17, pp. 966–967, 2005.
- [14] H. P. D. Yang, Y. H. Chang, F. I. Lai et al., “Singlemode InAs quantum dot photonic crystal VCSELs,” *Electronics Letters*, vol. 41, no. 20, pp. 1130–1132, 2005.
- [15] P. Debernardi, J. M. Ostermann, M. Feneberg, C. Jolics, and R. Michalzick, “Reliable polarization control of VCSELs through

- monolithically integrated surface gratings: a comparative theoretical and experimental study," *IEEE Journal on Selected Topics in Quantum Electronics*, vol. 11, no. 1, pp. 107–116, 2005.
- [16] K. D. Choquette, R. P. Schneider, K. L. Lear, and R. E. Leibenguth, "Gain-dependent polarization properties of vertical-cavity lasers," *IEEE Journal on Selected Topics in Quantum Electronics*, vol. 1, no. 2, pp. 661–666, 1995.
- [17] K. Panajotov, B. Ruykin, J. Danckaert, M. Peeters, H. Thienpont, and I. Veretennicoff, "Polarization switching in VCSELs due to thermal lensing," *IEEE Photonics Technology Letters*, vol. 10, no. 1, pp. 6–8, 1998.
- [18] M. Sciamanna, K. Panajotov, H. Thienpont, I. Veretennicoff, P. Mégret, and M. Blondel, "Optical feedback induces polarization mode hopping in vertical-cavity surface-emitting lasers," *Optics Letters*, vol. 28, no. 17, pp. 1543–1545, 2003.
- [19] I. Gatare, M. Sciamanna, J. Buesa, H. Thienpont, and K. Panajotov, "Nonlinear dynamics accompanying polarization switching in vertical-cavity surface-emitting lasers with orthogonal optical injection," *Applied Physics Letters*, vol. 88, no. 10, Article ID 101106, 2006.
- [20] G. R. Hadley, "Effective index model for vertical-cavity surface-emitting lasers," *Optics Letters*, vol. 20, no. 13, pp. 1483–1485, 1995.
- [21] H. Wenzel and H. J. Wünsche, "The effective frequency method in the analysis of vertical-cavity surface-emitting lasers," *IEEE Journal of Quantum Electronics*, vol. 33, no. 7, pp. 1156–1162, 1997.
- [22] C. W. Tee and S. F. Yu, "Design and analysis of cylindrical antiresonant reflecting optical waveguide," *Journal of Lightwave Technology*, vol. 21, no. 12, pp. 3379–3386, 2003.
- [23] R. Mittra and U. Pekel, "New look at the perfectly matched layer (PML) concept for the reflectionless absorption of electromagnetic waves," *IEEE Microwave and Guided Wave Letters*, vol. 5, no. 3, pp. 84–86, 1995.
- [24] D. Xu, C. Tong, S. F. Yoon et al., "Room-temperature continuous-wave operation of the In(Ga)As/GaAs quantum-dot VCSELs for the 1.3  $\mu\text{m}$  optical-fibre communication," *Semiconductor Science and Technology*, vol. 24, no. 5, Article ID 055003, 2009.
- [25] T. Czyszanowski, M. Dems, H. Thienpont, and K. Panajotov, "Full vectorial electromagnetic modeling of vertical-cavity surface-emitting diode lasers by the plane wave admittance method," in *VCSELs: Stability Control and High Performance*, Proceedings of SPIE, p. 36, Strasburg, France, April 2006.
- [26] T. Czyszanowski, M. Wasiak, R. P. Sarzała, and W. Nakwaski, "Exactness of simplified scalar optical approaches in modelling a threshold operation of possible nitride vertical-cavity surface-emitting diode lasers," *Physica Status Solidi (A)*, vol. 204, no. 10, pp. 3562–3573, 2007.
- [27] W. Nakwaski and P. Maćkowiak, "Transverse-mode selectivity in possible nitride vertical-cavity surface-emitting lasers," *Optical and Quantum Electronics*, vol. 35, no. 11, pp. 1037–1054, 2003.
- [28] R. P. Sarzała, "Modeling of the threshold operation of 1.3- $\mu\text{m}$  GaAs-based oxide-confined (InGa)As-GaAs quantum-dot vertical-cavity surface-emitting lasers," *IEEE Journal of Quantum Electronics*, vol. 40, no. 6, pp. 629–634, 2004.
- [29] C. Degen, I. Fischer, and W. Elsässer, "Transverse modes in oxide confined VCSELs: influence of pump profile, spatial hole burning, and thermal effects," *Optics Express*, vol. 5, no. 3, pp. 38–47, 1999.
- [30] R. P. Sarzała and W. Nakwaski, "Separate-Confined-Oxidation (SCO) VCSEL structure," *Journal of Applied Physics*, vol. 99, Article ID 123110, 2003.
- [31] R. P. Sarzała, P. Mendla, M. Wasiak, P. Maćkowiak, M. Bugajski, and W. Nakwaski, "Comprehensive self-consistent three-dimensional simulation of an operation of the GaAs-based oxide-confined 1.3- $\mu\text{m}$  quantum-dot (InGa)As/GaAs vertical-cavity surface-emitting lasers," *Optical and Quantum Electronics*, vol. 36, pp. 331–347, 2004.
- [32] W. Nakwaski, M. Wasiak, P. Maćkowiak et al., "Oxidation kinetics of AlAs and (AlGa)As layers in arsenide-based diode lasers: comparative analysis of available experimental data," *Semiconductor Science and Technology*, vol. 19, pp. 333–341, 2004.
- [33] M. B. Panish, H. C. Casey, S. Sumski, and P. W. Foy, "Reduction of threshold current density in GaAs/Al<sub>x</sub>Ga<sub>1-x</sub> As heterostructure lasers by separate optical and carrier confinement," *Applied Physics Letters*, vol. 22, no. 11, pp. 590–591, 1973.
- [34] W. C. Ng, Y. Liu, and K. Hess, "Resonant-wavelength control and optical-confinement analysis for graded SCH VCSELs using a self-consistent effective-index method," *Journal of Lightwave Technology*, vol. 21, no. 2, pp. 555–560, 2003.
- [35] N. Samal, S. R. Johnson, D. Ding, A. K. Samal, S. Q. Yu, and Y. H. Zhang, "High-power single-mode vertical-cavity surface-emitting lasers," *Applied Physics Letters*, vol. 87, no. 16, Article ID 161108, 3 pages, 2005.
- [36] T. Czyszanowski, M. Dems, H. Thienpont, and K. Panajotov, "Optimal radii of photonic crystal holes within DBR mirrors in long wavelength VCSEL," *Optics Express*, vol. 15, no. 3, pp. 1301–1306, 2007.
- [37] T. Czyszanowski, R. P. Sarzała, M. Dems, H. Thienpont, W. Nakwaski, and K. Panajotov, "Strong modes discrimination and low threshold in cw regime of 1300 nm AlInGaAs/InP VCSEL induced by photonic crystal," *Physica Status Solidi (A)*, vol. 206, no. 7, pp. 1396–1403, 2009.
- [38] T. Czyszanowski, R. P. Sarzała, M. Dems, W. Nakwaski, H. Thienpont, and K. Panajotov, "Optimal photonic-crystal parameters assuring single-mode operation of 1300 nm AlInGaAs vertical-cavity surface-emitting laser," *Journal of Applied Physics*, vol. 105, no. 9, Article ID 093102, 2009.
- [39] D. S. Song, Y. J. Lee, H. W. Choi, and Y. H. Lee, "Polarization-controlled, single-transverse-mode, photonic-crystal, vertical-cavity, surface-emitting lasers," *Applied Physics Letters*, vol. 82, no. 19, pp. 3182–3184, 2003.
- [40] M. Dems, T. Czyszanowski, H. Thienpont, and K. Panajotov, "Highly birefringent and dichroic photonic crystal VCSEL design," *Optics Communications*, vol. 281, no. 11, pp. 3149–3152, 2008.

## Review Article

# Semiconductor Disk Lasers: Recent Advances in Generation of Yellow-Orange and Mid-IR Radiation

**Mircea Guina, Antti Härkönen, Ville-Markus Korpijärvi,  
Tomi Leinonen, and Soile Suomalainen**

*Optoelectronics Research Centre, Tampere University of Technology, P.O. Box 692, 33101 Tampere, Finland*

Correspondence should be addressed to Mircea Guina, mircea.guina@tut.fi

Received 15 September 2011; Accepted 23 November 2011

Academic Editor: Rainer Michalzik

Copyright © 2012 Mircea Guina et al. This is an open access article distributed under the Creative Commons Attribution License, which permits unrestricted use, distribution, and reproduction in any medium, provided the original work is properly cited.

We review the recent advances in the development of semiconductor disk lasers (SDLs) producing yellow-orange and mid-IR radiation. In particular, we focus on presenting the fabrication challenges and characteristics of high-power GaInNAs- and GaSb-based gain mirrors. These two material systems have recently sparked a new wave of interest in developing SDLs for high-impact applications in medicine, spectroscopy, or astronomy. The dilute nitride (GaInNAs) gain mirrors enable emission of more than 11 W of output power at a wavelength range of 1180–1200 nm and subsequent intracavity frequency doubling to generate yellow-orange radiation with power exceeding 7 W. The GaSb gain mirrors have been used to leverage the advantages offered by SDLs to the 2–3  $\mu\text{m}$  wavelength range. Most recently, GaSb-based SDLs incorporating semiconductor saturable absorber mirrors were used to generate optical pulses as short as 384 fs at 2  $\mu\text{m}$ , the shortest pulses obtained from a semiconductor laser at this wavelength range.

## 1. Introduction

Conceptually, the idea of an optically pumped semiconductor disk laser (OP-SDLs) was suggested already in 1966 by Basov et al. in a paper describing lasers with radiating mirrors [1]. However, it was not until the 1990s that the concept was acknowledged and the first working devices were reported [2–6]. In its essence, the concept of an OP-SDL is based on using an optically pumped semiconductor gain structure (i.e., gain mirror) with vertical emission. We note here that in addition to OP-SDL, also acronyms like OP-VECSEL (optically pumped vertical external-cavity surface-emitting laser) and OPSL (optically pumped semiconductor laser) are commonly used in literature to describe the same type of laser. The laser resonator is typically formed between the gain mirror and one or more external-cavity mirrors. In many ways, this laser architecture is similar to that of traditional solid state disk lasers. An essential difference is that in traditional solid state lasers the emission wavelength is dependent on certain fixed atomic transitions in a host material, whereas in an SDL the wavelength can be specifically tailored in a wide range by engineering the composition of the semiconductor

material. This added wavelength versatility is one of the key factors that have made SDLs successful also commercially.

Technically speaking, the OP-SDL can be considered as a brightness and wavelength converter; it converts low brightness light from multimode diode pump lasers into a high brightness single mode beam at a wavelength that is longer than the pump wavelength. Compared to edge emitting diode lasers and vertical-cavity surface-emitting lasers (VCSELs), the external cavity and optical pumping make the SDLs more complicated but they also bring several benefits. First of all they enable upscaling of the mode area on the gain while still maintaining single transversal mode operation; consequently the output power can be increased to multiwatt levels without risk of catastrophic optical damage due to excessively high optical intensities. In addition, the external cavity allows for cascading multiple gain mirrors thus increasing even more the power scaling capability. The SDL cavity has a high Q-factor and therefore it stores optical energy allowing efficient nonlinear intracavity frequency conversion to visible wavelengths. Another benefit of the external cavity is that it enables incorporation of nonlinear components to initiate ultrashort pulse operation. We should

also note that lately, the cost of broad stripe edge emitting pump diodes at 790–980 nm wavelengths has decreased significantly, while at the same time the available power from both single emitters and diode bars has increased markedly. More recently, also high-power pump diodes at other important wavelengths, including 635–690 nm, 1480–1550 nm, and 2000 nm, have been commercialized more actively. These advances in the availability, cost, and performance of pump diodes have made the optical pumping concept even more attractive.

*1.1. Cavity Designs.* Structurally the SDL gain mirror resembles a half-VCSEL design that comprises a high reflectivity mirror and a semiconductor gain region. The gain region usually includes several quantum-well (QW) or quantum-dot (QD) layers separated by spacer/barrier layers. A typical mirror structure consists of a stack of quarter-wavelength semiconductor layers, forming a distributed Bragg reflector (DBR), although metallic, dielectric, or hybrid [7] mirror structures can be used in some cases as well. While in VCSELs the single transverse mode operation is achieved by confining the laser mode to a very small gain area, in SDLs the same functionality is achieved by controlling the fundamental mode size via cavity design to have it match with the pumped area on the gain. Figure 1 shows various cavity configurations of SDLs.

The simplest conventional SDL cavity has an I-shape that is formed between the gain mirror and a single external output coupler (OC) mirror. However, in practice it is often easier to use a V-shaped cavity formed between the gain mirror, one curved folding mirror, and a planar output coupler. The advantage of the V-cavity is that planar output couplers with various coupling ratios are often cheaper and more widely available on stock than equivalent curved couplers. Another practical advantage of the V-shaped cavity is related to the alignment of the laser; if the final alignment is done by monitoring the output of a photodiode placed behind the output coupler, the folding mirror in a V-shaped cavity collects the light efficiently to the photodiode enhancing the available signal while in I-shaped cavity the spontaneous emission from the gain is rapidly dispersed to all direction. More complex cavity configurations are often used for frequency conversion and mode-locking. For efficient frequency conversion the nonlinear crystal is often placed at a location near or at the mode waist. This is usually easier to do in a V-shaped or Z-shaped cavity than in an I-shaped cavity. More complicated Z-shaped cavities are typically used in mode-locking SDLs to accommodate also a semiconductor saturable absorber mirrors (SESAMs); the challenge here is to produce sufficiently small mode diameter on the absorber mirror, while at the same time maintaining reasonably large mode diameter on the gain [8]. One should notice though that the overall cavity length increases for more complex designs and the mode-locked pulse repetition rate is reduced. This in turn would reduce the efficiency; if the interval of consequent pulses is longer than the carrier-lifetime, which is typically in the ns-range or slightly below, there will be loss of pump energy in time. In other words, the gain element can store energy only for a limited time, and if it is not exploited

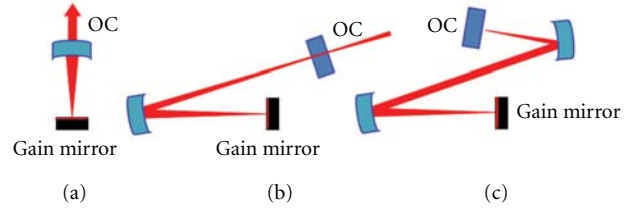


FIGURE 1: Typical SDL cavities. (a) I-shaped cavity; (b) V-shaped cavity; (c) Z-shaped cavity. OC: output coupler.

in that time window by an incoming pulse, a portion of that energy will be lost to spontaneous emission between the consequent pulses. This feature sets a practical upper limit for the cavity length in mode-locked laser with continuous wave pumping.

To scale up the power of an SDL, it is possible to deploy multiple gain elements in single cavity [9–11]. SDLs can also employ ring cavities [12], but probably due to the added complexity such lasers have not gained much popularity. In addition to different external cavity configurations, one can also produce an SDL with a semimonolithic cavity that may include a plane-plane design stabilized by a thermal lens [13, 14]. Such laser may be more limited in power and brightness but does possess an extremely rugged design. Furthermore, the semimonolithic cavity can be processed to have curved surfaces with mirror structures, thus avoiding the need for cavity stabilization by a thermal lens [15].

*1.2. Thermal Management of SDLs.* Efficient thermal management is a very important aspect required for high-power operation of SDLs. Although heroic in many ways, the early SDL experiments required the use of very low temperatures for high-power operation making the devices unpractical for use outside the laboratory. To large extent this was caused by a lack of adequate heat dissipation techniques. Excess heating reduces the emission efficiency via increased nonradiative recombination and carrier leakage and red-shifts the emission wavelength, which in a resonant periodic gain structure [16] leads also to a mismatch between the emission wavelength and the resonant wavelength further reducing the gain. Effectively, such heat-induced processes create a positive feedback loop with very negative impact on the laser performance. Consequently, the output power of the laser exhibits a roll-over characteristic when the pump power is increased beyond a critical point. For high-power operation, one should implement adequate ways of thermal management. Heating of the gain mirror originates from pump energy, which is converted to useful photons only partially while another part of the pump energy is transferred to phonons due to nonradiative recombination and the quantum defect (i.e., the photon energy difference between the pump photon and the laser photon). As a general strategy, one should try to minimize the heat generation and at the same time maximize the heat transfer from the gain.

Typically the pump photon has markedly higher photon energy than the emitted laser photon; for example, for a 1060 nm laser pumped with 808 nm radiation, the quantum

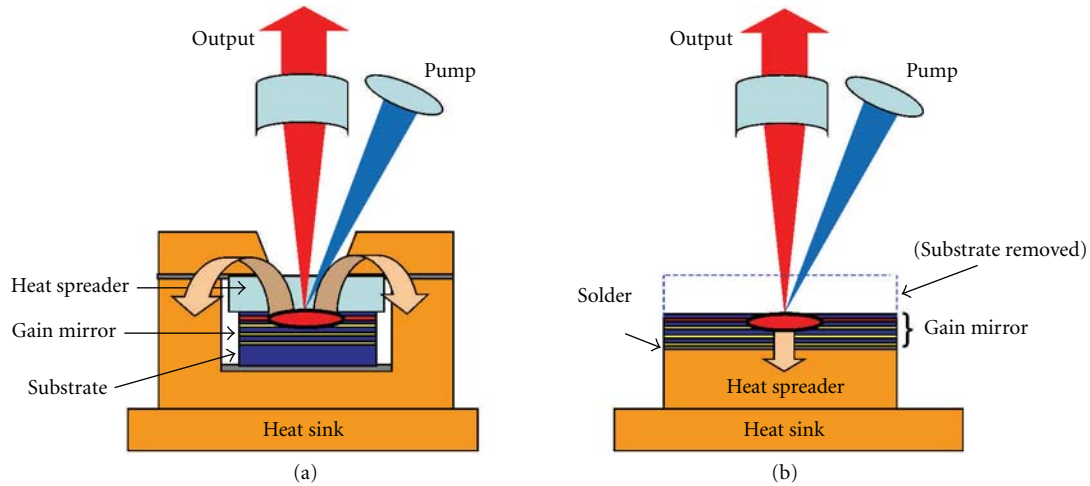


FIGURE 2: Description of two heat extraction strategies. (a) Laser equipped with intracavity heat spreader. (b) Flip-chip mounted thin-device from which the semiconductor substrate is removed.

defect is about 24% of the pump photon energy. In other words, the optical-to-optical conversion efficiency of such laser cannot exceed 76% even under theoretically perfect conditions. Usually, the laser is designed to absorb the pump radiation in the spacer/barrier layers separating the QWs because in this way the interaction length of light in matter is long enough to absorb sufficient amount of pump energy in a single pass. On the other hand, there must be a notable bandgap contrast between the spacer layers and the QWs in order to ensure a good carrier confinement and hence efficient operation at elevated temperatures. In most spacer pumped SDLs, the quantum defect is between 15% and 50% of the pump photon energy. An alternative for spacer pumping is direct “in-well” pumping [17–19] where the spacers are transparent to the pump radiation and the pump wavelength closely matches the QW emission wavelength. This approach minimizes the quantum defect but another technical difficulty arises from a short light-matter interaction length; the thickness of one QW is typically some nanometers and the total absorptive path length is rather small, as a gain mirror would typically include 5–15 QWs. To some extent, the pump absorption can be improved by adding more QWs to the structure but usually either a resonant pumping scheme or external pump recirculation optics is required for efficient pump absorption. We should note that an in-well pumped gain mirror provides by default a high reflection for the unabsorbed pump light, thus avoiding pump absorption in the DBR, and providing double-pass of pump radiation through the gain region. The selection of the pump laser for in-well pumping is more critical (and possibly more expensive) than in a spacer pumped laser where low-cost 808 nm diodes can be used for pumping 920 nm SDLs as well as 2000 nm SDLs. This is particularly true in the case of resonant in-well pumping. Nevertheless, in-well pumping offers an interesting option for reducing the quantum defect and the heating related to it. One should notice that quantum defect optimization makes sense only if the quantum efficiency of the laser is already high. If a significant majority of

pump photons are anyway lost to nonradiative processes, the benefits of quantum defect optimization become marginal to the overall performance of the system. Therefore, high-quality gain materials and proper structural designs are prerequisites for efficient operation of SDLs.

It is also very important to conduct the heat away from the gain region with minimal thermal resistance between the heat sink and the active region. Generally speaking, thermal resistance is dependent on the thermal conductance of the materials used and on the distance that heat needs to be transferred. In short, one should aim to minimize the distance between the heat sink and the gain and at the same time use materials that have high thermal conductance. Using a planar gain mirror geometry, the pumping is concentrated on an area that has typically a diameter of some tens or hundreds of micrometers, whereas the overall thickness of the semiconductor layer structure is only a few microns (e.g., 5–6  $\mu\text{m}$ ). In other words, the heated area is very large compared to the thickness of the layers. Thermal simulations show that in such a structure the heat flow is essentially one dimensional and is directed normal to the sample surface [21]. We should point out that the epitaxial layers are grown on a semiconductor substrate that is typically some 200–600  $\mu\text{m}$  thick and presents a major obstacle for the heat flow. Two assembling techniques of the gain mirror to the heat sink are typically employed to overcome this issue. The so-called “intracavity heat spreader” method, is conceptually simple and involves contacting a transparent heat spreader element onto the gain mirror [22] (see Figure 2 for general description). This method does not require substrate removal and the heat spreader is located right next to the gain region. The practical limitations arise from the fact that the heat spreader is located inside the laser cavity and that the number of transparent materials with high thermal conductance is limited; their cost may also be a limiting factor. By far the best material for this purpose is diamond due to its extremely high thermal conductance (up to  $\sim 2000 \text{ W/m}\cdot\text{K}$ ) and wide transmission window. Other suitable materials

include, for example, silicon carbide (SiC) [23] and sapphire (crystalline  $\text{Al}_2\text{O}_3$ ) [22]. A common technique for contacting the heat spreader and the semiconductor sample is based on capillary bonding [24] with deionized water or other suitable liquid. In this technique, two smooth and flat surfaces (here the gain mirror and heat spreader) are pulled together by surface tension of a liquid, and as the liquid evaporates, the two surfaces are brought to close optical contact and held together by surface forces. Simple mechanical clamping can be also used for optical contacting as long as the surfaces are sufficiently smooth, flat, and free from particles or other contaminants. However, capillary bonding is a good way to make sure that the surfaces meet these requirements and can be brought to close optical and thermal contact. The success of the bonding process can be simply monitored by observing the disappearance of the Newton's interference rings as the surfaces are brought together.

Another option for efficient heat dissipation was presented already in Kuznetsov's paper [25] and it involves growing the mirror and gain structures in reversed order (gain first, then the mirror) and bonding the component "upside-down" on a heat sink after which the substrate is removed by etching. Effectively this method transfers the epitaxial layers from a semiconductor substrate onto a substrate with higher thermal conductance. The process leaves only the Bragg reflector layers between the heated active region and the heat sink, which greatly reduces the thermal resistance in comparison to the situation where the semiconductor substrate would be located between the gain mirror and the heat sink. This process is often referred to as the "flip-chip" process or the "thin-device" process. Sometimes these components are also called bottom emitters, a term that is commonly used in VCSEL processing. From processing point of view, the flip-chip process requires longer overall time but can be done in batches of many devices. The major challenge of the flip-chip approach relates to the fact that without the support of the original substrate the epitaxial layers are mechanically very fragile. The bonding process requires usually the use of temperatures exceeding  $150^\circ\text{C}$ . Therefore, any differences in the coefficients of thermal expansion between the epitaxial layers and the heat sink may translate to mechanical stress as the sample cools down and the solder hardens. This is particularly critical issue with large samples bonded with hard solders such as AuSn that have high melting point. To alleviate the mechanical stress, one can resort to soft solders such as indium. However, it is a well-known fact that in high-power diode lasers indium solder tends to fail due to thermal diffusion and other effects. Such effects should be considered in connection with lifetime of high-power SDLs as the gain region is operated at relatively high temperatures. There are also many alternative bonding methods, such as InAu bonding [7, 26], that can be used instead. An important aspect related to soldering concerns the presence of voids within the solder; any voids in the solder will likely result in physical damage to the gain mirror under pumping. The voids can be monitored prior to substrate removal using a scanning acoustic microscope, for example. To further improve the heat dissipation, one can use a heat spreader, such as diamond, between the

sample and the metallic heat sink; the thermal energy is thus rapidly spread from a point source to a larger area over which it is conducted to the actual heat sink. The cost of the heat spreader is also markedly reduced when there is no need for optical quality surface polishing. In addition to soldering the substrate removal is an important step in the flip-chip process. To some extent the substrate can be thinned by lapping, prior to bonding, but in any case tens or hundreds of microns of semiconductor substrate must be removed by etching. This is done usually by wet etching employing an etch stop layer. It is important for the success of the process that the selectiveness of the etching is sufficiently high and that the process can be carried out in reasonable time. For GaAs removal one can use, for example, InGaP or Al(Ga)As etch stop layers and  $\text{NH}_4\text{OH}:\text{H}_2\text{O}_2$ -based etchants. InP etchants are often based on HCl [27], which may limit or hinder the use of indium as a solder for sample bonding. For GaSb-based compounds, good etchant-etch stop combinations are less developed; successful flip-chip SDLs based on this material system were just recently reported [26].

When compared to the flip-chip design, the intracavity heat spreader approach has proved to be very quick and simple to do in laboratory conditions. The heat spreaders can be also recycled almost endlessly, which overcomes their high initial cost at least for research use. The intrinsic disadvantage of the intracavity heat spreader is that it introduces a loss element in the cavity that can also act as an etalon. The etalon effect modulates the optical spectrum affecting the mode-locking mechanisms and making continuous wavelength tuning difficult. The etalon effect can be suppressed by using a wedged heat spreader with an antireflective coating [28]. The wedge angle usually increases the reflection losses despite the AR layer and hence decreases the output power. One should notice that inside the laser resonator, etalon effects may arise also from unexpected sources such as double-side polished semiconductor wafers onto which the gain mirror or the saturable absorber mirror may have been grown. Although the reflectivity of the gain mirror DBR is usually over 99.5%, the small transmitted portion of light may penetrate to the substrate (if transparent) and can be reflected back from its second surface, in which case an etalon is established in the system and the spectrum of the laser is affected. Both heat management strategies have been successfully used to achieve over 10 W output from standard InGaAs/GaAs gain structures, though the highest output powers have been achieved with the flip-chip components [29, 30]. However, if the thickness of the DBR stack increases (due to longer operation wavelength or poor index contrast of the materials), or if the DBR layers have very poor thermal conductance, it may be more advantageous to use the intracavity heat spreader technique. This is particularly true for InP- and GaSb-based SDLs. The thermal issues of SDLs have been discussed in detail in a number of papers reporting simulations and experimental results on the subject [21, 31–34].

To summarize, efficient heat removal is highly important for high-power operation of SDLs. Use of high thermal conductance heat spreader materials, such as diamond,

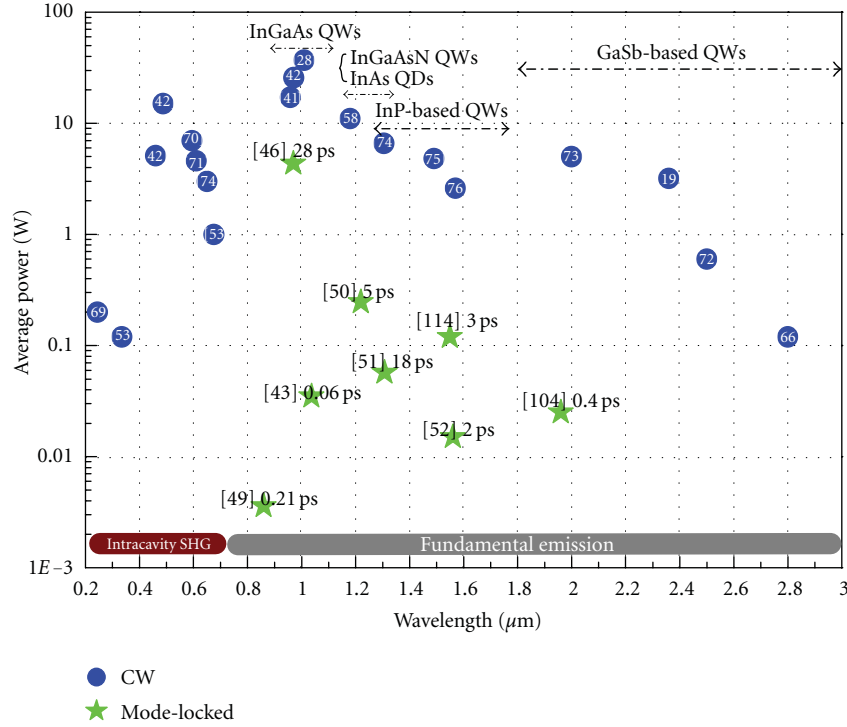


FIGURE 3: Selection of SDL results showing the maximum average power reached at different wavelengths. InGaAs(N)-based gain materials dominate the results up to 1.3 μm above which InP-based and GaSb-based QWs are used. Only SDLs incorporating single gain chips are included. Pulse durations related to mode-locked results are given in picoseconds.

greatly improves the heat extraction from the point source. The distance from the gain region to the heat spreader can be minimized by optically contacting the heat spreader onto the sample or by flip-chip bonding the component on a heat spreader/heat sink. The application and the type of gain material determine which process is more suitable. Flip-chip processing suits well for mode-locking, continuous spectral tuning, and single-frequency operation since the laser spectrum is not affected by the intracavity heat spreader element. The intracavity heat spreader approach suits particularly well for long wavelength (GaSb and InP) lasers and applications that are not spectrally sensitive.

**1.3. Wavelength Coverage.** During the last decade, the SDL research has been largely channelized along three major directions, namely, (i) power scaling, (ii) extending the wavelength coverage, and (iii) generation of ultrashort pulses. Along the way, many demonstrations concerned widely tunable [35–38] and narrow band lasers [39–41]. In terms of available output power, the 10 W level has been reached and exceeded using both single and multiple gain elements [29, 30, 42, 43]. Excellent results have been obtained lately in ultrashort pulse generation [44, 45], as well as in generation of pulses with high average output power [46, 47] and high repetition rate [48]. The spectral coverage of mode-locked [49] SDLs has also extended [50–53] outside the common InGaAs wavelengths near 1 μm. Interestingly, the spectral coverage of continuous wave SDLs (fundamental and frequency converted emission) spans today from 244 nm to 5000 nm [18, 20, 22, 23, 37, 54–76], although not without

gaps. Figure 3 gives an overview of maximum output powers achieved as a function of wavelength for both continuous-wave (CW) and mode-locking operation regimes. It also provides a correspondence to main classes of material systems used to reach a certain wavelength region.

In terms of more recent efforts and development directions, the 580–630 nm wavelength range is particularly interesting as it cannot be reached via direct emission from semiconductors. Nevertheless, it can be covered conveniently by frequency doubled 1160–1260 nm infrared lasers. We should note that it is also difficult to find suitable solid state materials for these visible and IR ranges. Because of these reasons, there has been a lot of scientific and commercial interest in extending the SDL technology to this particular wavelength range. In the following we will review different options for reaching emission at ~1150–1300 nm with semiconductors. First, it is important to understand the main features of the semiconductor structures we are considering for fabricating SDL mirrors. The gain mirror is essentially a stack of epitaxially grown semiconductor thin-films, fabricated on a GaAs, InP, GaSb, or other suitable semiconductor substrate by epitaxial growth. It is quite essential that one is able to grow high-quality gain material (QW, QD, or bulk) with desired bandgap energy, while keeping the material strain within reasonable limits. Secondly, the DBR should provide sufficient reflectance with a reasonable stack thickness and level of strain. Excessive material strain, arising from the difference between the lattice constants of the semiconductor layers, can lead to formation of crystalline defects and ultimately to relaxation of the layered structure. The

TABLE 1: Different technologies used for fabricating SDLs with emission at 1150–1300 nm.

Strategies for wavelength extension to 1150–1300 nm	Challenges
GaAsSb/GaAs QW gain material [81]	Low confinement of carriers in the QWs. Poor temperature behavior
InP-based gain with InP-based Bragg reflector [64]	Compromised reflectivity, Increased stack thickness, low thermal conductance of the DBR
Hybrid mirrors with InP-based gain [7]	Compromised thermal conductance
Wafer fusion of different gain and active regions [82]	More expensive processing. Two growths required for one component
InAs/GaAs QDs [83, 84]	Reduced design flexibility and low modal gain
Strain compensated high indium content InGaAs QWs [85]	Strain-related lifetime issues
Dilute nitride GaInNAs/GaAs QWs [20, 62]	Formation of nitrogen-related defects

1150–1300 nm wavelength range has previously been very challenging for the growth of SDLs for two main reasons. First, for conventional InGaAs/GaAs QW material a relatively large content of indium must be used to reduce the bandgap energy to the desired value and the high indium content increases the lattice constant of the material causing buildup of strain in the layer structure. Alternatively, one could also resort to the use of InP-based QWs which work at 1.2  $\mu\text{m}$ –1.6  $\mu\text{m}$ , but unlike with GaAs, the DBR materials lattice matched to InP have very low index contrast [77–80]. Therefore, the thickness of the Bragg reflector must be increased significantly in order to achieve high reflectance. A number of techniques have been proposed to extend the emission wavelength of GaAs-based structures beyond the typical InGaAs spectral window near 1  $\mu\text{m}$  or to enable the use of InP-based gain regions in surface normal lasers; the main techniques have been listed in Table 1 with related challenges.

In the next sections, we will review the basic technological aspects regarding the development of dilute nitrides gain mirrors and the recent achievements concerning dilute-nitride SDLs with yellow-orange emission. GaSb-based SDL emitting at around 2  $\mu\text{m}$  will be discussed in Section 3.

## 2. High-Power Yellow-Orange SDLs Based on Dilute Nitride Gain Mirrors

*2.1. Dilute Nitrides: Band-Gap Engineering and Gain Mirror Technology.* To produce yellow emission by second harmonic emission, the indium content of the conventional InGaAs/GaAs QWs needs to be relatively high ( $x > 35\%$ ). The high indium content increases the compressive lattice strain close to the point where misfit dislocations start to appear. The high lattice strain, together with high operation temperatures, can strongly deteriorate the lifetime of a device based on such QWs [86]. By adding a small amount of N (typically less than 3%) to InGaAs, one can reduce at the same time the lattice constant and the band-gap of the material. This opens up great opportunities for GaAs-based technology. For example, the compressive strain of InGaAs/GaAs material system can be compensated by N incorporation enabling emission at wavelengths up to 1.55  $\mu\text{m}$  [87]. These dilute nitride compounds can be in fact lattice matched to GaAs;

$\text{Ga}_{1-x}\text{In}_x\text{N}_y\text{As}_{1-y}$ , with  $x \approx 2.8 y$  is lattice matched to GaAs whereas compositions with  $x > 2.8 y$  and  $x < 2.8 y$  lead to compressively and tensile strained compounds, respectively. Furthermore, GaNAs layers exhibit a tensile strain that can be used for balancing the compressive strain of GaInAs layers.

The dramatic effect of nitrogen on the band gap is generally explained as being caused by the small size and large electronegativity of N atoms (radius  $\sim 0.068 \text{ \AA}$ , electronegativity  $\sim 3.04$  in units of Pauling scale) as compared to As atoms (radius  $\sim 0.121 \text{ \AA}$ , electronegativity  $\sim 2.18$ ) of the host crystal. Such impurity atoms create localized energy levels close to the conduction band edge and, as a result, modify the conduction band structure of the alloy. The interaction between the localized states and the conduction band is usually modeled using a so-called band anticrossing model (BAC). BAC has been very successful in explaining anomalous properties of the dilute nitrides, especially the conduction band structure and the related electron effective mass [88–91]. The theoretical dependence of the GaInNAs band-gap as a function of N and In composition is shown in Figure 4 (the material parameters used for calculation are taken from [91]). The band gap decreases strongly by incorporating only a few percent of nitrogen and the 1200 nm wavelength range is readily achievable by using GaInNAs with relatively low N content. We should also note that nitrogen incorporation is associated with an increase of the nonradiative recombination centers [92]. Incorporation of higher amounts of nitrogen can cause clustering and phase separation [93] having a detrimental effect on the optical quality of the material. To some extent, this effect can be alleviated by rapid thermal annealing (RTA) which, however, leads to a considerable blue shift of the PL wavelength [94], an effect that should be taken into account in order to achieve the desired laser performance.

In general, the control and understanding of epitaxial processes used to fabricate dilute nitrides is rather challenging. For example, the range of suitable growth temperatures for fabricating high-quality dilute nitrides is narrower than that for growing GaInAs. The typical growth temperature for GaInNAs is in the range of  $\sim 460^\circ\text{C}$ , while GaInAs QWs are grown typically at  $\sim 520^\circ\text{C}$ . The highest performance InGaAsN-based heterostructures are routinely fabricated by molecular beam epitaxy [95]. The standard

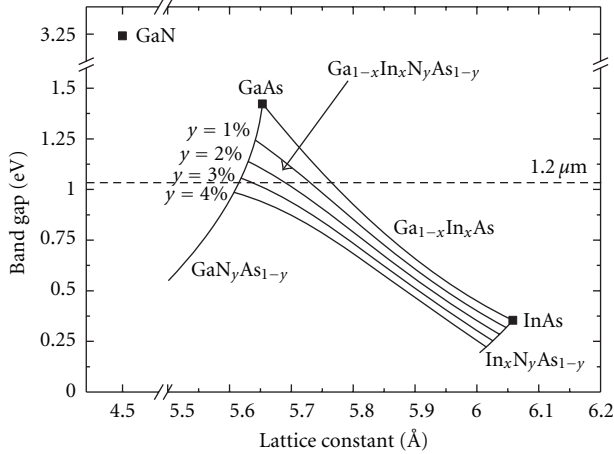


FIGURE 4: Band gap and lattice constant of dilute nitride GaInNAs.

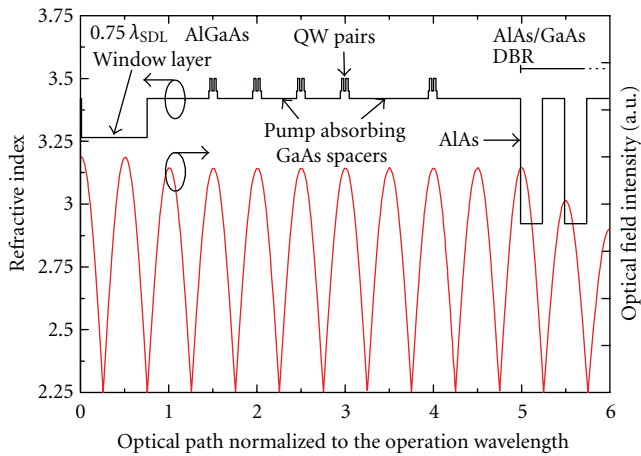


FIGURE 5: Typical structure of the quantum well region of a GaInNAs gain mirror [20].

technique used to incorporate N is dissociation of atomic nitrogen from molecular nitrogen using a radio-frequency (RF) plasma source attached to the MBE growth chamber [96]. Optimization of the plasma operation is one of the key issues that need to be addressed in order to fabricate high-quality dilute nitride heterostructures. The state of the nitrogen plasma depends on the RF power, the flow of  $N_2$ , and pressure. The main constituents of the plasma are the molecular nitrogen, atomic nitrogen, and nitrogen ions, each of them having a specific spectral signature that can be used for optimizing the plasma operation [97]. Although the energy of the ions is small, they can cause significant degradation of the optical quality as they impinge on the semiconductor structure during the formation of the QWs [94]. Another important growth parameter affecting the quality of dilute nitrides is the As pressure [98].

Figure 5 displays the structure of a typical dilute nitride gain mirror comprising 10  $Ga_{0.33}In_{0.67}N_{0.006}As_{0.994}$  QWs placed in five pairs. The  $GaN_{0.006}As_{0.994}$  layers surrounding the QWs shift their ground state to lower energy and compensate for the compressive strain. For achieving lasing at

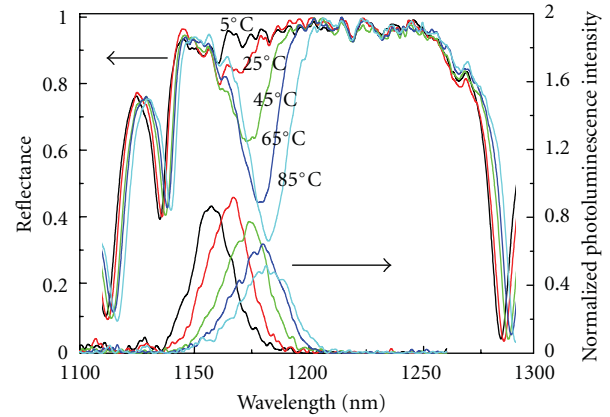


FIGURE 6: Reflectance and photoluminescence spectra of the 1180 nm GaInNAs gain mirror measured at different temperatures.

around 1180 nm, the room temperature emission wavelength of the QWs was designed to be  $\sim 1145$  nm. The first four QW pairs were equally spaced at one half wavelength distance apart from each other. The last QW pair was located a full wavelength distance apart from the fourth pair in order to compensate for the pump intensity drop along the gain structure. A  $0.75\text{-}\lambda$   $Al_{0.25}Ga_{0.75}As$  window layer was grown on top of the active region. The active region was grown on top of a 25.5-pair AlAs/GaAs DBR. The growth rate was  $0.95 \mu\text{m}/\text{hour}$  and the As/III beam equivalent ratio was 25. After the growth, the sample was kept in the growth chamber under As pressure for a 7 min *in situ* anneal at  $680^\circ\text{C}$  to improve the luminescence properties.

The reflectance and photoluminescence (PL) spectra measured for different temperatures of the gain mirror are displayed in Figure 6. The PL graph reveals a temperature dependent red-shift of about  $0.3 \text{ nm}/\text{K}$ . The reason for the decrease in the PL intensity is the increase in the nonradiative recombination rate with increasing temperature resulting in a quantum efficiency drop. The DBR exhibits a temperature red-shift of about  $0.06 \text{ nm}/\text{K}$ . The reflectance spectra were recorded from an as-grown sample, and the photoluminescence spectra were recorded from a sample with diamond heat spreader having an anti-reflective coating on it.

**2.2. Operation at Fundamental Wavelength.** The gain mirror wafer was cut into  $2.5 \times 2.5 \text{ mm}^2$  chips, which were then capillary-bonded to synthetic diamond heat spreaders with a wedge angle of about  $2^\circ$  to alleviate the spectral modulation caused by the etalon effect. In addition, we applied a 2-layer  $TiO_2/SiO_2$  antireflective coating on top of the diamond. The laser chip was clamped onto a copper heat sink having small water cooling channels. Despite the flow of cooling water within the heat sink, the heat load generated by pumping the gain mirror led to a slight increase in the mount temperature ( $T_{\text{mount}}$ ). The dependence of  $T_{\text{mount}}$  on the pump power is shown in Figure 7 for three different pump spot diameters ( $\phi_{\text{pump}}$ ) and two different temperatures of the cooling water ( $T_{\text{water}}$ ). For laser characterization, the gain chips were tested in a V-shaped SDL cavity shown in Figure 8. The distance

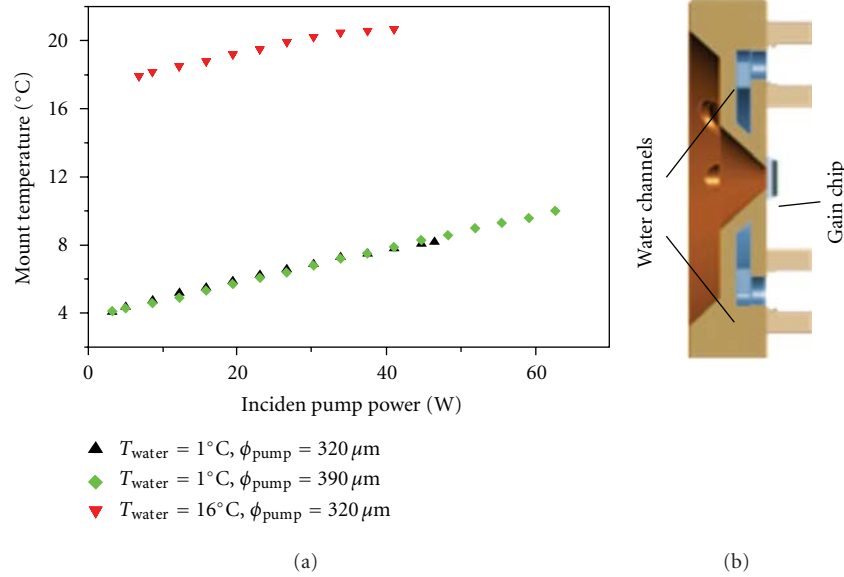


FIGURE 7: (a) The dependence of the mount temperature on the pump power for three diameters of the pump spot and two temperatures of the cooling water. (b) Drawing of the water-cooled mount.

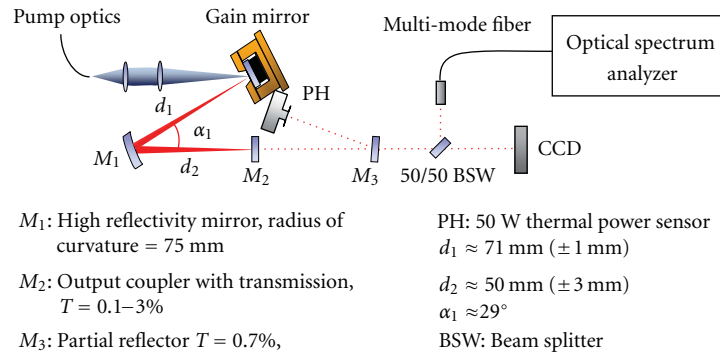


FIGURE 8: Description of the setup used for the spectrum and beam shape measurements.

between  $M_1$  and  $M_2$  was adjusted to match the size of the  $\text{TEM}_{00}$  mode to the pump spot on the gain chip, while monitoring the intensity of the output beam to resemble as close as possible a circular Gaussian geometry. In the experiments presented here the gain mirror was pumped by an 808 nm diode bar coupled to a  $200 \mu\text{m}$  multimode fiber. The incidence angle of the pump beam was about  $27^\circ$ .

The SDL output characteristics for different output couplers are shown in Figure 9. Here the water temperature was set to  $16^\circ\text{C}$  and the diameter of the pump spot to  $320 \mu\text{m}$ . The maximum output power before thermal roll-over was achieved with 1.5% transmissive output coupler. The highest slope efficiency, of 27%, corresponded to a coupling ratio of 3%. The threshold pump power varied in the range of 3–7 W when the output coupling ratio was varied from 0.1 to 3%.

Next, in order to optimize the pump spot for reaching highest possible power,  $T_{\text{water}}$  was set to  $1^\circ\text{C}$ . The results shown in Figure 10 reveal that the maximum output power increased when  $\phi_{\text{pump}}$  was increased from  $320 \mu\text{m}$  to  $390 \mu\text{m}$ .

Also the pump power at which the thermal roll-over was observed was increased from 45 W to 63 W. An output power of slightly more than 11 W was reached with a pump spot of  $\phi_{\text{pump}} = 390 \mu\text{m}$ ; the effective mount temperature was  $10^\circ\text{C}$ . When  $\phi_{\text{pump}}$  was increased from  $390 \mu\text{m}$  to  $460 \mu\text{m}$ , the thermal roll-over point increased slightly to 70 W. However, the slope efficiency dropped and the output power stayed below 11 W, allegedly because of nonideal heat extraction from the gain mirror [99] or overlapping of the larger pump beam with defects on the gain mirror.

**2.3. Frequency Doubling.** To generate yellow-orange radiation via frequency doubling, we have used V-shape cavity as shown in Figure 11. The nonlinear conversion experiments were performed in free-running mode, that is, without any wavelength control. Compared to the cavity used for fundamental wavelength, the output coupler has been replaced by a mirror that was highly reflective for both IR and visible, whereas the folding mirror reflects infrared but transmits

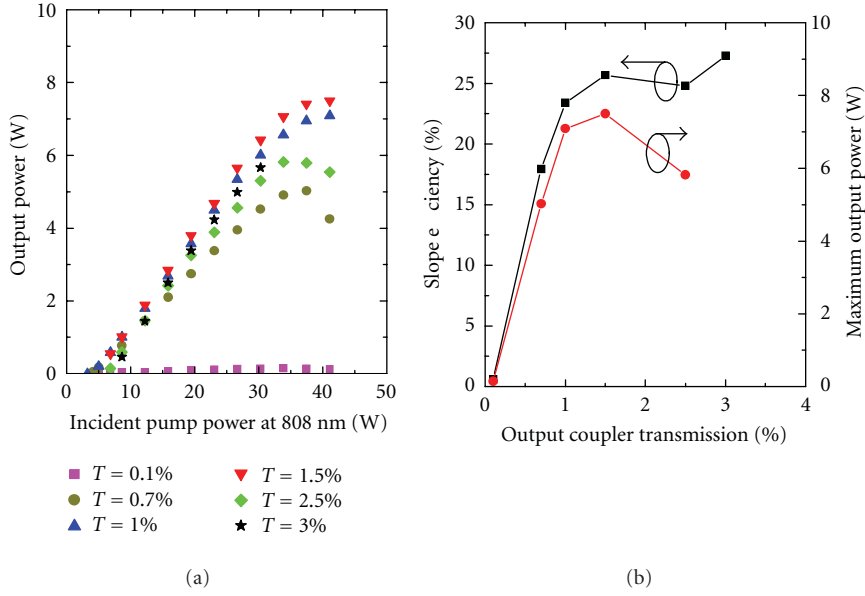


FIGURE 9: Output characteristics of the 1.18  $\mu\text{m}$  SDL for different output couplers. The temperature of the cooling water was set to 16°C and the diameter of the pump spot was  $\sim 320 \mu\text{m}$  [20].

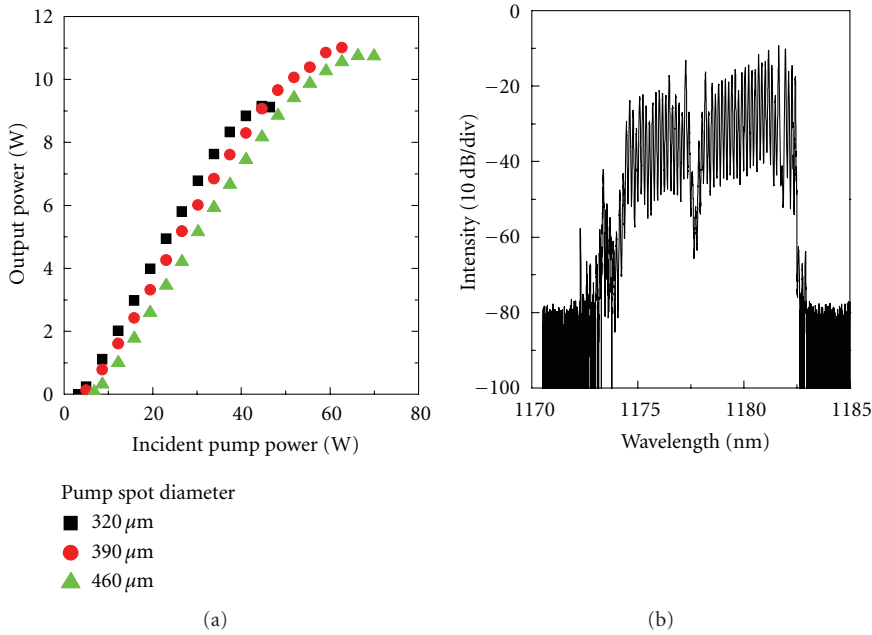


FIGURE 10: Output characteristic (a) and typical spectrum for an output power of 5 W (b). The temperature of the cooling water was set to 1°C and the transmission of output coupler was 1.5% [20].

visible light. The frequency conversion was achieved using a 4 mm long type-I critically phase-matched BBO crystal. Figure 12 shows a power transfer graph comparison between the SDL emitting at fundamental infrared wavelength of  $\sim 1180 \text{ nm}$  and frequency-doubled light at 590 nm. For a pump power of 41.5 W, we demonstrated a maximum

conversion efficiency (absorbed pump light to frequency-converted light) of 17%, which to our knowledge is the highest efficiency reported for a yellow SDL. The ratio of absorbed light to incident pump power was estimated to be  $\sim 0.94$ . At this pump power level, the output power of frequency-doubled light was about 77% of that obtained at

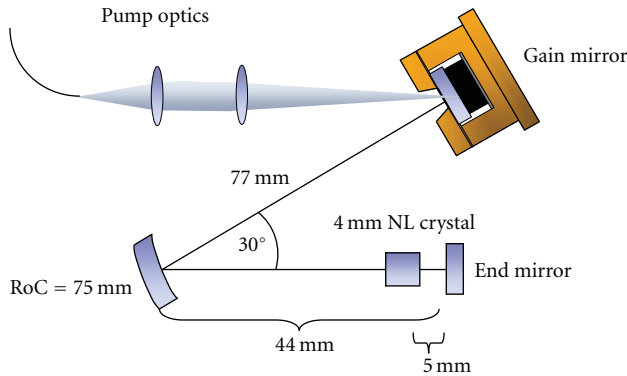
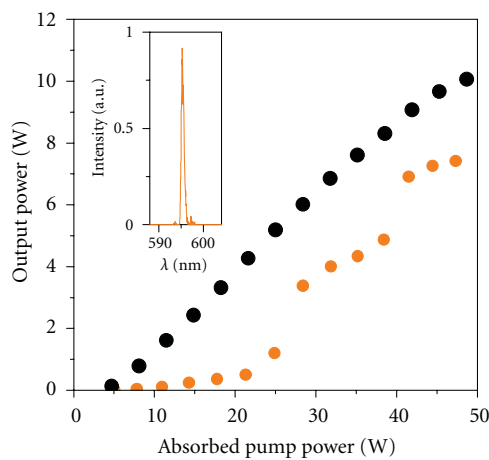
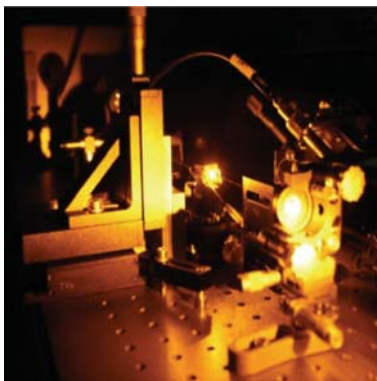


FIGURE 11: SDL setup used for yellow second-harmonic generation in free-running mode.



(a)



(b)

FIGURE 12: Power transfer graphs of an SDL emitting fundamental 1180 nm light (black) and of a frequency doubled SDL (orange). The inset shows the output spectrum of the frequency-doubled SDL. The photograph at right shows an SDL in operation.

the fundamental wavelength with similar lasing conditions. The inset of Figure 12 shows the emission spectrum of the frequency-doubled radiation at 7 W of output.

Based on the result discussed previously we can conclude that GaInNAs gain mirror technology is the leading

candidates for realizing high-power SDLs with emission at yellow-orange wavelengths.

### 3. GaSb-Based SDLs for 2–3 $\mu\text{m}$ Wavelength Range

Another commercially and scientifically very interesting spectral domain is that located between 2 and 3  $\mu\text{m}$ . This spectral range can be accessed using GaSb material system. GaSb-based SDLs with high-power (>1 W) and widely tunable (up to  $\sim 160$  nm) operations have been reported by several groups [19, 37, 65, 100, 101]. In addition to continuous wave lasers also ultrashort pulse SDLs in this wavelength range are of interest, as they could be used as seed sources for mid-IR supercontinuum sources [102] or for pumping of mid-IR optical parametric oscillators. However, because of limited availability of some essential components, such as like semiconductor saturable absorber mirrors (SESAMs), the first passively mode-locked 2  $\mu\text{m}$  GaSb-based SDLs were reported only very recently [103, 104].

The development of GaSb-based (AlGaIn)(AsSb) heterostructures designed for 2–3  $\mu\text{m}$  wavelength range has struggled with many obstacles, such as increased Auger recombination, typical in narrow bandgap semiconductors, and reduced carrier confinement leading to type-II band alignment in QWs instead of preferred type-I. Regardless, electrically pumped, edge-emitting lasers based on GaSb epitaxy have demonstrated CW operation even beyond 3  $\mu\text{m}$  [105, 106] with careful band-gap engineering and utilization of quinary AlGaInAsSb waveguides. For optical pumping, the decreased thermal properties of GaSb compared to conventional GaAs make thermal management more demanding for mid-IR SDLs. Typically, the optical pumping is based on commercially available diode pumps at 780–980 nm wavelength range, causing excessive heating due to a large quantum defect. The power scalability of GaSb-based SDLs is therefore limited by the effectiveness of thermal management [21]. To reduce the thermal load, different methods have been investigated, such as in-well pumping [19], a flip-chip process with GaSb substrate removal [26], and the use of high thermal conductivity substrate, such as Si or GaAs, in combination with metamorphic growth [107].

The benefits brought by GaSb-based material system to SDLs are the high index contrast ( $\Delta n \sim 0.6$ ) of lattice-matched AlAs<sub>0.08</sub>Sb<sub>0.92</sub>/GaSb DBR layers, which enables to achieve high reflectivity in exceptionally broad band ( $\sim 300$  nm [100]) with a relatively small number of layer pairs. This makes GaSb SDLs very attractive for spectroscopic application where broad tunability of the laser is needed. High-quality AlAsSb/GaSb DBR can also be used for SESAMs [108]. GaAs-based 1- $\mu\text{m}$  SESAMs have been exploited extensively and their properties can be nowadays tailored to produce ultrashort pulses in various laser types. However, investigation of GaSb-based SESAMs has received far less attention [109, 110]. SESAMs operating at wavelengths around 2  $\mu\text{m}$  and above would have a significant impact on the development of practical ultrafast lasers required in medical applications and time-resolved

molecular spectroscopy, or as seeders for optical amplifiers and mid-IR supercontinuum lasers.

To our knowledge the first diode-pumped GaSb-based SDL was demonstrated by Cerutti et al. [111] in 2004; the  $2.3\ \mu\text{m}$  laser reached lasing at temperatures up to 350 K with quite moderate output powers. Currently, the emission wavelengths of GaSb SDLs cover the  $1.96\text{--}2.8\ \mu\text{m}$  spectral range [66, 100]. At  $2\text{--}2.35\ \mu\text{m}$  the CW power levels have reached multiple watts [37, 112] for near room temperature operation. The achieved output powers of 0.6 W at  $2.5\ \mu\text{m}$  and 0.1 W at  $2.8\ \mu\text{m}$  [66, 72] have not yet reclaimed the position as such SDLs as high-power lasers. Here, our work had two primary targets: (1) obtain as high CW power as possible at  $2\ \mu\text{m}$  and (2) produce ultrashort pulses by passive mode locking at  $2\ \mu\text{m}$ . We have developed a gain mirror structure grown on GaSb substrate by solid source MBE. The design included an 18.5-pair DBR made of lattice matched AlAsSb/GaSb layers, and a gain region with 15 InGaSb QWs. For continuous wave experiments, the SDL mirrors were bonded to a planar intracavity diamond heat spreader in a similar manner as the GaInNAs samples described previously. Details of the fabrication process are provided in [37].

**3.1. Continuous Wave GaSb Disk Laser.** Our  $2\ \mu\text{m}$  range SDLs employed a V-shaped laser cavity. The output characteristics obtained with 99–97% reflective couplers are shown in Figure 13. Here the cooling water temperature was set to  $3.5^\circ\text{C}$  and the pump spot diameter was about  $350\ \mu\text{m}$ . The emission wavelength was about  $1990\ \text{nm}$  (Figure 13), slightly depending on the power and output coupler. We observed a general tendency for a spectrum shift towards longer wavelengths with increased coupler reflectance, which could be caused by different heat loads on the gain.

The output characteristics were also measured as a function of the cooling water temperature (Figure 14) using a 98% reflective coupler. The available maximum power was reduced with increasing temperature but it is worth noting that for a coolant temperature of  $45^\circ\text{C}$  the laser still produced nearly 1 W of output power. In order to further increase the output power, the pump spot diameter was increased from  $350\ \mu\text{m}$  to  $440\ \mu\text{m}$  which enabled a maximum power of 5.75 W to be achieved at a water temperature of  $3.5^\circ\text{C}$ .

While the power from a single gain chip was limited to less than 6 W, we studied also the possibility to increase the laser output by cascading 2 gain chips in one laser cavity. A W-shaped laser cavity was set up as shown in Figure 15. The pump spot diameter was further increased to  $500\ \mu\text{m}$  and the temperature was reduced to  $-2.5^\circ\text{C}$ . For this purpose a mixture of water and alcohol had to be used as coolant and a flow of nitrogen was provided to the samples to prevent condensation of water from the surrounding air. Eventually we were able to increase the power to 8.6 W (Figure 15) but could not achieve linear power scaling that should have theoretically resulted in more than 11 W of power with these two particular chips. Reasons for this can be many. One important contributing factor may be the output coupler that was 94.6% reflective; out of all available output couplers it enabled the highest output power but might not have been

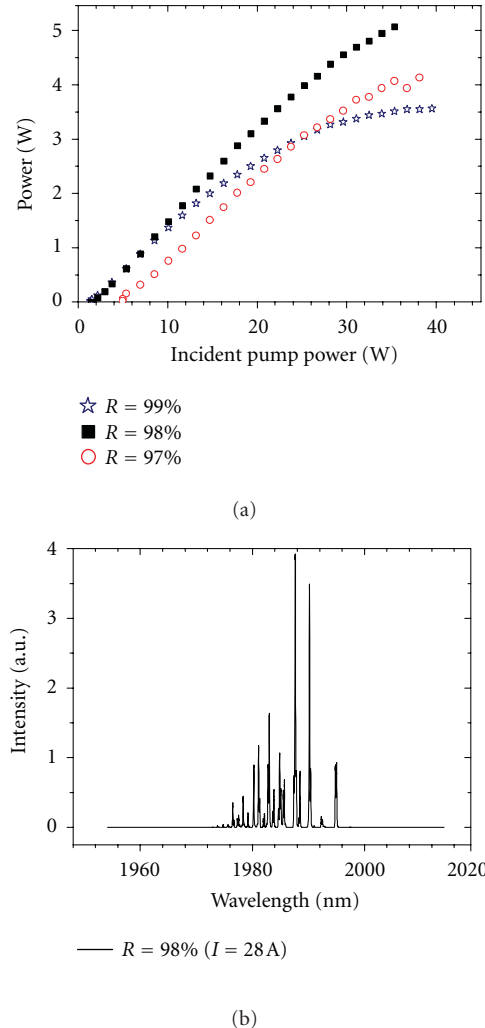


FIGURE 13: (a) Laser output for different output couplers.  $T = 3.5^\circ\text{C}$  (cooling water temperature). Pump spot  $\varnothing = 350\ \mu\text{m}$ . R : output coupler reflectivity. (b) Laser spectrum for a pump power of 35.2 W.

optimal for this particular laser configuration. The coolant mixture had also lower specific heat than pure water and therefore the cooling may not be as effective as the coolant temperature could suggest. The 2-gain laser alignment is also somewhat more complicated than a single chip laser which may hinder power scaling. Despite these difficulties, reasonable results were obtained in terms of output power at  $2\ \mu\text{m}$  wavelength.

**3.2. Femtosecond Pulse Generation.** As discussed earlier, ultrashort optical pulses have been generated in GaAs- and InP-based disk lasers in various configurations using both active and passive mode-locking schemes [2, 4, 6, 44, 45, 113, 114]. On the contrast, the development of ultrafast GaSb disk lasers has been much slower, possibly due to lack of SESAMs and more demanding SESAM characterization. We have shown only very recently that also GaSb-based disk laser can generate sub-picoseconds pulses at  $2\ \mu\text{m}$  [104]. The development of low-nonlinearity GaSb-based SESAMs was

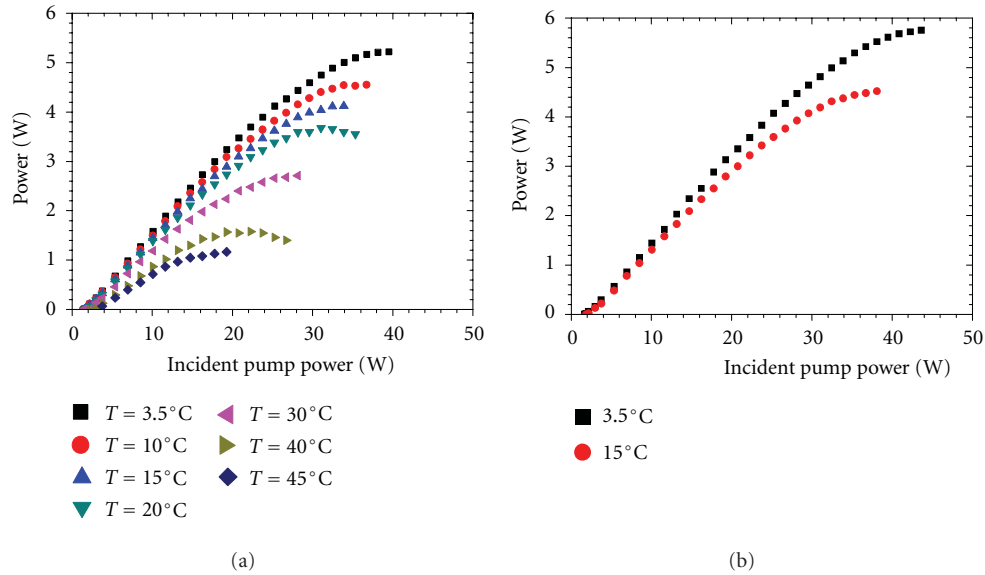


FIGURE 14: (a) Laser output characteristics at different cooling water temperatures. Output coupler  $R$  is 98%, and pump spot diameter is  $350 \mu\text{m}$ . (b) Laser output characteristics with  $440 \mu\text{m}$  pump spot diameter. Output coupler  $R$  is 98%.

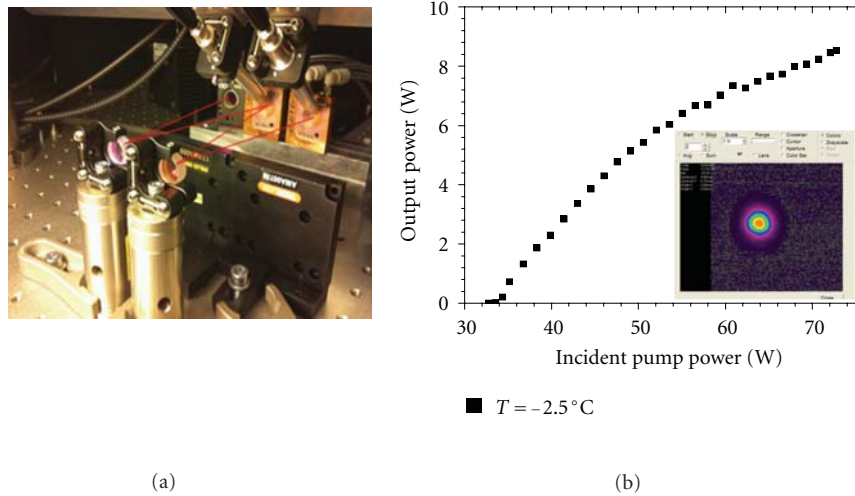


FIGURE 15: (a) Photograph of the W-shaped 2-gain laser cavity. (b) 2-gain laser output characteristics with  $500 \mu\text{m}$  pump spot diameter. Output coupler  $R$  is 94.6%. Inset: profile of the output beam.

instrumental for demonstrating ultrafast  $2 \mu\text{m}$  SDLs. The right combination of the dynamic properties of the SESAM (saturation fluence, absorption recovery time, nonlinear reflectivity, and nonsaturable losses) is quite essential for achieving stable mode-locking. An interesting finding was made that as-grown  $2 \mu\text{m}$  GaSb saturable absorber mirrors had much faster recovery time than typical as-grown GaAs-based components operating in the  $1 \mu\text{m}$  regime. Fabrication details of the SESAMs we have used are provided in reference [110]. The GaSb absorber mirrors were studied with pump probe measurements. The growth temperature and amount of strain were used as controlled variables. For the mode-locking experiments, we used a Z-shaped cavity (Figure 16)

that allowed convenient alignment of the SESAM and gain mirror.

The gain chip was cooled in a similar manner as the continuous wave  $2 \mu\text{m}$  laser, but the heat spreader diamond had a  $2^\circ$  wedge and AR coating to suppress the etalon effect arising from it. The gain mirror was pumped with a fiber-coupled  $980 \text{ nm}$  diode laser and the output coupler had a reflectivity of  $R = 99\%$  at the operation wavelength. Simulated mode diameter was  $\sim 230 \mu\text{m}$  on the gain and  $\sim 25 \mu\text{m}$  on the SESAM. The pulse repetition rate, defined by the cavity length, was in the order of  $890 \text{ MHz}$ . The output of the laser was monitored with an optical spectrum analyzer and a  $2.5 \text{ GHz}$  photodiode from which the signal

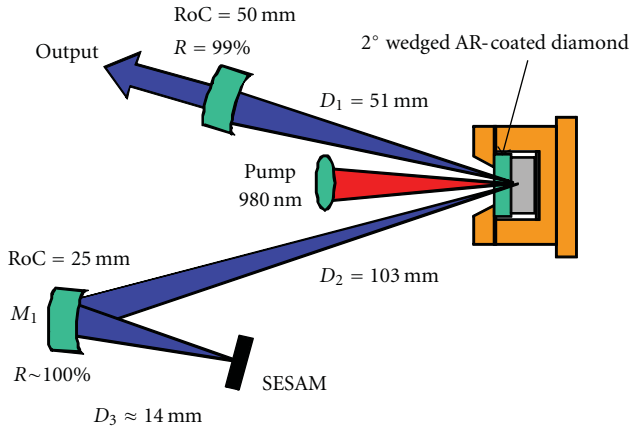
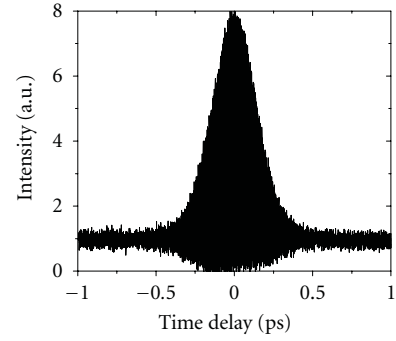


FIGURE 16: A Z-shaped cavity of the mode-locked GaSb laser.

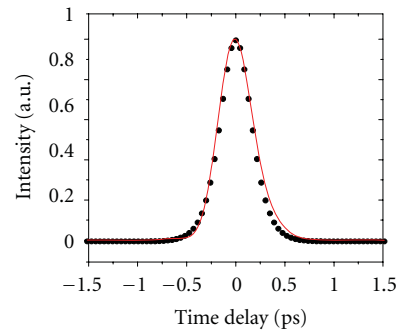
was coupled to an RF-analyzer and oscilloscope. The laser beam profile could be monitored with a pyroelectric camera for proper alignment. The pulses were characterized with an interferometric autocorrelator that was based on two-photon absorption in a silicon detector. Depending on the laser alignment, we were able to measure pulses with duration varying from slightly less than 400 fs to slightly more than 400 fs, with the shortest measured pulse being 384 fs. A typical autocorrelation trace is shown in Figure 17 with the optical spectrum, RF-spectrum, and retrieved pulse shape.

Quite surprisingly the output power level of the mode-locked laser was only some tens of milliwatts despite many watts of pump power. In continuous wave mode over 5 W of power was obtained from other devices having similar gain material. To some extent the differences can be explained by variations between individual chips, nonoptimal output coupling ratio, lossy cavity, and smaller pump spot diameter but clearly the average power in mode-locked operation should have been markedly higher. In order to study the potential of the laser, we replaced the SESAM with a high reflective mirror and then we measured the output power in continuous wave mode. As shown in Figure 18, for an incident pump power of 7.6 W, the power was ~23 mW with the SESAM, and slightly over 40 mW with the HR mirror.

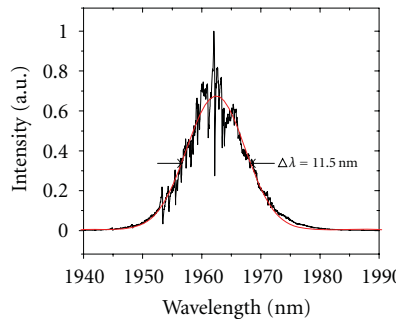
The precise position of the mirror could be determined from the RF-spectrum, which helped to monitor the output power as a function of the mirror position in regard to the original position of the SESAM. When the HR mirror was repositioned about 60  $\mu\text{m}$  closer to the curved mirror than the original SESAM position, the power increased from ~40 mW to 130 mW (see Figure 19 for details). The position of the HR/absorber mirror changes the mode diameter also on the gain and therefore it has an impact on the efficiency of the laser. The study revealed that the mirror position that was optimal for mode-locking may not have been optimal for achieving the highest average power. The result suggests that with further optimization of the cavity geometry and adjustments of the pump spot diameter and output coupling ratio, it should be possible to increase the average power to >100 mW also in mode-locked operation.



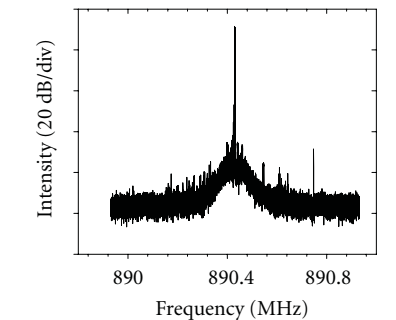
(a)



(b)



(c)



(d)

FIGURE 17: (a) Interferometric autocorrelation trace. (b) Intensity autocorrelation retrieved from the interferometric data, shown together with calculated Fourier limit. (c) Optical spectrum and a fitting. (d) Measured RF-spectrum.

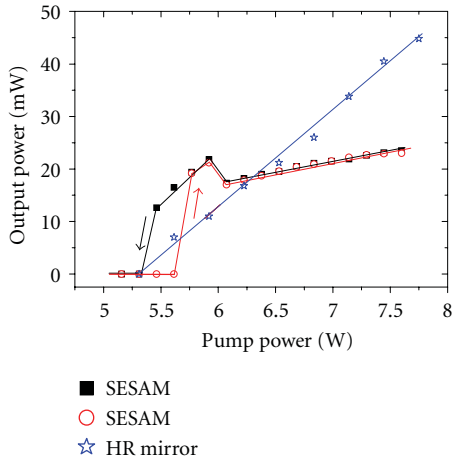


FIGURE 18: Average power of the GaSb SDL with a SESAM, and with a high reflective mirror. With the SESAM we can observe a hysteresis characteristic, typical for mode-locking.

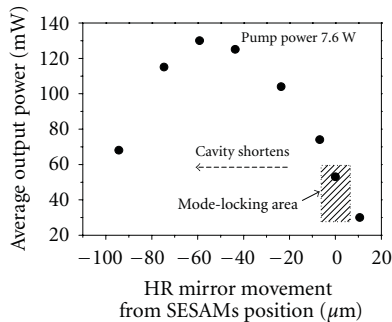


FIGURE 19: Output power of the GaSb disk laser with the high reflective mirror, given as a function of the HR mirror's position in regard to the original SESAM's position (point of optimal mode-locking).

To summarize, we have shown that nearly transform limited femtosecond pulses can be obtained from SESAM mode-locked GaSb disk lasers without use of additional dispersion compensating elements. So far the power levels are modest but there is reason to believe that the average power could be increased beyond 100 mW with further optimization of the laser.

#### 4. Future Outlook

SDLs (or VECSELs, or OPSLs) combine a small footprint, multiwatt output power capability, high beam quality, and the capability to fill spectral gaps that cannot be reached by traditional solid state disk lasers. In terms of semiconductor technology, OP-SDLs are in many aspects simpler than VCSELs; they do not require doping of the mirrors, usually make use of only one semiconductor mirror, and their processing is simpler. Owing to these advantageous features and intense developments efforts in the last decade, SDLs have reached a development stage that makes them very attractive for application deployments. While SDLs with emission at

green or blue have been commercialized for several years by Coherent Inc., there are other wavelength regions where SDLs could have a tremendous impact on the development of new applications. Leveraging the advantages of SDLs technology to broader wavelength domains is inherently linked to the development of new semiconductor structures enabling wavelength tailoring and increased functionality.

In this paper, we reviewed the main advances in the development of SDLs producing yellow-orange and  $2\ \mu\text{m}$  radiation, which are required in medicine, astronomy, life science research, sensing, or infrared countermeasures. GaInNAs/GaAs gain mirrors are now a reliable approach for the development of SDLs with fundamental emission of more than 11 W at around 1180–1200 nm. This material system has enabled generation of yellow-orange laser radiation with excellent beam quality and output power exceeding 7 W (the highest power obtained from a semiconductor-based laser at this wavelength range). The GaSb gain mirrors have been used to leverage the advantages offered by SDLs to the 2–3  $\mu\text{m}$  wavelength range. This material system is very robust in terms of reliability and life-time, enabling one to reach output powers in excess of several watts at wavelengths of 2–2.3  $\mu\text{m}$ . Most recently, we have demonstrated that GaSb SDLs are suitable for generation of femtosecond pulses at 2- $\mu\text{m}$ , a wavelength range that is particularly attractive for surgery, infrared counter measures, or LIDAR, and where there is a lack of compact high-power ultrashort pulse sources. Despite these achievements, there are certainly several development steps that are required for reaching new functionality and for advancing the technology to levels suitable for application deployment. The main development directions we undertake for the advances of dilute-nitride and GaSb-based SDLs are briefly discussed as follows.

*Development of flip-chip technology for dilute nitride SDLs*, would enable further improvements of the spectral and power characteristics. The main limitation of using intracavity heat spreader is related to spectral modulation caused by spurious etalon effects, which have a detrimental effect on wavelength tuning and mode-locking. Allegedly, the flip-chip technology would also enable a more predictable power scaling with increasing the area of the pump region on the gain mirror. The main difficulty related to the use of flip-chip technology for dilute-nitrides is apparently related to the high level of residual strain corresponding to the GaInNAs active region; the strain leads to occurrence of structural defects due to mechanical deformation once the substrate is removed. Advanced strain compensation techniques are expected to alleviate this problem.

*Flip-chip technology could provide advantages to GaSb-based SDLs* for increased functionality and development of a process that is more suitable for volume production. In particular, we should note that wavelength-tuning capability is very important for mid-IR SDLs as many of the applications could be related to spectroscopy. The main difficulty related to the use of flip-chip technology for GaSb is related to the fact that this material system is less developed from processing point of view. Successful steps in GaSb SDL flip-chip processing and development of adequate etch stop layers for substrate removal have been already made [26]. Very recently

we have also demonstrated that InPsb can be used effectively as an etch stop layer for the GaSb substrate removal; we have achieved an etch selectivity of GaSb substrate as high as 244 and excellent substrate removal rate of  $32.4 \mu\text{m}/\text{min}$  [115]. The flip-chip GaSb gain mirrors would be beneficial for ultrashort pulse operation and could ultimately enable to take full advantage of the broad gain bandwidth of GaSb.

*Development of electrically pumped GaSb SDLs.* While optically pumped SDLs can produce multiple watts of output power, they require a separate pump source that adds to the cost and complexity of the device. Direct electrical-pumping offers an interesting alternative that simplifies the overall laser scheme. If the power level is not the main target, electrically pumping of SDLs, more often termed as EP-VECSELs, can be realized conveniently [116]. The essential challenges of electrical pumping relate to nonuniform current spreading and optical losses in doped semiconductor material [117–119]. Doping is necessary for achieving low electrical resistance, but at the same time it does increase absorption. On the other hand, the current spreading problems limit the size of usable gain area and therefore hinder power scaling. Despite several technical challenges, EP-VECSELs have been studied actively and there have been also serious attempts to commercialize this type of laser [120, 121]. Using standard GaAs gain mirrors output power levels in excess of 400 mW have been reported [122]. On the contrary GaSb-based EP-VECSELs have been demonstrated only recently [123]. For this preliminary demonstration, we have used a (1/2)-VCSEL gain mirror ( $\lambda \sim 2.3 \mu\text{m}$ ) that was fabricated at the Walter Schottky Institute in Germany. An I-shaped cavity was formed between the gain mirror and a curved output coupler. In a first study we tested 7 different components with diameters of 30–90  $\mu\text{m}$ . Lasing was obtained from all components at 15°C mount temperature using pulsed current with 1  $\mu\text{s}$  pulse width and 3% duty cycle. A maximum peak power of 1.5 mW was obtained from the 60  $\mu\text{m}$  component. Thermal issues seemed to be the major factor limiting the power. We should note here that electrical pumping is particularly attractive for mid-IR GaSb VECSELs, as the requirements for deployment in spectroscopic applications are mainly related to compactness, tunability, single-frequency lasers, and less to the power level. An EP-VECSEL would be compact but at the same time would enable to include intracavity elements for wavelength tuning in a broad wavelength range or would enable the use of intracavity spectroscopy in compact and efficient laser architectures.

## Acknowledgments

The authors would like to thank several colleagues and external collaborators for continuous contribution to the development of SDLs reviewed here. In particular, Janne Puustinen, Jonna Paajaste, and Riku Koskinen are acknowledged for MBE fabrication of the semiconductor structures, and Lasse Orsila and Jari Nikkinen are acknowledged for their help with the deposition of antireflection coatings. They thank Jukka-Pekka Alanko, Christian Grebing, and Professor Günter Steinmeyer for their contribution to the demonstration

of 2- $\mu\text{m}$  mode-locked SDL. They acknowledge Professor Anne Tropper from the University of Southampton for useful discussion and sharing some of the data presented in Figure 3. They thank Professor Amann and his group from the Walter Schottky Institute for fabricating the 2.3  $\mu\text{m}$  EP-VECSEL samples they reported in [123]. They gratefully acknowledge the financial support provided by by Areté Associates, Pirkanmaa TE-center, the Finnish Funding Agency for Development and Innovation (TEKES), the Academy of Finland (no. 128364), the Graduate Schools in Material Science and GETA, and the United States Office of Naval Research Global (ONRG) under the Grant no. N62909-10-1-7030.

## References

- [1] N. Basov, O. Bogdankevich, and A. Grasyuk, “9B4—semiconductor lasers with radiating mirrors,” *Quantum Electronics*, vol. 2, no. 9, pp. 594–597, 1966.
- [2] W. B. Jiang, S. R. Friberg, H. Iwamura, and Y. Yamamoto, “High powers and subpicosecond pulses from an external-cavity surface-emitting InGaAs/InP multiple quantum well laser,” *Applied Physics Letters*, vol. 58, no. 8, pp. 807–809, 1991.
- [3] H. Q. Le, S. Di Cecca, and A. Mooradian, “Scalable high-power optically pumped GaAs laser,” *Applied Physics Letters*, vol. 58, no. 18, pp. 1967–1969, 1991.
- [4] W. H. Xiang, S. R. Friberg, K. Watanabe et al., “Sub-100 femtosecond pulses from an external-cavity surface-emitting InGaAs/InP multiple quantum well laser with soliton-effect compression,” *Applied Physics Letters*, vol. 59, no. 17, pp. 2076–2078, 1991.
- [5] D. C. Sun, S. R. Friberg, K. Watanabe, S. MacHida, Y. Horikoshi, and Y. Yamamoto, “High power and high efficiency vertical cavity surface emitting GaAs laser,” *Applied Physics Letters*, vol. 61, no. 13, pp. 1502–1503, 1992.
- [6] W. B. Jiang, R. Mirin, and J. E. Bowers, “Mode-locked GaAs vertical cavity surface emitting lasers,” *Applied Physics Letters*, vol. 60, no. 6, pp. 677–679, 1992.
- [7] C. Symonds, J. Dion, I. Sagnes et al., “High performance 1.55  $\mu\text{m}$  vertical external cavity surface emitting laser with broadband integrated dielectric-metal mirror,” *Electronics Letters*, vol. 40, no. 12, pp. 734–735, 2004.
- [8] D. Lorensen, H. J. Unold, D. J. H. C. Maas et al., “Towards wafer-scale integration of high repetition rate passively mode-locked surface-emitting semiconductor lasers,” *Applied Physics B*, vol. 79, no. 8, pp. 927–932, 2004.
- [9] M. Kuznetsov, F. Hakimi, R. Sprague, and A. Mooradian, “Design and characteristics of high-power (>0.5-W CW) diode-pumped vertical-external-cavity surface-emitting semiconductor lasers with circular TEM<sub>00</sub> beams,” *IEEE Journal on Selected Topics in Quantum Electronics*, vol. 5, no. 3, pp. 561–573, 1999.
- [10] E. J. Saarinen, A. Härkönen, S. Suomalainen, and O. G. Okhotnikov, “Power scalable semiconductor disk laser using multiple gain cavity,” in *Proceedings of the Conference on Lasers and Electro-Optics (CLEO ’07)*, 2007.
- [11] L. Fan, M. Fallahi, J. Hader et al., “Multichip vertical-external-cavity surface-emitting lasers: a coherent power scaling scheme,” *Optics Letters*, vol. 31, no. 24, pp. 3612–3614, 2006.

- [12] T. J. Ochalski, A. De Burea, G. Huyet et al., "Passively modulated bi-directional vertical external ring cavity surface emitting laser," in *Proceedings of the Conference on Quantum Electronics and Laser Science Conference on Lasers and Electro-Optics (CLEO/QELS '08)*, May 2008.
- [13] J. E. Hastie, J. M. Hopkins, C. W. Jeon et al., "Microchip vertical external cavity surface emitting lasers," *Electronics Letters*, vol. 39, no. 18, pp. 1324–1326, 2003.
- [14] S. A. Smith, J. M. Hopkins, J. E. Hastie et al., "Diamond-microchip GaInNAs vertical external-cavity surface-emitting laser operating CW at 1315 nm," *Electronics Letters*, vol. 40, no. 15, pp. 935–936, 2004.
- [15] N. Laurand, C. L. Lee, E. Gu, J. E. Hastie, S. Calvez, and M. D. Dawson, "Microlensed microchip VECSEL," *Optics Express*, vol. 15, no. 15, pp. 9341–9346, 2007.
- [16] S. W. Corzine, R. S. Geels, J. W. Scott, R. H. Yan, and L. A. Coldren, "Design of Fabry-Perot surface-emitting lasers with a periodic gain structure," *IEEE Journal of Quantum Electronics*, vol. 25, no. 6, pp. 1513–1524, 1989.
- [17] M. Schmid, S. Benchabane, F. Torabi-Goudarzi, R. Abram, A. I. Ferguson, and E. Riis, "Optical in-well pumping of a vertical-external-cavity surface-emitting laser," *Applied Letters*, vol. 84, no. 24, pp. 4860–4862, 2004.
- [18] S. S. Beyertt, U. Brauch, F. Demaria et al., "Efficient gallium-arsenide disk laser," *IEEE Journal of Quantum Electronics*, vol. 43, no. 10, pp. 869–875, 2007.
- [19] N. Schulz, M. Rattunde, C. Ritzenthaler et al., "Resonant optical in-well pumping of an (AlGaIn)(AsSb)-based vertical-external-cavity surface-emitting laser emitting at 2.35  $\mu\text{m}$ ," *Applied Physics Letters*, vol. 91, no. 9, Article ID 091113, 2007.
- [20] V. M. Korpjärvi, T. Leinonen, J. Puustinen, A. Härkönen, and M. D. Guina, "11 W single gain-chip dilute nitride disk laser emitting around 1180 nm," *Optics Express*, vol. 18, no. 25, pp. 25633–25641, 2010.
- [21] A. J. Kemp, G. J. Valentine, J. M. Hopkins et al., "Thermal management in vertical-external-cavity surface-emitting lasers: finite-element analysis of a heatspreader approach," *IEEE Journal of Quantum Electronics*, vol. 41, no. 2, pp. 148–155, 2005.
- [22] W. J. Alford, T. D. Raymond, and A. A. Allerman, "High power and good beam quality at 980 nm from a vertical external-cavity surface-emitting laser," *Journal of the Optical Society of America B*, vol. 19, no. 4, pp. 663–666, 2002.
- [23] J. E. Hastie, J. M. Hopkins, S. Calvez et al., "0.5-W single transverse-mode operation of an 850 nm diode-pumped surface-emitting semiconductor laser," *IEEE Photonics Technology Letters*, vol. 15, no. 7, pp. 894–896, 2003.
- [24] Z. L. Liao, "Semiconductor wafer bonding via liquid capillarity," *Applied Physics Letters*, vol. 77, no. 5, pp. 651–653, 2000.
- [25] M. Kuznetsov, F. Hakimi, R. Sprague, and A. Mooradian, "High-power (>0.5-W CW) diode-pumped vertical-external-cavity surface-emitting semiconductor lasers with circular TEM<sub>00</sub> beams," *IEEE Photonics Technology Letters*, vol. 9, no. 8, pp. 1063–1065, 1997.
- [26] J. P. Perez, A. Laurain, L. Cerutti, I. Sagnes, and A. Garnache, "Technologies for thermal management of mid-IR Sb-based surface emitting lasers," *Semiconductor Science and Technology*, vol. 25, no. 4, Article ID 045021, 2010.
- [27] A. R. Clawson, "Guide to references on III-V semiconductor chemical etching," *Materials Science and Engineering R*, vol. 31, no. 1, pp. 1–438, 2001.
- [28] A. J. Maclean, A. J. Kemp, S. Calvez et al., "Continuous tuning and efficient intracavity second-harmonic generation in a semiconductor disk laser with an intracavity diamond heatspreader," *IEEE Journal of Quantum Electronics*, vol. 44, no. 3, pp. 216–225, 2008.
- [29] T. L. Wang, Y. Kaneda, J. M. Yarborough et al., "High-power optically pumped semiconductor laser at 1040 nm," *IEEE Photonics Technology Letters*, vol. 22, no. 9, Article ID 5422654, pp. 661–663, 2010.
- [30] J. Chilla, Q. Shu, H. Zhou, E. Weiss, M. Reed, and L. Spinelli, "Recent advances in optically pumped semiconductor lasers," in *Solid State Lasers XVI: Technology and Devices*, vol. 6451 of *Proceedings of SPIE*, San Jose, Calif, USA, 2007.
- [31] H. Lindberg, M. Strassner, E. Gerster, J. Bengtsson, and A. Larsson, "Thermal management of optically pumped long-wavelength InP-based semiconductor disk lasers," *IEEE Journal on Selected Topics in Quantum Electronics*, vol. 11, no. 5, pp. 1126–1134, 2005.
- [32] A. J. Kemp, A. J. MacLean, J. E. Hastie et al., "Thermal lensing, thermal management and transverse mode control in microchip VECSELs," *Applied Physics B*, vol. 83, no. 2, pp. 189–194, 2006.
- [33] A. J. Maclean, R. B. Birch, P. W. Roth, A. J. Kemp, and D. Burns, "Limits on efficiency and power scaling in semiconductor disk lasers with diamond heatspreaders," *Journal of the Optical Society of America B*, vol. 26, no. 12, pp. 2228–2236, 2009.
- [34] A. R. Zakharian, J. Hader, J. V. Moloney, S. W. Koch, P. Brick, and S. Lutgen, "Experimental and theoretical analysis of optically pumped semiconductor disk lasers," *Applied Physics Letters*, vol. 83, no. 7, pp. 1313–1315, 2003.
- [35] L. Fan, M. Fallahi, J. T. Murray et al., "Tunable high-power high-brightness linearly polarized vertical-external-cavity surface-emitting lasers," *Applied Physics Letters*, vol. 88, no. 2, Article ID 021105, pp. 1–3, 2006.
- [36] L. Fan, M. Fallahi, A. R. Zakharian et al., "Extended tunability in a two-chip VECSEL," *IEEE Photonics Technology Letters*, vol. 19, no. 8, pp. 544–546, 2007.
- [37] J. Paajaste, S. Suomalainen, R. Koskinen, A. Härkönen, M. Guina, and M. Pessa, "High-power and broadly tunable GaSb-based optically pumped VECSELs emitting near 2  $\mu\text{m}$ ," *Journal of Crystal Growth*, vol. 311, no. 7, pp. 1917–1919, 2009.
- [38] C. Borgentun, J. Bengtsson, A. Larsson, F. Demaria, A. Hein, and P. Unger, "Optimization of a broadband gain element for a widely tunable high-power semiconductor disk laser," *IEEE Photonics Technology Letters*, vol. 22, no. 13, Article ID 5451056, pp. 978–980, 2010.
- [39] M. A. Holm, D. Burns, A. I. Ferguson, and M. D. Dawson, "Actively stabilized single-frequency vertical-external-cavity AlGaAs laser," *IEEE Photonics Technology Letters*, vol. 11, no. 12, pp. 1551–1553, 1999.
- [40] H. Lindberg, A. Larsson, and M. Strassner, "Single-frequency operation of a high-power, long-wavelength semiconductor disk laser," *Optics Letters*, vol. 30, no. 17, pp. 2260–2262, 2005.
- [41] A. Laurain, M. Myara, G. Beaudoin, I. Sagnes, and A. Garnache, "Multiwatt-power highly-coherent compact single-frequency tunable vertical-external-cavity-surface-emitting-semiconductor-laser," *Optics Express*, vol. 18, no. 14, pp. 14627–14636, 2010.
- [42] B. Rudin, A. Rutz, M. Hoffmann et al., "Highly efficient optically pumped vertical-emitting semiconductor laser with more than 20 W average output power in a fundamental transverse mode," *Optics Letters*, vol. 33, no. 22, pp. 2719–2721, 2008.
- [43] J. Chilla, S. Butterworth, A. Zeitschel et al., "High power optically pumped semiconductor lasers," in *Solid State Lasers*

- XIII: Technology and Devices*, vol. 5332 of *Proceedings of SPIE*, pp. 143–150, San Jose, Calif, USA, 2004.
- [44] A. H. Quarterman, K. G. Wilcox, V. Apostolopoulos et al., “A passively mode-locked external-cavity semiconductor laser emitting 60 fs pulses,” *Nature Photonics*, vol. 3, no. 12, pp. 729–731, 2009.
- [45] P. Klopp, F. Saas, M. Zorn, M. Weyers, and U. Griebner, “290 fs pulses from a semiconductor disk laser,” *Optics Express*, vol. 16, no. 8, pp. 5770–5775, 2008.
- [46] A. Aschwanden, D. Lorenser, H. J. Unold, R. Paschotta, E. Gini, and U. Keller, “2.1 W picosecond passively mode-locked external-cavity semiconductor laser,” *Optics Letters*, vol. 30, no. 3, pp. 272–274, 2005.
- [47] B. Rudin, V. J. Wittwer, D. J. H. C. Maas et al., “High-power MIXSEL: an integrated ultrafast semiconductor laser with 6.4 W average power,” *Optics Express*, vol. 18, no. 26, pp. 27582–27588, 2010.
- [48] D. Lorenser, D. J. H. C. Maas, H. J. Unold et al., “50 GHz passively mode-locked surface-emitting semiconductor laser with 100 mW average output power,” *IEEE Journal of Quantum Electronics*, vol. 42, no. 8, Article ID 01658136, pp. 838–847, 2006.
- [49] U. Keller and A. C. Tropper, “Passively modelocked surface-emitting semiconductor lasers,” *Physics Reports*, vol. 429, no. 2, pp. 67–120, 2006.
- [50] W. Zhang, A. McDonald, T. Ackemann, E. Riis, and G. McConnell, “Femtosecond synchronously in-well pumped vertical-external-cavity surface-emitting laser,” *Optics Express*, vol. 18, no. 1, pp. 187–192, 2010.
- [51] J. Rautiainen, V. M. Korpiljärvi, J. Puustinen, M. Guina, and O. G. Okhotnikov, “Passively mode-locked GaInNAs disk laser operating at 1220 nm,” *Optics Express*, vol. 16, no. 20, pp. 15964–15969, 2008.
- [52] A. Rutz, V. Liverini, D. J. H. C. Maas et al., “Passively mode-locked GaInNAs VECSEL at centre wavelength around 1.3  $\mu\text{m}$ ,” *Electronics Letters*, vol. 42, no. 16, pp. 926–927, 2006.
- [53] A. Khadour, S. Bouchoule, G. Aubin, J. C. Harmand, J. Decobert, and J. L. Oudar, “Ultrashort pulse generation from 1.56  $\mu\text{m}$  modelocked VECSEL at room temperature,” *Optics Express*, vol. 18, no. 19, pp. 19902–19913, 2010.
- [54] J. E. Hastie, L. G. Morton, A. J. Kemp, M. D. Dawson, A. B. Krysa, and J. S. Roberts, “Tunable ultraviolet output from an intracavity frequency-doubled red vertical-external-cavity surface-emitting laser,” *Applied Physics Letters*, vol. 89, no. 6, Article ID 061114, 2006.
- [55] S. H. Park, J. Kim, H. Jeon et al., “Room-temperature GaN vertical-cavity surface-emitting laser operation in an extended cavity scheme,” *Applied Physics Letters*, vol. 83, no. 11, pp. 2121–2123, 2003.
- [56] J. Y. Kim, S. Cho, S. J. Lim et al., “Efficient blue lasers based on gain structure optimizing of vertical-external-cavity surface-emitting laser with second harmonic generation,” *Journal of Applied Physics*, vol. 101, no. 3, Article ID 033103, 2007.
- [57] J. Lee, S. Lee, T. Kim, and Y. Park, “7 W high-efficiency continuous-wave green light generation by intracavity frequency doubling of an end-pumped vertical external-cavity surface emitting semiconductor laser,” *Applied Physics Letters*, vol. 89, no. 24, Article ID 241107, 2006.
- [58] S. Hilbich, W. Seelert, V. Ostroumov et al., “New wavelengths in the yellow orange range between 545 nm to 580 nm generated by an intracavity frequency-doubled Optically Pumped Semiconductor Laser,” in *Solid State Lasers XVI: Technology and Devices*, vol. 6451 of *Proceedings of SPIE*, San Jose, Calif, USA, 2007.
- [59] A. Härkönen, J. Rautiainen, M. Guina et al., “High power frequency doubled GaInNAs semiconductor disk laser emitting at 615 nm,” *Optics Express*, vol. 15, no. 6, pp. 3224–3229, 2007.
- [60] M. I. Müller, N. Linder, C. Karnutsch et al., “Optically pumped semiconductor thin-disk laser with external cavity operating at 660 nm,” in *Vertical-Cavity Surface-Emitting Lasers VI*, vol. 4649 of *Proceedings of SPIE*, pp. 265–271, San Jose, Calif, USA, 2002.
- [61] K. S. Kim, J. R. Yoo, S. H. Cho et al., “1060 nm vertical-external-cavity surface-emitting lasers with an optical-to-optical efficiency of 44% at room temperature,” *Applied Physics Letters*, vol. 88, no. 9, Article ID 091107, 2006.
- [62] J. Konttinen, A. Härkönen, P. Tuomisto et al., “High-power (>1 W) dilute nitride semiconductor disk laser emitting at 1240 nm,” *New Journal of Physics*, vol. 9, article 140, 2007.
- [63] J. M. Hopkins, S. A. Smith, C. W. Jeon et al., “0.6 W CW GaInNAs vertical external-cavity surface emitting laser operating at 1.32  $\mu\text{m}$ ,” *Electronics Letters*, vol. 40, no. 1, pp. 30–31, 2004.
- [64] H. Lindberg, M. Strassner, E. Gerster, and A. Larsson, “0.8 W optically pumped vertical external cavity surface emitting laser operating CW at 1550 nm,” *Electronics Letters*, vol. 40, no. 10, pp. 601–602, 2004.
- [65] J. Nikkinen, J. Paajaste, R. Koskinen, S. Suomalainen, and O. G. Okhotnikov, “GaSb-based semiconductor disk laser with 130 nm tuning range at 2.5  $\mu\text{m}$ ,” *IEEE Photonics Technology Letters*, vol. 23, no. 12, Article ID 5723696, pp. 777–779, 2011.
- [66] B. Rösener, M. Rattunde, R. Moser et al., “Continuous-wave room-temperature operation of a 2.8  $\mu\text{m}$  GaSb-based semiconductor disk laser,” *Optics Letters*, vol. 36, no. 3, pp. 319–321, 2011.
- [67] M. Rahim, A. Khair, F. Felder, M. Fill, and H. Zogg, “4.5  $\mu\text{m}$  wavelength vertical external cavity surface emitting laser operating above room temperature,” *Applied Physics Letters*, vol. 94, no. 20, Article ID 201112, 2009.
- [68] M. Rahim, F. Felder, M. Fill, and H. Zogg, “Optically pumped 5  $\mu\text{m}$  IV-VI VECSEL with Al-heat spreader,” *Optics Letters*, vol. 33, no. 24, pp. 3010–3012, 2008.
- [69] Y. Kaneda, J. M. Yarborough, L. Li et al., “Continuous-wave all-solid-state 244 nm deep-ultraviolet laser source by fourth-harmonic generation of an optically pumped semiconductor laser using CsLiB<sub>6</sub>O<sub>10</sub> in an external resonator,” *Optics Letters*, vol. 33, no. 15, pp. 1705–1707, 2008.
- [70] T. Leinonen, J. Puustinen, V.-M. Korpiljärvi, A. Härkönen, M. Guina, and R. J. Epstein, “Generation of high power (>7 W) yellow-orange radiation by frequency doubling of GaInNAs-based semiconductor disk laser,” in *Proceedings of the Conference on Lasers and Electro-Optics Europe and 12th European Quantum Electronics Conference (CLEO EUROPE/EQEC '11)*, 2011.
- [71] J. Rautiainen, A. Härkönen, V.-M. Korpiljärvi et al., “Red and UV generation using frequency-converted GaInNAs-based semiconductor disk laser,” in *Proceedings of the Conference on Lasers and Electro-Optics and 2009 Conference on Quantum Electronics and Laser Science Conference (CLEO/QELS '09)*, 2009.
- [72] J. Paajaste, R. Koskinen, J. Nikkinen, S. Suomalainen, and O. G. Okhotnikov, “Power scalable 2.5  $\mu\text{m}$  (AlGaIn)(AsSb) semiconductor disk laser grown by molecular beam epitaxy,” *Journal of Crystal Growth*, vol. 323, pp. 454–456, 2010.
- [73] J. M. Hopkins, N. Hempler, B. Rösener et al., “5 W Mid-IR optically-pumped semiconductor disk laser,” in *Proceedings of the Conference on Quantum Electronics and Laser Science*

- Conference on Lasers and Electro-Optics (CLEO/QELS '08)*, May 2008.
- [74] A. Rantamäki, A. Sirbu, A. Mereuta, E. Kapon, and O. G. Okhotnikov, "3 W of 650 nm red emission by frequency doubling of wafer-fused semiconductor disk laser," *Optics Express*, vol. 18, no. 21, pp. 21645–21650, 2010.
- [75] J. Lyytikäinen, J. Rautiainen, A. Sirbu et al., "High-power 1.48  $\mu\text{m}$  wafer-fused optically pumped semiconductor disk laser," vol. 23, no. 13, pp. 917–919, 2011.
- [76] J. Rautiainen, J. Lyytikäinen, A. Sirbu et al., "2.6 W optically-pumped semiconductor disk laser operating at 1.57- $\mu\text{m}$  using wafer fusion," *Optics Express*, vol. 16, no. 26, pp. 21881–21886, 2008.
- [77] B. Lambert, Y. Toudic, Y. Rouillard et al., "High reflectivity 1.55  $\mu\text{m}$  (Al)GaAsSb/AlAsSb Bragg reflector lattice matched on InP substrates," *Applied Physics Letters*, vol. 66, pp. 442–444, 1995.
- [78] I. F. L. Dias, B. Nabet, A. Kohl, J. L. Benchimol, and J. C. Harmand, "Electrical and optical characteristics of n-type-doped distributed bragg mirrors on InP," *IEEE Photonics Technology Letters*, vol. 10, no. 6, pp. 763–765, 1998.
- [79] Y. Imajo, A. Kasukawa, S. Kashiwa, and H. Okamoto, "GaInAsP/InP semiconductor multilayer reflector grown by metalorganic chemical vapor deposition and its application to surface emitting laser diode," *Japanese Journal of Applied Physics*, vol. 29, no. 7, pp. 1130–1132, 1990.
- [80] J. H. Baek, I. H. Choi, B. Lee, W. S. Han, and H. K. Cho, "Precise control of 1.55  $\mu\text{m}$  vertical-cavity surface-emitting laser structure with InAlGaAs/InAlAs Bragg reflectors by in situ growth monitoring," *Applied Physics Letters*, vol. 75, no. 11, pp. 1500–1502, 1999.
- [81] E. Gerster, I. Ecker, S. Lorch, C. Hahn, S. Menzel, and P. Unger, "Orange-emitting frequency-doubled GaAsSb/GaAs semiconductor disk laser," *Journal of Applied Physics*, vol. 94, no. 12, pp. 7397–7401, 2003.
- [82] J. Lyytikäinen, J. Rautiainen, L. Toikkanen et al., "1.3- $\mu\text{m}$  optically-pumped semiconductor disk laser by wafer fusion," *Optics Express*, vol. 17, no. 11, pp. 9047–9052, 2009.
- [83] T. D. Germann, A. Strittmatter, U. W. Pohl et al., "Quantum-dot semiconductor disk lasers," *Journal of Crystal Growth*, vol. 310, no. 23, pp. 5182–5186, 2008.
- [84] J. Rautiainen, I. Krestnikov, M. Butkus, E. U. Rafailov, and O. G. Okhotnikov, "Optically pumped semiconductor quantum dot disk laser operating at 1180 nm," *Optics Letters*, vol. 35, no. 5, pp. 694–696, 2010.
- [85] L. Fan, C. Hessenius, M. Fallahi et al., "Highly strained InGaAsGaAs multiwatt vertical-external-cavity surface-emitting laser emitting around 1170 nm," *Applied Physics Letters*, vol. 91, no. 13, Article ID 131114, 2007.
- [86] K. J. Beernink, P. K. York, J. J. Coleman, R. G. Waters, J. Kim, and C. M. Wayman, "Characterization of InGaAs-GaAs strained-layer lasers with quantum wells near the critical thickness," *Applied Physics Letters*, vol. 55, no. 21, pp. 2167–2169, 1989.
- [87] G. Jaschke, R. Averbeck, L. Geelhaar, and H. Riechert, "Low threshold InGaAsN/GaAs lasers beyond 1500 nm," *Journal of Crystal Growth*, vol. 278, no. 1–4, pp. 224–228, 2005.
- [88] W. Walukiewicz, W. Shan, J. Wu, K. M. Yu, and J. W. Ager, "Band anticrossing and related electronic structure in III-N-V alloys," in *Dilute Nitride Semiconductors*, M. Henin, Ed., pp. 325–359, Elsevier, 2005.
- [89] E. P. O'Reilly, A. Lindsay, S. Fahy, S. Tomic, and P. J. Klar, "A tight-binding based analysis of the band anti-crossing model and its application in Ga(In)NAs alloys," in *Dilute Nitride Semiconductors*, M. Henini, Ed., pp. 361–391, Elsevier, 2005.
- [90] W. Walukiewicz, K. Alberi, J. Wu, W. Shan, K. M. Yu, and J. W. Ager, *Electronic Band Structure of Highly Mismatched Semiconductor Alloys*, Springer, 2008.
- [91] I. Vurgaftman and J. R. Meyer, "Band parameters for nitrogen-containing semiconductors," *Journal of Applied Physics*, vol. 94, no. 6, pp. 3675–3696, 2003.
- [92] D. J. Palmer, P. M. Smowton, P. Blood, J. Y. Yeh, L. J. Mawst, and N. Tansu, "Effect of nitrogen on gain and efficiency in InGaAsN quantum-well lasers," *Applied Physics Letters*, vol. 86, no. 7, Article ID 071121, pp. 1–3, 2005.
- [93] W. M. McGee, R. S. Williams, M. J. Ashwin et al., "Structure, morphology, and optical properties of  $\text{Ga}_x\text{In}_{1-x}\text{N}_{0.05}\text{As}_{0.95}$  quantum wells: influence of the growth mechanism," *Physical Review B*, vol. 76, no. 8, Article ID 085309, 2007.
- [94] J. Miguel-Sánchez, A. Guzmán, J. M. Ulloa, A. Hierro, and E. Muñoz, "Effect of nitrogen ions on the properties of InGaAsN quantum wells grown by plasma-assisted molecular beam epitaxy," *IEEE Proceedings: Optoelectronics*, vol. 151, no. 5, pp. 305–308, 2004.
- [95] A. Y. Egorov, D. Bernklau, D. Livshits, V. Ustinov, Z. I. Alferov, and H. Riechert, "High power CW operation of InGaAsN lasers at 1.3  $\mu\text{m}$ ," *Electronics Letters*, vol. 35, no. 19, pp. 1643–1644, 1999.
- [96] O. Ambacher, "Growth and applications of group III-nitrides," *Journal of Physics D*, vol. 31, no. 20, pp. 2653–2710, 1998.
- [97] H. Carrère, A. Arnoult, A. Ricard, and E. Bedel-Pereira, "RF plasma investigations for plasma-assisted MBE growth of (Ga,In)(As,N) materials," *Journal of Crystal Growth*, vol. 243, no. 2, pp. 295–301, 2002.
- [98] E. M. Pavelescu, T. Hakkarainen, V. D. S. Dhaka et al., "Influence of arsenic pressure on photoluminescence and structural properties of GaInNAs/GaAs quantum wells grown by molecular beam epitaxy," *Journal of Crystal Growth*, vol. 281, no. 2–4, pp. 249–254, 2005.
- [99] S. Giet, A. J. Kemp, D. Burns et al., "Comparison of thermal management techniques for semiconductor disk lasers," in *Solid State Lasers XVII: Technology and Devices*, vol. 6871 of *Proceedings of SPIE*, San Jose, Calif, USA, 2008.
- [100] A. Härkönen, M. Guina, O. Okhotnikov et al., "1-W antimonide-based vertical external cavity surface emitting laser operating at 2- $\mu\text{m}$ ," *Optics Express*, vol. 14, no. 14, pp. 6479–6484, 2006.
- [101] J. M. Hopkins, N. Hempler, B. Rösener et al., "High-power, (AlGaIn)(AsSb) semiconductor disk laser at 2.0  $\mu\text{m}$ ," *Optics Letters*, vol. 33, no. 2, pp. 201–203, 2008.
- [102] J. H. V. Price, T. M. Monro, H. Ebindorff-Heidepriem et al., "Mid-IR supercontinuum generation from nonsilica microstructured optical fibers," *IEEE Journal on Selected Topics in Quantum Electronics*, vol. 13, no. 3, pp. 738–749, 2007.
- [103] A. Härkönen, J. Paajaste, S. Suomalainen et al., "Picosecond passively mode-locked GaSb-based semiconductor disk laser operating at 2  $\mu\text{m}$ ," *Optics Letters*, vol. 35, no. 24, pp. 4090–4092, 2010.
- [104] A. Härkönen, C. Grebing, J. Paajaste et al., "Modelocked GaSb disk laser producing 384 fs pulses at 2 m wavelength," *Electronics Letters*, vol. 47, no. 7, pp. 454–456, 2011.
- [105] L. Shterengas, G. Belenky, T. Hosoda, G. Kipshidze, and S. Suchalkin, "Continuous wave operation of diode lasers at 3.36  $\mu\text{m}$  at 12°C," *Applied Physics Letters*, vol. 93, no. 1, Article ID 011103, 2008.

- [106] T. Hosoda, G. Kipshidze, L. Shterengas, and G. Belenky, "Diode lasers emitting near  $3.44\ \mu\text{m}$  in continuous-wave regime at 300 K," *Electronics Letters*, vol. 46, no. 21, pp. 1455–1457, 2010.
- [107] Y. Y. Lai, J. M. Yarborough, Y. Kaneda et al., "340-W peak power from a GaSb  $2\text{-}\mu\text{m}$  optically pumped semiconductor laser (OPSL) grown mismatched on GaAs," *IEEE Photonics Technology Letters*, vol. 22, no. 16, Article ID 5512584, pp. 1253–1255, 2010.
- [108] U. Keller, K. J. Weingarten, F. X. Kärtner et al., "Semiconductor saturable absorber mirrors (SESAM's) for femtosecond to nanosecond pulse generation in solid-state lasers," *IEEE Journal on Selected Topics in Quantum Electronics*, vol. 2, no. 3, pp. 435–453, 1996.
- [109] R. Koskinen, S. Suomalainen, J. Paajaste et al., "Highly nonlinear GaSb-based saturable absorber mirrors," in *Nonlinear Optics and Applications III*, vol. 7354 of *Proceedings of SPIE*, 2009.
- [110] J. Paajaste, S. Suomalainen, R. Koskinen, A. Härkönen, G. Steinmeyer, and M. Guina, "GaSb-based semiconductor saturable absorber mirrors for mode-locking  $2\ \mu\text{m}$  semiconductor disk lasers," *Physica Status Solidi (C), Special Issue: 38th International Symposium on Compound Semiconductors (ISCS 2011)*, vol. 9, no. 2, pp. 294–297, 2012.
- [111] L. Cerutti, A. Garnache, A. Ouvrard, and F. Genty, "High temperature continuous wave operation of Sb-based vertical external cavity surface emitting laser near  $2.3\ \mu\text{m}$ ," *Journal of Crystal Growth*, vol. 268, no. 1-2, pp. 128–134, 2004.
- [112] M. Rattunde, N. Schulz, C. Ritzenthaler et al., "High brightness GaSb-based optically pumped semiconductor disk lasers at  $2.3\ \mu\text{m}$ ," in *Quantum Sensing and Nanophotonic Devices IV*, vol. 6479 of *Proceedings of SPIE*, 2007.
- [113] A. Garnache, S. Hoogland, A. C. Tropper, I. Sagnes, G. Saint-Girons, and J. S. Roberts, "Sub-500-fs soliton-like pulse in a passively mode-locked broadband surface-emitting laser with 100 mW average power," *Applied Physics Letters*, vol. 80, no. 21, pp. 3892–3894, 2002.
- [114] H. Lindberg, M. Sadeghi, M. Westlund et al., "Mode locking a 1550 nm semiconductor disk laser by using a GaInNAs saturable absorber," *Optics Letters*, vol. 30, no. 20, pp. 2793–2795, 2005.
- [115] J. Lindfors, J. Paajaste, R. Koskinen, A. Härkönen, S. Suomalainen, and M. Guina, "Highly selective etch stop layer for GaSb substrate removal," in *Proceedings of the 16th Semiconducting and Insulating Materials Conference (SIMC-XVI '11)*, 2011.
- [116] N. Yokouchi, T. Miyamoto, T. Uchida, Y. Inaba, F. Koyama, and K. Iga, "40 angstrom continuous tuning of a GaInAsP/InP vertical-cavity surface-emitting laser using an external mirror," *IEEE Photonics Technology Letters*, vol. 4, no. 7, pp. 701–703, 1992.
- [117] P. Kreuter, B. Witzigmann, D. J. H. C. Maas, Y. Barbarin, T. Südmeyer, and U. Keller, "On the design of electrically pumped vertical-external-cavity surface-emitting lasers," *Applied Physics B*, vol. 91, no. 2, pp. 257–264, 2008.
- [118] J. R. Orchard, D. T.D. Childs, L. C. Lin, B. J. Stevens, D. M. Williams, and R. A. Hogg, "Design rules and characterisation of electrically pumped vertical external cavity surface emitting lasers," *Japanese Journal of Applied Physics*, vol. 50, no. 4, Article ID 04DG05, 2011.
- [119] W. Schwarz, "Cavity optimization of electrically pumped VECSELs," II Annual Report, Institute of Optoelectronics, Ulm University, 2006.
- [120] M. Jansen, B. D. Cantos, G. P. Carey et al., "Visible laser and laser array sources for projection displays," in *Liquid Crystal Materials, Devices, and Applications XI*, vol. 6135 of *Proceedings of SPIE*, 2006.
- [121] A. Mooradian, S. Antikichev, B. Cantos et al., "High power extended vertical cavity surface emitting diode lasers and arrays and their applications," in *Proceedings of the Micro-Optics Conference*, pp. 1–4, 2005.
- [122] J. G. McInerney, A. Mooradian, A. Lewis et al., "High-power surface emitting semiconductor laser with extended vertical compound cavity," *Electronics Letters*, vol. 39, no. 6, pp. 523–525, 2003.
- [123] A. Härkönen, A. Bachmann, S. Arafin et al., " $2.34\ \mu\text{m}$  electrically-pumped VECSEL with buried tunnel junction," in *Semiconductor Lasers and Laser Dynamics IV*, vol. 7720 of *Proceedings of SPIE*, 2010.

## Review Article

# Spin-Controlled Vertical-Cavity Surface-Emitting Lasers

**Nils C. Gerhardt and Martin R. Hofmann**

*Photonics and Terahertz Technology, Ruhr University Bochum, 44780 Bochum, Germany*

Correspondence should be addressed to Nils C. Gerhardt, [nils.gerhardt@rub.de](mailto:nils.gerhardt@rub.de)

Received 29 April 2011; Revised 8 December 2011; Accepted 20 December 2011

Academic Editor: Rainer Michalzick

Copyright © 2012 N. C. Gerhardt and M. R. Hofmann. This is an open access article distributed under the Creative Commons Attribution License, which permits unrestricted use, distribution, and reproduction in any medium, provided the original work is properly cited.

We discuss the concept of spin-controlled vertical-cavity surface-emitting lasers (VCSELs) and analyze it with respect to potential room-temperature applications in spin-optoelectronic devices. Spin-optoelectronics is based on the optical selection rules as they provide a direct connection between the spin polarization of the recombining carriers and the circular polarization of the emitted photons. By means of optical excitation and numerical simulations we show that spin-controlled VCSELs promise to have superior properties to conventional devices such as threshold reduction, spin control of the emission, or even much faster dynamics. Possible concepts for room-temperature electrical spin injection without large external magnetic fields are summarized, and the progress on the field of purely electrically pumped spin-VCSELs is reviewed.

## 1. Introduction

Concepts for the use of the electron spin as an information carrier have become an important research field called “spintronics.” The goal of spintronic research is to exploit the carrier spin degree of freedom additionally to the charge degree of freedom in order to develop novel devices, which offer new functionalities or a better performance as their conventional counterparts. Semiconductor spintronics in general includes the search for alternative device concepts as well as the investigation of the fundamental physical processes as spin injection, spin transport, spin manipulation, and spin detection. This research area was strongly stimulated by the suggestion of the so-called spin transistor by Datta and Das in 1990 [1]. Although such a spin transistor has yet to be realized even about 20 years after its suggestion, a lot of progress has been made in terms of understanding the above-mentioned fundamental physical processes. Moreover, new spintronic device concepts have been developed which might have a more realistic application perspective than the spin transistor. For example, spin-optoelectronic devices might be very promising. In such devices the direct connection between carrier spin momentum and photon spin momentum upon radiative recombination will be utilized in order to generate a spin-controlled net circular polarization degree for the light emission. While spin light-emitting diodes (spin-LEDs)

are already established tools in order to characterize and optimize electrical spin injection [2–9], spin controlled semiconductor lasers (spin-lasers) seem to be more promising for mass applications. Spin-lasers might provide properties superior to those of their conventional counterparts. For example, they promise to have faster modulation dynamics [10–14], to operate with lower threshold [15–20] and to offer a stronger polarization determination than conventional lasers with up to a 100% polarization control [17, 21–26]. However, such spin-optoelectronic device concepts are only attractive for applications if they operate at room temperature and without the need for large external magnetic fields, and if they really provide new or superior properties. Therefore, while earlier reviews have nicely discussed the physical background of spin-optoelectronic devices and the scientific achievements [24, 27, 28], we concentrate on approaches operating at room temperature without the need for superconducting magnets. In particular, we analyze the potential for new and superior performance of spin-controlled lasers.

In this article, we first discuss the fundamentals of spin-optoelectronics and then analyze the concepts for spin injection with respect to their potential for room temperature and low magnetic field operation. Then, we discuss the concepts for spin-controlled semiconductor lasers, namely, spin-controlled vertical-cavity surface-emitting lasers (VCSELs), and analyze which properties are particularly attractive for

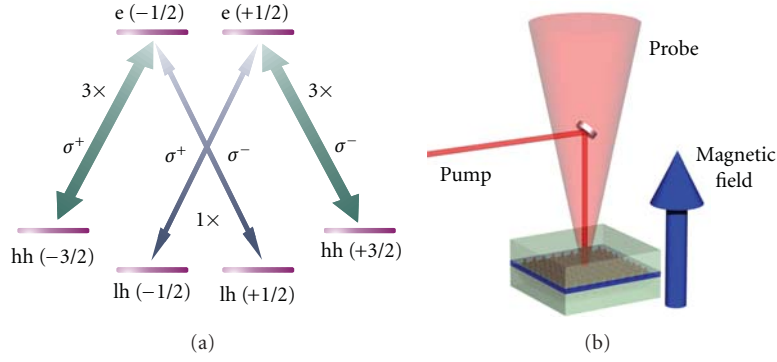


FIGURE 1: (a) Selection rules for optical transitions in direct semiconductor quantum well. The quantum numbers  $m_j$  which correspond to the  $z$ -projections of the total angular momentum of each Bloch state are printed in brackets. The transition rates and the associated circular polarization states are plotted next to the transition. (b) Vertical geometry for the selection rules in case of quantum well structure.

applications. Finally, we briefly review the state-of-the-art for electrically pumped VCSELs.

## 2. Fundamentals of Spin-Optoelectronics

**2.1. Optical Selection Rules.** Spin-optoelectronics is based on the fact that the total spin angular momentum of an electron-hole pair is directly linked to the angular momentum of a photon, which is either absorbed or emitted radiatively. This link is a consequence of the conservation of the angular momentum and is expressed by the so-called optical quantum selection rules for dipole radiation which are shown schematically for direct band-gap semiconductors in Figure 1(a) [29]. This schematic reduces the band structure of a typical direct semiconductor like GaAs in the vicinity of the  $\Gamma$ -point to a 6-level diagram in accordance with usual Bloch states. The Bloch states in Figure 1(a) are denoted by the quantum number  $m_j$  which corresponds to the projection of the total angular momentum  $\vec{J}$  including orbital and spin momentum onto the positive  $z$  axis. The s-like conduction band is represented by two electron (e) levels with opposite spins (+1/2 and -1/2). The p-like valence band is represented by four states: two heavy hole (hh) states with  $m_j = \pm 3/2$ , and two light hole (lh) states with  $m_j = \pm 1/2$ . The split-off band is energetically separated by the spin-orbit splitting energy  $\Delta_{SO}$  and therefore usually not included in the considerations. However, it should be noted that a sufficiently large spin-orbit splitting is a basic requirement for spin-optoelectronic devices otherwise optically induced spin injection as well as optical detection of carrier spin would not be achievable. In bulk GaAs, the hh and lh states are degenerated at the  $\Gamma$ -point. The energetic splitting of hh and lh states in Figure 1(a) appears because we consider a two-dimensional system, for example, a GaAs quantum well (QW), which is mostly used in spin-optoelectronic devices. Here different confinement energies for heavy and light hole states and possible strain contributions lead to a separation of the hole band states. The projection of the angular momentum of circularly polarized photons of the wave

vector matches  $\pm 1 \hbar$ . From this it follows that optical transitions between conduction and valence band states involving circularly polarized light are allowed for  $\Delta m_j = \pm 1$  only. In direct bulk semiconductors, this optical selection rule is valid for all directions, but in the case of lower dimensional active regions like quantum wells or quantum dots (QDs) the situation is a little more complex. In narrow QWs, the transitions depicted in Figure 1(a) are only valid for a vertical geometry, where the carrier spin orientation as well as the light emission is perpendicular to the quantum well plane (Figure 1(b)). Sometimes this geometry is denoted as Faraday geometry, even though a magnetic field is not obligatory in this case. The possible transitions are indicated by arrows in Figure 1(a). Due to the different geometries of the wave functions of the hh and lh states, the transitions involving hh and lh states have different probabilities. In detail, the hh transitions are three-times more probable than lh transitions.

As mentioned above, these selection rules directly link the spin polarization of the carriers and the polarization of the emitted or absorbed light. For example, we assume a spin polarization of 100% in the electron  $m_j = -1/2$  state. Then, the emission consists of a part with circular right polarization ( $\sigma^+$ , -1/2 to -3/2) and a part with circular left polarization ( $\sigma^-$ , -1/2 to +1/2), whereas the right polarized part is three-times stronger than the left one. The electron spin polarization is defined as [27]:

$$P_n = \frac{n_+ - n_-}{n_+ + n_-}. \quad (1)$$

Here,  $n_{\pm}$  are the densities of electrons in the +1/2 and -1/2 electron states, respectively. If  $I(\sigma^+)$  and  $I(\sigma^-)$  are the intensities for the right and left circularly polarized light fields, the circular polarization degree can be described as [27]:

$$P_{\text{circ}} = \frac{I(\sigma^+) - I(\sigma^-)}{I(\sigma^+) + I(\sigma^-)}. \quad (2)$$

In the following we assume that each hole state is sufficiently populated and thus the electron densities are the only limiting factors for optical transitions. Then the equation can be reformed to [27]:

$$P_{\text{circ}} = \frac{I(\sigma^+) - I(\sigma^-)}{I(\sigma^+) + I(\sigma^-)} = \frac{(n_+ + 3n_-) - (3n_+ + n_-)}{(n_+ + 3n_-) + (3n_+ + n_-)} \quad (3)$$

$$= -\frac{P_n}{2}.$$

From this it follows that the circular polarization degree (CPD) of the light field emitted from an electron spin-polarized QW is always  $-1/2$ -times the electron spin-polarization degree. In our example with  $P_n = -1$  the resulting light field would be right circularly polarized with a CPD of 50%. This correlation is valid as long as we consider both lh and hh transitions. However, the energetic separation of hh and lh states even allows for higher polarization degrees: If the emission or absorption is energy selective, that is, if only the hh-electron transition takes place, a CPD of up to 1 can be obtained for an electron spin-polarization degree of  $-1$ .

The situation would change completely, if split-off band related transitions were involved. If we assume, for example, an excitation with right circular polarized light with a photon energy larger than the band-gap energy  $E_g$  plus the spin-orbit splitting energy  $\Delta_{\text{so}}$ , no net spin-polarization degree would be achieved due to the additional split-off transitions. Since split-off-transitions have a transition rate of 2, they equalize the summarized transition rates for right and left circularly polarized light [27]. Correspondingly, in order to achieve a spin-polarization degree for the electrons (and holes) using optical pumping, the excitation photon energy has to be less than  $E_g + \Delta_{\text{so}}$ . This indicates that spin-orbit coupling is principally necessary for spin-optoelectronics. However, we will see in next chapter that the spin-orbit interaction is also the origin for the most relevant spin relaxation mechanisms which are often obstructive for the development of spin-optoelectronic devices.

These selection rules are the basis for spin-optoelectronics because they directly link optical and carrier spin polarizations. In detail, for spin-optoelectronic devices with electrical spin injection (spin-LEDs or spin-VCSELs) they enable an estimate of the spin injection efficiency from the measured light polarization degree of the optical emission. On the other hand, they can be used also to inject carrier spin polarizations optically, by means of circularly polarized light. This is an important tool in order to investigate spin-dependent effects fundamentally, if electrical spin injection is not available.

**2.2. Spin Transport and Spin Relaxation.** Unfortunately the carrier spin in a semiconductor is not permanently stable like the electron charge but relaxes to equilibrium within a relatively short time called spin relaxation time. This is often a fundamental challenge for the development of spin-optoelectronic devices especially in case of the spin transport. The spin relaxation is due to many reasons like the Elliot-Yafet (EY) [30, 31], the D'yakonov-Perel (DP) [32], and the Bir-Aronov-Pikus (BAP) [33] mechanisms, and others like the hyperfine interaction. These relaxation mechanisms can

basically be described as a result of the interaction between the spin magnetic moments and fluctuating effective magnetic fields, originating mainly from the spin-orbit coupling. This interaction forces a group of aligned electron spins into equilibrium of both allowed spin states. Typical spin relaxation times vary over a huge range from 10 ps up to 100 ns. They are depending on various band structure and environment parameters like lattice symmetry, spin-orbit interaction, confinement, carrier, dopant, defect densities, temperature, and others. A detailed recapitulation of the different spin relaxation mechanisms and their dependencies is beyond the scope of this article. However, a nice overview can be found, for example, in [27]. Here we will concentrate on the fundamentals of spin relaxation important for the development of spin-optoelectronic devices operating at higher temperatures.

Usually, the spin relaxation time strongly decreases with temperature. In semiconductors without inversion symmetry like (100) GaAs and at low hole densities, the DP mechanism is the dominant spin relaxation mechanism at elevated temperature. Here the spin states in the conduction band for  $k \neq 0$  are no longer degenerated, resulting in an effective magnetic field  $B_{\text{eff}} = f(k)$ . Consequently, momentum scattering processes lead to magnetic fields fluctuating in time and inducing a spin dephasing and relaxation process [34]. Typical spin relaxation times for (100) GaAs bulk vary from approximately 100 ns at low temperatures [35] to some tens of ps at room temperature [36]. The confinement energy in low-dimensional active regions is an important factor, too. In (100)-GaAs-QWs at room temperature, the spin relaxation rate exhibits a quadratic increase with increasing confinement energy [37]. Accordingly, typical relaxation times for (100)-GaAs-QWs at room temperature are in the regime of several tens of picoseconds for electron spins. Anyway low-dimensional structures can also provide longer spin relaxation times, because their higher degree of spatial confinement limits the carrier motion and possibly reduces relaxation mechanisms like the DP mechanism. This is the reason for the long spin lifetimes, predicted for quantum dots, which are consequently a very promising material system for spin-optoelectronics [24, 38]. Other possibilities in order to obtain long spin lifetimes are to make use of materials with inversion symmetry like Si or (110)-GaAs, because here the usually dominant DP mechanism is suppressed. Especially silicon, which provides electron spin relaxations times up to 7 ns at RT [38] is a very interesting material system, because of its compatibility with the highly developed complementary metal oxide semiconductor (CMOS) technology. Unfortunately, because of its indirect nature, the development of sufficient spin-optoelectronic devices based on silicon remains a fundamental challenge.

Up to now we have concentrated on the electron spin relaxation only. Hole spins usually relax much faster than electron spins. Typical values at room temperature are in the range of 100 fs [39]. Consequently it is often adequate to assume a statistic contribution of the hole spin even after optical spin injection. Nevertheless there are some concepts for hole spin injection and transport but they suffer from a rather low efficiency [3, 40].

However, even the spin relaxation time of the electrons is typically shorter than the transport time of the carriers through a spin-optoelectronic device, for example, a spin-LED. The selection rules provide a direct link between the polarization of the spin-LED emission and the spin polarization of the carriers when they recombine. However, the longer the time is between the generation of the spin-polarized carriers (by optical absorption or electrical spin injection) the more spins relax before they recombine. This relaxation takes place both on the transport path and within the active region where the carriers recombine radiatively. Consequently, the light polarization emitted by a spin-LED only provides a lower estimate of the spin injection. Presuming a sufficient number of holes for recombination, for example, in a p-doped semiconductor, the spin relaxation within the active region can be accounted using [34]

$$P_{\text{circ, eff}} = \frac{P_{\text{circ}}}{1 + (\tau/\tau_s)}. \quad (4)$$

Here  $\tau_s$  is the spin lifetime,  $\tau$  the electron lifetime, and  $P_{\text{circ, eff}}$  the effectively measured degree of circular polarization. This has important consequences: the impact of spin relaxation in the active medium is not determined by the spin lifetime alone, but by the electron-to-spin-lifetime ratio  $\tau/\tau_s$  [41] which has to be minimized. This can be accomplished either by a long spin relaxation time or by a short electron lifetime. Furthermore, to ensure a minimized spin relaxation during transport, all transport path lengths in spin-optoelectronic devices should be kept as short as possible. Typical electron spin relaxation lengths for a drift related transport in vertical geometry in *n*-doped GaAs at room temperature are theoretically predicted to be in the range of 25–50 nm [42]. Recently, these predictions could be verified experimentally using a series of spin-LEDs with varying spin-injection transport path length in vertical drift-based transport geometry by Soldat et al. [43]. The results demonstrate an exponential decrease of the circular polarization degree and thus of the spin-polarization degree in the active region with increasing injection path length. A spin relaxation length of 26 nm at room temperature in undoped GaAs was determined, which corresponds to the lower bound of the theoretically predicted values.

Consequently, the development of electrically pumped spin-optoelectronic devices at room temperature is a huge challenge, because in standard optoelectronic devices in particular lateral carrier transport path lengths easily reach values of several micrometers. In the following section, we briefly review the concepts for electrical spin injection into semiconductors.

**2.3. Electrical Spin Injection into Semiconductors.** On the long run, spin-optoelectronic devices will only be application relevant if the spin injection can be performed electrically and when the devices operate at room temperature and without the need for high external magnetic fields which would require superconducting magnets. As we will discuss below, this implies that many of the spin injection concepts reported in the literature will never be usable in practical devices. Firstly, we briefly describe the state-of-the-art and the

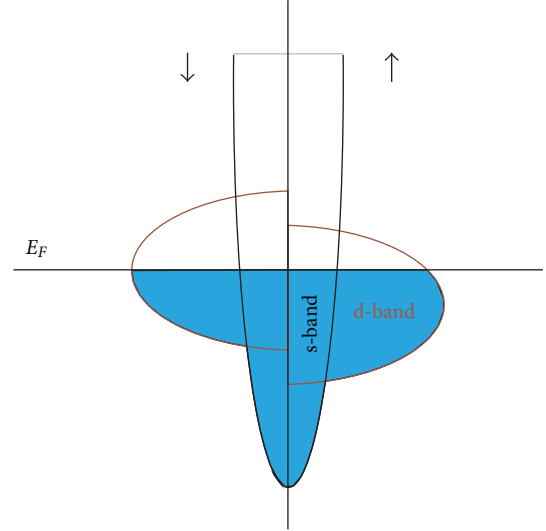


FIGURE 2: Schematics of the exchange field induced spin-splitting of the d-like density of states in a ferromagnetic metal.  $E_F$  denotes the Fermi level (Illustration analogous to [44]).

different concepts for spin injection into semiconductors. Again, we are concentrating on concepts which are relevant for the development of room temperature devices.

In general, the alignment of spins upon injection into a semiconductor implies the presence of a magnetic layer somewhere in the vicinity of the contact of the spin-optoelectronic device. The straightforward approach would be to use ferromagnetic contacts, for example, iron contacts. In a ferromagnetic metal like iron, the density of states at the Fermi level has both s- and d-character. The exchange interaction in the ferromagnet leads to a spin splitting of the d-states and therefore to a different density of states for spin-up and spin-down states at the Fermi level [44]. The density of states of a ferromagnetic metal is schematically depicted in Figure 2. Since s-electrons have significantly smaller effective masses than electrons in d-states, the current flow in the metal is dominated by the s-electrons. However, due to the splitting of the d-like density of states, spin-up and spin-down electrons have different probabilities for scattering into the d-states which results in different mobilities for spin-up and spin-down s-electrons. Consequently, the current will be dominated by s-electrons in a spin-state with less d-like density of states at the Fermi level. This can principally be used for spin injection in a nonmagnetic semiconductor [44].

But with a normal ohmic contact between the magnetic iron contact and the semiconductor, the large conductivity mismatch [45] leads to nearly negligible spin injection efficiency. Two different solutions of this problem have been suggested: the first is injection by tunnel contacts from a ferromagnetic metal layer into the semiconductor [46, 47] and the second is to use diluted magnetic semiconductors. Spin injection using dilute magnetic semiconductors is either possible with spin injection out of ferromagnetic semiconductors [3] or with spin alignment with paramagnetic semiconductor layers [2]. Though the highest spin injection

efficiencies were realized with diluted magnetic semiconductors, these approaches suffer from fundamental drawbacks. Spin aligners for example, a paramagnetic BeMnZnSe layer in the n-doped region of a GaAs/Al-GaAs LED structure, require large external magnetic fields in the order of a few Tesla for spin alignment. Such high fields can only be provided by superconducting magnets. The ferromagnetic semiconductors used for spin injection so far, have Curie temperatures far below room temperature. Consequently, such concepts require cryogenic cooling. Various candidates for ferromagnetic semiconductors with Curie temperatures above room temperature have been suggested and discussed. The most promising materials are GaMnN [48, 49] and MnAs clusters in GaAs environment [50] due to their compatibility to existing optoelectronic semiconductor technology. Materials like ZnCrTe [51], Cr-doped In<sub>2</sub>O<sub>3</sub> [52], CdMnGeP<sub>2</sub> [53], or ZnMnO [54] offer high Curie temperatures but are far from being compatible with established optoelectronic technology, yet. Actually, efficient spin injection from ferromagnetic semiconductors at room temperature has yet to be demonstrated and it is not clear whether this demonstration will happen at all.

Many ferromagnetic metals, in contrast, have Curie temperatures far above room temperature. But other problems appear for spin injection from ferromagnetic metals. As mentioned above, the conductivity mismatch between metal and semiconductor prevents spin injection via ohmic contacts. This problem can be solved using tunnel contacts either via Schottky contacts or via isolating tunnel barriers as, for example, MgO. In tunnel contacts the tunnel rates for the electrons are proportional to the product of the densities of states of the materials on both sides of the tunnel barriers [44]. Due to the spin splitting of the d-states in ferromagnetic metals discussed above, this enables a robust spin injection from the metal into the semiconductor circumventing the problem of conductivity mismatch.

Spin injection at room temperature has indeed been successfully realized both with Schottky barriers [4, 7] and with isolating tunnel barriers [8, 55]. While the first approaches reached only spin injection efficiencies of a few percent [4], the record value for spin injection from ferromagnetic metals into semiconductors at room temperature is 32% using MgO tunnel barriers [8]. However, as mentioned above, the optical selection rules usually require an orientation of the injected spins perpendicular to the semiconductor surface. Most ferromagnetic contacts, in contrast, have an easy magnetization axis and thus a spontaneous remanent magnetization in the film plane, that is, parallel to the surface. Accordingly, large magnetic fields in the order of 2 Tesla have to be applied in order to turn the magnetization into the required perpendicular orientation. Similar to the spin aligner concept, this induces the need for a superconducting magnet which is not attractive for device applications. This problem can be solved using ferromagnetic materials with perpendicular magnetization even without external magnetic field. Possible candidates include Fe/Tb multilayers [6, 9, 56–58] and alloys, FePt [59], and PtCo [60]. Indeed, room temperature spin injection has successfully been demonstrated in remanence and at room

temperature with Fe/Tb-contacts [9, 58] and FePt [59]. The polarization degrees of the spin-LED emission and thus the injection efficiencies were in the few percent region in all cases. One reason for this is that the magnetization orientation of the ferromagnetic contacts is not completely perpendicular to the surface. Typical values for the angle between magnetization direction and surface normal are  $\sim 30^\circ$  for FeTb alloys and  $\sim 40^\circ$  for FeTb multilayers [57, 58]. Thus, further material optimization is required to ensure perfect vertical alignment of the ferromagnetic contacts in remanence. Then, it can be expected that this efficiency can be increased up to about 30% combining the vertically magnetized ferromagnetic contacts with the optimized injector structure of Jiang et al. [8]. Thus, from the actual point of view, the optimum room-temperature spin-LED would look like it is schematically shown in Figure 3.

However, even this optimized spin-LED will probably not become relevant for applications other than the characterization and optimization of spin injection contacts. This is because LEDs are generally too slow for information technology. Moreover, the injection efficiencies that could be obtained even in the best case are still rather low. In contrast, spin-controlled lasers might offer a much higher application potential. In the following section, we will analyze this potential.

### 3. Spin-Controlled Vertical-Cavity Surface-Emitting Lasers

The first step on the way to a spin-polarized laser is to identify a qualified laser concept. Principally a choice has to be made, whether an edge- or a vertical-emitting geometry suites best. Figure 4 compares schematically the structures of a vertical-cavity surface-emitting laser (VCSEL) and of a conventional edge-emitting laser. On the first glance, an edge-emitting laser might be more promising. It is obvious from the comparison of both laser structures with the spin-LED in Figure 3 that it would be rather easy to transfer the injector concept of a spin-LED to an edge-emitter while electrical spin injection into the VCSEL is much more complicated due to the larger vertical path length. In addition, an edge-emitting concept would allow for an easy remanent spin injection utilizing the natural in-plane magnetization of the ferromagnetic layers due to the shape anisotropy. But the requirement for the Faraday geometry in spin-optoelectronics implies that lasers with vertical architecture such as VCSELs are the first candidates for spin-controlled lasers. At least for narrow quantum wells the angular momentum of the holes lies in the quantum well plane, and the connection between carrier and photon spin is only straightforward for the vertical geometry as discussed in Section 2.1. In principle, an edge-emitting concept utilizing a bulk active region might still be a possibility. Recent experimental results have demonstrated spin injection in an edge-emitting LED utilizing bulk-like wide GaAs QWs [61]. In a wide QW, the heavy-hole angular momentum can principally lie in the QW plane comparable to the case in bulk semiconductors. However, due to the restriction on bulk-like active systems, an edge-emitting concept for room temperature operation would be

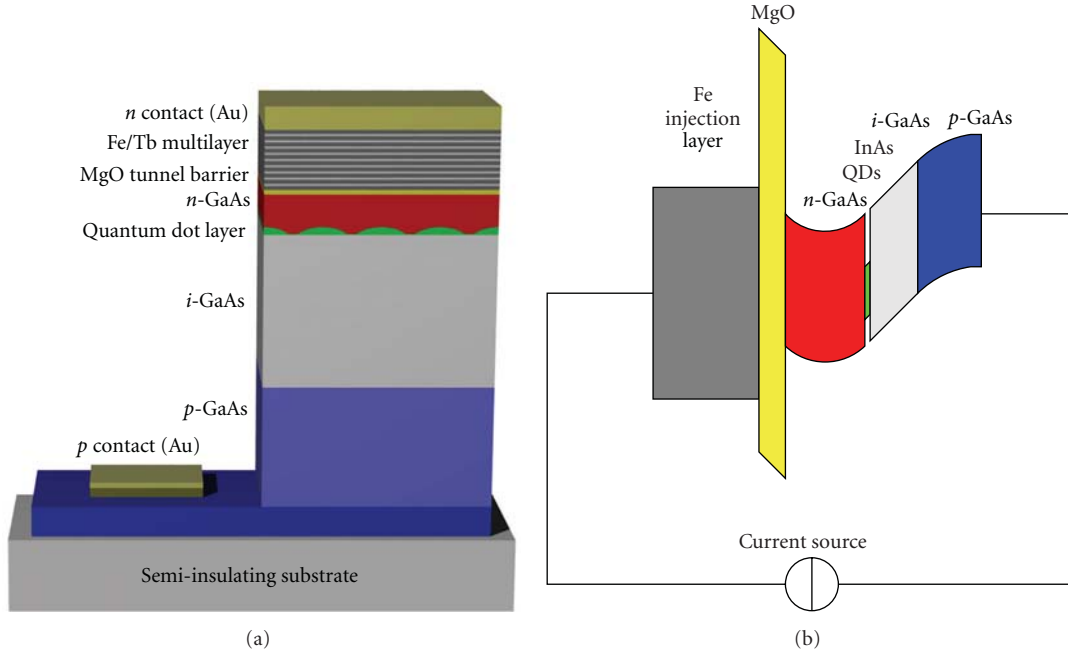


FIGURE 3: Optimized structure for a room temperature spin-LED. The design combines a Fe/Tb-multilayer contact structure with spontaneous perpendicular magnetization, a highly efficient MgO tunnel barrier for spin injection, a minimized electron path length, and InAs QDs with enhanced spin lifetime at room temperature (a), (b) depicts the schematic energy diagram of the spin-LED in growth direction. Spin-polarized electrons will be injected from the lowest Fe layer of the Fe/Tb multilayer contact into n-GaAs via the MgO tunnel barrier and recombine with unpolarized holes in the QDs.

a tough challenge and it remains questionable whether such a concept can be competitive to conventional laser devices. Additionally, waveguide effects have a relevant impact on the polarization state of an edge-emitting laser, usually leading to a linearly polarized laser emission parallel or perpendicular to the waveguide plane. With respect to this, VCSELs have a big advantage, because generally a VCSEL is a laterally isotropic device with nearly perfect circular symmetry, which leads to weak pinning of the polarization state.

Altogether, because of the above-mentioned fundamental disadvantages of edge-emitting concepts a VCSEL seems to be the most qualified concept for a spin-polarized laser at room temperature. Thus, the challenge of a more complicated spin injection concept has to be faced.

As a consequence of the long vertical spin transport path, room temperature spin-VCSELs with electrical spin injection are not available yet. Thus, at this stage, the potential of spin-VCSELs at room temperature has to be analyzed theoretically or with alternative experimental techniques. Since the selection rules shown in Figure 1(a) enable controlled optical spin excitation, most experimental work on this field has been done on spin-VCSELs with optical spin injection. In the following section, we review theoretical and experimental work on room-temperature spin-VCSELs in order to work out the specific advantages spin-VCSELs might deliver for applications.

**3.1. Basics and Properties of Spin-VCSELs.** The idea that spin-controlled lasers might offer a much higher potential than spin-LEDs arises from the fact that lasers show a dynamical

behavior much different from that of LEDs. One important example affects the influence of the spin relaxation in the active region. In spin-LEDs the effective circular polarization degree will be reduced. This reduction is usually accounted for by the factor  $1 + (\tau/\tau_s)$  [34] including the electron-to-spin-lifetime ratio (see Section 2.2). At room temperature the ratio is typically very large due to a small spin lifetime, which leads to a small circular polarization degree. In spin lasers, in contrast, the electron lifetime will be reduced significantly due to the strong stimulated emission, resulting in a vanishing electron lifetime to spin lifetime ratio and a correction factor of approximately 1. Accordingly the spin relaxation rate in the active medium should be less important in spin-VCSELs in comparison to spin-LEDs. This is a first fundamental advantage. Nevertheless the spin relaxation during carrier transport remains still an issue.

The dynamic behavior of spin-polarized laser can be investigated theoretically using a spin-dependent rate-equation model. Several different models have been used in the literature for this purpose [12–15, 19, 24, 62, 63]. In the following a common dynamic spin-flip model (SFM) will be used, originally developed by San Miguel et al. in order to describe the polarization switching and bistability in conventional VCSEL devices [64–66]. The SFM is based on a four-energy-level approximation and takes only transitions between electron and heavy-hole states into account. It describes the polarization dynamics for the two hh-related circularly polarized transitions, considering two distinguished carrier densities for spin-up and spin-down carriers [65]. These two carrier reservoirs are coupled by the spin

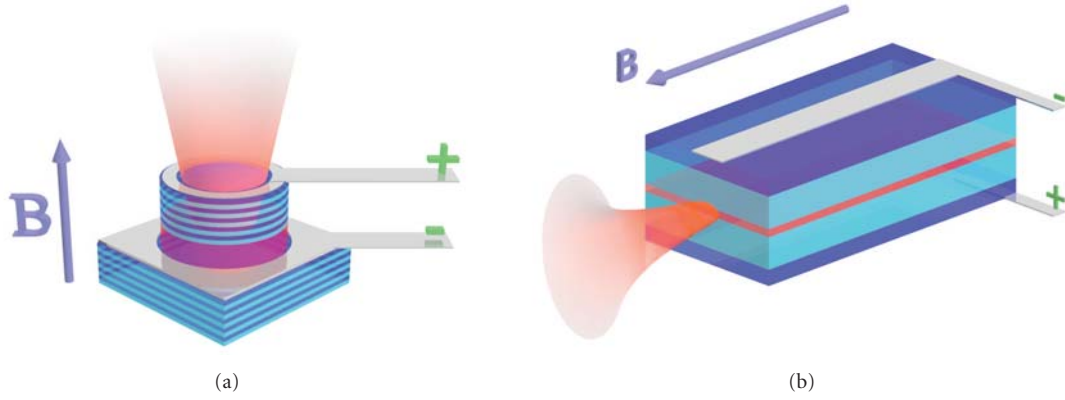


FIGURE 4: Comparison between spin-VCSEL (a) and spin-edge emitter (b).

relaxation rate  $\gamma_s$ . The spin relaxation rate  $\gamma_s$  describes all kinds of microscopic spin relaxation processes mentioned in Section 2.2 by means of a single phenomenological parameter [66]. The circularly polarized light fields  $E_{\pm}$  are coupled by the cavity anisotropies birefringence ( $\gamma_p$ ) and dichroism ( $\gamma_a$ ). The four coupled rate equations are as follows:

$$\begin{aligned} \dot{E}_{\pm} &= \kappa(1 + i\alpha)(N \pm m_z - 1)E_{\pm} - (\gamma_a + i\gamma_p)E_{\mp} \\ &\quad + \xi_{\pm}\sqrt{\beta}\gamma(N \pm m_z), \\ \dot{N} &= \gamma[\eta_+ + \eta_- - (1 + I_+ + I_-)N - (I_+ - I_-)m_z], \\ \dot{m}_z &= \gamma(\eta_+ - \eta_-) - [\gamma_s + \gamma(I_+ + I_-)]m_z - \gamma(I_+ - I_-)N. \end{aligned} \quad (5)$$

In the SFM the light field is coupled to two population inversion variables [66]. The first variable  $N$  is the total carrier population, that is, the sum of the populations of spin-up and spin-down states, normalized to the population at laser threshold. Its decay rate is  $\gamma$ . The second variable  $m_z$  is the so-called carrier spin magnetization which represents the normalized value of the population difference between spin-up and spin-down states [63]. The intensity  $I_{\pm}$  of the circularly polarized optical laser modes can be described by the complex amplitudes  $E_{\pm}$  of the circularly polarized light fields via  $I_{\pm} = |E_{\pm}|^2$ .  $\kappa$  is the cavity decay rate which can be related to the photon lifetime using  $1/2\kappa$  [66].  $\alpha$  is the linewidth enhancement factor. The influence of the spontaneous emission to the laser mode is considered using the spontaneous emission factor  $\beta$  and the spontaneous emission noise terms  $\xi_{\pm}$  which are usually described by complex Gaussian shaped distributions. Optical as well as electrical pumping can be modelled using the pump terms  $\eta_{\pm}$ . The optical gain is implemented in the model by using a simple linear dependence of the population inversion. Since the optical gain for the circularly polarized light intensities  $I_{\pm}$  is proportional to  $(N \pm m_z - 1)$ , the gain values for  $I_+$  and  $I_-$  are unequal in case of a carrier spin polarization. This is one of the fundamental concepts of the spin-polarized VCSEL and will be described later in detail. Gain compression, frequency dependencies or temperature effects are not included in this model. However, since a VCSEL operates spectrally single-mode with a usually

small detuning between the cavity mode and the gain mode, the reduction of heavy-hole transitions and neglecting the frequency dependencies are sufficient to describe the main features of conventional and spin-polarized VCSELs. We will use this model in the following in order to discuss the advantages and properties of spin-VCSELs in comparison to spin-LEDs and conventional lasers.

One important difference between a spin-laser and a spin-LED is the nonlinearity of a laser at the laser threshold which enables a kind of amplification of spin information with a spin-controlled carrier injection. Figure 5 shows schematically the gain spectra of a laser with conventional unpolarized pumping in comparison to the case with spin-polarized pumping. Note that only the gain differences at the cavity energy  $E_{\text{cavity}}$  are relevant for the dynamics so that the spectral dependence of the gain is not considered in our simple model.

The anisotropic pumping leads to a small spin polarization of the carriers in the active region. We assume here a small excess in the occupation of the  $e(-1/2)$  state (compare Figure 1) with respect to the  $e(+1/2)$  state. This excess is in the regime of a few percent only which is, in principle, accessible by electrical spin injection. This small excess occupation of one spin band leads to a higher inversion in the  $e(-1/2)$  state and, accordingly, the corresponding  $\sigma^+$ -transition from  $e(-1/2)$  to the  $hh(-3/2)$  state sees a higher gain than the  $\sigma^-$ -transition from  $e(+1/2)$  to  $hh(+3/2)$ . The transitions to the lh states do not play a role here because they are usually not in resonance with the VCSEL cavity mode and have a lower transition strength. In other words, the spin anisotropic pumping leads directly to a gain anisotropy at the photon energy of the cavity resonance  $E_{\text{cavity}}$  for the circularly polarized laser modes. We further consider a polarization independent loss level indicated by the horizontal line in Figure 5. In the situation shown in Figure 5(b), the laser is just above threshold for  $\sigma^+$  emission and still below threshold for  $\sigma^-$  emission, which results in a nearly 100% right circularly polarized laser emission. This behavior has been investigated experimentally by Ando et al. for the first time [21]. They demonstrated that the laser polarization in optically pumped VCSEL structures at room temperature can be

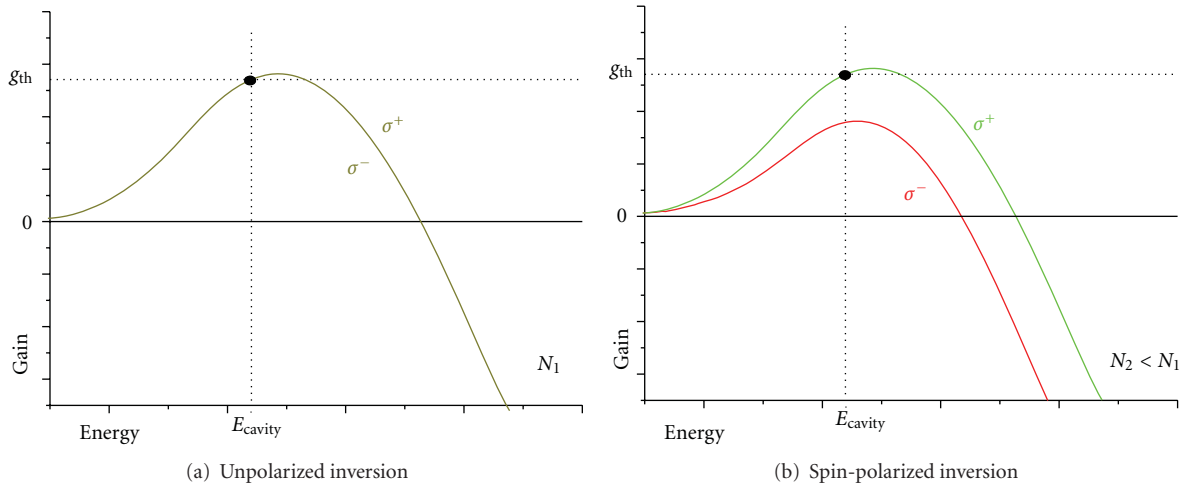


FIGURE 5: Schematic illustration of the optical gain as a function of photon energy in a VCSEL with conventional unpolarized pumping (a) and for a small spin polarization of the carriers in the active region (b). The spin-polarized pumping leads to separation of the gain spectra for the  $\sigma^+$  and  $\sigma^-$  transition. This results in a gain anisotropy at the cavity resonance energy  $E_{\text{cavity}}$ , which marks the relevant photon energy for the laser emission.

controlled via optical spin injection. In an ideal case, even a small excess in the spin polarizations of the electrons in the active region should be efficient in order to generate a 100%  $\sigma^+$  polarization of the optical emission. Accordingly, it can be expected that a spin-VCSEL, in contrast to a spin-LED, provides a kind of spin amplification, that is, the polarization degree of the optical emission becomes higher than the spin-polarization degree in the active region in the vicinity of the laser threshold. This expectation was confirmed by Hövel et al. [22, 23]. They showed that in an optically pumped spin-VCSEL the circular polarization degree can indeed become higher than the input polarization degree.

In these experiments, a Ti:sapphire laser was taken for optical pumping an InGaAs/GaAs-QW-VCSEL-structure at room temperature. The spin injection was obtained by pulsed excitation with a pulse length of 80 fs. Figure 6(a) shows the measured circular polarization degree of the VCSEL emission as a function of the injected spin polarization of the carriers in the active region. To circumvent the stopband of the VCSEL Bragg mirrors, the excitation was performed with some excess energy leading to excitation of heavy hole- and light hole-transitions in the GaAs barriers. According to the selection rules in Figure 1(a) the maximum spin-polarization degree of the excited electrons is 50%. Accordingly, a circular polarization of 100% leads to an injected carrier spin polarization of 50% at most, if we neglect any kind of spin relaxation in the barriers and in the quantum wells. The results in Figure 6 confirm the expectation of spin amplification with a spin-VCSEL. A circular polarization degree of 100% is already obtained with a spin polarization of 30%, and a spin-polarization of 13% still provides a polarization degree of 50%. The results are in a good agreement with theoretical calculations based on the SFM mentioned above. The simulations also shown in Figure 6(a) were obtained for a spin relaxation time of 40 ps

in the active region. Later experimental and numerical work confirmed that spin amplification also works for continuous wave excitation [23]. Nevertheless it has to be noted that both effects, the possibility to control the light polarization by the carrier spin and the amplification of spin information are restricted to a pump region near the laser threshold. In a simple steady-state picture this can easily be understood taking the clamping of the carrier density at the laser threshold into account. If we consider the situation in Figure 5(b), the laser emission with a 100%  $\sigma^+$  polarization state leads to a clamping of the carrier density in the  $e(-1/2)$  electron spin band but not in the  $e(+1/2)$  electron spin band. Accordingly, if the carrier density will be increased and the spin-polarization degree is less than 100%, the gain anisotropy will be reduced and the  $\sigma^-$  gain spectrum reaches threshold for a high carrier density, too. Thus the  $\sigma^-$  polarization starts to emit and diminishes the spin control and amplification effects.

Accordingly, a spin-VCSEL has two threshold carrier densities  $N_{\text{th1}}$  and  $N_{\text{th2}}$  for the two circularly polarized laser modes. Their difference depends on the spin-polarization degree of the carriers in the active medium. If the device operates in a carrier density regime  $N$  with  $N_{\text{th2}} < N < N_{\text{th1}}$ , predominantly the electrons with the correct spin-polarization participate in the laser process. From this it follows that less injected carriers are sufficient to reach threshold in a spin-VCSEL in comparison to a conventional VCSEL without spin-control. This spin polarization induced threshold reduction can be seen from the data depicted in Figure 6(b). The laser threshold is significantly reduced for a carrier spin polarization of 50% in comparison to unpolarized pumping. Threshold reduction in spin-VCSELs has motivated a lot of work in the field of spin-lasers, because the direct pumping of only one spin state basically allows reducing the threshold by up to 50% [15]. However this implies 100% spin-polarization degree in the active medium and a sufficiently long spin lifetime, taking simple rate equations into

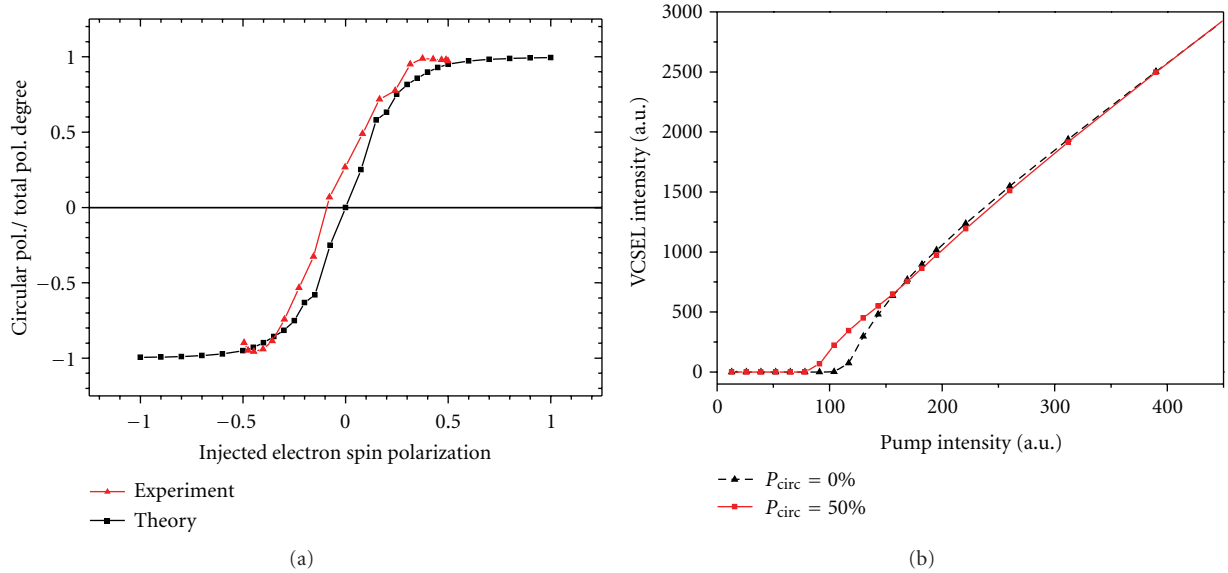


FIGURE 6: Circular polarization degree as a function of the carrier spin polarization in the active region (a). The experiments have been obtained at room temperature for pulsed excitations and show a good agreement with theoretical results based on the SFM for a spin relaxations time of 40 ps. (b) shows the calculated laser characteristics for a carrier spin polarization of 0% and 50%.

account. This threshold reduction was indeed observed. At low temperatures, Rudolph et al. have reported a threshold reduction of 23% in optically pumped devices [15], while at room temperature still a reduction of 2.5% was observable [16]. Recent theoretical work about threshold reduction even predicts threshold reductions significantly higher than 50% depending on several device parameters like nonradiative recombination [18], hole spin relaxation [67], and valence-band mixing [20]. Anyway, the best result for electrically pumped devices so far is a threshold reduction of 14% at 200 K [68]. However, even though threshold reduction is an important property of spin-VCSEL, its efficiency depends strongly on the spin lifetime and it is still questionable whether in terms of threshold reduction a spin-VCSEL will be ever competitive with optimized conventional devices at room temperature. This spin-induced threshold reduction will probably be overcompensated by the additional effort needed for spin injection by using ferromagnetic contacts, for example.

A closer look onto the experimental details of the work done on purely optically pumped spin-VCSELs indicates problems that might occur in electrically pumped devices, too. In order to obtain the effects like spin amplification and threshold reduction great care had to be taken to ensure a perfectly circularly symmetric pump spot. Otherwise additional anisotropic carrier density and temperature effects introduce parasitic anisotropies into the cavity, which lead to a coupling of both circular polarized laser modes and result in linearly polarized laser emission. Such cavity anisotropies like birefringence and dichroism are known to have an enormous impact on the polarization dynamics of electrically pumped VCSEL [69–71]. The anisotropies, caused for example, by the internal electric fields and anisotropic strain induce a pinning of the polarization mode to a certain

linearly polarized state and thus are the origin of chaotic polarization behavior in electrically pumped VCSEL devices [64, 70–74]. Accordingly, for the development of electrically pumped spin-VCSELs the role of cavity anisotropies on the laser dynamics is an important issue and might in the worst case be stronger than any spin-induced effects. Hövel et al. have investigated whether the influence of cavity anisotropies can be overcompensated by the spin in electrically pumped devices [25]. The experiments were performed using a special hybrid pumping scheme for a conventional electrically pumped VCSEL structure. The VCSEL was pumped electrically with a continuous spin unpolarized current in the vicinity of the electrical threshold. Additionally, a short circularly polarized light pulse with 3 ps pulse length was used to inject a small amount of spin-polarized carriers in the active region. The experimental setup shown in Figure 7 was used for these experiments. Just, instead of the streak camera shown in Figure 7, a time integrating photodetector was used to analyze the time averaged output of the VCSEL. The results indeed confirmed that spin control and spin amplification are also feasible in electrically pumped VCSEL devices. In other words, the spin effects are strong enough to overcompensate the above-mentioned cavity anisotropies at least for time-integrated measurements [25].

So far, we have only discussed time averaged stationary effects. But, besides spin amplification, spin control, and threshold reduction in continuously operating spin-VCSELs, dynamical effects might be even more promising. For example, it was predicted that spin-VCSELs might be considerably faster than their conventional counterparts. First fundamental investigations by Hallstein et al. confirmed this potential [10]. They investigated an optically pumped VCSEL structure at low temperature and in a high magnetic field and observed a fast modulation of the VCSEL polarization

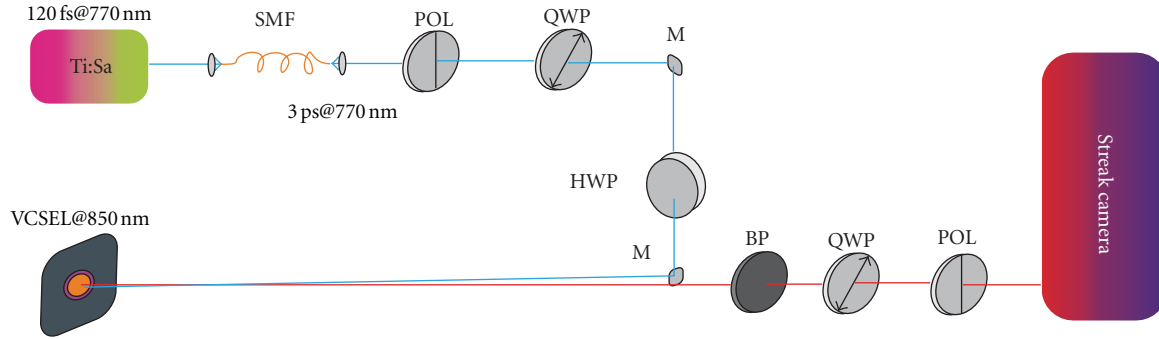


FIGURE 7: Setup for hybrid excitation and spin control of a commercial VCSEL device. (SMF) single mode fiber, (POL) linear polarizer, (QWP) quarter wave plate, (M) mirror, (HWP) half wave plate, and (BP) bandpass.

due to spin precession of the carriers in the magnetic field with modulation frequencies up to 120 GHz [10, 11]. But also under realistic device conditions, strong indications for improved dynamical performance of spin-VCSELs have been found. Li et al. investigated an electrically pumped commercial VCSEL device with additional optical spin injection at room temperature [14]. Now, the entire experimental arrangement shown in Figure 7 was used for these experiments. Instead of the time integrated detection used by Hövel et al. [25], a time and polarization resolved analysis of the VCSEL emission was performed with a streak camera synchronized to the exciting Ti:sapphire laser. The time-resolution of the setup was approximately 3 ps. Again, the above-mentioned hybrid excitation scheme for the electrically pumped VCSEL was used and the VCSEL was operated in the vicinity of the threshold.

The results for a pulsed spin injection into the  $e(-1/2)$  electron spin band are presented in Figure 8. While the intensity dynamics exhibits a typical short pulse response, followed by some relaxation oscillations, the dynamics of the circular polarization degree perform a very fast oscillation within the first VCSEL pulse. The corresponding oscillation frequency is in the range of 10 GHz and thus much faster than the relaxation oscillation in the device for the same pump conditions. Accordingly, even in electrically pumped devices at room temperature, the combination of the spin dynamics with the photon dynamics in a laser cavity obviously leads to an improved speed of spin-VCSEL devices in comparison to conventional devices. The results are in a good agreement with simulations utilizing the rate equation spin-flip-model discussed before (Figures 8(c) and 8(d)) [14, 75]. A detailed analysis based on the SFM additionally revealed that the observed dynamics are a consequence of an interplay between the spin dynamics of the carriers and the birefringence in the laser cavity which can be described as follows: in case of a zero spin polarization as in a conventional VCSEL, only one linearly polarized mode is lasing. In case of spin injection, we have an imbalance of the spin band populations, which results in laser emission with a nonzero circular polarization degree. This corresponds to a simultaneous emission of two orthogonal linearly polarized laser modes. Due to the birefringence in the cavity, their frequencies are different [70]. The resulting beating of both

modes leads to an oscillation of the circular polarization degree [76]. The polarization oscillations feed back into the carrier spin dynamics and can stabilize the dynamics which potentially results in a long oscillation lifetime. The damping of polarization oscillations depends on the effective dichroism in the cavity and the oscillations are sustained the longer, the smaller the dichroism is. Since the effective dichroism and thus the damping of the oscillations can be controlled by the current, this allows for both very long and very short oscillation lifetimes. This is potentially interesting to stabilize spin information, as well as for the generation of short polarization bursts which are interesting for information transmission. This concept has been verified experimentally very recently by Gerhardt et al. [76]. They demonstrated polarization oscillations with a frequency of 11.6 GHz for a device with a modulation bandwidth of only less than 4 GHz at room temperature. The oscillation lifetimes could be controlled by the current in the vicinity of a polarization switching point significantly above threshold, where the effective dichroism is minimized. It should be added that while the damping of the oscillations is current dependent the oscillations themselves are not restricted to any current region. In comparison to the other spin effects in VCSELs this is an important advantage for applications and will be discussed later. At the polarization switching point, oscillation lifetimes of at least 5 ns could be demonstrated which is 200-times longer than the estimated spin lifetime in the device [76]. The oscillation frequency is determined by the linear birefringence and small corrections due to non-linear spin effects only and is principally independent of the carrier dynamics. Hence, by tuning the birefringence, for example, by applying additional strain, the oscillation frequency can possibly be enhanced significantly. It is not restricted by conventional relaxation oscillations. Since strain-induced birefringence values of 80 GHz have already been reported in the literature [77] this concept has a strong potential for future ultrahigh bandwidth lasers in the 100 GHz region [75, 76].

The ability for enhance speed and modulation bandwidth is a very promising advantage of spin-VCSELs, which is attractive for a lot of applications, for example, high-speed optical data communication technology. Accordingly, a lot of work has been concentrated on this issue, and

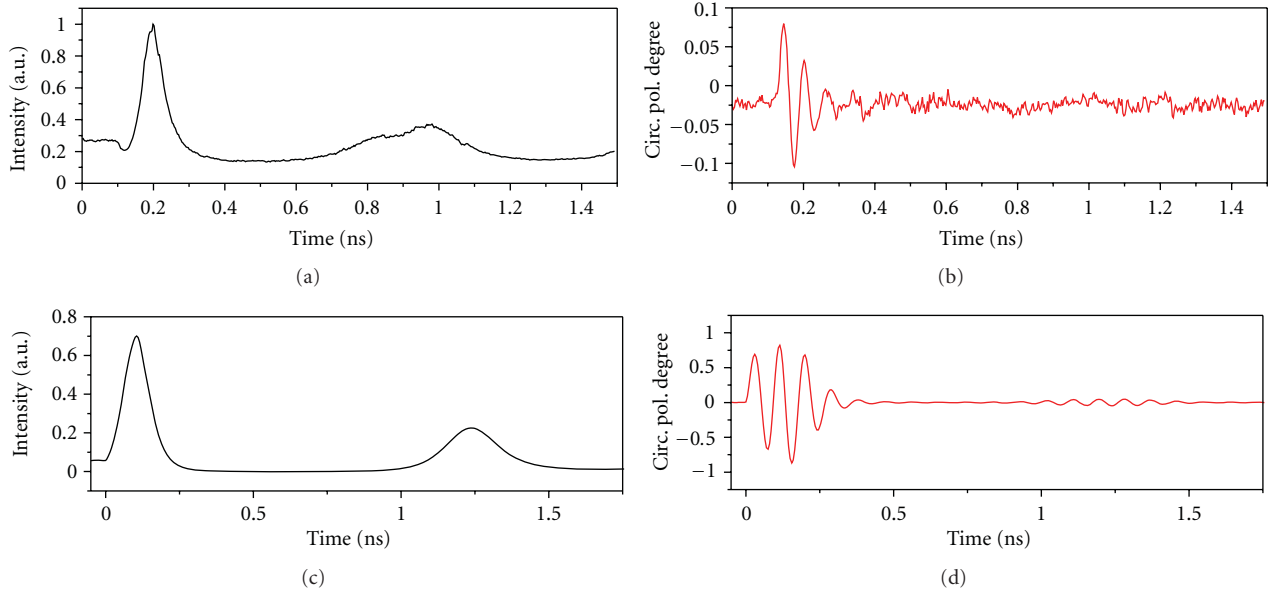


FIGURE 8: Dynamics of the total intensity (a) and the circular polarization degree (b) of an electrically pumped VCSEL after additional spin injection using a short right circularly polarized light pulse. Theoretical calculations based on the SFM are depicted ((c), (d)).

several other concepts have been presented, recently. Lee et al. investigated the small-signal modulation properties of both circularly polarized laser modes in a spin-polarized VCSEL, theoretically [13]. They predict that the modulation bandwidth can be enhanced for the favored circularly polarized laser mode as compared to conventional devices, due to spin injection. This concept is directly correlated to the threshold reduction for this laser mode and accordingly restricted to this current region close to threshold. In another recent publication Saha et al. have studied both the small-signal and the large signal modulation properties using a rate equation model [12]. The results for small-signal modulation support the reported prediction of Lee et al. and emphasize that the laser dynamics can be improved, when only one circularly polarized mode is operating. Additionally, they demonstrate experimentally using an electrically pumped InAs-QD-based spin-VCSEL that the amplification of spin information and the polarization control can significantly be enhanced for pulsed operation (see Section 3.3).

However, even though a lot of progress has been made in emphasizing the advantages of spin-polarized laser devices in comparison to conventional ones and a lot of promising properties have already been identified, a device with superior performance in comparison with conventional devices is still missing. One important challenge which has to be solved is the realization of efficient electrically pumped spin-VCSELs at room temperature. The current state of technology for electrically pumped VCSELs will be discussed in the next section. However, another important problem is that most concepts for spin-VCSELs are restricted to an operation near the laser threshold. This can be an important drawback on the way to realistic applications, because here the efficiency and the power of a laser are low and the laser dynamics is inherently slow. Accordingly, the search for other

spin-dependent properties which are not restricted to this current region is one of the most relevant tasks in the near future. Anyway, the usable current region can be significantly enhanced by improving the spin polarization degree. Here the development of spin-VCSELs using (110) GaAs quantum wells might deliver an important progress due to the long spin relaxations time in this material. Recently the first optically pumped spin-VCSEL grown on (110) GaAs substrate and operating at room temperature could be demonstrated by Iba et al. [26]. They reported circularly polarized lasing with a circular polarization degree of 0.96 at room temperature using pulsed excitation. The spin lifetime in the active region was estimated to be 0.7 ns which is significantly larger than in conventional (100) GaAs QWs. First transient investigations using a (110) GaAs-based VCSEL with an (110) InGaAs active region operating at 77 K additionally demonstrate optically induced switching of the circular polarization mode in the GHz range [78]. Even though these results are very promising, the realization of exceptional (110) based electrically pumped devices is still a big challenge. This is because “standard” all electrically pumped spin-VCSELs on conventional (100) oriented substrates already induce severe technological difficulties which have not yet been solved completely. We will review this work in the next section.

**3.2. Electrically Pumped Spin-VCSELs.** All electrically pumped spin-polarized VCSEL devices published so far have been developed at the University of Michigan, USA. The first device was presented in 2005 by Holub et al. [40]. Here a GaMnAs spin aligner, located intracavity underneath the top mirror was used for electrical spin injection. Because GaMnAs is an intrinsically p-doped material, the spin-VCSEL concept based on hole spin injection, accepting the associated ultrafast spin relaxation. Five  $\text{In}_{0.2}\text{Ga}_{0.8}\text{As}$

quantum wells served as active gain media. Polarization measurements as a function of the magnetic field revealed a maximum circular polarization degree 4.6% at 80 K. The concept to implement the spin-injection contact directly into the cavity of the VCSEL, which displays a direct transfer of a spin-LED concept to spin-VCSELs, has the advantage that the lateral transport length equals zero whereas the vertical transport length could be minimized to  $\sim 0.25 \mu\text{m}$  [40]. Unfortunately, the intracavity spin-aligner layer has a critical impact on the cavity quality and induces additional magnetic circular dichroism (MCD). The latter has a potentially strong influence on the polarization state of the emission, depending on the number of reflection within the laser cavity [24]. Accordingly, due to the impact of the MCD and the utilized hole spin injection, the results have been critically discussed in the literature [79, 80]. However, a small amount of circular polarization degree of approximately 1% has finally been stated to be due to the injection of spin polarized holes [24, 80], thus demonstrating the first realization of purely electrically pumped spin-polarized VCSEL.

Taking the difficulties due to hole spin injection and MCD in the cavity into account, the next concept for an electrically pumped spin-VCSEL consequently based on electron spin injection contacts. This concept was realized by Holub et al. in 2007 [17] using a  $\text{Fe}/\text{Al}_{0.1}\text{Ga}_{0.9}\text{As}$  Schottky tunnel barrier for electron spin injection in combination with an  $n$ -doped intracavity contact. The VCSEL design is depicted in the inset of Figure 9(b). Again, an active region containing five compressively strained  $\text{In}_{0.2}\text{Ga}_{0.8}\text{As}$  QWs was used for the laser operation. One important advantage of this concept is the utilization of a magnetic layer free cavity, reducing the impact of MCD to a minimum. However this led to a significantly increased average electron spin transport length of  $\sim 4.5 \mu\text{m}$  for a circular post VCSEL with a mesa diameter of  $15 \mu\text{m}$ . Nevertheless laser operation with a maximum CPD of 23% at 50 K and for an external magnetic field of 2.2 T could be realized with this device (Figure 9(a)). Additionally, threshold reduction in electrically pumped spin-VCSELs could be demonstrated for the first time, showing a maximum value of 11% at 50 K (Figure 9(b)) [17, 81]. Using this value, a cavity spin polarization degree of 16.8% was estimated for the barrier layers using a spin-dependent rate equation model comparable to the model used by Rudolph et al. [15, 16]. This value is significantly higher than the carrier spin polarization in the InGaAs-QWs estimated to be 7%. However, the circular polarization degree of the laser is stated to be dominantly determined by the cavity spin degree, while the spin polarization in the active region is less important due to the short carrier lifetime. Comparing the 16.8% cavity spin polarization with the maximum value of 23% for the CPD, the results nevertheless demonstrate the predicted amplification of the spin information.

In order to optimize the spin-VCSEL concepts for an operation at elevated temperatures, the next concept published by Basu et al. in 2008 based on InAs/GaAs quantum dots as active gain medium [68]. Electron spin injection was obtained using a  $\text{MnAs}/\text{Al}_{0.1}\text{Ga}_{0.9}\text{As}$  Schottky tunnel contact in a comparable VCSEL design comparable to that

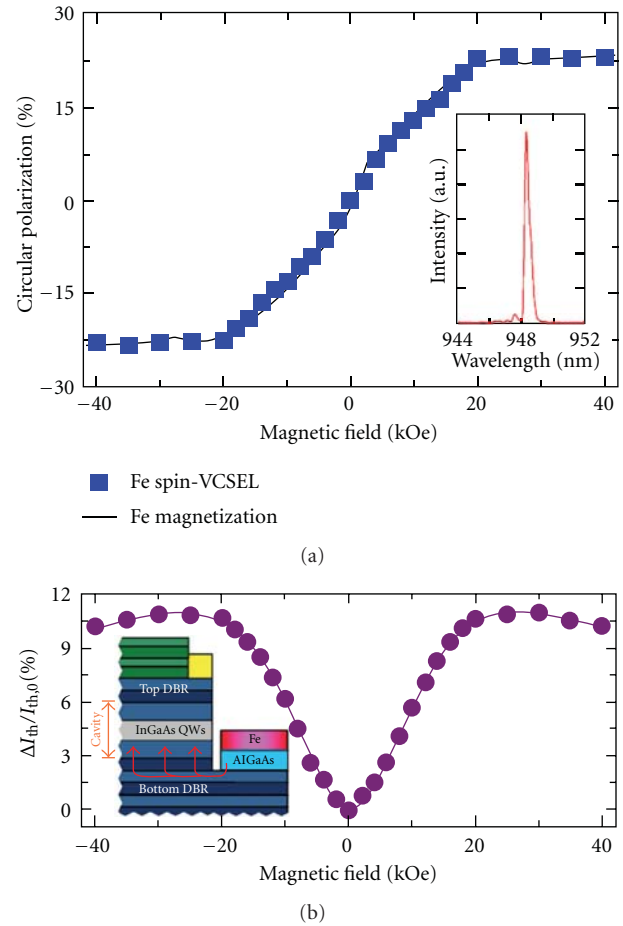


FIGURE 9: Circular polarization degree (a) and threshold current reduction (b) as a function of the magnetic field in an electrically pumped spin-VCSEL at 50 K. The VCSEL design is displayed in the inset of (b). The spin-VCSEL based on electron spin injection utilizing a  $\text{Fe}/\text{AlGaAs}$  Schottky tunnel contact design. (from [17]).

displayed in the inset of Figure 9(b)). The active region contains 10 layers of self-organized QDs grown by molecular beam epitaxy (MBE) with a QD density of  $3 \times 10^{10} \text{cm}^{-2}$ . The utilization of InAs-QDs represented an important progress, allowing to increase the operation temperature of the laser up to 200 K. Here a CPD of 8% and a maximum threshold reduction of 14% could be demonstrated for external magnetic fields of approximately 2 T, using a device with  $15 \mu\text{m}$  mesa diameter. A following publication based on comparable devices showed values of  $\sim 15\%$  CPD and  $\sim 8\%$  threshold reduction at 200 K and demonstrates the electrically controlled modulation of the output polarization in the vicinity of the threshold for the first time [19]. The issues of polarization control and high-frequency dynamics in such devices have been addressed recently in 2010 by Saha et al. [12]. They investigated the transient characteristics of an electrically pumped spin-VCSEL structure, comparable to the devices in [19, 68] but with mesa diameters down to  $10 \mu\text{m}$ . The operation temperature could be increased to 230 K and an average CPD of up to 55% could be realized for pulsed bias conditions with a pulse length of 3 ns. These

results were obtained for an estimated spin polarization in the active region of  $\sim 6\%$ , demonstrating a significant amplification process for the spin information, due to the stimulated emission in spin-VCSELS.

Though impressive progress has been made concerning the development of electrically pumped spin-VCSELS, a device operating at room temperature is still missing. However, the realization of this goal is absolutely necessary to develop spin-VCSELS in order to benefit from the potential for superior performance in comparison to conventional devices in the near future. Thus, additional intensive research effort is required in this field in the next years. But the already demonstrated results are encouraging and raise the hope that this goal can be reached soon.

#### 4. Conclusions and Outlook

In this paper we review the state-of-the-art of spin-controlled VCSELS with a particular focus on the most promising concepts for real devices. After discussing the fundamentals of spin-optoelectronics we discuss the concepts for electrical spin injection into semiconductor light-emitting diodes (LEDs). However, spin-controlled lasers are generally more attractive for applications than spin-controlled LEDs. Lasers have much faster dynamics than LEDs and the non-linearity of the laser at threshold potentially enables a strong amplification of spin-dependent effects. Among the different concepts for semiconductor lasers, VCSELS are most attractive for spin-control because of their vertical device architecture and circular symmetry. Fundamental studies confirm that spin-VCSELS promise to have lower thresholds than their conventional counterparts and that they enable spin-control of the output polarization. But their most promising advantage is that they might be much faster than their conventional counterparts. For practical applications, the interaction of the spin effects with cavity anisotropies like birefringence and dichroism might enable enormously high modulation frequencies. Recently, Li et al. and Gerhardt et al. [14, 76] have reported spin-induced oscillations much faster than the relaxation oscillation frequency which, in conventional devices, roughly determines the upper modulation frequency limit. Since the damping of the spin induced oscillations and thus their lifetime can be tuned by the current, this concept is interesting for many applications like high-bandwidth data communication or spin information storage. However, in order to realize a device with superior performance, this concept has to be further analyzed in detail. In particular, a clever cavity design with careful engineering of the birefringence might open the door to modulation frequencies significantly above 100 GHz. While most spin-induced effects work only in the vicinity of threshold, such polarization oscillations can be utilized at higher pump levels. This is potentially an important breakthrough, because the usual restriction to an operation near the laser threshold is a major drawback for applications.

The greatest challenge in the field of spin-VCSELS still remains the realization of room temperature operation with pure electrical spin injection. Further massive effort will have to be invested into the engineering of appropriate

spin injectors, injection paths in the semiconductor, and of materials with weak spin relaxation such as (110) GaAs, for example. Additionally a successful integration of efficient spin injection contacts with perpendicular magnetization, providing low switching fields would be an important issue towards realistic applications. However, there has been considerable progress in this area of electrically pumped VCSELS in the past few years. Together with the above-mentioned high potential of spin-VCSELS it can thus be expected that spin-controlled VCSELS remain a scientifically stimulating research area with growing application potential within the next decade.

#### Acknowledgments

The authors thank the German science foundation for financial support within the SFB 491. Helpful discussions with and technical support from T. Ackemann, C. Brenner, M. Li, and H. Höpfner are gratefully acknowledged.

#### References

- [1] S. Datta and B. Das, "Electronic analog of the electro-optic modulator," *Applied Physics Letters*, vol. 56, no. 7, pp. 665–667, 1990.
- [2] R. Flederling, M. Kelm, G. Reuscher et al., "Injection and detection of a spin-polarized current in a light-emitting diode," *Nature*, vol. 402, no. 6763, pp. 787–790, 1999.
- [3] Y. Ohno, D. K. Young, B. Beschoten, F. Matsukura, H. Ohno, and D. D. Awschalom, "Electrical spin injection in a ferromagnetic semiconductor heterostructure," *Nature*, vol. 402, no. 6763, pp. 790–792, 1999.
- [4] H. J. Zhu, M. Ramsteiner, H. Kostial, M. Wassermeier, H. P. Schönherr, and K. H. Ploog, "Room-temperature spin injection from Fe into GaAs," *Physical Review Letters*, vol. 87, no. 1, Article ID 016601, 4 pages, 2001.
- [5] A. T. Hanbicki, B. T. Jonker, G. Itskos, G. Kioseoglou, and A. Petrou, "Efficient electrical spin injection from a magnetic metal/tunnel barrier contact into a semiconductor," *Applied Physics Letters*, vol. 80, no. 7, pp. 1240–1242, 2002.
- [6] N. C. Gerhardt, S. Hövel, C. Brenner et al., "Electron spin injection into GaAs from ferromagnetic contacts in remanence," *Applied Physics Letters*, vol. 87, no. 3, Article ID 32502, 3 pages, 2005.
- [7] C. Adelman, X. Lou, J. Strand, C. J. Palmström, and P. A. Crowell, "Spin injection and relaxation in ferromagnet-semiconductor heterostructures," *Physical Review B*, vol. 71, no. 12, Article ID 121301, 4 pages, 2005.
- [8] X. Jiang, R. Wang, R. M. Shelby et al., "Highly spin-polarized room-temperature tunnel injector for semiconductor spintronics using MgO(100)," *Physical Review Letters*, vol. 94, no. 5, Article ID 056601, 2005.
- [9] S. Hövel, N. C. Gerhardt, M. R. Hofmann et al., "Room temperature electrical spin injection in remanence," *Applied Physics Letters*, vol. 93, no. 2, Article ID 021117, 2008.
- [10] S. Hallstein, J. D. Berger, M. Hilpert et al., "Manifestation of coherent spin precession in stimulated semiconductor emission dynamics," *Physical Review B*, vol. 56, no. 12, pp. R7076–R7079, 1997.
- [11] M. Oestreich, J. Hübner, D. Hägele et al., "Spintronics: spin electronics and optoelectronics in semiconductors," in *Advances in Solid State Physics*, B. Kramer, Ed., pp. 173–186, Springer, Berlin, Germany, 2001.

- [12] D. Saha, D. Basu, and P. Bhattacharya, "High-frequency dynamics of spin-polarized carriers and photons in a laser," *Physical Review B*, vol. 82, no. 20, Article ID 205309, 2010.
- [13] J. Lee, W. Falls, R. Oszałdowski, and I. Žutić, "Spin modulation in semiconductor lasers," *Applied Physics Letters*, vol. 97, no. 4, Article ID 041116, 2010.
- [14] M. Y. Li, H. Jähme, H. Soldat, N. C. Gerhardt, M. R. Hofmann, and T. Ackemann, "Birefringence controlled room-temperature picosecond spin dynamics close to the threshold of vertical-cavity surface-emitting laser devices," *Applied Physics Letters*, vol. 97, no. 19, Article ID 191114, 2010.
- [15] J. Rudolph, D. Hägele, H. M. Gibbs, G. Khitrova, and M. Oestreich, "Laser threshold reduction in a spintronic device," *Applied Physics Letters*, vol. 82, no. 25, pp. 4516–4518, 2003.
- [16] J. Rudolph, S. Döhrmann, D. Hägele, M. Oestreich, and W. Stolz, "Room-temperature threshold reduction in vertical-cavity surface-emitting lasers by injection of spin-polarized electrons," *Applied Physics Letters*, vol. 87, no. 24, Article ID 241117, pp. 1–3, 2005.
- [17] M. Holub, J. Shin, D. Saha, and P. Bhattacharya, "Electrical spin injection and threshold reduction in a semiconductor laser," *Physical Review Letters*, vol. 98, no. 14, Article ID 146603, 2007.
- [18] I. Vurgaftman, M. Holub, B. T. Jonker, and J. R. Meyer, "Estimating threshold reduction for spin-injected semiconductor lasers," *Applied Physics Letters*, vol. 93, no. 3, Article ID 031102, 2008.
- [19] D. Basu, D. Saha, and P. Bhattacharya, "Optical polarization modulation and gain anisotropy in an electrically injected spin laser," *Physical Review Letters*, vol. 102, no. 9, Article ID 093904, 2009.
- [20] M. Holub and B. T. Jonker, "Threshold current reduction in spin-polarized lasers: role of strain and valence-band mixing," *Physical Review B*, vol. 83, no. 12, Article ID 125309, 2011.
- [21] H. Ando, T. Sogawa, and H. Gotoh, "Photon-spin controlled lasing oscillation in surface-emitting lasers," *Applied Physics Letters*, vol. 73, no. 5, pp. 566–568, 1998.
- [22] S. Hövel, N. Gerhardt, M. Hofmann, J. Yang, D. Reuter, and A. Wieck, "Spin controlled optically pumped vertical cavity surface emitting laser," *Electronics Letters*, vol. 41, no. 5, pp. 251–253, 2005.
- [23] N. Gerhardt, S. Hövel, M. Hofmann, J. Yang, D. Reuter, and A. Wieck, "Enhancement of spin information with vertical cavity surface emitting lasers," *Electronics Letters*, vol. 42, no. 2, pp. 88–89, 2006.
- [24] M. Holub and P. Bhattacharya, "Spin-polarized light-emitting diodes and lasers," *Journal of Physics D*, vol. 40, no. 11, article R01, pp. R179–R203, 2007.
- [25] S. Hövel, A. Bischoff, N. C. Gerhardt et al., "Optical spin manipulation of electrically pumped vertical-cavity surface-emitting lasers," *Applied Physics Letters*, vol. 92, no. 4, Article ID 041118, 2008.
- [26] S. Iba, S. Koh, K. Ikeda, and H. Kawaguchi, "Room temperature circularly polarized lasing in an optically spin injected vertical-cavity surface-emitting laser with (110) GaAs quantum wells," *Applied Physics Letters*, vol. 98, no. 8, Article ID 81113, 2011.
- [27] I. Žutić, J. Fabian, and S. D. Sarma, "Spintronics: fundamentals and applications," *Reviews of Modern Physics*, vol. 76, no. 2, pp. 323–410, 2004.
- [28] M. Oestreich, M. Bender, J. Hübner et al., "Spin injection, spin transport and spin coherence," *Semiconductor Science and Technology*, vol. 17, no. 4, pp. 285–297, 2002.
- [29] F. Meier and B. P. Zakharchenya, *Optical Orientation. Modern Problems in Condensed Matter Sciences*, vol. 8, North-Holland-Elsevier Science, New York, NY, USA, 1984.
- [30] R. J. Elliott, "Theory of the effect of spin-Orbit coupling on magnetic resonance in some semiconductors," *Physical Review*, vol. 96, no. 2, pp. 266–279, 1954.
- [31] Y. Yafet, "Solid state physics," in *Advances in Research and Applications*, F. Seitz and D. Turnbull, Eds., pp. 2–96, Academic Press, 1963.
- [32] M. I. D'Yakonov and V. I. Perel, "Optical orientation in a system of electrons and lattice nuclei in semiconductors. Theory," *Soviet Physics*, vol. 38, pp. 177–183, 1974.
- [33] G. Bir, A. Aronov, and G. Pikus, "Spin relaxation of electrons due to scattering by holes," *Soviet Physics*, vol. 42, pp. 705–712, 1976.
- [34] M. Dyakonov, *Spin Physics in Semiconductors*, Springer, 2008.
- [35] R. I. Dzhiyev, K. V. Kavokin, V. L. Korenev et al., "Low-temperature spin relaxation in n-type GaAs," *Physical Review B*, vol. 66, no. 24, Article ID 245204, 7 pages, 2002.
- [36] A. V. Kimel, F. Bentivegna, V. N. Gridnev, V. V. Pavlov, R. V. Pisarev, and T. Rasing, "Room-temperature ultrafast carrier and spin dynamics in GaAs probed by the photoinduced magneto-optical Kerr effect," *Physical Review B*, vol. 63, no. 23, Article ID 235201, 8 pages, 2001.
- [37] A. Malinowski, R. S. Britton, T. Grevatt, R. T. Harley, D. A. Ritchie, and M. Y. Simmons, "Spin relaxation in GaAs/AlM<sub>x</sub>Ga<sub>1-x</sub>As quantum wells," *Physical Review B*, vol. 62, no. 19, pp. 13034–13039, 2000.
- [38] J. Fabian, A. Matos-Abiague, C. Ertler, P. Stano, and I. Žutić, "Semiconductor spintronics," *Acta Physica Slovaca*, vol. 57, no. 4-5, pp. 565–907, 2007.
- [39] D. J. Hilton and C. L. Tang, "Optical orientation and femtosecond relaxation of spin-polarized holes in GaAs," *Physical Review Letters*, vol. 89, no. 14, Article ID 146601, 4 pages, 2002.
- [40] M. Holub, J. Shin, S. Chakrabarti, and P. Bhattacharya, "Electrically injected spin-polarized vertical-cavity surface-emitting lasers," *Applied Physics Letters*, vol. 87, no. 9, Article ID 91108, pp. 1–3, 2005.
- [41] M. Ramsteiner, H. Y. Hao, A. Kawaharazuka et al., "Electrical spin injection from ferromagnetic MnAs metal layers into GaAs," *Physical Review B*, vol. 66, no. 8, Article ID 081304, 4 pages, 2002.
- [42] S. Saikin, M. Shen, and M. C. Cheng, "Spin dynamics in a compound semiconductor spintronic structure with a Schottky barrier," *Journal of Physics Condensed Matter*, vol. 18, no. 5, pp. 1535–1544, 2006.
- [43] H. Soldat, M. Li, N. C. Gerhardt et al., "Room temperature spin relaxation length in spin light-emitting diodes," *Applied Physics Letters*, vol. 99, no. 5, Article ID 051102, 2011.
- [44] J. F. Gregg, I. Petej, E. Jouguelet, and C. Dennis, "Spin electronics—a review," *Journal of Physics D*, vol. 35, no. 18, pp. R121–R155, 2002.
- [45] G. Schmidt, D. Ferrand, L. W. Molenkamp, A. T. Filip, and B. J. Van Wees, "Fundamental obstacle for electrical spin injection from a ferromagnetic metal into a diffusive semiconductor," *Physical Review B*, vol. 62, no. 8, pp. R4790–R4793, 2000.
- [46] E. I. Rashba, "Theory of electrical spin injection: tunnel contacts as a solution of the conductivity mismatch problem," *Physical Review B*, vol. 62, no. 24, Article ID R16267, pp. R16267–R16270, 2000.
- [47] A. Fert and H. Jaffrès, "Conditions for efficient spin injection from a ferromagnetic metal into a semiconductor," *Physical Review B*, vol. 64, no. 18, Article ID 184420, 9 pages, 2001.

- [48] T. Dietl, H. Ohno, F. Matsukura, J. Cibert, and D. Ferrand, "Zener model description of ferromagnetism in zinc-blende magnetic semiconductors," *Science*, vol. 287, no. 5455, pp. 1019–1022, 2000.
- [49] M. L. Reed, N. A. El-Masry, H. H. Stadelmaier et al., "Room temperature ferromagnetic properties of (Ga, Mn)N," *Applied Physics Letters*, vol. 79, no. 21, pp. 3473–3475, 2001.
- [50] M. Tanaka, "Ferromagnet (MnAs)/III-V semiconductor hybrid structures," *Semiconductor Science and Technology*, vol. 17, no. 4, pp. 327–341, 2002.
- [51] H. Saito, S. Yamagata, and K. Ando, "Room-temperature ferromagnetism in a II-VI diluted magnetic semiconductor Zn<sub>1-x</sub>CrxTe," *Physical Review Letters*, vol. 90, no. 20, Article ID 207202, 4 pages, 2003.
- [52] J. Philip, A. Punnoose, B. I. Kim et al., "Carrier-controlled ferromagnetism in transparent oxide semiconductors," *Nature Materials*, vol. 5, no. 4, pp. 298–304, 2006.
- [53] G. A. Medvedkin, T. Ishibashi, T. Nishi, K. Hayata, Y. Hasegawa, and K. Sato, "Room temperature ferromagnetism in novel diluted magnetic semiconductor Cd<sub>1-x</sub>MnxGeP<sub>2</sub>," *Japanese Journal of Applied Physics*, vol. 39, no. 10 A, pp. L949–L951, 2000.
- [54] T. Dietl and H. Ohno, "Ferromagnetic III-V and II-VI semiconductors," *MRS Bulletin*, vol. 28, no. 10, pp. 714–719, 2003.
- [55] T. Manago and H. Akinaga, "Spin-polarized light-emitting diode using metal/insulator/semiconductor structures," *Applied Physics Letters*, vol. 81, no. 4, pp. 694–696, 2002.
- [56] N. C. Gerhardt, S. Hövel, C. Brenner et al., "Spin injection light-emitting diode with vertically magnetized ferromagnetic metal contacts," *Journal of Applied Physics*, vol. 99, no. 7, Article ID 073907, 2006.
- [57] E. Schuster, R. A. Brand, F. Stromberg et al., "Epitaxial growth and interfacial magnetism of spin aligner for remanent spin injection: [Fe/Tb]<sub>n</sub>/Fe/MgO/GaAs -light emitting diode as a prototype system," *Journal of Applied Physics*, vol. 108, no. 6, Article ID 063902, 2010.
- [58] A. Ludwig, R. Roescu, A. K. Rai et al., "Electrical spin injection in InAs quantum dots at room temperature and adjustment of the emission wavelength for spintronic applications," *Journal of Crystal Growth*, vol. 323, no. 1, pp. 376–379, 2011.
- [59] A. Sinsarp, T. Manago, F. Takano, and H. Akinaga, "Electrical spin injection from out-of-plane magnetized FePt/MgO tunneling junction into GaAs at room temperature," *Japanese Journal of Applied Physics Part 2*, vol. 46, no. 1–3, pp. L4–L6, 2007.
- [60] L. Grenet, M. Jamet, P. N6 et al., "Spin injection in silicon at zero magnetic field," *Applied Physics Letters*, vol. 94, no. 3, Article ID 032502, 2009.
- [61] O. M. J. Van't Erve, G. Kioseoglou, A. T. Hanbicki, C. H. Li, and B. T. Jonker, "Remanent electrical spin injection from Fe into AlGaAs/GaAs light emitting diodes," *Applied Physics Letters*, vol. 89, no. 7, Article ID 072505, 2006.
- [62] M. J. Adams and D. Alexandropoulos, "Parametric analysis of spin-polarized VCSELs," *IEEE Journal of Quantum Electronics*, vol. 45, no. 6, pp. 744–749, 2009.
- [63] R. Oszwadowski, C. G6thgen, and I. Žutić, "Theory of quantum dot spin lasers," *Physical Review B*, vol. 82, Article ID 85316, 2010.
- [64] M. San Miguel, Q. Feng, and J. V. Moloney, "Light-polarization dynamics in surface-emitting semiconductor lasers," *Physical Review A*, vol. 52, no. 2, pp. 1728–1739, 1995.
- [65] A. Gahl, S. Balle, and M. San Miguel, "Polarization dynamics of optically pumped VCSELs," *IEEE Journal of Quantum Electronics*, vol. 35, no. 3, pp. 342–351, 1999.
- [66] J. Martin-Regalado, F. Prati, M. San Miguel, and N. B. Abraham, "Polarization properties of vertical-cavity surface-emitting lasers," *IEEE Journal of Quantum Electronics*, vol. 33, no. 5, pp. 765–783, 1997.
- [67] C. G6thgen, R. Oszwadowski, A. Petrou, and I. Žutić, "Analytical model of spin-polarized semiconductor lasers," *Applied Physics Letters*, vol. 93, no. 4, Article ID 042513, 2008.
- [68] D. Basu, D. Saha, C. C. Wu, M. Holub, Z. Mi, and P. Bhattacharya, "Electrically injected InAsGaAs quantum dot spin laser operating at 200 K," *Applied Physics Letters*, vol. 92, no. 9, Article ID 091119, 2008.
- [69] M. Travagnin, M. P. Van Exter, A. K. Jansen Van Doorn, and J. P. Woerdman, "Role of optical anisotropies in the polarization properties of surface-emitting semiconductor lasers," *Physical Review A*, vol. 54, no. 2, pp. 1647–1660, 1996.
- [70] M. P. Van Exter, M. B. Willemsen, and J. P. Woerdman, "Polarization fluctuations in vertical-cavity semiconductor lasers," *Physical Review A*, vol. 58, no. 5, pp. 4191–4205, 1998.
- [71] M. Sondermann, M. Weinkath, and T. Ackemann, "Polarization switching to the gain disfavored mode in vertical-cavity surface-emitting lasers," *IEEE Journal of Quantum Electronics*, vol. 40, no. 2, pp. 97–104, 2004.
- [72] M. B. Willemsen, M. P. Van Exter, and J. P. Woerdman, "Anatomy of a polarization switch of a vertical-cavity semiconductor laser," *Physical Review Letters*, vol. 84, no. 19, pp. 4337–4340, 2000.
- [73] E. L. Blansett, M. G. Raymer, G. Khitrova et al., "Ultrafast polarization dynamics and noise in pulsed vertical-cavity surface-emitting lasers," *Optics Express*, vol. 9, no. 6, pp. 312–318, 2001.
- [74] T. Ackemann and M. Sondermann, "Characteristics of polarization switching from the low to the high frequency mode in vertical-cavity surface-emitting lasers," *Applied Physics Letters*, vol. 78, no. 23, pp. 3574–3576, 2001.
- [75] R. Al-Seyab, D. Alexandropoulos, I. D. Henning, and M. J. Adams, "Instabilities in spin-polarized vertical-cavity surface-emitting lasers," *IEEE Photonics Journal*, vol. 3, no. 5, pp. 799–809, 2011.
- [76] N. C. Gerhardt, M. Y. Li, H. Jähme, H. Höpfner, T. Ackemann, and M. R. Hofmann, "Ultrafast spin-induced polarization oscillations with tunable lifetime in vertical-cavity surface-emitting lasers," *Applied Physics Letters*, vol. 99, no. 15, Article ID 151107, 2011.
- [77] K. Panajotov, B. Nagler, G. Verschaffel et al., "Impact of in-plane anisotropic strain on the polarization behavior of vertical-cavity surface-emitting lasers," *Applied Physics Letters*, vol. 77, no. 11, pp. 1590–1592, 2000.
- [78] K. Ikeda, T. Fujimoto, H. Fujino, and T. Katayama, "Switching of lasing circular polarizations in a (110)-VCSEL," *IEEE Photonics Technology Letters*, vol. 21, no. 18, pp. 1350–1352, 2009.
- [79] D. Hägele, M. Oestreich, M. Holub, and P. Bhattacharya, "Comment on "electrically injected spin-polarized vertical-cavity surface-emitting lasers" [Applied Physics Letters vol. 87, article 091108, 2005]," *Applied Physics Letters*, vol. 88, no. 5, Article ID 56101, p. 1, 2006.
- [80] M. Holub and P. Bhattacharya, "Response to Comment on "Electrically injected spin-polarized vertical-cavity surface-emitting lasers" [Applied Physics Letters, vol. 87, article 091108, 2005]," *Applied Physics Letters*, vol. 88, no. 5, Article ID 56102, p. 1, 2006.
- [81] M. Holub, P. Bhattacharya, J. Shin, and D. Saha, "Electron spin injection from a regrown Fe layer in a spin-polarized vertical-cavity surface-emitting laser," *Journal of Crystal Growth*, vol. 301–302, pp. 602–606, 2007.

## Review Article

# Single-Fiber Bidirectional Optical Data Links with Monolithic Transceiver Chips

**Alexander Kern, Sujoy Paul, Dietmar Wahl, Ahmed Al-Samaneh, and Rainer Michalzik**

*Institute of Optoelectronics, Ulm University, Albert-Einstein-Allee 45, 89081 Ulm, Germany*

Correspondence should be addressed to Rainer Michalzik, rainer.michalzik@uni-ulm.de

Received 18 August 2011; Accepted 23 September 2011

Academic Editor: Krassimir Panajotov

Copyright © 2012 Alexander Kern et al. This is an open access article distributed under the Creative Commons Attribution License, which permits unrestricted use, distribution, and reproduction in any medium, provided the original work is properly cited.

We report the monolithic integration, fabrication, and electrooptical properties of AlGaAs-GaAs-based transceiver (TRx) chips for 850 nm wavelength optical links with data rates of multiple Gbit/s. Using a single butt-coupled multimode fiber (MMF), low-cost bidirectional communication in half- and even full-duplex mode is demonstrated. Two design concepts are presented, based on a vertical-cavity surface-emitting laser (VCSEL) and a monolithically integrated p-doped-intrinsic-n-doped (PIN) or metal-semiconductor-metal (MSM) photodetector. Whereas the VCSEL-PIN photodiode (PD) chips are used for high-speed bidirectional data transmission over 62.5 and 50  $\mu\text{m}$  core diameter MMFs, MSM TRx chips are employed for 100 or 200  $\mu\text{m}$  large-area fibers. Such a monolithic transceiver design based on a well-established material system and avoiding the use of external fiber coupling optics is well suited for inexpensive and compact optical interconnects over distances of a few hundred meters. Standard MMF networks can thus be upgraded using high-speed VCSEL-PIN transceiver chips which are capable to handle data rates of up to 10 Gbit/s.

## 1. Introduction

Over the last decades, the well-known AlGaAs-GaAs mixed compound semiconductor material system paved the way for the tremendous development of vertical-cavity surface-emitting lasers (VCSELs) as excellent light sources. Their inherent property of light emission perpendicular to the wafer surface and therefore the ability of fabrication in densely packed two-dimensional arrays make VCSELs distinguished inexpensive candidates for many applications [1]. Further advances in VCSEL technology have enabled higher chip functionalities such as monolithic integration with photodiodes. Such a device combination can be used for monitoring the laser output power [2], for realizing an ultracompact laser self-mixing interference sensor [3], or for biomedical fluorescence sensing [4]. Favorable properties like low threshold currents and operating voltages, circular beam profiles and high modulation bandwidths are ideal for VCSEL use in optical communications [1]. In contrast to conventional interconnections with one MMF

per transmission direction, one could potentially lower the link cost, weight, and size by employing a single optical fiber, as presented in [5]. Here, the VCSEL is used as a dual-purpose device, namely, an efficient laser source and a resonant-cavity-enhanced avalanche photodetector. Since it is switched between two operation modes, only half-duplex operation at 1.25 Gbit/s data rate over a 50  $\mu\text{m}$  core diameter MMF with 500 m length could be demonstrated. Hence, data transmission in full-duplex mode is only possible for single-purpose, that is, spatially separated devices. Similar to [5], monolithic integration can be achieved by using only one epitaxial layer structure for VCSEL and resonant photodetector [6]. However, both attempts need temperature control at each fiber end in order to tune the very narrow spectral range of the photodetector in case of temperature differences. The use of separate epitaxial layers for nonresonant detection, as reported in [7, 8], can avoid higher costs for the temperature stabilization of such an optical link. In [7], the small-signal 3 dB bandwidth of the presented PIN PD array is 2.3 GHz and only static operation is reported in [8].

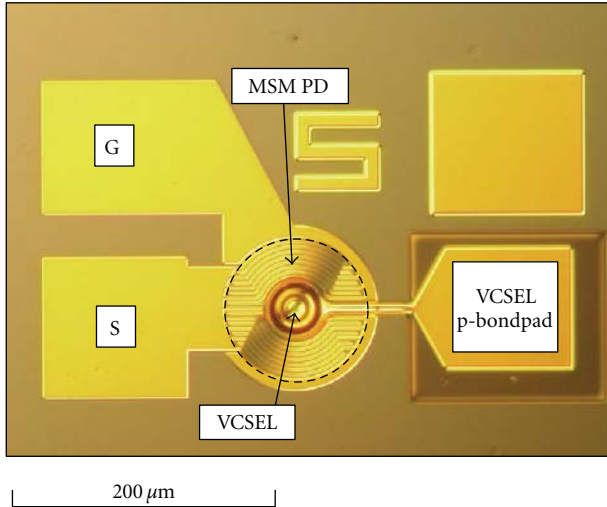


FIGURE 1: Photograph of a transceiver chip consisting of a VCSEL and an MSM photodiode with indicated ground-signal (GS) microwave probe contacts. The VCSEL is positioned in the center of the photodetector in order to achieve best fiber coupling. The dashed line indicates the optimum alignment of a MMF with  $100\ \mu\text{m}$  core diameter (from [9]).

The main feature of our approach is the combination of monolithic integration of a laser source and a nonresonant photodetector while retaining the capability of half- and full-duplex data transmission over a single butt-coupled multimode fiber. Modules based on those chips can enable compact, efficient, and low-cost optical interconnection for short-reach local area, premises, and even mobile networks. Such true bidirectional optical links are presented in this paper, based on an 850 nm wavelength VCSEL and MSM-type as well as PIN-type photodetectors.

## 2. Previous Work

In our first approach, several designs of monolithically integrated VCSELs and MSM photodiodes for 200 and  $100\ \mu\text{m}$  core diameter MMFs were presented in [9–18]. Figure 1 shows a transceiver chip based on an 850 nm VCSEL centered in the MSM PD for efficient coupling to a  $100\ \mu\text{m}$  MMF. MSM PDs are preferred for short-reach applications with large-core MMFs for larger fiber alignment tolerances. Here, PIN photodiodes with the same size of MSM PDs would lead to larger parasitic capacitances and thus lower bandwidths [19]. For this reason, MSM photodetectors with  $210\ \mu\text{m}$  diameter were employed for 1 Gbit/s half-duplex and 0.5 Gbit/s full-duplex data transmission over a 50 m long butt-coupled  $200\ \mu\text{m}$  core diameter semi-graded-index polymer-clad silica (semi-GI PCS) fiber [17]. Since those transceiver chips were capable to transmit 3 Gbit/s in back-to-back (BTB) mode [12, 13], the maximum data rate was limited by the low bandwidth-distance product ( $B \times L$ ) of  $40\ \text{GHz} \times \text{m}$  of the semi-GI PCS fiber. With an improved chip design, even 4 Gbit/s BTB data transmission was possible [18]. In a further miniaturization step, 1 Gbit/s

half-duplex operation was demonstrated with  $110\ \mu\text{m}$  TRx MSM PDs over a 100 m long multimode fiber with  $100\ \mu\text{m}$  core diameter [15, 16], thus exploiting the most from its bandwidth-distance product of  $100\ \text{GHz} \times \text{m}$ .

Fibers with even higher bandwidths are required for longer and faster interconnects. Pursuing this goal, a  $50\ \mu\text{m}$  core diameter MMF of 500 m length and a  $B \times L$  of about  $2\ \text{GHz} \times \text{km}$  was used with similar  $110\ \mu\text{m}$  MSM TRx chips for data transmission of 1 Gbit/s in both, half- and full-duplex mode [9], where the size mismatch required very careful lateral and longitudinal alignment. Also here, with an improved chip design, even data rates of 5 Gbit/s were possible in BTB mode [18]. The results are summarized in [21].

In order to push the data rate further, our approach aims at a miniaturization of transceiver chips, thus ensuring the compatibility with standard MMFs with core diameters of 50 and  $62.5\ \mu\text{m}$ . Since MSM photodiodes suffer from relatively low responsivities of around  $0.4\ \text{A/W}$  [18] and a higher optical crosstalk owing to their metal contact fingers that partially shadow the detector area, the further downscaling of VCSEL-MSM TRx chips would strongly decrease the effectively detected signal power. Therefore, the fraction of optical crosstalk in bidirectional full-duplex operation would further increase. Thus, for the next miniaturization step, better performance is expected by moving to PIN-type photodetectors. Both, their responsivity is sufficiently higher and the amount of light reflected at metal contacts is minimized, which decreases the relative optical crosstalk within the system. Additionally, the inherent PIN PD capacitance decreases with the smaller fiber core diameter, boosting the maximum possible data rate of the transceiver.

Figure 2 shows a TRx chip with  $60\ \mu\text{m}$  diameter PIN PD and a miniaturized laterally offset VCSEL, maximizing the effective photodetecting area of such a transceiver configuration.

## 3. Chip Design and Processing

For the full-monolithic integration, the transceiver chip comprises all epitaxial layers necessary for signal generation and detection. Figure 3 illustrates schematically such a layer structure grown by molecular beam epitaxy on an n-doped GaAs substrate.

**3.1. VCSEL.** The VCSEL layer structure consists of a distributed Bragg reflector (DBR) with 38.5 n-doped  $\text{Al}_{0.2}\text{Ga}_{0.8}\text{As}/\text{Al}_{0.9}\text{Ga}_{0.1}\text{As}$  mirror periods with graded aluminum content. The three 8 nm thick GaAs quantum wells are designed for 850 nm wavelength emission at room temperature. They are separated by 10 nm  $\text{Al}_{0.27}\text{Ga}_{0.73}\text{As}$  barrier layers forming the active region in the center of a one-wavelength optical thickness inner cavity. A 32 nm thick highly p-doped AlAs layer in the first top-mirror period above the active region is designated for current confinement after an oxidation step. The upper p-doped DBR with 23.5 periods completes the VCSEL cavity and is equivalent to the bottom n-DBR. The VCSEL growth is terminated with

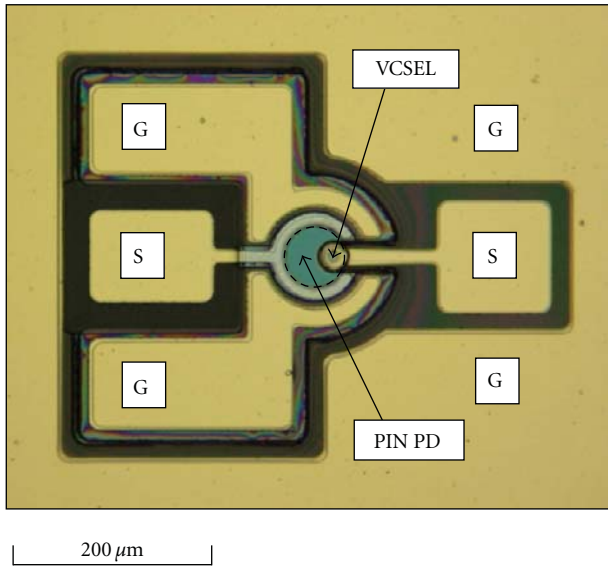


FIGURE 2: Photograph of a transceiver chip consisting of a VCSEL and a PIN photodiode, each with indicated ground-signal-ground (GSG) microwave probe contacts. The VCSEL is positioned off-center with respect to the photodetector in order to maximize the effective photodetecting area of the transceiver. The dashed circle indicates the alignment of a MMF with  $50\ \mu\text{m}$  core diameter (from [20]).

a 30 nm highly p-doped GaAs layer, which provides a low resistance p-contact and at the same time prevents oxidation of the subjacent aluminum-containing Bragg layers.

**3.2. PIN Photodiode.** A monolithic integration of PIN photodiodes with VCSELs was realized by growing the PD layers on top of the VCSEL structure in the same growth run. This guarantees an improved crystal quality compared to an overgrowth process [23]. Hence, the PIN PD layer stack is grown on top of the intrinsic  $\text{Al}_{0.9}\text{Ga}_{0.1}\text{As}$  etch stop layer, which also partially acts as an insulator, reducing the capacitive coupling between the two devices. Additionally, the reverse-biased PD has its grounded p-doped side facing the VCSEL layers, which minimizes possible capacitive effects. The main part of the PIN-type photodiode is the 2 to  $3\ \mu\text{m}$  thick undoped GaAs absorption layer sandwiched by p- and n-doped  $\text{Al}_{0.3}\text{Ga}_{0.7}\text{As}$  of 250 nm thickness, which enables sufficient current spreading for large diameter PDs [24]. The higher band gap energy of these two contact layers provides a spectral window for the wavelengths of interest at around 850 nm. Linearly graded n- and p- $\text{Al}_x\text{Ga}_{1-x}\text{As}$  ( $x = 0 \rightarrow 0.3$ ) in Figure 3 is employed between the absorption and contact layers in order to minimize the energy band discontinuities, thus ensuring an easier escape of the light-induced carriers from the undoped GaAs. To prevent the top n- $\text{Al}_{0.3}\text{Ga}_{0.7}\text{As}$  from oxidation, a 10 nm thick n-doped GaAs cap layer terminates the complete VCSEL-PD stack.

**3.3. Fabrication.** The fabrication of transceiver chips is based on lithographic structuring with photosensitive resists

and subsequent etching or material deposition steps. At least eight lithographic steps are necessary for the full processing of the transceiver chip shown in Figure 4. In the first step, the detector layers on top of the VCSEL structure are removed to uncover the future laser device. In order to ensure that the uppermost VCSEL layer is not affected by the etching, it is protected by an etch stop layer with a high aluminum content, as mentioned above. Combining nonselective with selective dry-etching processes such as reactive-ion etching (RIE) with  $\text{SiCl}_4$  alone and with an appropriate  $\text{SF}_6/\text{SiCl}_4$  ratio afterwards [25], the p- $\text{Al}_{0.3}\text{Ga}_{0.7}\text{As}$  can be exposed. It is subsequently removed by a citric acid/hydrogen peroxide solution, since it provides the best achievable etching selectivity with a possibility of visual control between  $\text{Al}_{0.3}\text{Ga}_{0.7}\text{As}$  and  $\text{Al}_{0.9}\text{Ga}_{0.1}\text{As}$  layers [26]. Followed by an  $\text{Al}_{0.9}\text{Ga}_{0.1}\text{As}/\text{GaAs}$  highly selective wet-etching with hydrofluoric acid [26], also the etch stop layer covering the p-doped cap layer of the VCSEL can now be removed. Despite the fact that the last 300 to 400 nm above the p-Bragg mirror are wet-etched, thus providing rather flat mesa side walls in this region, more than 90% of the total etch depth was reached by the dry-etching process resulting in nearly vertical mesa edges. Unlike MSM PDs with planar contact structure, PIN PDs have vertically displaced contacts and thus require an additional etch step to expose the p-doped  $\text{Al}_{0.3}\text{Ga}_{0.7}\text{As}$  layer as can be seen in the left part of Figure 4. This step can be accomplished in analogy to the previous dry-etching processes, where the AlGaAs p-contact layer with just 30% aluminum content acts also as an etch stop layer. By means of the described selective etching techniques, a uniform layer topography all over the wafer can be guaranteed in spite of the layer thickness inhomogeneity due to the epitaxial growth process. The third etching process spatially separates the VCSEL and the photodetector by a 2 to  $4\ \mu\text{m}$  narrow trench and thus provides access to the current confinement layer, as seen in the right part of Figure 4. It is performed by reactive-ion etching with  $\text{SiCl}_4$  and thus without selectivity. Also this process step requires dry-etching, since steep mesa side walls are crucial for the miniaturization and dense integration of VCSEL and PIN PD for  $50\ \mu\text{m}$  core diameter fibers.

In the next processing step, selective oxidation in a hot water vapor atmosphere forms a current aperture in the AlAs layer. Its diameter is chosen to obtain transverse multimode operation of the laser. An aluminum content of 90% in the 150 nm thick etch stop layer ensures a much decreased oxidation rate compared to the current confinement layer [27]. A deep oxidation of the etch stop layer associated with a volume change would induce strain in the surrounding layers, which could cause cracks and damage of the edges of the PD after the subsequent annealing process for the n-contacts [22]. On the other hand, a low aluminum content could result in a lower etching selectivity of the hydrofluoric acid [26]. The fourth and fifth lithography step provides passivation and planarization with polyimide. Afterwards, both p- and n-contacts of the PD and VCSEL are evaporated and annealed, in order to form low-resistance contacts. In the last lithography step, an  $\text{Al}_2\text{O}_3$  quarter-wave antireflection layer is sputtered on the area of the transceiver chip which

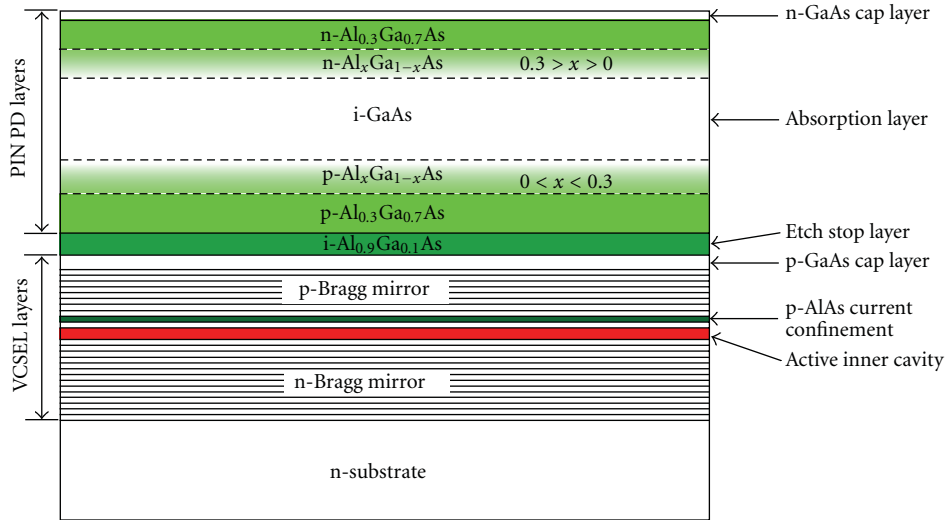


FIGURE 3: Schematic layer structure design for the monolithically integrated transceiver chip. The layers for the PIN PD on top of the VCSEL layers are separated by an etch stop layer (from [22]).

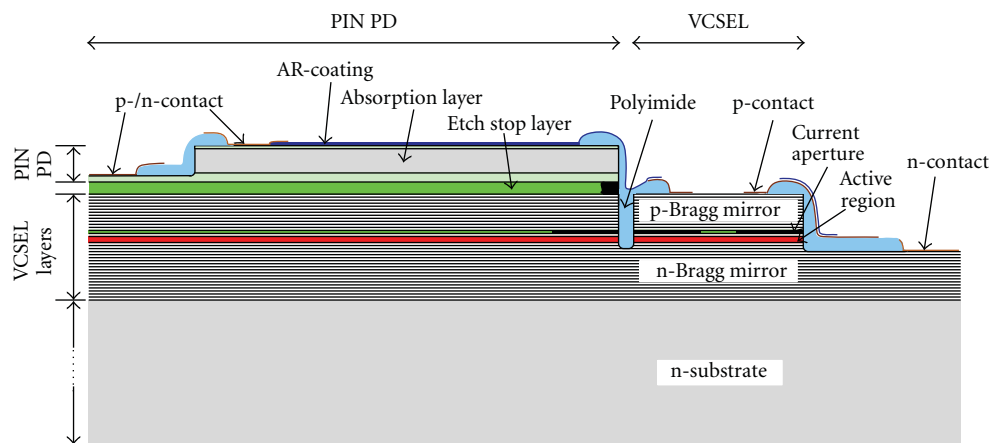


FIGURE 4: Schematic cross-sectional view of the fully processed transceiver chip consisting of a monolithically integrated PIN photodetector separated by a 2 to 4  $\mu\text{m}$  wide trench from the top-emitting, oxide-confined VCSEL. Both devices feature top-accessible contacts (from [24], ©2011 IEEE).

is exposed to the incident light. The reflectivity of the semiconductor surface is thus reduced from approximately 30% to 1.3% over a spectral width of nearly 50 nm [21].

#### 4. Device Characteristics

As can be seen in Figures 2 and 4, all PD and VCSEL contacts are accessible from the top, thus allowing on-wafer testing with two coplanar microwave probes with ground-signal-ground (GSG) configuration.

**4.1. VCSEL.** Small-signal modulation transfer functions of an integrated VCSEL with about 8  $\mu\text{m}$  oxide aperture and 25  $\mu\text{m}$  mesa diameter are shown in Figure 5. Their typical second-order low-pass behavior is clearly visible with the shift of the resonance peak for bias currents above threshold.

The increase of the damping coefficient flattens the shape of the frequency response without limiting its bandwidth for currents up to 9 mA. A maximum 3 dB bandwidth of around 11.5 GHz is observed, providing a suitable frequency characteristic for large-signal experiments. For the given device generation, unintentional cavity detuning has led to optical emission at around 810 nm, a rather high threshold current of 3.5 mA, and a relatively low maximum output power of 3.5 mW [24].

**4.2. PIN Photodiode.** The VCSEL structure underneath the photodetector leads to backreflection of the incident non-absorbed light and thus to double-pass absorption. The responsivity of the transceiver PIN photodiode with 3  $\mu\text{m}$  thick GaAs absorption layer increases to 0.61 A/W at 850 nm, which corresponds to a quantum efficiency of nearly 88%

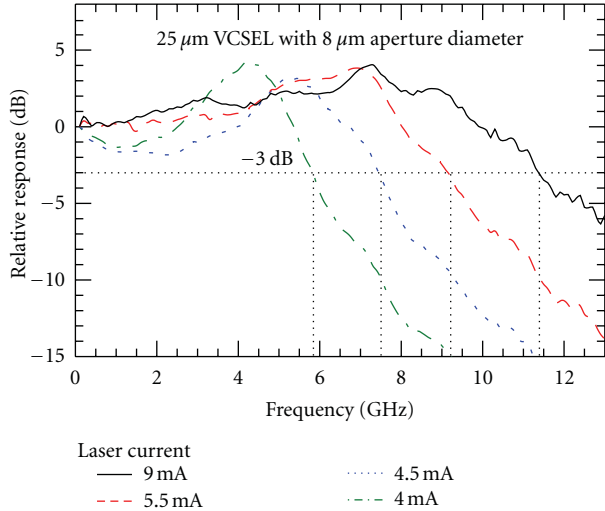


FIGURE 5: Small-signal frequency response curves of a typical transceiver multimode VCSEL for different bias currents (from [24]).

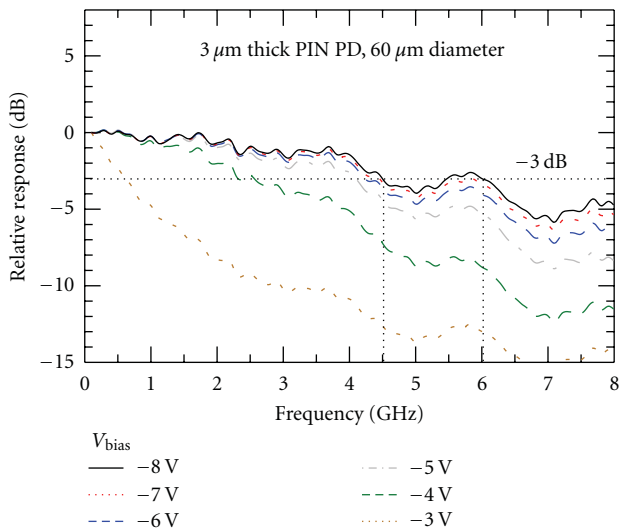


FIGURE 6: Small-signal frequency response curves of an integrated  $3\ \mu\text{m}$  thick transceiver PIN photodetector for reverse bias voltages from  $-3$  to  $-8\ \text{V}$  (from [28]).

[29]. It is almost independent of the bias voltage. The small-signal frequency response of the  $3\ \mu\text{m}$  thick and  $60\ \mu\text{m}$  diameter photodetector can be sufficiently improved by increasing its reverse bias voltage, as shown in Figure 6. It saturates at  $-8\ \text{V}$  enabling a 3 dB-bandwidth in the range of 4.5 to 6 GHz [28]. Despite the fact that the 3 dB bandwidth of the PIN PD is about a factor of two smaller than that of the VCSEL, the rather slow roll-off of the response curve still provides sufficient signals for frequencies somewhat beyond the 3 dB limit. From simple estimations, the resistor-capacitor ( $RC$ ) low-pass and drift time bandwidths of the PD are expected to be 14 GHz (for  $R = 50\ \Omega$  and neglecting the bond pad capacitances) and 15 GHz, respectively. We attribute the

much smaller experimental values and the corrugations of the frequency responses predominantly to parasitic coupling with the highly doped VCSEL layers underneath the PD layers as well as to the parasitic contributions of the PD bondpads.

## 5. Data Transmission

According to the results presented in the previous subsection, the lower small-signal bandwidths of the PIN PDs compared to those of the VCSELs are expected to limit the maximum achievable data rate of the transceivers. For half-duplex operation, the VCSEL is biased by a constant current superimposed with a high-speed modulating signal, which is generated by a bit pattern generator (Anritsu MP1763B) that itself is driven by a signal generator (Rohde & Schwarz SMR40). An attenuator between bias tee and bit pattern generator is used to weaken the backward microwave reflections due to impedance mismatch between the VCSEL and the  $50\ \Omega$  signal driver. For back-to-back (BTB) data transmission, the laser beam is focused via free-space optics on the transceiver PIN photodetector, as shown in Figure 8 (top). In case of fiber-based data transmission in Figure 7 (top), a MMF is butt-coupled (about  $30\ \mu\text{m}$  distance) to each TRx chip. The PIN photodiode is reverse biased with a constant voltage of  $-8\ \text{V}$  using a bias tee. It separates the modulated and direct current signals on the receiver side. The high-speed signal is subsequently amplified by a wideband amplifier (Anritsu A3HB3102) with 10 GHz bandwidth, 28 dB gain, and 4.5 dB noise figure before its analysis with a wide-bandwidth oscilloscope (Agilent 86100B) or bit error detector (Anritsu MP1764A). For full-duplex operation, in order to build an equivalent transmission link in the opposite direction, the inverted output of the bit pattern generator is used for the second channel.

**5.1. Standard MMF.** Investigations into digital data transmission were made using a 500 m long  $50\ \mu\text{m}$  core diameter OM3-type MMF with a bandwidth-distance product of about  $2\ \text{GHz} \times \text{km}$ . For evaluation purposes, two different transceiver chips with 2 and  $3\ \mu\text{m}$  thick PIN PDs were used in this experiment [28]. The thinner photodiode has a larger capacitance and a smaller 3 dB-bandwidth of approximately 4.2 GHz. First, data transmission in half-duplex mode was performed in order to avoid the influence of optical and electrical crosstalk in the system. The optical eye diagrams in Figure 7 (bottom) show error-free operation with the  $2\ \mu\text{m}$  (left) and  $3\ \mu\text{m}$  (center) thick PIN PDs at 7 Gbit/s, thus fully utilizing the  $B \times L$  of the MMF. For the  $2\ \mu\text{m}$  PD, the maximum data rate is additionally limited by the rising and falling edges caused by  $RC$  parasitics. In contrast, for the opposite channel with a  $3\ \mu\text{m}$  thick PIN PD, the error-free eye with smaller amplitude (caused by the smaller on-off ratio of the VCSEL on TRx chip 2) shows the  $RC$  limit to a much smaller extent. The signals detected by the PDs on the transmitter side (i.e., on the same chip) correspond to optical crosstalk, predominantly due to the reflections at both fiber endfaces as well as at the opposite TRx chip.

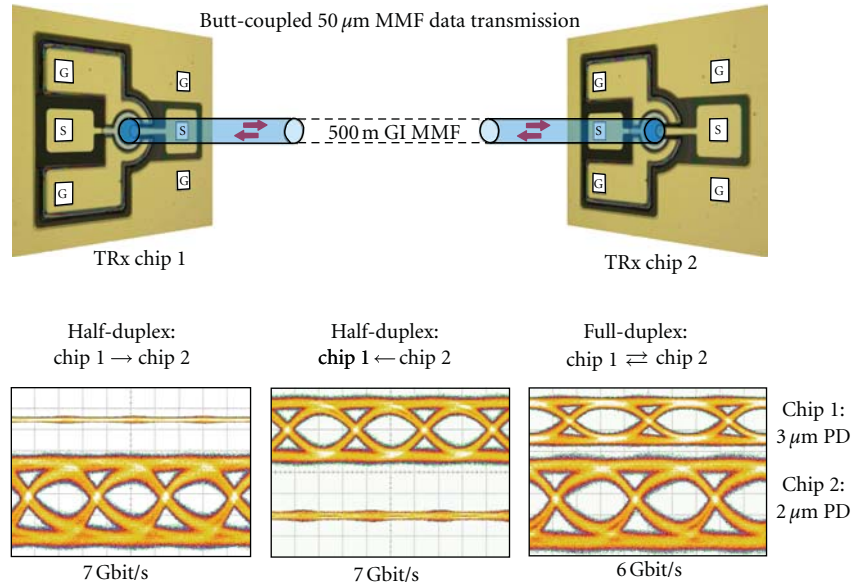


FIGURE 7: Optical eye diagrams (from [28]) for error-free half-duplex  $2^{15} - 1$  word length non-return-to-zero (NRZ) pseudorandom bit sequence (PRBS) data transmission at 7 Gbit/s (bottom left and center), as well as 6 Gbit/s error-free full-duplex operation (bottom right), all over 500 m graded-index (GI) MMF, as indicated in the schematic setup (top).

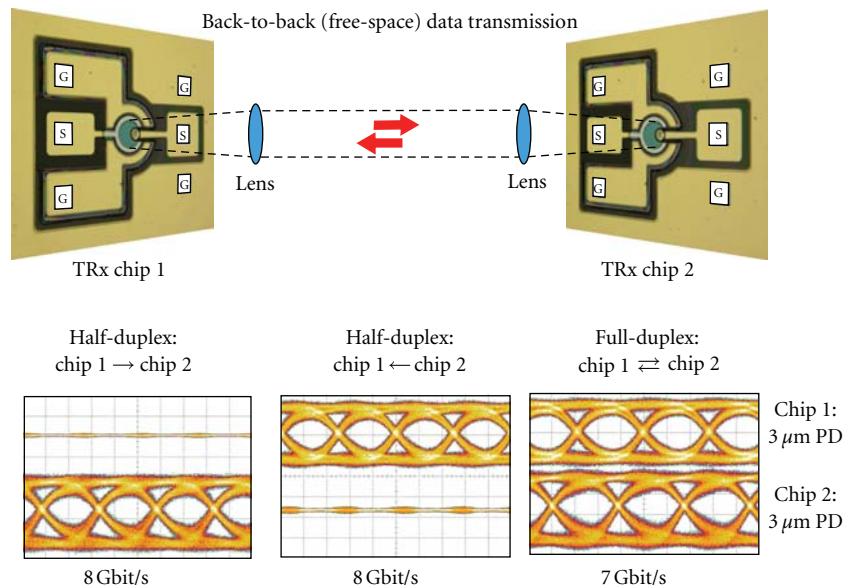


FIGURE 8: Optical eye diagrams (bottom) for back-to-back (top) error-free half-duplex  $2^{15} - 1$  word length NRZ PRBS data transmission at 8 Gbit/s (bottom left and center), as well as 7 Gbit/s error-free full-duplex operation (bottom right).

Their contributions are still sufficiently smaller than the trace widths of the operating channel. Thus, quasi error-free data transmission in full-duplex mode could be achieved at 6 Gbit/s, as shown in Figure 7 (bottom right). The slightly smaller data rate can be clearly attributed to the higher noise level inherently present in the setup for full-duplex mode operation.

In the present experiment, disturbances of the VCSELs owing to injected light from the opposite laser could not

be observed since the emission wavelengths were slightly different. In a previous experiment with VCSEL-MSM chips, we tried to enforce such a potentially critical operation condition by matching the VCSELs through thermal tuning. Nevertheless, no adverse effects have been found [21]. With the result from Figure 7, the full-duplex data rate has been increased by a factor of six compared to [9] and is to our knowledge the highest reported full-duplex throughput for single-fiber optical links with monolithic transceivers so far.

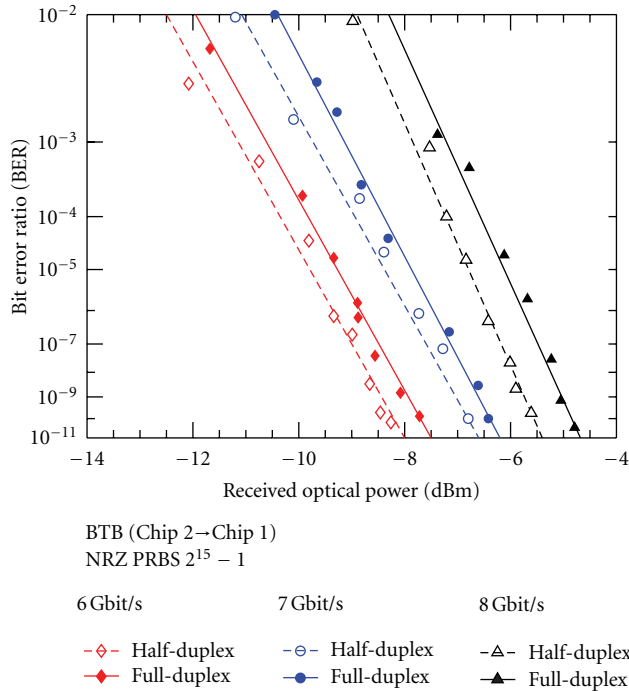


FIGURE 9: BER characteristics for back-to-back half- and full-duplex  $2^{15} - 1$  word length NRZ PRBS data transmission.

5.2. *Back-to-Back.* Additional data transmission experiments were performed in back-to-back mode in order to avoid dispersion and optical crosstalk effects of the glass fiber and thus to demonstrate the maximum achievable data rate of the transceivers. Here,  $3\ \mu\text{m}$  thick PIN PDs were used in both TRx chips. As can be seen in Figure 8 (bottom left and center), quasi error-free data transmission in half-duplex mode is well possible up to 8 Gbit/s. Owing to lower optical crosstalk contributions in BTB mode, error-free full-duplex operation is even possible up to 7 Gbit/s. In such free-space communication, there is no limit of the maximum data rate by the bandwidth-distance product of the fiber as was the case in the previous subsection.

The back-to-back operation mode also allows the insertion of optical elements into the transmission channel. In order to perform bit error measurements, a variable optical attenuator was used to adjust the optical output power of the VCSELs. In Figure 9, bit error ratios (BERs) are shown for different data rates in both, half- and full-duplex mode. For simplicity, only one transmission direction (here from chip 2 to 1) is presented. On average, there is 0.5 dB power penalty for full-duplex compared to half-duplex transmission at the same data rate. At a relatively high optical power of approximately  $-4.5\ \text{dBm}$ , even 8 Gbit/s could be transmitted quasi error-free simultaneously in both directions.

## 6. Conclusion

In summary, we have presented the past and current achievements on the fabrication and properties of monolithically integrated 850 nm wavelength transceiver chips for

bidirectional data transmission over a single butt-coupled multimode fiber. The two kinds of chips consist of a VCSEL and either an MSM- or a PIN-type photodetector. Using MSM photodiodes for signal detection with  $100\ \mu\text{m}$  diameter large-core MMFs, data transmission of 1 Gbit/s in half- and full-duplex mode was possible. Maximum values of up to 5 Gbit/s were shown in back-to-back mode.

The VCSEL-PIN transceiver chips were miniaturized in order to match with standard MMFs of  $50\ \mu\text{m}$  core diameter. The main challenge in chip processing was the sophisticated combination of selective dry- and wet-etching techniques for mesa formation. PIN PDs with maximum bandwidths of 4.5 to 6 GHz and VCSELs with 11.5 GHz can handle data rates of up to 8 Gbit/s in BTB half- and full-duplex data transmission. Over a 500 m long butt-coupled standard MMF, 7 Gbit/s in half-duplex and 6 Gbit/s in full-duplex mode could be demonstrated. With optimized TRx chips, even further improvements reaching to around 10 Gbit/s are realistic.

## Acknowledgments

The authors would like to thank R. Rösch, R. Blood, A. Bergmann, A. Hein, and F. Demaria for their support with chip processing. They also thank W. Schwarz for his technical assistance with device measurements and M. Stach and M. T. Haidar for the work on VCSEL-MSM chips and previous-generation VCSEL-PIN PD chips, respectively. Ulm University gratefully acknowledges partial funding of this work by the German Research Foundation (DFG).

## References

- [1] R. Michalzik, Ed., *VCSELs—Fundamentals, Technology and Applications of Vertical-Cavity Surface-Emitting Lasers*, vol. 166 of *Springer Series in Optical Sciences*, Springer, Berlin, Germany, 2012.
- [2] K. D. Choquette, R. P. Schneider Jr., K. L. Lear, and K. M. Geib, “Monolithic integration of photodetector with vertical cavity surface emitting laser,” *Electronics Letters*, vol. 27, no. 18, pp. 1630–1632, 1991.
- [3] A. Pruijboom, M. Schemmann, J. Hellmig, J. Schutte, H. Moench, and J. Pankert, “VCSEL-based miniature laser-Doppler interferometer,” in *Vertical-Cavity Surface-Emitting Lasers XII*, C. Lei and J. K. Guenter, Eds., vol. 6908 of *Proceedings of SPIE*, pp. 1–7, San Jose, Calif, USA, January 2008.
- [4] E. Thrush, O. Levi, W. Ha et al., “Integrated semiconductor vertical-cavity surface-emitting lasers and PIN photodetectors for biomedical fluorescence sensing,” *IEEE Journal of Quantum Electronics*, vol. 40, no. 5, pp. 491–498, 2004.
- [5] J. D. Ingham, R. V. Penty, and I. H. White, “Bidirectional multimode-fiber communication links using dual-purpose vertical-cavity devices,” *Journal of Lightwave Technology*, vol. 24, no. 3, pp. 1283–1294, 2006.
- [6] O. Sjölund, D. A. Loudereback, E. R. Hegblom, J. Ko, and L. A. Coldren, “Individually optimized bottom-emitting vertical-cavity lasers and bottom-illuminated resonant photodetectors sharing the same epitaxial structure,” *Journal of Optics A: Pure and Applied Optics*, vol. 1, no. 2, pp. 317–319, 1999.

- [7] P. Kazlas, J. Wasserbauer, J. Scott, D. Paananen, S. Swirhun, and D. Lewis, "Monolithic vertical-cavity laser/p-i-n photodiode transceiver array for optical interconnects," *IEEE Photonics Technology Letters*, vol. 10, no. 11, pp. 1530–1532, 1998.
- [8] A. M. Kasten, A. V. Giannopoulos, C. Long, C. Chen, and K. D. Choquette, "Fabrication and characterization of individually addressable vertical-cavity surface-emitting laser arrays and integrated VCSEL/PIN detector arrays," in *Vertical Cavity Surface Emitting Lasers XI*, K. D. Choquette and J. K. Guenter, Eds., vol. 6484 of *Proceedings of SPIE*, pp. 1–6, San Jose, Calif, USA, 2007.
- [9] M. Stach, F. Rinaldi, D. Wahl, D. Rimpf, S. Lorch, and R. Michalzik, "1 Gbit/s full-duplex bidirectional optical data transmission over 500 m of 50  $\mu\text{m}$ -core graded-index multimode fiber with novel monolithically integrated transceiver chips," in *Proceedings of the 33rd European Conference on Optical Communication (ECOC '07)*, vol. 5, pp. 127–128, Berlin, Germany, 2007.
- [10] M. Stach, L. Stöferle, F. Rinaldi, and R. Michalzik, "Monolithically integrated optical transceiver chips at 850 nm wavelength consisting of VCSELs and MSM photodiodes," in *Proceedings of the Lasers and Electro-Optics Europe, (CLEO/Europe '05)*, CI2-4-THU, p. 1, Munich, Germany, June 2005.
- [11] M. Stach, L. Stöferle, F. Rinaldi, and R. Michalzik, "3 Gbit/s data transmission with monolithically integrated optical transceiver chips for very short reach applications," in *Proceedings of the 31st European Conference on Optical Communication (ECOC '05)*, vol. 3, pp. 529–530, Glasgow, UK, 2005.
- [12] M. Stach, M. Chandran, and F. Rinaldi, "Monolithically integrated transceiver chips for bidirectional optical interconnection," in *Micro-Optics, VCSELs, and Photonic Interconnects II: Fabrication, Packaging, and Integration*, vol. 6185 of *Proceedings of SPIE*, Strasbourg, France, 2006.
- [13] M. Stach, F. Rinaldi, M. Chandran, S. Lorch, and R. Michalzik, "Monolithically integrated GaAs-based transceiver chips for bidirectional optical data transmission," *Electronics Letters*, vol. 42, no. 12, pp. 716–718, 2006.
- [14] M. Stach, F. Rinaldi, M. Chandran, S. Lorch, and R. Michalzik, "Bidirectional optical interconnection at Gb/s data rates with monolithically integrated VCSEL-MSM transceiver chips," *IEEE Photonics Technology Letters*, vol. 18, no. 22, pp. 2386–2388, 2006.
- [15] M. Stach, F. Rinaldi, A. Gadallah et al., "1 Gbit/s bidirectional data transmission over 100 m graded-index glass optical fiber with monolithically integrated transceiver chips," in *Proceedings of the European Conference on Optical Communication (ECOC '06)*, vol. 3, pp. 493–494, Cannes, France, 2006.
- [16] R. Michalzik, M. Stach, F. Rinaldi, and S. Lorch, "Monolithic integration of VCSELs and MSM photodiodes for bidirectional multimode fiber communications," in *Vertical-Cavity Surface-Emitting Lasers XI*, K. D. Choquette and J. K. Guenter, Eds., vol. 6484 of *Proceedings of SPIE*, pp. 1–10, San Jose, Calif, USA, 2007.
- [17] M. Stach, F. Rinaldi, J. Scharpf, S. Lorch, and R. Michalzik, "1 Gbit/s bidirectional optical data transmission over 50m semi-GI PCS fiber with monolithically integrated transceiver chips," in *Proceedings of the EOS Conference on Trends in Optoelectronics, Sub-conference on Information and Communication*, pp. 61–62, Munich, Germany, 2007.
- [18] M. Stach, F. Rinaldi, D. Wahl, D. Rimpf, S. Lorch, and R. Michalzik, "Monolithically integrated miniaturized transceiver chips for bidirectional graded-index fiber systems," in *Proceedings of the 14th ITG Symposium on Communication Cable Networks*, vol. 204 of *ITG-Fachbericht Kommunikationskabelnetze*, pp. 115–119, Köln, Germany, 2007.
- [19] J. B. D. Soole and H. Schumacher, "InGaAs metal-semiconductor-metal photodetectors for long wavelength optical communications," *IEEE Journal of Quantum Electronics*, vol. 27, no. 3, pp. 737–752, 1991.
- [20] A. Kern, D. Wahl, S. Paul et al., "Up to 9 Gbit/s data transmission with monolithically integrated VCSELs and PIN photodiodes," in *Proceedings of the Conference on Lasers and Electro-Optics Europe, (CLEO/Europe '11)*, CB1.4, p. 1, Munich, Germany, May 2011.
- [21] R. Michalzik, A. Kern, M. Stach, F. Rinaldi, and D. Wahl, "True bidirectional optical interconnects over multimode fiber," in *Optoelectronic Interconnects and Component Integration IX*, A. L. Glebov and R. T. Chen, Eds., vol. 7607 of *Proceedings of SPIE*, pp. 1–17, San Francisco, Calif, USA, 2010.
- [22] A. Kern, D. Wahl, and M. T. Haidar, "Monolithic integration of VCSELs and PIN photodiodes for bidirectional data communication over standard multimode fibers," in *Semiconductor Lasers and Laser Dynamics IV*, K. P. Panayotov, M. Sciamanna, A. A. Valle, and R. Michalzik, Eds., vol. 7720 of *Proceedings of SPIE*, pp. 1–9, Brussels, Belgium, 2010.
- [23] D. Wahl, A. Kern, M. Stach, F. Rinaldi, R. Rösch, and R. Michalzik, "VCSELs with monolithically integrated photodiodes for single-fiber bidirectional data transmission in the Gbit/s range," *Journal of Crystal Growth*, vol. 323, no. 1, pp. 438–441, 2011.
- [24] A. Kern, S. Paul, W. Schwarz, D. Wahl, R. Blood, and R. Michalzik, "Bidirectional multimode fiber interconnection at Gb/s data rates with monolithically integrated VCSEL-PIN transceiver chips," *IEEE Photonics Technology Letters*, vol. 23, no. 15, pp. 1058–1060, 2011.
- [25] S. Salimian and C. B. Cooper III, "Selective dry etching of GaAs over AlGaAs in  $\text{SF}_6/\text{SiCl}_4$  mixtures," *Journal of Vacuum Science and Technology B*, vol. 6, pp. 1641–1644, 1988.
- [26] J.-H. Kim, D. H. Lim, and G. M. Yang, "Selective etching of AlGaAs/GaAs structures using the solutions of citric acid/ $\text{H}_2\text{O}_2$  and de-ionized  $\text{H}_2\text{O}$ /buffered oxide etch," *Journal of Vacuum Science and Technology B: Microelectronics and Nanometer Structures*, vol. 16, no. 2, pp. 558–560, 1998.
- [27] K. D. Choquette, R. P. Schneider, K. L. Lear, and K. M. Geib, "Low threshold voltage vertical-cavity lasers fabricated by selective oxidation," *Electronics Letters*, vol. 30, no. 24, pp. 2043–2044, 1994.
- [28] A. Kern, S. Paul, and D. Wahl, "6 Gbit/s full-duplex multimode fiber link with monolithic VCSEL-PIN transceiver chips," in *Proceedings of the 37th European Conference on Optical Communication, (ECOC '11)*, p. 3, Geneva, Switzerland, 2011.
- [29] A. Kern, D. Wahl, S. Paul et al., "7 Gbit/s data transmission over 500 m multimode fiber with monolithically integrated bidirectional VCSEL-based transceiver chips," in *Proceedings of the Conference on Lasers and Electro-Optics, (CLEO '11)*, Baltimore, MD, USA, May 2011.

## Review Article

# Advances in Red VCSEL Technology

**Klein Johnson, Mary Hibbs-Brenner, William Hogan, and Matthew Dummer**

*Vixar, 2950 Xenium Lane, Suite 104, Plymouth, MN 55441, USA*

Correspondence should be addressed to Mary Hibbs-Brenner, [mhibbsbrenner@vixarinc.com](mailto:mhibbsbrenner@vixarinc.com)

Received 6 July 2011; Revised 4 November 2011; Accepted 8 November 2011

Academic Editor: Rainer Michalzik

Copyright © 2012 Klein Johnson et al. This is an open access article distributed under the Creative Commons Attribution License, which permits unrestricted use, distribution, and reproduction in any medium, provided the original work is properly cited.

Red VCSELs offer the benefits of improved performance and lower power consumption for medical and industrial sensing, faster printing and scanning, and lower cost, higher speed interconnects based upon plastic optical fiber (POF). However, materials challenges make it more difficult to achieve the desired performance than at the well-developed wavelength of 850 nm. This paper will describe the state of the art of red VCSEL performance and the results of development efforts to achieve improved output power and a broader temperature range of operation. It will also provide examples of the applications of red VCSELs and the benefits they offer. In addition, the packaging flexibility offered by VCSELs, and some examples of non-Hermetic package demonstrations will be discussed. Some of the red VCSEL performance demonstrations include output power of 14 mW CW at room temperature, a record maximum temperature of 115°C for CW operation at an emission wavelength of 689 nm, time to 1% failure at room temperature of approximately 200,000 hours, lifetime in a 50°C, 85% humidity environment in excess of 3500 hours, digital data rate of 3 Gbps, and peak pulsed array power of greater than 100 mW.

## 1. Introduction

Multimode 850 nm VCSELs based upon the AlGaAs materials system have been the standard optical source for glass fiber optic-based data communication links since the mid-1990s. Although the first demonstration of red VCSELs followed fairly quickly after the demonstration of the industry standard “all-semiconductor” 850 nm VCSEL, the commercialization of red VCSEL technology has proceeded much more slowly due to the materials limitations that have made the development more challenging.

The AlGaAs materials system which is used for 850 nm VCSELs provides good lattice matching over the full range of compositions, a reasonably good refractive index contrast between the high index (AlGaAs with approximately 15–20% mole fraction AlAs) and low index (AlAs) materials used for the mirrors, and a high (approximately 0.35 eV) conduction band offset between the GaAs quantum wells and the AlGaAs compositions normally used as quantum well barriers. However, the 650–700 nm emission wavelength range requires use of GaInP quantum wells with AlGaInP barrier layers, with the compositions limited to those which are nearly lattice matched to a GaAs substrate. The AlGaAs materials system is usually used for the mirrors. Several

limitations for these shorter wavelength VCSELs exist: (1) the available conduction band offset is smaller and ranges from approximately 0.17 eV at 650 nm to 0.23 eV at 700 nm [1]. Therefore, thermal carrier overflow limits the maximum temperature of operation and peak power, limitations that become more apparent at shorter wavelengths. (2) The requirement that the mirrors be nonabsorbing limits the mirror compositions available to AlGaAs materials with AlAs mole fraction greater than 0.4–0.5. This reduces the available range of refractive index, requiring more mirror periods to achieve the same reflectivity. Furthermore, the 50% AlGaAs composition has a higher thermal and electrical resistivity than compositions closer to the binary AlAs or GaAs. This results in a higher conversion of input power to heat, and more difficulty in removing heat from the device, resulting in higher junction temperatures. The development of red VCSELs over the past nearly two decades has focused on ameliorating these issues. Since the early 1990s when the initial red VCSEL research was done, several groups have reported performance improvements in peak output power, temperature range of operation, wavelength range, modulation speed, and reliability. Significant strides in developing red VCSELs have been made, and devices are now being implemented in a number of applications. This

paper will first review the progress that has been made, will then discuss recent developments, and finally discuss some applications of the technology.

## 2. Background

The earliest reports of red VCSEL demonstrations were in 1993 from Sandia National Labs and Chiao Tung University in Taiwan [2, 3]. Some of this work was initially based upon the use of InGaAlP materials for both the quantum well active region and the mirrors, but fairly quickly most researchers adopted a structure that retained the InGaAlP-based quantum well active region, but used AlGaAs materials in the mirrors, all on a GaAs substrate, thus simplifying the challenge of growing lattice-matched structures. The initial devices were limited in output power and temperature range, as might be expected from the earliest demonstrations of a new technology.

Due to the wavelength dependence of the conduction band offset available in the AlGaInP materials system, the peak output power achieved and the temperature range of operation is a strong function of wavelength. A fairly early paper [4] reported 8.2 mW of maximum multimode output power, and 1.9 mW of single-mode output power at 687 nm at room temperature. This device was fabricated using a proton implant process. Several improvements to the red VCSEL structure, including the use of carbon doping in the mirror, graded interfaces in the mirror, separate confinement structure in the active region, an oxide aperture, and the removal of the GaAs contact layer from the aperture resulted in the demonstration of room temperature peak output power of 4 mW at 650 nm and 10 mW at 670 nm [5, 6]. Johnson and Hibbs-Brenner reported an output power of 11.5 mW at 673 nm at room temperature [7].

The temperature range of operation is also a strong function of wavelength. The first demonstrations of red VCSELs in 1993 required pulsed operation to lase [2, 3]. However, by 1994 CW operation to 45°C had been achieved at 670 nm [8]. Room temperature operation for wavelengths as short as 645 nm was demonstrated in 1995, although the output power was very low (0.04 mW) [9]. Calvert et al. [10] reported the continuous wave operation of 670 nm single-mode devices to a heat sink temperature of 80°C. Sale et al. [11] also demonstrated CW lasing at 666 nm over the temperature range from -180°C to +80°C. Knigge et al. [5] extended the temperature range by demonstrating 650 nm VCSELs achieving output powers of 4.3 mW at room temperature, with lasing to 65°C, and 10 mW at 670 nm (room temperature) with lasing to 86°C. The temperature range of operation can further be extended by pulsing the devices, with a temperature up to 160°C for a 670 nm device and up to 172°C for a 660 nm VCSEL [12, 13].

Efforts have been made to extend the feasible wavelength range of red VCSELs, both to shorter wavelengths (<650 nm) and to longer wavelengths (>700 nm). The first red VCSELs reported below 699 nm actually included wavelengths as short as 639 nm, although they only operated under pulsed conditions [2]. Choquette et al. [9] were able to achieve

0.25 mW CW room temperature emission at 652 nm and 0.04 mW CW room temperature operation at 645 nm. Knigge et al. [14] were able to achieve pulsed operation down to 629 nm, although no power was reported, and 2.1 mW of room temperature CW power at 647 nm. Several groups have reported efforts to extend the VCSEL wavelength into the range from 700 to 740 nm [15–20]. All of these efforts above 700 nm have been based upon the AlGaAs materials system for both the mirrors and the active regions. The performance has been limited in output power and maximum temperature of operation. In some cases [18–20] the device only operated in pulsed mode at room temperature, while in other results [15–17] the devices did operate CW at room temperature, but the output power was limited to less than 1 mW.

Reliability data has been fairly limited. An early report on aging and failure analysis performed the testing under fairly unrealistic conditions, that is, current drive that was 3x past the rollover point, resulting in a junction temperature of around 250°C [21]. This is likely to result in a degradation mechanism that is not representative of normal use conditions. Low-temperature testing was performed on 655 nm VCSELs [22], demonstrating little degradation over 1000 hours at 20°C for a 7 μm diameter device operated at 2.5 mA, but a 3 dB degradation in output power after 500 hours at 40°C. A second report indicated widely varying results at 665 nm, with one wafer remaining fairly stable during life testing at 6 mA and 100°C for 1000 hours, while a second wafer with a different design (the design differences were not described), where it is noted that the resistance is higher and required drive voltage in the range of 5-6 V, failed after 300 hours at the same condition [23]. The device diameter was not reported in this case. The most complete report was published in 2008 [24]. Although the device diameter was not specified, 128 devices were placed on test at 8 different acceleration conditions, ranging from 40 to 85°C, and current drive of 3, 4, or 5 mA. The devices remained on test for close to 8000 hours. From the multiple acceleration conditions, the authors estimated an empirical failure acceleration model of an Arrhenius dependence on temperature with an activation energy of 0.6 eV, and a squared dependence upon current. From this data they estimated time to 1% failure of several hundred thousand hours for use conditions of 40°C and 1.5 mA.

Since one of the main applications for red VCSELs is for data communication over plastic optical fiber, the achievable modulation rate is a key parameter of interest. An early measurement [25] showed a small signal 3 dB bandwidth of around 2.5 GHz and also demonstrated low error rate large signal modulation at 1 Gbps. A subsequent study with better performing VCSELs measured a 3 dB bandwidth of 11 GHz [26]. Duggan et al. [24] demonstrated a 3 dB bandwidth in excess of 3 GHz at bias currents of less than 10 mA. Large signal modulation at 1.25 Gbps was demonstrated over temperatures ranging from -20 to +60°C. Transceiver modules and connector systems operating at 1.25 Gbps have been developed for plastic optical fiber-based communication links [27, 28].

Novel approaches for dealing with the limited electrical and thermal conductivity have included the incorporation of transparent indium tin oxide (ITO) contacts that extend across the entire VCSEL aperture [29] and the incorporation of plated copper interconnects around the VCSEL mesa [30]. While the latter approach reduced the thermal resistance, it was postulated that the stress created by the approach prevented improvements in output power and temperature range.

Mode control, that is, for achieving single transverse mode VCSELs, is also a challenge and is typically achieved by reducing the aperture size. Kasten et al. used a photonic crystal approach to achieve single-mode performance [31].

### 3. VCSEL Development Approach

The goals of the work reported here were to increase the output power, temperature range of operation, achievable wavelength range, and reliability of red VCSELs. Specifically, the targets were a minimum of 1 mW single-mode power from 0–60°C, 10 mW multimode power up to 40°C, and at least 1 mW of useable multimode power at 80°C. Another goal was to extend performance to 720 nm with >1 mW of useable output power.

The red VCSEL structure is illustrated schematically in Figure 1. The structure is grown on off-axis 4" n+-GaAs substrates. Mirrors are AlGaAs based with graded interfaces between the high and low index layers. The results in this paper come from several different wafers, but in all cases the bottom mirror consisted of between 50 and 56 periods, and the number of top mirror periods ranged from 28 to 36. The active region consists of 3–5 compressively strained InGaP quantum wells with unstrained or tensile strained AlGaInP barriers and a graded (50–70%) AlGaInP separate confinement heterostructure (SCH). The p-spacer is doped with Zn. A highly doped contact layer is grown at the top surface to facilitate formation of ohmic contacts.

Current and index confinement is provided by an oxide confinement layer located 2 periods above the quantum well active region. The devices are top-emitting with a ring contact patterned around the current aperture on the front side of the device. The substrate was thinned to 200  $\mu\text{m}$  before the deposition of a broad area gold contact on the substrate side of the wafer. A variety of aperture sizes were fabricated to evaluate performance as a function of aperture size. Some die consisted of an array of apertures connected to a common anode in order to increase the total power output per die.

Wafers were probed on an automated probe station with wafer temperature control. 100% probe testing of the light output and voltage versus drive current ( $L-I-V$ ) and wavelength was performed.  $L-I-V$  measurements were made over a range of temperatures on a sample basis. Devices were mounted on a TO-46 header for measurement of beam profiles, and for measurement of pulsed characteristics.

Reliability measurements under pulsed conditions were carried out on devices in hermetic TO-46 packages. Resistance to humidity was evaluated at 50°C, 85% humidity

on devices packaged in TO-46 headers but with the glass window removed from the lid. In both cases devices are biased during life testing at the accelerated environmental conditions. However, the devices are removed from the oven at each test point and tested at room temperature and room humidity, which was typically 20–25°C and 40% relative humidity.

## 4. Results

**4.1. Temperature Performance.** One of the most challenging aspects of designing red VCSELs has been achieving useable output power over the temperature ranges required by the applications of interest. Figure 2 illustrates the temperature performance of two red VCSELs: a single-mode design, emitting at 689 nm and a multimode design emitting at 693 nm. The single mode device (Figure 2(a)) lases up to 115°C, with 1 mW of output power achievable at 75°C, and 0.5 mW at 95°C. (The vertical scale is expanded to allow a closer look at the  $L-I-V$  characteristics at the highest temperature.) We believe that this is the highest temperature operation achieved in red VCSELs under CW conditions. Generally, the temperature range of operation of larger diameter devices is more limited. Figure 2(b) illustrates the temperature performance of a multimode 693 nm VCSEL. This device was tested at increments of 20°C, and output 1.5 mW peak power at 80°C, but ceased lasing between 80°C and 100°C. The improved temperature performance is the result of attention to a number of details, such as mirror design for low thermal and electrical resistance, engineering of the active region, and the proper choice of the gain peak-Fabry-Perot resonance offset. While the longer wavelength of approximately 690 nm also makes the higher temperature operation easier to achieve due to the larger band discontinuities, the result is still a record temperature even when compared to other results at the same wavelength.

**4.2. Single-Mode Performance.** Figure 3 further illustrates the performance of single-mode devices at 25°C. Figure 3(a) overlays the  $L-I-V$  curves of an array of single-mode VCSELs. Figure 3(b) shows the beam profile of one of the devices in the array. Profiles in the  $x$ - and  $y$ -direction are taken at three different currents, that is, 4, 5, and 6 mA and are overlaid in the figure of intensity versus angle. It is difficult to distinguish more than one plot since the three plots overlap so closely. Single spatial mode performance is maintained up to the current corresponding to the peak output power.

**4.3. Wafer Uniformity: Wavelength and Device Performance.** One of the key questions of interest in the production of devices is the uniformity across a wafer. The wavelength of a VCSEL is approximately proportional to thickness of the layers, so a 1% variation of thickness can result in approximately a 7 nm variation in wavelength. In addition, the oxidation diameter can also vary across a wafer due to small differences in layer thickness, doping, or composition. Both of these effects can impact performance of a VCSEL. For instance, the temperature characteristics of a VCSEL depend

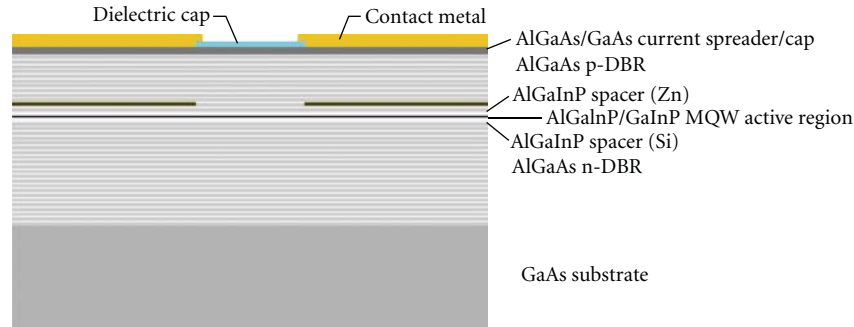


FIGURE 1: Schematic of VCSEL structure (From Proceedings of the SPIE, Vol. 7952, paper 795208).

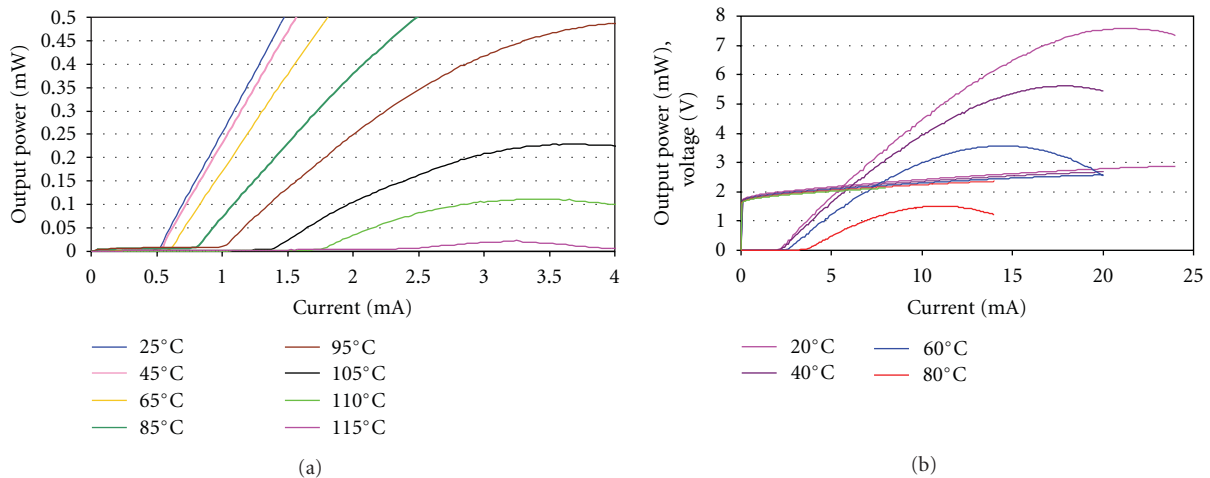


FIGURE 2: Light output and voltage versus current ( $L$ - $I$ - $V$ ) at a range of temperatures for (a) a 689 nm single-mode device, and (b) a 693 nm multimode device (from Proceedings of the SPIE, Vol. 7952, paper 795208).

upon the offset between the gain peak and the Fabry-Perot resonance. Since the gain peak wavelength is less sensitive to thickness and therefore nearly constant across the wafer, while the Fabry-Perot resonance may have a range of 5–10 nm, this offset varies across the wafer. The ability to do automated wafer scale testing allows us to gather statistics on uniformity.

Figure 4 shows the results of probing approximately 60,000 VCSELs on a 4" wafer. A histogram of the wavelength distribution of the devices is shown in Figure 4(a). While the distribution ranges from 675 nm to 709 nm, the vast majority of the devices on the wafer lie in the range from 681 to 692 nm. Figure 4(b) illustrates the uniformity of threshold current as a function of emission wavelength for four different laser aperture sizes. This data (and the data in Figure 4(c)) was taken at 40°C. The shaded region in the figure corresponds to the wavelength range constituting the majority of the devices on the wafer. Threshold currents are less than 0.5 mA for the smallest devices and from 1.5 to 2.5 mA for the 12  $\mu\text{m}$  apertures at 40°C. While the largest diameter devices appear to be quite a bit less uniform than the smallest diameter, on a percentage basis the threshold current range of the 12  $\mu\text{m}$  device is similar to that of the 7 and 10  $\mu\text{m}$  devices.

As one might expect, the threshold current is U-shaped and rises at the longer wavelengths, due to a larger offset between the gain peak and the Fabry-Perot cavity, but devices are still lasing at 709 nm, where the offset is approximately 40 nm. Peak output power at 40°C versus wavelength for several aperture sizes is shown in Figure 4(c). Within the wavelength region included in the shaded region, which includes the majority of the VCSELs on the wafer, the peak output power is quite uniform.

**4.4. Maximum Achievable Output Power.** Red VCSELs have typically been limited in the maximum output power that can be achieved in part because the larger aperture devices are more sensitive to temperature. Improved design has allowed larger devices to be built. Improvements include the use of quantum well barrier layers with tensile strain to improve the conduction band offset, tailoring of the doping profile in the mirrors to reduce series resistance, and the use of a slightly thicker high aluminum-containing mirror layers, and thinner low aluminum-containing mirror layers (while keeping the sum of the two equal to  $\lambda/2$ ) in each mirror period to improve thermal conductivity. Figure 5 illustrates the 25°C output power achievable from two types of devices. Figure 5(a) shows the  $L$ - $I$ - $V$  from a single aperture

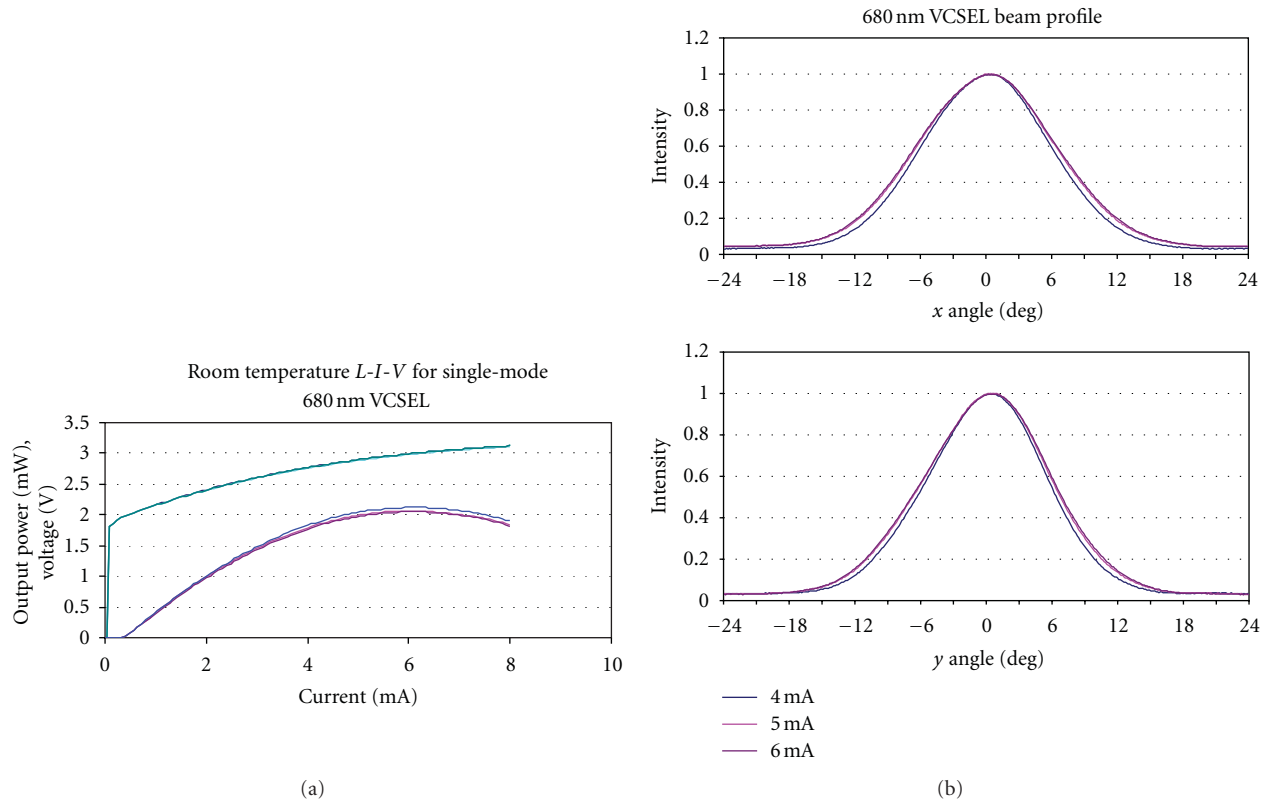


FIGURE 3: Performance of single-mode 680 nm VCSELs at 25°C. (a) Overlaid  $L$ - $I$ - $V$  curves from a  $1 \times 3$  array. (b) Beam intensity (normalized, arbitrary units) versus angle in the  $x$ - and  $y$ -direction at three current levels: 4, 5, and 6 mA (from Proceedings of the SPIE, Vol. 7952, paper 795208).

device with a wavelength of 685 nm which emits a peak output power of 14 mW. If beam size or profile is not an issue, an alternative way of achieving high output power is to use multiple apertures with a common anode contact. Figure 5(b) illustrates that nearly 45 mW of output power can be generated from a  $4 \times 4$  array of apertures emitting at 680 nm within a  $200 \mu\text{m} \times 200 \mu\text{m}$  area.

**4.5. Extended Wavelength Performance.** We have fabricated devices with wavelengths in the range from 700 to 720 nm, but unlike previous reports [15–20] our devices are based upon GaInP/AlGaInP active regions. A large variation in wavelength across a single wafer was achieved by not rotating the wafer during growth. The gain peak wavelength was fairly constant at around 678 nm, while the Fabry-Perot resonance varied from 680 up to nearly 720 nm. The longest wavelengths, therefore, corresponded to a very large gain peak-resonance offset, as large as 40 nm. Figure 6 shows the results from two devices lasing CW at 25°C. A 716 nm device (Figure 6(a)) had a threshold current of 7 mA and a peak output power of nearly 3.5 mW, while a 719 nm device (Figure 6(b)) had a threshold current of 7 mA and a peak output power of over 2 mW. The threshold current is high due to the large gain peak-resonance offset, so it is believed that even better performance could be achieved if the devices were optimally designed for this wavelength. We therefore

believe that good VCSEL performance spanning the entire wavelength range from 650 to 850 nm can be achieved using either the AlGaAs materials system, or the AlGaInP materials for the active region.

**4.6. Pulsed Operation and Reliability.** There are some applications where lasers are typically pulsed at a low duty cycle, such as industrial sensors, or the computed radiography application described in the applications section below. Pulse widths in the range of  $1 \mu\text{sec}$  and a duty cycle less than 25% are common. It has been demonstrated at other wavelengths that the peak output power can be extended significantly due to the reduction in self-heating when pulsed. Red VCSELs are even more limited by thermal effects and hence we desired to quantify the magnitude of potential improvement that could be achieved if the devices were pulsed.

Figure 7 illustrates the performance of a multimode 680 nm VCSEL operated in pulsed mode. The relevant parameters affecting pulsed performance are pulse width, duty cycle, and ambient temperature. Since  $1 \mu\text{sec}$  is a nominal thermal time constant for a VCSEL chip, pulse widths substantially longer than this provide little benefit. We have used  $1 \mu\text{sec}$  pulse width for the evaluation, although shorter pulse widths can provide even higher peak power. Figure 7(a) illustrates the effect of the duty cycle. A 10% duty cycle can provide nearly a 4x improvement in peak power,

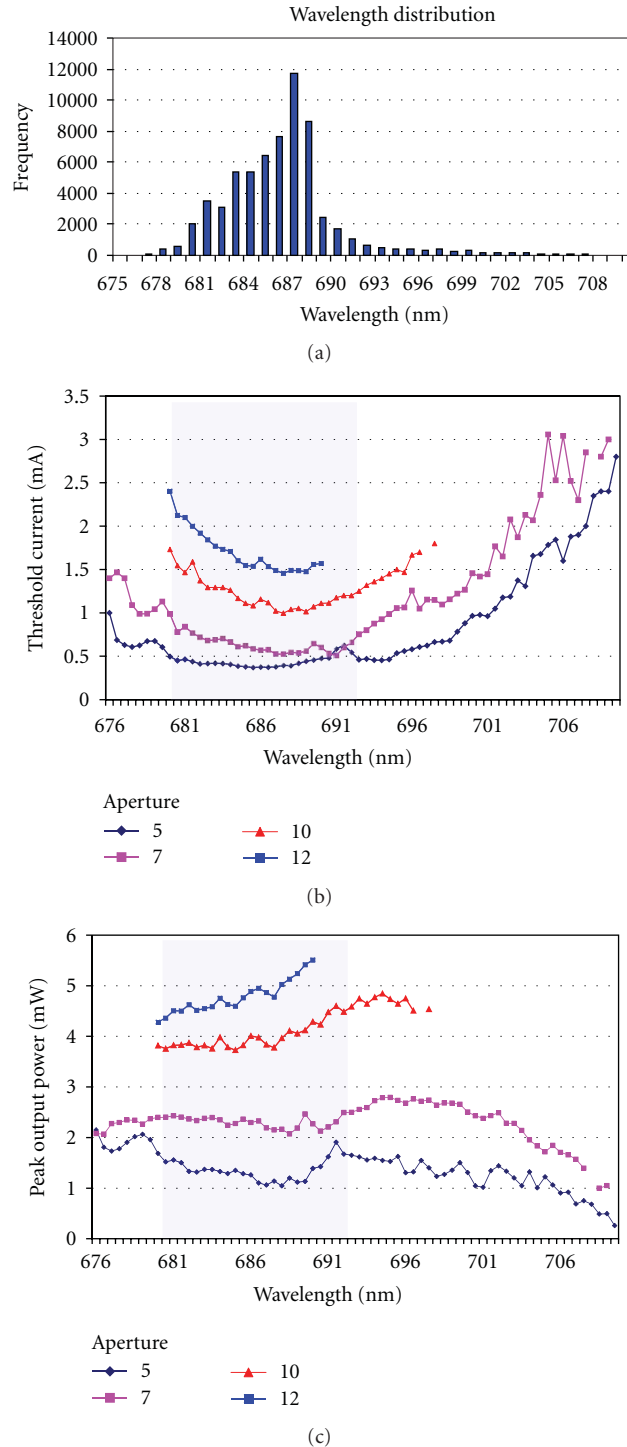


FIGURE 4: (a) Histogram showing the wavelength distribution of 60,000 VCSELs tested at 40°C on a 4" wafer. (b) Threshold current versus wavelength. (c) Peak output power versus wavelength. The shaded regions in (b) and (c) indicate the wavelength range corresponding to the vast majority of devices on the wafer (from Proceedings of the SPIE, Vol. 7952, paper 795208).

while a 50% duty cycle still provides nearly a 2x increase in peak power. Also note that the peak power achieved at a 10% duty cycle exceeds 35 mW. This is a multimode device with a single aperture. Figure 7(b) illustrates the improvement in the temperature range of operation that can be achieved when the device is pulsed at a 25% duty cycle. The peak

power of the device at 60°C reaches 15 mW, while under CW operation, the same device might only reach a peak power of 3-4 mW.

Pulsing can also increase the peak output power of the arrays described above. Figure 8 illustrates the benefits of pulsing an array 680 nm device. The figure demonstrates that

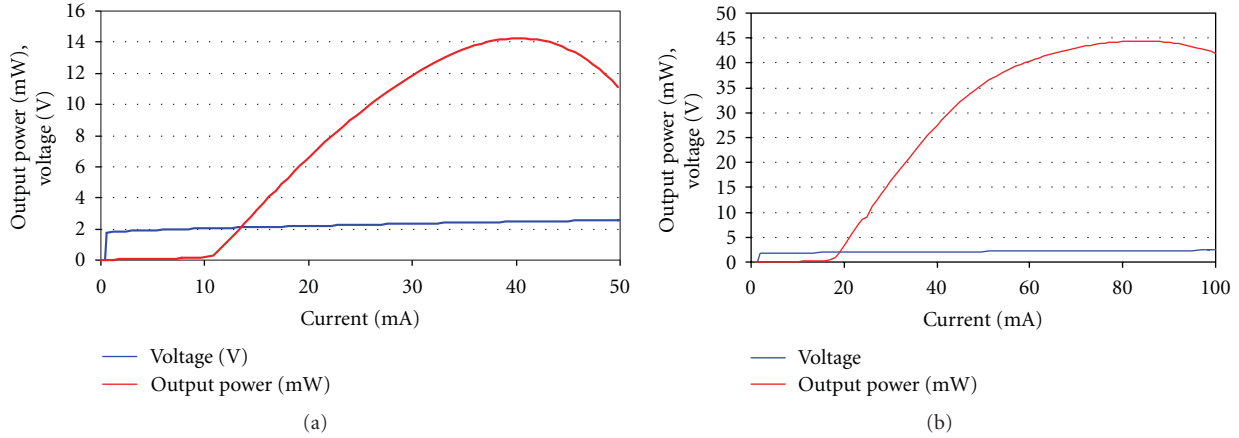


FIGURE 5: High output power devices at 25°C. (a) *L-I-V* curve from a 685 nm device with a single large aperture, demonstrating a peak output power of 14 mW. (b) *L-I-V* from a 680 nm device with multiple apertures in a  $200\ \mu\text{m} \times 200\ \mu\text{m}$  area, demonstrating a peak output power of 44 mW (from Proceedings of the SPIE, Vol. 7952, paper 795208).

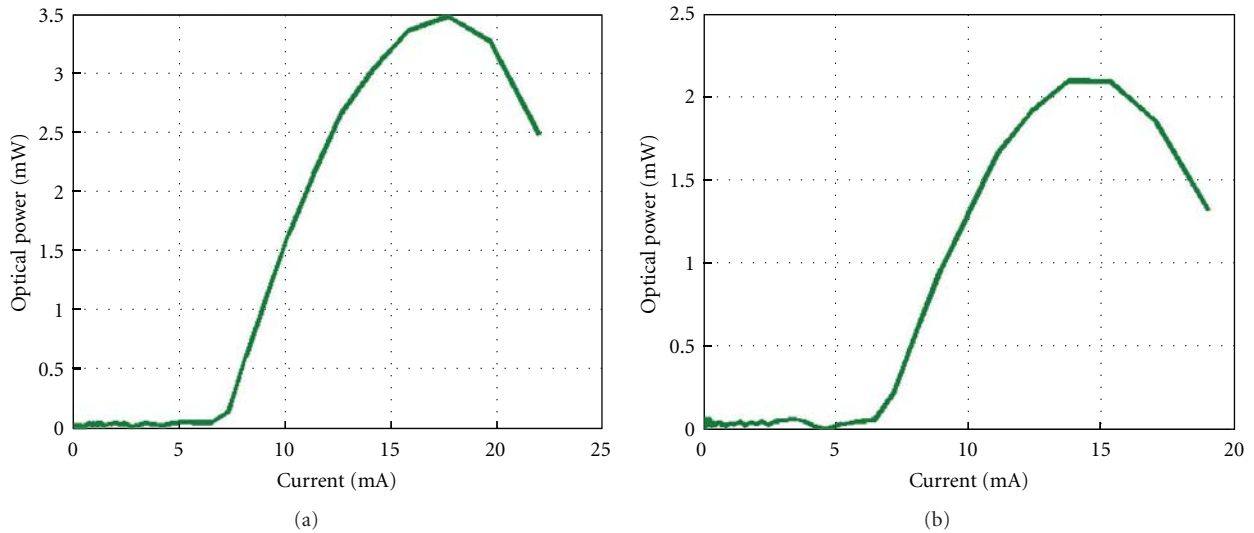


FIGURE 6: Performance at 25°C of an AlGaInP QW-based VCSEL at (a) 716 nm, and (b) at 719 nm (from Proceedings of the SPIE, Vol. 7952, paper 795208).

nearly 120 mW of peak power can be reached in a  $3 \times 3$  array on a single die, using a pulse width of  $1\ \mu\text{sec}$  and a 1% duty cycle.

In pulsed mode the device self-heating is reduced, and therefore the device rollover point (where increasing the current actually results in a reduction of output power) is extended to significantly higher drive current. However, this leads to a question: if device lifetime is reduced by higher current (or, more accurately, current density) can one operate a device in pulsed mode at these higher current ranges for useful periods of time? Furthermore, are there any transient effects, such as stress created by repeated junction temperature cycling resulting from the current cycling that might actually accelerate the degradation of the devices beyond what is normally expected from the current drive alone? For instance, the VCSEL lifetime is commonly found to be reduced proportionally to the square of the current

density. An increase of drive current from 8 mA to 30 mA might be expected to reduce the lifetime by a factor of 14 due to current density alone. Under CW conditions, the increase in junction temperature from the higher current adds to the acceleration of failure. Using the empirical model for acceleration of failure, we estimate that a 30 mA CW drive current would reduce lifetime by a factor of 500 under CW conditions.

To experimentally evaluate the effect of pulsing on reliability we developed a capability for testing the VCSELs in pulsed mode. Both single-mode and multimode devices were packaged in TO-46 headers and mounted on boards that were placed in ovens. The devices were pulsed with a pulse width of  $1\ \mu\text{sec}$ , and a duty cycle of 12.5%. Thus 8 hours of test time correspond to 1 hour of actual “on-time” The devices were periodically removed from the oven and tested CW at room temperature, and then returned to the oven

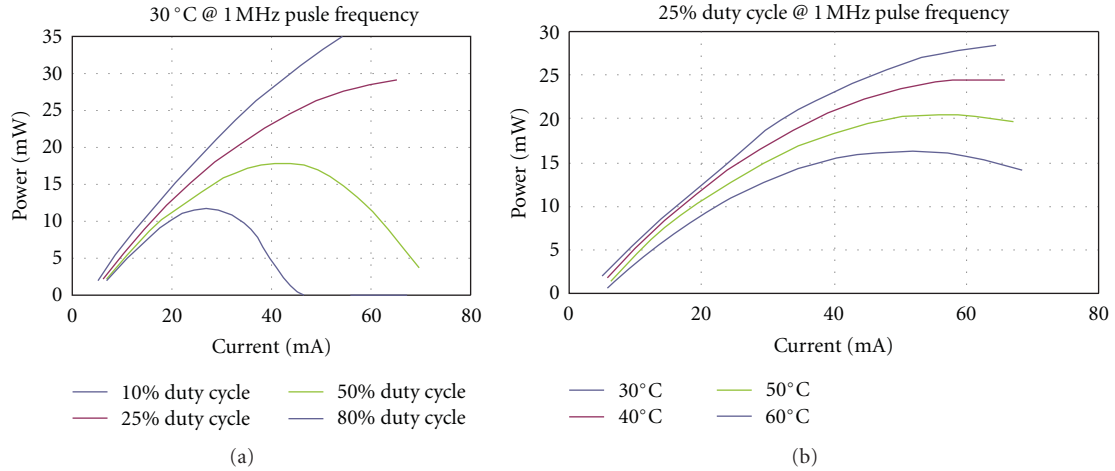


FIGURE 7: Output power versus current for multimode 680 nm VCSELs operated in pulsed mode with a  $1 \mu\text{sec}$  pulse width. (a) illustrates the effect of varying the duty cycle at  $30^\circ\text{C}$ , while (b) illustrates the improved temperature performance associated with pulsed operation (from Proceedings of the SPIE, Vol. 7952, paper 795208).

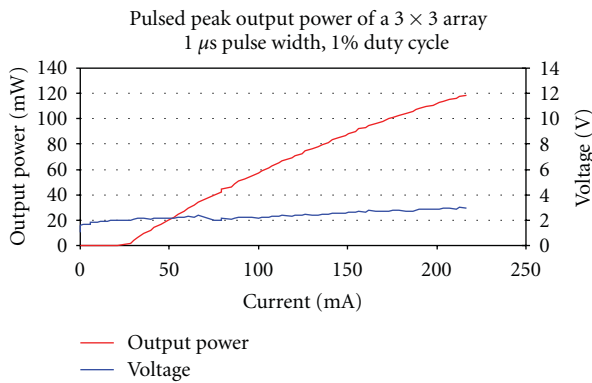


FIGURE 8: An output power of nearly 120 mW is achieved from a  $3 \times 3$  680 nm array under pulsed conditions.

for further aging under pulsed conditions. The results are illustrated in Figure 9.

The multimode devices have a CW peak output power around 5 mW and were pulsed to one of two different current levels, 18 mA or 30 mA. The single-mode devices have a CW peak output power of approximately 2.5 to 3 mW and were pulsed to 7 mA. A burn-in effect can be seen in the first 100–200 hours, where the output power increases, but after the burn-in period, the output power has been stable during the 6596 hours of test at  $50^\circ\text{C}$ , corresponding to 824 hours of actual pulsed on-time.

Table 1 illustrates the differences in acceleration factor one might expect for the CW and pulsed current cases. In this table we compare acceleration factors based on the assumption of a use condition at  $25^\circ\text{C}$  and 10 mA. We have measured the thermal resistance of the multimode device, and found it to be  $1.4^\circ\text{C}/\text{mW}$ . We assume acceleration factors which have been reported in [24] for red VCSELs, that is, an Arrhenius relationship for temperature dependence with an activation energy of 0.6 eV, and a squared dependence on

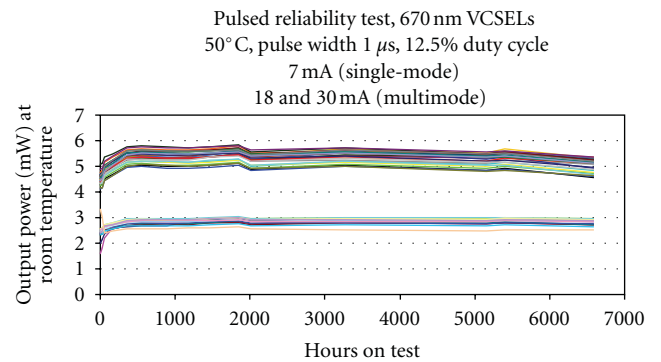


FIGURE 9: Peak output power versus test time for 670 nm VCSELs tested in pulsed mode. The output power testing was performed at room temperature. The lower curves correspond to a smaller diameter single-mode device, while the upper curves correspond to a multimode device (from Proceedings of the SPIE, Vol. 7952, paper 795208).

TABLE 1: Calculation of acceleration factors assuming an acceleration temperature of  $50^\circ\text{C}$  and a use condition of 10 mA and  $25^\circ\text{C}$ .

DC or pulsed	Acceleration current	Acceleration factor
DC	10	4.5
	18	88
	30	2438
Pulsed	10	6
	18	20
	30	55

current. These acceleration factors are also representative of that routinely reported for 850 nm VCSELs. We also assumed a thermal resistance of 0 in the pulsed case, that is, that the junction temperature does not rise above ambient. This assumption may not be completely accurate, but it helps



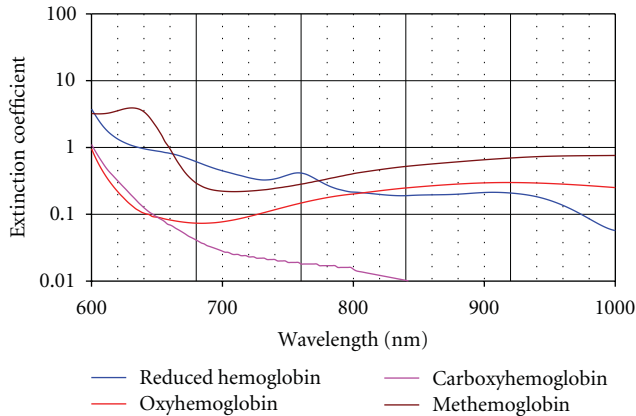


FIGURE 12: The absorption spectra versus wavelength for four different components of hemoglobin (from <http://www.masimo.com/Rainbow/about.htm>).

which measures venous or capillary blood, is an emerging application. Near-infrared spectroscopic-based imaging, which relies on differing absorption and scattering as a function of quantity and oxygenation of blood for image contrast, is an active area of research. All versions of oximetry take advantage of the varying absorption coefficient as a function of wavelength for different types of hemoglobins, that is, oxyhemoglobin, reduced hemoglobin, carboxyhemoglobin, or methemoglobin as is illustrated in Figure 12. The sensors rely on the absorption of wavelengths in the range from 650 nm to 1000 nm, and as the number of blood components one wishes to distinguish increases, the number of different wavelengths that one needs to employ also increases. These applications benefit from the narrow spectral line width and the slow spectral shift with temperature of the VCSEL, while wireless implementations make use of the reduced power consumption of VCSELs as compared to LEDs. In imaging applications, the high speed modulation characteristics of VCSELs are also useful in distinguishing absorption loss from scattering loss.

These sensors are often disposable, body worn sensors requiring a low cost, very compact package that can accommodate multiple chips of various wavelengths. Figure 13(a) illustrates a package that can accommodate multiple devices, potentially of different wavelengths, in a single package. Up to three individually modulated devices can be incorporated, and four devices can be accommodated if they are operated in alternating forward-bias/reverse-bias pairs. Devices are mounted on a lead using conductive epoxy and wire bonded. They are then embedded in an optically clear encapsulant that protects the wire bond and allows the package to be attached to a circuit board via solder reflow. This packaging approach is non-Hermetic, and hence requires the humidity resistance described earlier. Figure 13(b) illustrates the  $L$ - $I$ - $V$  (output power and voltage versus current) for the three wavelengths incorporated into a single package. An example of the application of the multiwavelength technology for near-infrared spectroscopic-based brain imaging has been demonstrated at Drexel University [32].

A second example application is plastic optical fiber (POF) links based upon PMMA fiber materials which have been implemented for sensor and data links in automobiles, and are being considered for home networks. PMMA-based fiber has secondary absorption minima in the red. Absorption at 850 nm is too high for links more than a few meters. While the potential for high speed data rates and the packaging simplicity of VCSELs makes them ideal for this application, wavelengths in the range of 650–680 nm are a necessity for low loss links. POF links based upon LEDs have been implemented in automobile sensors and entertainment networks. POF links for home networking are being developed and will require data rates in the 1 Gbps range and above at low cost, making VCSELs an attractive solution. Figure 14 illustrates eye diagrams for devices coupled into a 2 meter glass 62  $\mu\text{m}$  multimode fiber and modulated at 1.25 Gbps and 3 Gbps with a pseudorandom bit sequence, demonstrating wide open eyes to at least 3 Gbps. The measurement of the bandwidth of VCSELs coupled into plastic optical fiber is planned in the near future.

A third application example takes advantage of the ease with which VCSELs can be fabricated in multilaser arrays on a single chip. Vixar has been developing a laser scanner with no moving parts for computed radiography, a form of X-ray imaging that results in a digitized image by storing the X-ray image in a storage phosphor screen, and then reading out the phosphor with a red laser. The red laser stimulates the emission of blue light which is detected and digitized. However, the width of the standard screen, 14 inches, requires a fairly long optical path for scanning with a single laser. A linear laser array could reduce the size of the scanning mechanism and make the equipment more robust. This application requires a wavelength in the 650–700 nm range. However, creating a linear array of lasers 14 inches long requires tiling array chips in a chip on board configuration.

An early report on this product was published by Dummer et al. [33]. We have since built a 2-inch scanner, pictured in Figure 15, in a much more compact format. The VCSEL array was made up of 16 arrays of  $1 \times 32$  VCSELs for a total count of 512 VCSELs. The VCSEL pitch is 100  $\mu\text{m}$ , which is maintained within a chip and from the edge of one chip to the next. The scanner is operated by pulsing each laser sequentially with a 1  $\mu\text{sec}$  wide pulse. A pulsed output power of approximately 8 mW is achieved for 14 mA drive current. This assembly is combined with a GRIN lens array to produce focused spots of less than 50  $\mu\text{m}$  diameter at a distance of 9 mm from the top of the GRIN lens array. The total size of the assembly, including GRIN lens array, is 116 mm  $\times$  27 mm  $\times$  38 mm.

## 5. Summary and Conclusions

The results reported in this paper describe improvements in the temperature range of operation, the magnitude of output power and the range of wavelengths that can be achieved in red VCSELs. The improved performance is the result of attention to many details of the design including

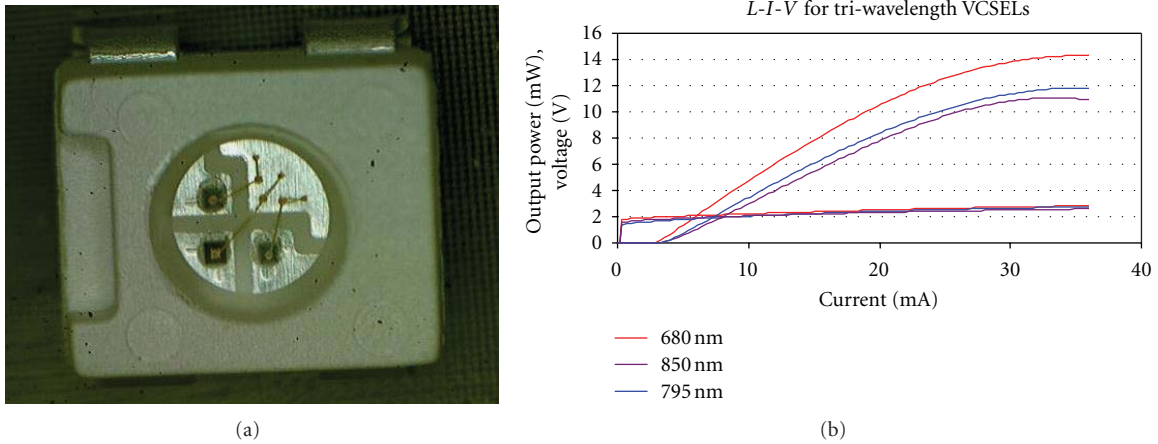


FIGURE 13: (a) A PLCC package incorporating 3 VCSEL chips. The package dimensions are 2.8 mm × 3.2 mm. (b) Room temperature *L-I-V* curves for three VCSELs (680 nm, 795 nm, and 850 nm) packaged in a single PLCC-4 package.

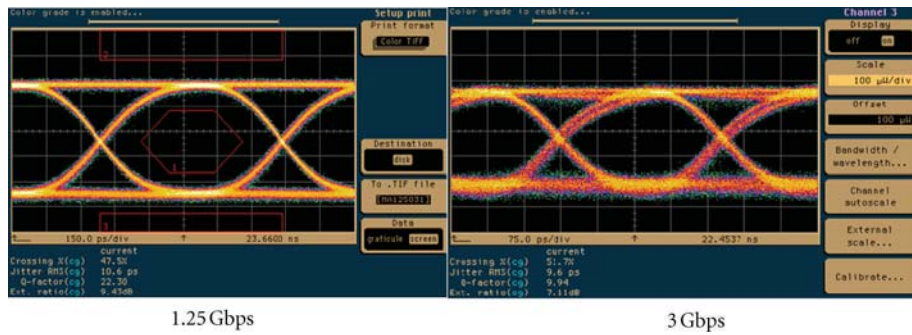


FIGURE 14: Eye diagrams of a pseudorandom bit sequence at 1.25 Gbps (left) and 3 Gbps (right) measured with a Vixar red VCSEL emitting at 670 nm.

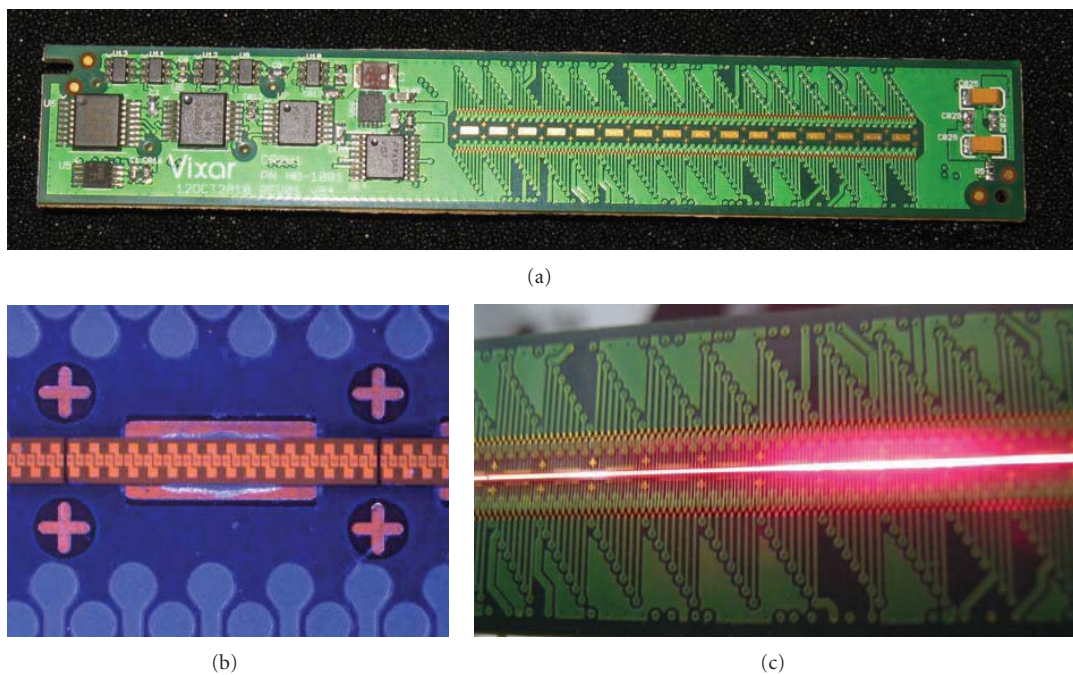


FIGURE 15: Photos of the 2'' solid-state scanner. (a) The circuit board including the electronics for controlling the scanner function. (b) A closeup of the board with the VCSEL chips attached but without wire bonding. One full VCSEL array is visible, and the edges of two others. The intersections between chips are between the alignment crosses. (c) A picture of the scanner in operation.

quantum well active layer design, mirror design, mask layout, proper choice of gain peak resonance cavity offset, and epitaxial materials quality. There is no silver bullet, but the improvement is the result of the accumulation of many incremental steps of optimization.

We have demonstrated red VCSELs lasing at 689 nm up to 115°C for smaller aperture single mode devices. Of more importance is the temperature range of “useable” power. Single mode devices have produced 1 mW of output power up to 60°C, and multimode devices provide up to 1.5 mW of power at 80°C. 14 mW of output power at room temperature has been achieved from a single VCSEL aperture, and as much as 44 mW of power from a chip containing multiple apertures within a small area.

The range of wavelengths achievable from this materials system has been extended out to 719 nm, with 2 mW of output power at room temperature at that wavelength. While VCSELs in this wavelength range have been demonstrated in the AlGaAs materials system, the results demonstrate improved output power as compared to the previously reported results. We have not explored the wavelength region below 670 nm to any substantial degree, but the improvements we have seen at 670 nm and above, combined with previous reports of devices operating at 650 nm, suggest that operation over a useful power and temperature range at 650 nm should be feasible. However, operation at wavelengths substantially below 650 nm with useful power or temperature ranges remains questionable in this materials system.

The benefits of pulsing the VCSEL have been investigated. Peak output power of 35 mW from one multimode aperture has been demonstrated for a 10% duty cycle and 1  $\mu$ sec pulse width. Pulsing also allows an extension the temperature range of operation of the VCSELs. Concerns about potential additional acceleration of failure due to repeated thermal transitions have been allayed by reliability data showing stable operation out to nearly 6500 hours when pulsed at 30 mA and a 12.5% duty cycle.

A 4” wafer diameter process and automated wafer probe testing that allows the gathering of statistics on uniformity have been developed. Wavelength uniformity across the wafer is approximately 8 nm, and average threshold current and output power uniformity do not vary significantly within that wavelength range.

The feasibility of using low cost non-Hermetic packages was demonstrated by 3500 hours of continuous operation at 50°C and 85% humidity in a package open to the environment.

Red VCSEL technology has struggled to reach the marketplace due to performance limitations caused by the materials challenges in overcoming thermal and environmental demands. We believe that the results reported here illustrate devices that are ready for use in a wide variety of applications.

## Acknowledgments

This material is based upon work supported by the National Science Foundation under Grant no. IIP-0823022. Any

opinions, findings, and conclusions or recommendations expressed in this material are those of the author(s) and do not necessarily reflect the views of the National Science Foundation. The laser scanner work was funded by the National Institutes of Health under Award no. R44RR025874 from the National Center for Research Resources. The content is solely the responsibility of the authors and does not necessarily represent the official views of the National Center for Research Resources or the National Institutes of Health.

## References

- [1] W. W. Chow, K. D. Choquette, M. H. Crawford, K. L. Lear, and G. R. Hadley, “Design, fabrication, and performance of infrared and visible vertical-cavity surface-emitting lasers,” *IEEE Journal of Quantum Electronics*, vol. 33, no. 10, pp. 1810–1823, 1997.
- [2] J. A. Lott and R. P. Schneider, “Electrically injected visible (639–661 nm) vertical cavity surface emitting lasers,” *Electronics Letters*, vol. 29, no. 10, pp. 830–832, 1993.
- [3] K. F. Huang, K. Tai, C. C. Wu, and J. D. Wynn, “Continuous wave visible InGaP/InGaAlP quantum well surface emitting laser diodes,” in *Proceedings of the Annual Meeting of the IEEE Lasers and Electro-Optics Society, (LEOS’93)*, pp. 613–614, November 1993.
- [4] M. H. Crawford, R. P. Schneider Jr., K. D. Choquette, and K. L. Lear, “Temperature-dependent characteristics and single-mode performance of AlGaInP-based 670–690 nm vertical-cavity surface-emitting lasers,” *IEEE Photonics Technology Letters*, vol. 7, no. 7, pp. 724–726, 1995.
- [5] A. Knigge, M. Zorn, M. Weyers, and G. Tränkle, “High-performance vertical-cavity surface-emitting lasers with emission wavelength between 650 and 670 nm,” *Electronics Letters*, vol. 38, no. 16, pp. 882–883, 2002.
- [6] M. Zorn, A. Knigge, U. Zeimer et al., “MOVPE growth of visible vertical-cavity surface-emitting lasers (VCSELs),” *Journal of Crystal Growth*, vol. 248, pp. 186–193, 2003.
- [7] K. Johnson and M. Hibbs-Brenner, “High output power 670 nm VCSELs 1648404,” in *Vertical-Cavity Surface-Emitting Lasers XI*, vol. 6484 of *Proceedings of SPIE*, January 2007.
- [8] R. P. Schneider Jr., K. D. Choquette, J. A. Lott, K. L. Lear, J. J. Figiel, and K. J. Malloy, “Efficient room-temperature continuous-wave AlGaInP/AlGaAs visible (670 nm) vertical-cavity surface-emitting laser diodes,” *IEEE Photonics Technology Letters*, vol. 6, no. 3, pp. 313–316, 1994.
- [9] K. D. Choquette, R. P. Schneider, M. H. Crawford, K. M. Geib, and J. J. Figiel, “Continuous wave operation of 640–660 nm selectively oxidised AlGaInP vertical-cavity lasers,” *Electronics Letters*, vol. 31, no. 14, pp. 1145–1146, 1995.
- [10] T. Calvert, B. Corbett, and J. D. Lambkin, “80°C continuous wave operation of AlGaInP based visible VCSEL,” *Electronics Letters*, vol. 38, no. 5, pp. 222–223, 2002.
- [11] T. E. Sale, G. C. Knowles, S. J. Sweeney et al., “–180 to +80°C CW lasing in visible VCSELs,” in *Proceedings of the IEEE LEOS Annual Meeting*, p. MB5, 2000.
- [12] R. Rossbach, R. Butendeich, T. Ballmann et al., “160°C pulsed laser operation of AlGaInP-based vertical-cavity surface-emitting lasers,” *Electronics Letters*, vol. 39, no. 23, pp. 1654–1655, 2003.

- [13] M. Eichfelder, R. Roßbach, M. Jetter, H. Schweizer, and P. Michler, "Red high-temperature AlGaInP-VCSEL," in *Proceedings of the Conference on Lasers and Electro-Optics, Quantum Electronics and Laser Science*, 2007.
- [14] A. Knigge, M. Zorn, H. Wenzel, M. Weyers, and G. Tränkle, "High efficiency AlGaInP-based 650 nm vertical-cavity surface-emitting lasers," *Electronics Letters*, vol. 37, no. 20, pp. 1222–1223, 2001.
- [15] H. Q. Hou, K. D. Choquette, B. E. Hammons, W. G. Breiland, M. Hagerott Crawford, and K. L. Lear, "Highly uniform and reproducible visible to near-infrared vertical-cavity surface-emitting lasers grown by MOVPE," in *Vertical-Cavity Surface-Emitting Lasers*, vol. 3003 of *Proceedings of SPIE*, pp. 34–45, February 1997.
- [16] H. Q. Hou, M. H. Crawford, B. E. Hammons, and R. J. Hickman, "Metalorganic vapor phase epitaxial growth of all-AlGaAs visible (700 nm) vertical-cavity surface-emitting lasers on misoriented substrates," *Journal of Electronic Materials*, vol. 26, no. 10, pp. 1140–1144, 1997.
- [17] F. Rinaldi, J. M. Ostermann, A. Kroner, and R. Michalzik, "High-performance AlGaAs-based VCSELs emitting in the 760 nm wavelength range," *Optics Communications*, vol. 270, no. 2, pp. 310–313, 2007.
- [18] T. E. Sale, J. S. Roberts, J. Woodhead, J. P. R. David, and P. N. Robson, "Room temperature visible (683–713 nm) all-AlGaAs vertical-cavity surface-emitting lasers (VCSELs)," *IEEE Photonics Technology Letters*, vol. 8, no. 4, pp. 473–475, 1996.
- [19] B. Tell, R. E. Leibenguth, K. F. Brown-Goebeler, and G. Livescu, "Short wavelength (699 nm) electrically pumped vertical-cavity surface-emitting lasers," *IEEE Photonics Technology Letters*, vol. 4, no. 11, pp. 1195–1196, 1992.
- [20] B. Tell, K. F. Brown-Goebeler, and R. E. Leibenguth, "Low temperature continuous operation of vertical-cavity surface-emitting lasers with wavelength below 700 nm," *IEEE Photonics Technology Letters*, vol. 5, no. 6, pp. 637–639, 1993.
- [21] R. W. Herrick and P. M. Petroff, "Annealing and aging in GaInP-based red VCSELs," in *Proceedings of the 10th IEEE Lasers and Electro-Optics Society Annual Meeting, (LEOS'97)*, pp. 66–67, 1997.
- [22] A. Knigge, R. Franke, S. Knigge et al., "650-nm vertical-cavity surface-emitting lasers: laser properties and reliability investigations," *IEEE Photonics Technology Letters*, vol. 14, no. 10, pp. 1385–1387, 2002.
- [23] T. E. Sale, D. Lancefield, B. Corbett, and J. Justice, "Ageing studies on red-emitting VCSELs for polymer optical fibre applications," in *Proceedings of the IEEE 19th International Semiconductor Laser Conference*, pp. 75–76, September 2004.
- [24] G. Duggan, D. A. Barrow, T. Calvert et al., "Red vertical cavity surface emitting lasers (VCSELs) for consumer applications," in *Vertical-Cavity Surface-Emitting Lasers XII*, vol. 6908 of *Proceedings of SPIE*, January 2008.
- [25] D. M. Kuchta, R. P. Schneider, K. D. Choquette, and S. Kilcoyne, "Large- and small-signal modulation properties of RED (670 nm) VCSELs," *IEEE Photonics Technology Letters*, vol. 8, no. 3, pp. 307–309, 1996.
- [26] J. A. Lehman, R. A. Morgan, D. Carlson, M. H. Crawford, and K. D. Choquette, "High-frequency modulation characteristics of red VCSELs," *Electronics Letters*, vol. 33, no. 4, pp. 298–300, 1997.
- [27] T. Wipiejewski, G. Duggan, D. Barrow et al., "Red VCSELs for POF data transmission and optical sensing applications," in *Proceedings of the 57th Electronic Components and Technology Conference, (ECTC '07)*, pp. 717–721, June 2007.
- [28] T. Wipiejewski, T. Moriarty, V. Hung et al., "Gigabits in the home with plugless plastic optical fiber (POF) interconnects," in *Proceedings of the 2nd Electronics System Integration Technology Conference, (ESTC'08)*, pp. 1263–1266, September 2008.
- [29] R. Thornton, Y. Zou, J. Tramontana, M. Hagerott Crawford, R. P. Schneider, and K. D. Choquette, "Visible (670 nm) vertical cavity surface emitting lasers with indium tin oxide transparent conducting top contacts," in *Proceedings of the 8th Annual Meeting of the IEEE Lasers and Electro-Optics Society*, pp. 108–109, November 1995.
- [30] R. Safaisini, K. Johnson, M. Hibbs-Brenner, and K. L. Lear, "Stress analysis in copper plated red VCSELs," *Proceedings of the 23rd Annual Meeting of the IEEE Photonics Society, (PHOTONICS '10)*, pp. 246–247, 2010.
- [31] A. M. Kasten, D. F. Siriani, M. K. Hibbs-Brenner, K. L. Johnson, and K. D. Choquette, "Beam properties of visible proton implanted photonic crystal VCSELs," *IEEE Journal of Selected Topics in Quantum Electronics*, vol. 17, no. 6, pp. 1648–1655, 2011.
- [32] E. Sultan, K. Manseta, A. Khwaja et al., "Modeling and tissue parameter extraction challenges for free space broadband fNIR brain imaging systems," in *Imaging, Manipulation, and Analysis of Biomolecules, Cells and Tissues IX*, vol. 7902 of *Proceedings of SPIE*, 2011.
- [33] M. M. Dummer, K. Johnson, M. Witte, W. K. Hogan, and M. Hibbs Brenner, "Computed radiography imaging based on high-density 670 nm VCSEL arrays," in *Multimodal Biomedical Imaging V*, vol. 7557 of *Proceedings of SPIE*, January 2010.

## Review Article

# Single Mode Photonic Crystal Vertical Cavity Surface Emitting Lasers

**Kent D. Choquette,<sup>1</sup> Dominic F. Siriani,<sup>1</sup> Ansas M. Kasten,<sup>2</sup> Meng Peun Tan,<sup>1</sup> Joshua D. Sulkin,<sup>1</sup> Paul O. Leisher,<sup>3</sup> James J. Raftery Jr.,<sup>4</sup> and Aaron J. Danner<sup>5</sup>**

<sup>1</sup>Department of Electrical and Computer Engineering, University of Illinois, Urbana, IL, 61801, USA

<sup>2</sup>Micro and Nano Structures Technologies, GE Global Research, Niskayuna NY 12309, USA

<sup>3</sup>Department of Physics and Optical Engineering, Rose-Hulman Institute of Technology, Terre Haute, IN 47803, USA

<sup>4</sup>Department of Electrical Engineering, United States Military Academy, West Point, NY 10996, USA

<sup>5</sup>Department of Electrical and Computer Engineering, National University of Singapore, Singapore 117576

Correspondence should be addressed to Kent D. Choquette, choquett@illinois.edu

Received 27 July 2011; Accepted 5 October 2011

Academic Editor: Krassimir Panajotov

Copyright © 2012 Kent D. Choquette et al. This is an open access article distributed under the Creative Commons Attribution License, which permits unrestricted use, distribution, and reproduction in any medium, provided the original work is properly cited.

We review the design, fabrication, and performance of photonic crystal vertical cavity surface emitting lasers (VCSELs). Using a periodic pattern of etched holes in the top facet of the VCSEL, the optical cavity can be designed to support the fundamental mode only. The electrical confinement is independently defined by proton implantation or oxide confinement. By control of the refractive index and loss created by the photonic crystal, operation in the Gaussian mode can be insured, independent of the lasing wavelength.

## 1. Introduction

Vertical cavity surface emitting lasers (VCSELs) have emerged as the commercial laser source of choice for short distance digital fiber optical interconnects and sensing applications. The principle advantage that VCSELs have in many of these applications are their low operating power requirements (only a few mW) as well as their low cost and large volume manufacturing. Compared to edge emitting semiconductor lasers, VCSELs also possess the benefits of a circular output beam, on wafer testing, and the ability to form 2-dimensional arrays. The most common emission wavelength is 850 nm, although wavelengths from 640 to 1300 nm have been demonstrated for VCSELs monolithically grown on GaAs substrates.

Unlike an edge emitting laser, VCSELs have a single longitudinal mode but tend to operate in multiple transverse optical modes. This arises because the optical cavity of the VCSEL is short in the direction of light propagation (typically the cavity is 1 wavelength long, or approx. 265 nm for 850 nm emission), but the transverse cavity width defined by a selectively oxidized or ion implanted aperture [1]

is much greater (typically a few to tens of microns in diameter). Edge emitting semiconductor lasers have much longer cavities (several hundreds of microns in length) supporting numerous longitudinal modes, but with a cavity cross-section that supports a few or a single transverse/lateral mode. The number of laser emission modes will influence the spectral width of the laser emission, while the near field and far field beam profile is determined by the transverse mode profiles. For a typical multimode 850 nm VCSEL, the emission bandwidth can be roughly 3 nm, while the far field is often a ring shape, due to the higher order mode operation. The multimode VCSEL bandwidth can be a limiting factor for high speed digital modulation through optical fiber due to spectral dispersion, while the smallest focused spot size will come from operation only in the fundamental Gaussian mode.

Many approaches to achieve single fundamental mode operation in VCSELs have been reported. The simplest approach is reducing the oxide [2] or implant [3] cavity diameter, but this comes at the expense of high current density and inferior laser reliability. Other approaches include a hybrid combination of oxide/implant apertures [4], surface

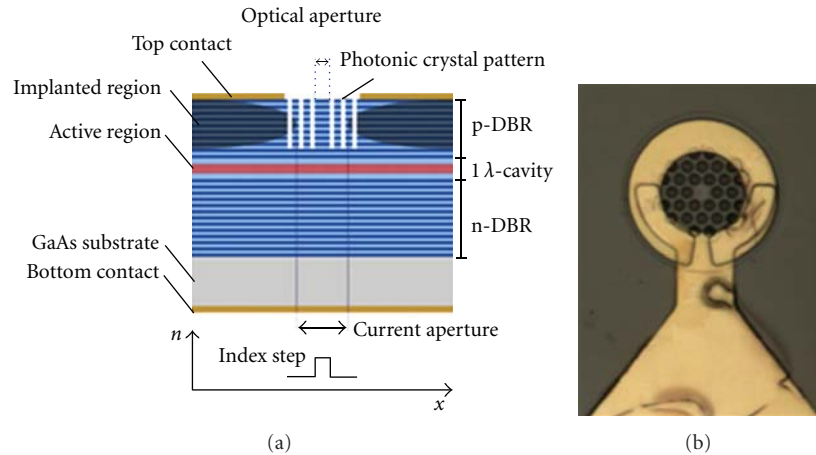


FIGURE 1: (a) Cross-section sketch and (b) top view image of planar ion implanted photonic crystal VCSEL.

relief etched structures [5], increasing the optical cavity length [6], etched holey patterns [7, 8], and etched photonic crystal VCSELs [9–14].

In most cases, the technique for achieving single mode operation requires an added epitaxial semiconductor layer or etched feature that has a stringent dimension control related to the wavelength. All of these approaches favor single fundamental mode operation by either increasing the gain for the fundamental mode, increasing the loss of higher order modes, or by engineering the transverse index profile of the VCSEL to support only the lowest order mode.

In this review, we will focus on index-guided single mode photonic crystal (PhC) VCSELs. In these devices, a 2-dimensional periodic pattern of holes is etched into the top distributed Bragg reflector mirror (DBR). The lasing cavity is defined by the absence of one or more holes as depicted in Figure 1. Unlike in-plane 2-dimensional photonic crystal structures where the defect mode often lies within a frequency bandgap, the type of out-of-plane defect mode in the PhC VCSEL is not created by a photonic band gap. Instead, the PhC VCSEL out-of-plane mode is confined similarly to the case in a solid-core photonic crystal fiber, which guides by way of total internal reflection [15]. As we will show, the unetched defect has a higher refractive index as compared to the surrounding etched photonic crystal region.

The refractive index and optical loss arising from the PhC region can be engineered via the photonic crystal parameters of hole arrangement, period, diameter, and etch depth. A key feature is the periodicity of the etched pattern of holes which allows us to accurately calculate the effective refractive index. The modified index is not a geometric average of the low index etched regions within the semiconductor, but is actually much less [12]. Note that nonperiodic but symmetric etched features, such as wedges or rings, can also be used to engineer the refractive index [16, 17]. However, this approach does rely upon geometrically averaging the index and thus is very sensitive to feature size and fabrication error. Moreover, etched features that are continuous, such as rings, will lead to degraded electrical injection.

The index confinement and optical loss can be exploited to create fundamental mode photonic crystal VCSELs. As shown in the comparison of Figure 2, conventional multimode VCSELs can be altered to show single mode lasing emission more than 30 dB above the nonlasing modes. Moreover, insuring single mode behavior can be maintained independent of the lasing wavelength or crystal design [18], precluding the need for accurate and/or wavelength specific features. Finally, the electrical diameter can be increased independent to the optical cavity to enable lower current density operation [13, 19] and thus potentially long laser lifetime [20].

In Section 2, we review the fabrication details for both oxide-confined and ion implanted PhC VCSELs. In Section 3, a description of the design approach which incorporates both index and loss confinement effects from the photonic crystal is introduced. In Section 4, the performance of various PhC VCSELs are presented. Finally, Section 5 summarizes this review.

## 2. Fabrication

The epitaxial materials used are conventional all-semiconductor VCSELs consisting of upper p-type and lower n-type DBR mirrors which surround a quantum well active region [1]. In our studies, we have fabricated PhC VCSELs grown on GaAs substrates which emit at 670, 780, 850, 980, or 1300 nm [18, 21]. The device fabrication for oxide-confinement or ion implantation follows the typical steps as detailed below, with the addition of the patterning and anisotropic etching of the photonic crystal. In our PhC VCSELs, the optical cavity confinement is determined by the photonic crystal parameters of hole diameter ( $a$ ), period ( $b$ ), and hole depth, whereas the electrical confinement is provided by the proton-implanted or oxide aperture. This allows for precise engineering of the index guidance effect of the photonic crystal independent of the electrical confinement of the VCSEL.

Implant-confined photonic crystal VCSELs are fabricated as follows [1]. Ohmic ring contacts (Ti/Au) for the top

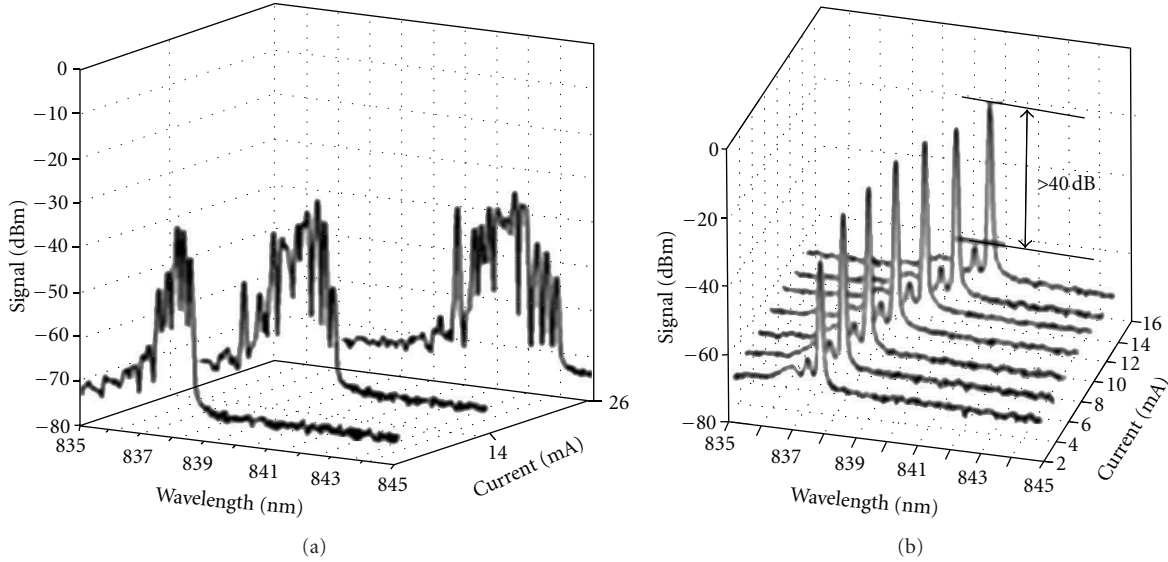


FIGURE 2: Optical spectrum of (a) oxide-confined and (b) photonic crystal VCSEL.

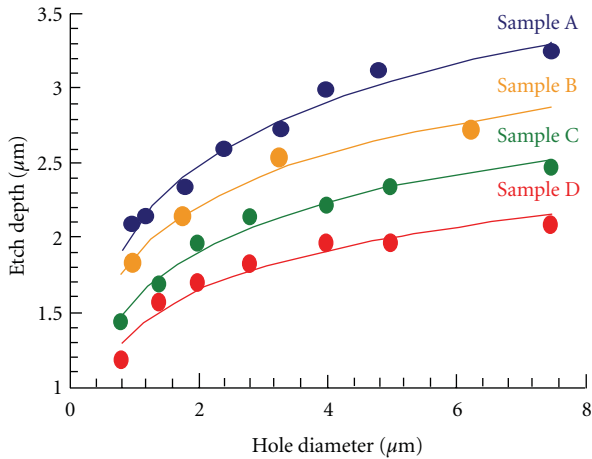


FIGURE 3: Etch depth versus hole diameter for  $b/a = 0.4, 0.5, 0.6,$  and  $0.7$ .

p-type DBR are patterned using optical photolithography, deposited by electron-beam evaporation, and formed using conventional liftoff. A backside contact (AuGe/Ni/Au) is deposited to form an ohmic contact to the n-type substrate. A thin protective layer of SiO<sub>2</sub> is deposited, and thick (12 μm) photoresist pillars are patterned in the center of each top ring contact with diameter varying from 6 to 20 μm. The exposed SiO<sub>2</sub> is etched using CF<sub>4</sub> reactive ion etching (RIE). These pillars serve to mask and define the apertures for the implant process. Protons are next implanted at typically 340 keV (the implant energy will depend on the intended implant projected range [1]) with a dose of  $4 \times 10^{14} \text{ cm}^{-2}$  and afterwards the resist pattern is removed. Another larger resist mask is used for a second multiple implantation step to create a stacked implant from the implant aperture to the

surface for electrical isolation between devices in a planar device topology. The implant isolation can be done either before or after the photonic crystal etch.

The photonic crystal patterns are defined by optical lithography in an SiO<sub>2</sub> mask. Note that the periodic index variation of the hole pattern needs not be of the same size as the light wavelength, since the light is propagating parallel to the hole patterns [12]; hence micron-sized holes are sufficient, which allows for optical photolithographic patterning. The photonic crystal holes are etched into the top DBR using SiCl<sub>4</sub>/Ar inductively coupled plasma RIE. The etch rate of the holes will depend on their diameter,  $b$ , due to size-dependent etch effects [22]. The etch depth for the samples A, B, C, and D, which have a  $b/a = 0.4, 0.5, 0.6,$  and  $0.7$ , respectively, is shown in Figure 3 as a function of photonic crystal hole diameter ( $b$ ). The holes were inspected in a scanning electron microscope at an angle of 35° off-normal, and the etch depth was calculated by counting the number of DBR periods etched and multiplying by the thickness of one period. For a given etching time, smaller diameter holes etched to a shallower depth. The etch depth data can be empirically fit with a logarithmic function. The hole etch depth is limited by the large aspect ratio, but as we show below etching to and/or through the active region is undesirable. However, an important consequence is that the optical mode only experiences the photonic crystal in part of the longitudinal cavity; we will show below that this creates optical loss and confinement. After etching the photonic crystal pattern, the oxide mask is removed by CF<sub>4</sub> RIE, and the samples are subjected to 30 sec rapid thermal annealing at 325°C for ohmic contact formation. Figure 1(a) illustrates a schematic of a completed implant-confined photonic crystal VCSEL and Figure 1(b) shows a top view of a planar implant PhC VCSEL.

For oxide-confined VCSELs, a high aluminum content layer (Al<sub>0.98</sub>Ga<sub>0.02</sub>As) is placed above the active region for

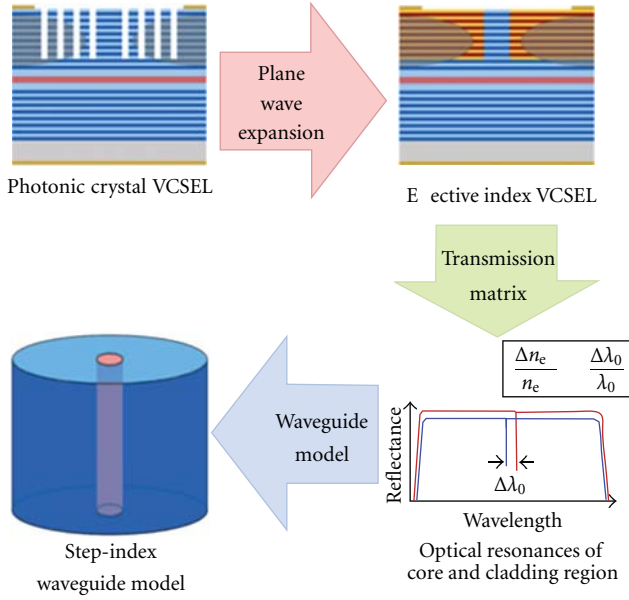


FIGURE 4: Design approach for photonic crystal VCSELs.

fabrication of an oxide aperture [1, 23]. After top and bottom contact metals are defined and deposited, photonic crystal patterns and an oxidation mesa or trench are defined by standard optical lithography and are etched by ICP-RIE. The hole pattern and the oxidation trench are simultaneously patterned by optical lithography but can be etched separately or simultaneously [24]. This results in self-alignment of the PhC defect to the oxide aperture. After removal of the etch mask, selective oxidation at 420°C in a steam environment creates the oxide aperture.

The index step of the PhC defect cavity can be engineered by carefully designing the periodic hole pattern as well as by controlling the etch depth of the air holes. However, to simply achieve single fundamental mode operation, PhC parameters such as lattice constant, hole diameter, or etching depths of the air holes do not need to be stringently controlled [18]. The large tolerances in the fabrication process makes PhC VCSELs suitable for mass-production and thus an excellent candidate for low cost/high volume consumer applications.

### 3. Design

The design of the photonic crystal has been developed to incorporate both the index confinement [10] as well as the confinement that arises due to optical loss [25, 26]. The photonic crystal has a reduced effective refractive index, due to the periodic refractive index variation (see Figure 1). The basic design approach is schematically shown in Figure 4. The VCSEL is modeled using a simplified step-index optical fiber waveguide model: the defect in the photonic crystal is considered to be the core of the fiber with index  $n_{\text{core}}$ , and the photonic crystal region surrounding is taken as the reduced-index cladding region with  $n_{\text{clad}}$ . More computationally intensive and rigorous methods, such

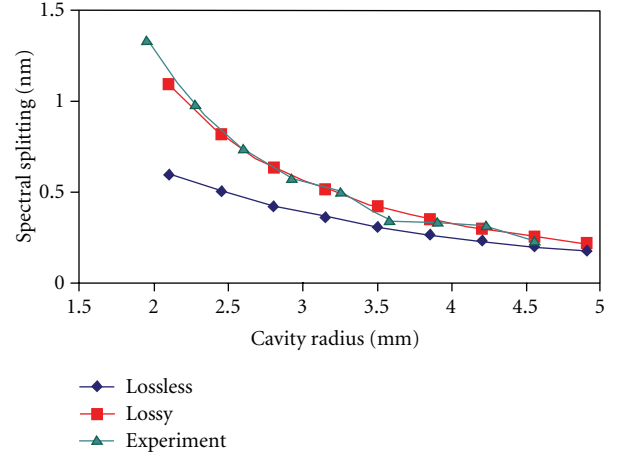


FIGURE 5: Spectral splitting between fundamental and first higher order mode versus cavity radius.

as finite-difference time-domain, finite element, or vectorial and three-dimensional calculations [27–29] can also be employed.

The waveguiding and optical loss effects are incorporated by using a complex refractive index in the PhC clad region. The real part of the effective refractive index of the PhC cladding is found from the band diagram calculated using the plane wave expansion method. The slope of the band for out-of-plane propagation determines the effective refractive index for each high and low index layer of the DBR mirror. This effective homogeneous index is used to replace the DBR layers that are penetrated by the photonic crystal, thereby accounting for the finite etch depth. The index step difference between the core and clad regions can be found using the difference in the calculated resonance wavelengths [30] of a matrix calculation [26]. This procedure intrinsically accounts for the finite etch depth of the holes.

The optical loss introduced by the finite etch depth of the holes is accounted for using a complex refractive index in the cladding region [31]:

$$n_{\text{clad}} = n'_{\text{PhC}} + im''_{\text{loss}}. \quad (1)$$

To determine the magnitude of the imaginary component, we rely upon the confinement induced by the loss. This can be inferred from the cold cavity spectral splitting between the modes observed below threshold, as discussed below. From the Helmholtz equation:

$$\nabla^2 U + n^2(r)k_0^2 U = 0, \quad (2)$$

where  $U$  is the field in three spatial dimensions,  $n$  is the radial-dependent refractive index profile, and  $k_0$  is the free-space wave number, we assume separable solutions of the form:

$$U(r, \phi, z) = u(r)e^{-im\phi}e^{-ik_z z}, \quad (3)$$

where  $u$  is the radial field profile,  $m$  is an integer, and  $k_z$  is an effective propagation constant. The propagation constant  $k_z$

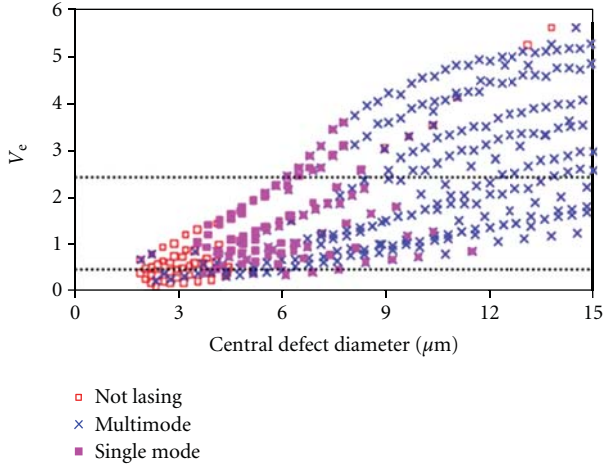


FIGURE 6: Normalized frequency and modal properties of oxide-confined 850 nm VCSELs.

is set by Fabry-Perot cavity. Inserting the solutions in (3) into (2) gives

$$\frac{d^2u}{dr^2} + \frac{1}{r} \frac{du}{dr} + \left( n^2(r)k_0^2 - k_z^2 - \frac{m^2}{r^2} \right) u(r) = 0. \quad (4)$$

Solving the eigenvalue equation (4) using finite differences produces eigenvectors  $u$  and eigenvalues  $k_0$ , which are set of solutions for the resonant modes of the waveguide whose wave numbers are  $k_0$ . The resonant wavelength is

$$\lambda_0 = \frac{2\pi c}{\text{Re}\{\omega_0\}} = \frac{2\pi}{\text{Re}\{k_0\}}, \quad (5)$$

and the loss experienced by the mode is

$$\alpha_i = \text{Im}\{k_0\}. \quad (6)$$

We compare the calculated resonances (fundamental and first higher order mode) to spectral measurements from a fabricated PhC VCSEL with injection current less than threshold [25]. Figure 5 shows spectral splitting between the fundamental and first higher order mode as a function of cavity radius. The lossless (lossy) curve corresponds to a real (complex) PhC refractive index used to solve (4). Note that the splitting increases for reduced cavity size but is greater for a nonzero  $n'_{\text{loss}}$ . By varying this parameter, we can match the experimental curve shown in Figure 5. Hence, the effect of optical loss from the photonic crystal is to increase the cavity confinement.

For a lossless waveguide, the modal properties can be quantified from the normalized frequency parameter,  $V_{\text{eff}}$ :

$$V_{\text{eff}} = \frac{2\pi R}{\lambda} \sqrt{n_{\text{core}}^2 - n_{\text{clad}}^2}, \quad (7)$$

where  $R = a - b/2$  is the core radius and  $\lambda$  is the free-space optical wavelength. For a lossless guide, the single-mode cutoff is  $V_{\text{eff}} < 2.405$  [32]. Note that in (7), the finite etch depth dependence is accounted in the determination of the purely real  $n_{\text{clad}}$ . In the next section, we compare the

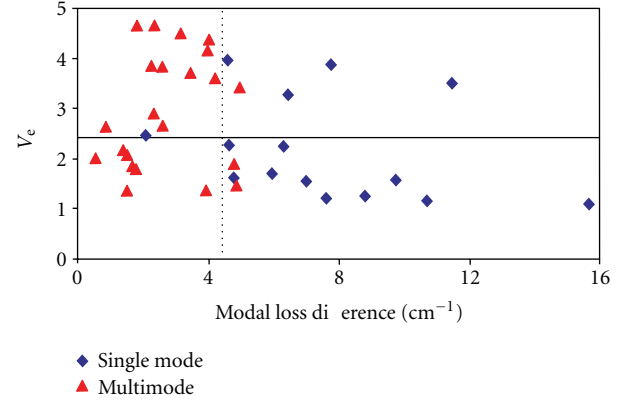


FIGURE 7: Normalized frequency versus modal loss difference between fundamental and first higher order mode of oxide-confined 850 nm VCSELs.

calculated values of  $V_{\text{eff}}$  and the extracted values of optical loss, with the modal characteristics of PhC VCSELs.

#### 4. Performance

The characteristics of PhC VCSELs were measured using on-wafer probing at room temperature. For continuous wave light versus current measurements, the input current was varied and both the device voltage and the output from a silicon photodetector were measured using a semiconductor parameter analyzer. The spectral characteristics were measured using an optical spectrum analyzer with resolution bandwidth of 0.06 nm. At maximum power, each VCSEL was categorized as either not lasing, multimode lasing, or single mode lasing, where single mode is defined as a single spectral peak at the fundamental (lowest energy) wavelength with greater than 30 dB side mode suppression ratio. Note that VCSELs that lased single mode at threshold with higher order mode lasing at maximum power are defined as multimode.

In Figure 6 we show the calculated  $V_{\text{eff}}$  and the observed modal properties for approximately 1500 different photonic crystal designs with differing period,  $b/a$  ratios, and etch depth [33]. For many of these 850 nm oxide-confined VCSELs with  $V_{\text{eff}} < 2.4$ , single mode lasing is observed, particularly for cavity diameters less than  $6 \mu\text{m}$ . However, multi-mode VCSELs with  $V_{\text{eff}} < 2.4$  can be seen, as well as single mode PhC VCSELs with  $V_{\text{eff}} > 2.4$ . Hence, the loss induced confinement is a critical design parameter.

In Figure 7, we show a smaller population of approximately 40 oxide-confined 850 nm photonic crystal VCSELs with differing designs where  $V_{\text{eff}}$  and the modal loss difference between the fundamental and the first higher order mode are determined. The single mode cutoff is shown by a horizontal line in Figure 7. Again, we observe that the normalized frequency parameter is not a good determination for single mode VCSELs. However, if optical loss is considered, a cutoff can be seen between single and multimode lasing at approximately  $5 \text{ cm}^{-1}$  of loss difference

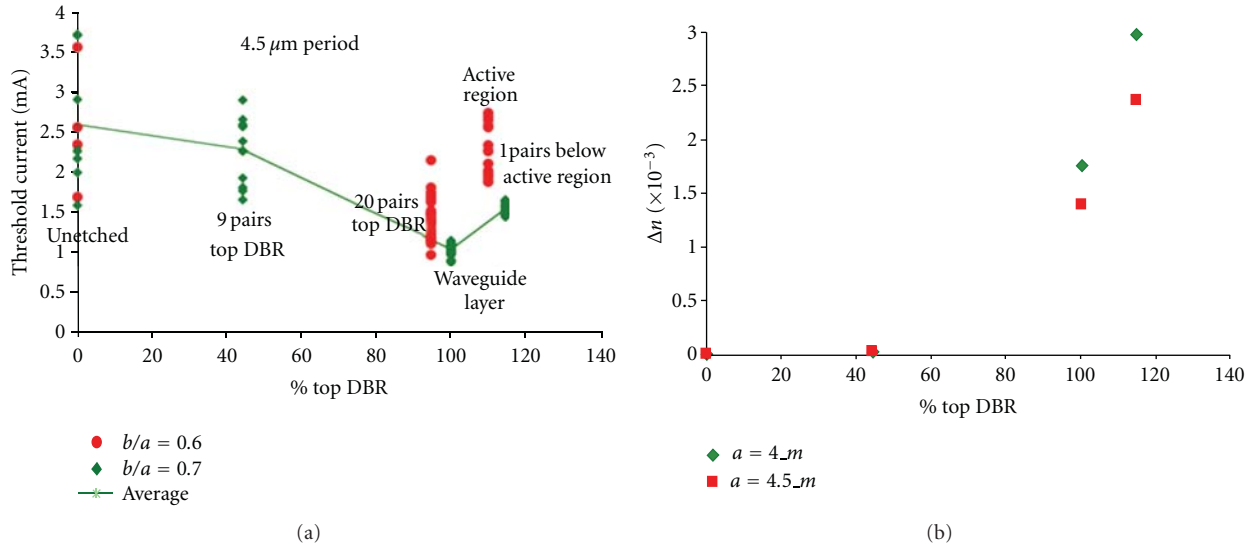


FIGURE 8: (a) Threshold current and (b) index contrast versus etch depth into top DBR for ion implanted 850 nm VCSELs.

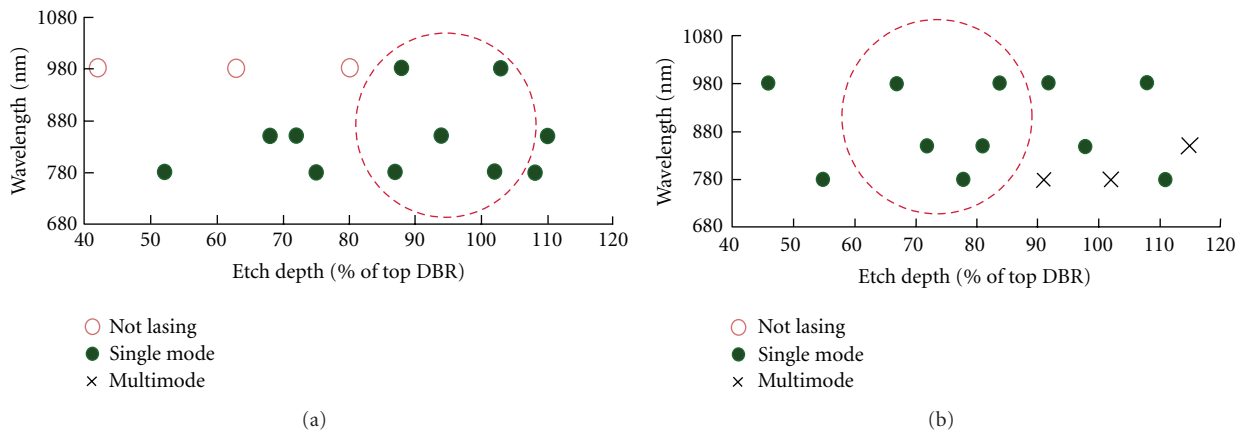


FIGURE 9: Modal properties of oxide-confined PhC VCSELs; designs that are independent of wavelength are shown in dashed circles: (a)  $b/a = 0.7$ ,  $a = 4 \mu\text{m}$ , oxide aperture =  $12 \mu\text{m}$  and (b)  $b/a = 0.7$ ,  $a = 4.5 \mu\text{m}$ , oxide aperture =  $12 \mu\text{m}$  [18].

(dotted vertical line in Figure 7). This condition corresponds to the point at which the loss to higher order mode is too great for gain to compensate and thus lasing to occur.

The effect of the etch depth on confinement is explicitly shown for implanted 850 nm photonic crystal VCSELs in Figure 8(a). Here, we calculate the difference between the core and clad index as a function of the percent etch depth into the top DBR for two  $b/a$  ratios. The confinement increases as the hole depth increases. However, etching through the active region leads to increased threshold current, as seen in Figure 8(b). Multiple VCSELs with two  $b/a$  ratios etched at different depths into the top DBR are shown. The highest threshold currents are for lasers with no etching, which arises from the diffraction loss inherent to ion implanted VCSELs [34]. The threshold current decreases with increased etch depth (increased confinement), reaching the lowest values when the photonic crystal is etched precisely through the

top DBR. However, when the VCSELs are etched through the active region, the threshold current increases, presumably due to nonradiative recombination occurring at the edges of the penetrating holes into the quantum wells.

A notable feature of photonic crystal designs is that the designs are wavelength agnostic. In Figure 9, we present the modal properties of 780, 850, and 980 nm VCSELs, all with the same photonic crystal pattern [18]. In this study, single mode operation is defined as  $>35$  dB side mode suppression, and all lasers emit  $>1$  mW of single mode output. In other studies, we have achieved as high as 3 mW of fundamental mode emission [13].

For Gaussian fundamental mode emission, we expect to see a Gaussian far field mode with a minimum of divergence. The far field divergence for visible implanted PhC VCSELs is plotted in Figure 10 as a function of their measured side mode suppression ratio (SMSR). The insets in Figure 10 are false color representation of the far field intensity

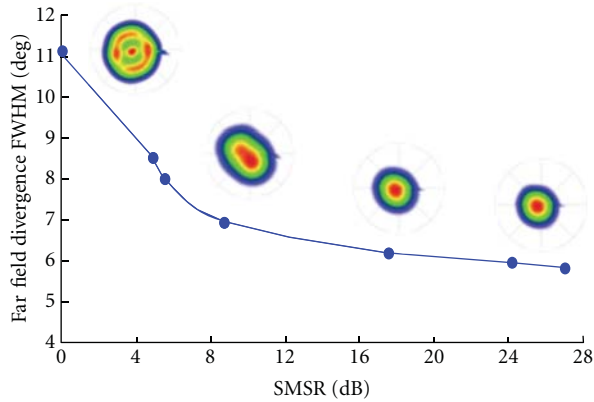


FIGURE 10: Far field divergence of implanted 670 nm PhC VCSELs as a function of side mode suppression ratio; the insets show representative far field patterns.

patterns. For multimode VCSELs (0 dB SMSR), a ring-like far field is observed. For increasing single mode operation, the divergence angle monotonically decreases.

## 5. Summary

Implant and oxide-confined photonic crystal VCSELs emitting from 670 to 1300 nm were designed, fabricated, and characterized to parametrically study the effects of photonic crystal design and etch depth on single mode operation. A lossy model for the photonic crystal waveguide used for transverse confinement in VCSELs has been developed. We have found a wide range of designs and fabrication approaches to achieve reproducible single fundamental mode operation. Moreover, these designs are found to be independent of wavelength and lead to 1–3 mW of output power in single aperture devices.

These developments in the control of transverse modes can significantly advance the use of VCSELs for a number of applications. With the methods developed here, photonic crystal VCSELs can be designed to operate only on a single mode while maintaining a larger aperture size and higher efficiency. Thus, these advancements could enable a single mode VCSEL with high output powers and greater reliability for sensing and long-haul communication applications.

## Acknowledgments

The authors thank many former University of Illinois students for extensive VCSEL characterization. This work was partially supported by the National Science Foundation under Awards nos. 03-35082, DMI 0328162, and NDSEG Graduate Fellowship.

## References

- [1] K. D. Choquette and K. M. Geib, "Fabrication and performance of vertical cavity surface emitting lasers," in *Vertical Cavity Surface Emitting Lasers*, C. Wilmsen, H. Temkin, L. Coldren et al., Eds., chapter 5, Cambridge University Press, Cambridge, UK, 1999.
- [2] C. Jung, R. Jager, M. Grabherr et al., "4.8 mW single-mode oxide confined top surface emitting vertical-cavity laser diodes," *Electronics Letters*, vol. 33, no. 21, pp. 1790–1791, 1997.
- [3] R. A. Morgan, G. D. Guth, M. W. Focht et al., "Transverse mode control of vertical-cavity top-surface-emitting lasers," *IEEE Photonics Technology Letters*, vol. 5, no. 4, pp. 374–377, 1993.
- [4] E. W. Young, K. D. Choquette, S. L. Chuang, K. M. Geib, A. J. Fischer, and A. A. Allerman, "Single-transverse-mode vertical-cavity lasers under continuous and pulsed operation," *IEEE Photonics Technology Letters*, vol. 13, no. 9, pp. 927–929, 2001.
- [5] H. Martinsson, J. A. Vukušić, M. Grabherr et al., "Transverse mode selection in large-area oxide-confined vertical-cavity surface-emitting lasers using a shallow surface relief," *IEEE Photonics Technology Letters*, vol. 11, no. 12, pp. 1536–1538, 1999.
- [6] H. J. Unold, S. W. Z. Mahmoud, R. Jager, M. Kicherer, M. C. Riedl, and K. J. Ebeling, "Improving single-mode VCSEL performance by introducing a long monolithic cavity," *IEEE Photonics Technology Letters*, vol. 12, no. 8, pp. 939–941, 2000.
- [7] A. Furukawa, S. Sasaki, M. Hoshi, A. Matsuzono, K. Moritoh, and T. Baba, "High-power single-mode vertical-cavity surface-emitting lasers with triangular holey structure," *Applied Physics Letters*, vol. 85, no. 22, pp. 5161–5163, 2004.
- [8] P. O. Leisher, A. J. Danner, J. J. Raftery Jr., and K. D. Choquette, "Proton implanted singlemode holey vertical-cavity surface-emitting lasers," *Electronics Letters*, vol. 41, no. 18, pp. 1010–1011, 2005.
- [9] D. S. Song, S. H. Kim, H. G. Park, C. K. Kim, and Y. H. Lee, "Single-fundamental-mode photonic-crystal vertical-cavity surface-emitting lasers," *Applied Physics Letters*, vol. 80, no. 21, p. 3901, 2002.
- [10] N. Yokouchi, A. J. Danner, and K. D. Choquette, "Two-dimensional photonic crystal confined vertical-cavity surface-emitting lasers," *IEEE Journal on Selected Topics in Quantum Electronics*, vol. 9, no. 5, pp. 1439–1445, 2003.
- [11] A. J. Danner, J. J. Raftery Jr., T. Kim, P. O. Leisher, A. V. Giannopoulos, and K. D. Choquette, "Progress in photonic crystal vertical cavity lasers," *IEICE Transactions on Electronics*, vol. E88-C, no. 5, pp. 944–949, 2005.
- [12] N. Yokouchi, A. J. Danner, and K. D. Choquette, "Etching depth dependence of the effective refractive index in two-dimensional photonic-crystal-patterned vertical-cavity surface-emitting laser structures," *Applied Physics Letters*, vol. 82, no. 9, pp. 1344–1346, 2003.
- [13] A. J. Danner, T. S. Kim, and K. D. Choquette, "Single fundamental mode photonic crystal vertical cavity laser with improved output power," *Electronics Letters*, vol. 41, no. 6, pp. 325–326, 2005.
- [14] H. P. D. Yang, F. I. Lai, Y. H. Chang et al., "Singlemode (SMSR<40dB) proton-implanted photonic crystal vertical-cavity surface-emitting lasers," *Electronics Letters*, vol. 41, no. 6, pp. 326–328, 2005.
- [15] T. A. Birks, J. C. Knight, and P. S. J. Russell, "Endlessly single-mode photonic crystal fiber," *Optics Letters*, vol. 22, no. 13, pp. 961–963, 1997.
- [16] A. Furukawa, S. Sasaki, M. Hoshi, A. Matsuzono, K. Moritoh, and T. Baba, "High-power single-mode vertical-cavity surface-emitting lasers with triangular holey structure," *Applied Physics Letters*, vol. 85, no. 22, pp. 5161–5163, 2004.

- [17] P. O. Leisher, A. J. Danner, J. J. Raftery, D. Siriani, and K. D. Choquette, "Loss and index guiding in single-mode proton-implanted holey vertical-cavity surface-emitting lasers," *IEEE Journal of Quantum Electronics*, vol. 42, no. 10, pp. 1091–1096, 2006.
- [18] A. M. Kasten, M. P. Tan, J. D. Sulkin, P. O. Leisher, and K. D. Choquette, "Photonic crystal vertical cavity lasers with wavelength-independent single-mode behavior," *IEEE Photonics Technology Letters*, vol. 20, no. 23, pp. 2010–2012, 2008.
- [19] C. Chen, Z. Tian, K. D. Choquette, and D. V. Plant, "25-Gb/s direct modulation of implant confined holey vertical-cavity surface-emitting lasers," *IEEE Photonics Technology Letters*, vol. 22, no. 7, pp. 465–467, 2010.
- [20] A. M. Kasten, J. D. Sulkin, P. O. Leisher, D. K. McElfresh, D. Vacar, and K. D. Choquette, "Manufacturable photonic crystal single-mode and fluidic vertical-cavity surface-emitting lasers," *IEEE Journal on Selected Topics in Quantum Electronics*, vol. 14, no. 4, pp. 1123–1131, 2008.
- [21] P. O. Leisher, A. J. Danner, and K. D. Choquette, "Single-mode 1.3- $\mu\text{m}$  photonic crystal vertical-cavity surface-emitting laser," *IEEE Photonics Technology Letters*, vol. 18, no. 20, pp. 2156–2158, 2006.
- [22] R. A. Gottscho and C. W. Jurgensen, "Microscopic uniformity in plasma etching," *Journal of Vacuum Science & Technology B*, vol. 10, p. 2133, 1992.
- [23] K. D. Choquette, R. P. Schneider Jr., K. L. Lear, and K. M. Geib, "Low threshold voltage vertical-cavity lasers fabricated by selective oxidation," *Electronics Letters*, vol. 30, no. 24, pp. 2043–2044, 1994.
- [24] M. S. Alias, S. Shaari, P. O. Leisher, and K. D. Choquette, "Single transverse mode control of VCSEL by photonic crystal and trench patterning," *Photonics and Nanostructures*, vol. 8, no. 1, pp. 38–46, 2010.
- [25] D. F. Siriani, P. O. Leisher, and K. D. Choquette, "Loss-induced confinement in photonic crystal vertical-cavity surface-emitting lasers," *IEEE Journal of Quantum Electronics*, vol. 45, no. 7, pp. 762–768, 2009.
- [26] D. F. Siriani, M. P. Tan, A. M. Kasten et al., "Mode control in photonic crystal vertical-cavity surface-emitting lasers and coherent arrays," *IEEE Journal on Selected Topics in Quantum Electronics*, vol. 15, no. 3, Article ID 4781555, pp. 909–917, 2009.
- [27] P. Bienstman, R. Baets, J. Vukusic et al., "Comparison of optical VCSEL models on the simulation of oxide-confined devices," *IEEE Journal of Quantum Electronics*, vol. 37, no. 12, pp. 1618–1631, 2001.
- [28] T. Czynszanowski, M. Dems, and K. Panajotov, "Single mode condition and modes discrimination in photonic-crystal 1.3  $\mu\text{m}$  AlInGaAs/InP VCSEL," *Optics Express*, vol. 15, no. 9, pp. 5604–5609, 2007.
- [29] T. Czynszanowski, M. Dems, and K. Panajotov, "Optimal parameters of photonic-crystal vertical-cavity surface-emitting diode lasers," *Journal of Lightwave Technology*, vol. 25, no. 9, pp. 2331–2336, 2007.
- [30] G. R. Hadley, "Effective index model for vertical-cavity surface-emitting lasers," *Optics Letters*, vol. 20, no. 13, pp. 1483–1485, 1995.
- [31] A. E. Siegman, "Propagating modes in gain-guided optical fibers," *Journal of the Optical Society of America A*, vol. 20, no. 8, pp. 1617–1628, 2003.
- [32] R. S. Quimby, *Photonics and Lasers*, John Wiley & Sons, New Jersey, NJ, USA, 2006.
- [33] A. J. Danner, J. J. Raftery Jr., P. O. Leisher, and K. D. Choquette, "Single mode photonic crystal vertical cavity lasers," *Applied Physics Letters*, vol. 88, no. 9, Article ID 091114, 2006.
- [34] G. Hasnain, K. Tai, L. Yang et al., "Performance of gain-guided surface emitting lasers with semiconductor distributed Bragg reflectors," *IEEE Journal of Quantum Electronics*, vol. 27, no. 6, pp. 1377–1385, 1991.

## Review Article

# Collective Micro-Optics Technologies for VCSEL Photonic Integration

V. Bardinal,<sup>1,2</sup> T. Camps,<sup>1,2</sup> B. Reig,<sup>1,2</sup> D. Barat,<sup>1,2</sup> E. Daran,<sup>1,2</sup> and J. B. Doucet<sup>1,2</sup>

<sup>1</sup> LAAS, CNRS, 7 Avenue du Colonel Roche, F-31077 Toulouse, France

<sup>2</sup> Université de Toulouse, UPS, INSA, INP, ISAE, LAAS, F-31077 Toulouse, France

Correspondence should be addressed to V. Bardinal, bardinal@laas.fr

Received 1 June 2011; Accepted 13 September 2011

Academic Editor: Rainer Michalzik

Copyright © 2011 V. Bardinal et al. This is an open access article distributed under the Creative Commons Attribution License, which permits unrestricted use, distribution, and reproduction in any medium, provided the original work is properly cited.

We describe the main recent technological approaches that associate micro-optical elements to VCSELs in order to control their output beam and to improve their photonic integration. These approaches imply either a hybrid assembly or a direct integration technique. They are compared with regards to their tolerance to alignment errors and to their ease of implementation onto arrays of devices at a wafer level. In particular, we detail the integration techniques we have developed for self-aligned polymer microlens fabrication for beam collimation and short distance beam focusing. Finally, designs to achieve active micro-optics or to exploit novel nanophotonic effects are discussed.

## 1. Introduction

Due to their unique advantages such as low threshold, parallel operation, symmetrical and circular beam, on-wafer test capability, and high bandwidth modulation, VCSELs now constitute strategic light sources for photonic applications, ranging from optical communications to instrumentation as well as optical storage or printing [1]. Current research on these devices concerns enhancement of emission performances by means of novel confinement designs, spectral extension to UV-visible and mid-infrared ranges, but also improvement of their photonic integration. For this latter issue, precise beam control is strongly in demand. Despite a limited far-field beam divergence, typically in the range from  $10^\circ$  to  $20^\circ$ , (half angle at  $1/e^2$ ), these laser diodes have indeed to be more and more associated with microoptical elements to improve the performance of the system in which they are inserted and to develop their use in novel application fields. In this paper, we review the main approaches recently proposed in the literature to combine free-space micro-optics with VCSEL arrays. In the first part, we sum up the main requirements for VCSEL beam shaping in function of the aimed application. In Sections 2 and 3, we review different fabrication methods for passive micro-optics integration on VCSELs, from hybrid report to direct fabrication on device

surface. In Section 4, we describe recent advances in the field of active micro-optics for VCSEL beam adaptation to a dynamic environment. Finally, we discuss on emerging approaches based on nanostructured integrated lenses.

## 2. Micro-Optics for VCSELs: Main Requirements

Up to now, the major market for VCSEL devices remains short-distance high-speed optical interconnects. In this area, key considerations concern coupling efficiency of VCSEL arrays to optical fibers. This efficiency depends strongly on the laser natural beam divergence and on two correlated parameters: VCSEL to fiber lateral alignment and VCSEL to fiber distance (Figure 1(a)). For instance, to keep a coupling efficiency as high as 85% in a silica multimode fiber, tolerances on lateral positioning do not exceed  $\pm 5 \mu\text{m}$  [2–4]. The efficiency also decreases with the VCSEL-fiber distance, with typical optical losses of  $\sim 3 \text{ dB}$  at  $500 \mu\text{m}$ . These last years, a strong effort has been put towards enhancing tolerances to vertical and lateral misalignments through passive alignment designs based on etched silicon V-grooves or indium flip-chip bonding. Nevertheless, insertion of a focusing microlens in the optical path between the VCSEL and the fiber could greatly

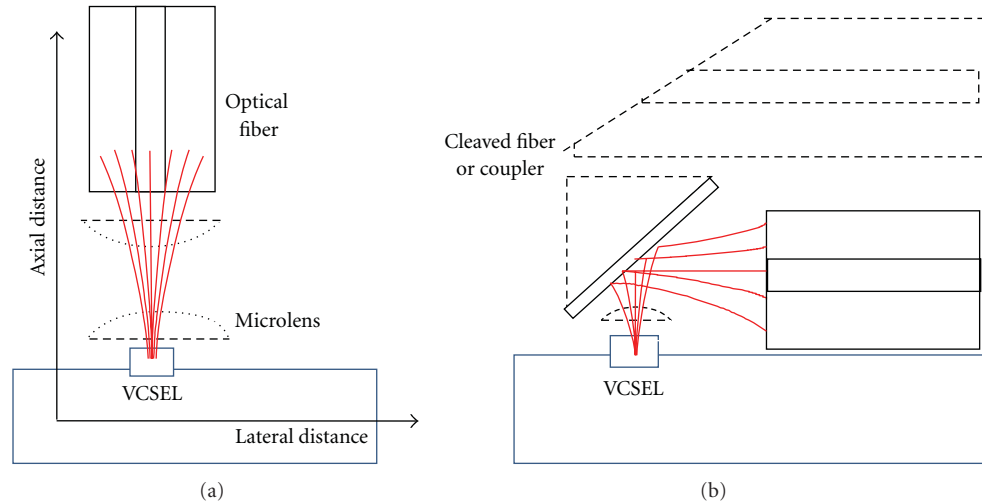


FIGURE 1: (a) Critical parameters for VCSEL-to-fiber coupling efficiency and possible configuration for lens insertion. (b) Schematic view of an horizontal VCSEL-to-fiber association through the use of a 45° tilted mirror or a TIR microprism for light deflection in the horizontal plane. Direct coupling with a 45°-ended fiber or coupler is also possible.

improve coupling tolerances. However, the technique to be used for lens fabrication should allow a simple alignment procedure and be of low cost for mass production.

Additionally, VCSEL beams emitting in the horizontal plane are strongly in demand to reduce packaging volume and costs, as well as to make easier intrachip and interchip communications with photodetectors. Therefore, out-of-plane coupling by means of a deflection of light at 90° is often preferred. This can be done using specific element such as 45° tilted micromirrors or TIR (total internal reflection) microprisms (Figure 1(b)). These elements can be also combined with a focusing microlens to improve light collection.

As for emerging applications such as sensing, VCSEL beam generally propagates in free space and its beam waist has to be precisely controlled to fit the detection area, at distances from few hundred of  $\mu\text{ms}$  [5, 6] to several centimeters [7]. Consequently, major requirements concern beam collimation with divergences of  $\sim 1^\circ$ . Beam focusing and beam steering at precise working distances are also necessary. For example, in reflection-based sensing microsystems, the laser light must be focused towards photodiodes located on the same chip. Besides, in VCSEL-based optical tweezers, focused beams from single-mode or multimodes devices are required [8]. More specific requirements concern the development of optical microprobes arrays for near-field scanning optical microscopy (NSOM) [9, 10] or high-density data storage and optical reading [11]. In these cases, a strong beam focusing is desired at short distances (micrometric range) thanks to high throughput microtips. Finally, active micro-optics instead of passive is more and more in demand to allow dynamic lateral beam steering as well as vertical beam scanning [12].

As indicated in Figure 2, collimation and focusing of the Gaussian beam emitted by a VCSEL are usually achieved using a refractive microlens (a), a Fresnel-like microlens, or a diffractive lens (b). Microtips are more suited for strong focusing at short distances (c). Diffractive optical elements (DOEs), fabricated with continuous relief, binary or multi-

level structures, present specific advantages for size and volume reduction as well as for achieving beam steering [13], but they are more complex to fabricate and wavelength dependent. Note that diffractive and refractive lenses can also be combined to minimize optical aberrations [14].

Whatever the aimed optical function, lens dimensions have to match with VCSEL arrays topology and to fit with the initial Gaussian beam properties of individual devices. To avoid cross-talk from adjacent beams, maximal diameters are limited by the VCSEL channel spacing (or pitch), which is generally equal to 250  $\mu\text{m}$ . For top-emitting devices, the maximum propagation distance of the beam in free space is thus more limited, for instance, it should not exceed 350  $\mu\text{m}$  for an initial beam divergence of 20° FWHM.

The vertical positioning of microoptical elements relatively to the laser is highly critical since it influences the whole system performance. Lenses can be positioned directly on the VCSEL output facet in both top- and bottom-emitting configurations. However, large numerical apertures ( $NA = f/D$ ,  $f$  being the focal length and  $D$  the lens diameter) are typically desired to achieve an optimal light coupling in the lens as well as low aberrations. Most used refractive lenses are plano-convex rather than ball lenses. Consequently, for top-emitting VCSELs, a thick transparent pedestal (dotted lines in Figure 2) has to be inserted to place the back focal plane of the lens in VCSEL plane. Depending on the used fabrication technique, pedestal and microoptical elements can be realized with the same or a different material. A trade-off has often to be found on the pedestal thickness in function of the pitch and of the initial and the aimed optical properties of the VCSEL beam.

The choice of the most suitable shape and dimension is not only a function of optical performance but also of fabrication considerations. Hence, tolerances to fabrication fluctuations or to alignment errors decrease when the lens is close to the surface. Moreover, microlens geometry can be easily optimized if the chosen fabrication technique is able

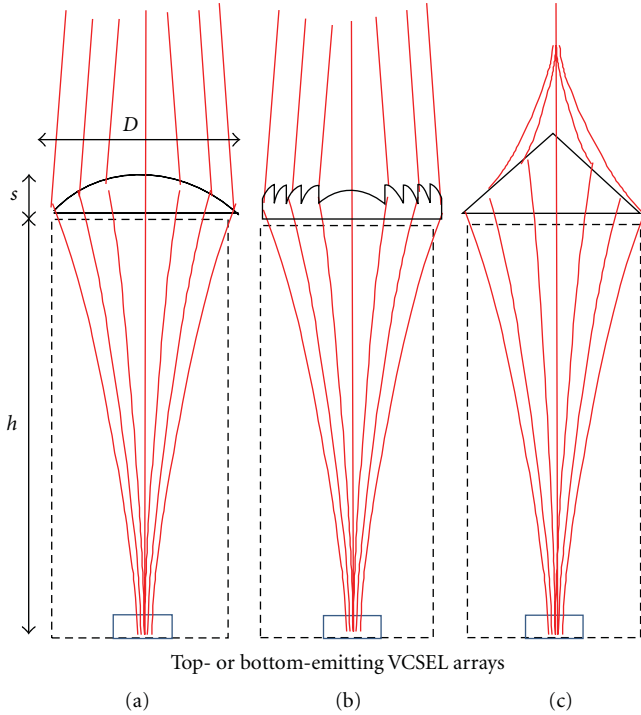


FIGURE 2: Main microoptical elements developed for VCSEL beam shaping: refractive lens (a), Fresnel-like or diffractive microlens (b), microtip (c). These objects can be fabricated either directly on the emitting surface (top or bottom) or above an intermediate transparent pedestal layer (dot line).

to control and to adjust separately pedestal height  $h$ , lens thickness (or sag)  $s$ , diameter  $D$ , and focal length. For refractive lenses, this optimization can be achieved using a simple Gaussian beam propagation tool. However, more sophisticated methods taking into account diffraction effects are often necessary for a precise optical design. Taking into account the optical feedback in the semiconductor microcavity laser due to the lens presence can be useful to control VCSEL modal properties and/or to render lasing operation robust to lens lateral misalignments [13, 15]. In the following sections, we review main techniques proposed for integration of such microoptical elements on VCSEL devices. First, a short description of hybrid assembly solutions is presented. Secondly, direct integration methods are detailed, ranging from modifications of the internal semiconductor laser structure to surface engineering techniques implying polymer-based technologies.

### 3. Passive Micro-Optics for VCSEL: Hybrid Assembly

To achieve VCSEL beam collimation, hybrid assembly of commercial glass or plastic lenslet is the most usual way (Figure 3). By assembling silica-based microlenses on 2D broad-area bottom-emitting devices, H. Chen et al. first reported beam divergences of  $1.6^\circ$  ( $1/e^2$ ) over  $1\text{ cm}^2$  [16]. Similar results were also demonstrated on top-emitting

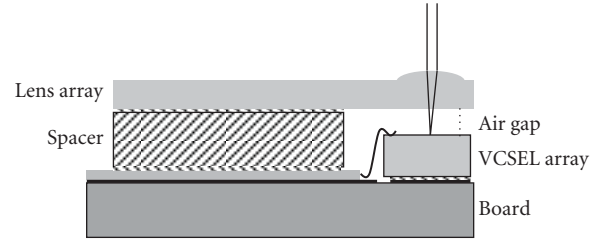


FIGURE 3: Basic principle of hybrid assembly of a lenslet array on a VCSEL array for beam collimation (reprint from [17], SPIE 2005).

VCSELs by mounting lens arrays with the convex side directed towards [2] or backwards [17] the laser. This method enables the use of “on the shelf” microlenses but implies tricky alignment steps to meet the requirements on vertical and lateral positioning relatively to the VCSEL sources. Usually, lateral alignment is controlled by the precision of the chip report equipment used (typically  $2\text{--}3\ \mu\text{m}$  for a Karl Suss FC-150 flip-chip bonder), whereas vertical positioning is highly sensitive to uncertainties on spacer and adhesive thicknesses. To improve alignment accuracy, S. Eitel et al. inserted additional Fresnel plates to use focusing alignment spots during the assembly step and reduced the beam divergence to  $5^\circ$  FWHM with a lateral alignment better than  $2\ \mu\text{m}$  [18].

For optical links applications, more sophisticated configurations were developed to combine beam shaping with a coupling in the horizontal plane (Figure 2(b)). One can cite, for example, passive alignment of micro-Fresnel lens arrays with side-mounted VCSELs [19]. A low-cost plastic multi-channel interconnection module including a lenslet and a high-quality microprism was also successfully developed for increasing misalignments tolerances to  $\pm 40\ \mu\text{m}$  (Figure 4) [20].

More recently, fabrication by inkjet printing of an elliptical mirror on a planar waveguide was reported for lateral coupling with a lensed VCSEL [21]. The use of polymer-lensed fibers instead of standard ones was also proposed to improve tolerances [22] as well as the polymer bonding of  $90^\circ$  connectors [23]. In the past several years, diverse assembly designs including a  $45^\circ$  end facet optical guide equipped with an integrated mirror close to the VCSEL surface were reported to achieve coupling and deflection with no need for a lens [24]. A fully flexible optoelectronic foil based on such direct coupling configuration was also recently demonstrated [25]. Despite significant advances on alignments tolerances, hybrid assembly remains sensitive to positioning errors and is not totally collective. Therefore, direct integration of microoptical elements on VCSEL surface can constitute a better solution for packaging cost reduction.

### 4. Direct Integration Techniques for Passive Micro-Optics on VCSEL

Direct integration methods can be classified in two types: the firsts imply a modification of the III-V semiconductor

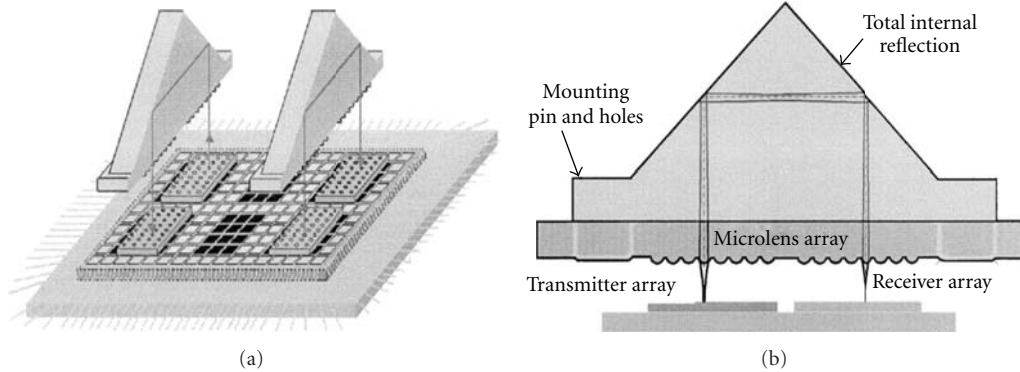


FIGURE 4: (a) Optical interconnection module (OIM) for intrachip interconnections. (b) Side view with a beam trace of the optical link (reprinted from [20], SPIE 2003).

structure; the seconds can be applied on the device surface using polymeric materials.

**4.1. Monolithic Integration with III-V Technology.** Monolithic lenses can be realized by modifying the semiconductor structure on both faces of the VCSEL wafer. A first way consists in etching the back side of the device. This was first reported in 1991 by K. Rastani et al. using selective ion milling of binary-phase diffractive lenses for focusing the emitted beam of bottom-emitting InGaAs-based VCSELs [26]. Reactive ion etching was also developed to fabricate refractive microlenses on bottom-emitting devices (Figure 5(a)). These studies enabled an efficient board-to-board interconnection with no need for any other external optics [27]. More recently, Wang et al. implemented refractive lenses fabrication on a densely packed 2D-VCSEL array using a one-step diffusion limited wet etching method. An emitted power of 1 W and a reduced divergence of  $6.6^\circ$  for each individual pixel were demonstrated with this technique [28]. Design and fabrication of hybrid microlens—both refractive and diffractive—to compensate aberrations and achieve athermalization was also proven, with the achievement of a very low beam divergence ( $0.3^\circ$  half-angle) (Figure 5(b)) [14]. Finally, GaAs-integrated microtips were also etched on the back surface of VCSELs for light-emitting cantilever microprobes realization (Figure 5(c)) [9]. The main drawback of these solutions is the restriction to bottom-emitting devices, due to optical absorption of GaAs substrate below 870 nm. Moreover, they are difficult to apply to devices that need a substrate thinning for thermal management purposes.

Application of similar etching techniques to top-emitting devices requires the insertion of an additional thick transparent material on the top surface. Epitaxial growth of a transparent semiconductor layer such as InGaP over the top mirror was investigated by S. Park et al. [29]. These authors reported a significant beam divergence reduction of oxide-confined VCSELs as well as a modal selection. Hybrid assembly of stacked GaN was also suggested for this goal [30]. An alternative solution was recently proposed by K.S. Chang et al.: it is based on an internal oxide lens fabrication by selective oxidation of a composition-graded AlGaAs layer above the

top-Bragg mirror (Figure 6) [31]. This approach is very attractive as it allows for a self-alignment of the oxide lens with the emission zone, although it requires high control of the epitaxial step. With this method, VCSEL beam focusing was demonstrated at distances of  $\sim 30 \mu\text{m}$ , limited by lens location close to the active zone. To conclude on this part, monolithic integration methods present the advantages of being powerful and collective. However, most of them are not applicable to top-emitting devices or are still technically challenging for mass production.

**4.2. Surface Engineering Using Polymer Materials.** Microlens fabrication using polymer materials has been a key topic in micro-optics for more than 15 years because of their low cost and their ease of use [13, 32, 33]. Research is currently very active in this field, and many fabrication techniques are possible: thermal resist reflow, deep lithography by protons, LIGA process, photopolymerization, inkjet printing, UV imprint, laser ablation, direct writing by electronic beam or laser beam. Among all possible methods, those compatible with a postprocess treatment are the most attractive for VCSEL devices as they allow for a direct integration at a wafer scale.

**4.2.1. Self-Assembly by Thermal Reflow.** A simple way to fabricate refractive microlens arrays is to use resist thermal reflow. This self-assembly technique is based on the patterning of cylindrical resist posts by photolithography, followed by a controlled melting. This leads to the formation of hemispherical lenses owing to surface tension effects. The final lens dimensions depend on diameter and height of the initial posts and on the wettability properties of the substrate. Fabrication of sags of up to  $\sim 20 \mu\text{m}$  is possible, as well as achievement of high optical quality lens due to low surface roughness. Application to VCSELs was thus successfully performed using different types of resists, such as polyimide, on the back surface for beam collimation [34] or on top-emitting devices surfaces for beam focusing [35]. This method was also applied to the fabrication of  $\mu$ -lensed optically pumped fiber VCSELs using a UV-curable epoxy resist [36]. It is noteworthy that it can be also combined to a dry etching technique

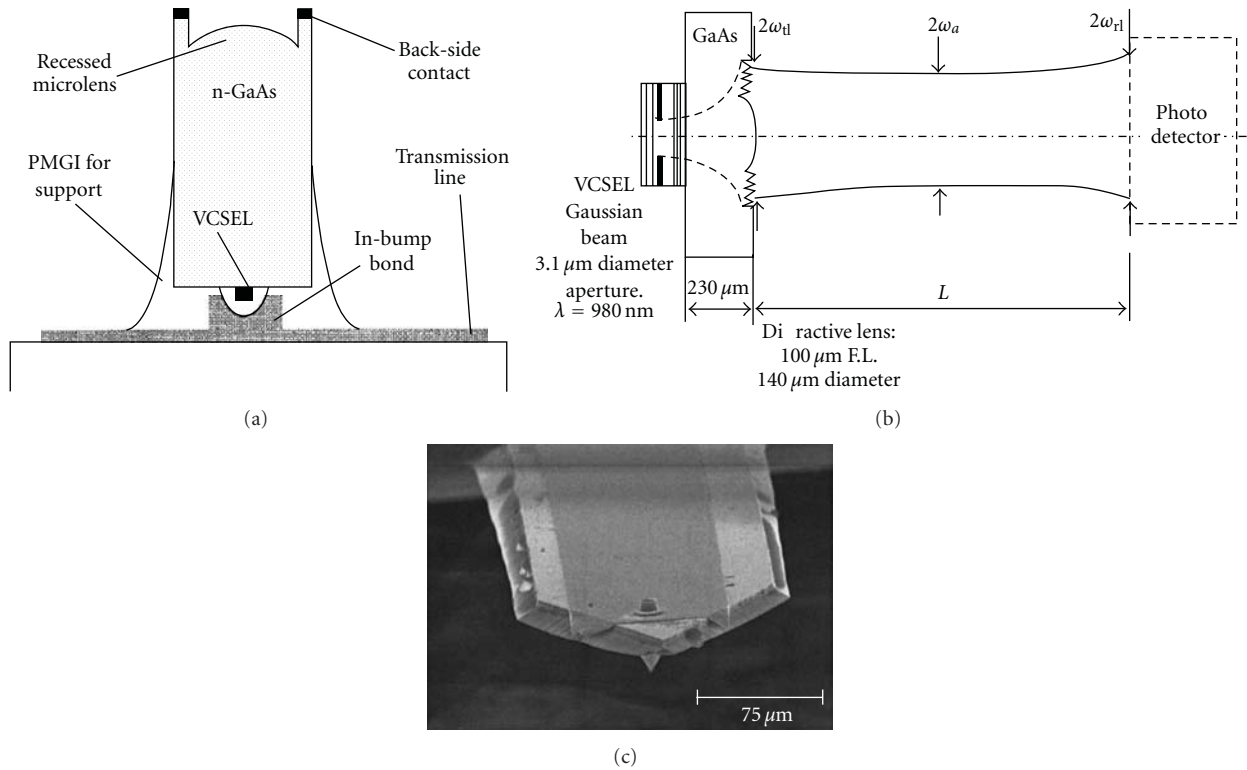


FIGURE 5: Lens fabrication by etching the back surface of a bottom-emitting VCSEL (a) refractive lens [27], (b) hybrid (refractive + diffractive) lens [14], (c) VCSEL with an integrated GaAs microtip (bottom) for light emitting cantilever microprobe [9] (reprinted, resp., from [27] OSA 2004, [14] IEEE 2001, [9] American Institute of Physics 2000).

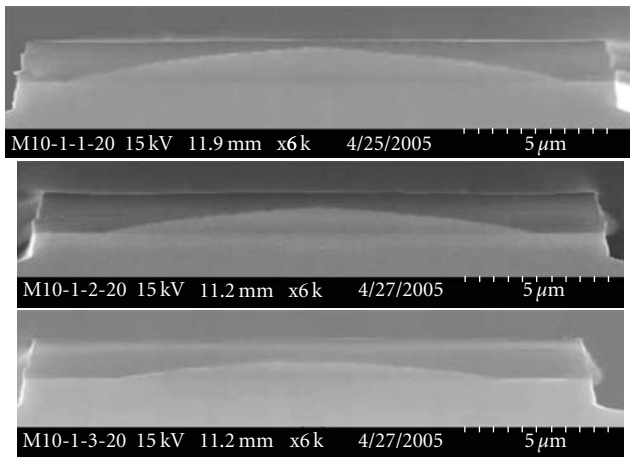


FIGURE 6: Cross-sectional SEM (scanning electron microscopy) images of 20- $\mu\text{m}$ -wide stripe mesa after oxidation of composition-graded digital alloy Al Ga As. Oxidation time: (a) 20, (b) 30, and (c) 45 min for a self-aligned oxide integrated lens (reprinted from [31], IEEE 2006).

in order to transfer lens patterns in inorganic materials [18]. This simple technology is convenient for collective integration at a postprocessing stage but requires a thermal treatment which can be conflicting with prior fabrication of a polymer pedestal. Consequently, development of alternative self-assembly methods that would not require any thermal

step, such as localized hydrophilic/hydrophobic treatments, could give more degrees of freedom in lens geometry [37].

**4.2.2. Replication Methods.** Replication methods are of major interest for the direct integration of micro-optics on VCSELs at a wafer scale. Several techniques are possible either for original mould fabrication (dry etching, e-beam, or laser writing) than for replication process: injection molding, hot embossing, or UV casting with transparent moulds. It can be applied to liquid polymers or to more robust materials such as organically modified sol-gel. Moreover, this technique enables thick pedestal fabrication for accurate lens vertical positioning. Collective replication of refractive as well as diffractive elements was successfully demonstrated on multi-mode VCSEL wafers using sol-gel materials (Figure 7) [38]. Note that this technique is better suited for mass production than for custom-made prototyping, since the lens mould has to be modified in case the real numerical aperture of the devices does not match exactly with the aimed value.

**4.2.3. SU-8 Technology.** Microoptical fabrication involving epoxy-based negative-tone SU-8 photoresist is currently in strong development, as it leads to the definition of high-aspect-ratio patterns with vertical sidewalls using a single photolithography step. For instance, SU-8 was used to fabricate integrated guiding holes for coupling plastic optical fibers to VCSELs [39]. Three-dimensional SU-8 microprisms

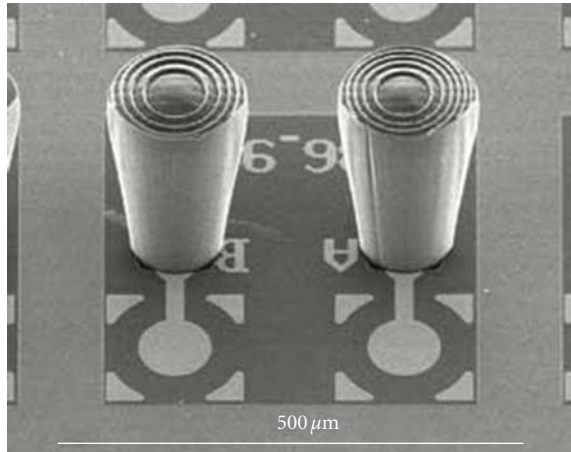


FIGURE 7: SEM image of a sol-gel diffractive lens replicated on VCSEL arrays (reprinted from [38], SPIE 2004).

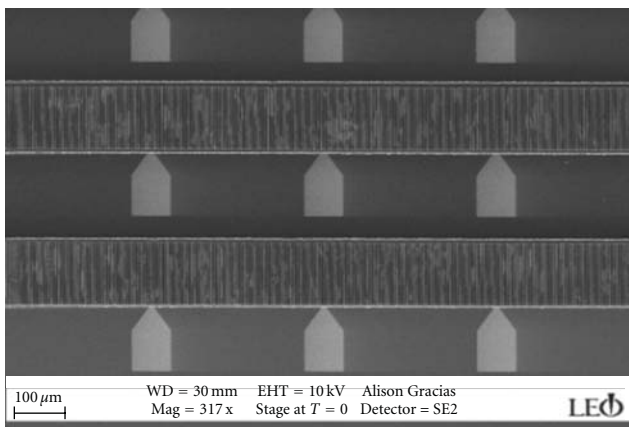


FIGURE 8: SEM images of a DOE (diffractive optical element) replicated on SU-8 pedestals on VCSEL arrays for beam steering (reprinted from [42], SPIE 2008)

were also directly integrated on VCSEL surface by inclined exposure photolithography for in-plane optical coupling [40]. Moreover, SU-8 micropisms were fabricated by electron beam grey-scale lithography for static VCSEL beam steering [41]. Additionally, wafer-scale replication of DOEs phase-shift gratings on SU-8 rectangular pedestals was reported for the same application [42] (Figure 8). Foremost, as reported hereafter, SU-8 properties were successfully combined to local polymer dispensing methods for accurate VCSEL beam shaping.

**4.2.4. Local Dispensing Methods.** Liquid polymer drop-on-demand techniques are highly competitive for micro-optics fabrication. They indeed offer numerous advantages such as high flexibility, wafer-level and maskless technology, high surface quality, and compatibility with nonplanar process. In particular, inkjet printing ensures a wide range of lens shapes and numerical apertures by simply modifying the number of printed polymer droplets [3, 43]. An additional advantage for VCSELs is to enable lens fabrication on thick

polymer pedestals for vertical positioning. For instance, by inkjet printing a UV-curable polymer on the top of a thick “bank,” previously fabricated with a higher-volume dispensing method, Y. Ishii et al. succeeded to improve VCSEL-to-fiber coupling tolerances up to  $\pm 2$  mm for axial misalignments and  $\pm 10 \mu\text{m}$  for lateral ones [4]. As for lens lateral positioning issue, it was solved by A. Nallani et al. [44] by associating inkjet printing with SU-8 cylindrical pedestals (Figure 9(a)). These authors demonstrated a precise control of lens dimensions owing to a liquid self-positioning on the SU-8 pillar (Figure 9(b)). They successfully applied this method for VCSEL beam collimation and for VCSEL beam focusing in optical fibers. More recently, we have exploited the same self-centering properties using an alternative low-volume deposition technique based on a robotized silicon-cantilever spotter (Figure 9(c)) [45]. With this low-cost contact method, fabrication of small  $f$ -number lenses is also possible. Moreover, in our case, deposition conditions are only ruled by surface tension effects, leading to a constant dispensed volume on the SU-8 pedestal surface, that is to say, to a stable lens contact angle. Thanks to these properties, we have demonstrated that VCSEL beam divergence can be tailored by adjusting only pedestal diameter during the SU-8 photolithography step. The efficiency of our approach has been demonstrated with divergence reduction of 850 nm single-mode devices to values as low as  $1.2^\circ$  (half-angle at  $1/e^2$ ) [46].

**4.2.5. Self-Writing by NIR Photopolymerization.** To go further and achieve a perfect alignment with the emitted beam, the integrated microlens should be ideally created by the laser source itself. With this aim, we have exploited novel near infra-red (NIR) photopolymers [47] to fabricate collectively microoptical elements by self-guided photopolymerization (Figure 10) [48]. The main advantages of this promising method are to require a single fabrication step and to be compatible with postprocess at a wafer-scale and with post-packaging stages. We have applied it to 760 nm emitting single-mode VCSELs to fabricate self-aligned microtips for strong laser beam focusing at short distances ( $\sim 1 \mu\text{m}$ ). These devices could be used in novel miniaturized near-field optical probes or for compact optical storage heads. Current work on this method now concerns the increase of focal length and the optimization of lens geometry for beam collimation. Extension to longer wavelengths is also under study.

A comparison of the main approaches reported in the literature or explored by the authors for integrating microoptical elements on VCSEL arrays by means of collective and self-aligned techniques can be found in Table 1.

## 5. Towards Active Micro-Optics on VCSELs

The possibility to dynamically control VCSEL beam shape or VCSEL beam axis during laser operation constitutes a significant advantage for increasing device functionalities and systems performances. This could for instance give birth to novel types of reconfigurable optical routers or to miniaturized vertical scanners. To fulfill this goal, several silicon-based

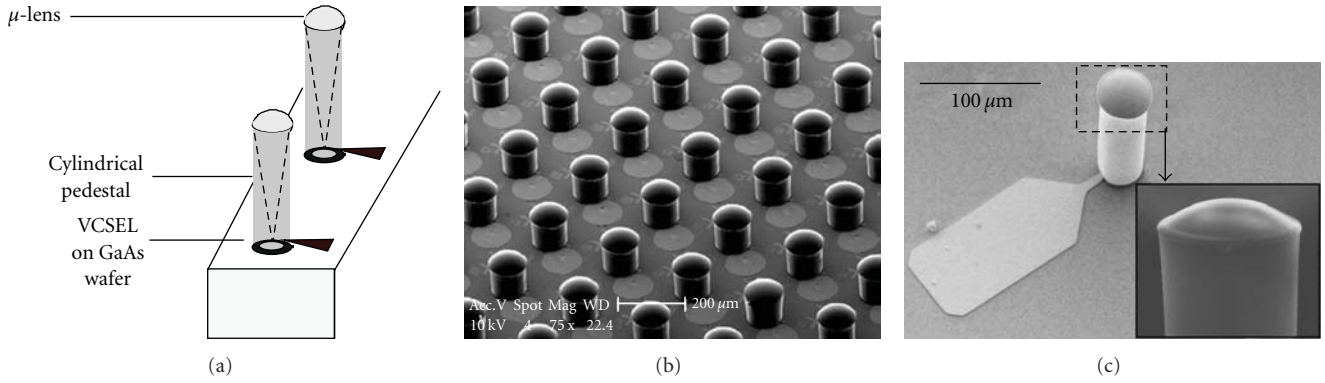


FIGURE 9: (a) Principle of lens integration on VCSEL wafer using a local dispensing method coupled to high aspect ratio cylindrical SU-8 pedestals: the low-viscosity polymer is self-centered on the top of the pedestal owing to surface tension properties. (b) SEM images of inkjet-printed lenses (reprinted from [44], SPIE 2005). (c) SEM image of a spotted lens. Inset: SEM image of a microlens self-centered on SU-8 cylindrical pedestal (reprinted from [46], IEEE 2010).

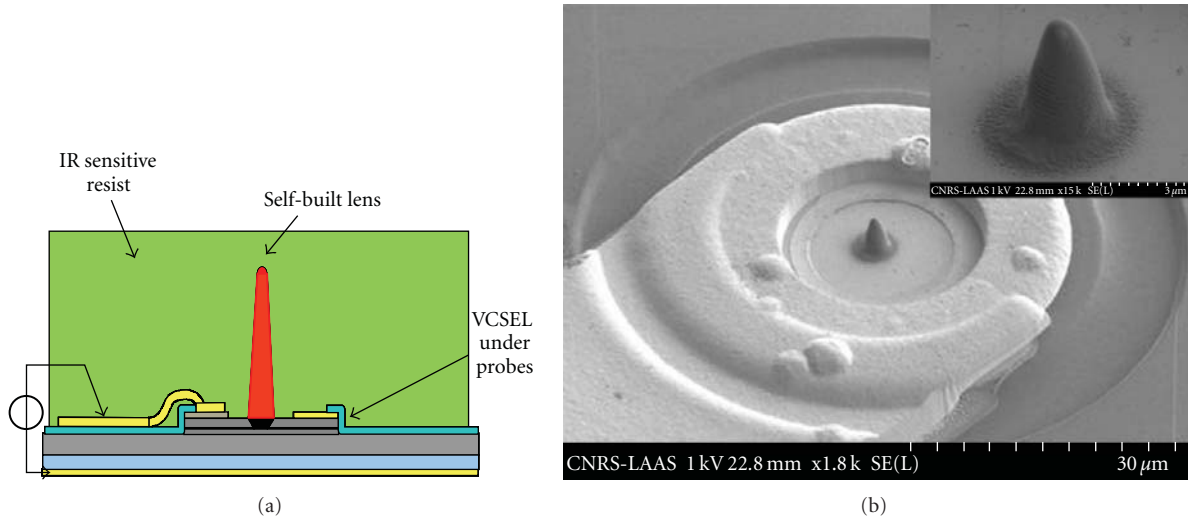


FIGURE 10: (a) Principle of lens self-writing using NIR photoresists. (b) SEM image of a microtip self-written at 760 nm for beam focusing at short distances (reprinted from [48], American Institute of Physics 2010).

TABLE 1: Summary of main approaches proposed in the literature for integrating microlens on VCSEL devices. The three last columns concern polymer-based technologies.

Integration method	Hybrid assembly	Monolithic integration	UV photolithography	Replication	NIR self-writing
Lateral alignment precision	~2-3 $\mu\text{m}$ (flip-chip ~1 $\mu\text{m}$ )	~1-2 $\mu\text{m}$ (Top-oxidation = self-aligned)	~1 $\mu\text{m}$	~1 $\mu\text{m}$	Self-aligned
Vertical positioning	Controlled by spacer and adhesive thicknesses	Controlled by semiconductor process fabrication	Controlled by spin coating conditions	Controlled by molding conditions	Controlled by exposure conditions
Wafer-scale process	No	Yes	Yes	Yes	Yes
Applicable after packaging	Yes	No	No	No	Yes
References	[2, 16–21]	[14, 26–31]	[3, 4, 34–36, 44, 46]	[38, 42]	[48]

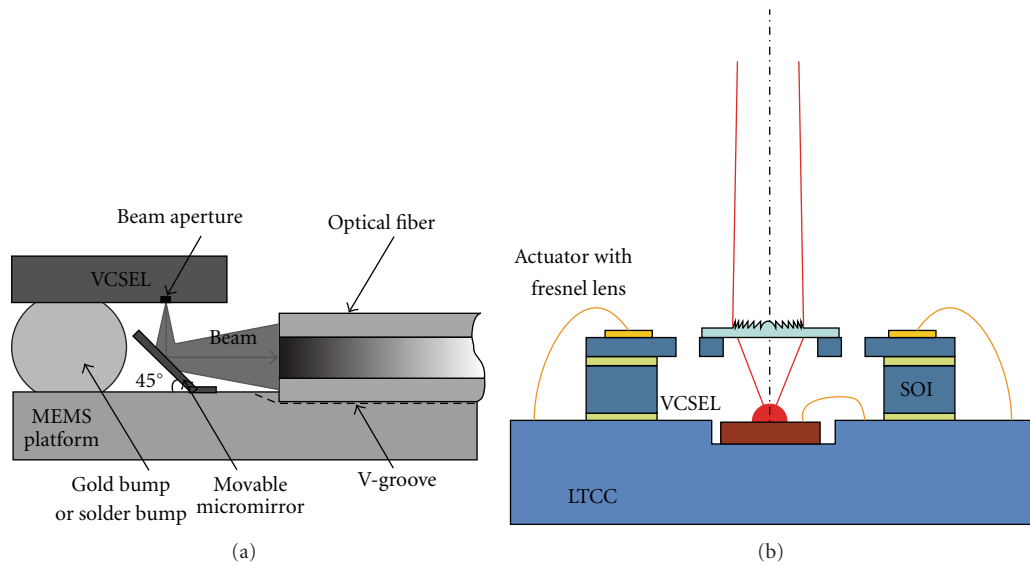


FIGURE 11: (a) Hybrid assembly of a movable silicon 45°-micromirror for VCSEL-fiber active alignment (reprinted from [52] Elsevier 2003). (b) MEMS-based VCSEL including a diffractive lens on a reported silicon MEMS for optical beam steering (reprinted from [53] Elsevier 2008).

MEMSs (micro-electrical mechanical systems) have been associated to VCSEL devices by means of hybrid assembly techniques [49, 50]. Up to now, most attempts have concerned top-emitting devices and beam steering applications. For instance, flip-chip bonding of a silicon XY translatable plate integrating a polymer refractive lens controlled by electrothermal actuators was assembled on a  $4 \times 4$  VCSEL array for lens off-axis dynamic displacement [51]. Using the same actuation principle, a movable silicon 45°-micromirror was also reported for VCSEL-to-fiber active alignment with alignment tolerances up to  $25 \mu\text{m}$  (Figure 11(a)) [52]. More recently, K. Hedsten et al. reported lateral deflections up to  $\sim 10 \mu\text{m}$  with applied voltages of  $\sim 70 \text{V}$  by assembly of an electrostatic silicon MEMS including a Fresnel lens fabricated by a hot embossing collective method (Figure 11(b)) [53].

Design of such MEMS with dimensions compatible with VCSEL pitch remains quite challenging. Moreover, as mentioned before, direct integration fabrication methods are often preferred to avoid tricky assembly steps. Recent progress on tunable lasers technology could be inspiring to solve these issues. In such devices, a vertical shift in the optical path is achieved thanks to a micromachined sacrificial layer in the semiconductor microcavity [54–56] or owing to an intracavity liquid crystal layer [57]. These geometries are not directly usable for active beam shaping but derivative designs could be conceived. For instance, integrated SU-8-based optical MEMS could meet active beam shaping requirements [58].

## 6. Conclusions and Future Prospects

The main needs for VCSEL beam shaping have been presented, along with collective methods for passive and active micro-optics integration on VCSEL arrays. Among possible solutions, the self-aligned and postprocessing ones, and the

ones applicable to all types of VCSELs and suitable with mass production have been highlighted. In particular, direct fabrication of polymer microlens on VCSELs surface was found of major interest. Several demonstrations based either on thermal reflow, molding methods or dispensing techniques were reported. To our knowledge, most advanced results were obtained using localized dispensing methods such as microjet printing or microspotting. These methods open indeed the possibility to adjust lens dimensions during the fabrication process. Moreover, they lead to a good surface morphology and to high optical quality, since lens formation originates from surface tension of liquid polymer droplets. Furthermore, combination of such methods with cylindrical SU-8 transparent pedestals allows for lens self-centering with an alignment accuracy provided by photolithography precision ( $\sim 1 \mu\text{m}$ ). To achieve a perfect alignment, we have demonstrated that the use of NIR photopolymers, sensitive at the laser wavelength, could be a very promising tool. Main issues for this approach now concern lens shape control for beam collimation as well as spectral range extension. Finally, VCSEL association with optical MEMS in view of active beam shaping has been discussed, as well as wafer-scale integration abilities of such microsystems.

Prospectively, several designs involving e-beam lithography have been recently proposed for VCSEL output beam profiling. In particular, introduction of a photonic crystal (PC) in the top mirror of a VCSEL not only achieves a reproducible singlemode operation but also enables a beam divergence reduction to  $5.5^\circ$ , owing to the weakly guiding waveguide characteristic of the PC [59]. Interest of photonic crystals was also proven for 2D electronically driven beam steering of in-phase coupled VCSELs arrays [60]. A narrow beam divergence of  $3.2^\circ$  was also demonstrated in a two-dimensional petal-shaped holey VCSEL thanks to a suited refractive index profile in the holey region and near the optical

aperture [61]. In addition, the use of nonperiodic high-contrast subwavelength mirrors (SWG) proposed recently to replace thick Bragg mirrors in tunable MEMS-VCSEL [62] is considered as a future solution for active phase front correction and dynamic focusing [63, 64]. Nonetheless, precise fabrication of these nanostructures using low-cost and collective techniques, such as nanoimprint UV lithography, is still challenging, as well as their association to integrated MEMS.

## Acknowledgments

The authors would like to thank Corinne Vergnenègre for helping in optical modeling, Christophe Levallois for his work on device collimation, Thierry Leichlé and Jean-Bernard Pourciel for micromanipulations, Olivier Soppera (IS2M-CNRS, Mulhouse, France) for fruitful collaboration on NIR photopolymerization, Guilhem Almuneau for assistance in oxide-confined VCSEL fabrication, Franck Carcenac for technical assistance on SEM measurements, Chantal Fontaine and Liviu Nicu for fruitful discussions, as well as the partners of the Optonanogen IST STREP project for initiating these studies. The French National Research Agency (ANR) is gratefully acknowledged for financial support (ANR-09-BLAN-0168-01) as well as Region Midi-Pyrénées (FIAB SU-8 project).

## References

- [1] K. Iga, "Vertical-cavity surface-emitting laser: its conception and evolution," *Japanese Journal of Applied Physics*, vol. 47, no. 1, pp. 1–10, 2008.
- [2] G. Kim, X. Han, and R. T. Chen, "Crosstalk and interconnection distance considerations for board-to-board optical interconnects using 2-D VCSEL and microlens array," *IEEE Photonics Technology Letters*, vol. 12, no. 6, pp. 743–745, 2000.
- [3] A. K. Nallani, T. Chen, D. J. Hayes, W. S. Che, and J. B. Lee, "A method for improved VCSEL packaging using MEMS and ink-jet technologies," *Journal of Lightwave Technology*, vol. 24, no. 3, pp. 1504–1512, 2006.
- [4] Y. Ishii, S. Koike, Y. Arai, and Y. Ando, "Hybrid integration of polymer microlens with VCSEL using drop-on-demand technique," in *Optoelectronic Interconnects VII; Photonics Packaging and Integration II*, vol. 3952 of *Proceedings of SPIE*, pp. 364–374, January 2000.
- [5] E. Thrush, O. Levi, W. Ha et al., "Integrated semiconductor vertical-cavity surface-emitting lasers and PIN photodetectors for biomedical fluorescence sensing," *IEEE Journal of Quantum Electronics*, vol. 40, no. 5, pp. 491–498, 2004.
- [6] L. M. Lechuga, J. Tamayo, M. Alvarez et al., "A highly sensitive microsystem based on nanomechanical biosensors for genomics applications," *Sensors and Actuators B*, vol. 118, no. 1-2, pp. 2–10, 2006.
- [7] J. Perchoux and T. Bosch, "Multimode VCSELs for self-mixing velocity measurements," in *Proceedings of the 6th IEEE Conference on SENSORS*, pp. 419–422, October 2007.
- [8] R. Michalzik, A. Kroner, and F. Rinaldi, "VCSEL-based optical trapping for microparticle manipulation," in *Vertical-Cavity Surface-Emitting Lasers XIII*, K. D. Choquette and C. Lei, Eds., vol. 7229 of *Proceedings of SPIE*, pp. 722908-1–722908-13, 2009.
- [9] S. Heisig, O. Rudow, and E. Oesterschulze, "Scanning near-field optical microscopy in the near-infrared region using light emitting cantilever probes," *Applied Physics Letters*, vol. 77, no. 8, pp. 1071–1073, 2000.
- [10] D. Heinis, C. Gorecki, C. Bringer et al., "Miniaturized scanning near-field microscope sensor based on optical feedback inside a single-mode oxide-confined vertical-cavity surface-emitting laser," *Japanese Journal of Applied Physics 2*, vol. 42, no. 12 A, pp. L1469–L1471, 2003.
- [11] K. Goto, Y. J. Kim, S. Mitsugi, K. Suzuki, K. Kurihara, and T. Horibe, "Microoptical two-dimensional devices for the optical memory head of an ultrahigh data transfer rate and density system using a vertical cavity surface emitting laser (VCSEL) array," *Japanese Journal of Applied Physics 1*, vol. 41, no. 7 B, pp. 4835–4840, 2002.
- [12] C. Gorecki, L. Nieradko, S. Bargiel et al., "On-chip scanning confocal microscope with 3D MEMS scanner and VCSEL feedback detection," in *Proceedings of the 4th International Conference on Solid-State Sensors, Actuators and Microsystems (TRANSDUCERS '07)*, pp. 2561–2564, June 2007.
- [13] H. Zappe, *Fundamentals of Micro-Optics*, Cambridge University Press, 2010.
- [14] Y. Fu, "Integration of microdiffractive lens with continuous relief with vertical-cavity surface-emitting lasers using focused ion beam direct milling," *IEEE Photonics Technology Letters*, vol. 13, no. 5, pp. 424–426, 2001.
- [15] I. S. Chung, P. Debernardi, Y. T. Lee, and J. Mørk, "Transverse-mode-selectable microlens vertical-cavity surface-emitting laser," *Optics Express*, vol. 18, no. 5, pp. 4138–4147, 2010.
- [16] H. L. Chen, D. Francis, T. Nguyen, W. Yuen, G. Li, and C. Chang-Hasnain, "Collimating diode laser beams from a large-area VCSEL-array using microlens array," *IEEE Photonics Technology Letters*, vol. 11, no. 5, pp. 506–508, 1999.
- [17] C. Vergnenègre, T. Camps, V. Bardinal, C. Bringer, C. Fontaine, and A. Muñoz-Yagüe, "Integrated optical detection subsystem for functional genomic analysis biosensor," in *Photonics Applications in Biosensing and Imaging*, vol. 5969 of *Proceedings of SPIE*, pp. 596912.1–596912.10, 2005.
- [18] S. Eitel, S. J. Fancey, H. P. Gauggel, K. H. Gulden, W. Bächtold, and M. R. Taghizadeh, "Highly uniform vertical-cavity surface-emitting lasers integrated with microlens arrays," *IEEE Photonics Technology Letters*, vol. 12, no. 5, pp. 459–461, 2000.
- [19] S. S. Lee, L. Y. Lin, K. S. J. Pister, M. C. Wu, H. C. Lee, and P. Grodzinski, "Passively aligned hybrid integration of  $8 \times 1$  micromachined micro-Fresnel lens arrays and  $8 \times 1$  vertical-cavity surface-emitting laser arrays for free-space optical interconnect," *IEEE Photonics Technology Letters*, vol. 7, no. 9, pp. 1031–1033, 1995.
- [20] C. Debaes, M. Vervaeke, V. Baukens et al., "Low-cost microoptical modules for MCM level optical interconnections," *IEEE Journal on Selected Topics in Quantum Electronics*, vol. 9, no. 2, pp. 518–530, 2003.
- [21] H. S. Lee, I. Park, K. S. Jeon, and E. H. Lee, "Fabrication of micro-lenses for optical interconnection using micro ink-jetting technique," *Microelectronic Engineering*, vol. 87, no. 5-8, pp. 1447–1450, 2010.
- [22] J. K. Kim, D. U. Kim, B. H. Lee, and K. Oh, "Arrayed multimode fiber to VCSEL coupling for short reach communications using hybrid polymer-fiber lens," *IEEE Photonics Technology Letters*, vol. 19, no. 13, pp. 951–953, 2007.
- [23] D. W. Kim, T. W. Lee, M. H. Cho, and H. H. Park, "High-efficiency and stable optical transmitter using VCSEL-direct-bonded connector for optical interconnection," *Optics Express*, vol. 15, no. 24, pp. 15767–15775, 2007.

- [24] A. Suzuki, Y. Wakazono, S. Suzuki et al., "High optical coupling efficiency using 45°-ended fibre for low-height and low-cost optical interconnect modules," *Electronics Letters*, vol. 44, no. 12, pp. 724–725, 2008.
- [25] E. Bosman, G. Van Steenberge, I. Milenkovic et al., "Fully flexible optoelectronic foil," *IEEE Journal on Selected Topics in Quantum Electronics*, vol. 16, no. 5, Article ID 5404348, pp. 1355–1362, 2010.
- [26] K. Rastani, M. Orenstein, E. Kapon, and A. C. Von Lehmen, "Integration of planar Fresnel microlenses with vertical-cavity surface-emitting laser arrays," *Optics Letters*, pp. 919–921, 1991.
- [27] E. M. Strzelecka, D. A. Louderback, B. J. Thibeault, G. B. Thompson, K. Bertilsson, and L. A. Coldren, "Parallel free-space optical interconnect based on arrays of vertical-cavity lasers and detectors with monolithic microlenses," *Applied Optics*, vol. 37, no. 14, pp. 2811–2821, 1998.
- [28] Z. Wang, Y. Ning, Y. Zhang et al., "High power and good beam quality of two-dimensional VCSEL array with integrated GaAs microlens array," *Optics Express*, vol. 18, no. 23, pp. 23900–23905, 2010.
- [29] S. H. Park, Y. Park, H. Kim et al., "Microlensed vertical-cavity surface-emitting laser for stable single fundamental mode operation," *Applied Physics Letters*, vol. 80, no. 2, p. 183, 2002.
- [30] C. H. Hou, C. C. Chen, B. J. Pong et al., "GaN-based stacked micro-optics system," *Applied Optics*, vol. 45, no. 11, pp. 2396–2398, 2006.
- [31] K. S. Chang, Y. M. Song, and Y. T. Lee, "Microlens fabrication by selective oxidation of composition-graded digital alloy AlGaAs," *IEEE Photonics Technology Letters*, vol. 18, no. 1, pp. 121–123, 2006.
- [32] H. P. Herzig, *Micro-Optics, Elements, Systems and Applications*, Taylor and Francis, London, UK, 1997.
- [33] H. Ottevaere, R. Cox, H. P. Herzig et al., "Comparing glass and plastic refractive microlenses fabricated with different technologies," *Journal of Optics A*, vol. 8, no. 7, pp. S407–S429, 2006.
- [34] O. Blum, S. P. Kilcoyne, M. E. Warren et al., "Vertical-cavity surface-emitting lasers with integrated refractive microlenses," *Electronics Letters*, vol. 31, no. 1, pp. 44–45, 1995.
- [35] A. Kroner, I. Kardosh, F. Rinaldi, and R. Michalzik, "Towards VCSEL-based integrated optical traps for biomedical applications," *Electronics Letters*, vol. 42, no. 2, pp. 93–94, 2006.
- [36] N. Laurand, C. L. Lee, E. Gu, J. E. Hastie, S. Calvez, and M. D. Dawson, "Microlensed microchip VECSEL," *Optics Express*, vol. 15, no. 15, pp. 9341–9346, 2007.
- [37] D. M. Hartmann, S. C. Esener, and O. Kibar, "Precision fabrication of polymer microlens arrays," United States patent 7.771, 630 B2, 2010.
- [38] C. Gimkiewicz, M. Moser, S. Obi et al., "Wafer-scale replication and testing of micro-optical components for VCSELs," in *Micro-Optics, VCSELs, and Photonic Interconnects*, vol. 5453 of *Proceedings of SPIE*, pp. 13–26, April 2004.
- [39] T. Ouchi, A. Imada, T. Sato, and H. Sakata, "Direct coupled packaging of plastic optical fibers on vertical-cavity surface-emitting lasers with patterned polymer guide holes," *Japanese Journal of Applied Physics A*, vol. 41, no. 7 B, pp. 4813–4816, 2002.
- [40] K. Y. Hung, H. T. Hu, and F. G. Tseng, "Application of 3D glycerol-compensated inclined-exposure technology to an integrated optical pick-up head," *Journal of Micromechanics and Microengineering*, vol. 14, no. 7, pp. 975–983, 2004.
- [41] C. Reardon, A. Di Falco, K. Welna, and T. Krauss, "Integrated polymer microprisms for free space optical beam deflecting," *Optics Express*, vol. 17, no. 5, pp. 3424–3428, 2009.
- [42] U. A. Gracias, N. Tokranova, and J. Castracane, "SU8-based static diffractive optical elements: wafer-level integration with VCSEL arrays," in *Photonics Packaging, Integration, and Interconnects VIII*, vol. 6899 of *Proceedings of SPIE*, p. 68990J, January 2008.
- [43] D. J. Hayes, M. E. Grove, D. B. Wallace, T. Chen, and W. R. Cox, "Ink-jet printing in the manufacturing of electronics, photonics, and displays," in *Nanoscale Optics and Applications*, vol. 4809 of *Proceedings of SPIE*, pp. 94–99, July 2002.
- [44] A. Nallani, T. Chen, J. B. Lee, D. Hayes, and D. Wallace, "Wafer level optoelectronic device packaging using MEMS," in *Smart Sensors, Actuators, and MEMS II*, vol. 5836 of *Proceedings of SPIE*, pp. 116–127, May 2005.
- [45] C. Levallois, V. Bardinal, T. Camps et al., "VCSEL collimation using self-aligned integrated polymer microlenses," in *Micro-Optics 2008*, vol. 6992 of *Proceedings of SPIE*, p. 69920W, April 2008.
- [46] V. Bardinal, B. Reig, T. Camps et al., "Spotted custom lenses to tailor the divergence of vertical-cavity surface-emitting lasers," *IEEE Photonics Technology Letters*, vol. 22, no. 21, Article ID 5560728, pp. 1592–1594, 2010.
- [47] O. Soppera, C. Turck, and D. J. Loughnot, "Fabrication of micro-optical devices by self-guiding photopolymerization in the near IR," *Optics Letters*, vol. 34, no. 4, pp. 461–463, 2009.
- [48] V. Bardinal, B. Reig, T. Camps et al., "A microtip self-written on a vertical-cavity surface-emitting laser by photopolymerization," *Applied Physics Letters*, vol. 96, no. 5, Article ID 051114, 2010.
- [49] L. Fan, M. C. Wu, H. C. Lee, and P. Grodzinski, "Dynamic beam switching of vertical-cavity surface-emitting lasers with integrated optical beam routers," *IEEE Photonics Technology Letters*, vol. 9, no. 4, pp. 505–507, 1997.
- [50] M. C. Wu, L.-Y. Lin, S.-S. Lee, and K. S. J. Pister, "Micromachined free-space integrated micro-optics," *Sensors and Actuators A*, vol. 50, no. 1-2, pp. 127–134, 1995.
- [51] A. Tuantranont, V. M. Bright, J. Zhang, W. Zhang, J. A. Neff, and Y. C. Lee, "Optical beam steering using MEMS-controllable microlens array," *Sensors and Actuators A*, vol. 90, no. 3, pp. 363–372, 2001.
- [52] K. Ishikawa, J. Zhang, A. Tuantranont, V. M. Bright, and Y. C. Lee, "An integrated micro-optical system for VCSEL-to-fiber active alignment," *Sensors and Actuators A*, vol. 103, no. 1-2, pp. 109–115, 2003.
- [53] K. Hedsten, J. Melin, J. Bengtsson et al., "MEMS-based VCSEL beam steering using replicated polymer diffractive lens," *Sensors and Actuators A*, vol. 142, no. 1, pp. 336–345, 2008.
- [54] C. J. Chang-Hasnain, "Tunable VCSEL," *IEEE Journal on Selected Topics in Quantum Electronics*, vol. 6, no. 6, pp. 978–987, 2000.
- [55] M. Maute, F. Riemenschneider, G. Böhm et al., "Micro-mechanically tunable long wavelength VCSEL with buried tunnel junction," *Electronics Letters*, vol. 40, no. 7, pp. 430–431, 2004.
- [56] B. Kögel, A. Abbaszadehbanaeiyan, P. Westbergh et al., "Integrated tunable VCSELs with simple MEMS technology," in *Proceedings of the 22nd IEEE International Semiconductor Laser Conference (ISLC '10)*, pp. 26–30, 2010.
- [57] O. Castany, L. Dupont, A. Shuaib, J. P. Gauthier, C. Levallois, and C. Paranthoen, "Tunable semiconductor vertical-cavity surface-emitting laser with an intracavity liquid crystal layer," *Applied Physics Letters*, vol. 98, no. 16, pp. 161105-1–161105-3, 2011.
- [58] B. Reig, T. Camps, D. Bourrier, E. Daran, C. Vergnenègre, and V. Bardinal, "Design of active lens for VCSEL collimation," in

- Micro-Optics 2010*, vol. 7716 of *Proceedings of SPIE*, p. 771620, 2010.
- [59] A. Liu, M. Xing, H. Qu, W. Chen, W. Zhou, and W. Zheng, "Reduced divergence angle of photonic crystal vertical-cavity surface-emitting laser," *Applied Physics Letters*, vol. 94, no. 19, Article ID 191105, 2009.
- [60] A. J. Liu, W. Chen, H. W. Qu et al., "Single-mode holey vertical-cavity surface-emitting laser with ultra-narrow beam divergence," *Laser Physics Letters*, vol. 7, no. 3, pp. 213–217, 2010.
- [61] D. F. Siriani and K. D. Choquette, "Electronically controlled two-dimensional steering of in-phase coherently coupled vertical-cavity laser arrays," *IEEE Photonics Technology Letters*, vol. 23, no. 3, pp. 167–169, 2011.
- [62] M. C. Y. Huang, Y. Zhou, and C. J. Chang-Hasnain, "Single mode high-contrast subwavelength grating vertical cavity surface emitting lasers," *Applied Physics Letters*, vol. 92, no. 17, Article ID 171108, 2008.
- [63] D. Fattal, J. Li, Z. Peng, M. Fiorentino, and R. G. Beausoleil, "Flat dielectric grating reflectors with focusing abilities," *Nature Photonics*, vol. 4, no. 7, pp. 466–470, 2010.
- [64] L. Chrostowski, "Optical gratings: nano-engineered lenses," *Nature Photonics*, vol. 4, no. 7, pp. 413–415, 2010.

## Review Article

# Wafer-Fused Optically Pumped VECSELs Emitting in the 1310-nm and 1550-nm Wavebands

A. Sirbu,<sup>1</sup> N. Volet,<sup>1</sup> A. Mereuta,<sup>1</sup> J. Lyytikäinen,<sup>2</sup> J. Rautiainen,<sup>2</sup> O. Okhotnikov,<sup>2</sup> J. Walczak,<sup>3</sup> M. Wasiaik,<sup>3</sup> T. Czystanowski,<sup>3</sup> A. Caliman,<sup>1</sup> Q. Zhu,<sup>1</sup> V. Iakovlev,<sup>1</sup> and E. Kapon<sup>1</sup>

<sup>1</sup>Swiss Federal Institute of Technology (EPFL), Laboratory of Physics of Nanostructures, 1015 Lausanne, Switzerland

<sup>2</sup>Optoelectronics Research Centre, Tampere University of Technology, 33720 Tampere, Finland

<sup>3</sup>Institute of Physics, Technical University of Łódź, 90-924 Łódź, Poland

Correspondence should be addressed to A. Sirbu, alexei.sirbu@epfl.ch

Received 1 June 2011; Accepted 9 August 2011

Academic Editor: Krassimir Panajotov

Copyright © 2011 A. Sirbu et al. This is an open access article distributed under the Creative Commons Attribution License, which permits unrestricted use, distribution, and reproduction in any medium, provided the original work is properly cited.

1300-nm, 1550-nm, and 1480-nm wavelength, optically pumped VECSELs based on wafer-fused InAlGaAs/InP-AlGaAs/GaAs gain mirrors with intracavity diamond heat spreaders are described. These devices demonstrate very low thermal impedance of 4 K/W. Maximum CW output of devices with 5 groups of quantum wells shows CW output power of 2.7 W from 180  $\mu\text{m}$  apertures in both the 1300-nm and the 1550-nm bands. Devices with 3 groups of quantum wells emitting at 1480 nm and with the same aperture size show CW output of 4.8 W. These VECSELs emit a high-quality beam with  $M^2$  beam parameter below 1.6 allowing reaching a coupling efficiency as high as 70% into a single-mode fiber. Maximum value of output power of 6.6 W was reached for 1300 nm wavelength devices with 290  $\mu\text{m}$  aperture size. Based on these VECSELs, second harmonic emission at 650 nm wavelength with a record output of 3 W and Raman fiber lasers with 0.5 W emission at 1600 nm have been demonstrated.

## 1. Introduction

Vertical-cavity surface-emitting lasers (VCSELs) [1, 2] and vertical-external-cavity surface-emitting lasers (VECSELs) [3–5] emitting in the 1310-nm and 1550-nm wavelength bands are ideally based on gain medium grown in the InP material system, with InGaAsP or InAlGaAs quantum wells (QWs) that produce high optical gain in the spectral region from 1270 nm to 1610 nm. Besides fibre-optic communications, this spectral range presents increasing interest in other fields of optics applications like gas sensors, free-space communications, biomedical, Raman optical amplifiers, and so forth. In recent years, the performance of 1310-nm and 1550-nm VCSELs has been considerably improved by the introduction of InAlGaAs QWs and tunnel junction injection, resulting in fundamental mode output close to 10 mW of wafer-fused VCSELs with AlGaAs/GaAs distributed Bragg reflectors (DBRs) [6]. Although emission in the mW range is sufficient for an important part of the mentioned applications, there is a number of emerging novel applications, such as in 1300-nm lasers for frequency

doubled 650-nm high-power red lasers applied in laser displays [7] and 1300–1600-nm optical pumping of Raman amplifiers [8] at high output power levels in the range of several watts. This high optical power domain is accessible by the realization of optically pumped VECSELs that are capable of producing intense, high-quality beams from a large pumped area as initially demonstrated for short-wavelength VECSELs in 1999 [9]. In addition, VECSELs are suitable for insertion of optical elements inside the laser cavity not only for frequency doubling but also, for example, for subpicosecond pulse generation [10] and for reaching narrow spectral linewidths of less than 5 kHz [11].

In order to reach the inherent advantage of VECSELs, which is the possibility of power scaling with increasing the pump area, an efficient mechanism for heat dissipation from the active region is of paramount importance. Thus, the thermal impedance of the VECSEL gain mirror that includes a semiconductor active region placed on a DBR is a quality factor that finally determines the output power level of the device. In the case of long-wavelength VECSEL gain mirrors that incorporate a DBR formed in the same

material system as the multi-QW (MQW) active region, the heat dissipation through the InP-based quaternary alloys (InGaAsP or InAlGaAs) that form the DBR is hampered by the very low thermal conductivity of these materials, resulting in thermal impedance as high as 470 K/W [3]. One solution to this problem consists of replacing the as-grown InP-based DBR with an AlGaAs/GaAs DBR with better thermal conductivity either in the form of a metamorphic mirror grown on the InP-based MQW active region [4] or bonded to the active region by wafer fusion as implemented in wafer-fused long-wavelength VCSELs [5]. In addition, an intracavity diamond heat-spreader that is directly bonded to the top side of the active region is very effective in considerably improving the heat dissipation in the gain mirror [12].

In this work, we present the fabrication and characterization results of wafer-fused InAlGaAs/AlGaAs optically pumped long-wavelength VCSELs with intracavity diamond heat-spreaders. We demonstrate thermal impedance as low as 4 K/W, room-temperature (RT) CW output power values of 2.7–6.6 W and high-quality beam emission with 70% coupling efficiency into single-mode fibres.

## 2. Gain Mirror Development

**2.1. 1550-nm Wavelength Gain Mirrors.** The active regions of the 1550-nm VCSELs were grown by low-pressure metal-organic vapour phase epitaxy (LP MOVPE) on (100)-InP substrates as previously described in [13]. The periodic gain structures comprise 5 groups of 2 compressively strained (1%)  $\text{Al}_{0.06}\text{Ga}_{0.26}\text{In}_{0.68}\text{As}$  QWs. The QWs are sandwiched between tensile strained (−0.5%), 10-nm thick  $\text{Al}_{0.16}\text{Ga}_{0.38}\text{In}_{0.46}\text{As}$  barriers and lattice-matched  $\text{Al}_{0.23}\text{Ga}_{0.24}\text{In}_{0.53}\text{As}$  spacers and are positioned at the antinodes of the standing wave of the electromagnetic field confined by a  $3\lambda$ -thick subcavity. Figure 1 shows the schematic structure of the gain medium, and the calculated near field intensity profile superimposed on the refractive index distribution of the core of the gain mirror. The photoluminescence (PL) spectrum of the active region is peaked near 1520 nm, at room temperature (cf. Figure 2).

With increasing temperature, the PL intensity decreases, and the spectral peak shifts to longer wavelengths at a rate of 0.6 nm/K due to the temperature variation of the bandgap energy in the QWs. This material system shows quite efficient high-temperature luminescence at temperatures as high as 130°C, which resulted in high performance, state of the art VCSELs [14]. The DBR was grown by solid-source MBE as previously described in [15] and consists of 35 pairs of quarter wave thick  $\text{Al}_{0.9}\text{Ga}_{0.1}\text{As}$  and GaAs layers with a high-reflectivity stop band centered at 1570 nm. The fused gain mirror cavity emission spectrum has a room temperature maximum at 1570 nm (cf. Figure 3). The spectra on Figure 3 were acquired under optical pumping with a 980-nm pump laser emitting 65 mW under 200 mA driving current. The shift of the cavity emission peak with temperature is 0.23 nm/K and is mainly due to the temperature variation of the refractive index in the active region.

**2.2. 1300-nm Wavelength Gain Mirrors.** The active regions of 1300-nm wavelength gain mirrors were also grown by LP MOVPE. The periodic gain structure consists of  $5 \times 2$  compressively strained (1%)  $\text{Al}_{0.14}\text{Ga}_{0.18}\text{In}_{0.68}\text{As}$  quantum wells. The QWs are sandwiched between  $\text{Al}_{0.28}\text{Ga}_{0.26}\text{In}_{0.46}\text{As}$  tensile strained compensation barriers as in previously reported 1310 nm band VCSELs [16]. The QW pairs are separated by lattice-matched  $\text{Al}_{0.31}\text{Ga}_{0.16}\text{In}_{0.53}\text{As}$  spacers. An InP layer on the surface acts as a window layer (cf. Figure 4). The DBR, grown by MBE on a GaAs substrate, comprises 35 pairs of quarter-wave thick  $\text{Al}_{0.9}\text{Ga}_{0.1}\text{As}$  and GaAs layers.

The PL spectrum at room temperature of this MQW active region, with a full width at half maximum of 60 nm, is centered at 1263 nm (cf. Figure 5). A subcavity resonance dip of the fused gain mirror situated at 1315 nm within the high-reflectivity stop band sets a detuning of 52 nm (cf. Figure 6).

**2.3. 1480-nm Wavelength Gain Mirrors.** Both the active MQW structure and the DBR for the 1480-nm wavelength devices were grown by a solid-source MBE [17]. Compressively strained (1%) 7 nm thick  $\text{Al}_{0.1}\text{Ga}_{0.22}\text{In}_{0.68}\text{As}$  QWs were sandwiched between 10 nm thick  $\text{Al}_{0.22}\text{Ga}_{0.31}\text{In}_{0.47}\text{As}$  strain compensation barriers and separated by  $\text{Al}_{0.31}\text{Ga}_{0.16}\text{In}_{0.53}\text{As}$ /InP spacers (cf. Figure 7). The topmost InP window layer of the gain section provides additional carrier confinement and prevents carrier diffusion to and subsequent nonradiative recombination at the surface. As for the designs discussed earlier, the QWs are located at the antinodes of the standing wave pattern of the electromagnetic field intensity. Distribution of the QWs was changed to 4-2-2 in order to improve pump absorption efficiency; moreover, the more compact subcavity allowed better heat extraction.

The room temperature PL spectrum of the QW structure peaked near 1445 nm with a full-width at half maximum of 71 nm, as illustrated in Figure 8. The DBR is comprised of 35 pairs of quarter-wave thick  $\text{Al}_{0.9}\text{Ga}_{0.1}\text{As}$ /GaAs layers with the high-reflectivity stop band centered at 1490 nm. The dip at the center of the stop band is caused by the absorption of the QWs.

**2.4. Gain Mirror Assembled by Wafer Fusion.** The InAlGaAs/InP active regions grown on InP substrates and the AlGaAs/GaAs DBRs grown on the GaAs substrates are fused together to form long-wavelength gain mirrors using the wafer fusion technique. In the standard fusion process that was previously developed for the fabrication of long-wavelength VCSELs [2], InP-based and GaAs-based 2-inch wafers are brought into contact at 600°C in vacuum, or purified nitrogen, while applying a force of 7000 N for 30 min in an industrial custom-built wafer bonding machine. At these values of temperature and pressure, both wafers undergo a slight plastic deformation resulting in a uniform contacting on a nanometer scale. As a result, covalent bonds are formed between the InP-based and GaAs-based wafers. After cooling down, the stack that includes the InAlGaAs/InP-AlGaAs/GaAs half cavity with InP and GaAs substrates on respective sides is bowed. This bowing, with a radius of curvature of about 1 m, occurs because of different values

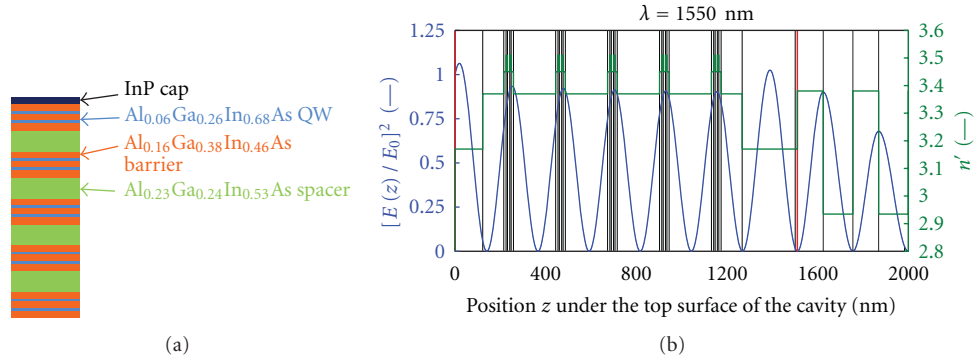


FIGURE 1: Schematic of layer design in the active region (a) and normalized electric field (blue line) and refractive index (green line) distributions in the 1550-nm wavelength gain mirror. Black lines show the different layers in the VECSEL subcavity (delimited by red lines) and the first 4 layers in the DBR section.

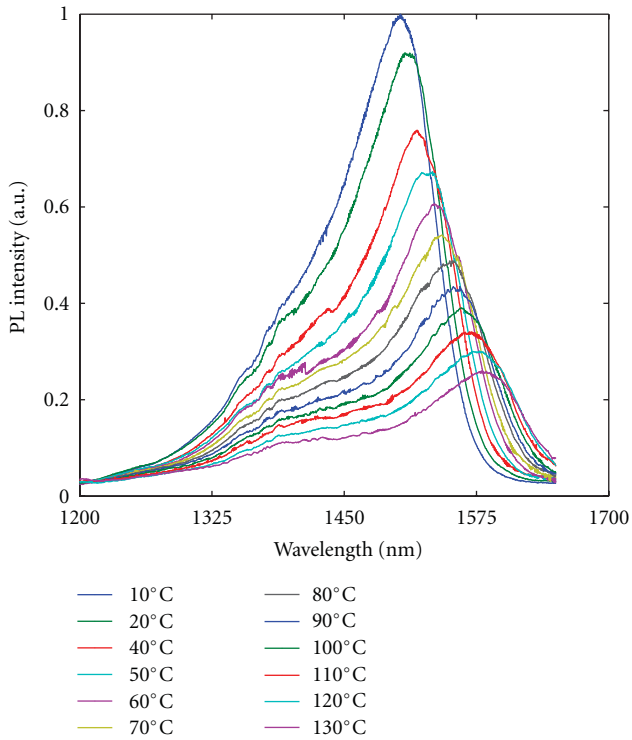


FIGURE 2: Photoluminescence spectra of the gain medium of 1550-nm wavelength VECSELs versus temperature.

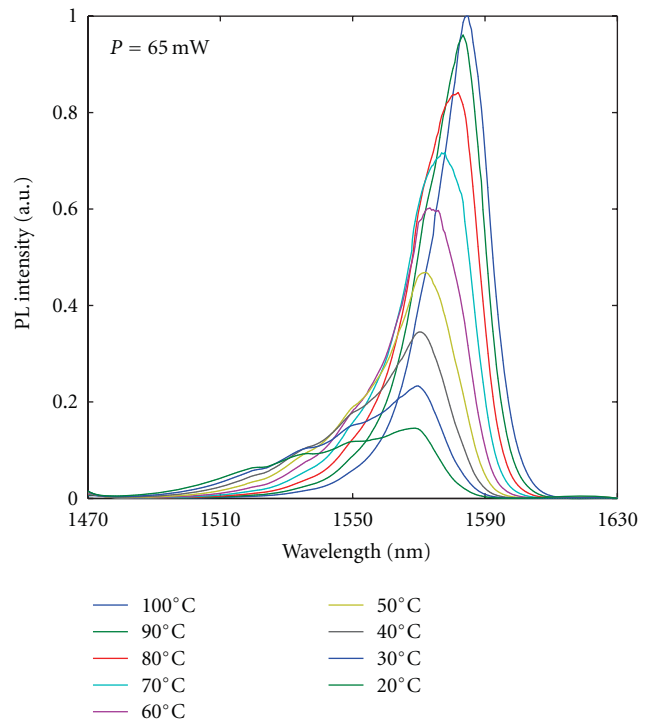


FIGURE 3: Gain mirror emission spectra of the 1550-nm devices versus temperature.

of thermal expansion coefficients of the GaAs-based wafers with lattice parameter of  $5.6535 \text{ \AA}$  and the InP-based wafers with lattice parameter of  $5.86875 \text{ \AA}$ , ( $5.8 \cdot 10^{-6} \text{ K}^{-1}$  for GaAs and  $4.8 \cdot 10^{-6} \text{ K}^{-1}$  for InP). After selectively etching the InP substrate, the remaining GaAs substrate containing the fused stack regains its planarity. As a result of this process, some dark-line defects are formed in the active region, which normally do not affect devices of small aperture size of about  $7 \mu\text{m}$ . In the case of high-power VECSELs with an aperture size of the order of  $100 \mu\text{m}$ , special care needs to be taken for decreasing the defect formation appearing due to the different thermal expansion coefficients of the GaAs-based

and InP-based wafers during cooling down from  $600^\circ\text{C}$  to RT. In this work, we applied a modified fusion technique that allows reducing the formation of dark-line defects in the active region [18]. The new approach consists of transferring the AlGaAs/GaAs DBRs on InP substrates before fusing them on the InAlGaAs/InP wafers. Thus, in the fused stack, both wafers have the same InP substrates and practically no strain is introduced in the active region during the cooling down to room temperature.

We studied a 1300 nm gain mirror with cathodoluminescence (CL) spectroscopy, which allows revealing defects in a field of  $50 \times 50 \mu\text{m}^2$ . For CL mapping of larger areas, we

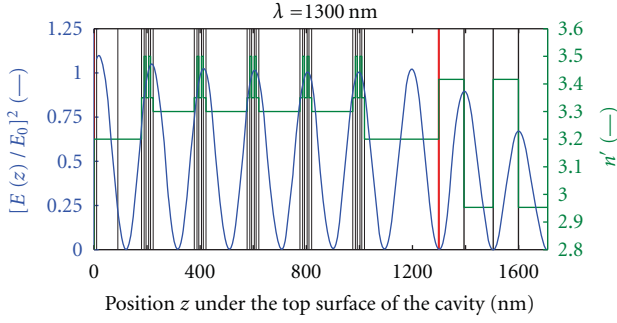


FIGURE 4: Normalized electric field (blue line) and refractive index (green line) distributions in the 1300-nm wavelength gain mirror. Black lines show the different layers in the VECSEL subcavity (delimited by red lines) and the first 4 layers in the DBR section.

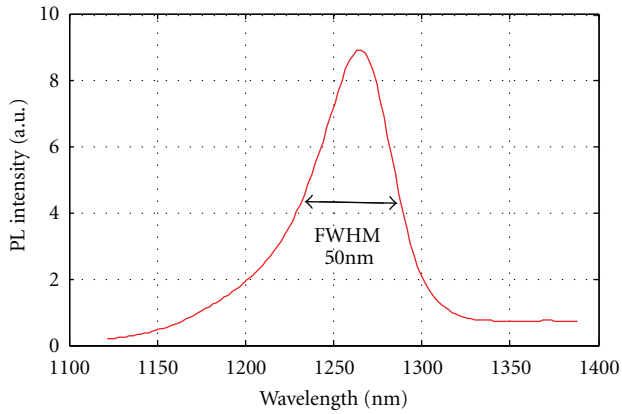


FIGURE 5: PL spectrum of the 1300-nm wavelength active region at room temperature.

deposited on a 1300 nm InAlGaAs/InP-AlGaAs/GaAs fused gain mirror (described in Section 2.2) a grid of Ti-Au stripes with exposed cells of  $25 \times 25 \mu\text{m}^2$  and performed CL analysis of different regions of  $50 \times 50 \mu\text{m}^2$ . By assembling, these images, a CL mapping of the whole sample presented on Figure 9 was reconstructed (cf. Figure 10).

In Figure 10, we can observe just one dark line on the gain mirror of  $150 \times 250 \mu\text{m}^2$  area. We can also identify 5 dark points that represent dust particles. In one cell on the left side of the sample, marked with a yellow arrow on Figure 9, the gold film did not lift off, and hence, this area appears dark in the CL image.

**2.5. Heat Dissipation Scheme.** Recently, two efficient heat dissipation schemes have emerged to produce high-power optically pumped VECSELs in the wavelength range of 1–3  $\mu\text{m}$  [19–21]. In the first approach [19], the VECSEL structure that demonstrated 20 W at  $-20^\circ\text{C}$  at 950 nm was first grown in a reverse order on a GaAs substrate, then, after soldering it to a diamond heat spreader, the GaAs substrate was selectively etched. In the second approach [20, 21] that has been adopted in the current work, effective heat dissipation is obtained by introducing an optically transparent intracavity diamond that is directly bonded to the gain

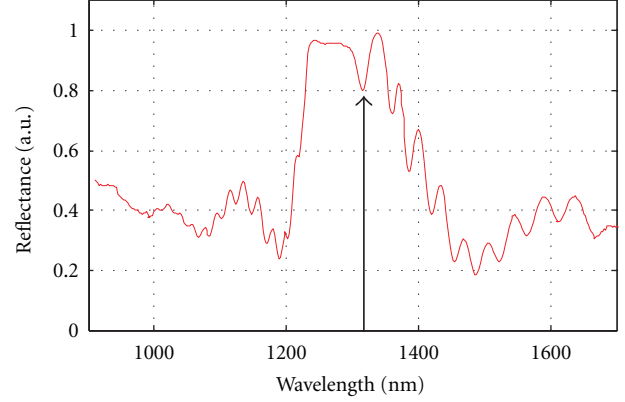


FIGURE 6: Reflectance spectrum of the 1300-nm wavelength gain mirror. Subcavity resonance at 1315 nm is indicated by an arrow.

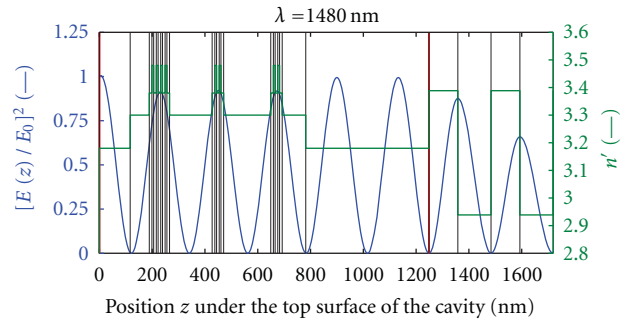


FIGURE 7: Refractive index profile and distribution of the electric field in the 1480-nm gain mirror. Black lines show the different layers in the VECSEL subcavity (delimited by red lines) and the first 4 layers in the DBR section.

mirror. In this study, we used a  $3 \times 3 \times 0.3 \text{ mm}^3$  natural type IIa diamond that was bonded to the InP window layer of the gain mirror by molecular bonding as described in [22].

We performed thermal modelling of the wafer-fused gain mirror with diamond heat spreader mounted on a water-cooled copper block by solving the thermal equation using a finite element method for a generated heat power of 3.3 W in the active region [18]. To simplify the calculations, the gain mirror design was transformed from 3D Cartesian to 2D cylindrical coordinate system by keeping the volumes of the active region layers unchanged. We assumed Gaussian distribution of the pumped beam in the lateral direction and exponential decay depending on the absorption coefficient of particular layers in the vertical direction. The heat generation distribution reflects the distribution of the energy absorbed by the device. Results depicted on Figure 11 demonstrate that the diamond thickness of 300  $\mu\text{m}$  used in this work is quite sufficient for efficient heat removal from the active region.

The distribution of the temperature within the gain mirror, depicted in Figure 12, shows that the temperature decreases quite fast with increasing distance from the pumped part of the active region in the lateral direction. The heat dissipation mechanism consists in effective heat flow from the active region into the diamond slab followed by heat

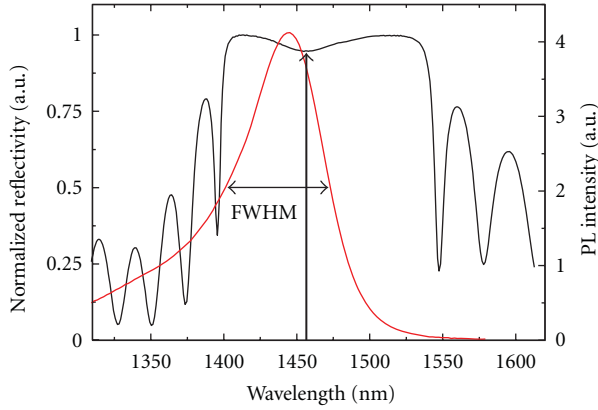


FIGURE 8: Spectral distributions of room-temperature PL of the QWs and DBR reflectivity for the 1480-nm wavelength structures.

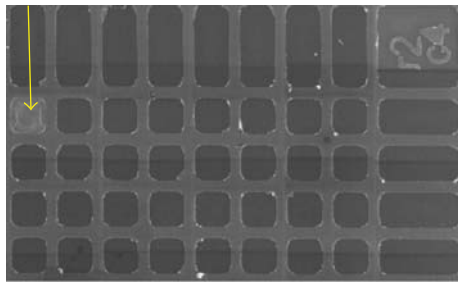


FIGURE 9: Ti/Au grid on the surface of a 1300 nm gain mirror sample. Yellow arrow points to a cell in which the Ti/Au did not lift off.

reinjection into the unpumped part of the active region and further dissipation through the AlGaAs/GaAs DBR.

The procedure of thermal impedance determination consists of calculating the temperature distribution within the gain mirror for three different lasing conditions: 3 W and 300 K, 3 W and 300.1 K, and 3.01 W and 300 K. The temperature distribution is further transformed into a distribution of the refractive index, and the emission wavelength is derived. The value of thermal impedance determined in such a way should be close to the top limit value estimated from direct temperature determination, since the temperature in the active region is the highest, and there is no modification of the refractive index in the region between the gain mirror and the external mirror. If one replaces the air by diamond and assumes a thermo-optic coefficient of diamond  $dn/dT = 0$ , thermal impedance will be equal to the value determined with air. Since the thermo-optic properties of the diamond are not well known, we performed the determination of thermal impedance in a broad range of thermo-optic coefficient values of  $0-2 \cdot 10^{-5} \text{ K}^{-1}$ . Figure 13 depicts the calculated dependence of the thermal impedance  $Z$  as a function of the thermo-optic coefficient  $dn/dT$ . The experimental value  $Z = 4 \text{ K/W}$  (see Section 3.2) is shown as a line in Figure 13.

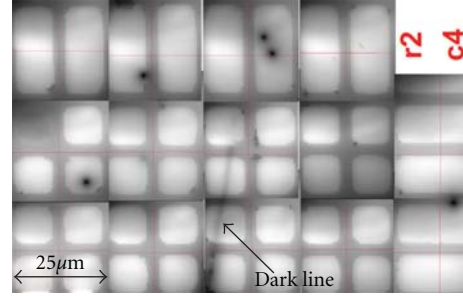


FIGURE 10: CL mapping of the sample depicted on Figure 9.

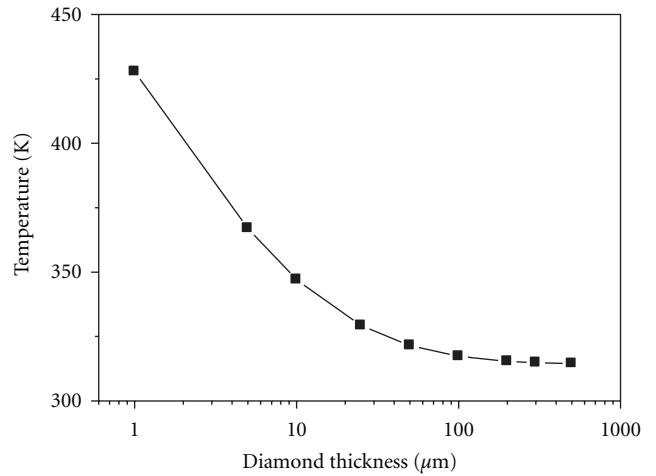


FIGURE 11: Maximum temperature in the active region versus diamond thickness.

### 3. VECSEL Characteristics

**3.1. Optically Pumped VECSEL Cavity.** Gain mirrors that are bonded to intra cavity diamond are further mounted between two copper plates with indium foil in between to ensure reliable thermal contact between the surfaces. This assembly is placed on a thermoelectric cooler mounted on a copper water-cooled block. The topmost copper plate has a circular aperture for signal and pump beams (cf. Figure 14). The lasing measurements are done with reflective plane output couplers with different values of output coupling of 1%–2.5%. The pump source is a fibre-coupled 980-nm diode laser. The cavity of the VECSEL is of V-type and is composed of a planar output coupler, a curved mirror and the gain mirror, as shown in Figure 15. The cavity is simulated numerically to ensure that the mode size at the gain mirror matches the pump spot.

**3.2. 1550-nm VECSELs Test Results.** Output characteristics of the 1550-nm wavelength VECSEL [23] for different operation temperatures are shown in Figure 18. In the temperature range of  $10^{\circ}\text{C}$ – $35^{\circ}\text{C}$ , the output power increases up to 2.62 W at  $10^{\circ}\text{C}$  and 1.6 W at  $35^{\circ}\text{C}$ . These values are limited by the maximum available input pump power of 25 W. With increasing pump power, the emission wavelength shifts to

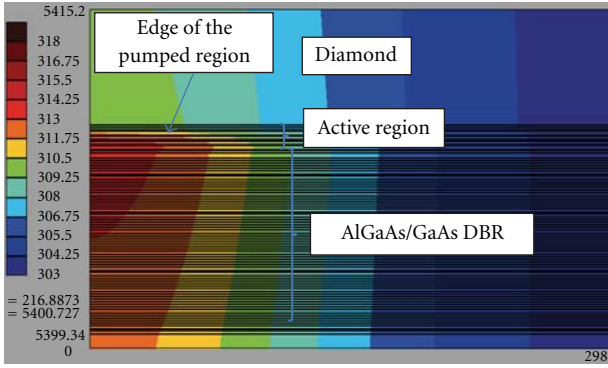


FIGURE 12: Temperature distribution in the active region.

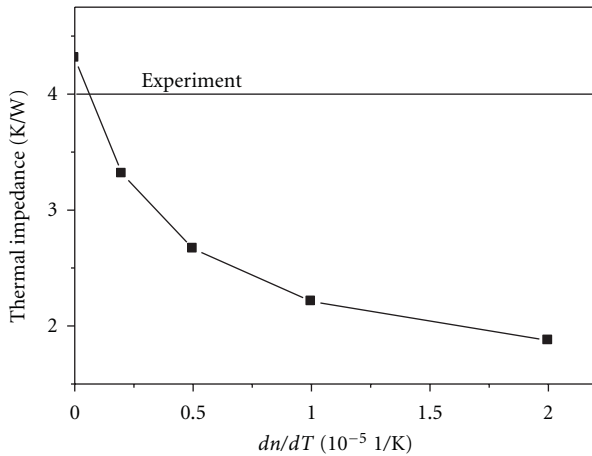


FIGURE 13: Thermal impedance  $Z$  as a function of thermo-optic coefficient  $dn/dT$ .

longer wavelengths at a rate of  $1 \text{ nm} \cdot \text{W}^{-1}$ . The effective thermal impedance is estimated as  $4 \text{ K} \cdot \text{W}^{-1}$  from the ratio of wavelength shift at different pump power levels and the wavelength shift with temperature of the gain mirror sub-cavity at a low pump power level determined in Section 2.1. Light-light characteristics are linear up to 15 W pumping power with a slope efficiency of 12% at  $10^\circ\text{C}$  (Figure 17). The recalculated efficiency inside the structure is equal to 16% when taking into consideration that the gain mirror, not containing an antireflective coating, reflects 30% of the incident pumping power. At higher pumping levels the light-light characteristics are sublinear, which is probably due to excessive heating as a consequence of a large defect energy  $\Delta E_d$  at 980 nm pumping wavelength ( $\Delta E_d = 0.48 \text{ eV}$ , 38% of pump photons energy is heating the lattice).

**3.3. 1310-nm VECSELS Test Results.** Output power versus pump power characteristics of the 1310-nm VECSELS with a pump spot of  $180 \mu\text{m}$  diameter [24] (cf. Figure 18) demonstrate values of 1.9 W, 2.4 W, and 2.7 W for output coupling of 1%, 2% and 2.5%, respectively. Any roll-over in the output characteristics was not observed with this gain medium for pump power up to 25 W, which limited also the achievable output power. The slope efficiency for these

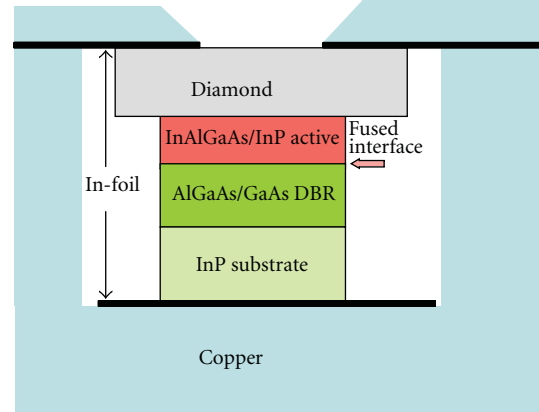


FIGURE 14: The gain mirror assembly.

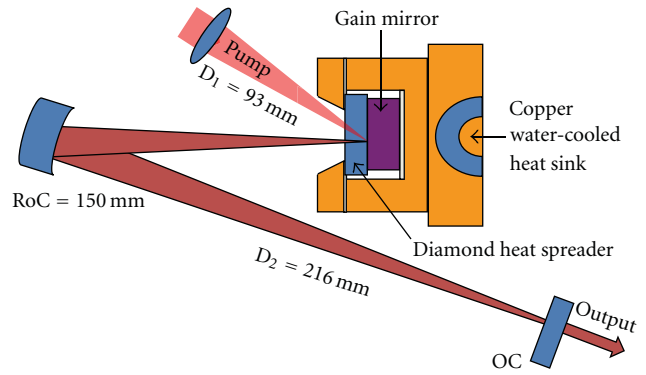


FIGURE 15: Schematic representation of the VECSEL cavity.

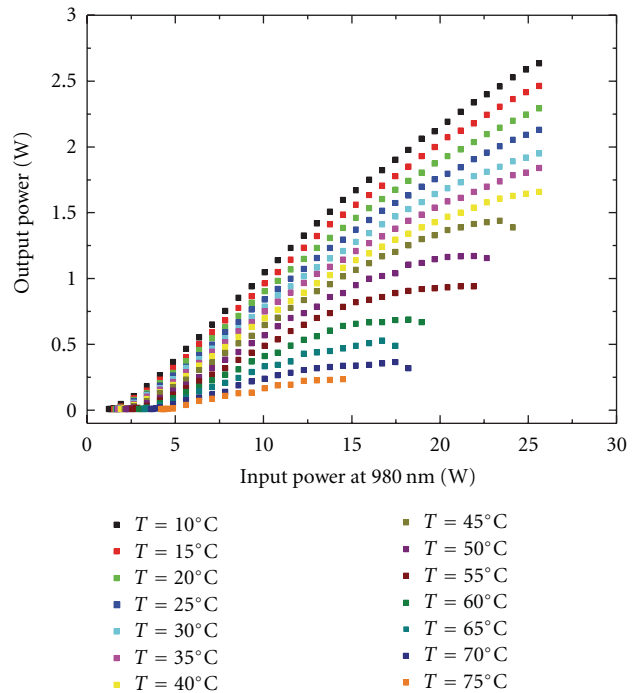


FIGURE 16: Output characteristics for different operating temperatures for a 1550-nm VECSEL. The output coupling is 2%.

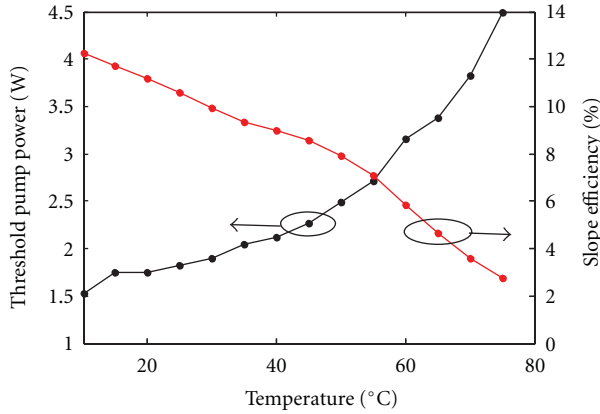


FIGURE 17: Threshold pump power and slope efficiency as a function of gain mirror temperature for the 1550-nm VECSEL.

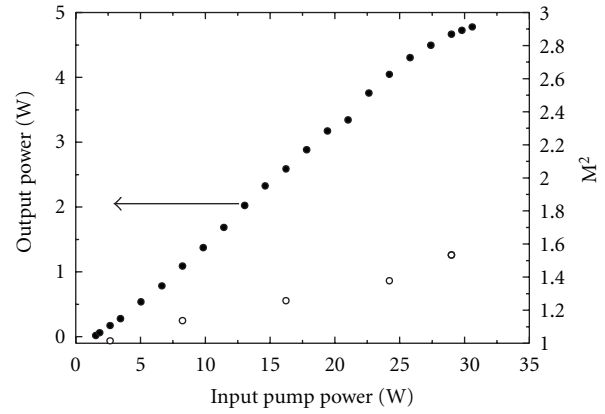


FIGURE 20: Output power and  $M^2$  versus pump power.

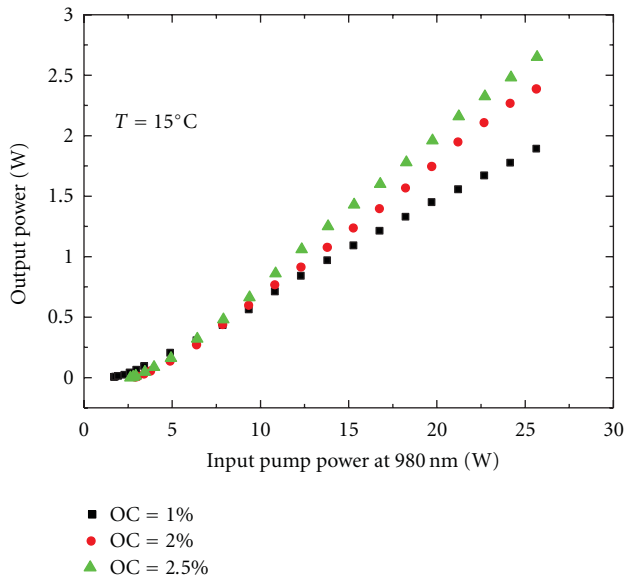


FIGURE 18: Output characteristics of 1310 nm wavelength 180  $\mu\text{m}$  aperture VECSEL device.

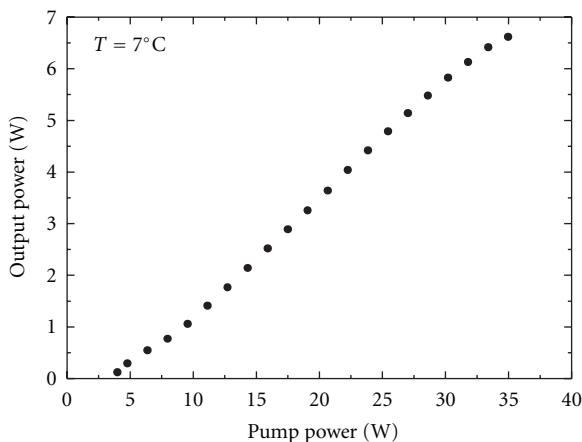


FIGURE 19: Output characteristics of the 1310 nm wavelength 290  $\mu\text{m}$  aperture VECSEL device.

devices ranges from 8.2% to 12.2% and the threshold pump power varies between 2.0 W and 3.1 W.

In another test, the optical pumping beam of a 980 nm pump laser diode was focused onto a spot with a diameter of about 290  $\mu\text{m}$  at the gain mirror [25]. At 7°C, the maximum output power of 6.6 W is reached with a 2.5% output coupler (Figure 19), which represents the highest reported value of power at this wavelength, to our knowledge. Based on these devices, second harmonic emission at 650 nm with a continuous wave output of 3 W was demonstrated for the first time [25].

**3.4. 1480-nm VECSEL Results.** The 1480-nm VECSELs have been tested at a pump spot diameter of 180  $\mu\text{m}$  to enable single transverse mode operation. Figure 20 presents the output power and  $M^2$  beam parameter versus pump power characteristics measured with an output coupler of 2.5% at 8°C. Maximum output power of 4.8 W, slope efficiency of 0.18 and  $M^2$  beam parameter below 1.6 for all pump power levels have been achieved. This high-quality emission beam allowed coupling into a single mode fiber with a coupling efficiency of 70% and a Raman fiber laser emitting 0.5 W at 1600 nm was demonstrated [26].

## 4. Conclusions

We have developed wafer-fused InAlGaAs/AlGaAs optically pumped VECSELs with intracavity diamond heat spreaders emitting at wavelengths of 1300, 1550, and 1480 nm, based on a modified wafer-fusion process allowing reduced defect formation in the active region. These devices produce record high levels of continuous wave power of 2.7, 2.62 and 4.8 W, respectively, with aperture diameter of 180  $\mu\text{m}$ , and 6.6 W at 1300 nm with increased aperture diameter of 290  $\mu\text{m}$ . A substantial increase of output power is observed when the configuration of the QWs is changed from 5 groups of 2 QWs to 3 groups of 4, 2, 2 QWs. Reaching high levels of output power as well as power scaling with increasing aperture size is possible as a result of the very low thermal impedance value of 4 K/W, which is predicted by thermal modeling and confirmed by experiment. These devices emit a high-quality

beam with  $M^2$  beam parameter below 1.6, allowing reaching a coupling efficiency into a single mode fiber as high as 70%. Based on VCSELS developed in this work, second harmonic emission at 650 nm with a record output of 3 W and Raman fiber lasers with 0.5 W emission at 1600 nm have been demonstrated.

## Acknowledgment

This work was partially supported by the Swiss Nano-Tera project MIXSEL.

## References

- [1] W. H. Hofmann, M. Müller, G. Böhm, M. Ortsiefer, and M.-C. Amann, "1.55  $\mu\text{m}$  InP-based VCSEL with enhanced modulation bandwidths > 10 GHz up to 85°C," in *Optical Fiber Communication (OFC) Conference*, March 2009.
- [2] A. Syrbu, A. Mircea, A. Mereuta et al., "1.5-mW single-mode operation of wafer-fused 1550-nm VCSELS," *IEEE Photonics Technology Letters*, vol. 16, no. 5, pp. 1230–1232, 2004.
- [3] C. Symonds, I. Sagnes, J. L. Oudar et al., "Room temperature CW lasing operation of monolithically grown 1.55  $\mu\text{m}$  vertical external cavity surface emitting laser," *Optics Communications*, vol. 230, no. 4–6, pp. 419–423, 2004.
- [4] J. P. Tournenc, S. Bouchoule, A. Khadour et al., "Thermal optimization of 1.55  $\mu\text{m}$  OP-VECSEL with hybrid metal-metamorphic mirror for single-mode high power operation," *Optical and Quantum Electronics*, vol. 40, no. 2–4, pp. 155–165, 2008.
- [5] J. Lyytikäinen, J. Rautiainen, A. Sirbu et al., "Wafer fused InP-GaAs optically-pumped semiconductor disk laser operating at 1.57- $\mu\text{m}$ ," in *Photon Counting Applications, Quantum Optics, and Quantum Information Transfer and Processing II*, Proceedings of SPIE, April 2009.
- [6] A. Caliman, V. Iakovlev, A. Mereuta, A. Sirbu, G. Suruceanu, and E. Kapon, "8 mW fundamental mode output of wafer-fused VCSELS emitting in the 1550-nm band," in *the Conference on Lasers and Electro-Optics/International Quantum Electronics (CLEO/IQEC) Conference*, 2009.
- [7] J. L. A. Chilla, H. Zhou, E. Weiss et al., "Blue & green optically-pumped semiconductor lasers for display," in *Projection Displays XI*, Proceedings of SPIE, pp. 41–47, January 2005.
- [8] M. N. Islam, "Raman amplifiers for telecommunications," *IEEE Journal on Selected Topics in Quantum Electronics*, vol. 8, no. 3, pp. 548–559, 2002.
- [9] M. Kuznetsov, F. Hakimi, R. Sprague, and A. Mooradian, "Design and characteristics of high-power (>0.5-W CW) diode-pumped vertical-external-cavity surface-emitting semiconductor lasers with circular TEM<sub>00</sub> beams," *IEEE Journal on Selected Topics in Quantum Electronics*, vol. 5, no. 3, pp. 561–573, 1999.
- [10] S. Hoogland, S. Dhanjal, A. C. Tropper et al., "Passively mode-locked diode-pumped surface-emitting semiconductor laser," *IEEE Photonics Technology Letters*, vol. 12, no. 9, pp. 1135–1137, 2000.
- [11] R. H. Abram, K. S. Gardner, E. Riis, and A. I. Ferguson, "Narrow linewidth operation of a tunable optically pumped semiconductor laser," *Optics Express*, vol. 12, no. 22, pp. 5434–5439, 2004.
- [12] H. Lindberg, A. Larsson, and M. Strassner, "Single-frequency operation of a high-power, long-wavelength semiconductor disk laser," *Optics Letters*, vol. 30, no. 17, pp. 2260–2262, 2005.
- [13] A. Mereuta, V. Iakovlev, A. Caliman et al., "High single mode power wafer fused InAlGaAs/InP - AlGaAs/GaAs VCSELS emitting in the 1.3–1.6  $\mu\text{m}$  wavelength range," in *the 19th IEEE International Conference on Indium Phosphide and Related Materials (IPRM '07)*, pp. 430–433, May 2007.
- [14] E. Kapon, A. Sirbu, V. Iakovlev, A. Mereuta, A. Caliman, and G. Suruceanu, "Recent developments in long wavelength VCSELS based on localized wafer fusion," in *the 11th International Conference on Transparent Optical Networks (ICTON '09)*, July 2009.
- [15] J. Lyytikäinen, J. Rautiainen, S. Suomalainen et al., "MBE grown optically pumped semiconductor disk lasers emitting at 940 nm," *Materials Science and Engineering B*, vol. 147, no. 2–3, pp. 161–165, 2008.
- [16] A. Mereuta, G. Suruceanu, A. Caliman, V. Iakovlev, A. Sirbu, and E. Kapon, "10-Gb/s and 10-km error-free transmission up to 100°C with 1.3- $\mu\text{m}$  wavelength wafer-fused VCSELS," *Optics Express*, vol. 17, no. 15, pp. 12981–12986, 2009.
- [17] J. Lyytikäinen, J. Rautiainen, A. Sirbu et al., "High-power 1.48- $\mu\text{m}$  wafer-fused optically pumped semiconductor disk laser," *IEEE Photonics Technology Letters*, vol. 23, no. 13, pp. 917–919, 2011.
- [18] A. Sirbu, A. Mereuta, A. Caliman et al., "High-power optically-pumped VCSELS emitting in the 1310-nm and 1550-nm wavebands," in *Vertical External Cavity Surface Emitting Lasers, VCSELS*, vol. 7919 of *Proceedings of SPIE*, January 2011.
- [19] B. Rudin, A. Rutz, D. J. Maas et al., "Efficient High-power VCSEL generates 20 W continuous-wave radiation in a fundamental transverse mode," in *Advanced Solid-State Photonics (ASSP)*, 2009.
- [20] M. Rattunde, B. Rösener, S. Kaspar et al., "GaSb-based semiconductor disk lasers for the 2 - 3  $\mu\text{m}$  wavelength range: Versatile lasers for high-power and narrow linewidth emission," in *the Lasers and Electro-Optics/Quantum Electronics and Laser Science Conference (CLEO/QELS '10)*, May 2010.
- [21] V. M. Korpijärvi, T. Leinonen, J. Puustinen, A. Härkönen, and M. D. Guina, "11 W single gain-chip dilute nitride disk laser emitting around 1180 nm," *Optics Express*, vol. 18, no. 25, pp. 25633–25641, 2010.
- [22] Z. L. Liao, "Semiconductor wafer bonding via liquid capillarity," *Applied Physics Letters*, vol. 77, no. 5, pp. 651–653, 2000.
- [23] J. Rautiainen, J. Lyytikäinen, A. Sirbu et al., "2.6 W optically-pumped semiconductor disk laser operating at 1.57- $\mu\text{m}$  using wafer fusion," *Optics Express*, vol. 16, no. 26, pp. 21881–21886, 2008.
- [24] J. Lyytikäinen, J. Rautiainen, L. Toikkanen et al., "1.3- $\mu\text{m}$  optically-pumped semiconductor disk laser by wafer fusion," *Optics Express*, vol. 17, no. 11, pp. 9047–9052, 2009.
- [25] A. Rantamäki, A. Sirbu, A. Mereuta, E. Kapon, and O. G. Okhotnikov, "3 W of 650 nm red emission by frequency doubling of wafer-fused semiconductor disk laser," *Optics Express*, vol. 18, no. 21, pp. 21645–21650, 2010.
- [26] A. Chamorovskiy, J. Rautiainen, J. Lyytikäinen et al., "Raman fiber laser pumped by a semiconductor disk laser and mode locked by a semiconductor saturable absorber mirror," *Optics Letters*, vol. 35, no. 20, pp. 3529–3531, 2010.

## Review Article

# Cavity Solitons in VCSEL Devices

**S. Barbay,<sup>1</sup> R. Kuszelewicz,<sup>1</sup> and J. R. Tredicce<sup>2</sup>**

<sup>1</sup>Laboratoire de Photonique et de Nanostructures, CNRS-UPR20, Route de Nozay, 91 460 Marcoussis, France

<sup>2</sup>Institut Non Linéaire de Nice, UMR6618 CNRS-Université de Nice Sophia-Antipolis, 1361 Route de Lucioles, 06 560 Valbonne, France

Correspondence should be addressed to S. Barbay, sylvain.babay@lpn.cnrs.fr

Received 20 June 2011; Accepted 9 August 2011

Academic Editor: Krassimir Panajotov

Copyright © 2011 S. Barbay et al. This is an open access article distributed under the Creative Commons Attribution License, which permits unrestricted use, distribution, and reproduction in any medium, provided the original work is properly cited.

We review advances on the experimental study of cavity solitons in VCSELs in the past decade. We emphasize on the design and fabrication of electrically or optically pumped broad-area VCSELs used for CSs formation and review different experimental configurations. Potential applications of CSs in the field of photonics are discussed, in particular the use of CSs for all-optical processing of information and for VCSELs characterization. Prospects on self-localization studies based on vertical cavity devices involving new physical mechanisms are also given.

## 1. Introduction

In this paper we address experimental results on Cavity Solitons (CS) in VCSEL devices and focus on recent studies and developments. We emphasize on the design and fabrication of electrically or optically pumped broad-area VCSELs used for CS formation and review different experimental configurations. Applications of CS in the field of photonics are discussed, in particular the potential use of CS for all-optical processing of information and for VCSEL characterization. Prospects on self-localization studies based on vertical cavity devices involving new physical mechanisms are also given. The reader interested in the theory of CS formation in semiconductor devices can refer to recent reviews on the subject [1, 2] and also to [3] which provides a general review on CSs and their applications to photonics from a more fundamental viewpoint. A collection of articles on the most recent developments in the field can also be found in [4]. Our goal is to provide a complete and accessible review on past and most recent experimental results on CSs using vertical cavity semiconductor devices, while giving a prospect on future directions.

During the 80s, the main focus of experimental studies on nonlinear dynamics was on temporal dynamics (see, e.g., [5, 6]). Observation of period doubling, quasiperiodicity, intermittency, and chaos in a variety of systems ranging from fluids to chemical reactions appeared in the literature (see,

e.g., [7–9]). Optics was not an exception. After the report of period doubling and chaos in a modulated laser [10], several papers showed theoretically and experimentally the appearance of instabilities in optical systems [11]. In particular, laser with injected signal and optical amplifiers have been exhaustively studied [12–17]. Dynamics of semiconductor lasers under injection and delayed optical feedback were also objects of interests mainly because of the possible applications of such devices in optical communication systems [18–20]. Later, mainly during the 90s, the interest shifted towards spatiotemporal instabilities. The possibility of observing optical vortices [21] and finally reach optical turbulence was very attractive, because optical systems were somehow easier to model than hydrodynamical ones. Thus, the comparison between experimental and theoretical results was simpler than in other more complex systems. Several studies reported the appearance of complex spatio-temporal dynamics in optics [22–24] and in particular in laser systems [25–28]. Most of the experiments realized with broad area lasers, thus with a large transverse section or high Fresnel number, showed the appearance of large structures more or less complex but almost always with long correlation length in the transverse plane and, therefore, avoiding the appearance of a complex or turbulent behavior [29]. The reasons for such long correlation order is mainly that it is somehow difficult in lasers to reach a really high Fresnel number, because cavity lengths are usually too long. In

that sense, VCSEL represents an ideal laser to study spatio-temporal dynamics. Effective cavity lengths of the order of  $10\ \mu\text{m}$ , active medium lengths of the order of a quarter-wavelength, almost planar mirrors, and the possibility of having more than  $150\ \mu\text{m}$  in diameter makes this device an ideal candidate to observe structures with very short correlation length and, therefore, complex optical spatio-temporal structures. Several theoretical studies were centered around the formation of patterns in VCSELs [30–32] as well as some experimental ones [33–36].

However, the most interesting results have been obtained in general models of lasers with saturable absorbers [37–39] or optical absorber or amplifier [32, 40, 41]. Numerical and analytical results showed that it is possible to observe localized structures in these optical systems. The main property of a localized structure is that its correlation length is much smaller than the size of the system. Thus, each localized structure will behave as an independent object. In optics, localized structures with a single intensity peak have been called cavity solitons (CSs). Cavity solitons are self-localized states of light appearing in the transverse plane of a cavity as bright spots sitting on a dark background. Experimentally, they can be characterized by the following properties: (1) CSs are self-localized states, independent of the system boundaries whose shape and size is fixed by the system parameters and do not depend on the excitation that gave birth to them; (2) CSs can exist in several (ideally arbitrary) transverse locations of the cavity and can be independently manipulated (written, erased, ...); (3) CS can be “moved” or set into motion. At first sight, they possess characteristics resembling those of self-trapped beams [42] but constrained within a cavity whose propagation path is folded by the cavity mirrors. However, it is worthwhile to notice that single peak localized structures are different from self-trapped beams, because they are created by two fronts connecting two different spatial solutions in a dissipative system. This feature introduces important physical differences; however, that can be fully appreciated only when considering rather subtle theories on CS formation [43, 44]. Some of these physical differences were experimentally observed in a semiconductor-based system in [45]. On the other hand, the presence of a cavity is not necessary either as demonstrated by the observation of single peak localized structures in [46] in a single feedback mirror experiment performed in Na vapour. Thus, CS may be better called single peak localized structure (SPLS), but we will use both names in this review.

CS arise usually under the condition of coexistence of a homogeneous and a patterned stationary state; for the same control parameter values, the solution may approach one or the other state depending upon the initial condition. Localized structures are thus somehow intermediate, controllable states between the homogeneous state and the fully developed pattern. SPLS may also exist in optical systems, where two uniform states coexist, as a result of the locking of two fronts. This mechanism was first studied theoretically and numerically in [47] where self-localized states (then called “diffractive autosolitons”) were demonstrated to exist in a nonlinear, bistable, interferometer. Self-localized states were also found in the more general framework of the

Swift-Hohenberg equation, a model equation that describes pattern forming systems and applicable in nonlinear optics [39]. The stability conditions for localized structures in 1D were theoretically studied in [43]. The authors then proved theoretically that an infinity of localized structures presenting an arbitrary number of intensity peaks coexist and may be stable for a finite range of parameter values. Later, a similar method was used to study the region of coexistence and the order of the solutions in parameter space [44, 45].

The potential of CSs for applications to parallel information processing was then recognized and demonstrated in [40] and analyzed in the context of a model suited for semiconductor systems in [30]. CS can be excited and erased by a local perturbation at any transverse location of a nonlinear, broad-area cavity and as such play the role of pixels or spatial logical bits. They can be manipulated in phase or intensity gradients, where they can be moved or controlled, a property that relaxes considerably the addressing constraints if one wished to arrange them into 2D matrices.

The main advantages of semiconductor systems over other optical systems, where CS were predicted and observed lie in the fast timescales and small spatial scales associated with CS formation in semiconductor materials. Indeed, the characteristic timescale for CS formation in semiconductor systems is of the order of the carrier recombination time, which is in the nanosecond range, much shorter than other competing macroscopic systems based on photorefractive media [48], liquid crystals [49], or atomic vapors [46] in which CS were also found. Moreover, the characteristic size of a CS is governed by the diffraction length  $a \propto \sqrt{L\lambda\mathcal{F}}$ , where  $L$  is the cavity length,  $\lambda$  the wavelength of light and  $\mathcal{F}$  the resonator finesse and is of the order of  $10\ \mu\text{m}$  in microcavities, at least one order of magnitude smaller than in other macroscopic systems. CS necessitate a large and uniform aspect ratio system: a cavity whose transverse extent is much larger than the longitudinal extent such that it can host many transverse modes and allow for spatial decorrelation between different cavity locations. Therefore, broad-area VCSELs appear then as ideal devices to implement CS in semiconductor material systems. The first demonstration of CS in a broad-area VCSEL that stimulated all the ensuing investigations was reported in [50].

This paper is organized as follows. We present in Section 2 the characteristics of broad-area VCSELs with electrical injection and optical pumping designed for CS studies. In Section 3, we then describe experimental results obtained in the amplifying regime, with a cavity driven by an external coherent beam (holding beam). An important new conceptual and applicative step was obtained by the demonstration of a CS laser, that is, a system that does not require a coherent optical injection and emits self-localized microlasers having the properties of the CSs described earlier, as explained in Section 4. Possible applications of CS to photonics are presented in Section 5 with the experimental demonstrations of an optical delay line and of a soliton force microscope. The role of device defects and the applications of CS to device homogeneity characterization are also demonstrated. Finally, new directions in the field of self-localized states using VCSELs are presented in Section 6. We analyze CS

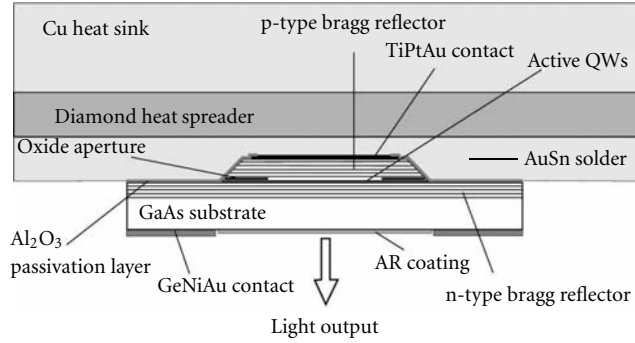


FIGURE 1: Schematic representation of a broad-area bottom emitter VCSEL structure with diamond heat spreader, after [51] (© 2011 IEEE).

in polarization, Cavity Light Bullets which are 3D-localized states of light traveling in a cavity and CS polaritons which explore new material nonlinearities.

## 2. VCSEL Fabrication and Design for CS Formation

Broad-area VCSELs play an important role in the development of CS studies in semiconductor systems. However, it was necessary to develop adequate devices, and there were major challenges to deal with, namely, uniformity (concerning pumping and cavity resonance) and thermal management. In the following, we review two solutions that have been proposed and used for CS experimental studies, one with electrical injection and the other with optical injection. The two approaches are presented and the various pros and cons are discussed.

**2.1. Electrically Pumped Broad-Area Devices.** The bottom emitter VCSEL structure is represented on Figure 1, a detailed description and characterization of which can be found in [51, 52]. The VCSEL is designed for laser operation around 980 nm and optimized for high-power, cw emission. The active zone is composed of three InGaAs/GaAs quantum wells, embedded in an AlGaAs spacer to fabricate the one-wavelength thick cavity. Two high reflectivity  $\text{Al}_{0.9}\text{Ga}_{0.1}\text{As}/\text{GaAs}$  Bragg mirrors close the cavity. The top mirror is p-doped with Carbon, while the back mirror is n-doped with Silicon. The back and front mirrors have respectively, 30 and 24.5 pairs of quarter wavelength-thick layers at the targeted cavity resonance of 980 nm. The whole cavity is grown on a GaAs substrate using molecular beam epitaxy (MBE). Circular mesas of diameter ranging from 100 to 250  $\mu\text{m}$  are then etched in the structure before oxidation of the current aperture down to the beginning of the back mirror, where a thin (30 nm) AlAs layer has been included. This layer is oxidized in a water-nitrogen environment at high temperature, leaving an oxidized ring of 25  $\mu\text{m}$  width. A TiPtAu contact is then deposited on top of the mesa and the device is soldered on the heat sink. Heat sinking is provided by metalized diamond sinks soldered with AuSn. On the other

side of the VCSEL, the substrate is thinned down to 180  $\mu\text{m}$  and antireflection coated in order to avoid back reflection from the air-semiconductor interface into the gain medium. The diamond can then be attached to a copper submount with a thermal paste. This design ensures a very good overall thermal conductivity of the VCSEL, compulsory for cw operation with large active areas. Cw operation was indeed obtained for 200  $\mu\text{m}$  or even higher diameter VCSELs with very good conversion efficiency and low threshold at room temperature. In [53], the group at the University of Ulm reported room-temperature, cw operation of 320  $\mu\text{m}$  VCSELs in diameter with a maximum output power of 0.89 W and a current density at threshold of 1  $\text{kA}/\text{cm}^2$ .

This VCSEL design has been successfully employed for the first demonstration of cavity solitons in a semiconductor optical amplifier [50], and subsequent studies on cavity soliton lasers in an extended configuration with a feedback grating [54] or face-to-face configuration [55] (see Section 4).

While a VCSEL possesses in theory a translational symmetry across its useful aperture, this is not the case in practice, and this has important consequences for CS studies. There are indeed two main types of spatial nonuniformities to consider: extended nonuniformities such as those of the cavity resonance wavelength and of the pump, and localized nonuniformities. Because of the growth conditions, layer thicknesses vary over the substrate that results in the appearance of a wedge along a given direction. This wedge does not affect much the spectral characteristics of the Bragg mirrors; however, the gradient in the cavity thickness translates into a cavity resonance wavelength gradient. The effect is all the more important when dealing with broad area devices, because then cavity resonance can vary appreciably across the VCSEL optical aperture. Since CS are sensitive to any parameter gradients [40, 56, 57], this may have major impact on their observation and control. In the seminal experiment on CS in VCSELs [50, 58], a large cavity resonance gradient of 2.34  $\text{GHz}/\mu\text{m}$  was measured which prevented the observation of cavity solitons over the entire VCSEL surface. Later, improvements in the growth conditions enhanced the VCSEL uniformity of about one order of magnitude (0.4  $\text{GHz}/\mu\text{m}$  [59]) and allowed the manipulation of CS over the whole transverse extent of the VCSEL. As for the pump uniformity, the bottom emitting structure allows to achieve a very good uniformity at the center of the device, whereas the borders suffer the well-known current crowding effect [60]. This manifests itself through the appearance of a high-order flower-like pattern [35] just above the laser threshold and limits the available area for CS manipulation. However, since bottom emitting devices grown on a GaAs substrate are limited to wavelengths above 900 nm to avoid absorption, shorter emission devices may require adopting other techniques. As an example, electrode patterning and use of semitransparent ITO electrodes were considered for the design of 850 nm, broad-area top emitting devices [61] and proved promising for improving electrical injection uniformity of top-emitters. A by-product of this technique would also be the possibility to address CS electrically with local electrodes. Electrode patterning was also used in [62] on a 960 nm top emitting VCSEL in the optical amplifier

regime. Bistability and optical pattern formation which are prerequisites for CS formation were observed. However, the insufficient transverse extension of the VCSEL together with the rather large grid period ( $4\ \mu\text{m}$ ) prevented CS formation on a uniformly injected background.

The spatially localized sources of nonuniformity that have also to be taken into account for CS studies are often termed as defects, and may precisely arise from crystallographic defects in the Bragg mirror materials or in the Quantum wells, and lead to CS pinning. More detailed studies on the sample uniformity have been conducted in [63], where CS were used as a spatial probe for defects, and in [64], where localized defects were used as a source of drifting CS. These aspects are detailed in Section 5.2.

*2.2. Optically Pumped Broad-Area Devices.* An alternative scheme for CS studies relies on the use of optically pumped devices. It may seem at first rather incongruous to deal with optically pumped VCSELs while electrical injection has always represented the ultimate goal in devices. However, the advent of high-power low-cost sources could make it a reasonable choice, all the more that integrated and compact sources can be fabricated. There are several advantages in using optical pumping for CS formation and studies. The first one is that optical pumping allows to easily shape the pump beam using conventional optics and to get rid of current crowding effects by using, for example, a top-hat shape illumination. Since the processing steps after the device growth are reduced, the second advantage one can expect is to reduce the number of defects, and thereby the stress on the final sample, hence the number of pinning sources. The third but not the least advantage is that the pump field may be shaped not only in the transverse but also in the propagation directions, as will be described further in the text and used in Section 4 to design new compact devices. Note also that optical pumping is commonly used in VECSELs for high power lasers [65, 66] and may also be used in the framework of studies on CLB (see Section 6.2). There are, however, problems to be circumvented in order for optical pumping to be a viable solution. The most important problem is the thermal management, to be addressed along its two components: heat production and heat dissipation. It is all the more important here as we consider broad area devices. Heat dissipation is common to the electrical pumping case and the same techniques can be somehow applied. On the converse, heat production is largely specific and depends on the material system considered. In some systems where all the pump power is not absorbed in the gain region, the substrate absorption at the pump wavelength may represent the major part of the heat production. Therefore, a special care has to be taken to avoid it while optimizing the pump absorption in the gain medium. The second contribution to heat production (and to pump energy waste) is the so-called quantum defect, that is, the energy difference between the pump energy and the laser transition (usually close to the bandgap of the semiconductor material). Pump photons absorbed by the semiconductor material produce electron-hole pairs at an energy higher than that of the band gap that cascade to the bottom of the bands through phonon exchange with

the crystal lattice (see Figure 2). At the end of the process, all the excess energy is transformed into heat and transferred to the lattice. There is very little to do against this fundamental mechanism except reducing the photon energy excess by choosing a proper wavelength.

As a result, an efficient optical design must minimize heat production and optimize pump absorption into the gain region. Such a design has been proposed in [67] and successfully applied to CS studies in [68] in the AlGaAs material system.

The design relies on the creation of a window at the pump wavelength around 800 nm. The pump window corresponds to a region in the optical spectrum of the cavity where transmission is minimized and pump absorption is maximized, while keeping the cavity properties at the operating wavelength of 870 nm unchanged. This is accomplished by an optimization procedure on the layer thicknesses composing the multilayer mirrors of the cavity. Target values of the transmission, reflection, and absorption spectra in given spectral regions are chosen. The procedure starts with a quarter-wavelength  $\text{Al}_{0.225}\text{Ga}_{0.775}\text{As}/\text{AlAs}$  multilayer stack centered at 870 nm. Then, all the layers composing the back and front multilayer mirrors are allowed to vary in order to reach the desired spectral targets. This is simply done by minimizing an error function that measures the deviation from the ideal target and the actual values, depending on all the layer thicknesses. A Simplex algorithm is used as a minimization algorithm. The algorithm eventually converges towards a set of layer thicknesses values (see Figure 2(b)). As can be readily seen, all the layer thicknesses have different values and the initial periodic structure is lost.

The calculated structure has been grown by metal-organic chemical vapor deposition and the reflectivity and calculated spectra are shown on Figure 3. There is a very good agreement between the calculated and the measured reflectivity spectra. The pump window is easily seen on the left around 800 nm, where absorption is maximized and at the same time pump transmission into the substrate is minimized. The cavity resonance structure at 890 nm is kept. This design ensures that very few pump photons will be absorbed into the substrate and contribute to heating while optimizing the pumping efficiency. The width of the pump window is 20 nm which introduces immunity against eventual temperature induced shifts of the reflectivity spectra through temperature-induced index change and subsequent dramatic effects on the pumping level. It also allows pumping with a large numerical aperture microscope objective or lens. The VCSEL can then be processed with other techniques to enhance heat removal, such as substrate removal and replacement with a high thermal conductivity substrate such as SiC substrate or diamond substrate. Note that this technique does not prevent heat absorption into the substrate, since, in general, the bonding layers absorb very efficiently the pump photons. Substrate removal and SiC bonding with Ti-InAu bonding has been employed in the sample used in [68].

The same design technique has been used and refined to fabricate a monolithic VCSEL with intracavity saturable absorber. VCSELs with intracavity saturable absorbers were

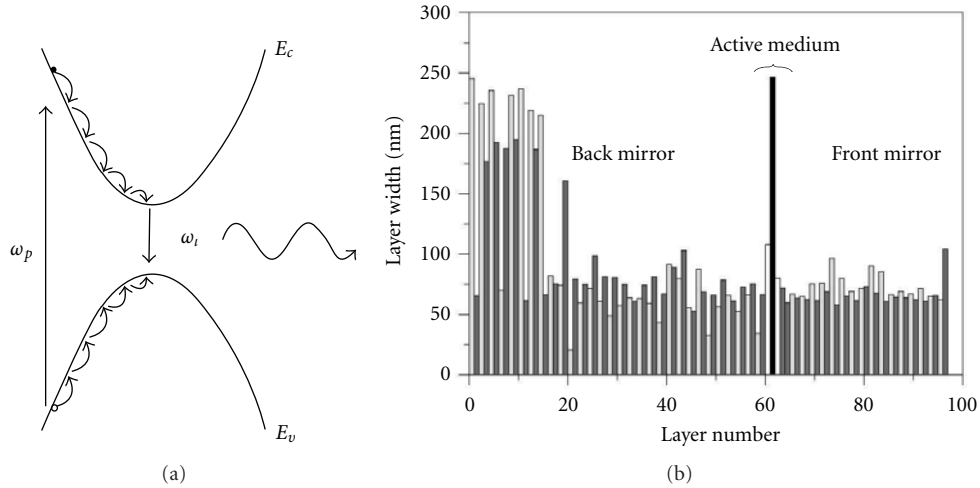


FIGURE 2: (a) Schematic representation of optical pumping in a semiconductor material: a pump photon of energy  $\hbar\omega_p$  is absorbed in the semiconductor material creating an electron-hole pair. The electron and hole cascade to the bottom of the bands releasing extra energy to the lattice and eventually recombine either radiatively or nonradiatively. (b) (after [67]): Layer widths of the optimized structure. The substrate is on the left side of the figure. The cavity is filled by two absorbing  $\text{Al}_{0.07}\text{Ga}_{0.93}\text{As}$  spacers (layers 61 and 63) white bars around a bulk GaAs active layer (layer 62, in black). The back and front Bragg mirrors are composed of alternating  $\text{Al}_{0.22}\text{Ga}_{0.78}\text{As}$  (dark gray) and AlAs (light gray) layers.

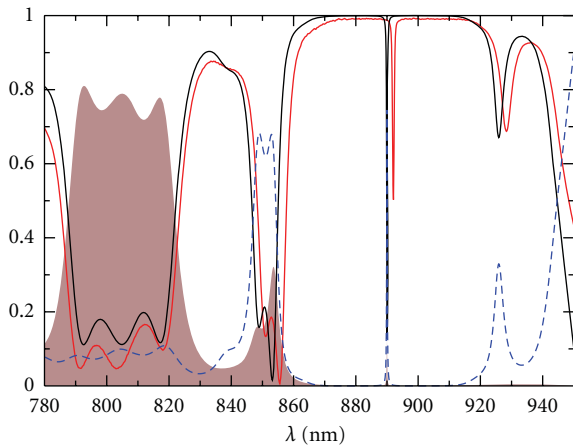


FIGURE 3: Calculated and measured spectra of the optimized cavity. Red line: experimental reflectivity spectra. Black line: corresponding calculated reflectivity spectrum. Brown: calculated absorption. Dashed blue: calculated cavity transmission.

already considered in the prospect of building self-pulsing or bistable vertical-cavity lasers. Several designs have been proposed for electrically injected devices. A quantum well may for example be placed in the upper or lower mirror stack with a shorter carrier lifetime [69] or with an additional contact for controllable operation [70]. Self-pulsing have also been observed in small area, oxide-confined VCSELs thanks to the difference between the carrier and the optical mode confinement [71]. A double cavity may also be used for controllable self-pulsing or bistable operation [72]. These techniques necessitate either a small area cavity, a fast saturable absorber, or a complex electrical design and are not

suitable for CS studies. An original design for a vertical cavity laser with intracavity saturable absorber has been proposed in [73]. Using the same technique as explained before, a cavity having a saturable absorber section and a gain section is designed. The gain region has two InGaAs/GaAs QW for lasing around 980 nm. The saturable absorber section has one InGaAs/AlGaAs QW. All the QWs are placed at the antinode of the resonant cavity field targeted at 980 nm. The cavity is designed for optimized optical pumping around 800 nm. Therefore, in addition to the previous optimizations, the multilayer mirror widths have also to be calculated in order to satisfy a condition on the pump field intensity inside the active zone of the cavity. The pump field is almost zero in the whole pump window at the location of the SA QW. The gain QW barriers absorb the 800 nm pump field, whereas the SA QW barriers are made transparent to the pump wavelength in the pumping window by aluminium incorporation inside the barriers. The design is depicted in Figure 4 and has been successfully used to demonstrate bistability, self-pulsing, and a compact cavity soliton laser (see Section 4).

### 3. CS in Semiconductor Optical Amplifiers

The most studied system in optics is represented in Figure 5. A nonlinear medium inside an optical cavity is driven by a homogeneous optical beam covering the whole transverse section of the device. The system can be set such that the output intensity is zero and all the incoming beam is absorbed by the saturable medium. If the condition for the bistable behavior is fulfilled, then a short and narrow optical pulse may ignite a small region of the device. Such an optical pulse is called the writing beam. If it is in phase with the holding beam, a CS is created at the location where it impinges that persists after the writing pulse disappears. In a similar

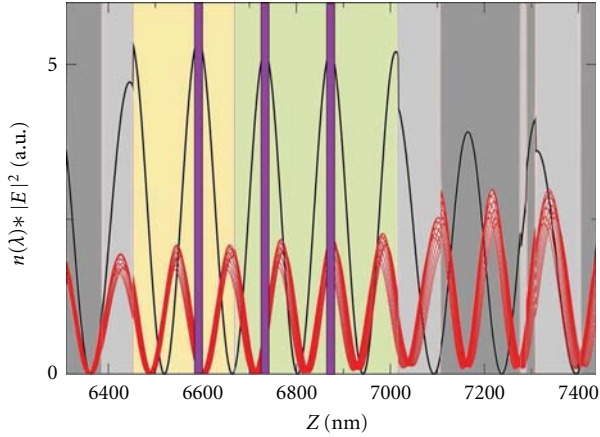


FIGURE 4: Active zone of the VCSEL-SA and field intensities at the cavity resonance (black, divided by 400) and at the pump wavelengths (in red, between 795 nm and 805 nm) versus the growth depth. The active zone is composed of two regions (in yellow and green): the SA region (yellow) with one InGaAs/Al<sub>0.22</sub>Ga<sub>0.78</sub>As quantum well and the amplifying region (green) with two InGaAs/Al<sub>0.05</sub>Ga<sub>0.95</sub>As quantum wells. The first few layers composing the the front and back mirrors is visible on the right and left respectively. of the active zone. Light grey: AlAs. Dark grey: Al<sub>0.22</sub>Ga<sub>0.78</sub>As. Note that the SA quantum well is at a node of the pump fields in the whole range of possible pump wavelength while being at an antinode of the field at cavity resonance. After [73].

way, another CS can be created in any other location provided the correlation length of the localized structure is significantly smaller than the transverse size of the device. CS written in the way described above can be erased by sending a pulse quite similarly to the writing pulse at the same location but with phase opposite to that the holding beam.

Experimentally, CS have been observed in several systems based on photorefractive crystals [48], Na vapors [46], liquid crystal light valves [49, 74], semiconductor optical amplifiers [50, 68], and lasers [54, 55, 73, 75]. In the latter, most experiments have been done in VCSELs, because their short cavity and large diameter insure a Fresnel number large enough to avoid the formation of patterns correlated over the whole extension of the system. CS have been observed in amplifiers both electrically [50] and optically pumped [68]. The pumping rate was set high enough to provide gain in the active medium but low enough to maintain the VCSEL below the laser threshold. However, it must be noted that similar results have been obtained with an injected VCSEL pumped slightly above threshold [59].

A typical experimental setup is shown in Figure 5. A bottom emitter VCSEL with a diameter of 150  $\mu\text{m}$  was injected by a coherent optical beam produced by an edge emitter laser with an external cavity in a Littrow configuration. Thus, the holding beam can be fine tuned in the range 960–980 nm. This beam was spatially filtered such that the intensity could be considered as almost uniform across the whole section of the VCSEL, and thus not introducing an additional gradient component. The holding beam power was controlled by an acousto-optic modulator together with a polarizer. The

second output coming from the external cavity laser was then used as a coherent writing beam (WB). This beam was prepared so as to obtain a 10  $\mu\text{m}$  waist; its power was controlled by an acousto-optic modulator. The phase relation between the writing beam and the holding beam was controlled by piezo-positioning a mirror on its own path. The reflected output of the VCSEL was monitored globally by a CCD camera or locally using a fast photodetector.

The observation of CS in an electrically pumped VCSEL amplifier [50, 58] and the demonstration of their mutual independence is explained in Figure 6. Similar results have been obtained in optically pumped VCSEL amplifiers [68]. The demonstration relies on the independent writing and erasure of two CS at two different locations of the VCSEL. In the first demonstrations, the locations where the independent manipulation of the CS could be obtained in practice were limited by the presence of a strong cavity resonance gradient. In the following experiments, new devices with much smaller gradients were provided and allowed manipulation over almost the whole transverse extent of the device, that is, 200  $\mu\text{m}$ . The switching characteristics were analyzed in [76]. A sequence of independent control of two CSs using in-phase local excitation with the holding beam (writing beam) or  $\pi$ -phase shifted beam (erasure beam) is shown in Figure 6.

The use of the phase parameter to control the writing or erasure process of a CS reveals in fact quite cumbersome in practical applications. However, an incoherent switching technique has been demonstrated by Barbay et al. in [68]. Using a specially designed optically pumped VCSEA as described earlier, they have shown that CS writing and erasure can be achieved by short pulses (60 ps duration), at a wavelength far from that of the holding beam, demonstrating a mechanism free of phase relationship. This technique relies on the observation that CS in semiconductor devices are compound objects. While a localized structure is formed in the intracavity field distribution, a counterpart forms in the carrier density. Hence, it is possible to excite CS by locally adding carriers. The fact that both writing and erasure are possible by local carrier injection, with slightly different HB parameters though, is intriguing and has been explained in terms of local temperature effects in [77]. As in the coherent case however, a delay is observed in the writing process which depends on the operating conditions and which is of the order of 100–200 ns (against several ns in the coherent case). The erasure process is faster and occurs without delay in a timescale of a few ns or less. The writing delay can be reduced by increasing the writing power.

In theory, one needs a translationally invariant system for CS formation and control. In practice, the presence of gradients in the system is unavoidable. They arise from different sources.

- (i) Device growth and fabrication: the VCSEL cavity resonance used in [50] had a linear variation along one diameter of the device. This variation creates a linear gradient of one of the most important control parameters in the experiment: the detuning between the cavity resonance frequency and the frequency of the holding beam. Though generating important

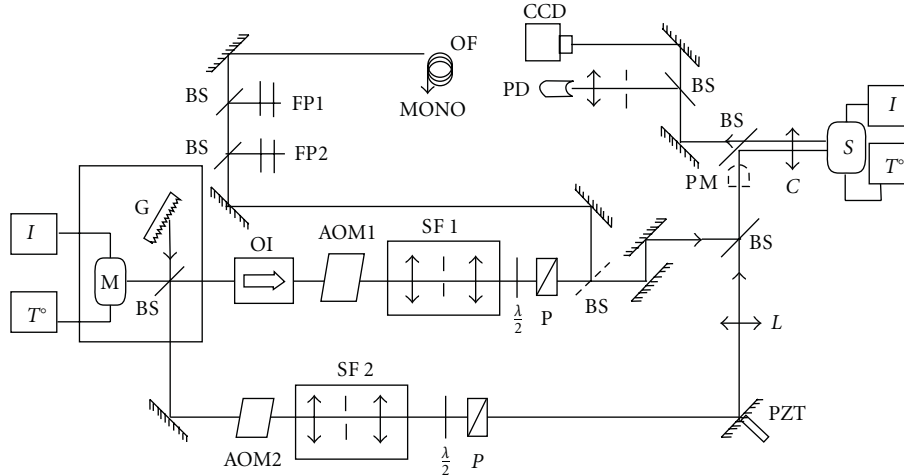


FIGURE 5: Experimental setup. M, high power edge emitter laser; I, current driver stabilized up to 0.01 mA; TO, temperature controller; G, grating; OI, optical isolator; FP, Fabry-Perot resonators; AOM, Acousto-optic modulators; SF1, beam expander configurator with spatial filtering; SF2, beam reducer configurator with spatial filtering; S, broad-area vertical cavity surface emitting laser; C, collimator; CCD, camera; PD, Photodetector; PZT, piezoelectric ceramic; M and BS, mirrors and beam splitters; PM, power meter (optional);  $\lambda/4$ ,  $\lambda/2$  wave plates; P, polarizers; OF and MONO, optical fiber and monochromator.

consequences, it can be controlled by the growth conditions.

- (ii) Nonuniform distributions of carrier injection in electrically injected devices. Usually, electrically pumped broad area devices present a current density higher at the borders than in the center of the active zone (current crowding effect). For this reason, a bottom emitter structure was preferred in the first demonstration of the generation of localized structures in a VCSEL because the longer distance between the ring electrode and the active medium translates into a more uniform current distribution.
- (iii) Misalignment of the holding beam with respect to the optical axis of the VCSEL.
- (iv) Not completely uniform intensity distribution of the holding beam.
- (v) Defects in the VCSEL structure. Some defects may repel the localized structure while others tend to pin them (see Section 5.2).

All these gradients could affect the generation and the stability of CSs. Localized structures move under the effect of a gradient and in semiconductor devices can move fast enough to prevent a CDD camera from detecting them. Fortunately, some defects or unwanted gradients of the device or induced by the imperfections in the experiment would pin them so that they remain stable and steady. During the first experiments, CS appeared always at the same set of positions. The introduction of external intensity or phase gradients allowed to move them around in a controllable way demonstrating the independence from the boundaries and the possibility to observe them in the whole transverse plane of the device which can be relevant for some applications as we will explain in Section 5.

Later, cavity solitons have been observed in electrically pumped VCSEL above threshold (see Section 4). The main properties of localized structures in optical amplifiers are the intensity and phase stability. The good stability in intensity is defined by the fact that the low and high intensity of the bistable cycle are very well defined at all positions and remain the same as much as the parameters are kept constant over the whole transverse section of the device. If the optically injected VCSEL is driven above threshold instead, the lower branch of the bistable cycle is usually unstable and the CS intensity fluctuates in time. The holding beam defines the phase of the CS so that the phase is fixed all across the transverse section of the device. Thus, a possible transverse phase wave generated by the fast change in intensity at the position of the CS will not propagate. If a phase wave is created, then it will act as a phase gradient for a second CS and it will move towards the border of the device as explained in [78].

In all cases, the experimental results have been compared with numerical ones showing very good qualitative agreement and in some cases even quantitative agreement with semiclassical models.

#### 4. CS Lasers

Vertical cavity semiconductor optical amplifiers (VCSOAs) allowed to demonstrate many useful properties of CS for possible applications to all-optical processing of information (see Section 5). However, they necessitate the use of a coherent holding beam for optical injection which makes the experimental implementation more difficult, bulky, and costly. Moreover, CSs in such a case sit on a nonzero background and the contrast between the CS peak intensity and the background intensity is reduced. This is why laser CS would be needed to circumvent all these problems.

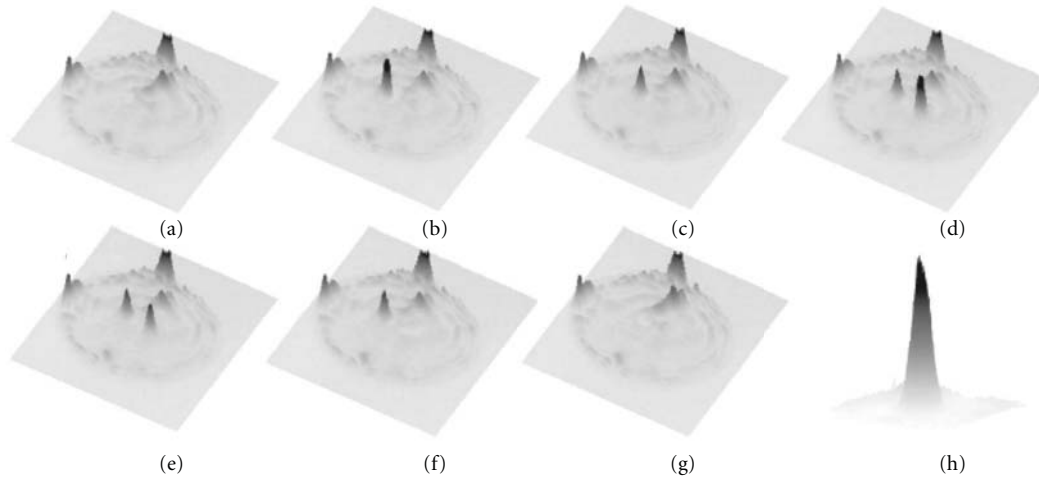


FIGURE 6: 3D representation of the VCSEA near-field intensity distribution, after [58]. The holding beam is always on, and all parameters are kept constant in the sequence (a)–(g). (a) The writing beam (WB) is off; (b) the WB induces the appearance of a single CS; (c) the WB is off again, and the CS remains; (d) the WB is displaced in position, and switched-on again and generates a second CS; (e) the WB is off again and the two bright spots coexist; (f) the WB targets the second CS, but the relative phase of WB with respect to HB has been changed, and the CS is erased; (g) the WB targets the first CS, and it is erased in the same manner as in (f). Once the WB is blocked, the intensity distribution is identical to (a). In (h) is shown the CS profile.

It is to be noted that contrarily to what was believed at the early stages of their studies, CS in the laser regime can indeed exist in a VCSEA. As a laser with injected signal is known to develop temporal (Hopf) instabilities that can couple to the spatial degrees of freedom and drive the system to a regime of spatio-temporal chaos, this seemed *a priori* not favorable to the formation of CS which require a stable background to form on. It was nevertheless shown in [59], both experimentally and theoretically, that CS can be observed in a driven VCSEL above threshold. The theoretical modeling indicate that CS can exist even on the oscillatory background generated by the onset of a Hopf instability. This is confirmed in the experiment, where it is shown that CS can survive in a narrow parameter range. Still, the laser CS thus obtained is limited by the necessity of a coherent holding beam (HB), which in addition to injecting energy, fixes the phase of the CS. This is in contrast to the case of a true, “free-running” CS laser (CSL) which can be described as a self-confined microlaser for which the phase is not fixed. This last point has important consequences regarding CS interactions.

Theoretically, CSL have been found in two-photon active media [79] or in dense two-level systems [80]. In the context of semiconductor CSLs, two possible bistable laser schemes have been studied. The first one is the VCSEL with frequency selective feedback, which led also to the first demonstration of CSL in a semiconductor system [54], and the second one is the VCSEL with saturable absorber, studied in a compact and an extended cavity configuration.

The VCSEL with a frequency selective feedback scheme is depicted in Figure 7. A broad area VCSEL of  $200\ \mu\text{m}$  diameter emitting around  $980\ \text{nm}$  is used in an external cavity configuration where a grating in Littrow configuration here, or a volume Bragg grating in later experiments, is used to close the cavity. A pair of lenses is inserted inside the cavity in

the self-imaging configuration in order to keep a high Fresnel number cavity hence the possibility to have a high number of transverse modes and allow for spatial decorrelation. A half-wave plate is used to match the VCSEL polarization direction of the laser emission to those of the beam splitters—BS1 and BS2—and of the grating. The grating is tuned such that its maximum reflection is red detuned with respect to the VCSEL longitudinal mode. Above a certain threshold in the injected current (lower than the solitary laser threshold), the system starts to emit and displays several isolated spots whose characteristics are those of a CSL [54]. The spots are bistable, almost identical in shape and size ( $10\ \mu\text{m}$ ), individually controllable in certain transverse locations of the laser (see Figure 7(b)), and can be put into motion or “dragged” by an appropriate intensity gradient obtained by inserting a comb filter in the cavity. The emission spectrum of each spot is narrow as expected in a laser. The writing beam that provides a temporary and localized excitation is not coherent with the spots. Further details on the different switching techniques are described in [81], and a model that qualitatively agrees very well with the observations is proposed in [82]. Interestingly, the switch-on and off are obtained with an incoherent beam and the function (writing or erasure) is controlled by the position of the localized excitation with respect to CSL location. This position depends on the grating orientation. The minimum writing beam pulse width needed to ignite a CSL is below  $15\ \text{ns}$  (lower limit not known due to experimental limitations), while the shorter the writing beam pulse, the higher the intensity is required [83]. Spontaneous switch is also observed following an uncontrolled perturbation (being of mechanical, thermal, optical origin). In such a case, the switch on is accompanied by short transient pulses, a feature of interest with respect to Section 6.2. Multiplex structures are also observed [84] and

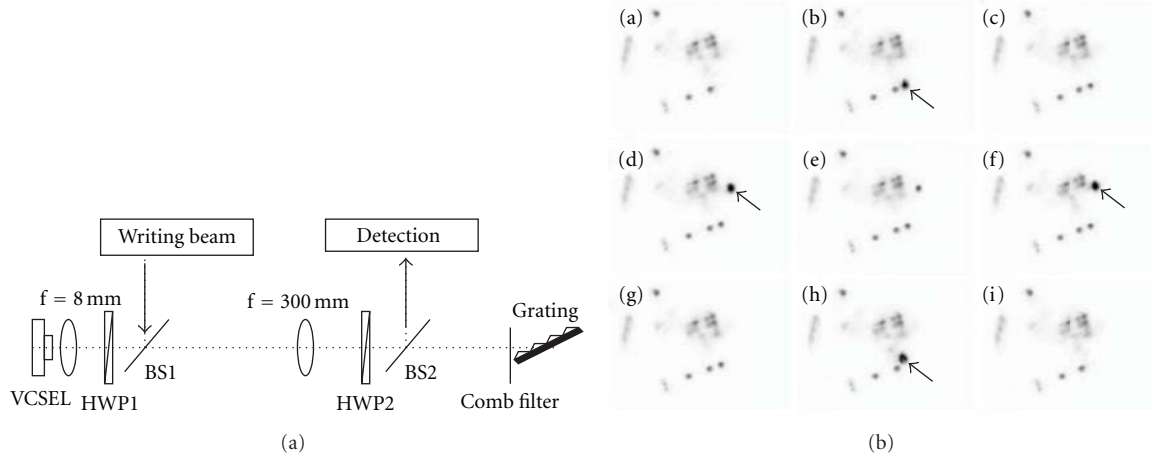


FIGURE 7: (a) Experimental setup of a CSL consisting in a VCSEL with frequency selective feedback. One pair of lenses are inserted inside the cavity in the self-imaging configuration. Beam splitters BS1 and BS2 are used for writing beam input port and for output detection. (b) Sequence of images (inverted contrast) of the VCSEL surface showing the independent writing and erasure of two CSL. Reprinted with permission from [54]. (© 2011) by the American Physical Society.

associated with a CS-splitting phenomenon reminiscent of the homoclinic snaking curve observed in amplifier systems [45].

It has been long known that semiconductor lasers with saturable absorbers can be bistable. They constitute thus the second system of choice for CSL studies. The first demonstration of a CSL with a saturable absorber has been reported in [55]. The experimental setup consists of two mutually coupled, face-to-face, VCSELs depicted in Figure 8. It is composed of two broad area ( $200\ \mu\text{m}$  diameter) 980 nm VCSELs, provided by the same company (ULM Photonics) as in the previous demonstration. The VCSELs are optically coupled by lenses in the self-imaging configuration. A beam splitter is used for detection and for localized excitation. One VCSEL is biased above transparency and operated in the gain regime, while the other VCSEL is biased below transparency and operates in the saturable absorption regime. The temperature of the gain VCSEL is set such that its emission is slightly (1 nm) blue detuned with respect to the below-threshold spontaneous emission of the second VCSEL. The output detected when the gain laser current is varied is shown in Figure 8. For low currents, light emitted by the gain device is almost fully reflected by the second VCSEL because of the frequency mismatch. The system starts to lase with a threshold lower than that of the solitary laser (Figures 8(a) and 8(b)). When laser emission starts to saturate with increasing current, and because of its thermal red-shift, laser emission starts to decrease as its coupling with the second VCSEL progressively increases. When enough intensity can enter the saturable-absorber cavity, absorption saturation takes place, and a bistable characteristics is locally recorded. In the near-field image of the sample, bistable laser spots appear that can be controlled independently with an external beam. Here, a localized excitation whose wavelength is close to that of the emitted light is used. The switching process is analyzed in [85]. Switch-on is accompanied by rather long (600 ns) transients composed of 150 ps pulses with a period equal to

the round-trip time of the external cavity, relevant in the context of Section 6.2. Multistability among several, multi-colored monochromatic CSL is analyzed and modeled in [86, 87]. The proposed model also explains the observation and control of bistable laser vortices reported in [88], that were predicted earlier in wide-aperture, class-A lasers with saturable absorption in [89].

A compact CSL has been demonstrated in [73, 75]. The device, a monolithic, optically pumped, vertical cavity laser with intracavity saturable absorber, is described in Section 2.2. At difference with the previous demonstrations, this system is purely single-longitudinal mode. Its theoretical description is intrinsically simpler and laser CS models have been studied in [90, 91] and in [92–94] for semiconductor laser models (see also [2] for a recent theoretical review). The vertical-cavity is optically pumped uniformly on a  $70\ \mu\text{m}$  diameter.

Fast and sequential independent and incoherent writing/erasure are demonstrated with short (60 ps) pulses at a maximum rate of 82 MHz (see Figure 9). Note that the switch-on time is very fast (several ns) and only limited by relaxation oscillations [75], while the switch-off time is of the order of 1 or 2 ns, as expected in this kind of systems [95]. The same beam characteristics were used for both switch-on and switch-off. Theoretical work [95] suggests the important role played by the writing/erasure beam width in the spatiotemporal dynamics that may explain why the same intensity distribution can allow exciting or erasing a laser CS.

One important point in CSL with respect to CS in amplifying systems is that the phase of the localized state is not fixed and may have *a priori* arbitrary value. Nevertheless, the phase profile of a laser CS is larger than its intensity profile, and it was shown in [94] that CSLs at a distance shorter than  $60\ \mu\text{m}$  will interact and form a cluster. The practical value in experimental systems above which LCS may be independent is however, smaller because of system's inhomogeneities that destroy the long-range interactions. If the distance between

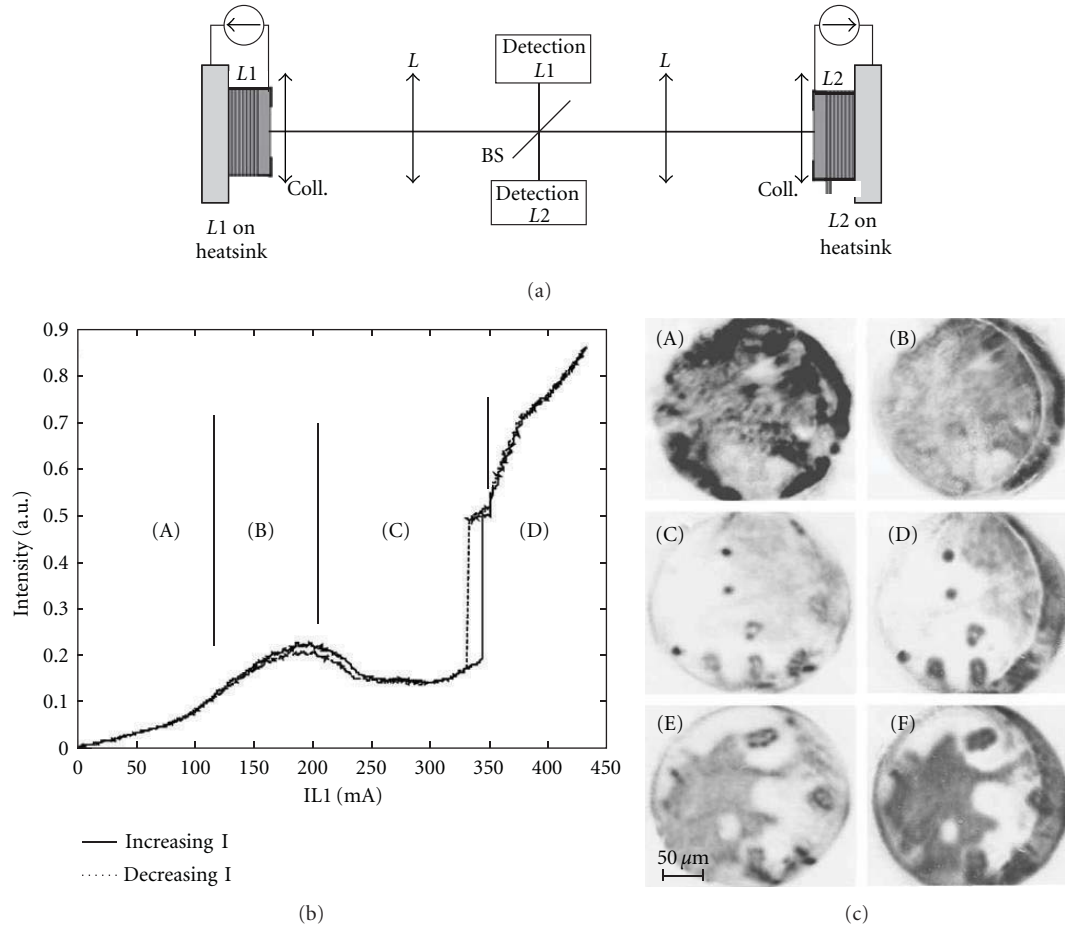


FIGURE 8: Experimental setup (a) and experimental results (b) and (c) obtained in the face-to-face VCSELs configuration (see text for details). Reprinted with permission from [55]. (© 2011) by the American Physical Society.

each laser CS is too small then laser CS shall not be independently controllable anymore [75]. The properties of clusters of laser localized structures and the associated motion is thoroughly studied in the theoretical paper of [96, 97]. Experimentally, clusters arise either spontaneously [75] or following a “splitting” process as the pump is increased as in [84, 98]. An experimental confirmation that uncoupled, single-peaked Laser CS are mutually incoherent is given in [84, 98], while clusters are found to have a well-defined phase relationship as reported in [98].

An important feature of CSL not yet clearly experimentally demonstrated is related to the control of their motion. In amplifying systems, motion can be induced either by a phase or intensity mask on the holding beam (see Section 5). In laser systems, one cannot use the phase degree of freedom anymore. Motion can be induced by instabilities, as studied in [99, 100], where spontaneous motion is expected when the ratio of the carrier lifetimes in the active and passive medium, respectively, is below a critical value. If boundaries are included, for example, circular boundaries, CS move along the boundaries, an effect that can be exploited for an optical clock [100]. Experimentally, techniques to control the index of refraction of the cavity by using a spatial light

modulator [101] may prove interesting, at the expense of a greater complexity of the experimental setup. Controlling the CSL motion remains therefore an important challenge.

## 5. Applications of CS to Photonics

The main properties of localized structures or cavity solitons in optical systems are twofold (1) They can be switched-on and off independently so that one can control their appearance and disappearance. (2) If the system is homogeneous in the transverse plane, CSs are free to move, thus they will feel the existence of any gradient. In other words, their position and their velocity can be controlled by adjusting a gradient of intensity and/or phase. These properties raise the idea that one can use localized structures in applications related to information processing. The most natural one is an all optical memory [38, 40, 50, 102, 103] due to the controllability in position and switching capabilities of CSs. However, there are several other possible applications not so obvious at first sight. In the following, we present two possible applications of cavity solitons: one in the optical information processing context, an all optical delay line; and

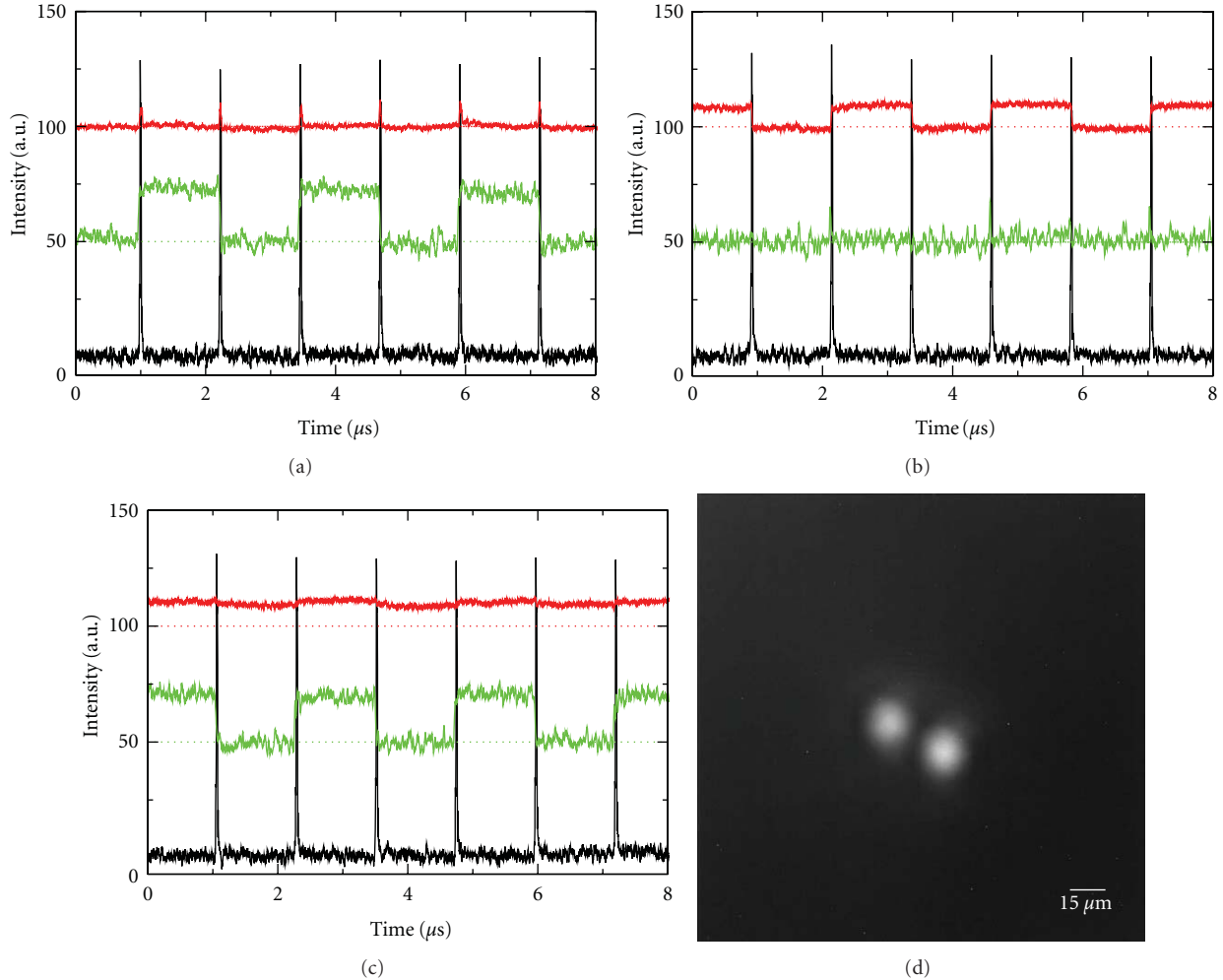


FIGURE 9: Independent and sequential writing-erasure of one cavity soliton while keeping the neighboring cavity soliton unchanged (a,b,c). The black trace corresponds to the incoming localized excitation pulse, and the middle (upper resp.) trace, green (red resp.) online, corresponds to the leftmost (rightmost resp.) cavity soliton. The zero intensity levels of the upper and middle traces (dashed lines) have been artificially offset by 100 and 50, respectively for clarity. An averaged image of the two-cavity solitons considered is shown in (d). After [73].

another for material structure determination: a soliton force microscope.

**5.1. All-Optical Delay Line.** Apart from the existing electronic devices that are used today as shift registers, there has been increasing interest in all optical delay lines in the last few years. Most of the proposed all-optical systems are based on slowing down light by modifying the group velocity. Such variation can be a consequence of a nonlinear process like electromagnetically induced transparency (EIT), stimulated Brillouin scattering (SBS), and so forth. In [104–108], it is possible to find several schemes based on slow-light in order to realize a delay line (Figure 10).

Using localized structures, it is possible to propose a completely different approach based on injecting a stream of optical pulses into a nonlinear device. Each injected pulse will create a CS. If a linear gradient is somehow superimposed, the CS will drift along this line at a speed which,

for some range of parameter values, is proportional to the gradient. The CS can be recovered later at a different spatial position. This method was proposed for the first time by Firth and Scroggie in 1996 [40, 57] and demonstrated experimentally in Na vapors by Schäpers et al. in 2001 [109] and by Pedaci et al. in 2008 in a VCSEL [110].

The optical system used in [110] is a bottom emitter VCSEL as described in Section 2.1. The broad area device (200 microns in diameter) is injected by a collimated beam focused by a cylindrical lens. This allows the generation of a homogeneous injection beam along a line transverse to the direction of propagation of light on the microresonator. The intensity of the injected field, the detuning between the cavity resonance and the injected field frequencies, and the pumping current of the VCSEL were set at typical values for which the CS may exist in such devices (see [58]). Five fast avalanche photodiode detectors are placed in the near-field image plane so as to detect the output intensity of the device

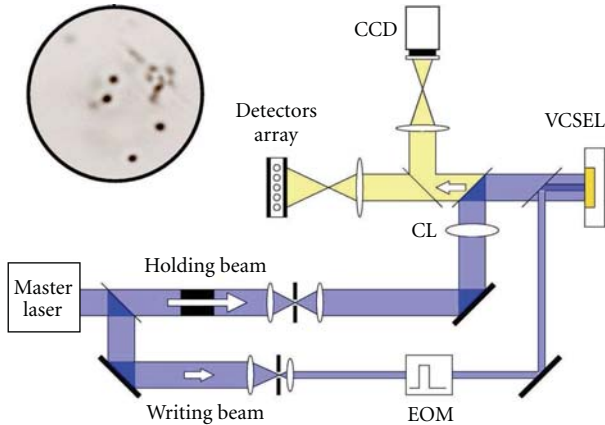


FIGURE 10: Experimental setup. Vertical cavity surface emitting laser (VCSEL); cylindrical lens (CL); electro-optic modulator (EOM); tunable master laser (ML). Inset: transverse profile emission (negative image) of a  $200\ \mu\text{m}$  section VCSEL, in the regime of CS existence under injection by a broad holding beam. Four CSs are present in the image. (figure reproduced from [110]).

along the line defined by the holding beam. A linear phase gradient is generated by tilting the holding beam with respect to the axis normal to the VCSEL. The amount of gradient is then controlled by the angle of incidence of the holding beam. A CS is then created by applying a  $100\ \text{ns}$  writing beam pulse at some point of the microresonator. This CS drifts as a consequence of the presence of a phase gradient along the line defined by the cylindrical lens and its passage is detected by the fast photodiodes. The detected output intensity as a function of time is displaced depending on the detector considered, as can be seen in Figure 11. It is clear then that the CS generated at one point in the transverse section of the device is drifting along a line and detected sequentially by the five fast detectors. Knowing the distance between the corresponding points detected by the fast photodiodes ( $7\ \mu\text{m}$ ), the speed of the CS is measured as a function of the tilt-induced phase gradient. In the case represented in Figure 11, the average speed of the CS is  $4.7\ \mu\text{m}/\text{ns}$ . The observation provides a proof-of-principle for an all optical delay line based on the property of motion of the CS under the influence of a phase gradient.

The experimental results obtained in [110] are in good agreement with numerical ones obtained by integration of a semiclassical model. In Figure 12, numerical results are shown corresponding to the speed of CS as a function of the gradient strength which are compatible with the experimental ones. For a large interval of the gradient strength, the velocity of the CS is almost linear and can be easily controlled between 1 and 4 micrometer/ns. This is much smaller than those obtained on the devices based on slowing down the speed of light by changing the index of refraction of the medium. Furthermore, those theoretical results indicate that the speed of the CS can be increased by increasing the decay rate  $\gamma$  of the carrier density in the semiconductor device (Figure 12(b)). The system proposed in [110] provides not only an operation of the device as an all optical delay line but

also an all optical pulse reshaping of the incoming optical pulse. Amplitude fluctuations of the incoming pulse are eliminated because of the threshold response of the medium to generate a CS. This functionality may be very useful in order to avoid deterioration of the transmitted signal.

*5.2. Soliton-Force Microscope/Role of Defects.* As stated before the position of a CS or localized structure can be controlled by a gradient. In [103], it was shown that it is possible to position the CS at the maximum of an intensity or phase gradient. On the other hand, CS can be pinned by defects in the structure of the device. The defects act by generating a gradient. If all other parameters are considered uniform, only the gradients generated by the defects will determine the final position of the CS. One may distinguish between two types of defects: those that are able to pin the CS and those that repel them. Thus, in presence of gradients of different origins, the stable positions of CSs will be those where the forces applied on them compensate. This view may however, be mitigated by the recent theoretical demonstration in [111] that CS may also feel the boundaries, even if they are far from them, so that only a finite set of positions are allowed. This point lacks; however, a clear experimental demonstration.

In [63], it was proposed to monitor the motion of CS under the effects of externally applied gradients. Deviation of the CS trajectory from the one imposed by external gradient reflects the presence of a defect of the structure revealing its attractive or repulsive character. As a consequence, a map of the inhomogeneities of the device is given by the frequency of visits of the areas of the device when the motion of CSs is imposed across the entire section of the system.

The experimental setup used in [63] to record the map of inhomogeneities is similar to the one described in the previous section. The motion of the CS is induced by creating a gradient in the transverse direction to the propagation of light. In particular, a spatial modulation of the holding beam intensity was introduced. In order to control the gradient strength and position of the intensity maxima a Mach-Zender interferometer was inserted in the path of the holding beam. The interferometer is set to generate an intensity profile on the VCSEL formed by fringes of  $10\ \mu\text{m}$  size. The pattern allows confining the position of CSs along the direction perpendicular to the fringe. No gradient is present in principle along each interference fringe. In such conditions, only the imposed intensity gradient or intrinsic gradients in the device can induce a motion of the CS. The fringes are adiabatically shifted horizontally by just moving a mirror of the Mach-Zender interferometer controlled by a PZT ceramics. The CS is expected to be dragged in a straight line while the fringe is moved, but it was observed that it deviates from this line. The deviation is attributed to the presence of internal gradients generated by defects in the device. The procedure was repeated for different orientation of the fringes. For an ideal defect-free medium, such analysis would result in a uniformly gray map. As long as inhomogeneities are present, some regions are visited very often by the CS while others are almost never visited. Thus, high-intensity regions in the map correspond to attractive defects while

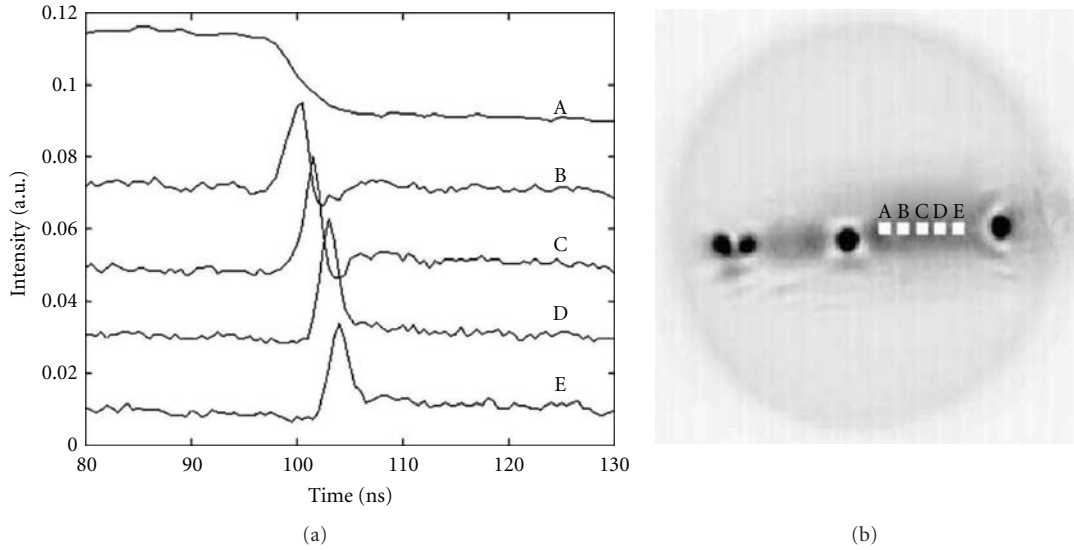


FIGURE 11: Passage of a CS in front of a linear array of five detectors (A)–(E). (a) Time traces of these detectors, displaced vertically by 0.02 units for clarity. Detector A monitors the point addressed by the writing beam, applied at time  $t = 0$ . (b) Positions of the detectors in the transverse plane (indicated by squares). The area monitored by each detector has a diameter of less than  $7.2 \mu\text{m}$  and the separation between neighboring detectors is  $8.9 \mu\text{m}$ . Also shown is a time-averaged output image of the VCSEL during the CS drift (charge coupled device camera exposure time of about 1 ms). Figure reproduced from [110].

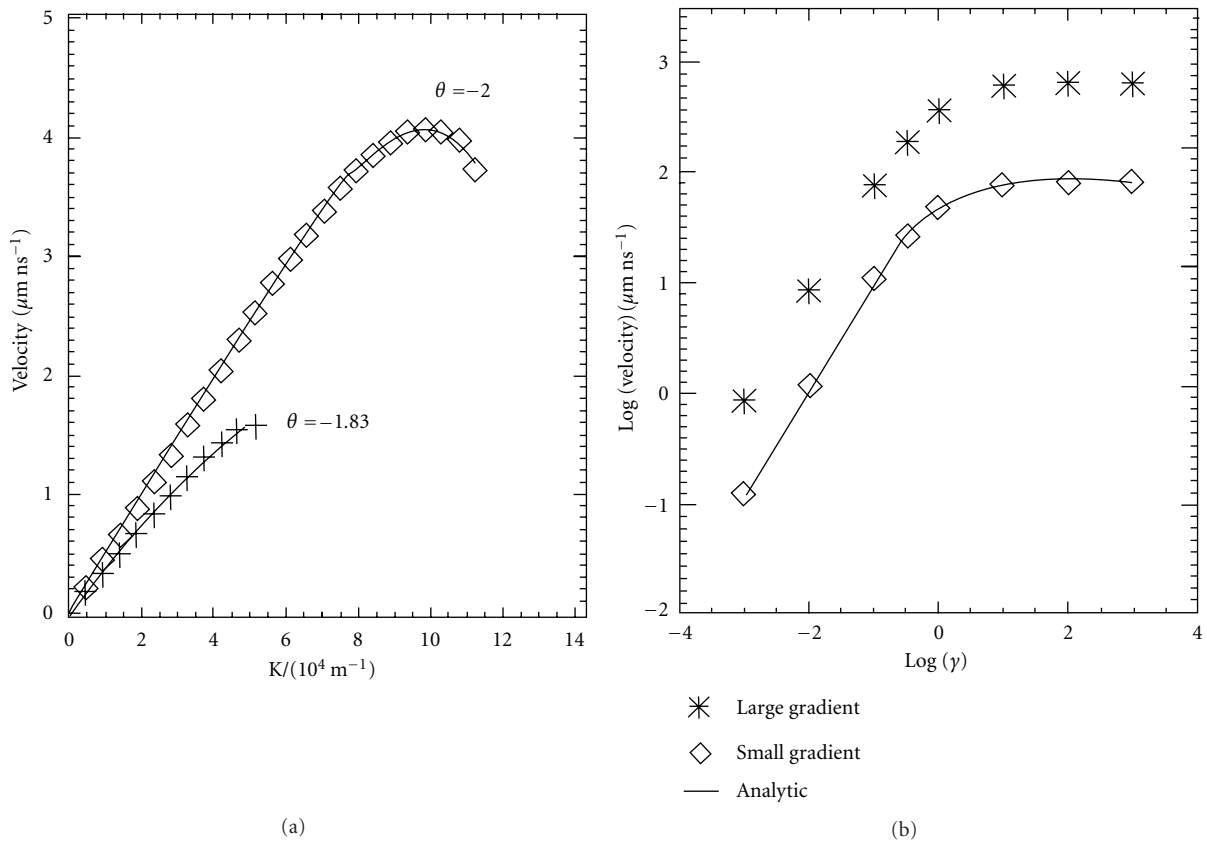


FIGURE 12: (a) Drift speed versus phase gradient (wave-vector tilt of holding beam) for a scaled cavity photon to carrier recombination rate  $\gamma = 0.01$  (corresponding to a nonradiative carrier lifetime of  $1 \text{ ns}^{-1}$ ) and two-cavity detuning values. The cavity photon lifetime is 10 ps. (b) Log-log plot of CS drift speed versus  $\gamma$  for a fixed scaled detuning ( $\theta = -2$ ) and for two values of the gradient: (stars)  $K = 2.38 \times 10^4 \text{ m}^{-1}$ ; (diamonds)  $K = 1.91 \times 10^5 \text{ m}^{-1}$ . Here, the cavity photon lifetime is 1.5 ps. Figure reproduced from [110].

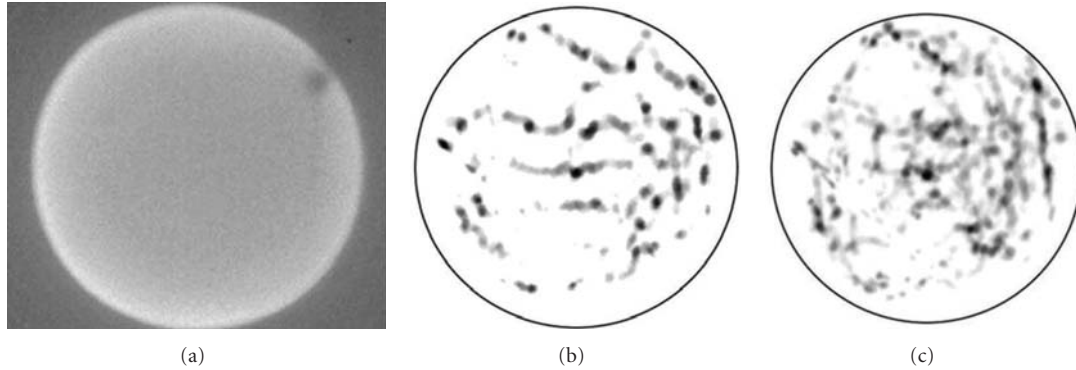


FIGURE 13: (a) Spontaneous emission profile of the VCSEL. (b) CSs trajectories when dragged toward the left. (c) Map of the defects in the VCSEL structure as the result of the complete analysis of the CSs trajectories. After [62].

low-intensity regions to repulsive ones. The experimental map is shown in Figure 13 with an inverted contrast. [63] gives a clear proof of the possibility to use the motion properties of localized structures in order to determine the position and strength of defects in semiconductor devices. The spatial resolution is determined by the size of the CS which is in this experiment of the order of  $10\ \mu\text{m}$ . Such a spatial resolution could in principle be increased by working in a different region of parameter space or using devices emitting at shorter wavelength. However, the strength of the proposed method lies in the sensitivity of the CS trajectory to any gradient, should they be smaller than the CS size itself. The practical limitation comes from the preparation of the external gradient and therefore, the quality of the optics that limits the uniformity of the holding beam. Moreover, the method not only allows to detect surface defects, but also can probe bulk defects in the device. This technique has been called soliton force microscopy, since it uses the various potentials felt by CSs in the VCSEL to reveal the map of defects. A similar dragging of CS has also been demonstrated in [54] in a CSL with filtered feedback. In this latter system, an attempt to control the inhomogeneities has also been undertaken in [101] using a Spatial Light Modulator. The idea is to create with an additional, spatially patterned, control beam a gradient that counteracts the effect of the local inhomogeneities by locally varying the refractive index. This results in displaced hysteresis cycles for individual CSs allowing two CSs initially not simultaneously bistable to become controllable in the same parameter regions.

Another interesting aspects of defects in VCSEL devices has been unveiled in [64, 112]. Indeed, defects can under certain circumstances be the source of CSs that may subsequently drift under a gradient, being a controlled gradient or a cavity resonance gradient. This results in the appearance of an almost periodic source of drifting localized states. The average period can be controlled by the phase gradient or by the kind of defect itself. Drifting excitations were also found in a CSL with filtered feedback in [81], while the CS properties remained to be established.

## 6. Prospects and New Developments

The previous demonstrations of CS using VCSEL devices, either in the optical amplifier or laser regimes, relied on absorptive or gain nonlinearities. CS were observed in the optical field intensity and carrier density components. Several other interesting new directions have been stimulated by these findings, exploring self-localization of different degrees of freedom, using different nonlinearities (see, e.g., [113–115] for theoretical studies of CS in quantum dot materials) or extrapolating the CS concept to three dimensions. In the following, we describe the advances in the fields of polarization CS, cavity soliton polariton and cavity light bullets.

**6.1. Polarization CS.** Due to the generally circular aperture of VCSELs, polarization of the emission is not constrained into a single direction as in edge-emitting lasers but rather may vary in the whole output plane, depending on the operating conditions (temperature and injection level). This fact has been long recognized and studied in real devices [116–118]. The understanding of the polarization dynamics in VCSELs has been the subject of many theoretical studies and a model [119] now well accepted has emerged, the so-called spin flip model (SFM). Whereas polarization control of VCSELs has represented a major goal of research, polarization switches can also be used in optical communications schemes [120, 121], where stochastic resonance in the polarization dynamics enhances transmission of binary information. The light emitted by a VCSEL is, in general polarized along one of the two crystallographic directions  $[110]$  or  $[\bar{1}\bar{1}0]$  because of crystal anisotropies, and since these anisotropies are weak, it is possible to control the state of emitted polarization. This is also true in broad-area devices [122], while the situation may be more complex for highly divergent modes in even larger devices [123]. In VCSELs with cylindrical symmetry, optical injection [124] or feedback [125, 126] can be employed to control the polarization of light. Since polarized optical injection or optical feedback can both induce bistability [127, 128], all the necessary ingredients are available for CS formation in large-aperture devices. Polarization CS

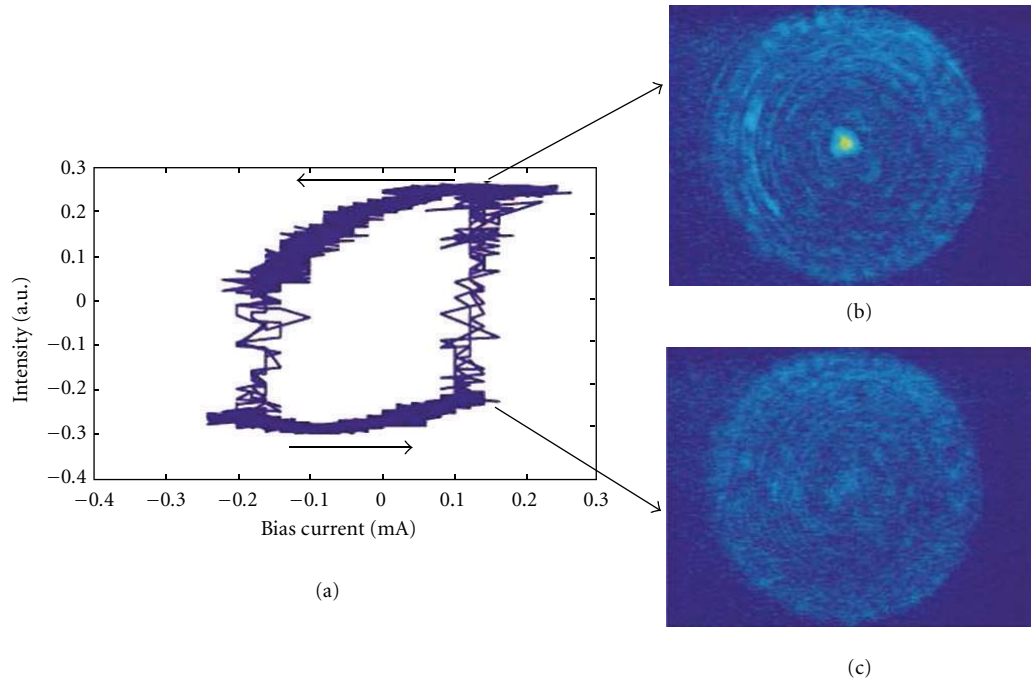


FIGURE 14: Near-field image of the VCSEL surface when injected by an orthogonally polarized holding beam in the lower (c) and upper (b) branch of the bistability curve (a) obtained by ramping the injected current in the laser. Reprinted with permission from [131]. (© 2011) by the American Physical Society.

could offer the practical advantage of ultrafast switching with low switching energy as was demonstrated in small polarization-bistable devices [129]. Polarization CS were predicted theoretically in [130] in a Kerr cavity with different losses for the two polarization components of the field. They have been experimentally investigated in [131] in a  $40\ \mu\text{m}$  diameter VCSEL. The laser, which is shown to emit in a well-defined polarization state just above the laser threshold, is injected by an orthogonally polarized holding beam. A localized state that sits in the center of the device spontaneously switches on and displays a bistable behavior when the injected current is ramped (see Figure 14). These results, though not demonstrating the independence of the localized state from the boundaries principally because of the moderate size of the laser used in the experiment, are encouraging steps towards the demonstration of polarization CS in VCSELs.

**6.2. Cavity Light Bullets.** Self-localization of light in 3D remains an open challenge [132–136]. The idea of combining the characteristics of a spatial soliton with those of a temporal soliton has been proposed more than 20 years ago [137], and the corresponding object has been termed a light bullet. Light bullets are self-localized states of light in space and time that keep their spatial and temporal profile in the course of propagation: self-focusing can compensate for diffraction and at the same time group velocity dispersion can be compensated by self-phase modulation. Because of the particle-like behavior of optical solitons, 3D self-localized states of light would be intriguing objects possibly leading to new application breakthroughs [138]. Dissipative light bullets are often considered in the context of the complex

Ginzburg-Landau equation [139, 140], a model used to describe pulses in mode-locked lasers with a fast saturable absorber. Cavity light bullets share the same properties as dissipative light bullets, in the sense that they are 3D nonlinearly localized states of light. However, CLBs form in a cavity and are thus not freely propagating. CLBs have been proposed and theoretically demonstrated in an extended cavity filled with a saturable absorber medium [141, 142] injected by a holding beam. It was shown that under certain circumstances, spatial filament solitons can destabilize in the propagation direction and form a 3D soliton (cf. Figure 15). These CLBs are addressable and independently controllable as their 2D counterpart. An important feature is that they sit on a non zero background, the stable uniform steady-state. CLBs have also been studied in a similar model including a Kerr focusing nonlinearity, showing that the unstable 3D localized structures then formed can be stabilized via higher-order processes such as multiphoton absorption [143]. A model more suitable for semiconductor systems was studied in [144] with MQWs as the nonlinear material. The model showed that the formation of CLBs requires fast carrier recombination times, since otherwise, the carrier dynamics lags behind the photon dynamics and prevents the formation of a CLB.

CLBs are a theoretical as well as experimental challenge. While the choice of a VCSEL for CS studies in semiconductor systems seems obvious, a variety of semiconductor devices may eventually be used for CLB studies. Among these, bisection edge-emitting lasers are good candidates [145]. Freely propagating light bullets have also been investigated theoretically in nonlinear waveguide arrays, which can be

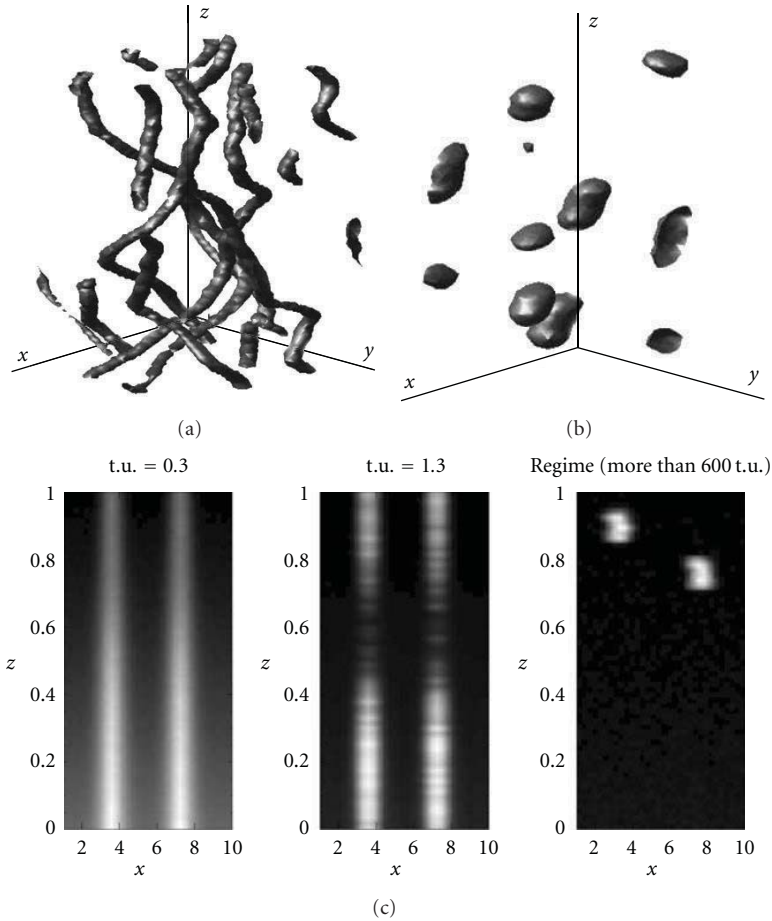


FIGURE 15: (a, b) Snapshot of 3D filaments and self-confined states in an extended cavity with transverse directions ( $x, y$ ) and propagation direction  $z$ . (c) Three snapshots of a 1D transverse cavity after injection of a writing beam:  $t = 0.3$ , initial injection;  $t = 1.3$ , destabilization of the longitudinally uniform solution;  $t > 600$ , two independent CLBs are formed and propagate in the cavity. Reprinted with permission from [141]. (© 2011) by the American Physical Society.

easily realized in semiconductor materials, in [146–148] and in Bragg gratings [149].

However, the extended cavity configurations used in Section 4 could reveal very interesting regarding CLB demonstration. The idea is to extend the VCSEL cavity to allow for multiple longitudinal modes and temporal mode-locking to take place, while preserving a high Fresnel number ensuring the possibility of multitransverse mode operation [150]. In this configuration, a CLB can be viewed as a mode-locked 2D CS. In [83, 151, 152], using a VCSEL with a frequency selective feedback by a volume Bragg grating in the self-imaging configuration, it was shown that depending on the writing pulse intensity a transient multiple frequency laser CS can be switched on. In most cases the transient oscillations die away after several tens of ns and the final state is a steady, cw laser CS. However, for a high writing pulse intensity an oscillating laser CS can stabilize with a frequency of 3.8 GHz. Because of experimental limitations the modulation depth of the oscillation is not known. Numerical simulations of the system [153] are in fairly good qualitative agreement with the observed behavior and predict

the stability of multifrequency laser CSs. The observations can then be interpreted in terms of partially phase-locked external cavity-modes giving rise to quasiperiodically or irregularly pulsing multifrequency laser CSs sitting on a non-zero background.

Self-pulsing localized laser structures are also observed in VCSEL-based schemes with a saturable absorber. In a monolithic vertical cavity laser with saturable absorber [73], self-pulsing localized states are observed. The physical origin of self-pulsing in that case has to be attributed to a Q-switching instability since the cavity has a single-longitudinal mode. The observed behavior is consistent with the experimental observations. In a face to face VCSEL configuration, self-pulsing optical structures have been observed [85] with a pulsing period of 400 ps corresponding to the cavity round-trip time. The physical mechanism for self-pulsing is thus in that case similar to that of the frequency-selective feedback experiment describes earlier. In both cases, the self-pulsing state could not be controlled by an external beam and was not bistable anymore. Control by an external beam of an irregular self-pulsing state has nevertheless been shown in [73].

It has been obtained on a structure composed of several localized spots but the physical mechanism at stake is not clear at the moment. These states are, however, not CLBs, because they develop in microcavities, but they probably constitute a good starting point for further investigation in an extended configuration.

Research on VCSEL-based CLBs is thus concentrated for the moment on extended cavity schemes. While there has been some interesting and encouraging results so far, no conclusive result has been obtained though. One reason lies certainly in the theoretical and numerical difficulty in modeling semiconductor extended cavity systems, since they are nonlinear, multilongitudinal and—transverse mode systems. Moreover, the CLBs obtained this way seem rather different from the original theoretical proposition in [141], and the link to the Ginzburg-Landau type approach to light bullets is not completely clear either. It is anticipated that further studies in the field will help clarify all the physics and the properties of these new self-localized objects and maybe help improve the theoretical comprehension and modeling of semiconductor-based mode-locked lasers [65, 66].

**6.3. Cavity Soliton Polariton.** Exciton polaritons (also called more simply cavity polaritons or polaritons) are mixed light-matter states arising when an exciton and a cavity-mode are strongly coupled ([154, 155] for a recent review). These states appear when a photon coming from the recombination of an exciton (a bound electron-hole pair) is reabsorbed and reemitted several times before the photon escapes from the microcavity. The cavity-exciton coupling gives rise to two resonances separated by the so-called Rabi splitting observed in the reflectivity spectrum of the microcavity, through a mechanism analogous to the anticrossing in the eigenenergies of a system composed of two coupled oscillators. This normal-mode coupling [156] is characterized by the dispersion curve depicted, for example, in Figure 1(a) in [157]. Exciton polaritons are fascinating quantum objects with bosonic properties in which Bose-Einstein condensation was recently observed [158] at temperatures much higher than in atomic clouds (and even at room temperature in [159]). An important feature in the context of CS is the giant  $\chi^3$ -type nonlinearity exhibited by exciton polaritons due to the coherent polariton-polariton scattering: two pump polaritons with in-plane wave vector  $k_p$  can scatter in one polariton with in-plane wave vector  $2k_p$  and one with 0 in-plane wave-vector. This coherent process must fulfill phase matching and energy conservation conditions, and can be obtained in two different ways. The first one, in the degenerate case, with normal incidence pump beam which gives rise to an optical nonlinearity analogous to a Kerr nonlinearity, with the difference that the index of refraction no longer depends on the input beam intensity but rather on the polariton density. The second one in the nondegenerate case in a parametric amplification configuration, at the so-called “magic-angle” (inflection point in the lower-polariton dispersion curve) with nonzero pump wave vector [160]. Bistability has been observed in both the degenerate [161] and the nondegenerate case [162]. Another mechanism is also predicted to lead to bistability in the strong coupling

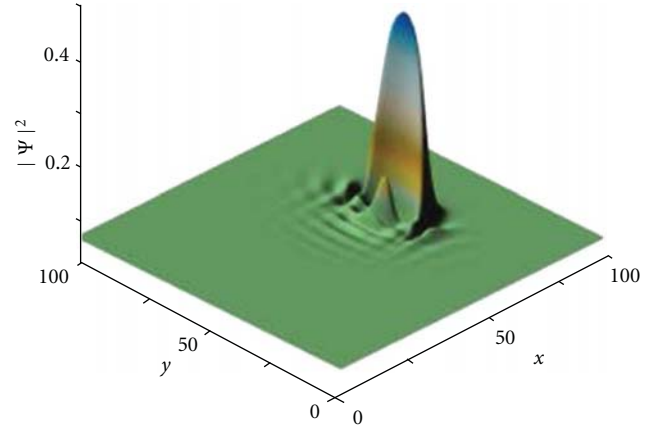


FIGURE 16: 2D self-localized bright CS polariton as predicted in [170]. Reprinted with permission from [170]. (© 2011) by the American Physical Society.

regime using the nonlinear bleaching of the Rabi-splitting [163] under high pumping excitation. However, there has been no convincing experimental observations of such a mechanism so far. A few experimental observations are associated with the simultaneous presence of the weak and strong coupling signatures in the spectrum, and bistability is associated to the bare cavity mode [164, 165]. Bistability has also been observed in a polariton diode [166], where the intracavity electric field is responsible for the strong to weak coupling abrupt switching.

Bistability being again one key ingredient for CS formation, several authors have studied how nonlinear and spatial effects (diffraction in particular) can mix to allow self-localized states appearance. Indications of self-localization were reported in [167], where local bistability, as well as localized bright and dark optical structures are reported in a microcavity with several QWs as active medium, brought to low temperature (4 K). However, a clear demonstration of polariton CS is missing, since no demonstration of independent excitation has been reported. All these results stimulated theoretical work on polariton CS. In addition to the large optical nonlinearity exhibited in this system, which is interesting because it allows the realization of low pump-power nonlinear optical devices [168], exciton polariton-based systems are expected to display very fast switching times too [169], a few orders of magnitude smaller than in the weak-coupling regime. Moreover, the quantum nature of exciton polaritons could open new prospects in the field of CS applied to information processing or parallel computation though practical schemes are not very clear at the moment (Figure 16).

Dark polariton solitons were first predicted to appear [171] in a cavity sustaining exciton polaritons, when the lower polariton branch is excited at normal incidence. The fact that bright CS polaritons were found to be unstable in that case is related to the defocusing nature of the exciton-polariton nonlinearity. Using the dispersion properties of the lower polariton branch near its inflection point ( $|k| \simeq 1$  in Figure 1(a) in [157]), it was later shown [172] that 1D bright

CS polaritons could be obtained. The stabilization of these states rely on the existence of higher-order spatial dispersion terms that can counteract the repulsive nonlinearity. These CS polaritons are moving objects, since the first order dispersion is nonzero at the inflection point. In 2D, use of a confining potential in the perpendicular direction to the inclined pump beam has been proposed to obtain 2D localized states. The authors claim that their theoretical predictions are in good agreement with the almost simultaneous experimental observation reported in [157] of moving “quasilocalized” polaritons. The latter authors have however a different interpretation in terms of the straightening of the Bogolyubov dispersion in superfluids.

In spite of the opposite signs of dispersion in polaritons excited close to the magic angle, truly 2D self-confined polaritons have nevertheless been obtained numerically in a recent work [170]. Starting from the 1D bright CS polariton conditions demonstrated in [172], the authors show that there exists a range of excitation intensities for which the width of the localized state remains constant in both directions. While in the propagation direction the explanation for self-localization remains the same as in the 1D case, in the perpendicular direction self-localization is attributed to the parametric nonlinearity: the 2D CS polariton is thus stable in both directions thanks to different physical mechanisms, each of them sustaining their family of 1D self-localized states.

Other theoretical studies have focused on different physical mechanism for CS polariton formation. In [173], taking into account the polarization degree of freedom of exciton polaritons, the authors show 1D vectorial bright and dark CS polaritons formation. Exploring in [174] the saturation of exciton-photon coupling, the author shows that normal incidence, resting CS polaritons may exist. However, stability conditions impose then unrealistically large exciton dispersions (or very small exciton effective mass).

In conclusion, even though the experimental observations in [157] are encouraging, CS polaritons observation and control remain an open challenge and may open new prospects in the field because of the different physics involved. In terms of possible applications, in spite of the quantitative improvements in the switching speed and holding beam power needed for their formation, the question remains whether the quantum nature of the exciton-polariton may be used for still unexplored functionalities.

## Acknowledgments

The authors wish to thank A. Amo and J. Bloch for useful discussions and comments on the paper.

## References

- [1] L. Lugiato, F. Prati, G. Tissoni et al., “Cavity solitons in semiconductor devices,” in *Dissipative Solitons: From Optics to Biology and Medicine*, vol. 751 of *Lecture Notes in Physics*, pp. 1–42, Springer, Berlin Heidelberg, Germany, 2008.
- [2] G. Tissoni, K. M. Aghdami, F. Prati, M. Brambilla, and L. A. Lugiato, “Cavity soliton laser based on a VCSEL with saturable absorber,” in *Localized States in Physics: Solitons and Patterns*, O. Descalzi, M. Clerc, S. Residori, and G. Assanto, Eds., pp. 187–211, Springer, Berlin Heidelberg, Germany, 2011.
- [3] T. Ackemann, W. J. Firth, and G. L. Oppo, “Fundamental-sand applications of spatial dissipative solitons in photonic devices,” in *Advances in Atomic Molecular and Optical Physics*, P. R. B. E. Arimondo and C. C. Lin, Eds., vol. 57 of *Advances In Atomic, Molecular, and Optical Physics*, chapter 6, pp. 323–421, Academic Press, 2009.
- [4] R. Kuszelewicz, S. Barbay, G. Tissoni, and G. Almuneau, “Editorial on dissipative optical solitons,” *European Physical Journal D*, vol. 59, no. 1, pp. 1–2, 2010.
- [5] H. G. Solari, M. Natiello, and G. Mindlin, *Nonlinear Dynamics: A Two-Way Trip from Physics to Math*, IOP Publishers, London, UK, 1996.
- [6] R. Gilmore and M. Lefranc, *The Topology of Chaos, Alice in Stretch and Squeeze land*, Wiley, New York, NY, USA, 2002.
- [7] F. Moss, L. A. Lugiato, and W. Schleigh, Eds., *Noise and Chaos in Nonlinear Dynamical Systems*, Cambridge University Press, New York, NY, USA, 1990.
- [8] B. Belousov, “A periodic reaction and its mechanism,” in *Oscillations and Traveling Waves in Chemical Systems*, R. Field and M. Burger, Eds., pp. 605–613, Wiley, New York, NY, USA, 1985.
- [9] J. C. Roux, R. H. Simoyi, and H. L. Swinney, “Observation of a strange attractor,” *Physica D*, vol. 8, no. 1–2, pp. 257–266, 1983.
- [10] F. T. Arecchi, R. Meucci, G. Puccioni, and J. Tredicce, “Experimental evidence of subharmonic bifurcations, multistability, and turbulence in a Q-switched gas laser,” *Physical Review Letters*, vol. 49, no. 17, pp. 1217–1220, 1982.
- [11] N. B. Abraham, P. Mandel, and L. M. Narducci, “Dynamical instabilities and pulsations in lasers,” *Progress in Optics*, vol. 25, pp. 1–190, 1988.
- [12] F. T. Arecchi, G. L. Lippi, G. P. Puccioni, and J. R. Tredicce, “Deterministic chaos in laser with injected signal,” *Optics Communications*, vol. 51, no. 5, pp. 308–314, 1984.
- [13] J. R. Tredicce, F. T. Arecchi, G. L. Lippi, and G. P. Puccioni, “Instabilities in lasers with an injected signal,” *Journal of the Optical Society of America B*, vol. 2, no. 1, pp. 173–183, 1985.
- [14] L. A. Lugiato, L. M. Narducci, D. K. Bandy, and C. A. Pennise, “Breathing, spiking and chaos in a laser with injected signal,” *Optics Communications*, vol. 46, no. 1, pp. 64–68, 1983.
- [15] L. M. Narducci, J. R. Tredicce, L. A. Lugiato, N. B. Abraham, and D. K. Bandy, “Multimode laser with an injected signal: steady-state and linear stability analysis,” *Physical Review A*, vol. 32, no. 3, pp. 1588–1595, 1985.
- [16] H. G. Solari and G. L. Oppo, “Laser with injected signal: perturbation of an invariant circle,” *Optics Communications*, vol. 111, no. 1–2, pp. 173–190, 1994.
- [17] F. A. N. B. Abraham and I. Lugiato, Eds., *Instabilities and Chaos in Quantum Optics*, vol. 2, Plenum Press, New York, 1988.
- [18] S. Wicczorek, B. Krauskopf, and D. Lenstra, “Unifying view of bifurcations in a semiconductor laser subject to optical injection,” *Optics Communications*, vol. 172, no. 1, pp. 279–295, 1999.
- [19] G. Vaschenko, M. Giudici, J. J. Rocca, C. S. Menoni, J. R. Tredicce, and S. Balle, “Temporal dynamics of semiconductor lasers with optical feedback,” *Physical Review Letters*, vol. 81, no. 25, pp. 5536–5539, 1998.
- [20] B. Krauskopf and D. Lenstra, Eds., *Fundamental Issues of Nonlinear Laser Dynamics*, AIP, New York, NY, USA, 2000.

- [21] P. Couillet, L. Gil, and F. Rocca, "Optical vortices," *Optics Communications*, vol. 73, no. 5, pp. 403–408, 1989.
- [22] J. R. Tredicce, E. J. Quel, A. M. Ghazzawi et al., "Spatial and temporal instabilities in a CO<sub>2</sub> laser," *Physical Review Letters*, vol. 62, no. 11, pp. 1274–1277, 1989.
- [23] P. L. Ramazza, S. Ducci, S. Boccaletti, and F. T. Arecchi, "Localized versus delocalized patterns in a nonlinear optical interferometer," *Journal of Optics B*, vol. 2, no. 3, pp. 399–405, 2000.
- [24] R. Holzner, P. Eschle, A. W. McCord, and D. M. Warrington, "Transverse "bouncing" of polarized laser beams in sodium vapor," *Physical Review Letters*, vol. 69, no. 15, pp. 2192–2195, 1992.
- [25] M. Brambilla, L. A. Lugiato, V. Penna, F. Prati, C. Tamm, and C. O. Weiss, "Transverse laser patterns. II. Variational principle for pattern selection, spatial multistability, and laser hydrodynamics," *Physical Review A*, vol. 43, no. 9, pp. 5114–5120, 1991.
- [26] C. Green, G. B. Mindlin, E. J. D'Angelo, H. G. Solari, and J. R. Tredicce, "Spontaneous symmetry breaking in a laser: the experimental side," *Physical Review Letters*, vol. 65, no. 25, pp. 3124–3127, 1990.
- [27] R. L. Ruiz, G. B. Mindlin, C. Pérez García, and J. Tredicce, "Mode-mode interaction for a CO<sub>2</sub> laser with imperfect O(2) symmetry," *Physical Review A*, vol. 47, no. 1, pp. 500–509, 1993.
- [28] A. B. Coates, C. O. Weiss, C. Green et al., "Dynamical transverse laser patterns. II. Experiments," *Physical Review A*, vol. 49, no. 2, pp. 1452–1466, 1994.
- [29] G. Huyet, M. C. Martinoni, J. R. Tredicce, and S. Rica, "Spatiotemporal dynamics of lasers with a large fresnel number," *Physical Review Letters*, vol. 75, no. 22, pp. 4027–4030, 1995.
- [30] M. Brambilla, L. A. Lugiato, F. Prati, L. Spinelli, and W. J. Firth, "Spatial soliton pixels in semiconductor devices," *Physical Review Letters*, vol. 79, no. 11, pp. 2042–2045, 1997.
- [31] D. Michaelis, U. Peschel, and F. Lederer, "Multistable localized structures and superlattices in semiconductor optical resonators," *Physical Review A*, vol. 56, no. 5, pp. R3366–R3369, 1997.
- [32] G. Tissoni, L. Spinelli, M. Brambilla, T. Maggipinto, I. M. Perrini, and L. A. Lugiato, "Cavity solitons in passive bulk semiconductor microcavities. I. Microscopic model and modulational instabilities," *Journal of the Optical Society of America B*, vol. 16, no. 11, pp. 2083–2094, 1999.
- [33] R. Kuszelewicz, I. Ganne, I. Sagnes, G. Sleky, and M. Brambilla, "Optical self-organization in bulk and multi-quantum well GaAlAs microresonators," *Physical Review Letters*, vol. 84, no. 26, pp. 6006–6009, 2000.
- [34] V. B. Taranenko, I. Ganne, R. J. Kuszelewicz, and C. O. Weiss, "Patterns and localized structures in bistable semiconductor resonators," *Physical Review A*, vol. 61, no. 6, pp. 063818–063811, 2000.
- [35] T. Ackemann, S. Barland, M. Cara et al., "Spatial mode structure of bottom-emitting broad-area vertical-cavity surface-emitting lasers," *Journal of Optics B*, vol. 2, no. 3, pp. 406–412, 2000.
- [36] T. Ackemann, S. Barland, J. R. Tredicce et al., "Spatial structure of broad-area vertical-cavity regenerative amplifiers," *Optics Letters*, vol. 25, no. 11, pp. 814–816, 2000.
- [37] N. N. Rosanov and G. V. Khodova, "Autosolitons in bistable interferometers," *Optics and Spectroscopy*, vol. 65, pp. 449–450, 1988.
- [38] G. S. McDonald and W. J. Firth, "Spatial solitary-wave optical memory," *Journal of the Optical Society of America B*, vol. 7, pp. 1328–1335, 1990.
- [39] M. Tlidi, P. Mandel, and R. Lefever, "Localized structures and localized patterns in optical bistability," *Physical Review Letters*, vol. 73, no. 5, pp. 640–643, 1994.
- [40] W. J. Firth and A. J. Scroggie, "Optical bullet holes: robust controllable localized states of a nonlinear cavity," *Physical Review Letters*, vol. 76, no. 10, pp. 1623–1626, 1996.
- [41] L. Spinelli, G. Tissoni, M. Tarengi, and M. Brambilla, "First principle theory for cavity solitons in semiconductor microresonators," *European Physical Journal D*, vol. 15, no. 2, pp. 257–266, 2001.
- [42] G. I. A. Stegeman, D. N. Christodoulides, and M. Segev, "Optical spatial solitons: historical perspectives," *IEEE Journal on Selected Topics in Quantum Electronics*, vol. 6, no. 6, pp. 1419–1427, 2000.
- [43] P. Couillet, C. Riera, and C. Tresser, "Stable static localized structures in one dimension," *Physical Review Letters*, vol. 84, no. 14, pp. 3069–3072, 2000.
- [44] W. J. Firth, L. Columbo, and A. J. Scroggie, "Proposed resolution of theory-experiment discrepancy in homoclinic snaking," *Physical Review Letters*, vol. 99, no. 10, Article ID 104503, 2007.
- [45] S. Barbay, X. Hachair, T. Elsass, I. Sagnes, and R. Kuszelewicz, "Homoclinic snaking in a semiconductor-based optical system," *Physical Review Letters*, vol. 101, no. 25, Article ID 253902, 2008.
- [46] B. Schäpers, M. Feldmann, T. Ackemann, and W. Lange, "Interaction of localized structures in an optical pattern-forming system," *Physical Review Letters*, vol. 85, no. 4, pp. 748–751, 2000.
- [47] N. N. Rosanov and G. V. Khodova, "Diffractive autosolitons in nonlinear interferometers," *Journal of the Optical Society of America B*, vol. 7, pp. 1057–1065, 1990.
- [48] M. Saffman, D. Montgomery, and D. Z. Anderson, "Collapse of a transverse-mode continuum in a self-imaging photorefractively pumped ring resonator," *Optics Letters*, vol. 19, no. 8, pp. 518–520, 1994.
- [49] R. Neubecker, G. L. Oppo, B. Thuerling, and T. Tschudi, "Pattern formation in a liquid-crystal light valve with feedback, including polarization, saturation, and internal threshold effects," *Physical Review A*, vol. 52, no. 1, pp. 791–808, 1995.
- [50] S. Barland, J. R. Tredicce, M. Brambilla et al., "Cavity solitons work as pixels in semiconductors," *Nature*, vol. 419, no. 6908, pp. 699–702, 2002.
- [51] M. Grabherr, R. Jäger, M. Miller et al., "Bottom-emitting VCSELs for high-CW optical output power," *IEEE Photonics Technology Letters*, vol. 10, no. 8, pp. 1061–1063, 1998.
- [52] M. Grabherr, M. Miller, R. Jäger et al., "High-power VCSELs: single devices and densely packed 2-D-arrays," *IEEE Journal on Selected Topics in Quantum Electronics*, vol. 5, no. 3, pp. 495–502, 1999.
- [53] M. Miller, M. Grabherr, R. King, R. Jäger, R. Michalzik, and K. J. Ebeling, "Improved output performance of high-power VCSELs," *IEEE Journal on Selected Topics in Quantum Electronics*, vol. 7, no. 2, pp. 210–216, 2001.
- [54] Y. Tanguy, T. Ackemann, W. J. Firth, and R. Jäger, "Realization of a semiconductor-based cavity soliton laser," *Physical Review Letters*, vol. 100, no. 1, Article ID 013907, 2008.
- [55] P. Genevet, S. Barland, M. Giudici, and J. R. Tredicce, "Cavity soliton laser based on mutually coupled semiconductor microresonators," *Physical Review Letters*, vol. 101, no. 12, Article ID 123905, 2008.
- [56] S. Fedorov, D. Michaelis, U. Peschel et al., "Effects of spatial inhomogeneities on the dynamics of cavity solitons in

- quadratically nonlinear media," *Physical Review E*, vol. 64, no. 3, Article ID 036610, pp. 366101–366108, 2001.
- [57] A. J. Scroggie, J. Jeffers, G. McCartney, and G. L. Oppo, "Reversible soliton motion," *Physical Review E*, vol. 71, no. 4, Article ID 046602, pp. 046602/1–046602/5, 2005.
- [58] X. Hachair, S. Barland, L. Furfaro et al., "Cavity solitons in broad-area vertical-cavity surface-emitting lasers below threshold," *Physical Review A*, vol. 69, no. 4, article 043817, 2004.
- [59] X. Hachair, F. Pedaci, E. Caboche et al., "Cavity solitons in a driven VCSEL above threshold," *IEEE Journal on Selected Topics in Quantum Electronics*, vol. 12, no. 3, pp. 339–351, 2006.
- [60] R. Michalzik, M. Grabherr, and K. J. Ebeling, "High-power vcsels: modeling and experimental characterization," in *Proceedings of the SPIE 3286 (SPIE '98)*, K. D. Choquette and R. A. Morgan, Eds., vol. 3286, pp. 206–219, 1998.
- [61] T. Camps, V. Bardinal, E. Havard et al., "Management of the electrical injection uniformity in broad-area top-emitting VCSELs," *European Physical Journal D*, vol. 59, no. 1, pp. 53–57, 2010.
- [62] M. Dabbicco, T. Maggipinto, and M. Brambilla, "Optical bistability and stationary patterns in photonic-crystal vertical-cavity surface-emitting lasers," *Applied Physics Letters*, vol. 86, no. 2, Article ID 021116, 2005.
- [63] F. Pedaci, G. Tissoni, S. Barland, M. Giudici, and J. Tredicce, "Mapping local defects of extended media using localized structures," *Applied Physics Letters*, vol. 93, no. 11, Article ID 111104, 2008.
- [64] E. Caboche, F. Pedaci, P. Genevet et al., "Microresonator defects as sources of drifting cavity solitons," *Physical Review Letters*, vol. 102, no. 16, Article ID 163901, 2009.
- [65] U. Keller, "Recent developments in compact ultrafast lasers," *Nature*, vol. 424, no. 6950, pp. 831–838, 2003.
- [66] U. Keller and A. C. Tropper, "Passively modelocked surface-emitting semiconductor lasers," *Physics Reports*, vol. 429, no. 2, pp. 67–120, 2006.
- [67] S. Barbay, Y. Ménesguen, I. Sagnes, and R. Kuszelewicz, "Cavity optimization of optically pumped broad-area microcavity lasers," *Applied Physics Letters*, vol. 86, no. 15, Article ID 151119, pp. 1–3, 2005.
- [68] S. Barbay, Y. Ménesguen, X. Hachair, L. Leroy, I. Sagnes, and R. Kuszelewicz, "Incoherent and coherent writing and erasure of cavity solitons in an optically pumped semiconductor amplifier," *Optics Letters*, vol. 31, no. 10, pp. 1504–1506, 2006.
- [69] D. G. H. Nugent, R. G. S. Plumb, M. A. Fisher, and D. A. O. Davies, "Self-pulsations in vertical-cavity surface-emitting lasers," *Electronics Letters*, vol. 31, no. 1, pp. 43–44, 1995.
- [70] S. F. Lim, J. A. Hudgings, G. S. Li, W. Yuen, K. Y. Lau, and C. J. Chang-Hasnain, "Self-pulsating and bistable VCSEL with controllable intracavity quantum-well saturable absorber," *Electronics Letters*, vol. 33, no. 20, pp. 1708–1710, 1997.
- [71] K. D. Choquette, H. Q. Hou, K. L. Lear et al., "Self-pulsing oxide-confined vertical-cavity lasers with ultralow operating current," *Electronics Letters*, vol. 32, no. 5, pp. 459–460, 1996.
- [72] A. J. Fischer, W. W. Chow, K. D. Choquette, A. A. Allerman, and K. M. Geib, "Q-switched operation of a coupled-resonator vertical-cavity laser diode," *Applied Physics Letters*, vol. 76, no. 15, pp. 1975–1977, 2000.
- [73] T. Elsass, K. Gauthron, G. Beaudoin, I. Sagnes, R. Kuszelewicz, and S. Barbay, "Control of cavity solitons and dynamical states in a monolithic vertical cavity laser with saturable absorber," *European Physical Journal D*, vol. 59, no. 1, pp. 91–96, 2010.
- [74] U. Bortolozzo, S. Residori, and P. L. Ramazza, "Optical structures and their control in a liquid-crystal-light-valve experiment," *Molecular Crystals and Liquid Crystals*, vol. 450, no. 1, pp. 141–162, 2006.
- [75] T. Elsass, K. Gauthron, G. Beaudoin, I. Sagnes, R. Kuszelewicz, and S. Barbay, "Fast manipulation of laser localized structures in a monolithic vertical cavity with saturable absorber," *Applied Physics B*, vol. 98, no. 2-3, pp. 327–331, 2010.
- [76] X. Hachair, L. Furfaro, J. Javaloyes et al., "Cavity-solitons switching in semiconductor microcavities," *Physical Review A*, vol. 72, no. 1, Article ID 013815, 2005.
- [77] S. Barbay and R. Kuszelewicz, "Physical model for the incoherent writing/erasure of cavity solitons in semiconductor optical amplifiers," *Optics Express*, vol. 15, no. 19, pp. 12457–12463, 2007.
- [78] L. Columbo, L. Gil, and J. Tredicce, "Could cavity solitons exist in bidirectional ring lasers?" *Optics Letters*, vol. 33, no. 9, pp. 995–997, 2008.
- [79] R. Vilaseca, M. C. Torrent, J. García-Ojalvo, M. Brambilla, and M. S. Miguel, "Two-photon cavity solitons in active optical media," *Physical Review Letters*, vol. 87, no. 8, Article ID 083902, pp. 839021–839024, 2001.
- [80] V. Ahufinger, J. García-Ojalvo, J. Mompert, M. C. Torrent, R. Corbalán, and R. Vilaseca, "Cavity solitons in two-level lasers with dense amplifying medium," *Physical Review Letters*, vol. 91, no. 8, pp. 839011–839014, 2003.
- [81] Y. Tanguy, N. Radwell, T. Ackemann, and R. Jäger, "Characteristics of cavity solitons and drifting excitations in broad-area vertical-cavity surface-emitting lasers with frequency-selective feedback," *Physical Review A*, vol. 78, no. 2, Article ID 023810, 2008.
- [82] P. V. Paulau, D. Gomila, T. Ackemann, N. A. Loiko, and W. J. Firth, "Self-localized structures in vertical-cavity surface-emitting lasers with external feedback," *Physical Review E*, vol. 78, no. 1, Article ID 016212, 2008.
- [83] N. Radwell, C. McIntyre, A. J. Scroggie, G. L. Oppo, W. J. Firth, and T. Ackemann, "Switching spatial dissipative solitons in a VCSEL with frequency selective feedback," *European Physical Journal D*, vol. 59, no. 1, pp. 121–131, 2010.
- [84] N. Radwell and T. Ackemann, "Characteristics of laser cavity solitons in a vertical-cavity surface-emitting laser with feedback from a volume Bragg grating," *IEEE Journal of Quantum Electronics*, vol. 45, no. 11, pp. 1388–1395, 2009.
- [85] P. Genevet, S. Barland, M. Giudici, and J. R. Tredicce, "Stationary localized structures and pulsing structures in a cavity soliton laser," *Physical Review A*, vol. 79, no. 3, Article ID 033819, 2009.
- [86] P. Genevet, L. Columbo, S. Barland, M. Giudici, L. Gil, and J. R. Tredicce, "Multistable monochromatic laser solitons," *Physical Review A*, vol. 81, no. 5, Article ID 053839, 2010.
- [87] L. Columbo, L. Gila, and P. Genevet, "Theoretical description of the transverse localised structures in a face to face VCSEL configuration," *European Physical Journal D*, vol. 59, no. 1, pp. 97–107, 2010.
- [88] P. Genevet, S. Barland, M. Giudici, and J. R. Tredicce, "Bistable and addressable localized vortices in semiconductor lasers," *Physical Review Letters*, vol. 104, no. 22, Article ID 223902, 2010.
- [89] N. N. Rozanov, S. V. Fedorov, and A. N. Shatsev, "Nonstationary multivortex and fissionable soliton-like structures of laser radiation," *Optics and Spectroscopy*, vol. 95, no. 6, pp. 843–848, 2003.
- [90] S. V. Fedorov and N. N. Rosanov, "Diffraction switching waves and autosolitons in a laser with saturable absorption," *Optics and Spectroscopy*, vol. 72, no. 6, pp. 782–785, 1992.

- [91] A. G. Vladimirov, S. V. Fedorov, N. A. Kaliteevskii, G. V. Khodova, and N. N. Rosanov, "Numerical investigation of laser localized structures," *Journal of Optics B*, vol. 1, no. 6, pp. 101–106, 1999.
- [92] M. Bache, F. Prati, G. Tissoni et al., "Cavity soliton laser based on VCSEL with saturable absorber," *Applied Physics B*, vol. 81, no. 7, pp. 913–920, 2005.
- [93] S. V. Fedorov, N. N. Rozanov, and A. N. Shatsev, "Two-dimensional solitons in B-class lasers with saturable absorption," *Optics and Spectroscopy*, vol. 102, no. 3, pp. 449–455, 2007.
- [94] F. Prati, P. Caccia, G. Tissoni, L. A. Lugiato, K. M. Aghdami, and H. Tajalli, "Effects of carrier radiative recombination on a VCSEL-based cavity soliton laser," *Applied Physics B*, vol. 88, no. 3, pp. 405–410, 2007.
- [95] K. M. Aghdami, F. Prati, P. Caccia et al., "Comparison of different switching techniques in a cavity soliton laser," *European Physical Journal D*, vol. 47, no. 3, pp. 447–455, 2008.
- [96] N. N. Rosanov, S. V. Fedorov, and A. N. Shatsev, "Two-dimensional laser soliton complexes with weak, strong, and mixed coupling," *Applied Physics B*, vol. 81, no. 7, pp. 937–943, 2005.
- [97] N. N. Rosanov, S. V. Fedorov, and A. N. Shatsev, "Curvilinear motion of multivortex laser-soliton complexes with strong and weak coupling," *Physical Review Letters*, vol. 95, no. 5, Article ID 053903, pp. 1–4, 2005.
- [98] P. Genevet, M. Turconi, S. Barland, M. Giudici, and J. R. Tredicce, "Mutual coherence of laser solitons in coupled semiconductor resonators," *European Physical Journal D*, vol. 59, no. 1, pp. 109–114, 2010.
- [99] S. V. Fedorov, A. G. Vladimirov, G. V. Khodova, and N. N. Rosanov, "Effect of frequency detunings and finite relaxation rates on laser localized structures," *Physical Review E*, vol. 61, no. 5, pp. 5814–5824, 2000.
- [100] F. Prati, G. Tissoni, L. A. Lugiato, K. M. Aghdami, and M. Brambilla, "Spontaneously moving solitons in a cavity soliton laser with circular section," *European Physical Journal D*, vol. 59, no. 1, pp. 73–79, 2010.
- [101] N. Radwell, P. Rose, C. Cleff, C. Denz, and T. Ackemann, "Compensation of spatial inhomogeneities in a cavity soliton laser using a spatial light modulator," *Optics Express*, vol. 18, no. 22, pp. 23121–23132, 2010.
- [102] N. N. Rosanov, "Switching waves, autosolitons, and parallel digital-analogous optical computing," in *Transverse Patterns in Nonlinear Optics*, N. N. Rosanov, Ed., vol. 1840, pp. 130–143, 1992.
- [103] F. Pedaci, P. Genevet, S. Barland, M. Giudici, and J. R. Tredicce, "Positioning cavity solitons with a phase mask," *Applied Physics Letters*, vol. 89, no. 22, Article ID 221111, 2006.
- [104] L. V. Hau, S. E. Harris, Z. Dutton, and C. H. Behroozi, "Light speed reduction to 17 metres per second in an ultracold atomic gas," *Nature*, vol. 397, no. 6720, pp. 594–598, 1999.
- [105] Y. Okawachi, M. S. Bigelow, J. E. Sharping et al., "Tunable all-optical delays via Brillouin slow light in an optical fiber," *Physical Review Letters*, vol. 94, no. 15, article 153902, 2005.
- [106] J. E. Sharping, Y. Okawachi, and A. L. Gaeta, "Wide bandwidth slow light using a Raman fiber amplifier," *Optics Express*, vol. 13, no. 16, pp. 6092–6098, 2005.
- [107] M. van der Poel, J. Mørk, and J. M. Hvam, "Controllable delay of ultrashort pulses in a quantum dot optical amplifier," *Optics Express*, vol. 13, no. 20, pp. 8032–8037, 2005.
- [108] J. T. Mok, C. M. de Sterke, I. C. M. Littler, and B. J. Eggleton, "Dispersionless slow light using gap solitons," *Nature Physics*, vol. 2, no. 11, pp. 775–780, 2006.
- [109] B. Schäpers, T. Ackemann, and W. Lange, "Characteristics and possible applications of localized structures in an optical pattern-forming system," in *Proceedings of the 2nd Nonlinear Optical Beam and Pulse Propagation (SPIE '01)*, vol. 4271, pp. 130–137, 2001.
- [110] F. Pedaci, S. Barland, E. Caboche et al., "All-optical delay line using semiconductor cavity solitons," *Applied Physics Letters*, vol. 92, no. 1, article 011101, 2008.
- [111] G. Kozyreff, P. Assemat, and S. J. Chapman, "Influence of boundaries on localized patterns," *Physical Review Letters*, vol. 103, no. 16, article 164501, 2009.
- [112] E. Caboche, S. Barland, M. Giudici, J. Tredicce, G. Tissoni, and L. A. Lugiato, "Cavity-soliton motion in the presence of device defects," *Physical Review A*, vol. 80, no. 5, Article ID 053814, 2009.
- [113] S. Barbay, J. Koehler, R. Kuszelewicz, T. Maggipinto, I. M. Perrini, and M. Brambilla, "Optical patterns and cavity solitons in quantum-dot microresonators," *IEEE Journal of Quantum Electronics*, vol. 39, no. 2, pp. 245–254, 2003.
- [114] I. M. Perrini, S. Barbay, T. Maggipinto, M. Brambilla, and R. Kuszelewicz, "Model for optical pattern and cavity soliton formation in a microresonator with self-assembled semiconductor quantum dots," *Applied Physics B*, vol. 81, no. 7, pp. 905–912, 2005.
- [115] M. Brambilla, T. Maggipinto, I. M. Perrini, S. Barbay, and R. Kuszelewicz, "Modeling pattern formation and cavity solitons in quantum dot optical microresonators in absorbing and amplifying regimes," *Chaos*, vol. 17, no. 3, article 037119, 2007.
- [116] K. D. Choquette, D. A. Richie, and R. E. Leibenguth, "Temperature dependence of gain-guided vertical-cavity surface emitting laser polarization," *Applied Physics Letters*, vol. 64, no. 16, pp. 2062–2064, 1994.
- [117] C. J. Chang-Hasnain, J. P. Harbison, L. T. Florez, and N. G. Stoffel, "Polarisation characteristics of quantum well vertical cavity surface emitting lasers," *Electronics Letters*, vol. 27, no. 2, pp. 163–165, 1991.
- [118] C. J. Chang-Hasnain, J. P. Harbison, G. Hasnain, A. C. von Lehmen, L. T. Florez, and N. G. Stoffel, "Dynamic, polarization, and transverse mode characteristics of vertical cavity surface emitting lasers," *IEEE Journal of Quantum Electronics*, vol. 27, no. 6, pp. 1402–1409, 1991.
- [119] M. S. Miguel, Q. Feng, and J. V. Moloney, "Light-polarization dynamics in surface-emitting semiconductor lasers," *Physical Review A*, vol. 52, no. 2, pp. 1728–1739, 1995.
- [120] S. Barbay, G. Giacomelli, and F. Marin, "Noise-assisted transmission of binary information: theory and experiment," *Physical Review E*, vol. 63, no. 5, pp. 511101–511109, 2001.
- [121] S. Barbay, G. Giacomelli, and F. Marin, "Experimental evidence of binary aperiodic stochastic resonance," *Physical Review Letters*, vol. 85, no. 22, pp. 4652–4655, 2000.
- [122] S. P. Hegarty, G. Huyet, J. G. McInerney, and K. D. Choquette, "Pattern formation in the transverse section of a laser with a large Fresnel number," *Physical Review Letters*, vol. 82, no. 7, pp. 1434–1437, 1999.
- [123] I. V. Babushkin, M. Schulz-Ruhtenberg, N. A. Loiko, K. F. Huang, and T. Ackemann, "Coupling of polarization and spatial degrees of freedom of highly divergent emission in broad-area square vertical-cavity surface-emitting lasers," *Physical Review Letters*, vol. 100, no. 21, article 213901, 2008.
- [124] Z. G. Pan, S. Jiang, M. Dagenais et al., "Optical injection induced polarization bistability in vertical-cavity surface-emitting lasers," *Applied Physics Letters*, vol. 63, no. 22, pp. 2999–3001, 1993.

- [125] P. Besnard, M. L. Charès, G. Stéphan, and F. Robert, "Switching between polarized modes of a vertical-cavity surface-emitting laser by isotropic optical feedback," *Journal of the Optical Society of America B*, vol. 16, no. 7, pp. 1059–1063, 1999.
- [126] M. Giudici, S. Balle, T. Ackemann, S. Barland, and J. R. Tredicce, "Polarization dynamics in vertical-cavity surface-emitting lasers with optical feedback: experiment and model," *Journal of the Optical Society of America B*, vol. 16, no. 11, pp. 2114–2123, 1999.
- [127] B. S. Ryvkin, K. Panajotov, E. A. Avrutin, I. Veretenicoff, and H. Thienpont, "Optical-injection-induced polarization switching in polarization-bistable vertical-cavity surface-emitting lasers," *Journal of Applied Physics*, vol. 96, no. 11, pp. 6002–6007, 2004.
- [128] I. Gatare, M. Sciamanna, M. Nizette, and K. Panajotov, "Bifurcation to polarization switching and locking in vertical-cavity surface-emitting lasers with optical injection," *Physical Review A*, vol. 76, no. 3, article 031803, 2007.
- [129] H. Kawaguchi, "Polarization-bistable vertical-cavity surface-emitting lasers: application for optical bit memory," *Opto-Electronics Review*, vol. 17, no. 4, pp. 265–274, 2009.
- [130] V. J. Sánchez-Morcillo, I. Pérez-Arjona, F. Silva, G. J. de Valcárcel, and E. Roldán, "Vectorial Kerr-cavity solitons," *Optics Letters*, vol. 25, no. 13, pp. 957–959, 2000.
- [131] X. Hachair, G. Tissoni, H. Thienpont, and K. Panajotov, "Linearly polarized bistable localized structure in medium-size vertical-cavity surface-emitting lasers," *Physical Review A*, vol. 79, no. 1, article 011801, 2009.
- [132] F. W. Wise, "Generation of light bullets," *Physicss*, vol. 3, p. 107, 2010.
- [133] S. Minardi, F. Eilenberger, Y. V. Kartashov et al., "Three-dimensional light bullets in arrays of waveguides," *Physical Review Letters*, vol. 105, no. 26, article 263901, 2010.
- [134] H. C. Gurgov and O. Cohen, "Spatiotemporal pulse-train solitons," *Optics Express*, vol. 17, no. 9, pp. 7052–7058, 2009.
- [135] B. A. Malomed, D. Mihalache, F. Wise, and L. Torner, "Spatiotemporal optical solitons," *Journal of Optics B*, vol. 7, no. 5, pp. R53–R72, 2005.
- [136] F. Wise and P. Di Trapani, "Spatiotemporal solitons," *Optics and Photonics News*, vol. 13, no. 2, pp. 28–32, 2002.
- [137] Y. Silberberg, "Collapse of optical pulse," *Optics Letters*, vol. 15, pp. 1282–1284, 1990.
- [138] M. O. Williams, C. W. McGrath, and J. N. Kutz, "Light-bullet routing and control with planar waveguide arrays," *Optics Express*, vol. 18, no. 11, pp. 11671–11682, 2010.
- [139] N. N. Rozanov, "On solitonlike optical structures on nonlinear optical media with gain," *Optics and Spectroscopy*, vol. 76, no. 4, pp. 555–557, 1994.
- [140] N. A. Veretenov, N. N. Rosanov, and S. V. Fedorov, "Motion of complexes of 3D-laser solitons," *Optical and Quantum Electronics*, vol. 40, no. 2–4, pp. 253–262, 2008.
- [141] M. Brambilla, T. Maggipinto, G. Patera, and L. Columbo, "Cavity light bullets: three-dimensional localized structures in a nonlinear optical resonator," *Physical Review Letters*, vol. 93, no. 20, article 203901, 2004.
- [142] M. Brambilla, L. Columbo, and T. Maggipinto, "Three-dimensional self-organized patterns in the field profile of a ring cavity resonator," *Journal of Optics B*, vol. 6, no. 5, pp. S197–S204, 2004.
- [143] S. D. Jenkins, F. Prati, L. A. Lugiato, L. Columbo, and M. Brambilla, "Cavity light bullets in a dispersive Kerr medium," *Physical Review A*, vol. 80, no. 3, Article ID 033832, 2009.
- [144] L. Columbo, I. M. Perrini, T. Maggipinto, and M. Brambilla, "3D self-organized patterns in the field profile of a semiconductor resonator," *New Journal of Physics*, vol. 8, p. 312, 2006.
- [145] L. Columbo, F. Prati, M. Brambilla, and T. Maggipinto, "Self-pulsing localized structures in a laser with saturable absorber," *European Physical Journal D*, vol. 59, no. 1, pp. 115–120, 2010.
- [146] F. Lederer and W. Biehlig, "Bright solitons and light bullets in semiconductor waveguides," *Electronics Letters*, vol. 30, no. 22, pp. 1871–1872, 1994.
- [147] A. A. Sukhorukov and Y. S. Kivshar, "Slow-light optical bullets in arrays of nonlinear Bragg-grating waveguides," *Physical Review Letters*, vol. 97, no. 23, article 233901, 2006.
- [148] M. O. Williams and J. N. Kutz, "Spatial mode-locking of light bullets in planar waveguide arrays," *Optics Express*, vol. 17, no. 20, pp. 18320–18329, 2009.
- [149] M. Blaauboer, G. Kurizki, and B. A. Malomed, "Spatiotemporally localized solitons in resonantly absorbing Bragg reflectors," *Physical Review E*, vol. 62, no. 1, pp. R57–R59, 2000.
- [150] X. Hachair, S. Barbay, T. Elsass, I. Sagnes, and R. Kuszelewicz, "Transverse spatial structure of a high fresnel number vertical external cavity surface emitting laser," *Optics Express*, vol. 16, no. 13, pp. 9519–9527, 2008.
- [151] T. Ackemann, N. Radwell, and R. Jäger, "Optically controllable microlasers and 3D light confinement based on cavity solitons in vertical-cavity devices," in *Proceedings of the 2nd IEEE/LEOS Winter Topicals (WTM '09)*, pp. 136–137, 2009.
- [152] T. Ackemann, N. Radwell, C. Mcintyre, G. L. Oppo, and W. J. Firth, "Self pulsing solitons: a base for optically controllable pulse trains in photonic networks?" in *Proceedings of the 12th International Conference on Transparent Optical Networks (ICTON '10)*, pp. 1–4, 2010.
- [153] A. J. Scroggie, W. J. Firth, and G. L. Oppo, "Cavity-soliton laser with frequency-selective feedback," *Physical Review A*, vol. 80, no. 1, article 013829, 2009.
- [154] C. Weisbuch, M. Nishioka, A. Ishikawa, and Y. Arakawa, "Observation of the coupled exciton-photon mode splitting in a semiconductor quantum microcavity," *Physical Review Letters*, vol. 69, no. 23, pp. 3314–3317, 1992.
- [155] H. M. Gibbs, G. Khitrova, and S. W. Koch, "Exciton-polariton light-semiconductor coupling effects," *Nature Photonics*, vol. 5, p. 273, 2011.
- [156] G. Khitrova, H. M. Gibbs, F. Jahnke, M. Kira, and S. W. Koch, "Nonlinear optics of normal-mode-coupling semiconductor microcavities," *Reviews of Modern Physics*, vol. 71, no. 5, pp. 1591–1639, 1999.
- [157] A. Amo, D. Sanvitto, F. P. Laussy et al., "Collective fluid dynamics of a polariton condensate in a semiconductor microcavity," *Nature*, vol. 457, no. 7227, pp. 291–295, 2009.
- [158] J. Kasprzak, M. Richard, S. Kundermann et al., "Bose-Einstein condensation of exciton polaritons," *Nature*, vol. 443, no. 7110, pp. 409–414, 2006.
- [159] S. Christopoulos, G. B. H. von Högersthal, A. J. D. Grundy et al., "Room-temperature polariton lasing in semiconductor microcavities," *Physical Review Letters*, vol. 98, no. 12, article 126405, 2007.
- [160] P. G. Savvidis, J. J. Baumberg, R. M. Stevenson, M. S. Skolnick, D. M. Whittaker, and J. S. Roberts, "Angle-resonant stimulated polariton amplifier," *Physical Review Letters*, vol. 84, no. 7, pp. 1547–1550, 2000.
- [161] A. Baas, J. P. Karr, H. Eleuch, and E. Giacobino, "Optical bistability in semiconductor microcavities," *Physical Review A*, vol. 69, no. 2, pp. 238091–238098, 2004.

- [162] A. Baas, J. P. Karr, M. Romanelli, A. Bramati, and E. Giacobino, "Optical bistability in semiconductor microcavities in the nondegenerate parametric oscillation regime: analogy with the optical parametric oscillator," *Physical Review B*, vol. 70, no. 16, Article ID 161307, pp. 1–4, 2004.
- [163] A. Tredicucci, Y. Chen, V. Pellegrini, M. Börger, and F. Bassani, "Optical bistability of semiconductor microcavities in the strong-coupling regime," *Physical Review A*, vol. 54, no. 4, pp. 3493–3498, 1996.
- [164] M. Gurioli, L. Cavigli, G. Khitrova, and H. M. Gibbs, "Bistable optical response in quantum well semiconductor microcavity," *Semiconductor Science and Technology*, vol. 19, no. 4, pp. S345–S347, 2004.
- [165] L. Cavigli and M. Gurioli, "Optical bistability and laserlike emission in a semiconductor microcavity," *Physical Review B*, vol. 71, no. 3, Article ID 035317, pp. 1–7, 2005.
- [166] D. Bajoni, E. Semenova, A. Lemaître et al., "Optical bistability in a GaAs-based polariton diode," *Physical Review Letters*, vol. 101, no. 26, article 266402, 2008.
- [167] Y. Larionova, W. Stolz, and C. O. Weiss, "Optical bistability and spatial resonator solitons based on exciton-polariton nonlinearity," *Optics Letters*, vol. 33, no. 4, pp. 321–323, 2008.
- [168] D. Bajoni, P. Senellart, E. Wertz et al., "Polariton laser using single micropillar GaAs-GaAlAs semiconductor cavities," *Physical Review Letters*, vol. 100, no. 4, article 047401, 2008.
- [169] A. Amo, T. C. H. Liew, C. Adrados et al., "Exciton-polariton spin switches," *Nature Photonics*, vol. 4, no. 6, pp. 361–366, 2010.
- [170] O. A. Egorov, A. V. Gorbach, F. Lederer, and D. V. Skryabin, "Two-dimensional localization of exciton polaritons in microcavities," *Physical Review Letters*, vol. 105, no. 7, article 073903, 2010.
- [171] A. V. Yulin, O. A. Egorov, F. Lederer, and D. V. Skryabin, "Dark polariton solitons in semiconductor microcavities," *Physical Review A*, vol. 78, no. 6, article 061801, 2008.
- [172] O. A. Egorov, D. V. Skryabin, A. V. Yulin, and F. Lederer, "Bright cavity polariton solitons," *Physical Review Letters*, vol. 102, no. 15, article 153904, 2009.
- [173] W. L. Zhang and S. F. Yu, "Vectorial polariton solitons in semiconductor microcavities," *Optics Express*, vol. 18, no. 20, pp. 21219–21224, 2010.
- [174] O. A. Egorov, D. V. Skryabin, and F. Lederer, "Polariton solitons due to saturation of the exciton-photon coupling," *Physical Review B*, vol. 82, no. 16, article 165326, 2010.

## Review Article

# Surface-Emitting Metal Nanocavity Lasers

**Martin T. Hill and Milan J. H. Marell**

*Department of Electrical Engineering, Eindhoven University of Technology, Postbus 513, 5600 MB Eindhoven, The Netherlands*

Correspondence should be addressed to Martin T. Hill, m.t.hill@ieee.org

Received 6 June 2011; Accepted 9 July 2011

Academic Editor: Krassimir Panajotov

Copyright © 2011 M. T. Hill and M. J. H. Marell. This is an open access article distributed under the Creative Commons Attribution License, which permits unrestricted use, distribution, and reproduction in any medium, provided the original work is properly cited.

There has been considerable interest in metallic nanolasers recently and some forms of these devices constructed from semiconductor pillars can be considered as surface-emitting lasers. We compare two different realized versions of these nanopillar devices, one with a trapped cutoff mode in the pillar, another with a mode that propagates along the pillar. For the cutoff mode devices we introduce a method to improve the output beam characteristics and look at some of the challenges in improving such devices.

## 1. Introduction

Since the invention of the first laser by Maiman [1] in 1960, different lines of development have yielded lasers the size of buildings, or as small as a few tens of nanometers. Perhaps the greatest impact on society has been had with making lasers smaller. In particular, the invention of the semiconductor laser [2] has allowed small, electrically driven lower power coherent light sources. One of the later developments in the miniaturization of the laser has been the vertical cavity surface-emitting laser or VCSEL [3]. The VCSEL was the first laser with dimensions which approached the wavelength scale. The VCSEL has found many applications due in part to the following characteristics: electrical pumping, room temperature operation, reasonable efficiency, small threshold current, useful output beam characteristics, and ease of test and manufacture owing to the surface normal output.

In the last few years the use of metals to form nanoscale resonators for lasers has been explored. Metals have allowed a dramatic decrease in both the size of the optical mode and also the overall size of the laser. Some of the initial devices are given roughly in chronological order in [4–12]. Some of these devices involve plasmonic waveguide modes [5, 7]. Others show lasing with a nanoparticle as a resonator [6]. Others involve the encapsulation of small pillars of semiconductor material [4, 10, 12]. In these particular devices, light escapes from one end of the pillar. Such devices can be considered

as surface-emitting lasers. In this article we will look at a number of aspects of such devices.

## 2. Pillar-Based Metal Nanolasers

Two main types of surface-emitting devices have been proposed thus far. The first sort of device involves encapsulating a heterostructure pillar [4, 10], which has a higher index in the center of the pillar, Figure 1(a). In the devices we have made, the lower index material consists of InP and the higher index InGaAs. The mode of interest which resonates in such a pillar has a frequency close to the cutoff frequency of the circular waveguide with the InGaAs core. Since the cutoff frequency of the waveguide above and below the InGaAs region is higher than the resonant frequency, the mode is trapped on the InGaAs region, see Figure 1(b). The modal energy in such a cutoff waveguide is actually bouncing back and forth between the sidewalls of pillar. This can be seen in the Figure 1(b), where the Poynting vector is shown. Due to the optical losses of the encapsulating metal, net energy flow is into the sidewalls of the pillar. However, due to the finite length of the bottom InP region in the pillar, there is some coupling of the modal energy into the substrate below the pillar. The amount of power emitted into the substrate can be tuned by adjusting the amount of cutoff waveguide below the InGaAs, and this will be discussed in a later section. The light escaping from the aperture at the base of the pillar

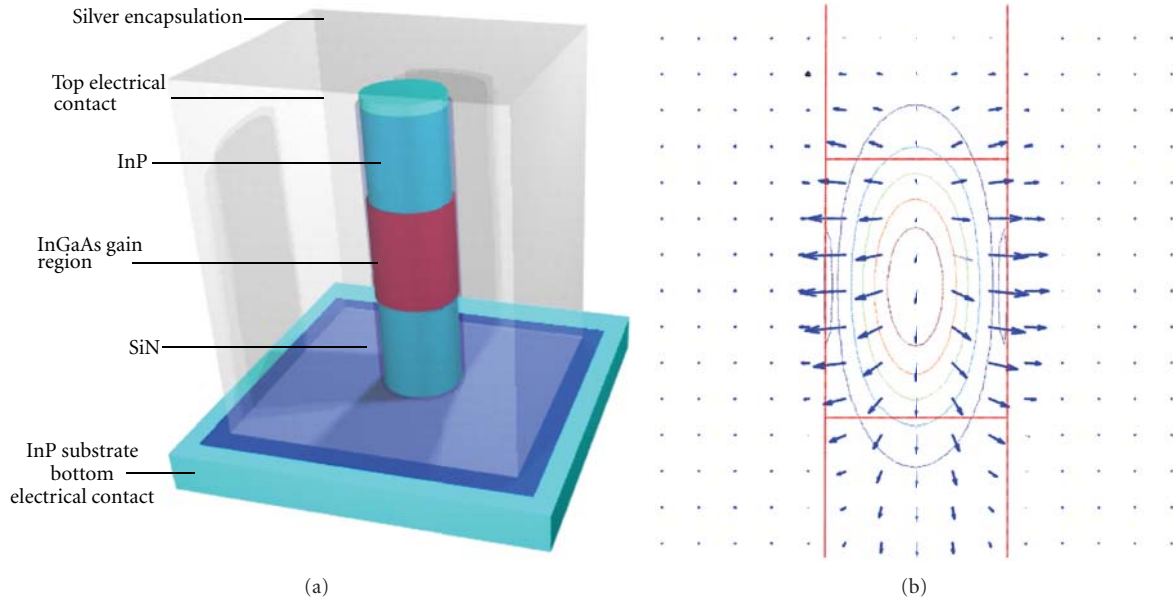


FIGURE 1: (a) One approach for metallic nanolasers with surface-emitting properties is to encapsulate a semiconductor heterostructure pillar in an insulator then a low optical loss metal such as silver or aluminium. Such an approach is particularly suitable for electrical pumping of the laser. In the figure shown an InP/InGaAs heterostructure is used with SiN insulator. Some light in the optical mode escapes through the bottom of the pillar and the substrate. (b) The optical mode in such structures is trapped on the InGaAs gain region in the center of the pillar due to refractive index differences. The figure shows just the center section of the pillar containing the InGaAs. The contour lines show  $|E|^2$  of the trapped optical mode in a slice through the pillar center, with color giving intensity. The arrows show the magnitude and direction of the time averaged Poynting vector for this slice of the mode and show that the energy of the mode is mostly being dissipated as heat in the metal sidewalls.

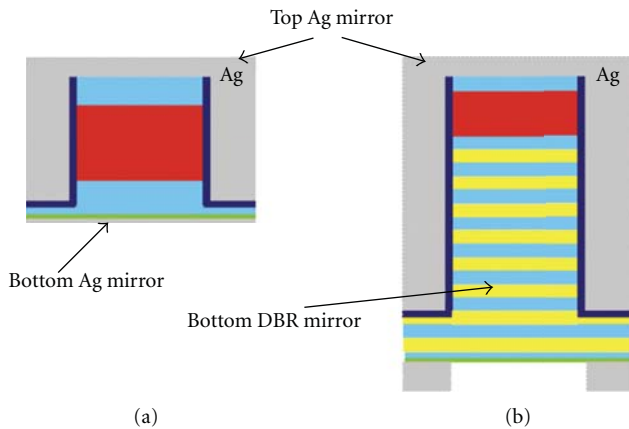


FIGURE 2: Another form of a pillar cavity appears very similar to that of Figure 1. However, here the mode propagates up and down in the pillar, and the resonant wavelength is always below the cutoff wavelength in the pillar waveguide [12, 13]. The mirror at the pillar top is formed by the silver contact. (a) In one case, the mirror at the bottom of the pillar is formed by a thin silver film. (b) In another case, the bottom mirror is formed by a Bragg reflector, similar to a traditional VCSEL. The red indicates the active region.

propagates with a component in the vertical direction, and hence the device can be used as a form of surface-emitting laser. More will be said on controlling the emission direction of the light later.

By adjusting the size and shape of the cross-section of the pillar different resonant modes can be obtained. At present,

perhaps the most interesting modes are the lower order modes of such cavities, for example HE<sub>11</sub> or TE<sub>01</sub> modes [4, 10], as these modes result in the smallest device and modal volumes. The benefits of small device and modal volumes include high Purcell factors helping to reduce threshold and nonradiative losses, smaller active regions reduce power and also improve prospects for heat sinking, and finally a large free spectral range to ensure single mode operation.

Another concept in metallic surface-emitting devices has also been demonstrated recently [12, 13], Figure 2. Although similar to the concept presented in Figure 1, in that both are round pillars containing heterostructures, there are a number of fundamental differences. In particular, the device of Figure 2 does not rely on a trapped cutoff mode in the center of the pillar. Rather, the resonant mode has a frequency above the cutoff frequency of the cylindrical metal waveguide. The mode is propagating up and down the waveguide. The resonator is formed by having mirrors at either end of the cylindrical waveguide. Typically, the top mirror is formed by the metal of the top contact. In the examples given in [12, 13], the bottom mirror can be formed by a Bragg grating or by a partially reflective metal mirror. This concept is closer to the original concept of a VCSEL, nanowire lasers, and also numerical studies of looking at lasing in metal coated nano-wires [14]. In this particular concept, the frequency of laser oscillation is determined by the length of the cavity in the vertical direction, in combination with any frequency selective mirrors that may be employed. Original VCSEL designs also incorporated metallic mirrors [15]. However, the metallic

propagating mode devices here also constrain the optical mode in the lateral direction, via the thick metallic waveguide. The lateral metallic confinement can lead to smaller size and better heat sinking compared to VCSELs. There are a number of advantages and disadvantages of this second approach compared to the cutoff mode devices discussed previously. In the following, these are listed to allow comparison between the two approaches. Aspects of each form of cavity can be considered an advantage or disadvantage depending on the application and point of view. For example, in the cutoff waveguide mode device, the pillar cross-section diameter determines the resonant frequency, which allows many different wavelength lasers to be easily produced on one wafer. However, the wavelength is also then sensitive to the lithographic precision employed in defining the pillar cross-section.

*Cutoff Mode Cavity Advantages:*

- (i) widely tunable wavelength and modal characteristics via pillar cross-section dimension;
- (ii) critical low resistance electrical contacts well separated from optical mode;
- (iii) good modal overlap between optical mode and gain medium;
- (iv) coupling of mode to free space can be tuned by cutoff region length;
- (v) optical mode properties independent of pillar length, emission pattern can be independently modified by horns or segments;
- (vi) do not require Bragg mirrors or critical metallic mirrors.

*Cutoff Mode Cavity Disadvantages:*

- (i) wavelength strongly dependent on lithographic control of pillar cross-section dimension;
- (ii) cannot make pillar width independent of wavelength and mode choice;
- (iii) energy flow in optical mode is not in the vertical direction;
- (iv) longer pillar required than for some propagating mode devices.

*Propagating Mode Cavity Advantages:*

- (i) wavelength better controlled over whole wafer due to Bragg mirrors or constant etch depth;
- (ii) mode energy propagation in direction of emission;
- (iii) waveguide (pillar) width independent of resonant wavelength and mode choice;
- (iv) smaller pillar height for some designs.

*Propagating Mode Cavity Disadvantages:*

- (i) wavelength difficult to widely tune via lithography;
- (ii) require special mirrors on the pillar base;

(iii) the critical top electrical contact material will form part of the optical cavity;

(iv) possibly smaller modal overlap with gain material.

The VCSEL has become a very successful form of semiconductor laser and it is good question to ask why should some other form of surface-emitting device be explored that could potentially replace it. The metallic cavity structures discussed above do have some significant positive features compared to conventional VCSELs and these are discussed below in point form.

- (i) Heat sinking. Having a nanoscale device encapsulated in a potentially large heat sink allows excellent heat removal from the active semiconductor material. In fact, simulations indicate that pumping densities into the MA/cm<sup>2</sup> region should be feasible, with only a few tens of degrees rise in device core temperature. Indeed, already current densities approaching 1 MA/cm<sup>2</sup> have been shown at low temperature for continuous operation [4] and at room temperature for pulsed operation [5]. Other experiments have reported excellent thermal characteristics for these devices [12]. The high pump densities possibly allow semiconductor gain material to be pushed close to its limits.
- (ii) High Purcell factor. A number of experiments have demonstrated that these cavities have a significant Purcell factor [4, 10]. Others have also pointed out that these cavities can have high Purcell factors over a broad bandwidth and that even for light-emitting diode applications they are interesting [16].
- (iii) Transfer to various substrates. The small size and malleable metallic encapsulation may be of benefit when transferring the devices to substrates such as Si or metals [12, 13].
- (iv) Lack of complex Bragg mirrors. The metallic mirrors required are in principle easy to construct and work over a very wide range of wavelengths.
- (v) Wide range of wavelengths on a single substrate.
- (vi) Potentially high intrinsic speed due to high Purcell effect and high pump density possible. Here we consider modulation of the laser by injection of optical signals, which is of interest in optical signal processing applications. Electrical modulation bandwidth may be significantly less due to limitations imposed by gain compression effects [17].
- (vii) Low power due to smaller active region.
- (viii) Closer packing of devices without interference, due to the strong lateral metallic mirrors, possibly allowing arrays of independent devices with subwavelength pitch.

### 3. Efficiency and Output Beam Quality

For applications, it is clearly desirable that any laser converts electrical energy into light which can be utilized, with as close

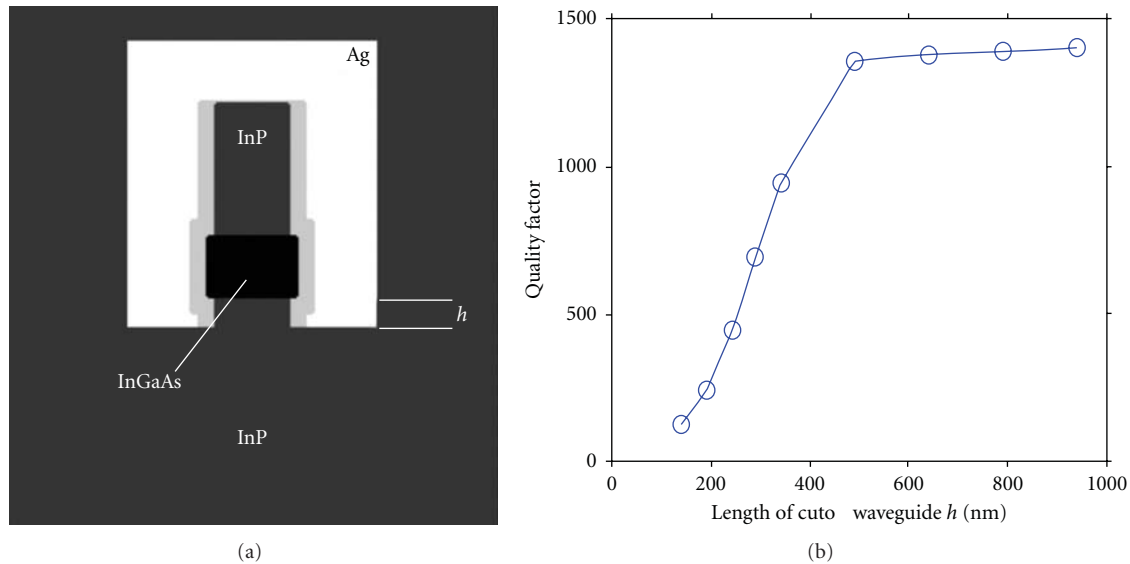


FIGURE 3: (a) Slice through silver-encapsulated semiconductor core pillar device, showing details of its structure used in a simulation. The height of the InGaAs core is 300 nm. The light gray region between the InGaAs core and silver is the dielectric. The substrate below the pillar is InP. The height parameter  $h$  can be varied to modify the  $Q$  of the cavity, allowing more or less light from the cavity mode to leak to the outside of the cavity. (b) Plot of quality factor of cavity ( $Q$ ) versus length of InP stub under the InGaAs. Values were obtained via FDTD simulations. Shows trade off can be made between  $Q$  and emission efficiency. The particular mode simulated here is the TE<sub>01</sub> mode, and due to less interaction with the metal, it has a reasonably large maximum  $Q$ .

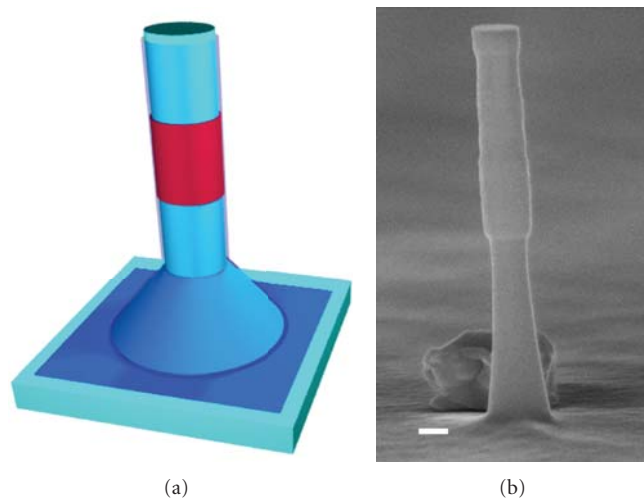


FIGURE 4: (a) The core of a cutoff mode pillar device with a horn antenna structure at the base of the pillar. The horn can radically change the output radiation pattern. (b) Scanning electron micrograph (SEM) of a semiconductor core of a pillar device, before encapsulation in dielectric and metal. The scale bar is 100 nm. The InGaAs region in the center can be seen, and has a slight bulge to enhance confinement. The base of the pillar flares out as often happens in reactive ion etch processes. Furthermore, the process parameters can be adjusted during the etch process to increase the sidewall slope and create horn-like structures at the pillar base.

as possible to one hundred percent efficiency. In practice, most lasers fall well short of perfect conversion efficiency. The optical loss of the lasing cavity mode is a combination of light escaping into free space, and also internal cavity losses. For metallic nanolasers in particular efficiency has been a contentious issue, as the high internal losses due to the metal require significant gain to be compensated. Further compensating the increased cavity loss due to emitting a significant

proportion of the optical mode energy to free space places even more demands on the material gain. However, a number of studies have shown that even with relatively strong confinement of the light, reasonable efficiency can be obtained with correct cavity design [18], and given published optical losses for the metal [19]. For the cutoff mode devices, larger pillars which employ higher order modes than the HE<sub>11</sub> mode, and also have thicker dielectric layers, can

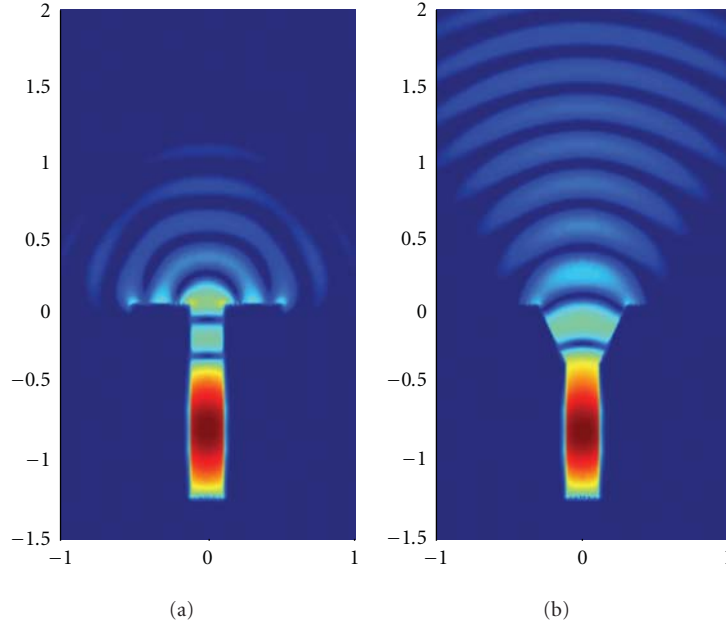


FIGURE 5: Simulations showing the electric field intensity of a cutoff pillar device with and without a horn antenna structure at the output. Note in this case the base of the device is at the zero point on the vertical axes. The scale is in microns. The resonant mode is a HE11 mode, and resonant wavelength approximately 1.55 microns. (a) Without horn: showing strong divergence of the output light. (b) With a modest horn. Note that already the output beam is much more directional.

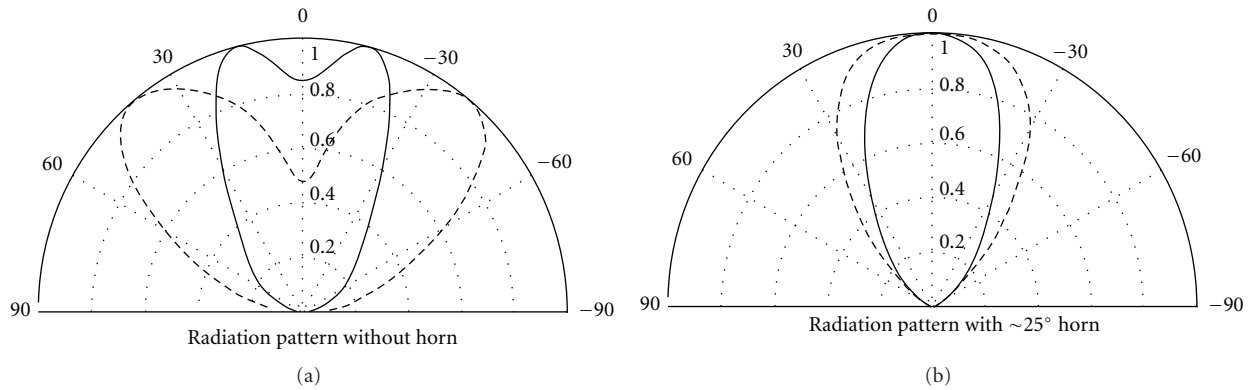


FIGURE 6: Far field radiation patterns derived from the simulations of Figure 5. Note that the HE11 mode does not have circular symmetry so that radiation patterns for the two axes are shown. (a) Without horn, showing a significant beam divergence. (b) With a modest horn, showing a much narrower beam.

suffer less from the metallic losses [20]. For these devices high efficiency could in theory be achieved as the material gain required for lasing can be low as several hundred per centimeter. Considering that semiconductor gains can reach several thousands per centimeter, there is room to make devices where a large proportion of the lasing mode energy is coupled out. Others have also indicated that for both lasers and LEDs, such pillar structures can in theory have quite acceptable efficiencies, in the order of 50% [16, 21].

For the propagating mode devices, controllable out coupling is achieved by adjusting the transmission characteristic of one of the mirrors, which with a metal mirror means controlling its thickness [17]. For the cutoff mode devices,

the amount of modal light coupled into the substrate can be controlled by adjusting the height of the cutoff waveguide under the gain region. Such a height adjustment can be readily achieved in fabrication. Figure 3 shows how such a change in height affects the cavity quality factor,  $Q$ . In the pillar devices the total  $Q$ ,  $Q_{tot}$ , depends on the  $Q$  due to metal absorption,  $Q_{abs}$ , and the  $Q$  due to radiation out the pillar base  $Q_{rad}$  [18].  $1/Q_{tot} = 1/Q_{abs} + 1/Q_{rad}$ . When the cutoff height is large,  $Q_{abs}$  dominates  $Q_{tot}$ . From Figure 3 it can be seen that for some modes  $Q_{abs}$  can reach into the thousands, allowing scope for significant out coupling of radiation.

A key advantage of the metallic devices described is that the resonant cavity has a subwavelength size. However,

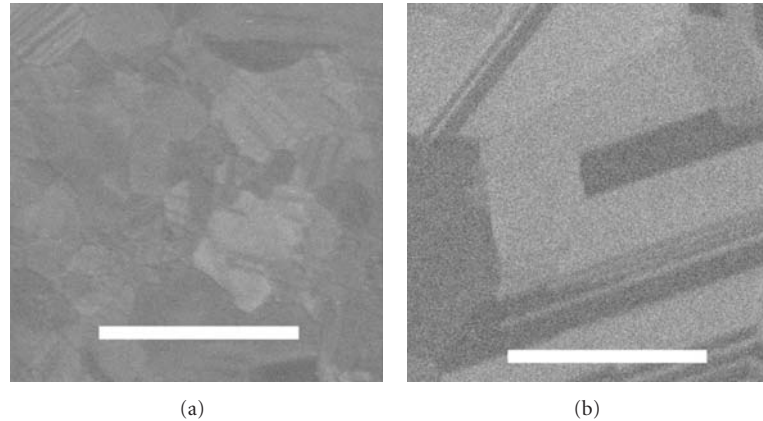


FIGURE 7: SEM images of deposited and annealed silver, showing different crystal sizes. The samples show the silver that occurs at the dielectric/silver interface, and the samples were prepared by removing the deposited and annealed silver films from the dielectric using adhesive tape. Both scale bars are 1 micron. (a) With 120 degrees C annealing for 2 hours. (b) With 400 degrees C annealing for 60 seconds. Note the much larger crystal grains, and also twinning defects.

the light exiting the cavity will in principle have to pass through some subwavelength aperture, which can lead to the light emitted over a wide solid angle. Some simulation studies have been done of these emission properties [21]. In many applications, a low divergence beam would be desired. The width of the propagating mode devices is independent of the mode choice, as long as the mode cutoff wavelength is longer than the lasing wavelength. Hence, here a wider device can be chosen to give less divergence in the output beam, although at the cost of a larger resonant cavity size.

Alternatively, some other form of patterning or structure at the subwavelength output could transform the highly divergent beam into narrow beam [22]. One possibility that exists for the cutoff mode cavities is the inclusion of some form of waveguide horn antenna [23] structure in the lower part of the pillar, Figure 4(a). Such an arrangement has the advantage that the properties of the subwavelength resonant cavity such as  $Q$ , and modal volume can be made independent of the output beam divergence. Such horn structures could be realized as part of the pillar etching process by adjusting the process parameters. Sidewall angles greater than 10 degrees can be achieved in reactive ion dry etching with methane/hydrogen etchants due to either polymer byproduct deposition or mask erosion [24]. Figure 4(b) gives an idea about how during reactive ion etch the sidewall angle can change at different stages in the process, and more strongly angled pillar bases could be made.

Simulations of the effects of such a horn structure are given in Figures 5 and 6. Here a pillar with a HE11 resonant mode is simulated. The far field radiation pattern and the electric field intensity of the beam show what a dramatic effect that even a modest horn structure a few hundred nanometers long can have.

#### 4. Technological Challenges

A number of teams have reported on attempts at producing these surface-emitting devices. However, often performance

falls short of what theory would predict. Certainly for the smaller devices with a HE11 or TE01 mode, continuous electrically pumped room temperature operation has yet to be shown. What are the possible major hurdles to overcome in such devices? At first sight surface recombination and surface defects caused by manufacture would seem to be the most difficult obstacle. However, our experience has been that with well-controlled dry-etching techniques, and surface treatments, surface damage, and surface recombination can be kept in check [25].

Good electrical contacts are required to support the very high injection current densities necessary. Very low resistance n-type contacts are in principle possible, and we see that indeed with care contact resistances well below  $10^{-6} \Omega\text{cm}^2$  can be obtained [26].

Likely, the largest deviation from theory in the manufactured devices that we see is the optical losses of the silver used as the confining metal. Estimates of cavity  $Q$  factor obtained from below threshold linewidths, in general yield a room temperature optical loss for the silver that is two to four times higher than some published measurements [19]. Other authors also report higher than expected optical losses in fabricated silver devices. Experiments have shown that the crystal structure of the metal can dramatically affect the optical losses [27]. Particular devices made from single crystal samples of metals have been shown to have much better performance than those made via deposition techniques such as evaporation [28]. Another aspect is that optical losses occur at the dielectric/metal interface where metal deposition starts, whereas most reported measurements are performed at the metal/air interface where deposition ends. In any case significant improvements in the metal dependent losses of the cavities are likely possible by improving the metal structure at the metal/dielectric interface. Figure 7 shows silver samples which were obtained by removing the treated silver layer from the dielectric (silicon nitride) surface via adhesive tape. The photos show the actual metal surface that in the device is responsible for optical losses, and they demonstrate

the wide range of metal structure possible due to different process parameters.

## 5. Conclusion

The last couple of years have seen a dramatic reduction in the size of the laser through the use of metallic resonators. Some of these metallic devices can be designed to have a VCSEL-like operation with light being emitted from a wafer surface. Such metallic devices may have advantages over conventional VCSELs such as higher intrinsic modulation speed, better thermal characteristics, and easier fabrication for a wider range of wavelengths. Such small low power devices, or even larger arrays of these devices, may generate new applications due to their unique properties.

We looked at two similar approaches based on nanopillars. Both of these approaches have already been demonstrated. For both approaches, it is in theory possible to create efficient laser light emitters with useful output beam characteristics. However, there appears to be still some technological challenges to reach the device performance that is predicted by theory. One of the key issues is reducing the optical loss of the deposited silver. In spite of difficulties, significant progress has occurred, and in just a few years electrically pumped room temperature devices have been realized.

## Acknowledgments

This work was supported by the Netherlands Organization for Scientific Research (NWO) through the NRC Photonics Grant and by the Dutch government through the MEMPHIS Grant.

## References

- [1] T. H. Maiman, "Stimulated optical radiation in Ruby," *Nature*, vol. 187, no. 4736, pp. 493–494, 1960.
- [2] R. N. Hall, G. E. Fenner, J. D. Kingsley, T. J. Soltys, and R. O. Carlson, "Coherent light emission from GaAs junctions," *Physical Review Letters*, vol. 9, no. 9, pp. 366–368, 1962.
- [3] K. Iga, "Surface-emitting laser—its birth and generation of new optoelectronics field," *IEEE Journal on Selected Topics in Quantum Electronics*, vol. 6, no. 6, pp. 1201–1215, 2000.
- [4] M. T. Hill, Y. S. Oei, B. Smalbrugge et al., "Lasing in metallic-coated nanocavities," *Nature Photonics*, vol. 1, no. 10, pp. 589–594, 2007.
- [5] M. T. Hill, M. Marell, E. S. P. Leong et al., "Lasing in metal-insulator-metal sub-wavelength plasmonic wave-guides," *Optics Express*, vol. 17, no. 13, pp. 11107–11112, 2009.
- [6] M. A. Noginov, G. Zhu, A. M. Belgrave et al., "Demonstration of a spaser-based nanolaser," *Nature*, vol. 460, no. 7259, pp. 1110–1112, 2009.
- [7] R. F. Oulton, V. J. Sorger, T. Zentgraf et al., "Plasmon lasers at deep subwavelength scale," *Nature*, vol. 461, no. 7264, pp. 629–632, 2009.
- [8] R. Perahia, T. P. M. Alegre, A. H. Safavi-Naeini, and O. Painter, "Surface-plasmon mode hybridization in subwavelength microdisk lasers," *Applied Physics Letters*, vol. 95, no. 20, Article ID 201114, 2009.
- [9] K. Yu, A. Lakhani, and M. C. Wu, "Subwavelength metal-optic semiconductor nanopatch lasers," *Optics Express*, vol. 18, no. 9, pp. 8790–8799, 2010.
- [10] M. P. Nezhad, A. Simic, O. Bondarenko et al., "Room-temperature subwavelength metallo-dielectric lasers," *Nature Photonics*, vol. 4, no. 6, pp. 395–399, 2010.
- [11] S. H. Kwon, J. H. Kang, C. Seassal et al., "Subwavelength plasmonic lasing from a semiconductor nanodisk with silver nanopan cavity," *Nano Letters*, vol. 10, no. 9, pp. 3679–3683, 2010.
- [12] C. Y. Lu, S. W. Chang, S. L. Chuang, T. D. Germann, and D. Bimberg, "Metal-cavity surface-emitting microlaser at room temperature," *Applied Physics Letters*, vol. 96, no. 25, Article ID 251101, 2010.
- [13] A. Matsudaira, C.-Y. Lu, S. L. Chuang, and L. Zhang, "Demonstration of metallic nano-cavity light emitters with electrical injection," in *Conference on Lasers and Electro-Optics (CLEO '11)*, 2011.
- [14] A. V. Maslov and C. Z. Ning, "Size reduction of a semiconductor nanowire laser by using metal coating," in *Physics and Simulation of Optoelectronic Devices XV*, Proceedings of SPIE, January 2007.
- [15] K. Iga, F. Koyama, and S. Kinoshita, "Surface emitting semiconductor lasers," *IEEE Journal of Quantum Electronics*, vol. 24, no. 9, pp. 1845–1855, 1988.
- [16] C. E. Hofmann, F. J. García De Abajo, and H. A. Atwater, "Enhancing the radiative rate in III-V semiconductor plasmonic core-shell nanowire resonators," *Nano Letters*, vol. 11, no. 2, pp. 372–376, 2011.
- [17] E. K. Lau, A. Lakhani, R. S. Tucker, and M. C. Wu, "Enhanced modulation bandwidth of nanocavity light emitting devices," *Optics Express*, vol. 17, no. 10, pp. 7790–7799, 2009.
- [18] S. W. Chang, T. R. Lin, and S. L. Chuang, "Theory of plasmonic Fabry-Perot nanolasers," *Optics Express*, vol. 18, no. 14, pp. 14913–14925, 2010.
- [19] P. B. Johnson and R. W. Christy, "Optical constants of the noble metals," *Physical Review B*, vol. 6, no. 12, pp. 4370–4379, 1972.
- [20] A. Mizrahi, V. Lomakin, B. A. Slutsky, M. P. Nezhad, L. Feng, and Y. Fainman, "Low threshold gain metal coated laser nanoresonators," *Optics Letters*, vol. 33, no. 11, pp. 1261–1263, 2008.
- [21] J. Huang, S. H. Kim, and A. Scherer, "Design of a surface-emitting, subwavelength metal-clad disk laser in the visible spectrum," *Optics Express*, vol. 18, no. 19, pp. 19581–19591, 2010.
- [22] H. J. Lezec, A. Degiron, E. Devaux et al., "Beaming light from a subwavelength aperture," *Science*, vol. 297, no. 5582, pp. 820–822, 2002.
- [23] S. Silver, *Microwave Antenna Theory and Design*, McGraw-Hill, New York, NY, USA, 1949.
- [24] B. T. Lee, T. R. Hayes, P. M. Thomas, R. Pawelek, and P. F. Sciortino, "SiO<sub>2</sub> mask erosion and sidewall composition during CH<sub>4</sub>/H<sub>2</sub> reactive ion etching of InGaAsP/InP," *Applied Physics Letters*, vol. 63, no. 23, pp. 3170–3172, 1993.
- [25] H. Wang, M. Sun, K. Ding, M. T. Hill, and C.-Z. Ning, "A top-down approach to fabrication of high quality vertical heterostructure nanowire arrays," *Nano Letters*, vol. 11, no. 4, pp. 1646–1650, 2011.
- [26] L. G. Shantharama, H. Schumacher, H. P. Leblanc, R. Esagui, R. Bhat, and M. Koza, "Evaluation of single ohmic metallizations for contacting both p- and n-type GaInAs," *Electronics Letters*, vol. 26, no. 15, pp. 1127–1129, 1990.

- [27] M. Kuttge, E. J. R. Vesseur, J. Verhoeven, H. J. Lezec, H. A. Atwater, and A. Polman, "Loss mechanisms of surface plasmon polaritons on gold probed by cathodoluminescence imaging spectroscopy," *Applied Physics Letters*, vol. 93, no. 11, Article ID 113110, 2008.
- [28] J. -S. Huang, V. Callegari, P. Geisler et al., "Atomically flat single-crystalline gold nanostructures for plasmonic nanocircuitry," *Nature Communications*, vol. 1, no. 9, article 150, 2010.

## Review Article

# Nonlinear Dynamics of Vertical-Cavity Surface-Emitting Lasers

**Krassimir Panajotov,<sup>1,2</sup> Marc Sciamanna,<sup>3</sup> Ignace Gatara,<sup>1</sup>  
Mikel Arteaga,<sup>4</sup> and Hugo Thienpont<sup>1</sup>**

<sup>1</sup> Department of Applied Physics and Photonics, Vrije Universiteit Brussel, Pleinlaan 2, 1050 Brussels, Belgium

<sup>2</sup> Laboratory of Optics and Spectroscopy, Institute of Solid State Physics, 72 Tzarigradsko Chaussee Boulevard, 1784 Sofia, Bulgaria

<sup>3</sup> Supélec, Optics & Electronics (OPTTEL), LMOPS EA-4423, 2 rue Edouard Belin, F-57070 Metz, France

<sup>4</sup> Department of Electrical and Electronic Engineering, Public University of Navarra, 31006 Pamplona, Spain

Correspondence should be addressed to Krassimir Panajotov, kpanajot@b-phot.org

Received 6 June 2011; Accepted 28 July 2011

Academic Editor: Rainer Michalzik

Copyright © 2011 Krassimir Panajotov et al. This is an open access article distributed under the Creative Commons Attribution License, which permits unrestricted use, distribution, and reproduction in any medium, provided the original work is properly cited.

Nonlinear dynamics of Vertical-Cavity Surface-Emitting Lasers (VCSELs) induced by optical injection, optical feedback, current modulation and mutual coupling is reviewed. Due to the surface emission and cylindrical symmetry VCSELs lack strong polarization anisotropy and may undergo polarization switching. Furthermore, VCSELs may emit light in multiple transverse modes. These VCSEL properties provide new features to the rich nonlinear dynamics induced by an external perturbation. We demonstrate for the case of orthogonal optical injection that new Hopf bifurcation on a two-polarization-mode solution delimits the injection locking region and that polarization switching and injection locking of first-order transverse mode lead to a new resonance tongue for large positive detunings. Similarly, the underlying polarization mode competition leads to chaotic-like behavior in case of gain switching and the presence of two transverse modes additionally reduces the possibility of regular dynamics. The bistable property of VCSEL makes it possible to investigate very fundamental problems of bistable systems with time-delay, such as the coherence resonance phenomenon. We also demonstrate that the synchronization quality between unidirectionally coupled VCSELs can be significantly enhanced when the feedback-induced chaos in the master laser involves both orthogonal LP fundamental transverse modes.

## 1. Introduction

The change of the semiconductor laser cavity geometry from facet to surface-emitting gave birth to the vertical-cavity surface-emitting lasers (VCSELs) [1] with significant advantages, such as single longitudinal mode emission, low cost, circular output beam, and easy fabrication in two-dimensional arrays. As a result, VCSELs are nowadays substituting the traditional semiconductor edge emitting lasers (EELs) in many applications, such as fiber to the home links, computer networks, optical interconnects, and optical sensing. Until recently, most of the commercially available VCSELs were emitting in the near infrared, around 850 nm or 970 nm, based on GaAs active region and GaAs/AlGaAs DBR mirrors but now they become available also at telecommunication wavelengths 1.3 or 1.55  $\mu\text{m}$  and at visible or even UV wavelengths. Emission in multiple transverse modes is usually found in VCSELs [2] as a result of spatial

hole burning effect [3, 4]. Furthermore, due to the surface emission and cylindrical symmetry VCSELs grown on (001) substrate lack strong polarization anisotropy and may undergo polarization switching (PS) [2, 5]. Different physical mechanisms can lead to PS, such as microscopic spin-flip processes in presence of birefringence and linewidth enhancement factor [6, 7], thermal lensing [8], spatial hole burning [9], or the relative modification of the net modal gain and losses with the injection current [5, 10]. The lack of polarization anisotropies and the multitransverse mode behavior of VCSELs provide new features to the rich nonlinear dynamics induced by optical injection (OI), gain switching (GS), and optical feedback (OF).

Locking of the frequency of the injected (slave) semiconductor laser to the one of the injecting (master) laser has long been known [11, 12] and is of great interest from an application point of view. It can be used for reduction of the laser linewidth [12] and the mode partition noise

[13] or for an enhancement of the modulation bandwidth [14] and for synchronizing an array of lasers onto a unique master [15]. Furthermore, OI dynamics is also of interest from a fundamental point of view and rich dynamics as period doubling route to chaos [16–18], resonance tongues [19], and excitability [20] have been reported. Orthogonal OI in VCSELS, that is, the linear polarization of the injected light is orthogonal to the one of the VCSEL, was first reported by Pan et al. [21] in 1993. It was shown that increasing the injection strength, the VCSEL switches its polarization to that of the injected light through a region of bistability and may exhibit an injection locking (IL) depending on the frequency detuning between the two lasers [22]. Hong et al. [23] have shown that the otherwise depressed LP mode may be excited by orthogonal OI and regions of chaotic competitions in the two linearly polarized (LP) modes of the VCSEL have been shown experimentally both for positive and negative detunings. The case of parallel OI has been investigated by Li et al. [24]. Transverse mode dynamics of a VCSEL with OI have been analyzed numerically [25] and experimentally [26, 27] for different configurations of the polarization of the injected light with respect to the light polarization of the free-running VCSEL.

Gain switching of semiconductor lasers has received a lot of attention, considering not only its potential to generate ultrafast sharp pulses but also because it can lead to complex dynamics such as period doubling and possibly chaotic pulsating [28–31]. Just a few reports of chaotic behavior can be found in the literature [30, 31] since only lasers with relatively small gain saturation and spontaneous emission noise parameters might undergo period doubling route to chaos under current modulation [32]. Studies of nonlinear dynamics in directly modulated VCSELS remain scarce [33–35]. Nonlinear dynamics have been theoretically analyzed for linearly polarized (LP) single transverse mode [33, 34] and multimode VCSELS [34, 35]. Chaotic behaviour appears in the multimode regime due to transverse mode competition [34, 35]. Only recently, theoretical and experimental studies have been undertaken with special attention on the role of light polarization [36–39].

Time-delayed optical feedback (OF) perturbs the steady state laser emission and leads to complex dynamics [40]. It can lead to quite irregular (chaotic) dynamics [41] and as much as 3 orders of magnitude increase of the optical linewidth [42]. The same sequence of dynamical regimes that has been observed in EEL [42] is also reported in VCSELS [43]. With increasing the feedback strength these are linewidth narrowing or broadening; external-cavity mode (ECM) hopping; stable emission; sustained relaxation oscillations; chaotic regimes (low-frequency fluctuations, coherence collapse). Low-frequency fluctuation (LFF) dynamics [41] consists of sudden dropouts in the emitted optical power followed by gradual recoveries. LFF in VCSELS was studied theoretically in [44, 45] and found experimentally in [46, 47]. The effect of optical feedback on the transverse mode selection in VCSELS has also been investigated by several authors, for example, in [48, 49].

Synchronization of chaotic systems has been a subject of both theoretical and experimental studies [50]. In particular,

the synchronization between two chaotic semiconductor lasers has attracted considerable attention owing to its application in secure chaos-based optical communications [51]. Recent theoretical works have focused on the synchronization properties in polarization-dependent optical injection schemes [52] or using multitransverse mode but not single LP mode VCSELS [53]. Chaos synchronization has also been recently shown experimentally [54]. The growing interest in implementing chaos communication using VCSELS motivates further investigations to better understand the influence of polarization dynamics on the synchronization properties.

In this paper we summarize recent results on nonlinear dynamics of VCSELS for the case of optical injection, gain switching, optical feedback, and unidirectional chaos synchronization. The paper is organized as follows: in Section 2, we demonstrate that, for the case of orthogonal OI, a new Hopf bifurcation on a two-polarization-mode solution delimits the injection locking region and that polarization switching and injection locking of first-order transverse mode lead to a new resonance tongue for large positive detunings. In Section 3 we show that the underlying polarization mode competition leads to chaotic-like behavior in case of gain switching and the presence of two transverse modes additionally reduces the possibility of regular dynamics as shown. In Section 4 we discuss optical feedback-induced polarization dynamics that allows investigating very fundamental problems of bistable systems with time delay, such as the coherence resonance phenomenon. In Section 5 we demonstrate that the synchronization quality between unidirectionally coupled VCSELS can be significantly enhanced when the feedback-induced chaos in the master laser involves both orthogonal LP fundamental transverse modes. Finally, in Section 6, a brief summary of the results is presented.

## 2. Nonlinear Polarization and Transverse Mode Dynamics in VCSEL with Orthogonal Optical Injection

The experiments on orthogonal OI have been performed with oxide-confined GaAs quantum well VCSEL emitting at 845 nm as a slave laser (SL). The solitary VCSEL is polarization bistable in the injection current region 2.25 mA–4.60 mA, displaying type II PS (from the low to the high frequency LP mode [10]). It is biased below the bistable region, at  $I = 2.105$  mA, and emits fundamental transverse mode with horizontal polarization ( $x$ -LP) and output power of  $P_{\text{out}} = 1.28$  mW. An external cavity tunable laser is used as a master laser (ML) and is set to emit vertically polarized light ( $y$ -LP).

In Figure 1 we show a typical route to PS through injection locking by presenting high resolution Fabry-Perot spectra for different injected powers and fixed negative detuning of  $-4$  GHz [22]. For very low injected power, the VCSEL keeps emitting in  $x$ -LP but is pulled toward the ML frequency proportionally to the strength of the injection. An increase of the injected power leads to undamping of relaxation oscillations—small side peaks appear on each side of the SL

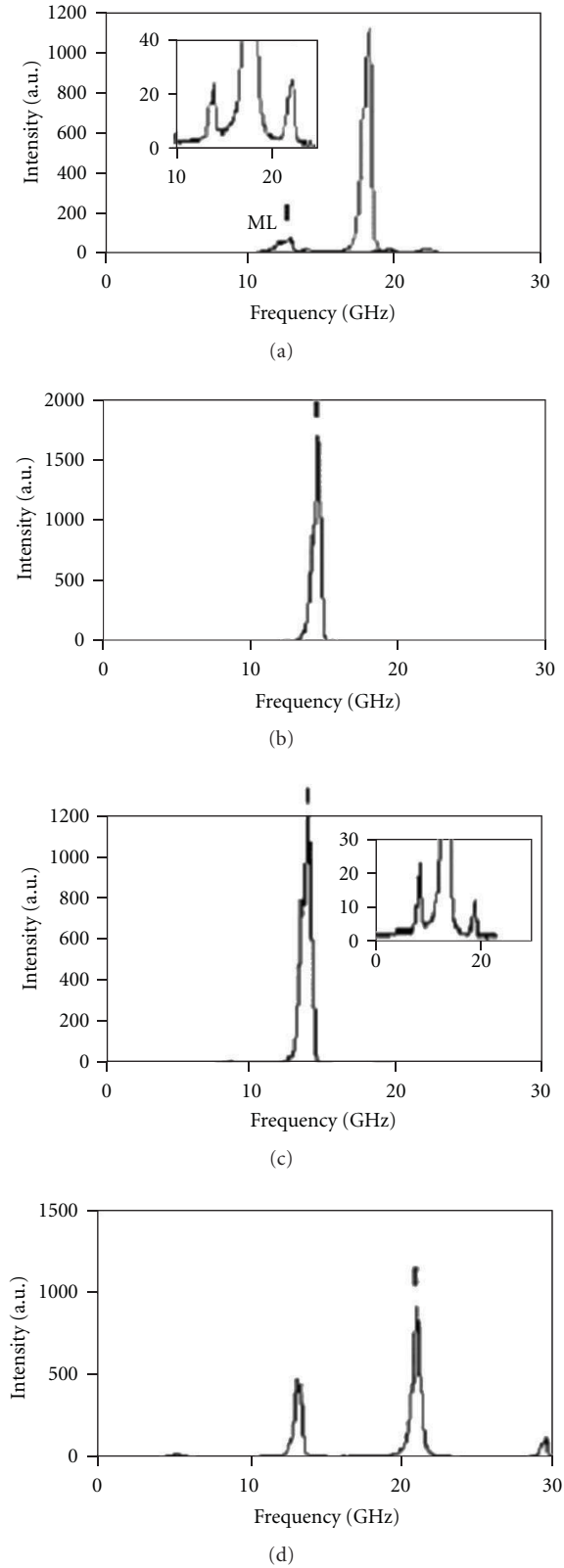


FIGURE 1: Polarization-resolved optical spectra of the VCSEL subject to optical injection at a frequency detuning of  $-4$  GHz. (a)  $P_{inj} = 40 \mu\text{W}$ . (b)  $76 \mu\text{W}$ . (c)  $103 \mu\text{W}$ . (d)  $210 \mu\text{W}$ . The vertical line shows the ML frequency. The insets in (a) and (c) show the same spectra magnified. After [22]. (Reprinted by permission from *IEEE J. Quantum Electronics*.)

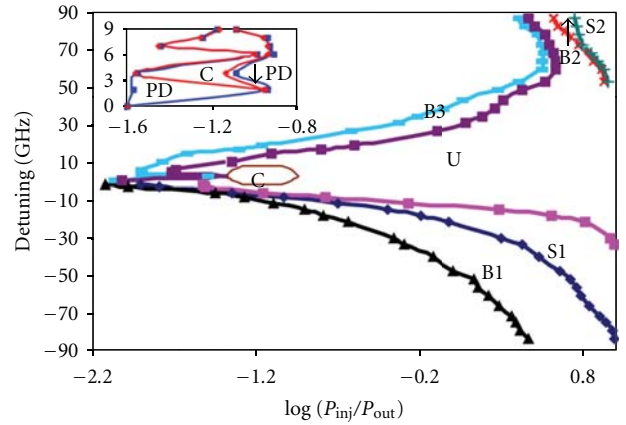


FIGURE 2: Experimental mapping of bifurcations to qualitatively different polarization dynamics in a VCSEL subject to orthogonal optical injection. Labels and symbols are explained in the text. After [55]. (Reprinted by permission from *Appl. Phys. Lett.*)

peak (Figure 1(a)). For still larger injection strength, PS with injection frequency locking of the fundamental transverse mode is achieved (Figure 1(b)). The locking region is excited by excitation of a limit cycle dynamics (Figure 1(c)). Harmonics of the limit cycle are resolved for higher injection power, and further the slave laser (SL) frequency is progressively pushed from the ML frequency (Figure 1(d)).

Figure 2 presents the boundaries of qualitatively different dynamics experimentally mapped in the plane of frequency detuning (master minus the slave laser frequency)—injection power (normalized to the solitary VCSEL power) [22, 55]. The polarization switch off and switch on points on the  $x$ -LP mode for increasing (decreasing) the injected power are represented by the dark blue and violet (light blue and black) lines. In the regions S1 and S2, the frequency of VCSEL emission is locked to the master laser. However, in the case of S2, it is the first order transverse mode rather than the fundamental transverse mode (as is the case of the S1 region) that locks to the master laser, the fundamental transverse mode being then suppressed when crossing the dark green line. The unlocking of the first order transverse mode happens at smaller values of  $P_{inj}$ , describing bistable region B2 between the fundamental and the first order transverse mode both with the same polarization (B2 is delimited by the dark green and red lines). We observe two polarization bistable regions in a regime of fundamental mode emission, which correspond to two different ways of PS. The first one is with frequency locking (B1), as presented in Figure 1, and is confined between the dark blue and the black lines. The second polarization bistable region (B3) is confined between the light blue and the violet lines where the PS happens without frequency locking. The two bistable regions are connected at a detuning of 2 GHz, which coincides with the birefringence frequency splitting between the two VCSEL LP modes. The bistable region B3 is strongly influenced by the locking of the first order LP mode (S2), its borderline turning backwards at a detuning of 50 GHz. The mapping of dynamical states shows that rich nonlinear dynamics including period-doubling route to

chaos and reverse period-doubling from the chaotic zone are found for detunings in the range 2–10 GHz (see the inset of Figure 2 and also [22]).

In Figure 3, the mapping of the VCSEL subject to optical injection is extended towards large positive detuning up to 180 GHz [56]. When the injection strength is increased, different PS scenarios are resolved depending on the frequency detuning. A switching from  $x$ -LP to  $y$ -LP fundamental transverse mode is observed for the whole frequency detuning range—denoted by black triangles in Figure 3. This boundary exhibits two minima for the switching power: the first located at a detuning of 2 GHz and the second one at a detuning of 150 GHz with injection powers of  $7.1 \mu\text{W}$  and  $623.9 \mu\text{W}$ , respectively. Injection locking of the first-order transverse mode together with suppression of the fundamental mode is observed for frequency detuning range from 60 to 120 GHz—denoted by black diamonds in Figure 3.

It is possible to reproduce theoretically the experimental results on the base of a set of rate equations that accounts for the polarization properties of VCSELs, namely, the spin-flip model (SFM) [6]. The SFM equations [6, 7], extended to the case of optical injection are given in [7, 57–59] for a single-transverse-mode VCSEL and in [56] for a multitransverse-mode VCSEL. For completeness, we list the SFM equations for the case of OI in a single-transverse mode VCSEL, namely,

$$\begin{aligned} \frac{dE_x}{dt} = & -(\kappa + \gamma_a)E_x - i(\kappa\alpha + \gamma_p + \Delta\omega)E_x \\ & + \kappa(1 + i\alpha)(NE_x + inE_y), \end{aligned} \quad (1)$$

$$\begin{aligned} \frac{dE_y}{dt} = & -(\kappa - \gamma_a)E_y - i(\kappa\alpha - \gamma_p - \Delta\omega)E_y \\ & + \kappa(1 + i\alpha)(NE_y - inE_x) + \kappa_{inj}E_{inj}, \end{aligned} \quad (2)$$

$$\begin{aligned} \frac{dN}{dt} = & -\gamma \left[ N \left( 1 + |E_x|^2 + |E_y|^2 \right) \right. \\ & \left. - \mu + in(E_y E_x^* - E_x E_y^*) \right], \end{aligned} \quad (3)$$

$$\frac{dn}{dt} = -\gamma_s n - \gamma \left[ n \left( |E_x|^2 + |E_y|^2 \right) + iN(E_y E_x^* - E_x E_y^*) \right]. \quad (4)$$

In addition to the coupling of the polarizations states through the carrier density (3), the SFM accounts for a coupling due to the finite spin-flip rate  $\gamma_s$  of the carriers [5], which, together with the linewidth enhancement factor  $\alpha$  and the inherent small VCSEL birefringence  $\gamma_p = (\omega_y - \omega_x)/2$  and dichroism  $\gamma_a$  leads to PS in a solitary laser [7]. The variable  $N$  is related to the total inversion between conduction and valence bands, while  $n$  accounts for the difference in the carrier numbers with opposite spins. The rest of the parameters are  $\mu$ : the normalized injection current;  $\kappa$ : the photon decay rate;  $\gamma$ : the carrier decay rate. OI of  $y$ -LP light is accounted for by  $\kappa_{inj}$ : the coupling coefficient,  $E_{inj}$ : the injected field amplitude, and  $\Delta\omega = \omega_{inj} - (\omega_x + \omega_y)/2$ —the

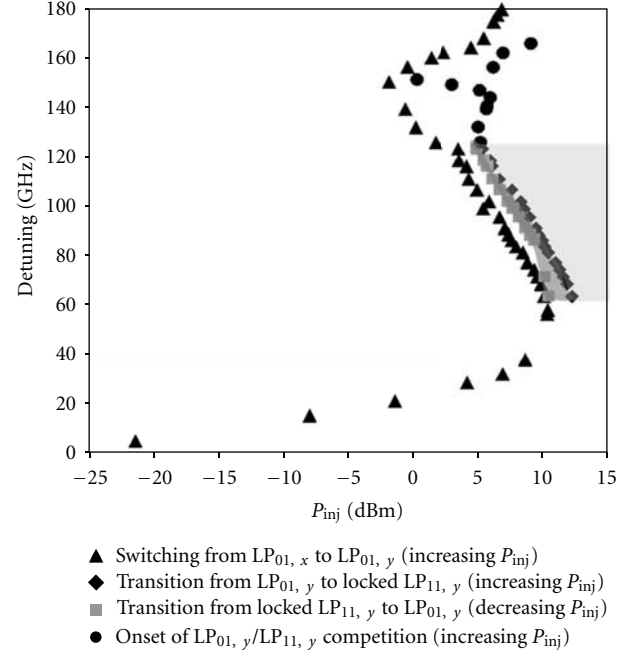


FIGURE 3: Experimental mapping of polarization switching and transverse modes competition extended towards large positive detunings. After [56]. (Reprinted, by permission, from *IEEE J. Quantum Electronics*.)

frequency detuning between the master and the mean of the VCSEL LP mode frequencies.

Figure 4 shows a typical bifurcation mapping for a single-transverse-mode VCSEL with parameters  $\mu = 1.5$ ,  $\kappa = 300 \text{ ns}^{-1}$ ,  $\gamma = 1 \text{ ns}^{-1}$ ,  $\gamma_p = 30 \text{ ns}^{-1}$ ,  $\gamma_a = 0.5 \text{ ns}^{-1}$ , and  $\gamma_s = 100 \text{ ns}^{-1}$ . Qualitative changes in the VCSEL dynamics are detected and followed using the continuation package AUTO 97. Different bifurcation curves are plotted: a saddle-node (SN), two Hopf ( $H_1$  and  $H_2$ ), and a torus (TR). The supercritical and subcritical parts of each bifurcation curve are represented in black and gray, respectively. When increasing the injection strength, the VCSEL switches its polarization to that of the injected field; these “PS off” ( $x$ -LP mode off) points are shown with circles. The PS curves interplay with the bifurcation curves. SN and  $H_1$  are bifurcations on a stationary injection-locked state and have also been reported in the case of optically injected edge-emitting laser. In the conventional case of EEL, the locking region is then delimited by the codimension two-point  $G_1$  where SN and  $H_1$  intersect [60]. In our VCSEL system, the locking region is delimited not only by SN,  $H_1$  but also by a new bifurcation  $H_2$  (see Figure 4(b)). The maximum detuning leading to injection locking therefore stays well below the codimension-two saddle-node-Hopf point  $G_1$ . Apart from its effect on the locking,  $H_2$  also affects the PS mechanism. The smallest injection strength needed to achieve PS is located on  $H_2$  and corresponds to a dramatic change in the PS curve ( $m_1$ , see the dot vertical arrow in Figure 4(c)). The regions of more complicated, possibly chaotic dynamics bounded by  $PD_1$  and  $PD_2$ , also affect the switching mechanism leading to a second local

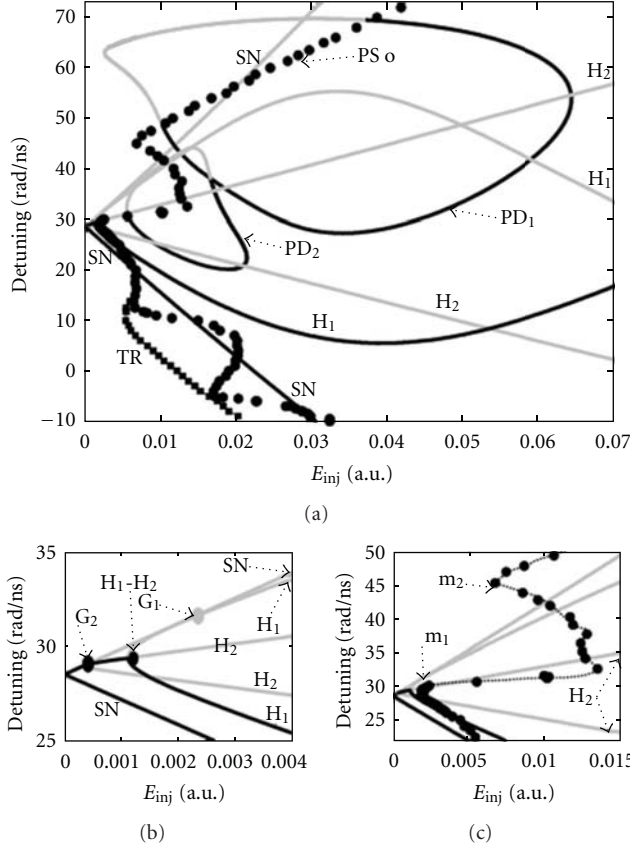


FIGURE 4: Bifurcation diagram in the plane injection strength-frequency detuning calculated by the SFM model for  $\kappa = 300 \text{ ns}^{-1}$ ,  $\gamma_p = 30 \text{ ns}^{-1}$ ,  $\gamma_a = 0.5 \text{ ns}^{-1}$ ,  $\gamma = 1 \text{ ns}^{-1}$ ,  $\gamma_s = 100 \text{ ns}^{-1}$  and  $\mu = 1.5$ . Close view of the codimension-two bifurcation mechanisms (b) and of the wobbling shape in the switching curve with local minima indicated by thick dotted arrows (c). (TR; “PS off”) and (TR) curves have been removed, respectively, in panels (b) and (c) for clarity. Black (gray) denotes supercritical (subcritical) bifurcation. After [57]. (Reprinted by permission from *Phys. Rev. A*.)

minimum denoted by  $m_2$  in Figure 4(c). As a result, the PS curve exhibits a wobbling shape with local minima of the injected power required for switching. The observed shape agrees qualitatively with the experimental results presented in Figure 2. The torus bifurcation TR corresponds to the excitation of two polarization mode dynamics in the route to PS and injection locking—a limit cycle in the  $x$ -LP and a wave mixing in the  $y$ -LP—which is also in agreement with the experiment [57]. The SFM model further predicts a two-mode injection-locked solution, that is, elliptically polarized injection-locked state for frequency detuning close to the VCSEL birefringence [58]. The bifurcation route to such solution has been studied in detail in [57].

### 3. Nonlinear Polarization and Transverse Mode Dynamics in Gain-Switched VCSEL

Polarization dynamics of gain-switched VCSELs was first investigated in [36] based on the spin-flip model for a single-

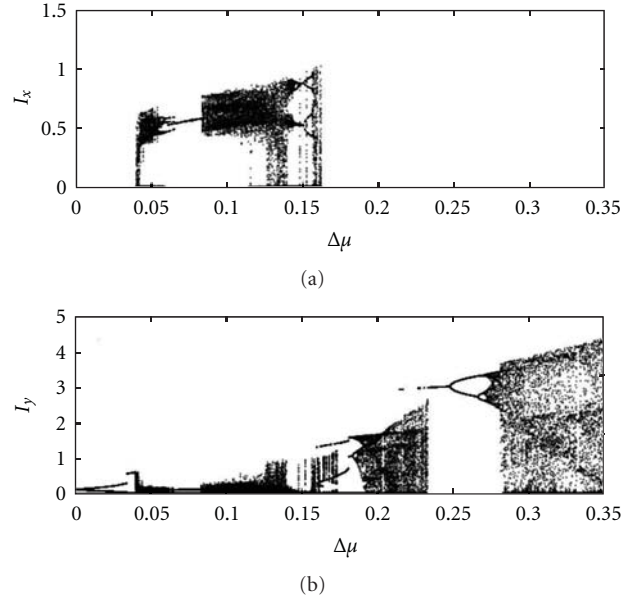


FIGURE 5: Bifurcation diagrams of the power of  $x$ -LP mode (a) and the  $y$ -LP mode (b) with the modulation amplitude  $\Delta\mu$  obtained by the SFM model for a single-mode VCSEL. The bias current is  $\mu_{dc} = 1.1$  and the modulation frequency is  $\nu_M = 1 \text{ GHz}$ . The VCSEL parameters are specified in the text. After [36]. (Reprinted by permission from *Phys. Rev. E*.)

transverse mode VCSEL given by (1)–(4) but without the optical injection term ( $\Delta\omega = 0$  and  $E_{inj} = 0$  in (2)) and with sinusoidally modulated injection current in (3):

$$\mu = \mu_{dc} + \Delta\mu \sin(2\pi\nu_M t), \quad (5)$$

where  $\mu_{dc}$  is the bias current and  $\Delta\mu$  and  $\nu_M$  are the amplitude and the frequency of modulation of the injection current, respectively.

Bifurcation diagrams of the polarization-resolved output power  $I_x$  and  $I_y$  are shown in Figure 5 as a function of amplitude of modulation  $\Delta\mu$  for  $\nu_M = 1 \text{ GHz}$  and  $\mu_{dc} = 1.1$ . The VCSEL parameters are  $\alpha = 3$ ,  $\gamma_a = 0.1 \text{ ns}^{-1}$ ,  $\gamma_p = 1 \text{ ns}^{-1}$ ,  $\gamma_s = 50 \text{ ns}^{-1}$ ,  $\kappa = 300 \text{ ns}^{-1}$ ,  $\gamma = 1 \text{ ns}^{-1}$ . The modulation frequency  $\nu_M$  is smaller than the relaxation oscillation frequency of the VCSEL  $\nu_{RO} = [2\kappa\gamma(\mu - 1)]^{1/2}/2\pi = 1.23 \text{ GHz}$ . As can be seen from Figure 5, the VCSEL initially lases in the  $y$ -LP mode, with increasing amplitude of sinusoidally modulated intensity at the modulation period with increasing  $\Delta\mu$ . For large enough  $\Delta\mu$ , such that the injection current goes from below to above the threshold current, gain switching occurs. In certain regions of  $\Delta\mu$ , the two LP modes coexist with chaotic or time-periodic dynamics and for still larger  $\Delta\mu$  the VCSEL lases only in the  $y$ -LP mode with a period-doubling route to chaos.

The LP mode dynamics is detailed in Figure 6, which shows time traces of the polarization resolved intensities for specific values of  $\Delta\mu$ . At  $\Delta\mu = 0.04$ , the depressed  $x$ -LP mode is also lasing, that is, the direct current modulation has excited the LP mode that was depressed in the VCSEL under dc operation. The two LP modes exhibit chaotic-like

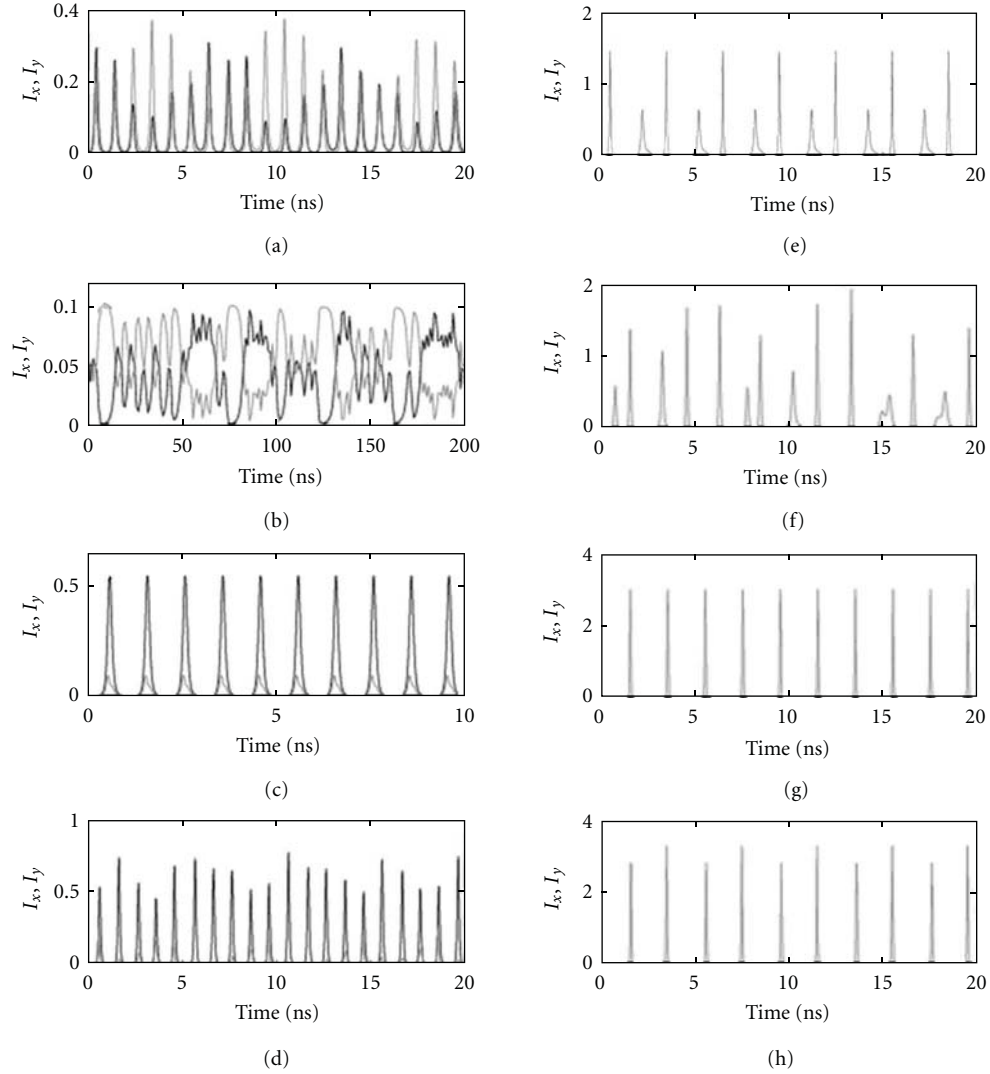


FIGURE 6: Time traces of  $I_x$  (black) and  $I_y$  (gray) for specific values of  $\Delta\mu$  in Figure 7: (a) and (b)  $\Delta\mu = 0.04$ , (c)  $\Delta\mu = 0.07$ , (d)  $\Delta\mu = 0.1$ , (e)  $\Delta\mu = 0.18$ , (f)  $\Delta\mu = 0.2$ , (g)  $\Delta\mu = 0.24$ , (h)  $\Delta\mu = 0.26$ . (b) is the same as (a) but averaged over 1 ns. After [36]. (Reprinted by permission from *Phys. Rev. E*.)

dynamics with a fast modulation of their intensities at the modulation frequency complemented by a slower envelope. Interestingly, the two LP modes emit in phase at the modulation frequency but the envelopes of their pulses are in partial antiphase: when one LP mode fires a large pulse, the other LP mode fires a small pulse. The partial antiphase dynamics is better seen in Figure 6(b), which presents the averaged over the modulation period output power in the two LP modes. For a slightly larger  $\Delta\mu = 0.07$ , Figure 6(c), the two LP modes exhibit in-phase time-periodic pulsing at the modulation frequency. For larger  $\Delta\mu$ , the  $y$ -LP mode is only lasing. At  $\Delta\mu = 0.18$ , Figure 6(e), the  $y$ -LP mode exhibits a period-3 time-periodic pulsing dynamics, which is followed by chaotic single mode dynamics at  $\Delta\mu = 0.2$ , Figure 6(f). For increasing modulation depth, the dynamics is single period one, Figure 6(g), followed by a period-doubling

route to chaos—the period 2 is shown for  $\Delta\mu = 0.24$  in Figure 6(h).

These theoretical predictions have been experimentally confirmed in [37]. A GaAs quantum-well oxide-confined VCSEL emitting at 851 nm is used in the experiments biased close to the PS point and then driven by an RF-signal through a bias-T. The temporal traces of the total and polarized powers are shown in Figure 7 for a modulation frequency of 2.88 GHz and current amplitude of  $\Delta I = 0.89I_{th}$ . A regular stream of pulses at each two periods of modulation is found for the total power. Small shoulders appear, that are remnants of the period-1 dynamics. When the amplitude of the modulation decreases, those shoulders become larger until similar heights are obtained for all the pulses in such a way that only one pulse appears each modulation cycle (period-1 dynamics). Pulses in individual polarizations also appear with that periodicity but their

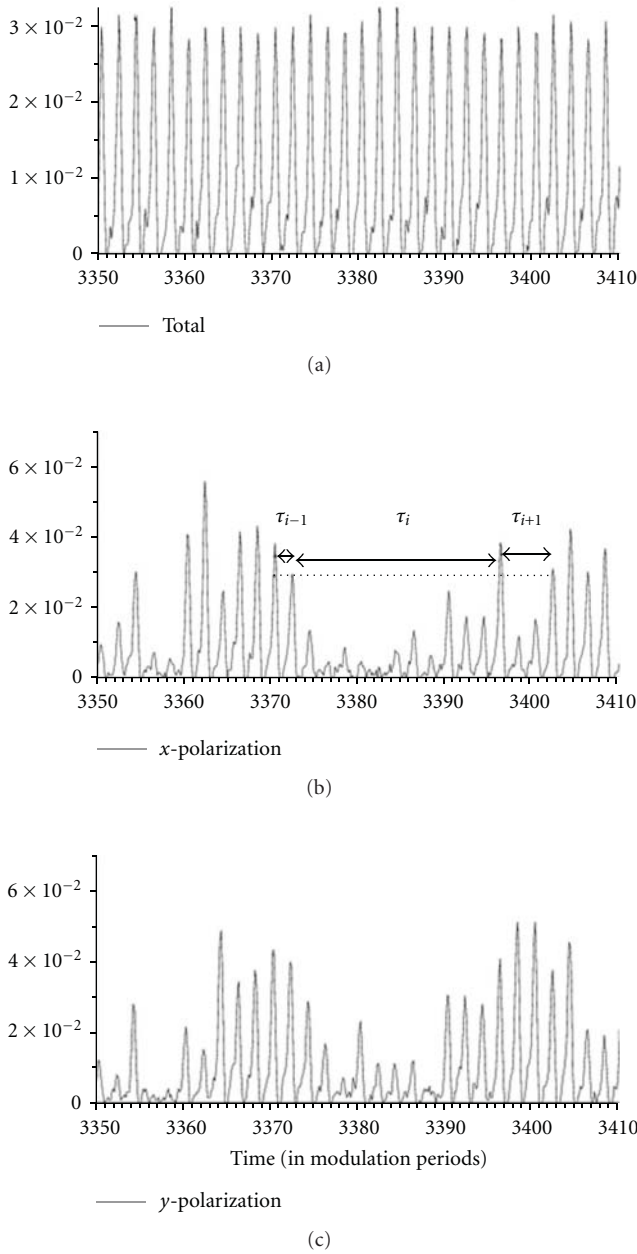


FIGURE 7: Experimental time traces of the intensities of the total (a), x-polarized (b), and y-polarized (c) powers. The current modulation is such that  $\nu_M = 2.88$  GHz,  $I = 1.26I_{th}$ , and  $\Delta I = 0.89I_{th}$ . After [37]. (Reprinted by permission from *IEEE J. Quantum Electronics*.)

heights are very irregular with wide temporal regions in which pulses in one polarization are very small while in orthogonal polarization are very high—as deduced from the regularity of the total power. Another indication for the regularity of the pulse dynamics is the statistical distribution of the residence times  $\tau_x$  ( $\tau_y$ ) given by the time between consecutive crossings of the corresponding  $P_x$  ( $P_y$ ) output power, from below to above, of certain reference level chosen as half of the total power maximum (see Figure 7(b)). Both the experimental and theoretical probability density

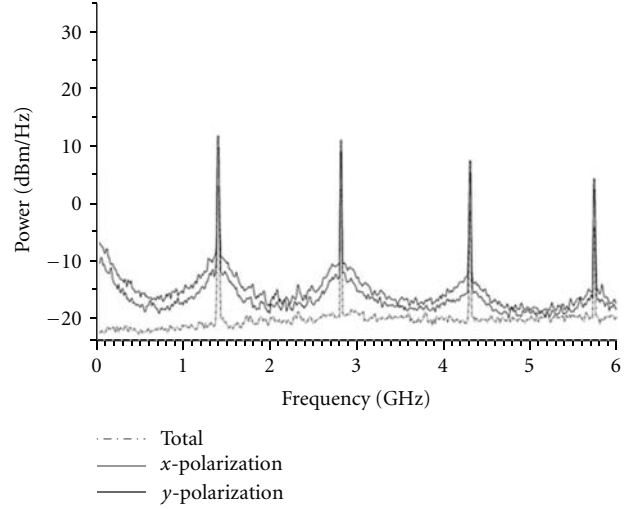


FIGURE 8: Experimental RF spectra of the total, x-polarized, and y-polarized power. The parameters of the modulation are the same as in Figure 7. After [37]. (Reprinted by permission from *IEEE J. Quantum Electronics*.)

distributions of the residence times for the individual polarizations present a multi-peaked structure with a long exponential envelope [37]. This long exponential tail is a signature of the irregularity of the stream of pulses—in contrast with the absence of such a tail for the total power.

The irregular behavior of individual polarizations, in contrast to the regular one of the total power, is also manifested in the corresponding RF spectra shown in Figure 8. Large peaks appear half of the modulation frequency and its multiples. These peaks are an indication of the period-doubling dynamics observed in the time series in Figure 7. The large pedestals that appear around the peaks of the spectra of individual polarizations indicate that the polarization-resolved dynamics is quite irregular. The power levels at low frequencies are much larger for the individual polarizations than for the total power, as a result of the anticorrelation between the two polarizations.

Gain-switched multitransverse mode VCSEL has been considered in [38]. The calculated bifurcation diagrams for the total and polarization resolved powers of the fundamental and first-order transverse modes display periodic and chaotic dynamics as well as for the total intensity. The  $LP_{11}$  mode is now excited with a significant power for all the modulation amplitudes. Time-periodic dynamics is now restricted to low values of  $\Delta\mu$ , that is, the excitation of the higher order transverse mode causes a disappearance of the windows of time-periodic regular pulsating dynamics found in the single-mode case.

These theoretical predictions were experimentally confirmed by using a GaAs quantum well VCSEL with medium oxide aperture size, such that it can operate on two transverse-modes simultaneously but in one linear polarization only [39]. A sinusoidal voltage is used to modulate the current around a bias value of 5.3 mA. Time traces obtained in the vertical polarization for a fixed amplitude

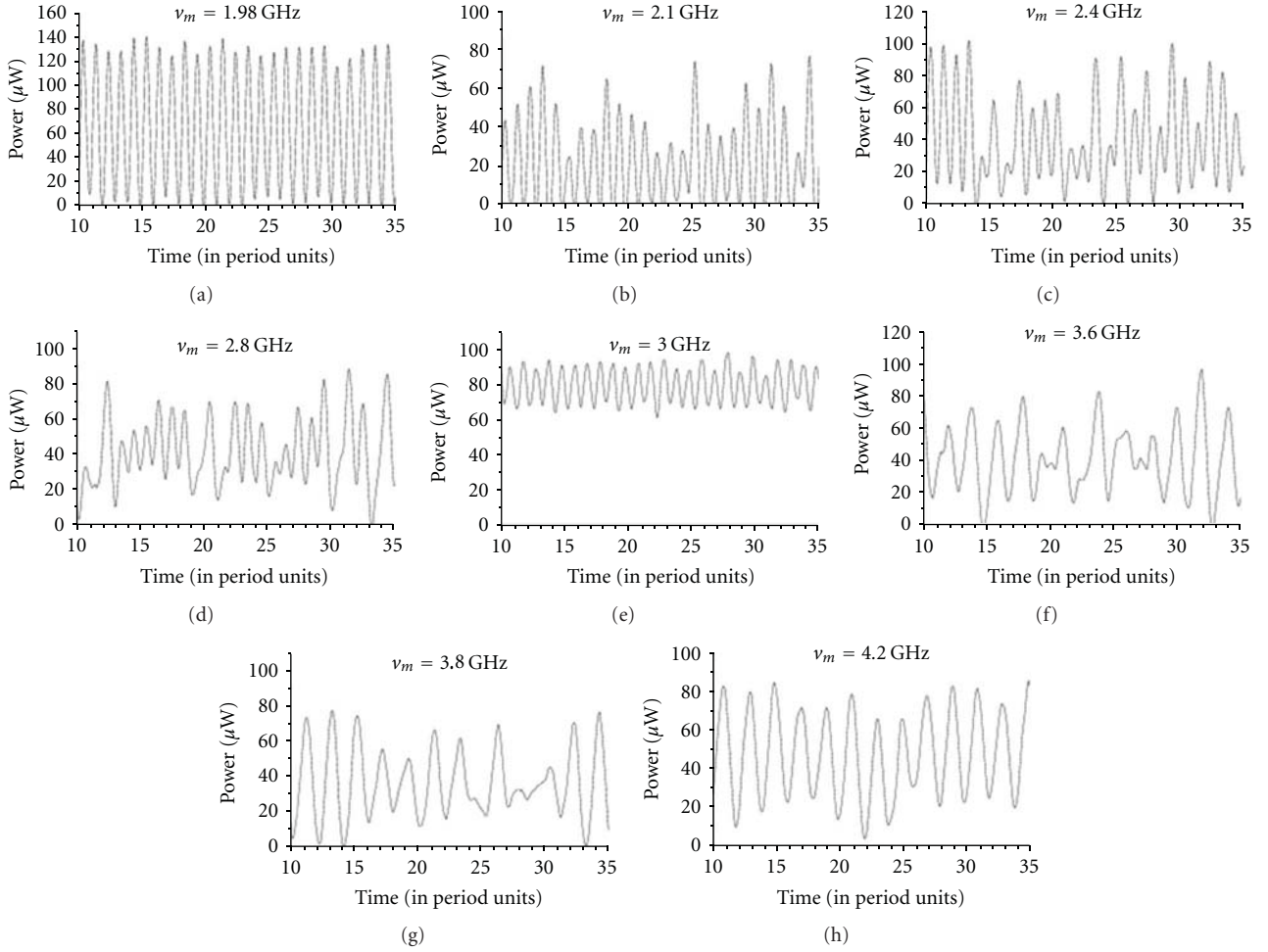


FIGURE 9: Time traces of the VCSEL output power for several values of the modulation frequency  $\nu_M$ , as denoted. The amplitude of the modulation is 20 dBm. After [39]. (Reprinted, by permission, from *Appl. Phys. Lett.*)

of 20 dBm—large enough to achieve gain-switching—and several modulation frequencies are shown in Figure 9. Time-periodic response of the system, with a period equal to the period of the modulation is obtained when  $\nu_M = 1.98$  GHz (Figure 9(a)). This situation is maintained in Figures 9(b), 9(c), and 9(d) but the pulse heights change in irregular way. 1T-periodic response with smaller modulation amplitudes again appears at  $\nu_M = 3$  GHz (Figure 9(e)) followed by irregular responses when increasing  $\nu_M$  (Figures 9(f) and 9(g)). The difference with respect to the irregular responses of Figures 9(b) and 9(c) is that now some of the pulses appear at 2T. For  $\nu_M = 4.2$  GHz in Figure 9(h), a more regular response but with a 2T periodicity is observed. We have measured a 2.4 GHz relaxation oscillation frequency at 5.3 mA, which roughly corresponds to the modulation frequency that separates the two situations in which the pulses switch off or do not switch off completely at each modulation cycle. In such a way, our experimental findings on the nonlinear dynamical behavior of a multitransverse-mode VCSEL when subject to high-frequency current modulation show that irregular pulsating dynamics can be obtained for a wide range of modulation frequencies as a result of the

competition between the different transverse modes of the laser, in agreement with the theoretical predictions.

#### 4. Polarization Dynamics of VCSEL with Optical Feedback: Coherence Resonance in Optical Bistable Time-Delayed System

Time-delayed optical feedback (OF) perturbs the steady state laser emission and leads to complex dynamics [40]. When a VCSEL is subject to isotropic (the same for any light polarization) OF, the route to dynamical instabilities is modified—see Figure 10 [62]. Due to the small frequency difference between the two solitary VCSEL LP modes, the modulation of the threshold gain as a result of the OF for the ECMs of different polarization differs. As can be seen from Figure 10(a), the change of the VCSEL injection current periodically destabilizes the laser operation through a Hopf bifurcation to a limit cycle [62]. The amplitude of the periodic oscillation initially increases but then the VCSEL undergoes a PS to a stable emission in the orthogonal LP state. Actually, the injection current, via the current induced

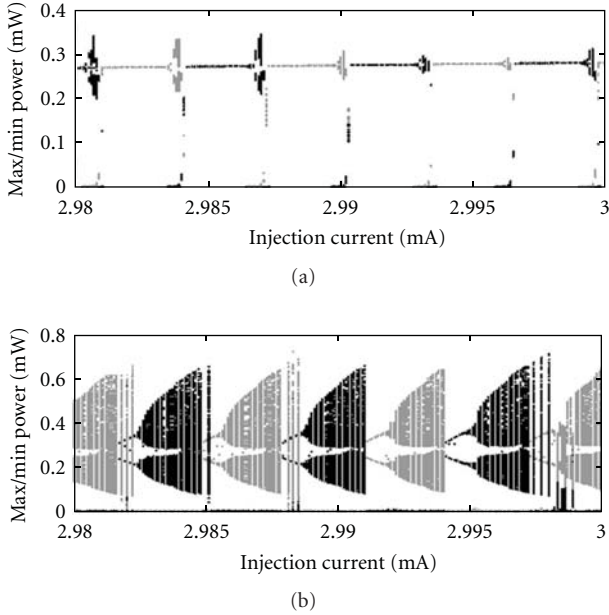


FIGURE 10: Numerically calculated bifurcation diagrams as a function of the injection current for external mirror reflectivity of  $r_{ex} = 0.005$  (a) and  $r_{ex} = 0.02$  (b). The two LP modes are represented with solid black ( $x$ -LP mode) and gray ( $y$ -LP mode) lines.

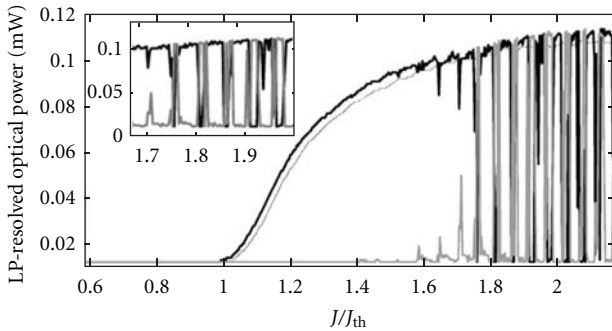


FIGURE 11: Experimental LI curve of a VCSEL subject to a weak optical feedback (thick lines), to be compared with the case without optical feedback (thin line). The  $x$ -LP ( $y$ -LP) mode intensity is plotted in black (gray). The inset shows enlargement to better illustrate the channeled LI curve with multiple PS points. After [61]. (Reprinted by permission from *Opt. Lett.*)

heating and the corresponding refractive index change, modifies the wavelength of the emitted light and therefore the phase of the light fed back into the VCSEL. In such a way, periodic regions of alternating lasing in the two LP modes are formed. For a fourfold increased reflectivity of the external mirror, the PS occurs between unstable LP modes, with different degree of destabilization—see Figure 10(b). Such a channeled light versus current (LI) curve has been found experimentally in [61, 63] and is shown in Figure 11 [61].

If we set the injection current close to a PS point light randomly alternates between emission of the  $x$ -LP mode and emission of the  $y$ -LP mode (see Figure 12). This situation

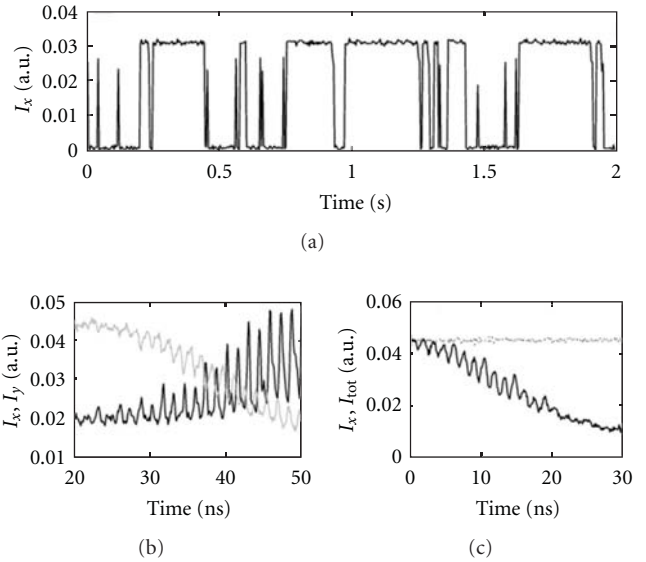


FIGURE 12: (a) Typical time-trace of mode hopping in the LP mode intensity of a VCSEL close to a polarization switching induced by weak optical feedback. (b) is an enlargement of (a) showing the two LP mode intensities when the light polarization hops between the two orthogonal directions. (c) shows a time-trace of the LP mode intensity (solid curve) together with the one of the total intensity (dotted curve). After [61]. (Reprinted by permission from *Opt. Lett.*)

is called polarization mode hopping for the case of solitary VCSEL [64–66], and from its statistical analysis it appears that the dwell time in a LP mode follows a Kramers law, that is, the probability distribution function exponentially decays with time. The mean dwell time depends on the injection current and the spontaneous emission level. In our OF experiment, superimposed on the slow polarization mode hopping (Figure 12(a)), a fast oscillatory behavior appears, at the frequency of the external cavity (750 MHz), that is, the inverse of the OF time delay (Figure 12(b)). These fast oscillations more clearly appear during an attempt to obtain successful polarization switch. The two LP intensities are strongly anticorrelated and therefore the oscillations vanish in the time trace of the total intensity (Figure 12(c)). It has been theoretically, [67] and experimentally [68] demonstrated that Kramers law is violated for VCSELs with OF: the time-delay strongly influences the residence time distribution leading to the appearance of an oscillatory behavior with peaks at the delay time and a valley connecting the statistics for short- and long-dwell times [68].

The coexistence of stochastic (noise driven) process of polarization mode hopping with the deterministic oscillatory behavior at the delay time brings an interesting question about the possibility to observe a coherence resonance in such a system, that is, a resonance of the dynamical regularity of the system at a certain noise level. It is indeed commonly accepted now that noise can play constructive role in nonlinear dynamical systems. After the seminal paper of Benzi et al. [69], the phenomenon of stochastic resonance, namely, the fact that adding noise can better

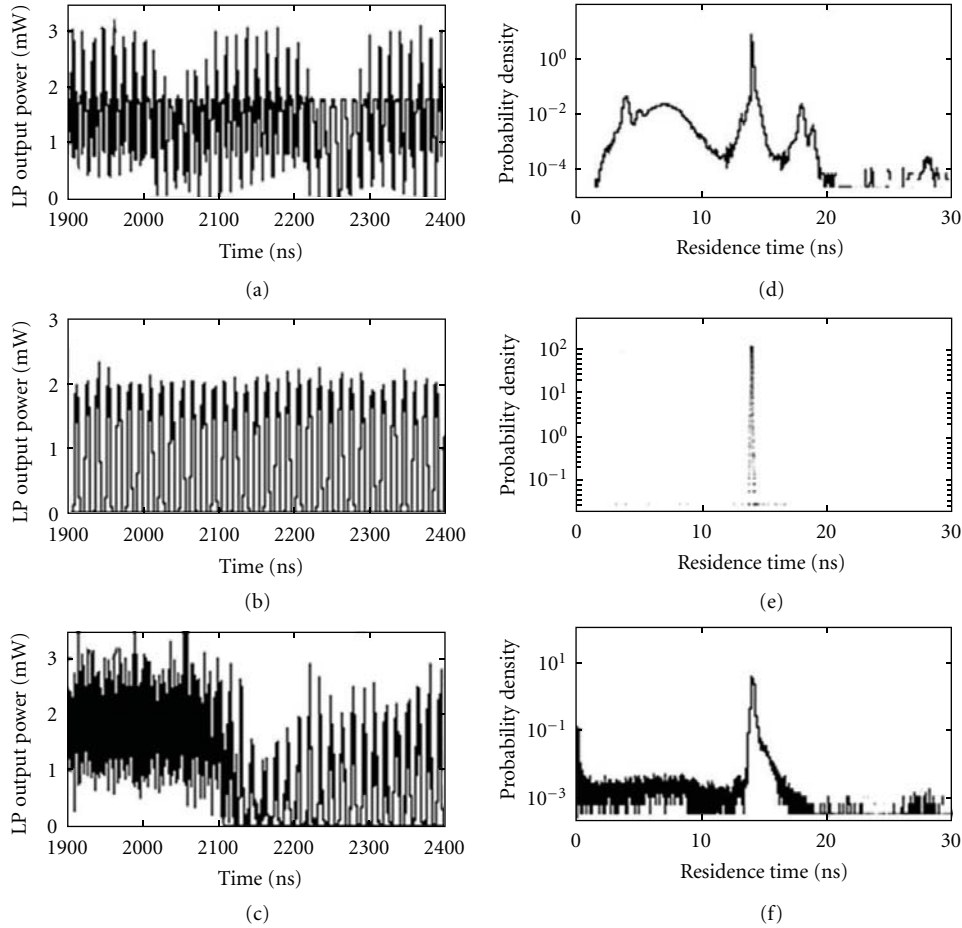


FIGURE 13: Numerical time traces of the  $x$ -LP mode (a), (b), (c), and joint residence-time distributions (d), (e), (f) for the case of long delay time ( $\tau = 13$  ns) and for different values of the external noise: (a), (d):  $J_{\text{var}} = 1.06 \cdot 10^{-7}$ ; (b), (e):  $J_{\text{var}} = 0.0066$ ; (c), (f):  $J_{\text{var}} = 0.0266$ . After [68]. (Reprinted by permission from *Phys. Rev. A*.)

synchronize dynamical system to an external periodic signal, has attracted a lot of interest in biology [70], physics [71], chemistry [72], and so forth (for a review see e.g., [73]). It has recently been realized that noise can enhance regular dynamics in nonlinear systems even in absence of external signal, when an internal time scale is present in the system [74]. This phenomenon is initially considered as stochastic resonance in autonomous system and lately named coherence resonance (CR) [75]. CR has been first predicted for excitable dynamical systems [74–77], that is, systems that emit quasiregular pulses as a result of an excitation threshold and with a refractory period. It has been demonstrated experimentally in semiconductor lasers subject to optical feedback and driven into chaotic excitable dynamics [78]. For a recent review see [79]. Theoretical works on different models furthermore reported that not only excitable but also bistable or multistable systems driven by noise can exhibit CR [80, 81], as also confirmed experimentally in bistable chaotic electronic Chua circuits [82]. Recently, CR has been predicted in another class of systems, which exhibit bistability together with time-delay [83]. These systems are interesting considering also that delay is an inherent

property of Nature, with examples found in biology [84] and economics [85].

A VCSEL subject to optical feedback is an example of a bistable time-delayed system and CR has been indeed observed in this system first numerically [68] and then experimentally [86]. The numerical prediction of CR for a VCSEL subject to isotropic OF is shown in Figure 13 [68]. In Figures 13(a)–13(c), we show the polarization resolved time traces of the output power for increased strength of the external noise added to the injection current and in Figures 13(d)–13(h) the corresponding joint residence time distribution (RTD). As can be seen from Figure 13, coherence resonance is indeed present in such a system. A continuous increase of the strength of the external noise results first in an increase of the peak amplitude and a decrease of the width of the joint RTD maximum at the delay time. The peak amplitude reaches a maximum and the peak width reaches a minimum for a given value of the noise (Figures 13(b), 13(e)), where the mode-hopping regime exhibits the most regular periodic behavior at the external cavity (EC) round-trip time. For larger external noise strengths, the RTD exhibits smaller peak amplitude at

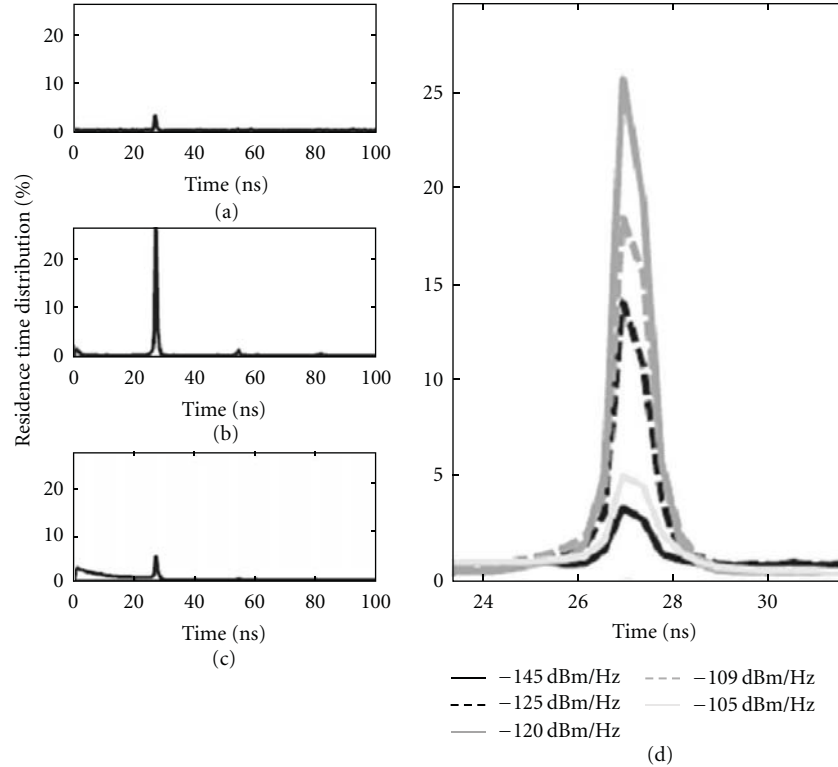


FIGURE 14: (a)–(c) Joint residence time distribution for three increasing noise levels, showing an optimal regularity at the delay time for an optimal noise level (case b). (d) is an enlargement of the JRTD around time values corresponding to the delay time, and for increasing values of noise added to the injection current. After [86]. (Reprinted by permission from *Phys. Rev. Lett.*)

the delay time and broadens towards smaller and larger time values. The mode-hopping time-trace exhibits windows of regular dynamics at the EC round-time but in general the dynamics is dominated by noise.

In order to observe CR experimentally, we have made use of the great possibility for tuning the PS current and hysteresis width by OF from an extremely short external cavity with a length of several  $10\ \mu\text{m}$  [88, 89]. The VCSEL is subject to OF from two external cavities. The first one is formed between the VCSEL output mirror and a fiber facet with enhanced reflectivity of 23% at a close distance (of the order of  $10\ \mu\text{m}$ ), that is, it is an extremely short external cavity used to tune the VCSEL polarization-switching current. The second cavity is the optical fiber itself and introduces a time delay of  $\tau = 27\ \text{ns}$  in the system. To look for a CR, an electrical noise with zero mean value and a flat spectrum until 300 MHz is added to the injection current of the VCSEL. The effect of the noise level on the distribution of the joint residence time (JRTD) is shown in Figure 14. If the noise is weak, the system needs a lot of time to consecutively visit the two stable states and the peak of the JRTD at the external cavity round trip time (27 ns) is very small (d). As the noise strength is increased, the peak at 27 ns dramatically increases reaching its maximum (e). For higher noise intensities, more and more fast PSs occur and the background masks the peak structure (f). The right panel (d) confirms the existence of an optimal noise level of  $-120\ \text{dBm/Hz}$  for which the JRTD exhibits a maximum

peak at the delay time. This constitutes a clear evidence of coherence resonance in our system. Different indicators have complemented our observations. In particular we have observed the radio-frequency (RF) spectrum of the laser output for different noise levels. A peak appears close to the long external cavity frequency and the peak height relative to the RF spectrum noise floor reaches a maximum for a given noise level (similar to the noise level that brings the maximum JRTD value at the delay time).

## 5. Light Polarization Specificities of Chaos Synchronization of Unidirectionally Coupled VCSEL

The growing interest in implementing chaos communication using VCSELs motivates further investigations to better understand the influence of polarization dynamics on the synchronization properties. In this section, we present a theoretical investigation of the effect of polarization mode competition on the synchronization characteristics of two unidirectionally coupled VCSELs [87]. The master VCSEL only is rendered chaotic by optical feedback, and its chaotic output is coupled to the slave VCSEL by use of an isotropic optical injection. We show that, depending on the injection conditions, the synchronization quality can be strongly enhanced when the master laser and therefore also the synchronized slave exhibit two LP mode dynamics.

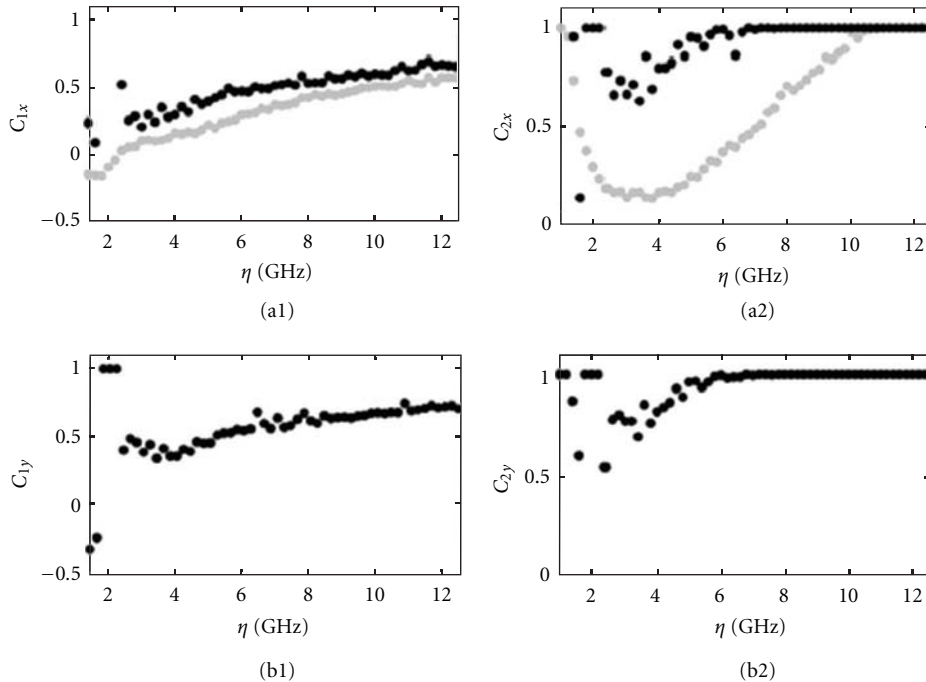


FIGURE 15: Evolution of the correlation coefficients related to isochronous (a1) and (b1) and anticipative (a2) and (b2) synchronization as a function of  $\eta$ . The gray (black) color corresponds to the case of single-mode (two-mode) chaos. After [87]. (Reprinted by permission from *Opt. Lett.*)

In isotropic optical feedback/injection configuration, the two VCSELs can exhibit either an anticipating or isochronous (injection-locking) type of synchronization [90]. Anticipating (perfect) synchronization is achieved when laser intensities for the  $x$ - and  $y$ -polarizations of the master laser as well as its carrier density at time  $t$  are synchronized with the corresponding light intensities and carrier density of the slave laser at time  $t - \tau$ , that is,  $I_{x,y}^m(t) = aI_{x,y}^s(t - \tau)$ . Necessary conditions for the existence of such a solution are that both lasers exhibit the same device parameters, bias currents, zero detuning, and also  $f = \eta$  with  $f$  being the feedback strength and  $\eta$  the coupling (injection) strength. The isochronous synchronization solution is of the type  $I_{x,y}^m(t) = aI_{x,y}^s(t)$ , with  $a$  being a constant. To evaluate the synchronization quality and to discriminate between isochronous and anticipative synchronizations, we use the cross-correlation coefficients for the  $x$ - and  $y$ -LP mode intensities  $C_{1x,y}(t, t)$  and  $C_{2x,y}(t + \tau, t)$ , respectively.

Figure 15 shows the evolution of the isochronous and the anticipative correlation coefficients when the injection rate  $\eta$  is varied but still equal to the feedback rate  $f$ . In Figures 15(a1) and 15(a2), we add gray curves that show the evolution of  $C_{1x}$  and  $C_{2x}$  in the case of single  $x$ -LP mode chaotic dynamics. In the whole range of  $\eta$ ,  $C_2 > C_1$ , whatever the LP modes that are analyzed ( $x$  or  $y$ ) and independently of the single  $x$ -LP mode or two LP mode cases in the laser dynamics (black or gray curves). The lasers therefore exhibit anticipative synchronization. The still large isochronous correlation coefficient  $C_1$  can be related to the presence of a periodicity at  $\tau$  in the intensity time

traces. For  $\eta < 3 \text{ ns}^{-1}$  the lasers exhibit either weakly synchronized irregular dynamics or locked steady states (see the small range of  $\eta$  with perfect synchronization in the two LP mode case). For larger  $\eta$ , the synchronization quality improves with  $\eta$ . Indeed, the lasers exhibit desynchronization bursts, but the average time between them increases as  $\eta$  increases, leading to better synchronization over a given time window. The comparison between the black and gray curves in Figures 15(a1) and 15(a2) unveils, moreover, that the correlation coefficients (and therefore the synchronization quality) improve in the two LP mode cases. Therefore, the synchronization quality between unidirectionally coupled VCSELs can be significantly enhanced when the feedback-induced chaos in the master laser involves both orthogonal LP fundamental transverse modes. Two regions of enhanced synchronization between the injected LP mode and the corresponding slave LP mode are identified in [91]. In the so-called region II, the slave VCSEL exhibits anticorrelated dynamics in its two LP modes while in the so-called region I, the slave VCSEL exhibits dynamics in only one LP mode, which corresponds to the polarization of the injected field. The two regions exhibit different synchronization properties in both the LP mode dynamics and total intensity dynamics.

## 6. Conclusions

In conclusions, we have shown that the nonlinear dynamics of vertical-cavity surface-emitting lasers (VCSELs) induced by optical injection, current modulation optical feedback

and unidirectional coupling are drastically modified due to the underlying polarization and transverse mode competition. This provides new features to the rich nonlinear dynamics such as, for the case of optical injection, the new Hopf bifurcation on a two-polarization-mode solution that delimits the injection locking region and the new resonance tongue of polarization switching and injection locking of first-order transverse mode for large positive detunings. Similarly, the underlying polarization mode competition leads to chaotic-like behavior in case of gain switching and the presence of two transverse modes additionally reduces the possibility of regular dynamics.

Since the polarization selection is very weak, a small amount of optical feedback is enough to significantly modify the VCSEL polarization behavior and observe laser dynamics that significantly differ from those typically observed in edge-emitting lasers. Typical dynamical instabilities such as low-frequency fluctuations and self-pulsations induced by optical feedback still exist in VCSELs but with the additional complexity of the anticorrelated dynamics between polarization modes. The bistable property of VCSEL makes it possible to investigate very fundamental problems of bistable systems with time-delay, such as the coherence resonance phenomenon. We also demonstrated that the synchronization quality between unidirectionally coupled VCSELs can be significantly enhanced when the feedback-induced chaos in the master laser involves both orthogonal LP fundamental transverse modes.

## Acknowledgments

Some of the works presented in this paper have been undertaken with other past and present colleagues and coworkers from other groups, as acknowledged via the relevant journal paper citations. The authors also acknowledge the support of COST MP0702 European Action, Conseil Régional de Lorraine, Fondation Supélec, IAP 6/10—Belgian Science Policy, FWO Flanders, GOA, and OZR of the VUB.

## References

- [1] H. Li and K. Iga, Eds., *Vertical-Cavity Surface-Emitting Laser Devices*, vol. 6 of *Springer Series in Photonics*, Springer, Berlin, Germany, 2002.
- [2] C. J. Chang-Hasnain, J. P. Harbison, G. Hasnain, A. C. Von Lehmen, L. T. Florez, and N. G. Stoffel, "Dynamic, polarization, and transverse mode characteristics of vertical cavity surface emitting lasers," *IEEE Journal of Quantum Electronics*, vol. 27, no. 6, pp. 1402–1409, 1991.
- [3] D. Vakhshoori, J. D. Wynn, G. J. Zydzik et al., "Top-surface emitting lasers with 1.9 v threshold voltage and the effect of spatial hole burning on their transverse mode operation and efficiencies," *Applied Physics Letters*, vol. 62, no. 13, pp. 1448–1450, 1993.
- [4] A. Valle, J. Sarma, and K. A. Shore, "Spatial holeburning effects on the dynamics of vertical cavity surface-emitting laser diodes," *IEEE Journal of Quantum Electronics*, vol. 31, no. 8, pp. 1423–1431, 1995.
- [5] K. D. Choquette, R. P. Schneider, K. L. Lear, and R. E. Leibenguth, "Gain-dependent polarization properties of vertical-cavity lasers," *IEEE Journal on Selected Topics in Quantum Electronics*, vol. 1, no. 2, pp. 661–666, 1995.
- [6] M. San Miguel, Q. Feng, and J. V. Moloney, "Light-polarization dynamics in surface-emitting semiconductor lasers," *Physical Review A*, vol. 52, no. 2, pp. 1728–1739, 1995.
- [7] J. Martin-Regalado, F. Prati, M. San Miguel, and N. B. Abraham, "Polarization properties of vertical-cavity surface-emitting lasers," *IEEE Journal of Quantum Electronics*, vol. 33, no. 5, pp. 765–783, 1997.
- [8] K. Panajotov, B. Ryvkin, J. Danckaert, M. Peeters, H. Thienpont, and I. Veretennicoff, "Polarization switching in VCSELs due to thermal lensing," *IEEE Photonics Technology Letters*, vol. 10, no. 1, pp. 6–8, 1998.
- [9] A. Valle, K. A. Shore, and L. Pesquera, "Polarization selection in birefringent vertical-cavity surface emitting lasers," *Journal of Lightwave Technology*, vol. 14, no. 9, pp. 2062–2068, 1996.
- [10] B. Ryvkin, K. Panajotov, A. Georgievski et al., "Effect of photon-energy-dependent loss and gain mechanisms on polarization switching in vertical-cavity surface-emitting lasers," *Journal of the Optical Society of America B*, vol. 16, no. 11, pp. 2106–2113, 1999.
- [11] J. I. Nishizawa and K. Ishida, "Injection-induced modulation of laser light by the interaction of laser diodes," *IEEE Journal of Quantum Electronics*, vol. 11, no. 7, pp. 515–519, 1975.
- [12] R. Lang, "Injection locking properties of a semiconductor laser," *IEEE Journal of Quantum Electronics*, vol. 18, no. 6, pp. 976–983, 1982.
- [13] K. Iwashita and K. Nakagawa, "Suppression of mode partition by laser diode light injection," *IEEE Journal of Quantum Electronics*, vol. 18, no. 10, pp. 1669–1674, 1982.
- [14] T. B. Simpson, J. M. Liu, and A. Gavrielides, "Bandwidth enhancement and broadband noise reduction in injection-locked semiconductor lasers," *IEEE Photonics Technology Letters*, vol. 7, no. 7, pp. 709–711, 1995.
- [15] L. Goldberg, H. F. Taylor, J. F. Weller, and D. R. Scifres, "Injection locking of coupled-stripe diode laser arrays," *Applied Physics Letters*, vol. 46, no. 3, pp. 236–238, 1985.
- [16] E. K. Lee, H. S. Pang, J. D. Park, and H. Lee, "Bistability and chaos in an injection-locked semiconductor laser," *Physical Review A*, vol. 47, no. 1, pp. 736–739, 1993.
- [17] V. Annovazzi-Lodi, S. Donati, and M. Manna, "Chaos and locking in a semiconductor laser due to external injection," *IEEE Journal of Quantum Electronics*, vol. 30, no. 7, pp. 1537–1541, 1994.
- [18] T. B. Simpson, J. M. Liu, A. Gavrielides, V. Kovanis, and P. M. Alsing, "Period-doubling cascades and chaos in a semiconductor laser with optical injection," *Physical Review A*, vol. 51, no. 5, pp. 4181–4185, 1995.
- [19] P. M. Varangis, A. Gavrielides, T. Erneux, V. Kovanis, and L. F. Lester, "Frequency entrainment in optically injected semiconductor lasers," *Physical Review Letters*, vol. 78, no. 12, pp. 2353–2356, 1997.
- [20] S. Wieczorek, B. Krauskopf, and D. Lenstra, "Multipulse excitability in a semiconductor laser with optical injection," *Physical Review Letters*, vol. 88, no. 6, pp. 063901/1–063901/4, 2002.
- [21] Z. G. Pan, S. Jiang, M. Dagenais et al., "Optical injection induced polarization bistability in vertical-cavity surface-emitting lasers," *Applied Physics Letters*, vol. 63, no. 22, pp. 2999–3001, 1993.
- [22] J. B. Altés, I. Gatare, K. Panajotov, H. Thienpont, and M. Sciamanna, "Mapping of the dynamics induced by orthogonal

- optical injection in vertical-cavity surface-emitting lasers," *IEEE Journal of Quantum Electronics*, vol. 42, no. 2, pp. 198–207, 2006.
- [23] Y. Hong, P. S. Spencer, P. Rees, and K. Alan Shore, "Optical injection dynamics of two-mode vertical cavity surface-emitting semiconductor lasers," *IEEE Journal of Quantum Electronics*, vol. 38, no. 3, pp. 274–278, 2002.
- [24] H. Li, T. L. Lucas, J. G. McInerney, M. W. Wright, and R. A. Morgan, "Injection locking dynamics of vertical cavity semiconductor lasers under conventional and phase conjugate injection," *IEEE Journal of Quantum Electronics*, vol. 32, no. 2, pp. 227–235, 1996.
- [25] J. Y. Law, G. H. M. Van Tartwijk, and G. P. Agrawal, "Effects of transverse-mode competition on the injection dynamics of vertical-cavity surface-emitting lasers," *Journal of Optics B*, vol. 9, no. 5, pp. 737–747, 1997.
- [26] S. Bandyopadhyay, Y. Hong, P. S. Spencer, and K. A. Shore, "Experimental observation of anti-phase polarisation dynamics in VCSELS," *Optics Communications*, vol. 202, no. 1–3, pp. 145–154, 2002.
- [27] Y. Hong, P. Spencer, S. Bandyopadhyay, P. Rees, and K. A. Shore, "Polarization resolved chaos and instabilities in a VCSEL subject to optical injection," *Optics Communications*, vol. 216, pp. 185–187, 2003.
- [28] C. H. Lee, T. H. Yoon, and S. Y. Shin, "Period doubling and chaos in a directly modulated laser diode," *Applied Physics Letters*, vol. 46, no. 1, pp. 95–97, 1985.
- [29] Y. C. Chen, H. G. Winful, and J. M. Liu, "Subharmonic bifurcations and irregular pulsing behavior of modulated semiconductor lasers," *Applied Physics Letters*, vol. 47, no. 3, pp. 208–210, 1985.
- [30] H. F. Liu and W. F. Ngai, "Nonlinear dynamics of a directly modulated 1.55  $\mu\text{m}$  InGaAsP distributed feedback semiconductor laser," *IEEE Journal of Quantum Electronics*, vol. 29, no. 6, pp. 1668–1675, 1993.
- [31] Y. Matsui, S. Kutsuzawa, S. Arahira, Y. Ogawa, and A. Suzuki, "Bifurcation in 20-GHz gain-switched 1.55- $\mu\text{m}$  MQW lasers and its control by CW injection seeding," *IEEE Journal of Quantum Electronics*, vol. 34, no. 7, pp. 1213–1222, 1998.
- [32] C. Mayol, R. Toral, C. R. Mirasso, S. I. Turovets, and L. Pesquera, "Theory of main resonances in directly modulated diode lasers," *IEEE Journal of Quantum Electronics*, vol. 38, no. 3, pp. 260–269, 2002.
- [33] S. F. Yu, "Nonlinear dynamics of vertical-cavity surface-emitting lasers," *IEEE Journal of Quantum Electronics*, vol. 35, no. 3, pp. 332–340, 1999.
- [34] A. Valle, L. Pesquera, S. I. Turovets, and J. M. López, "Nonlinear dynamics of current-modulated vertical-cavity surface-emitting lasers," *Optics Communications*, vol. 208, no. 1–3, pp. 173–182, 2002.
- [35] J. Y. Law and G. P. Agrawal, "Nonlinear spatio-temporal dynamics due to transverse-mode competition in gain-switched microcavity semiconductor lasers," *Optics Communications*, vol. 138, no. 1–3, pp. 95–98, 1997.
- [36] M. Sciamanna, A. Valle, P. Mégret, M. Blondel, and K. Panajotov, "Nonlinear polarization dynamics in directly modulated vertical-cavity surface-emitting lasers," *Physical Review E*, vol. 68, no. 1, Article ID 016207, 4 pages, 2003.
- [37] A. Valle, M. Sciamanna, and K. Panajotov, "Irregular pulsating polarization dynamics in gain-switched vertical-cavity surface-emitting lasers," *IEEE Journal of Quantum Electronics*, vol. 44, no. 2, pp. 136–143, 2008.
- [38] A. Valle, M. Sciamanna, and K. Panajotov, "Nonlinear dynamics of the polarization of multitransverse mode vertical-cavity surface-emitting lasers under current modulation," *Physical Review E*, vol. 76, no. 4, Article ID 046206, 2007.
- [39] A. Valle, M. Arizaleta, H. Thienpont, K. Panajotov, and M. Sciamanna, "Transverse mode competition effects on the dynamics of gain-switched vertical-cavity surface-emitting lasers," *Applied Physics Letters*, vol. 93, no. 13, Article ID 131103, 2008.
- [40] J. Mork, B. Tromborg, and J. Mark, "Chaos in semiconductor lasers with optical feedback: theory and experiment," *IEEE Journal of Quantum Electronics*, vol. 28, no. 1, pp. 93–108, 1992.
- [41] C. Risch and C. Voumard, "Self-pulsation in the output intensity and spectrum of GaAs-AlGaAs cw diode lasers coupled to a frequency-selective external optical cavity," *Journal of Applied Physics*, vol. 48, no. 5, pp. 2083–2085, 1977.
- [42] D. Lenstra, B. H. Verbeek, and A. J. den Boef, "Coherence collapse in single-mode semiconductor lasers due to optical feedback," *IEEE Journal of Quantum Electronics*, vol. 21, no. 6, pp. 674–679, 1984.
- [43] R. W. Tkach and A. R. Chraplyvy, "Regimes of feedback effects in 1.5- $\mu\text{m}$  distributed feedback lasers," *Journal of Lightwave Technology*, vol. 4, no. 11, pp. 1655–1661, 1986.
- [44] C. Masoller and N. B. Abraham, "Low-frequency fluctuations in vertical-cavity surface-emitting semiconductor lasers with optical feedback," *Physical Review A*, vol. 59, no. 4, pp. 3021–3031, 1999.
- [45] M. Sciamanna, C. Masoller, F. Rogister, P. Mégret, N. B. Abraham, and M. Blondel, "Fast pulsing dynamics of a vertical-cavity surface-emitting laser operating in the low-frequency fluctuation regime," *Physical Review A*, vol. 68, no. 1, Article ID 015805, 4 pages, 2003.
- [46] M. Giudici, S. Balle, T. Ackemann, S. Barland, and J. R. Tredicce, "Polarization dynamics in vertical-cavity surface-emitting lasers with optical feedback: experiment and model," *Journal of the Optical Society of America B*, vol. 16, no. 11, pp. 2114–2123, 1999.
- [47] M. Sondermann, H. Bohnet, and T. Ackemann, "Low-frequency fluctuations and polarization dynamics in vertical-cavity surface-emitting lasers with isotropic feedback," *Physical Review A*, vol. 67, no. 2, Article ID 021802(R), 4 pages, 2003.
- [48] J. Dellunde, A. Valle, L. Pesquera, and K. A. Shore, "Transverse-mode selection and noise properties of external-cavity vertical-cavity surface-emitting lasers including multiple-reflection effects," *Journal of the Optical Society of America B*, vol. 16, no. 11, pp. 2131–2139, 1999.
- [49] F. Marino, S. Barland, and S. Balle, "Single-mode operation and transverse-mode control in VCSELS induced by frequency-selective feedback," *IEEE Photonics Technology Letters*, vol. 15, no. 6, pp. 789–791, 2003.
- [50] L. M. Pecora and T. L. Carroll, "Synchronization in chaotic systems," *Physical Review Letters*, vol. 64, no. 8, pp. 821–824, 1990.
- [51] C. R. Mirasso, P. Colet, and P. García-Fernández, "Synchronization of chaotic semiconductor lasers: application to encoded communications," *IEEE Photonics Technology Letters*, vol. 8, no. 2, pp. 299–301, 1996.
- [52] R. Ju, P. S. Spencer, and K. A. Shore, "Polarization-preserved and polarization-rotated synchronization of chaotic vertical-cavity surface-emitting lasers," *IEEE Journal of Quantum Electronics*, vol. 41, no. 12, pp. 1461–1467, 2005.

- [53] M. S. Torre, C. Masoller, and K. A. Shore, "Synchronization of unidirectionally coupled multi-transverse-mode vertical-cavity surface-emitting lasers," *Journal of the Optical Society of America B*, vol. 21, no. 10, pp. 1772–1780, 2004.
- [54] Y. Hong, M. W. Lee, P. S. Spencer, and K. A. Shore, "Synchronization of chaos in unidirectionally coupled vertical-cavity surface-emitting semiconductor lasers," *Optics Letters*, vol. 29, no. 11, pp. 1215–1217, 2004.
- [55] I. Gatare, M. Sciamanna, J. Buesa, H. Thienpont, and K. Panajotov, "Nonlinear dynamics accompanying polarization switching in vertical-cavity surface-emitting lasers with orthogonal optical injection," *Applied Physics Letters*, vol. 88, no. 10, Article ID 101106, 2006.
- [56] A. Valle, I. Gatare, K. Panajotov, and M. Sciamanna, "Transverse mode switching and locking in vertical-cavity surface-emitting lasers subject to orthogonal optical injection," *IEEE Journal of Quantum Electronics*, vol. 43, no. 4, pp. 322–333, 2007.
- [57] I. Gatare, M. Sciamanna, M. Nizette, and K. Panajotov, "Bifurcation to polarization switching and locking in vertical-cavity surface-emitting lasers with optical injection," *Physical Review A*, vol. 76, no. 3, Article ID 031803, 2007.
- [58] M. Sciamanna and K. Panajotov, "Two-mode injection locking in vertical-cavity surface-emitting lasers," *Optics Letters*, vol. 30, no. 21, pp. 2903–2905, 2005.
- [59] M. Sciamanna and K. Panajotov, "Route to polarization switching induced by optical injection in vertical-cavity surface-emitting lasers," *Physical Review A*, vol. 73, no. 2, Article ID 023811, 17 pages, 2006.
- [60] S. Wiczorek, B. Krauskopf, T. B. Simpson, and D. Lenstra, "The dynamical complexity of optically injected semiconductor lasers," *Physics Reports*, vol. 416, no. 1–2, pp. 1–128, 2005.
- [61] M. Sciamanna, K. Panajotov, H. Thienpont, I. Veretennicoff, P. Mégret, and M. Blondel, "Optical feedback induces polarization mode hopping in vertical-cavity surface-emitting lasers," *Optics Letters*, vol. 28, no. 17, pp. 1543–1545, 2003.
- [62] K. Panajotov, M. Arizaleta, V. Gomez et al., "Semiconductor lasers for quantum sensing," in *Quantum Sensing and Nanophotonic Devices*, Proceedings of SPIE, pp. 360–375, January 2004.
- [63] P. Besnard, M. Chares, G. Stephan, and F. Robert, "Switching between polarization modes of a vertical-cavity surface-emitting laser by isotropic optical feedback," *Journal of the Optical Society of America B*, vol. 16, pp. 1059–1063, 1999.
- [64] G. Giacomelli, F. Marin, and I. Rabbiosi, "Stochastic and bona fide resonance: an experimental investigation," *Physical Review Letters*, vol. 82, no. 4, pp. 675–678, 1999.
- [65] M. B. Willemsen, M. U. F. Khalid, M. P. Van Exter, and J. P. Woerdman, "Polarization switching of a vertical-cavity semiconductor laser as a Kramers hopping problem," *Physical Review Letters*, vol. 82, no. 24, pp. 4815–4818, 1999.
- [66] B. Nagler, M. Peeters, J. Albert et al., "Polarization-mode hopping in single-mode vertical-cavity surface-emitting lasers: theory and experiment," *Physical Review A*, vol. 68, no. 1, Article ID 013813, 8 pages, 2003.
- [67] C. Masoller, "Distribution of residence times of time-delayed bistable systems driven by noise," *Physical Review Letters*, vol. 90, no. 2, Article ID 020601, 4 pages, 2003.
- [68] K. Panajotov, M. Sciamanna, A. Tabaka et al., "Residence time distribution and coherence resonance of optical-feedback-induced polarization mode hopping in vertical-cavity surface-emitting lasers," *Physical Review A*, vol. 69, no. 1, Article ID 011801(R), 4 pages, 2004.
- [69] R. Benzi, A. Sutera, and A. Vulpiani, "The mechanism of stochastic resonance," *Journal of Physics A*, vol. 14, no. 11, pp. L453–L457, 1981.
- [70] J. K. Douglass, L. Wilkens, E. Pantazelou, and F. Moss, "Noise enhancement of information transfer in crayfish mechanoreceptors by stochastic resonance," *Nature*, vol. 365, no. 6444, pp. 337–340, 1993.
- [71] B. McNamara, K. Wiesenfeld, and R. Roy, "Observation of stochastic resonance in a ring laser," *Physical Review Letters*, vol. 60, no. 25, pp. 2626–2629, 1988.
- [72] W. Hohmann, J. Müller, and F. W. Schneider, "Stochastic resonance in chemistry. 3. The minimal-bromate reaction," *Journal of Physical Chemistry*, vol. 100, no. 13, pp. 5388–5392, 1996.
- [73] L. Gammaitoni, P. Hänggi, P. Jung, and F. Marchesoni, "Stochastic resonance," *Reviews of Modern Physics*, vol. 70, no. 1, pp. 223–287, 1998.
- [74] H. Gang, T. Ditinger, C. Z. Ning, and H. Haken, "Stochastic resonance without external periodic force," *Physical Review Letters*, vol. 71, no. 6, pp. 807–810, 1993.
- [75] A. S. Pikovsky and J. Kurths, "Coherence resonance in a noise-driven excitable system," *Physical Review Letters*, vol. 78, no. 5, pp. 775–778, 1997.
- [76] A. Neiman, P. I. Saporin, and L. Stone, "Coherence resonance at noisy precursors of bifurcations in nonlinear dynamical systems," *Physical Review E*, vol. 56, no. 1, pp. 270–273, 1997.
- [77] S. Fauve and F. Heslot, "Stochastic resonance in a bistable system," *Physics Letters A*, vol. 97, no. 1–2, pp. 5–7, 1983.
- [78] G. Giacomelli, M. Giudici, S. Balle, and J. R. Tredicce, "Experimental evidence of coherence resonance in an optical system," *Physical Review Letters*, vol. 84, no. 15, pp. 3298–3301, 2000.
- [79] B. Lindner, J. García-Ojalvo, A. Neiman, and L. Schimansky-Geier, "Effects of noise in excitable systems," *Physics Reports*, vol. 392, no. 6, pp. 321–424, 2004.
- [80] B. Lindner and L. Schimansky-Geier, "Coherence and stochastic resonance in a two-state system," *Physical Review E*, vol. 61, no. 6 B, pp. 6103–6110, 2000.
- [81] C. Masoller, "Noise-induced resonance in delayed feedback systems," *Physical Review Letters*, vol. 88, no. 3, Article ID 034102, 4 pages, 2002.
- [82] C. Palenzuela, R. Toral, C. R. Mirasso, O. Calvo, and J. D. Gunton, "Coherence resonance in chaotic systems," *Europhysics Letters*, vol. 56, no. 3, pp. 347–353, 2001.
- [83] L. S. Tsimring and A. Pikovsky, "Noise-induced dynamics in bistable systems with delay," *Physical Review Letters*, vol. 87, no. 25, Article ID 250602, 4 pages, 2001.
- [84] L. Nunney, "The effect of long time delays in predator-prey systems," *Theoretical Population Biology*, vol. 27, no. 2, pp. 202–221, 1985.
- [85] M. C. Mackey, "Commodity price fluctuations: price dependent delays and nonlinearities as explanatory factors," *Journal of Economic Theory*, vol. 48, no. 2, pp. 497–509, 1989.
- [86] M. Arizaleta Arteaga, M. Valencia, M. Sciamanna, H. Thienpont, M. López-Amo, and K. Panajotov, "Experimental evidence of coherence resonance in a time-delayed bistable system," *Physical Review Letters*, vol. 99, no. 2, Article ID 023903, 4 pages, 2007.
- [87] I. Gatare, M. Sciamanna, A. Locquet, and K. Panajotov, "Influence of polarization mode competition on the synchronization of two unidirectionally coupled vertical-cavity surface-emitting lasers," *Optics Letters*, vol. 32, no. 12, pp. 1629–1631, 2007.
- [88] M. A. Arteaga, H. J. Unold, J. M. Ostermann, R. Michalzik, H. Theinpont, and K. Panajotov, "Investigation of polarization

- properties of VCSELs subject to optical feedback from an extremely short external cavity—part I: theoretical analysis,” *IEEE Journal of Quantum Electronics*, vol. 42, no. 2, pp. 89–101, 2006.
- [89] M. A. Arteaga, M. López-Amo, H. Thienpont, and K. Panajotov, “Role of external cavity reflectivity for achieving polarization control and stabilization of vertical cavity surface emitting laser,” *Applied Physics Letters*, vol. 90, no. 3, Article ID 031117, 3 pages, 2007.
- [90] A. Locquet, F. Rogister, M. Sciamanna, P. Mégret, and M. Blondel, “Two types of synchronization in unidirectionally coupled chaotic external-cavity semiconductor lasers,” *Physical Review E*, vol. 64, no. 4, Article ID 045203(R), 4 pages, 2001.
- [91] M. Sciamanna, I. Gatare, A. Locquet, and K. Panajotov, “Polarization synchronization in unidirectionally coupled vertical-cavity surface-emitting lasers with orthogonal optical injection,” *Physical Review E*, vol. 75, no. 5, Article ID 056213, 10 pages, 2007.

## Review Article

# Progress on High-Speed 980 nm VCSELs for Short-Reach Optical Interconnects

**Alex Mutig and Dieter Bimberg**

*Institut für Festkörperphysik and Zentrum für Nanophotonik, Technische Universität Berlin, Hardenbergstraße 36, 10623 Berlin, Germany*

Correspondence should be addressed to Alex Mutig, alex.mutig@berkeley.edu

Received 29 March 2011; Accepted 8 June 2011

Academic Editor: Krassimir Panajotov

Copyright © 2011 A. Mutig and D. Bimberg. This is an open access article distributed under the Creative Commons Attribution License, which permits unrestricted use, distribution, and reproduction in any medium, provided the original work is properly cited.

Progress of high-speed vertical cavity surface emitting lasers (VCSEL) operating around 980 nm is reviewed. A special focus is on their applications for future short-reach optical interconnects, for example, in high-performance computers (HPC). The wavelength of 980 nm has fundamental advantages for these applications and plays a significant role in VCSEL research today. The present data rates of 980 nm VCSELs exceed 40 Gbit/s, and excellent temperature stability has been reported. The major concepts leading to these impressive developments are presented.

## 1. Introduction

The perpetually increasing demand of our modern society for ever faster access to ever larger amounts of information requires a corresponding permanent increase of the computational power of data centres and high-performance computers (HPC) for rapid and efficient data processing and routing. The motor of the progress in HPC performance is the downscaling of Si-based integrated circuit (IC) technology, as predicted by Moore's Law. While currently the fabrication process of complementary metal-oxide-semiconductor (CMOS) ICs is based on the 32 nm technology node, future generations of CMOS chips based on 22, 15, 11, and 8 nm technology nodes are expected to appear just within a decade from now [1]. The ever increasing computational power of central processing units (CPU) and storage capability of memory elements logically and unavoidable requires a corresponding strong increase of the performance of data transmission lines connecting chips with each other. Traditional copper-based interconnects quickly run into their physical limitations as signal frequencies approach 10 GHz, which are among other high losses, large signal attenuation, large power dissipation, signal distortion, electromagnetic interference (EMI), and crosstalk [2–6]. The ultimate solution is brought by optical

interconnects [7–11], which are consistently replacing wire-based electrical links for rack-to-rack, box-to-box, and board-to-board communication and penetrating to even shorter transmission distances. It is expected that just within a decade from now optical links will reach module and chip levels [7].

The success of the optical technologies in the HPC applications originates from the decisive advantages of vertical cavity surface emitting lasers (VCSEL) [12–15] as a high-quality laser light source for short-reach optical interconnects with a large number of channels. The most important and beneficial VCSEL properties are: low-threshold and operating currents; high-efficiency and low-power consumption; a near-circular output beam enabling easy coupling into optical fibers, high-temperature stability, high reliability and easy packaging, straightforward fabrication of dense arrays, and planar fabrication technology with on-wafer characterization, enabling inexpensive production and testing of thousands of devices on a single wafer, resulting in a price of only several cents per laser. The availability of VCSELs enabled penetration of optical links first to the local area network (LAN) level and afterwards down to the intra-rack level in modern HPC applications [16, 17]. Today tens of thousands of optical interconnects based on oxide-confined

VCSELs [18, 19] and multimode fibers are routinely installed practically into each HPC system [20, 21].

Driven by the market demand for more bandwidth, many academic institutions and industrial companies focused their research on high-speed VCSELs, resulting in the demonstration of devices capable of error-free data transmission at bit rates of up to 40 Gbit/s at room temperature at the commercially important wavelength of 850 nm [22–40], which is the standard wavelength for LAN applications. However, as optical links penetrate to even shorter distances down to the board, module, and chip levels and the number of channels drastically increases, additional crucial requirements for laser light sources arise. Since temperatures inside computer racks can be as high as 85°C and even larger, high temperature stability of VCSELs becomes very important. Ability to operate in a wide temperature range, preferably without adjustment of the operating parameters to the temperature changes in order to reduce costs for the driver electronics, is vital for module-to-module and chip-to-chip optical interconnects. Additionally, the limited space and power budget in HPC systems requires fabrication of VCSELs with very high packaging densities and low power consumption. Already now up to one million VCSELs are encapsulated just in one supercomputer, and in the future Petaflop and Exaflop systems the number of optical links will reach hundreds of millions per machine [21]. Consequently, high bit rate, high-temperature stability, high packaging density and low power consumption are the major ultimate requirements for laser light sources of future optical links in HPC applications.

Appearance of these new challenges motivated the research and development of high-speed GaAs-based VCSELs emitting at longer wavelengths, as compared to the standard wavelength of 850 nm. In particular, devices operating between 980 nm and 1300 nm have been investigated with great success by different universities and industrial companies [41–82], whereby most impressive high-speed results were achieved in the wavelength range from 980 to 1100 nm [41–71]. Longer wavelengths provide decisive advantages to fulfil the described requirements for future short-reach optical interconnects in HPC systems as compared to 850 nm. The main advantage is the transparency of the GaAs material at, for example, 980 or 1100 nm. A transparent substrate facilitates a straightforward fabrication of bottom-emitting lasers, drastically increasing the packaging density. Incorporation of binary GaAs layers into distributed Bragg reflectors (DBR) significantly increases both thermal and electrical conductivity of the device, leading to lower internal temperatures and increasing high temperature stability. The increased potential modulation depth of the quantum wells (QW) additionally increases the temperature stability of the VCSELs, and the smaller bandgap of the active layers results in lower threshold and operating voltages, leading to lower power consumption. The higher In-content in the InGaAs QWs emitting at, for example, 980 nm leads to a larger compressive strain as compared to QWs emitting at 850 nm for a given QW thickness, increasing differential gain, the relaxation resonance frequency, and ultimately the VCSEL's bandwidth [83].

Analyzing all the described advantages, it appears logically that longer wavelengths, for example, 980 or 1100 nm, are the natural choice for GaAs-based VCSELs targeting future high-speed high-density applications in HPCs. They naturally provide higher speed, higher temperature stability, higher packaging density, and lower power consumption as compared to the standard wavelength of 850 nm. Indeed the first VCSELs operating at the bit rate of 40 Gbit/s at room temperature and at 25 Gbit/s at elevated temperatures were demonstrated at the wavelength of 1100 nm [41–44]. However, the wavelength of 980 nm has several physical advantages as compared to 1100 nm, among other lower free carrier absorption and more relaxed constraints regarding the growth of highly strained QWs, since the critical thickness of these layers is larger for the wavelength of 980 nm and major positive effects of the compressive strain are expected to appear already at moderate In compositions [38]. The wavelength of 980 nm is also preferable for optical links based on polymer waveguides, since their absorption and dispersion coefficients are wavelength dependent [7]. Because of these advantages, the fastest VCSELs at the moment both at room and elevated temperatures operate at 980 nm at bit rates as high as 44 Gbit/s at 25°C and 38 Gbit/s at 85°C [62, 63].

Considering the importance of the market demand for high-quality laser light sources for future high-speed high-density optical interconnects in HPC applications, as well as in view of record results with VCSELs emitting at 980 nm, we will review here the progress achieved over the last years in this field. Hereby we will mostly concentrate on the development of high-speed 980 nm VCSELs operating in a wide temperature range from room temperature up to elevated temperatures of 85°C and larger.

## 2. Laser Bandwidth and High-Temperature Stability

Semiconductor laser dynamics is commonly described in terms of the rate equation theory [83, 84], which is a relatively uncomplicated and at the same time powerful approach enabling both qualitative and quantitative analysis of high-speed laser properties. The laser performance for high-speed data transmission is determined by its small signal modulation response, which can be divided into two parts. The first part describes intrinsic properties of the laser structure and is given by the following equation:

$$H(f) = \frac{f_R^2}{f_R^2 - f^2 + j \cdot f \cdot (\gamma/2\pi)}, \quad (1)$$

where  $f_R$  represents the relaxation resonance frequency,  $\gamma$  stays for the damping factor,  $f$  is the frequency, and  $j$  is imaginary unit. Multiplied by the corresponding low-pass response, which represents electrical parasitic elements inside of the device, for example, parasitic resistances and capacitances associated with different parts of the laser structure like electrical contacts, oxide aperture and so forth, it gives the complete small signal modulation response of the semiconductor laser. Electrical parasitics are characterized by

the form of the low-pass function as well as by the electrical parasitics cut-off frequency  $f_p$ , at which the high-frequency electrical signal reaching the laser-active region decreases by 3 dB. It has been theoretically and experimentally demonstrated that the index-guided multimode VCSELs with highly overlapped transverse fields (e.g., oxide-confined VCSELs) exhibit a single relaxation resonance frequency [85, 86] similar to the single-mode devices, thus the single-mode rate equation theory presented here can be applied.

To achieve high bandwidth, a VCSEL should rapidly reach large relaxation resonance frequency, which increases with injected current, as determined by the following equation:

$$f_R = D \cdot \sqrt{I - I_{th}}, \quad (2)$$

where  $D$  is the so-called  $D$ -factor,  $I$  is the driving current, and  $I_{th}$  is the threshold current of the VCSEL. Therefore, it is important to realize structures with a high  $D$ -factor, which is determined by the physical and geometrical properties of the active region and of the cavity

$$D = \sqrt{\frac{v_g \cdot (\partial g / \partial N)}{4\pi^2 \cdot q \cdot V_p}} \eta_i, \quad (3)$$

where  $v_g$  is the group velocity of light,  $\partial g / \partial N$  is the differential gain,  $q$  is the elementary charge,  $V_p$  is the effective mode volume, and  $\eta_i$  is the current injection efficiency, which is the fraction of the terminal current that generates carriers in the active region.

In addition to high relaxation resonance frequencies, also low damping factors  $\gamma$  are decisive to achieve high bandwidth. The damping factor increases with increase of the relaxation resonance frequency, as described by the following equation:

$$\gamma = K \cdot f_R^2 + \gamma_0, \quad (4)$$

where  $K$  is the so-called  $K$ -factor and  $\gamma_0$  is the damping factor offset, whereby the damping factor offset  $\gamma_0$  normally plays a role only at small currents near the threshold. Thus to decrease the damping, it is very important to have a small  $K$ -factor, which is again determined by the physical and geometrical properties of the active region and cavity

$$K = 4\pi^2 \tau_p \left( 1 + \frac{\Gamma \cdot (-\partial g / \partial N_p)}{\partial g / \partial N} \right), \quad (5)$$

where  $\tau_p$  is the photon lifetime inside the cavity,  $\Gamma$  is the optical confinement factor, and  $\partial g / \partial N_p$  is a derivative of the gain with respect to the photon density, which depends on the empirical gain compression factor  $\epsilon$ .

The small signal modulation response and thus the high-speed physical properties of a VCSEL are determined by three parameters: the relaxation resonance frequency  $f_R$ , the damping factor  $\gamma$ , and the parasitic cut-off frequency  $f_p$ . Accordingly, there are three physical limitations controlling high-speed performance of a semiconductor laser: thermal, damping, and parasitic limits.

The thermal limitation arises from the fact that according to (2) the relaxation resonance frequency increases with current, but because of internal heating at high injection levels, it saturates at some maximum value  $f_{R,max}$  correspondingly leading to a saturation of the bandwidth  $f_{3\text{dB}}$ . Thus in the absence of negative effects of the damping and electrical parasitic, the maximum achievable bandwidth  $f_{3\text{dB},thermal}$  is given by:

$$f_{3\text{dB},thermal} = \sqrt{1 + \sqrt{2}} f_{R,max}. \quad (6)$$

Limitation by electrical parasitics comes mainly from the parasitic resistances and capacitances inside of the device. If a VCSEL would be limited only by electrical parasitic elements, its maximal achievable bandwidth  $f_{3\text{dB},parasitics}$  would be

$$f_{3\text{dB},parasitics} = (2 + \sqrt{3}) f_p. \quad (7)$$

Finally, the maximum achievable bandwidth in the case of the limitation only by the damping  $f_{3\text{dB},damping}$  would be determined by the  $K$ -factor:

$$f_{3\text{dB},damping} = \frac{2\sqrt{2}\pi}{K}. \quad (8)$$

In a common case, the bandwidth of a VCSEL is limited not only by one type of limitations but by two or even all the three limits: thermal effects, damping and electrical parasitics. The main task for achieving high speed is, therefore, a carefully optimization of different laser parameters, both in the epitaxial structure as well as in the device design, and an effective combination of many improvement concepts as well as identification of proper compromises between different competing processes. In addition, for future market applications, applied concepts are restricted to those, which would not have a significant negative impact onto the laser reliability and costs.

Equations (1)–(8) from the rate equation theory can be applied to analyze physical limitations of the fabricated devices and to identify and develop concepts for improving high-speed laser performance. Therefore, small signal modulation curves of the lasers are measured at different current levels and temperatures in a relatively straightforward experiment using calibrated network analyzer and photodetector. Thereafter, the theoretical function (1), multiplied by the appropriate low-pass curve of the electrical parasitics, can be fitted to experimental results, giving the relaxation resonance frequency  $f_R$ , the damping factor  $\gamma$ , and the parasitic cut-off frequency  $f_p$  for every measured small signal modulation response curve. However, to complete the fitting procedure, an assumption about the form of the low pass of electrical parasitics should be made. Therefore, a more accurate and precise way to extract the laser parameters is additionally to measure the electrical scattering parameters  $S_{11}$  in the same experiment and to extract the low-pass curve of electrical parasitics by fitting parameters of the equivalent circuit of the laser to the measurement results. The appropriate equivalent circuit of a VCSEL commonly reflects the basic parasitic resistances and capacitances in the device, including

resistances of the active region  $R_a$  and of the top and of the bottom DBR mirrors  $R_{mt}$  and  $R_{mb}$ , respectively, as well as the active region capacitance  $C_j$ , the capacitance of the oxide aperture and the underlying intrinsic region  $C_o$ , and the parasitic capacitance of the contact pads  $C_p$ , as demonstrated in Figure 1(a), where a typical structure of oxide-confined VCSELs together with the electrical parasitic elements is shown.

The equivalent circuit shown in Figure 1(a) can be simplified using common rules. Since the two capacitances  $C_o$  and  $C_j$  are connected in parallel, they can be combined to one capacitance  $C_a$ . Also both mirror resistances  $R_{mt}$  and  $R_{mb}$  together with eventually considerable contact resistances (not shown in the figure) can be represented by one common resistance  $R_m$ . These simplifications lead to the equivalent circuit demonstrated in Figure 1(b), which now has only four fitting parameters: both resistances and capacitances. For the case of, for example, wire bonding, also parasitic inductances could be included into the model.  $Z_0$  represents hereby the driver impedance and is usually 50 Ohm. Equivalent circuits identical or similar to the model demonstrated in the Figure 1(b) are commonly used to extract values of electrical parasitic element in VCSELs at different wavelengths, for example, 850 nm [24, 37], 980 nm [47, 53], and 1100 nm [41], leading to accurate analysis of the high-speed laser performance and its limiting factors.

By fitting the parameters of the laser equivalent circuit to the measured  $S_{11}$  curves, the low-pass curve of electrical parasitics can be calculated and used for the fitting of the small signal modulation response of the VCSELs together with (1). Following this procedure, limiting factors of the high-speed laser performance can be identified and physical processes in the VCSEL as well as their interactions can be properly understood.

Although the development of high-speed VCSELs operating at a defined ambient temperature is a very complicated and nontrivial task, realization of VCSELs capable of high-speed data transmission in a wide temperature range adds a new dimension of the complexity to the high-bandwidth problem. It arises from the fact that practically all physical quantities are more or less temperature dependent. This could be expressed by adding temperature dependence to all parameters in the basic equations (1)–(5). While some physical quantities, for example, effective mode volume  $V_P$  or optical confinement factor  $\Gamma$ , are less temperature sensitive, the majority of the important device parameters, for example, threshold current  $I_{th}$ , differential gain  $\partial g/\partial N$ , relaxation resonance frequency  $f_R$ , and many other are strongly temperature dependent, greatly increasing the complexity of the problem of maintaining a proper high-speed performance over a wide temperature range.

To achieve stable performance in a wide ambient temperature range, both the temperature dependence of the physical parameters, for example, differential gain, threshold current, damping, and so forth, as well as the temperature increase inside the device should be minimized. The complexity of the first task is the limited set of available semiconductor materials with defined physical properties and their dependence on temperature. Nevertheless, by applying novel concepts, for

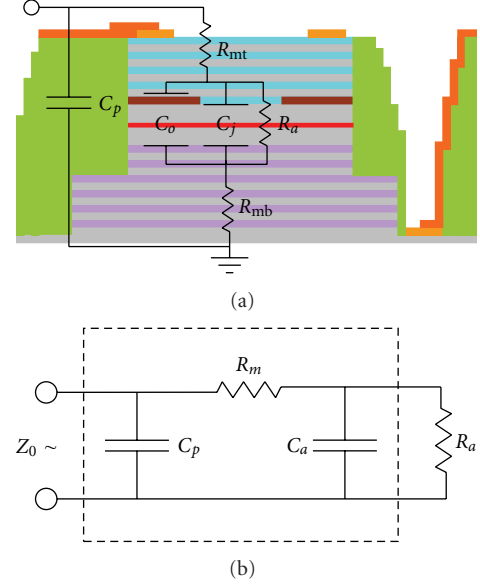


FIGURE 1: Electrical parasitic capacitances and resistances in VCSEL (a) and the corresponding equivalent circuit with two parallel capacitances  $C_o$  and  $C_j$  combined together to  $C_a$  and resistances of the both mirrors  $R_{mt}$  and  $R_{mb}$  joined to  $R_m$  (b).

example, for the growth of the active region, for example, submonolayer (SML) growth [50–53], temperature stability of the VCSELs can be significantly increased. Additionally, VCSELs have a very elegant and effective natural mechanism to increase the high temperature stability, which is the variable detuning between the wavelength of the laser cavity resonance and the gain peak wavelength, whereby both wavelengths are defined by the laser design. Because the gain peak wavelength shifts faster with the temperature than the cavity resonance wavelength, the decrease of the gain and of the differential gain as well as the increase of internal cavity losses at higher temperatures can be compensated or even overcompensated by applying a proper detuning.

The second task, which is the reduction of the temperature variations inside of the VCSEL, can be divided into two aspects, since internal device temperature changes are caused by two phenomena: internal heating and ambient temperature changes. The problem of the internal heating is generally solved by the reduction of the heat generated inside the device at different heat sources, for example, electrical resistances, optical absorbing layers, and so forth, and by the increase of the thermal conductivity of the laser, for example, by replacing ternary materials with binary alloys, which have a much better thermal conductivity, helping to dissipate the internally generated heat. Since the changes of the ambient temperature are defined by the application, the problem of the external temperature changes has no solutions on the device development level in this sense, so that the ambient operation temperature range should be considered as a given specification, which should be fulfilled.

In spite of the above-described constraints and the complexity of the task to achieve high-speed VCSEL operation

in a wide temperature range, impressive results have been achieved in this field with GaAs-based VCSELs emitting at different wavelengths. Following the motivation in the introduction, in the next sections we will review the progress of the VCSELs operating near the wavelength of 980 nm at bit rates from 20 Gbit/s up to 40 Gbit/s and even beyond.

### 3. High-Speed Operation up to 25 Gb/s at Elevated Temperatures

In the middle 2000s, IBM started the program “Terabus” [56], which targeted development of short-reach onboard optical interconnects for future HPC applications in collaboration with Agilent, which participated also in the program “MAUI: Multiwavelength Assemblies for Ubiquitous Interconnects” [55] with similar goals. In both programs, VCSELs emitting at longer wavelengths, in particular, near the wavelength of 980 nm, served as laser light sources because of their advantages described in the previous sections. The activity of such large companies in the field of high-speed 980-nm VCSELs promptly attracted many researchers worldwide to join this topic, which resulted in rapid progress of the VCSEL bandwidth and temperature stability.

Already in 2006, a fully functional optical link with a  $4 \times 12$  VCSEL array using lasers emitting at 985 nm has been demonstrated by the Agilent and IBM researchers [49, 56]. Each of the 48 VCSELs transmitted data at operation current density lower than  $10 \text{ kA/cm}^2$  at a bit rate of 20 Gbit/s, resulting in an aggregated data bit rate of 960 Gbit/s for the whole chip. Open eyes at bit rates of up to 25 Gbit/s at elevated temperatures of up to  $70^\circ\text{C}$  have been demonstrated, which would give an aggregated data rate of 1.2 Tbit/s for the  $4 \times 12$  VCSEL array, fully confirming the right choice of the program’s name “Terabus”.

In 2007, our group developed 980 nm VCSELs with active region grown in the SML growth mode [50, 51], further increasing the high temperature stability of the fabricated devices. These VCSELs have demonstrated error-free data transmission at a bit rate of 20 Gbit/s in a wide temperature range from 25 up to  $85^\circ\text{C}$  under constant driving conditions [50], for example, operation current and modulation voltage. The latter is very important for reducing the costs, the footprint and the power consumption of the driver electronics, since no active adjustment of the driving parameters is needed to compensate for changes in ambient temperature.

In 2008 we continued the development of high-speed high-temperature-stable 980 nm VCSELs based on the active region grown in the SML growth mode, since this type of active region has demonstrated its high-temperature stability in the first generation of our 980 nm VCSELs [50, 51] described above. Similarly to the first generation, the second generation of the 980 nm VCSELs developed in our group [52–54] has been grown by molecular beam epitaxy (MBE) on  $n^+$  GaAs (100) substrates and utilized a triple stack of highly strained SML grown InGaAs layers. The stack was placed into the middle of the low-index  $\text{Al}_{0.80}\text{Ga}_{0.20}\text{As}$  cavity, since the Al content of 80% provides a better

thermal conductivity and reduces the mesa capacitance due to the smaller dielectric constant as compared to for example,  $\sim 30\%$  Al used conventionally. To facilitate optical and electrical confinement, aperture layers consisted of a 12 nm thick binary AlAs surrounded by two 9.2 nm thick  $\text{Al}_{0.90}\text{Ga}_{0.10}\text{As}$  layers were utilized. During the selective wet oxidation, all three layers, including a part of the surrounding  $\text{Al}_{0.80}\text{Ga}_{0.20}\text{As}$  material, oxidized with different oxidation rates, leading to formation of a tapered  $\text{Al}_x\text{O}_y$  aperture, reducing optical scattering losses. The cavity length was  $3/2 \lambda$ . In order to improve the temperature stability of the lasers, the cavity was red shifted from the peak gain at  $25^\circ\text{C}$  by  $\sim 20 \text{ nm}$ . To simplify device fabrication and avoid critical etching steps, optimized doped  $\text{Al}_{0.90}\text{Ga}_{0.10}\text{As}/\text{GaAs}$  DBR mirrors were applied for both top and bottom mirrors. The top p-doped DBR contained 20.5 mirror pairs, while the bottom n-doped DBR consisted of 32.5 mirror pairs. To improve electrical conductivity, linear gradings with 10 nm thickness were utilized in the mirrors.

In addition to the appropriate epitaxial design, it is indispensable to develop a corresponding device design and device fabrication process, which will allow utilization of the internal high-speed properties of the VCSEL epitaxial material and in an ideal case without any external limitations. As described in the previous sections, important limitations of the laser speed arise from thermal heating, damping, and electrical parasitics. The electrical parasitic elements, for example, as well as most of the other limiting factors, are defined by the interplay of the internal properties of the epitaxial structure, for example, doping profiles and layer thicknesses, and of the fabrication process, for example, mesa and aperture diameters, contact dimensions, and so forth. Therefore, it is decisive to develop a fabrication flow which perfectly matches the epitaxial structure and results in the overall low electrical parasitics, low thermal heating, and low damping. While some concepts to reduce, for example, electrical parasitics, for example, reduction of the contact pad dimensions or planarization with thick dielectric layers, can be applied without negative effects on other VCSEL properties, some other concepts require a search for an appropriate compromise. For example, reducing the mesa diameter reduces not only parasitic capacitances but also decreases the thermal conductivity of the device; performing a deep mesa etch reduces electrical capacitances, but increases the thermal resistance of the laser and so on. Consequently, the overall design was optimized to reach a compromise between small electrical parasitics, good thermal conductivity, low damping, and good manufacturability.

To solve the dilemma of low electrical parasitics and high thermal conductivity, we have applied the two-mesa concept, as a novel feature of our device design. Hereby, the top mesa has a smaller diameter of only  $25\text{--}36 \mu\text{m}$ , which reduces device area and thus the electrical parasitics. The etching of the top mesa is stopped directly after the cavity region to ensure a proper exposure of the aperture layers. The bottom mesa is etched in the following steps and has a larger diameter, increasing the thermal conductivity and thus reducing the self-heating of the device. Consequently, the two-mesa concept allows a combination of low electrical

parasitics and high thermal conductivity of a laser. In order to reduce electrical parasitic capacitances further, 5–9  $\mu\text{m}$  thick layers of photosensitive polymer derived from the B-staged bisbenzocyclobutene (BCB) were employed.

Applying the two-mesa concept high-speed devices with coplanar top contacts in the ground-signal-ground (GSG) configuration and different aperture diameters were fabricated using standard techniques, for example, optical lithography, metal evaporation, dry etching, and so forth. VCSELs with aperture diameters smaller than 3  $\mu\text{m}$  have shown single mode behavior while lasers with larger aperture diameters were multimode. VCSELs fabricated with the two-mesa concept have shown very temperature-stable high-speed behavior in this and also in future experiments, thus we have applied different variations of this concept for all our devices in the next years.

In Figure 2, the scanning electron microscope image of a fabricated VCSEL with the SML-active region is demonstrated [53]. The smaller top mesa with the ring contact and a part of the contact pads in the ground-signal-ground configuration can be identified on the picture. Also the shape of the larger bottom mesa is clearly seen. All measured VCSELs have shown no noticeable degradation during the measurements, giving indications for good laser reliability.

From all fabricated devices, VCSELs with aperture diameters of 2–3  $\mu\text{m}$  exhibited the best high-temperature behavior and demonstrated open eye operation at 20 Gbit/s in a wide temperature range from 0 up to 120°C with signal-to-noise ratios (S/N) larger than 5 at all temperatures, as shown in Figure 3 for a VCSEL with the aperture diameter of 3  $\mu\text{m}$  [52]. The transmission experiments have been carried out in the back-to-back (BTB) configuration ( $\sim 3$  m of multimode fiber) using a  $2^7 - 1$  pseudorandom bit sequence (PRBS) in a nonreturn to zero (NRZ) format. The operation current and the modulation voltage were held constant at all temperatures, making complicated adjustments to the temperature changes and thus, expensive driver electronics redundant. Device with the 3  $\mu\text{m}$  aperture diameter demonstrated the output power of 4.6 mW at room temperature and was still operating even at 150°C with the output power of 1.2 mW.

Because of the relative small aperture diameter, the differential resistance of the 3  $\mu\text{m}$  aperture VCSEL was about 200 Ohms at room temperature. Coupled to the parasitic capacitances of the aperture and active regions, it resulted in a parasitic cut-off frequency of  $\sim 13$  GHz, limiting the high-speed performance of the laser. To decrease the differential resistance, larger apertures are favorable, but corresponding to (3), the increased mode volume reduces the  $D$ -factor and thus, the relaxation resonance frequency according to (2). While at lower aperture diameters the relaxation resonance frequency for the presented VCSELs with SML grown active region achieves values larger than 15 GHz at room temperature, increasing the aperture diameter decreases the maximum achievable relaxation resonance frequency to  $\sim 12$  GHz and below, which becomes smaller than the laser bandwidth of  $\sim 13$  GHz. Additionally, extracted  $K$ -factors according to (4) have shown limitations of the VCSELs by damping. Thus, further development of the VCSEL structure

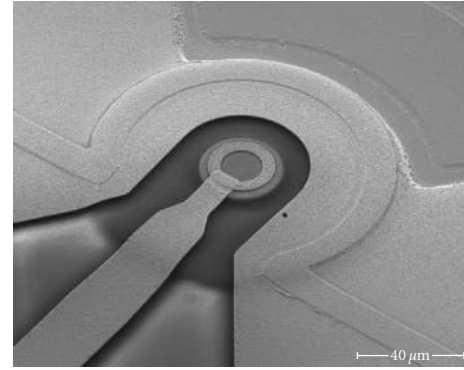


FIGURE 2: A scanning microscope image of a fabricated 980 nm VCSEL with the active region grown in the submonolayer growth mode. The smaller top mesa with the ring contact and a part of the contact pads in the ground-signal-ground configuration are demonstrated in the picture; also the shape of the larger bottom mesa can be identified.

was needed to achieve larger  $D$ -factors, relaxation resonance frequencies, and consequently bandwidths.

Based on the previous results described above we have decided to develop the next generation of high-speed high-temperature-stable VCSELs emitting at 980 nm [54, 60, 61]. To increase the relevance of our research for future commercial applications, we have decided to change the growth platform from MBE to metalorganic chemical vapor deposition (MOCVD), which is the standard and well-established growth technique for large-scale mass production of VCSELs. Since improvements of the active region were also needed to achieve larger  $D$ -factors, we have additionally decided to develop our VCSELs based on improved conventional quantum wells (QW), since they are routinely applied in commercial VCSELs today and have been proven to have excellent reliability, both GaAs QWs emitting at the standard wavelength of 850 nm [26, 27] as well as InGaAs QWs emitting at longer wavelengths [41, 66, 67]. Consequently in our new VCSEL generation active region consisted of five compressively strained InGaAs QWs each 4.2 nm thick with 6 nm thick GaAsP strain compensation layers in between and on both sides of the QW region [60, 61]. The compressive strain increases the differential gain and consequently the laser bandwidth [83]. The new active region enabled bandwidths of larger than 15 GHz and relaxation resonance frequencies larger than 14 GHz for aperture diameters as large as 7  $\mu\text{m}$ . Devices with aperture diameters of 10  $\mu\text{m}$  demonstrated similar bandwidths. Additional important improvement was the utilization of a double-oxide aperture [36] to decrease parasitic electrical capacitances. Together with the two-mesa design and thick BCB layers, this led to parasitic cut-off frequencies larger than 22 GHz at all temperatures [54, 60, 61].

In Figure 4, optical microscope image of the fabricated VCSEL array together with a zoomed view of a VCSEL with the top mesa diameter of 36  $\mu\text{m}$  is demonstrated. Devices with large aperture diameters of 7–10  $\mu\text{m}$  exhibited

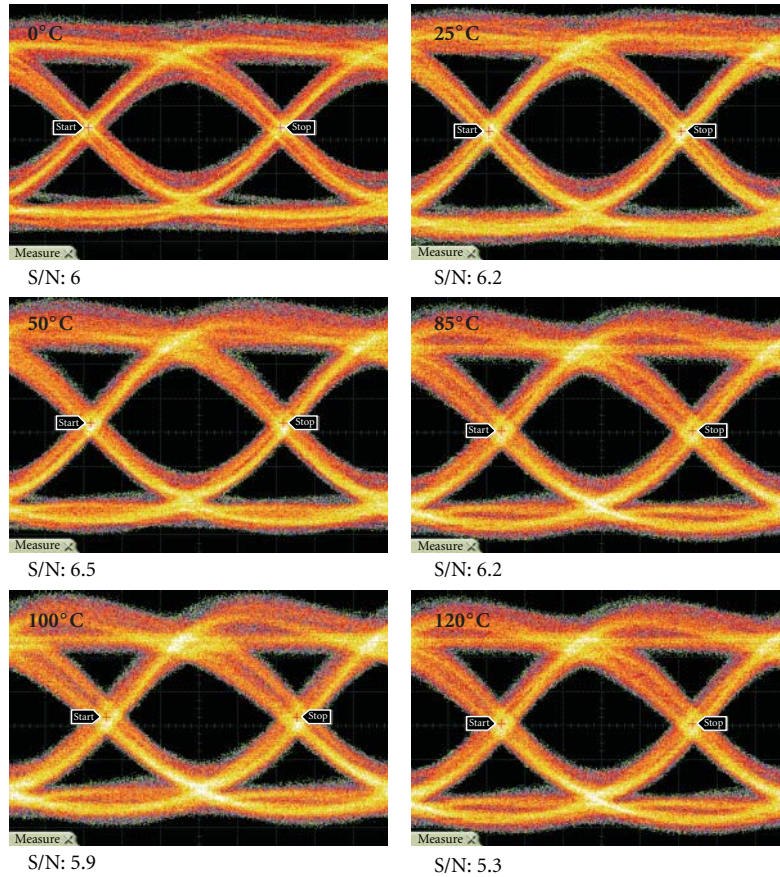


FIGURE 3: Measured optical eye diagrams for a 980 nm VCSEL with the active region grown in the submonolayer growth mode at the bit rate of 20 Gbit/s at different temperatures from 0 up to 120°C in the BTB, NRZ PRBS  $2^7 - 1$  configuration; the oxide aperture diameter of the VCSEL was 3  $\mu\text{m}$ .

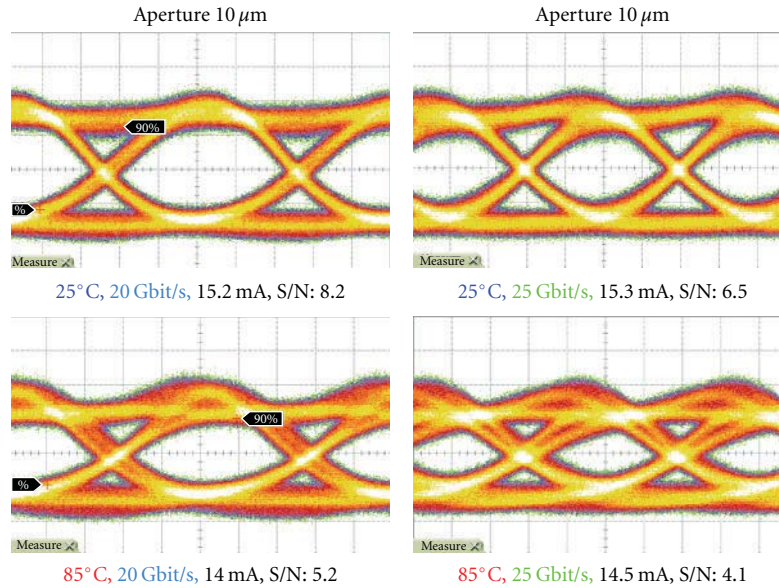
the best performance and demonstrated very-temperature-stable bandwidths around 13–15 GHz in a wide temperature range from room temperature up to 85°C. These large and very temperature stable bandwidths resulted in the very temperature-stable optical eye diagrams, as shown in Figure 5(a), and led to the demonstration of the worldwide first 980 nm VCSELs operating error-free at bit rates of up to 25 Gbit/s at temperatures of up to 85°C, as shown in Figure 5(b) [60]. All eye diagrams measured with the 10  $\mu\text{m}$  aperture VCSEL (Figure 5(a)) are clearly open with S/N larger than 6 at room temperature and larger than 4 at 85°C. Data transmission with the bit-error rate (BER) smaller than  $10^{-12}$  was achieved at both temperatures with the same device without adjustment of the driving parameters during the BER measurements at different temperatures (Figure 5(b)).

To achieve a very temperature-stable bandwidth, it is important to maintain a high relaxation resonance frequency in the whole temperature range, and thus a large and temperature-insensitive  $D$ -factor, as follows from (2). Since the  $D$ -factor is strongly dependent on the differential gain, accordingly to (3), it is indispensable to maintain the differential gain as large and as temperature stable as possible. Optimization of the detuning between the cavity resonance wavelength and the wavelength of the gain peak is a natural

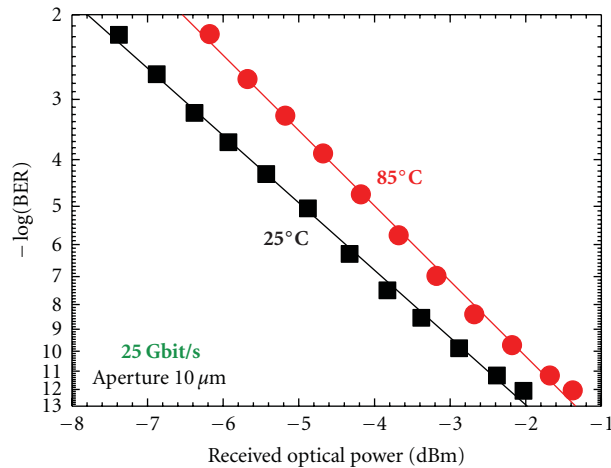


FIGURE 4: Top-down optical microscope image of the fabricated array of VCSELs with the quantum well active region, including an expanded view of a device with a mesa diameter of 36  $\mu\text{m}$ .

and elegant tool in a VCSEL to maintain a low threshold current density over a wide temperature range. Since differential gain decreases rapidly with increasing carrier density [83, 84], a low and temperature-insensitive threshold carrier



(a)



(b)

FIGURE 5: Eye diagrams at 20 and 25 Gbit/s and temperatures of 25 and 85°C with corresponding driving currents and signal to noise ratios in a BTB configuration with  $(2^7 - 1)$  PRBS in a NRZ format (a) and bit error rates at the bit rate of 25 Gbit/s at 25 and 85°C at the current of 12 mA for a BTB, NRZ,  $(2^7 - 1)$  PRBS configuration (b) for a VCSEL with 10  $\mu\text{m}$ -diameter oxide aperture.

density helps to maintain the large differential gain and thus high bandwidths at elevated temperatures. In our MOCVD grown VCSELs described above, we have applied a nominally 15 nm detuning between the cavity resonance wavelength and the wavelength of the photoluminescence (PL) peak of the active region. This optimized detuning resulted in very temperature-stable threshold currents with the variations smaller than 20% in the whole temperature range from 20 up to 85°C. The perfect alignment of the cavity-gain detuning manifested itself in the clear minimum of the threshold current as a function of the temperature near 50°C, just in the middle of the desired temperature interval [54, 60, 61].

As we can see VCSELs emitting around the wavelength of 980 nm have made rapid progress just within a couple of years and became able to transfer data at bit rates of up

to 25 Gbit/s in a wide temperature range. Nevertheless, the major and more challenging task to increase the bit rate of the 980 nm VCSELs at elevated temperatures towards 40 Gbit/s was still not solved. In the next section, we review the effort and achievements of the worldwide research community in this direction, which ultimately led to realization of 980 nm VCSELs capable of error-free data transmission at bit rates as high as 44 Gbit/s at room temperature and 38 Gbit/s at the elevated temperatures of up to 85°C [62, 63].

#### 4. Progress towards 40 Gb/S and Beyond

Already in 2007 researchers from the University of California, Santa Barbara developed advanced 980 nm bottom-emitting VCSELs which have demonstrated data rates as high as

35 Gbit/s [46, 47] at room temperature. To address the limitations of the high-speed laser performance, a number of elegant and effective concepts have been applied in these devices. The doping profiles were optimized to decrease optical losses and at the same time to maintain a large electrical conductivity. A thick oxide aperture with additional deep oxidation layers have been introduced, which together with a thick BCB layer decisively reduces electrical parasitics. It should be noted here that all GaAs-based VCSELs capable of data transmission at bit rates of 35 Gbit/s and larger utilize special advanced concepts to reduce electrical parasitics inside of the VCSEL mesa, for example, a double aperture and deep oxidation layers at the wavelength of 850 nm [22], a thick oxide aperture together with deep oxidation layers at the wavelength of 980 nm [46] or ion implantation at the wavelength of 1100 nm [41]. Consequently, to increase the bit rate towards 40 Gbit/s, it is indispensable to apply such concepts together with optimization of the contact pad capacitances, for example, via smaller dimensions and thick dielectric layers.

Another important point is the consideration of not only the high-speed performance of the laser, but additionally understanding the significance of all the components built into the complete optical link, especially of the high-speed photodetector. It is remarkable that all successful data transmission experiments at the record high bit rate of 40 Gbit/s using GaAs-based VCSELs utilized advanced photodetectors developed by industrial partners in special projects, for example, a special designed photodetector with the bandwidth of 30 GHz developed by the company VI Systems for the 850 nm link [22] or an advanced photoreceiver with integrated transimpedance amplifier (TIA) with the bandwidth of 20 GHz developed by NEC for the 1100 nm optical data transmission line [41, 45]. Therefore, we have concentrated our effort on both developing the next generation of our high-speed high-temperature-stable 980 nm VCSELs as well as searching for industrial partners to get access to advanced photodetectors in this wavelength range.

Based on the scientific results obtained from the previous generations of our 980 nm VCSELs, especially from the MOCVD grown devices presented at the end of the previous section, which were capable of error-free data transmission at the bit rate of 25 Gbit/s at temperatures up to 85°C, we have decided to develop a novel VCSEL structure targeting 40 Gbit/s data transmission. Therefore, all proven advanced concepts, which have demonstrated strong positive impact on the laser high-speed and high-temperature performance in the previous generations, should be consequently kept in the new VCSEL structure. On the other hand, all discovered limitations should be addressed by the application of new optimization concepts, which ideally should not have negative impact on the already achieved performance. We consistently investigated every of the three limiting factors: electrical parasitics, damping, and thermal processes and in a comprehensive study developed the new VCSEL design for high-speed operation at bit rates in the range of 40 Gbit/s in a wide temperature range from room temperature up to

85°C. In the following, we will describe the modifications and achieved results.

As we have already obtained from our previous VCSEL generation grown by MOCVD, electrical parasitic frequencies of larger than 22 GHz were achieved by utilizing a double oxide aperture and thick BCB layers [54, 60, 61]. Together with a small top mesa realized in the two-mesa concept and according to (7), electrical parasitics would not present a strong limitation of our devices, once we keep the double aperture and the thick BCB in the new VCSEL generation. Consequently, these concepts were transferred to our new laser structure without large modifications. Additionally, to decrease electrical resistance and optical losses, doping profiles were optimized further paying respect to dependence of the carrier mobility both on the material as well as on the type of the carriers, for example, electrons or holes. Also optical field distribution was taken into account more carefully, similarly to the procedure described, for example, in [47].

Since damping was one of the major limitations in our previous VCSELs, ultimate concepts for the reduction of the  $K$ -factor should be applied. The  $K$ -factor is strongly dependent on the photon lifetime, as shown by (5). Consequently, it is decisive to find concepts which would result in a significant decrease of the photon lifetime without having negative impact on other important laser parameters, for example, differential gain and so forth. As was demonstrated in a very impressive work by the researchers from the Chalmers University of Technology, reduction of the photon lifetime can decrease the damping and thus, increase the laser bandwidth significantly [39, 40]. In their work, the reflectivity of the top mirror was reduced by dry etching, leading to the reduction of the  $K$ -factor and thus damping. However, the increase of the mirror losses has negative impact on the threshold current and thus, the differential gain, resulting in decrease of the important  $D$ -factor and consequently of the maximum relaxation resonance frequency. Thus, to meet the compromise between increased losses and decreased damping, it is important to find a concept which not only decreases the photon lifetime, but simultaneously increases the modal gain, compensating for the increased losses.

An elegant concept for reduction of the photon lifetime without decreasing the differential gain is the application of a shorter VCSEL cavity. The photon lifetime decreases, but at the same time the optical confinement factor increases, compensating for the increase of the optical losses and maintaining the modal gain at a high level [83, 84]. Additionally, because of the changed balance between the mirror and the internal losses, also the differential efficiency of the laser increases, leading to larger output powers and thus a better S/N [83, 84]. Since our previous VCSEL structures utilized a  $3\lambda/2$  long cavity region, the only possibility to shorten the cavity was the introduction of a  $\lambda/2$  long cavity, which is known over many years and has been first investigated in the middle 1990s [87–89]. Consequently we have applied a  $\lambda/2$  cavity concept to our new structures and a comparison between the previous VCSEL design, which demonstrated error-free data transmission at the bit rate of 25 Gbit/s at temperatures of up to 85°C [54, 60, 61], as described at the

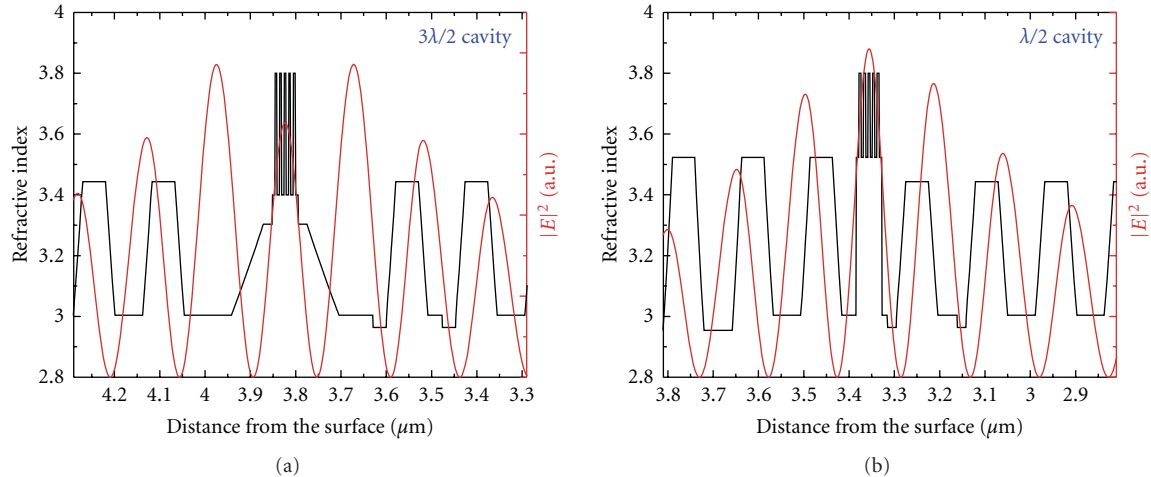


FIGURE 6: Comparison of the refractive index and simulated optical field intensity distribution inside the previous VCSEL structure with a  $3\lambda/2$  cavity (a) and inside the new VCSEL structure with a  $\lambda/2$  cavity (b).

end of the previous section and the new VCSEL structure [62, 63] is shown in Figure 6. While Figure 6(a) demonstrates the refractive index profile and the simulated optical field intensity distribution in our previous VCSELs with the  $3\lambda/2$  cavity, Figure 6(b) shows the new VCSEL structure with the  $\lambda/2$  cavity region. The wafer substrate is hereby to the left and the wafer surface to the right. As can be clearly seen, optical field distribution is more advantageous for the shorter cavity, because the middle intensity peak is much stronger as compared to the  $3\lambda/2$  case. Consequently, the overlap of the lasing mode with active region increases, leading to a strong increase of the optical confinement factor. The calculated value of the optical confinement factor for new VCSELs with the  $\lambda/2$  cavity is 5.1%, which is more than 70% larger than the value of the confinement factor for VCSELs based on the  $3\lambda/2$  cavity, which was only 3%. Consequently, the modal gain increases, compensating for increased losses and leaving the carrier density and thus the differential gain hardly affected. Simultaneously the cavity length decreases, leading to decrease of the  $K$ -factor and damping. In addition to the optimized doping profiles, the  $\lambda/2$  cavity is the second improvement of our previous VCSEL structure. Figure 6 shows also the double aperture in the two pairs of the top DBR directly adjacent to the cavity region both in the previous as well as in the new structure.

After investigations of the electrical parasitics and damping, also concepts to decrease thermal self-heating were studied. Therefore, it is important to increase thermal conductivity of a VCSEL. Introduction of binary materials, for example, binary GaAs and AlAs, instead of ternary AlGaAs alloys especially in the bottom DBR significantly increases the thermal conductivity of the devices. Consequently, we have replaced all layers in the bottom DBR, excepting for the first mirror pair adjacent to the cavity, by binary GaAs and AlAs, as can be also obtained from the refractive index profiles shown in Figure 6(b). Ternary AlGaAs in the first bottom mirror pair was maintained to ensure high yield during the dry etching step for the first mesa in the fabrication process.

Finally, we have carried out a series of experiments with several test structures with different active regions containing InGaAs QWs with different compositions, thicknesses, and quantity. As in our previous VCSELs, active regions with five QWs demonstrated the best performance, but in contrast to the previous devices, new active region contained InGaAs QWs with GaAs barriers, thus, without the GaAsP stress compensation layers. Additionally the thickness of the InGaAs QWs has been increased from 4.2 nm to 5.0 nm, increasing the optical confinement factor together with the previously described short cavity to the already mentioned value of 5.1%. The number of QWs can be identified also by taking a look onto Figure 6, where cavity region for both our previous and our new VCSELs are shown. To increase the high temperature stability of the lasers, optimized detuning between the cavity resonance and the PL peak of the active region has been applied, similarly to our previous VCSEL structures.

Summarizing the applied concepts, the new generation of our high-speed high-temperature-stable 980 nm VCSELs include the following significant design features, both in the epitaxial structure and in the device design:

- (i) double oxide aperture,
- (ii) small contact pad dimensions and thick BCB layers,
- (iii) two-mesa device design with a small top mesa and a larger bottom mesa,
- (iv) short  $\lambda/2$  cavity,
- (v) binary GaAs/AlAs bottom DBR,
- (vi) five compressively strained InGaAs QWs with GaAs barriers,
- (vii) optimized doping profiles,
- (viii) optimized gain-cavity detuning.

Combined together, the above-described concepts resulted in realization of VCSELs capable of the error-free data transmission at the record high bit rate of 44 Gbit/s

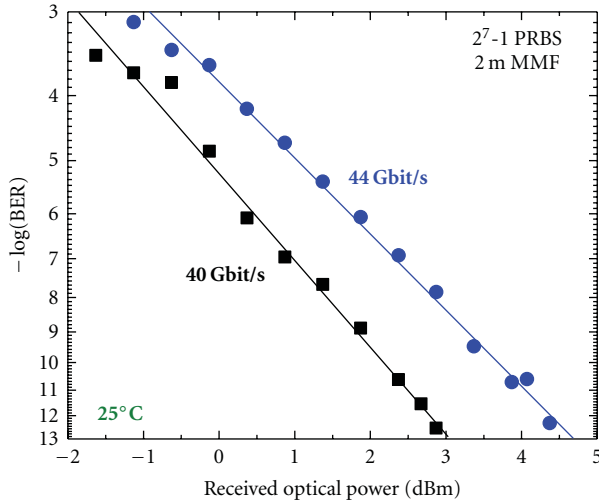


FIGURE 7: Measured bit error rates for the new VCSEL with the  $\lambda/2$  cavity and  $6\mu\text{m}$  aperture in the BTB, NRZ, PRBS  $2^7 - 1$  configuration at  $25^\circ\text{C}$  at the bit rates of 40 and 44 Gbit/s.

at room temperature [62, 63], as Figure 7 presents. The experiment was carried out in the BTB configuration ( $\sim 2\text{m}$  of multimode fiber) using a NRZ, PRBS  $2^7 - 1$  digital pattern, and a special advanced photoreceiver with an integrated TIA fabricated by the company  $u^2t$  and exhibiting  $\sim 30\text{GHz}$  bandwidth since the importance of the proper photodetector has been discussed above. For the data transmission experiment, a VCSEL with the oxide aperture diameter of  $6\mu\text{m}$  was measured at the current of 13 mA and the peak-to-peak modulation voltage of 0.8 V.

With the same device, also data transmission experiments at elevated temperatures up to  $120^\circ\text{C}$  have been carried out [62, 63] in the same configuration using the same photoreceiver from  $u^2t$ . Under the same driving conditions, error-free transmission at the elevated temperature of  $85^\circ\text{C}$  at the record high bit rate of 38 Gbit/s was demonstrated (Figure 8), which is an improvement of more than 10 Gbit/s compared to previous VCSEL records at elevated temperatures at any wavelength! Thus, our new generation of 980 nm lasers is currently the worldwide fastest of any VCSELs at any wavelength both at room as well as at elevated temperatures.

After several years of worldwide effort on the field of high-speed 980 nm VCSELs, these lasers have finally arrived at the very important milestone: realization of an optical link capable of error-free transmission at the bit rate of 40 Gbit/s. Additionally, bit rates close to 40 Gbit/s are maintained also at elevated temperatures, making these devices very suitable for parallel optical interconnects especially in future HPC applications.

## 5. Conclusions and Outlook

In the recent years, we have seen impressive progress in the field of high-speed VCSELs emitting around 980 nm. This wavelength has large advantages described in the introduction, which make it very suitable for future short-reach optical interconnects, especially in HPC applications.

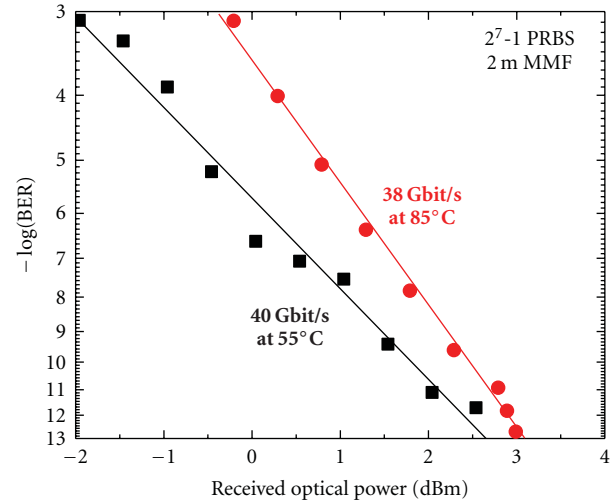


FIGURE 8: Measured bit error rates for the new VCSEL with the  $\lambda/2$  cavity and  $6\mu\text{m}$  aperture in the BTB, NRZ, PRBS  $2^7 - 1$  configuration at the bit rate of 40 Gbit/s at  $55^\circ\text{C}$  and at the bit rate of 38 Gbit/s at  $85^\circ\text{C}$ .

The worldwide effort of many excellent researchers from academic institutions as well as industrial companies led to a consequent increase of the data transmission speed of 980 nm VCSELs first to 25 Gbit/s, then to 35 Gbit/s and finally to 40 Gbit/s and now even beyond. Hereby, the increase of the transmission bit rate was achieved not only at one specific temperature, for example, room temperature, but also at elevated temperatures, resulting in VCSELs operating at ultrahigh speed in a wide temperature range, which is especially important for future HPC applications.

The increase of the bit rate was realized by a careful combination of advanced concepts, many of which are wellknown over years and have established themselves as very efficient and at the same time relative straightforward methods. Thus, the overall VCSEL design and fabrication could be maintained relatively inexpensive, making the achieved scientific results more valuable for future commercial applications.

Progress in the field of high-speed VCSELs will definitely continue, leading to further exciting results. In addition to further optimizations of the conventional VCSEL structure novel concepts, for example, VCSELs with photonic crystals [32] or high contrast gratings (HCG) [90, 91], as well as indirectly modulated VCSELs [92–94] and even exciting novel metal-cavity nanolasers based on VCSEL-like structures [95–99], are currently intensively investigated and certainly would generate significant knowledge with very high value for both fundamental science as well as application-oriented research.

## Acknowledgments

The authors would like to thank J. A. Lott, N. N. Ledentsov, P. Moser, P. Wolf, F. Hopfer, S. A. Blokhin, A. M. Nadtochiy, A. Payusov, V. A. Shchukin, G. Fiol, K. Pötschke, W. Hofmann,

V. Haisler, D. Arsenijevic, A. R. Kovsh, S. S. Mikhlin, I. L. Krestnikov, D. A. Livshits, and U. Pohl for significant contributions to this work. This work was supported by the EU FP7 program under agreement no. 224211, the Deutsche Forschungsgemeinschaft (Sfb 787), the State of Berlin (100 × 100 Optics), and grants of Saint Petersburg Government and Ministry of Education and Science of Russia.

## References

- [1] K. Skaugen, "Petascale to exascale: extending Intel's HPC commitment," in *Proceedings of the International Supercomputing Conference (ISC '10)*, Hamburg, Germany, May 2010.
- [2] E. Mohammed, A. Alduino, T. Thomas et al., "Optical interconnects system integration for ultra-short-reach applications," *Intel Technology Journal*, vol. 8, no. 2, pp. 115–128, 2004.
- [3] M. J. Kobrinsky, B. A. Block, J. F. Zheng et al., "On-chip optical interconnects," *Intel Technology Journal*, vol. 8, no. 2, pp. 129–142, 2004.
- [4] D. W. Dolfi, "Multi-channel optical interconnects for short-reach applications," in *Proceedings of the 53rd Electronic Components and Technology Conference (ECTC '03)*, pp. 1032–1039, May 2003.
- [5] D. A. B. Miller, "Physical reasons for optical interconnection," *International Journal of Optoelectronics*, vol. 11, no. 3, pp. 155–168, 1997.
- [6] D. G. Kam, M. B. Ritter, T. J. Beukema et al., "Is 25 Gb/s on-board signaling viable?" *IEEE Transactions on Advanced Packaging*, vol. 32, no. 2, pp. 328–344, 2009.
- [7] C. Schow, F. Doany, and J. Kash, "Get on the optical bus," *IEEE Spectrum*, vol. 47, no. 9, Article ID 5557513, pp. 32–56, 2010.
- [8] P. Pepeljugoski, M. Ritter, J. A. Kash et al., "Comparison of bandwidth limits for on-card electrical and optical interconnects for 100 Gb/s and beyond," in *Optoelectronic Integrated Circuits X*, vol. 6897, 68970I of *Proceedings of SPIE*, January 2008.
- [9] A. F. Benner, M. Ignatowski, J. A. Kash, D. M. Kuchta, and M. B. Ritter, "Exploitation of optical interconnects in future server architectures," *IBM Journal of Research and Development*, vol. 49, no. 4-5, pp. 755–775, 2005.
- [10] B. J. Offrein, C. Berger, R. Beyeler et al., "Parallel optical interconnects in printed circuit boards," in *Optically Based Biological and Chemical Sensing, and Optically Based Materials for Defence*, vol. 5990, 59900E of *Proceedings of SPIE*, Bruges, Belgium, September 2005.
- [11] N. Savage, "Linking with light," *IEEE Spectrum*, vol. 39, no. 8, pp. 32–36, 2002.
- [12] H. Soda, K. Iga, C. Kitahara, and Y. Suematsu, "GaInAsP/InP surface emitting injection lasers," *Japanese Journal of Applied Physics*, vol. 18, no. 12, pp. 2329–2330, 1979.
- [13] K. Iga, F. Koyama, and S. Kinoshita, "Surface emitting semiconductor lasers," *IEEE Journal of Quantum Electronics*, vol. 24, no. 9, pp. 1845–1855, 1988.
- [14] K. Iga, "Vertical-cavity surface-emitting laser: its conception and evolution," *Japanese Journal of Applied Physics*, vol. 47, no. 1, pp. 1–10, 2008.
- [15] F. Koyama, "Recent advances of VCSEL photonics," *Journal of Lightwave Technology*, vol. 24, no. 12, pp. 4502–4513, 2006.
- [16] D. Collins, N. Li, D. Kuchta et al., "Development of high-speed VCSELs: 10 Gb/s serial links and beyond," in *Vertical-Cavity Surface-Emitting Lasers XII*, vol. 6908, 690809 of *Proceedings of SPIE*, San Jose, Calif, USA, January 2008.
- [17] F. E. Doany, L. Schares, C. L. Schow et al., "Chip-to-chip optical interconnects," in *Proceedings of the Optical Fiber Communication Conference (OFC '06)*, OFA3, Anaheim, Calif, USA, March 2006.
- [18] D. L. Huffaker, D. G. Deppe, K. Kumar, and T. J. Rogers, "Native-oxide defined ring contact for low threshold vertical-cavity lasers," *Applied Physics Letters*, vol. 65, no. 1, pp. 97–99, 1994.
- [19] K. D. Choquette, R. P. Schneider, K. L. Lear, and K. M. Geib, "Low threshold voltage vertical-cavity lasers fabricated by selective oxidation," *Electronics Letters*, vol. 30, no. 24, pp. 2043–2044, 1994.
- [20] P. K. Pepeljugoski, J. A. Kash, F. Doany et al., "Low power and high density optical interconnects for future supercomputers," in *Proceedings of the Optical Fiber Communication Conference (OFC '10)*, San Diego, Calif, USA, March 2010, Paper OThX2.
- [21] W. Green, S. Assefa, A. Rylyakov, C. Schow, F. Horst, and Y. Vlasov, "CMOS integrated silicon nanophotonics: enabling technology for exascale computational systems," in *Proceedings of the SEMICON Japan*, Tokyo, Japan, December 2010.
- [22] P. Westbergh, J. S. Gustavsson, B. Kögel et al., "40 Gbit/s error-free operation of oxide-confined 850 nm VCSEL," *Electronics Letters*, vol. 46, no. 14, pp. 1014–1016, 2010.
- [23] S. A. Blokhin, J. A. Lott, A. Mutig et al., "Oxide-confined 850 nm VCSELs operating at bit rates up to 40 Gbit/s," *Electronics Letters*, vol. 45, no. 10, pp. 501–503, 2009.
- [24] A. Mutig, S. A. Blokhin, A. M. Nadtochiy et al., "Frequency response of large aperture oxide-confined 850 nm vertical cavity surface emitting lasers," *Applied Physics Letters*, vol. 95, no. 13, pp. 131101-1–131101-3, 2009.
- [25] A. Mutig, S. Blokhin, A. M. Nadtochiy et al., "High-speed 850 nm oxide-confined VCSELs for DATACOM applications," in *Vertical-Cavity Surface-Emitting Lasers XIV*, vol. 7615, 76150N of *Proceedings of SPIE*, San Francisco, Calif, USA, January 2010.
- [26] J. Wang, C. Ji, D. Soderstrom, T. Jian, and L. Giovane, "850 nm oxide high speed VCSEL development at Avago," in *Vertical-Cavity Surface-Emitting Lasers XV*, vol. 7952, 795205 of *Proceedings of SPIE*, San Francisco, Calif, USA, January 2011.
- [27] C. Xie, N. Li, C. Lei et al., "New high speed VCSEL product development at Emcore," in *Vertical-Cavity Surface-Emitting Lasers XV*, vol. 7952, 795206, San Francisco, Calif, USA, January 2011.
- [28] C. Ji, J. Wang, D. Söderström, and L. Giovane, "20 Gb/s 850 nm Oxide VCSEL operating at 25°C–70°C," *IEEE Photonics Technology Letters*, vol. 22, no. 10, pp. 670–672, 2010.
- [29] R. H. Johnson and D. M. Kuchta, "30 Gb/s directly modulated 850 nm datacom VCSELs," in *Proceedings of the Conference on Lasers and Electro-Optics Postdeadline Session II (CPDB '08)*, San Jose, Calif, USA, May 2008.
- [30] A. N. Al-Omari and K. L. Lear, "VCSELs with a self-aligned contact and copper-plated heatsink," *IEEE Photonics Technology Letters*, vol. 17, no. 9, pp. 1767–1769, 2005.
- [31] A. N. Al-Omari and K. L. Lear, "Polyimide-planarized vertical-cavity surface-emitting lasers with 17.0 GHz bandwidth," *IEEE Photonics Technology Letters*, vol. 16, no. 4, pp. 969–971, 2004.
- [32] C. Chen, P. O. Leisher, D. M. Kuchta, and K. D. Choquette, "High-speed modulation of index-guided implant-confined vertical-cavity surface-emitting lasers," *IEEE Journal on Selected Topics in Quantum Electronics*, vol. 15, no. 3, pp. 673–678, 2009.
- [33] J. A. Lott, V. A. Shchukin, N. N. Ledentsov et al., "20 Gbit/s error free transmission with ~850 nm GaAs-based vertical

- cavity surface emitting lasers (VCSELs) containing InAs-GaAs submonolayer quantum dot insertions,” in *Physics and Simulation of Optoelectronic Devices XVII*, vol. 7211, 721114 of *Proceedings of SPIE*, San Jose, Calif, USA, January 2009.
- [34] P. Westbergh, J. S. Gustavsson, A. Haglund et al., “32 Gbit/s transmission experiments using high speed 850 nm VCSELs,” in *Proceedings of the Conference on Lasers and Electro-Optics and International Quantum Electronics Conference (CLEO/IQEC '09)*, Baltimore, Md, USA, May 2009, Paper CMGG6.
- [35] P. Westbergh, J. S. Gustavsson, A. Haglund et al., “32 Gbit/s multimode fibre transmission using high-speed, low current density 850 nm VCSEL,” *Electronics Letters*, vol. 45, no. 7, pp. 366–368, 2009.
- [36] P. Westbergh, J. S. Gustavsson, A. Haglund, M. Sköld, A. Joel, and A. Larsson, “High-speed, low-current-density 850 nm VCSELs,” *IEEE Journal on Selected Topics in Quantum Electronics*, vol. 15, no. 3, pp. 694–703, 2009.
- [37] Y. Ou, J. S. Gustavsson, P. Westbergh, A. Haglund, A. Larsson, and A. Joel, “Impedance characteristics and parasitic speed limitations of high-speed 850 nm VCSELs,” *IEEE Photonics Technology Letters*, vol. 21, no. 24, Article ID 5291742, pp. 1840–1842, 2009.
- [38] S. B. Healy, E. P. O'Reilly, J. S. Gustavsson et al., “Active region design for high-speed 850 nm VCSELs,” *IEEE Journal of Quantum Electronics*, vol. 46, no. 4, pp. 506–512, 2010.
- [39] P. Westbergh, J. S. Gustavsson, and B. Kogel, “850 nm VCSEL operating error-free at 40 Gbit/s,” in *Proceedings of the 22nd IEEE International Semiconductor Laser Conference*, Kyoto, Japan, September 2010, Paper WC2.
- [40] P. Westbergh, J. S. Gustavsson, B. Kögel, A. Haglund, A. Larsson, and A. Joel, “Speed enhancement of VCSELs by photon lifetime reduction,” *Electronics Letters*, vol. 46, no. 13, pp. 938–940, 2010.
- [41] N. Suzuki, T. Anan, H. Hatakeyama et al., “High speed 1.1  $\mu\text{m}$ -range InGaAs-based VCSELs,” *IEICE Transactions on Electronics*, vol. E92-C, no. 7, pp. 942–950, 2009.
- [42] T. Anan, N. Suzuki, K. Yashiki et al., “High-speed InGaAs VCSELs for optical interconnects,” in *Proceedings of the International Symposium on VCSELs and Integrated Photonics*, Tokyo, Japan, December 2007.
- [43] H. Hatakeyama, T. Akagawa, K. Fukatsu et al., “25 Gbit/s 100°C operation of highly reliable InGaAs/GaAsP-VCSELs,” *Electronics Letters*, vol. 45, no. 1, pp. 45–46, 2009.
- [44] H. Hatakeyama, T. Anan, T. Akagawa et al., “Highly reliable high-speed 1.1  $\mu\text{m}$ -range VCSELs with InGaAs/GaAsP-MQWs,” *IEEE Journal of Quantum Electronics*, vol. 46, no. 6, pp. 890–897, 2010.
- [45] K. Fukatsu, K. Shiba, Y. Suzuki et al., “30 Gb/s over 100 m MMFs Using 1.1  $\mu\text{m}$  range VCSELs and photodiodes,” *IEEE Photonics Technology Letters*, vol. 20, no. 11, pp. 909–911, 2008.
- [46] Y. C. Chang, C. S. Wang, and L. A. Coldren, “High-efficiency, high-speed VCSELs with 35 Gbit/s error-free operation,” *Electronics Letters*, vol. 43, no. 19, pp. 1022–1023, 2007.
- [47] Y. C. Chang and L. A. Coldren, “Efficient, high-data-rate, tapered oxide-aperture vertical-cavity surface-emitting lasers,” *IEEE Journal on Selected Topics in Quantum Electronics*, vol. 15, no. 3, pp. 704–714, 2009.
- [48] Y. C. Chang, C. S. Wang, and L. A. Coldren, “Small-dimension power-efficient high-speed vertical-cavity surface-emitting lasers,” *Electronics Letters*, vol. 43, no. 7, pp. 396–397, 2007.
- [49] C. K. Lin, A. Tandon, K. Djordjev, S. W. Corzine, and M. R. T. Tan, “High-speed 985 nm bottom-emitting VCSEL arrays for chip-to-chip parallel optical interconnects,” *IEEE Journal on Selected Topics in Quantum Electronics*, vol. 13, no. 5, pp. 1332–1339, 2007.
- [50] F. Hopfer, A. Mutig, G. Fiol et al., “20 Gb/s 85°C error-free operation of vcsels based on submonolayer deposition of quantum dots,” *IEEE Journal on Selected Topics in Quantum Electronics*, vol. 13, no. 5, pp. 1302–1308, 2007.
- [51] F. Hopfer, A. Mutig, M. Kuntz et al., “Single-mode submonolayer quantum-dot vertical-cavity surface-emitting lasers with high modulation bandwidth,” *Applied Physics Letters*, vol. 89, no. 14, Article ID 141106, 2006.
- [52] A. Mutig, G. Fiol, P. Moser et al., “120°C 20 Gbit/s operation of 980 nm VCSEL,” *Electronics Letters*, vol. 44, no. 22, pp. 1305–1306, 2008.
- [53] A. Mutig, G. Fiol, K. Pötschke et al., “Temperature-dependent small-signal analysis of high-speed high-temperature stable 980 nm VCSELs,” *IEEE Journal on Selected Topics in Quantum Electronics*, vol. 15, no. 3, Article ID 4783017, pp. 679–686, 2009.
- [54] A. Mutig, *High Speed VCSELs for Optical Interconnects*, Springer Theses, Springer, New York, NY, USA, 2011.
- [55] B. E. Lemoff, M. E. Ali, G. Panotopoulos et al., “MAUI: enabling fiber-to-the-processor with parallel multiwavelength optical interconnects,” *Journal of Lightwave Technology*, vol. 22, no. 9, pp. 2043–2054, 2004.
- [56] L. Schares, J. A. Kash, F. E. Doany et al., “Terabus: terabit/second-class card-level optical interconnect technologies,” *IEEE Journal on Selected Topics in Quantum Electronics*, vol. 12, no. 5, pp. 1032–1043, 2006.
- [57] F. E. Doany, C. L. Schow, C. W. Baks et al., “160 Gb/s bidirectional polymer-waveguide board-level optical interconnects using CMOS-cased transceivers,” *IEEE Transactions on Advanced Packaging*, vol. 32, no. 2, pp. 345–359, 2009.
- [58] L. Olejniczak, M. Sciamanna, H. Thienpont et al., “Polarization switching in quantum-dot vertical-cavity surface-emitting lasers,” *IEEE Photonics Technology Letters*, vol. 21, no. 14, pp. 1008–1010, 2009.
- [59] L. Olejniczak, K. Panajotov, H. Thienpont et al., “Polarization switching and polarization mode hopping in quantum dot vertical-cavity surface-emitting lasers,” *Optics Express*, vol. 19, no. 3, pp. 2476–2484, 2011.
- [60] A. Mutig, J. A. Lott, S. A. Blokhin et al., “Highly temperature-stable modulation characteristics of multioxide-aperture high-speed 980 nm vertical cavity surface emitting lasers,” *Applied Physics Letters*, vol. 97, no. 15, Article ID 151101, 2010.
- [61] A. Mutig, J. A. Lott, and S. A. Blokhin, “High-speed highly temperature stable 980 nm VCSELs operating at 25 Gb/s at up to 85°C for short reach optical interconnects,” in *Vertical-Cavity Surface-Emitting Lasers XV*, vol. 7952, 79520H of *Proceedings of SPIE*, San Francisco, Calif, USA, January 2011.
- [62] W. Hofmann, P. Moser, P. Wolf, A. Mutig, M. Kroh, and D. Bimberg, “44 Gb/s VCSEL for optical interconnects,” in *Proceedings of the Optical Fiber Communication Conference and Exhibition and the National Fiber Optic Engineers Conference (OFC/NFOEC)*, Los Angeles, Calif, USA, March 2011, Paper PDP5.
- [63] A. Mutig, “High speed 850 and 980 nm VCSELs,” in *Proceedings of the OIDA's Short-Distance, High-Density Optical Interconnects Workshop*, Stanford, Calif, USA, April 2011.
- [64] A. N. Al-Omari, G. P. Carey, S. Hallstein, J. P. Watson, G. Dang, and K. L. Lear, “Low thermal resistance high-speed top-emitting 980 nm VCSELs,” *IEEE Photonics Technology Letters*, vol. 18, no. 11, pp. 1225–1227, 2006.
- [65] R. Safaisini, J. R. Joseph, D. Louderback, X. Jin, A. N. Al-Omari, and K. L. Lear, “Temperature dependence of 980 nm

- oxide-confined VCSEL dynamics,” *IEEE Photonics Technology Letters*, vol. 20, no. 14, pp. 1273–1275, 2008.
- [66] K. Takaki, S. Imai, S. Kamiya et al., “1060 nm VCSEL for inter-chip optical interconnections,” in *Vertical-Cavity Surface-Emitting Lasers XV*, vol. 7952, 795204 of *Proceedings of SPIE*, San Francisco, Calif, USA, January 2011.
- [67] K. Takaki, N. Iwai, S. Kamiya et al., “Experimental demonstration of low jitter performance and high reliable 1060 nm VCSEL arrays for 10 Gbpsx12ch optical interconnection,” in *Vertical-Cavity Surface-Emitting Lasers XIV*, vol. 7615, 761502 of *Proceedings of SPIE*, San Francisco, Calif, USA, January 2010.
- [68] F. Hopfer, I. Kaiander, A. Lochmann et al., “Vertical-cavity surface-emitting quantum-dot laser with low threshold current grown by metal-organic vapor phase epitaxy,” *Applied Physics Letters*, vol. 89, no. 6, Article ID 061105, 2006.
- [69] R. Safaisini, J. R. Joseph, and K. L. Lear, “Scalable high-CW-power high-speed 980 nm VCSEL arrays,” *IEEE Journal of Quantum Electronics*, vol. 46, no. 11, Article ID 5556436, pp. 1590–1596, 2010.
- [70] R. Safaisini, J. R. Joseph, G. Dang, and K. L. Lear, “Scalable high-power, high-speed CW VCSEL arrays,” *Electronics Letters*, vol. 45, no. 8, pp. 414–415, 2009.
- [71] A. N. Al-Omari, K. L. Lear, and H. Hamad, “High-speed 980 nm VCSELs with integrated distributed losses for mode control,” in *Vertical-Cavity Surface-Emitting Lasers XIV*, vol. 7615, 76150P of *Proceedings of SPIE*, San Francisco, Calif, USA, January 2010.
- [72] E. Soderberg, J. S. Gustavsson, P. Modh et al., “High-temperature dynamics, high-speed modulation, and transmission experiments using 1.3  $\mu\text{m}$  InGaAs single-mode VCSELs,” *Journal of Lightwave Technology*, vol. 25, no. 9, pp. 2791–2798, 2007.
- [73] E. Söderberg, P. Modh, J. S. Gustavsson et al., “High speed, high temperature operation of 1.28  $\mu\text{m}$  singlemode InGaAs VCSELs,” *Electronics Letters*, vol. 42, no. 17, pp. 978–979, 2006.
- [74] R. L. Naone, A. W. Jackson, S. A. Feld, D. Galt, K. J. Malone, and J. J. Hindi, “Monolithic GaAs-based 1.3  $\mu\text{m}$  VCSEL directly-modulated at 10 Gb/s,” in *Proceedings of the Conference on Lasers and Electro-Optics (CLEO '01)*, Baltimore, Md, USA, May 2001, Paper CPD13.
- [75] M. Laemmlin, G. Fiol, M. Kuntz et al., “Quantum dot based photonic devices at 1.3  $\mu\text{m}$ : direct modulation, mode-locking, SOAs and VCSELs,” *Physica Status Solidi C*, vol. 3, no. 3, pp. 391–394, 2006.
- [76] N. N. Ledentsov, J. A. Lott, V. A. Shchukin et al., “Quantum dot insertions in VCSELs from 840 to 1300 nm: growth, characterization, and device performance,” in *Quantum Dots, Particles, and Nanoclusters VI*, vol. 7224, 72240P of *Proceedings of SPIE*, San Jose, Calif, USA, January 2009.
- [77] H. Shimizu, C. Setiagung, M. Ariga et al., “1.3  $\mu\text{m}$ -range GaInNAsSb-GaAs VCSELs,” *IEEE Journal on Selected Topics in Quantum Electronics*, vol. 9, no. 5, pp. 1214–1219, 2003.
- [78] F. Koyama, “Wavelength engineering of surface emitting lasers for high capacity short reach systems,” in *Active and Passive Optical Components for WDM Communications III*, vol. 5246, 1 of *Proceedings of SPIE*, Orlando, Fla, USA, September 2003.
- [79] A. W. Jackson, R. L. Naone, L. Chirovsky et al., “1.3 micron InGaAsN VCSELs for telecom and datacom applications,” in *Semiconductor Lasers for Lightwave Communication Systems*, vol. 4533 of *Proceedings of SPIE*, Denver, CO, USA, August 2001.
- [80] D. A. Louderback, M. A. Fish, J. F. Klem et al., “Development of bottom-emitting 1300 nm vertical-cavity surface-emitting lasers,” *IEEE Photonics Technology Letters*, vol. 16, no. 4, pp. 963–965, 2004.
- [81] D. W. Kisker, L. M. F. Chirovsky, R. L. Naone et al., “1.3  $\mu\text{m}$  VCSEL production issues,” in *Vertical-Cavity Surface-Emitting Lasers VIII*, vol. 5364 of *Proceedings of SPIE*, San Jose, Calif, USA, January 2004.
- [82] H. Riechert, A. Ramakrishnan, and G. Steinle, “Development of InGaAsN based 1.3  $\mu\text{m}$  VCSELs,” *Semiconductor Science and Technology*, vol. 17, no. 8, pp. 892–897, 2002.
- [83] L. A. Coldren and S. W. Corzine, *Diode Lasers and Photonic Integrated Circuits*, Wiley, New York, NY, USA, 1995.
- [84] S. L. Chuang, *Physics of Photonic Devices*, Wiley, Hoboken, NJ, USA, 2009.
- [85] Y. Satuby and M. Orenstein, “Mode-coupling effects on the small-signal modulation of multitransverse-mode vertical-cavity semiconductor lasers,” *IEEE Journal of Quantum Electronics*, vol. 35, no. 6, pp. 944–954, 1999.
- [86] L. G. Zei, S. Ebers, J. R. Kropp, and K. Petermann, “Noise performance of multimode VCSELs,” *Journal of Lightwave Technology*, vol. 19, no. 6, pp. 884–892, 2001.
- [87] D. L. Huffaker, J. Shin, and D. G. Deppe, “Low threshold half-wave vertical-cavity lasers,” *Electronics Letters*, vol. 30, no. 23, pp. 1946–1947, 1994.
- [88] D. L. Huffaker and D. G. Deppe, “Half-wave cavity vertical-cavity surface-emitting lasers with native oxide/GaAs lower distributed Bragg reflectors,” in *Vertical-Cavity Surface-Emitting Lasers*, vol. 3003, 154 of *Proceedings of SPIE*, February 1997.
- [89] L. A. Graham, D. L. Huffaker, T. H. Oh, and D. G. Deppe, “Effects of steam oxidation on a single In<sub>0.20</sub>Ga<sub>0.80</sub>As quantum well in a half-wave microcavity VCSEL,” in *Vertical-Cavity Surface-Emitting Lasers*, vol. 3003, 63 of *Proceedings of SPIE*, San Jose, Calif, USA, February 1997.
- [90] M. C. Y. Huang, Y. Zhou, and C. J. Chang-Hasnain, “Single mode high-contrast subwavelength grating vertical cavity surface emitting lasers,” *Applied Physics Letters*, vol. 92, no. 17, Article ID 171108, 2008.
- [91] Y. Rao, C. Chase, and C. J. Chang-Hasnain, “Multiwavelength HCG-VCSEL array,” in *Proceedings of the 22nd IEEE International Semiconductor Laser Conference*, Kyoto, Japan, September 2010, Paper MB5.
- [92] N. N. Ledentsov, J. A. Lott, V. A. Shchukin et al., “Optical components for very short reach applications at 40 Gb/s and beyond,” in *Physics and Simulation of Optoelectronic Devices XVIII*, vol. 7597, 75971F of *Proceedings of SPIE*, San Francisco, Calif, USA, January 2010.
- [93] F. Hopfer, A. Mutig, A. Strittmatter et al., “High-speed directly and indirectly modulated VCSELs,” in *Proceedings of the 20th International Conference on Indium Phosphide and Related Materials (IPRM '08)*, Versailles, France, May 2008.
- [94] T. D. Germann, A. Strittmatter, A. Mutig et al., “Monolithic electro-optically modulated vertical cavity surface emitting laser with 10 Gb/s open-eye operation,” *Physica Status Solidi C*, vol. 7, no. 10, pp. 2552–2554, 2010.
- [95] C. Y. Lu, S. W. Chang, S. L. Chuang, T. D. Germann, and D. Bimberg, “Metal-cavity surface-emitting microlaser at room temperature,” *Applied Physics Letters*, vol. 96, no. 25, Article ID 251101, 2010.
- [96] C.-Y. Lu, S.-W. Chang, S. L. Chuang, T. D. Germann, U. W. Pohl, and D. Bimberg, “CW substrate-free metal-cavity surface microemitters at 300 K,” *Semiconductor Science and Technology*, vol. 26, no. 1, pp. 014012-1–014012-7, 2010.
- [97] C.-Y. Lu, S.-W. Chang, S. L. Chuang, T. D. Germann, U. W. Pohl, and D. Bimberg, “Characteristics of metal-cavity

- surface-emitting microlaser,” in *Proceedings of the 23rd Annual Meeting IEEE Photonics Society*, pp. 240–241, Denver, Colo, USA, November 2010, IEEE Catalog: CFP10LEO.CDR.
- [98] C.-Y. Lu, S.-W. Chang, S. L. Chuang, T. D. Germann, and D. Bimberg, “Substrate-free metal cavity surface-emitting laser with CW operation at room temperature,” in *Proceedings of the International Semiconductor Laser Conference (ISLC '10)*, pp. 15–16, Kyoto, Japan, September 2010.
- [99] C. Lu, S. L. Chuang, T. D. Germann, A. Mutig, and D. Bimberg, “Novel metal-cavity nanolasers at room temperature,” in *Proceedings of the Conference on Lasers and Electro-Optics (CLEO)*, Baltimore, Md, USA, May 2011, Paper JMA4.